AD_____

Award Number: DAMD17-03-1-0384

TITLE: Seamless Integration of Detection and Therapy for Breast Cancer using Targeted Engineered Nanoparticles

PRINCIPAL INVESTIGATOR: Naomi J. Halas, Ph.D.

CONTRACTING ORGANIZATION: William Marsh Rice University
                                                  Houston, TX 77005

REPORT DATE: June 2008

TYPE OF REPORT: Final

PREPARED FOR: U.S. Army Medical Research and Materiel Command
                          Fort Detrick, Maryland 21702-5012

REPORT DOCUMENTATION PAGE

Public reporting burden for this collection of information is estimated to average 1 hour per response, including the time for reviewing instructions, searching existing data sources, gathering and maintaining the data needed, and completing and reviewing this collection of information. Send comments regarding this burden estimate or any other aspect of this collection of information, including suggestions for reducing this burden to Department of Defense, Washington Headquarters Services, Directorate for Information Operations and Reports (0704-0188), 1215 Jefferson Davis Highway, Suite 1204, Arlington, VA 22202-4302. Respondents should be aware that notwithstanding any other provision of law, no person shall be subject to any penalty for failing to comply with a collection of information if it does not display a currently valid OMB control number. **PLEASE DO NOT RETURN YOUR FORM TO THE ABOVE ADDRESS.**

1. REPORT DATE	2. REPORT TYPE	3. DATES COVERED
1 Jun 2008	Final	15 May 2003 – 14 May 2008

4. TITLE AND SUBTITLE	5a. CONTRACT NUMBER
Seamless Integration of Detection and Therapy for Breast Cancer using Targeted Engineered Nanoparticles	5b. GRANT NUMBER DAMD17-03-1-0384
	5c. PROGRAM ELEMENT NUMBER

6. AUTHOR(S)	5d. PROJECT NUMBER
Naomi J. Halas, Ph.D.	5e. TASK NUMBER
	5f. WORK UNIT NUMBER
E-Mail: halas@rice.edu	

7. PERFORMING ORGANIZATION NAME(S) AND ADDRESS(ES)	8. PERFORMING ORGANIZATION REPORT NUMBER
William Marsh Rice University Houston, TX 77005	

9. SPONSORING / MONITORING AGENCY NAME(S) AND ADDRESS(ES)	10. SPONSOR/MONITOR'S ACRONYM(S)
U.S. Army Medical Research and Materiel Command Fort Detrick, Maryland 21702-5012	
	11. SPONSOR/MONITOR'S REPORT NUMBER(S)

12. DISTRIBUTION / AVAILABILITY STATEMENT
Approved for Public Release; Distribution Unlimited

13. SUPPLEMENTARY NOTES

14. ABSTRACT

This is a final cumulative report on the efforts of our team of researchers from Rice University and M. D. Anderson Cancer Center, in the DoD funded CDMRP award. The overall goal of the research was to develop an integrated diagnostic imaging and if needed therapy of breast cancers. We have demonstrated bioconjugation techniques to target the tumors by attaching antibodies and phage display ligand proteins to nanoparticles and studying the efficiency of nanoparticle attachment to cancer cells. We have demonstrated in mouse tumor models a number of diagnostic imaging modalities. The first molecular signature of cancer cells using surface enhanced Raman scattering was demonstrated. Finally we have optimized the size of nanoshell and demonstrated that it can be used both for diagnostic imaging and photothermal therapy as needed. In addition to meeting all the goals outlined in the original proposal, the research has lead to FDA approval for clinical trials for photothermal therapy of cancers. Numerous research laboratories have also started investigating nanoshell based cancer therapies.

15. SUBJECT TERMS
Nanoshells, targeting, Photothermal therapy, bioimaging

16. SECURITY CLASSIFICATION OF:			17. LIMITATION OF ABSTRACT	18. NUMBER OF PAGES	19a. NAME OF RESPONSIBLE PERSON USAMRMC
a. REPORT U	b. ABSTRACT U	c. THIS PAGE U	UU	244	19b. TELEPHONE NUMBER *(include area code)*

Table of Contents

Introduction

The vision of this research was to develop a nanoparticle based diagnostic imaging and therapy strategy such that in a single visit to a health care provider, our technology could be used to image the molecular and morphological features of the breast, provide real-time diagnosis of pathology, and if appropriate, provide same visit treatment based on the use of non-surgical photothermal methods to specifically destroy a detected tumor without harming surrounding normal tissue.

This final report summarizes the efforts of our highly synergistic team in achieving these goals. The strategy adopted is based on gold nanoshell nanoparticles. These nanoparticles consist of a spherical silica core surrounded by a thin gold shell. The optical properties of these nanoparticles strongly depend on the core to shell ratio and can be tuned across the visible and infrared. Nanoshells tuned to the NIR "optical window" a region of the spectrum where tissue is maximally transparent allow nanoshells to be used for bioimaging and for NIR light to penetrate into tissue for photothermal ablation of the targeted tissue.

Specifically the nanoshells are targeted to tumor sites by conjugating antibodies and specially engineered phage display ligand proteins. These targeted nanoshells called immunonanoshells have been demonstrated to bind to specific tumor cells both *in vitro* and *in vivo* experiments. Nanoshells attached to tumor tissue then act as agents to enhance the contrast in numerous imaging modalities explored such as dark field imaging, fixed fiber reflectance measurements, optical coherence tomography (OCT) etc. Nanoshells designed with high absorbance in the NIR absorb energy and cause a temperature rise in adjacent cells. A temperature rise of over 25°C has been demonstrated to cause cell death of the cells adjacent to the nanoshells.

We have implemented the entire strategy in mice tumors to image the tumors using OCT and then using higher powers of the same laser ablate the tumor cells. An overview of this nanoshell based techniques has been summarized in a review article published in the Accounts of Chemical Research.[1]

Body

A brief description of the accomplishments for each of the specific aims is outlined below. The references therein are for complete published articles. The published articles outline the experiments and results in complete details.

Specific Aim 1: Bioconjugation-based Targeting of Nanoparticles for imaging and therapy:
Task 1: Identification of optimal ligand-receptor pair for vascular targeted therapy in breast cancer
Task 2: Development of bioconjugate chemistry for binding targeting peptides and antibodies to nanoshells and nanoemitters.

Accomplishments: Human epidermal growth factor receptor 2 (HER2) has been identified as a proven molecular marker of breast cancer cells (SKBr3). Nanoshells labeled with HER2 have been prepared and were shown to successfully target the SKBr3 cancer cells. We have demonstrated that anti-human epidermal growth factor receptor 2 (anti-HER 2) can be consistently bound to gold nanoshells via a bi functional poly ethylene glycol (PEG) linker to form immunonanoshells. We have quantified the density of this antibody attached to the immunonanoshell surface by an ELISA style assay, developed specifically quantify the antibody attachment to the nanoshell surfaces. This

is confirmed visually by TEM imaging of gold colloid labeled antibodies attached to the immunonanoshells. Antibody densities of ~ 150 antibodies/nanoshells have been achieved.[2]

One of the techniques for directing nanoparticles to cancer cells for imaging and therapy is by attaching antibodies and peptides that bind specifically to cancer cell surfaces. More than 30% of breast cancer cells express Human Epidermal growth factor receptor- 2 (HER2) on the cell surface. We have developed bioconjugation techniques to attach anti-HER2 antibodies to nanoshells.[2] Filamentous bacteriophage (phage) can be easily engineered genetically to display ligand proteins that will bind to selected tissue. Integrating phage display technology with gold nanoparticles allows for targeting and optical imaging of specific tissue. We have investigated Au-phage networks for imaging and molecular finger printing of tumor cells, both *in vitro* and *in vivo* in tumor bearing mice.[3, 4]

Specific Aim 2: Nanoparticle-based Image Enhancement:

Task 1: Investigation of the effectiveness of gold nanoshells and rare earth nanoemitters as image enhancers in tomographic infrared imaging,
Task 2: Evaluation of the improvements in image contrast and resolution due to nanoshell-based and nanoemitter-based contrast enhancers.
Task 3: Demonstration of feasibility of targeted nanoshell-based imaging and nanoemitter-based imaging in a mouse tumor model.

Accomplishments: We have performed Monte-Carlo simulations of nanoshells embedded in tissue models. This allows us to optimize the size and concentration of nanoshells required for optical imaging. The results of the Monte-Carlo simulations have also been verified experimentally using a fixed fiber probe to measure the reflectance from a nanoshell solution.[5]

Gold nanoshell bioconjugates for optical imaging have been fabricated. The size of the nanoshells was controlled to provide the nanoshells with unique optical scattering capabilities in the NIR region of the spectrum, allowing optical imaging both in the visible and the NIR regions. The targeted nanoshell bioconjugates were utilized as high contrast agents to image human epidermal growth factor receptor 2 (HER2) expression in living human breast carcinoma cells. Our studies indicated that under dark-field microscopy, a significant increase in the imaging optical contrast was observed when HER2-positive SKBr3 breast cancer cells were targeted with anti-HER2-labeled nanoshells compared with cells targeted by either anti- IgG-labeled nanoshells (non-specific targeting) or cells not exposed to nanoshells bioconjugates. The average imaging contrast values in cells targeted by anti- HER2-labeled nanoshells was significantly ($p<0.05$) greater (142 16) than in cells targeted by anti-IgG (48 12) or cells not exposed to nanoshell bioconjugates (26 4). Images of HER2-negative MCF7 cells exposed to anti-HER2-labeled nanoshell bioconjugates showed significantly lower contrast (34 5) compared to HER2- positive SKBr3 cells (142 16). This provides additional evidence of contrast enhancement attributed to nanoshells targeting HER2 receptors.[6, 7]

We have investigated biologically active networks of gold nanoparticles-bacteriophage-imidazole as labels for non invasive optical detection of specific tumors. Spontaneous aggregation of Au-NPs on phage occurs without genetic modification of the pVIII major capsid proteins. The Au-NP- phage network depends upon the concentration of phage and can be further modified by the presence of

imidazole. The aggregation of the gold particles within the Au-NP-phage network broadens and red-shifts the surface plasmon resonance of the gold particles to the biologically accessible water window where light penetration through tissue is optimal. These biologically active networks effectively integrate the signal reporting properties of gold NPs, while preserving the biological activity of the phage. Melanoma cells that express high levels of α_v-integrins were chosen to demonstrate the immunofluorescence staining by the Au-phage network. The cell surface receptor is well characterized for displaying the peptide CDCRGD-CFC (RGD-4C) Figure 2 (supporting data) shows the results of the immunofluorescence based phage binding assay of Au-RGD-4C networks. When examined by confocal microscopy, Au–phage networks could serve as sensitive reporters to localize and evaluate ligand binding and receptor-mediated internalization events (Figure 3 supporting data). The differences in the structure of the targeting networks result in distinct kinetics of the internalization event that follows ligand–receptor binding. By incorporating imididazole into the nanoarchitecture of the networks, we were able to influence the localization of the Au–phage networks to either the cell surface or cytoplasm. More compact networks with a higher fractal dimension (Au–RGD-4C-imid) preferentially localized at the cell surface, whereas those with a lower fractal dimension (Au–RGD-4C) were internalized (Figure 3).[3, 4]

We have also demonstrated greater enhancement of nanoshell induced reflectance signals from angled fiber probes as compared to conventional orthogonal fiber geometry. These greatly enhanced signals have been measured in both tissue phantoms (suspensions of silica spheres) and in cancerous cervical tissue samples.[8]

We have successfully demonstrated the use of a single nanoshell to first increase the optical contrast for OCT imaging and subsequent photothermal ablation of the tumors in mouse tumor models.
Nanoshells with a 119 nm silica core and approximately 12 nm gold shell were synthesized. Mie scattering theory predicts 67% of the extinction of these shells is due to absorption and 33 % is due to scattering at 800 nm. Next the shells were passivated with thiolated poly ethylene (PEG) molecules. This provides steric stability and solubility while the nanoshells circulate and accumulate in the tumors due to the leaky neovasculature of the tumors. OCT images were collected after 20 hours, *in vivo* by placing the probe on shaved skin over the tumor site. This is compared to normal tissue with nanoshells and a control tumor tissue with a phosphate buffer injected instead of the nanoshell solution. There is a 56% increase in contrast with nanoshells as compared to mice injected with phosphate buffer solution.[9]

Specific Aim 3: Molecular Fingerprinting
Task 1: Examination of the feasibility of noninvasive "molecular fingerprinting" in a tissue culture model, (months 1-24).
Task 2: Investigation of spectroscopic detection of early lesions, (months 12-48).

Using a novel bi-functional linker constructed of paramercaptoanaline- poly(ethyleneglycol)-fluorescein (pMA-PEG-Fluor), and utilizing two independent techniques, fluorescence spectroscopy and surface enhanced Raman spectroscopy (SERS), our group has been able to quantitatively determine the number of pMA-PEG-Fluor molecules required to form a complete self-assembled monolayer (SAM) on the surface of gold nanoshells.[10] Surface enhanced Raman spectroscopy of pMA molecule was used to determine the surface coverage at various concentrations following the

relationship for a Langmuir isotherm.[10] Our studies indicate that both fluorescence spectroscopy and Raman spectroscopy can be correlated to obtain an effective strategy for obtaining quantitative information of SAMs on nanoshells. This holds promising future for designing efficient nanoshell bioconjugates for biological analysis and chemical identification with high sensitivity. Such nanoshells can be used for enhanced cancer detection and therapy and molecular fingerprinting applications.

We have also demonstrated the use of biologically active networks of Au NP-phage as optically active labels for non invasive detection using surface enhanced Raman spectroscopy (SERS). [3, 4] This is also one of the first *in vivo* SERS measurements.

Acidic pH is a common characteristic of human tumors.[11] Normal cells have a pH of 7.4 whereas most breast cancer tumors have a pH around 6.8. We have developed a nanoshell based pH sensor that can be used to monitor the pH in vivo to determine carcinogenicity. The Au nanoshell with a pH-sensitive molecular adsorbate (para-mercapto benzoic acid in this case) functions as a standalone, all-optical nanoscale pH meter that monitors its local environment through the pH-dependent surface-enhanced Raman scattering (SERS) spectra of the adsorbate molecules. By using a statistical learning theory analysis of the SERS spectra, a quantitative pH sensor has been developed. The average accuracy of the nano pH-meter was found to be ±0.10 pH units across its operating range.[12]

Specific Aim 4: Nanoshell-based Photothermal Cancer Therapy

Task 1: Evaluation of the therapeutic effect of targeted nanoshells in animal models of breast cancer, (months 1-36).
Task 2: Development of a strategy for combined imaging and therapy, (months 12-48).

Accomplishments: *In vivo* localized, irreversible photothermal ablation of tumor tissue have been demonstrated using nanoshells designed to absorb near infrared light. Nanoshells were injected interstially into solid tumors in female SCID mice. The injected nanoshells accumulated on the tumor sites were seen to induce no cell death until these sites were exposed to NIR light, where then localized cell death occurred. Temperatures were monitored via phase-sensitive, phase-spoiled gradient-echo MRI. Magnetic resonance temperature imaging (MRTI) demonstrated that tumor reached temperatures which caused irreversible tumor damage ($\Delta T = 37.4 \pm 6.6\ ^oC$) within 4-6 minutes. Controls which were exposed to a saline injection instead of nanoshell injection experienced significantly reduced average temperatures after exposure to the same dose of NIR light ($\Delta T < 10\ ^oC$).[13-15]

A novel nanoshell-based all-optical platform technology for integrating cancer imaging and therapy has been developed. We have demonstrated that immunotargeted nanoshells can provide scattering contrast for imaging while also exhibiting sufficient absorption to enable effective photothermal therapy.[16] Nanoshells, designed to both absorb and scatter in the NIR spectral region were conjugated with anti- HER2 antibody to specifically bind to SKBr3 breast cancer cells. Upon binding to the cells, nanoshells targeted against HER2 were seen to provide a significant increase in the scatter-based optical contrast compared to cells targeted by either no nanoshells or nanoshells conjugated with the non-specific antibody (anti-IgG). The anti- HER2-labeled nanoshells alone were

seen to be nontoxic to the cancer cells. However, after irradiation with NIR light, the conjugated nanoshells were seen to mediate photothermal effects that resulted in the death of the cancer cells. This effect was not observed in cells exposed to either nanoshells conjugated with the non-specific antibody (anti-IgG) or NIR alone. Greater silver staining intensity was seen in cells exposed to anti-HER2-labeled nanoshells as opposed to controls, indicating enhanced binding of the targeted nanoshells to cell surfaces expressing HER2.[16]

We have also demonstrated a single sized nanoshell can be used for combined imaging via OCT and photothermal ablation of cancerous cells. As described in specific aim 2 accomplishments, we synthesized nanoshells with a 119 nm silica core and approximately 12 nm gold shell. Mie scattering theory predicts 67% of the extinction of these shells is due to absorption and 33 % is due to scattering at 800 nm.
Next the shells were passivated with thiolated poly ethylene (PEG) molecules. This provides steric stability and solubility while the nanoshells circulate and accumulate in the tumors due to the leaky neovasculature of the tumors. The nanoshells were injected via the tail vein into mice with subcutaneously grown tumors. OCT imaging 20 hours post injection demonstrated a 56% enhanced contrast of the cancerous tissue. The subsequent photothermal ablation of the tumors demonstrated a 83% survival with no calculable median lifetime as all the mice survived longer than the study period (7 weeks). The mean survival lifetimes of the mice in the control and sham treatment groups were 10 and 14 days respectively.[9]

Key Research Accomplishments

- Nanoshells labeled with human epidermal growth factor receptor 2 (HER2) have been prepared and were shown to successfully target SKBR3 cancer cells.
- Anti-HER2-labeled nanoshells have demonstrated a significantly increased optical contrast for imaging cancer cells.
- Localized, irreversible photothermal ablation of tumor tissue in mice have been demonstrated using nanoshells designed to absorb near infrared light.
- Nanoshells targeted against a clinically relevant biomarker HER2 were demonstrated for the first time as both imaging and therapeutic agents of cancer.
- HER2 immunonanoshells were shown to specifically target SK BR3 in both imaging and photothermal ablation studies without destroying neighboring healthy cells.
- Au-phage and Au-phage-imidazole networks can be engineered to target specific tissue types. These networks have been shown to improve imaging and molecular fingerprinting of tumor sites (using the first demonstration of in vivo SERS), in both *in vitro* and *in vivo* studies.
- We have developed an all optical nanoshells based pH sensor with a sensitivity of 0.1 pH units. This will allow distinction of cancerous, precancerous and normal cells.
- Successful *in-vivo* (in mouse tumor) demonstration of a single nanoshell that enhances the scattering signal for OCT imaging and is subsequently used for photothermal ablation of the tumor.
- Monte Carlo simulations used to optimize the size and concentration of nanoshells needed to enhance reflectance and scattering based optical imaging of tumors.
- Optical signal optimized in fiber probe based optical spectroscopy. Experimentally demonstrated enhanced optical signals in tissue phantoms and cancerous cervical tissue.

Reportable Outcomes

Journal Articles Published

Papers

1. R. Drezek, J. West, and N. Halas, "Optical Technologies for Functional and Molecular Imaging of the Breast, (An editorial so does not cite any funding agencies but does discuss nanoshell work)." Breast Diseases **14**, 18-20 (2003).

3. A. W. Lin, C. H. Loo, L. R. Hirsch, J. K. Barton, M.-H. Lee, N. J. Halas, J. L. West, and R. A. Drezek, "Nanoshells for Integrated Diagnosis and Therapy of Cancer," Proceedings of SPIE **5593**, 308-316 (2004).

4. C. Loo, L. Hirsch, J. Barton, N. Halas, J. West, and R. Drezek, "Nanoshell-Enabled Photonics-Based Cancer Imaging and Therapy," Technology in Cancer Research and Treatment **3**, 33-40 (2004).

5. D. P. O'Neal, L. R. Hirsch, N. J. Halas, J. D. Payne, and J. L. West, "Photo-Thermal Tumor Ablation in Mice Using Near Infrared-Absorbing Nanoparticles," Cancer Letters **209**(2), 171-176 (2004).

6. A. W. H. Lin, N. J. Halas, and R. A. Drezek, "Optically tunable nanoparticle contrast agents for early cancer detection: model-based analysis of gold nanoshells," J. Biomed. Opt. **10**(6), 064035 (2005).

7. C. Loo, L. Hirsch, M.-H. Lee, E. Chang, J. West, N. Halas, and R. Drezek, "Gold nanoshell bioconjugates for molecular imaging in living cells," Optics Letters **30**(9), 1012-1014 (2005).

8. C. Loo, A. Lowery, N. J. Halas, J. L. West, and R. Drezek, ""Immunotargeted Nanoshells for Integrated Cancer Imaging and Therapy," Nano Letters **5**(4), 709-711 (2005).

9. D. P. O'Neal, L. R. Hirsch, N. J. Halas, J. D. Payne, and J. L. West, "Photo-thermal cancer therapy using intravenously injected near infrared-absorbing nanoparticles," Proceedings of SPIE **5689**, 149-157 (2005).

10. S. W. Bishnoi, C. J. Rozell, C. S. Levin, M. K. Gheith, B. R. Johnson, D. H. Johnson, and N. J. Halas, "An all-optical nanoscale pH meter," Nano Lett. **6**(8), 1687-1692 (2006).

11. A. Hajitou, M. Trepel, C. E. Lilley, S. Soghomonyan, M. M. Alauddin, F. C. Marini, B. H. Restel, M. G. Ozawa, C. A. Moya, R. Rangel, Y. Sun, K. Zaoui, M. Schmidt, C. v. Kalle, M. D. Weitzman, J. G. Gelovani, R. Pasqualini, and W. Arap, "A Hybrid Vector for Ligand-Directed Tumor Targeting and Molecular Imaging," Cell **125**, 385–398 (2006).

12. L. R. Hirsch, Andre M. Gobin, A. R. Lowery, R. A. Drezek, N. J. Halas, and J. L. West, "Metal Nanoshells," Annal. Biomed. Eng. **34**(1), 15–22 (2006).

13. M. G. Kolonin, Laura Bover, J. Sun, A. J. Zurita, K.-A. Do, J. Lahdenranta, M. Cardo´-Vila, R. J. Giordano, D. E. Jaalouk, M. G. Ozawa, C. A. Moya, G. R. Souza, F. I. Staquicini, A. Kunyiasu, D. A. Scudiero, S. L. Holbeck, E. A. Sausville, W. Arap, and R. Pasqualini, "Ligand-Directed Surface Profiling of Human Cancer Cells with Combinatorial Peptide Libraries," Can. Res. **66**(1), 34-40 (2006).

14. M. G. Kolonin, J. Sun, K.-A. Do, C. I. Vidal, Y. Ji, K. A. Baggerly, R. Pasqualini, and W. Arap, "Synchronous selection of homing peptides for multiple tissues by in vivo phage display," FASEB **20**, 979-981 (2006).

15. A. W. H. Lin, N. A. Lewinski, M.-H. Lee, and R. A. Drezek, "Reflectance spectroscopy of gold nanoshells: computational predictions and experimental measurements," Journal of Nanoparticle Research (2006).

16. A. R. Lowery, A. M. Gobin, E. S. Day, N. J. Halas, and J. L. West, "Immunonanoshells for targeted photothermal ablation of tumor cells," International Journal of Nanomedicine **1**(2)(2006).

17. G. R. Souza, D. R. Christianson, F. I. Staquicini, M. G. Ozawa, E. Y. Snyder, R. L. Sidman, J. H. Miller, W. Arap, and R. Pasqualini, "Networks of gold nanoparticles and bacteriophage as biological sensors and cell-targeting agents," Proc. Natl. Acad. Soc. **103**(5), 1215–1220 (2006).

18. G. R. Souza, C. S. Levin, A. Hajitou, R. Pasqualini, W. Arap, and J. H. Miller, "In Vivo Detection of Gold-Imidazole Self-Assembly Complexes: NIR-SERS Signal Reporters," Anal. Chem. (2006).

19. Choi, M.-R.; Stanton-Maxey, K. J.; Stanley, J. K.; Levin, C. S.; Bardhan, R.; Akin, D.; Badve, S.; Sturgis, J.; Robinson, J. P.; Bashir, R.; Halas, N. J.; Clare, S. E., A Cellular Trojan Horse for Delivery of Therapeutic Nanoparticles into Tumors. *Nano Lett.* **2007,** 7, 3759-3765.

20. L. C. Bover, M. Cardo´-Vila, A. Kuniyasu, J. Sun, R. Rangel, M. Takeya, B. B. Aggarwal, W. Arap, and R. Pasqualini, "A Previously Unrecognized Protein-Protein Interaction between TWEAK and CD163: Potential Biological Implications," The Journal of Immunology **178**, 8183– 8194 (2007).

21. P. Fortina, L. J. Kricka, D. J. Graves, J. Park, T. Hyslop, F. Tam, N. Halas, S. Surrey, and S. A. Waldman, "Applications of nanoparticles to diagnostics and therapeutics in colorectal cancer," TRENDS in Biotechnology **25**(4), 145-152 (2007).

22. K. Fu, J. Sun, A. Lin, H. Wang, N. Halas, and D. R., " Polarized Angular Dependent Light Scattering Properties of Bare and PEGylated Gold Nanoshells.," Current Nanoscience **3**, 167-170 (2007).

23. A. M. Gobin, M. H. Lee, N. J. Halas, W. D. James, R. A. Drezek, and J. L. West, "Near-Infrared Resonant Nanoshells for Combined Optical Imaging and Photothermal Cancer Therapy," Nano Lett. (2007).

24. A. Hajitou, R. Rangel, M. Trepel, S. Soghomonyan, J. G. Gelovani, M. M. Alauddin, R. Pasqualini, and W. Arap, "Design and construction of targeted AAVP vectors for mammalian cell transduction.," Nat. Protoc. **3**, 523-531 (2007).

25. D. E. Jaalouk, M. G. Ozawa, J. Sun, J. Lahdenranta, R. O. Schlingemann, R. Pasqualini, and W. Arap, "The Original Pathologische Anatomie Leiden-Endothelium Monoclonal Antibody Recognizes a Vascular Endothelial Growth Factor–Binding Site within Neuropilin-1," Cancer Research **67**(20), 9623–9629 (2007).

26. J. Lahdenranta, R. L. Sidman, R. Pasqualini, and W. Arap, "Treatment of hypoxia-induced retinopathy with targeted proapoptotic peptidomimetic in a mouse model of disease," FASEB Journal **21**, 3272–3278 (2007).

27. V. Nammalvar, A. Wang, and R. Drezek, "Enhanced gold nanoshell scattering contrast using angled fiber probes," J. Nanophoton **1**, 013510 (2007).

28. R. Rangel, Y. Sun, L. Guzman-Rojas, M. G. Ozawa, J. Sun, R. J. Giordano, C. S. Van Pelt, P. T. Tinkey, R. R. Behringer, R. L. Sidman, W. Arap, and R. Pasqualini, "Impaired angiogenesis in aminopeptidase N-null mice," Proc Natl Acad Sci U S A **104**, 4588-4593 (2007).

29. A. Hajitou, D. C. Lev, J. A. F. Hannay, B. Korchin, F. I. Staquicini, S. Soghomonyan, M. M. Alauddin, R. S. Benjamin, R. E. Pollock, J. G. Gelovani, R. Pasqualini, and W. Arap, "A preclinical model for predicting drug response in soft-tissue sarcoma with targeted AAVP molecular imaging," Proc Natl Acad Sci U S A **105**, 4471–4476 (2008).

30. D. O. Traktuev, S. Merfeld-Clauss, J. Li, M. Kolonin, W. Arap, R. Pasqualini, B. H. Johnstone, and K. L. March, "A Population of Multipotent CD34-Positive Adipose Stromal Cells Share Pericyte and Mesenchymal Surface Markers, Reside in a Periendothelial Location, and Stabilize Endothelial Networks," Circulation Research **102**, 77-85 (2008).

Invited Articles

1. R. A. Drezek, J. West, and N. J. Halas, " Optical Technologies for Functional and Molecular Imaging of the Breast", Brest Diseases. **14:** 18-20 (2003). (An editorial so does not cite funding agencies, but does discuss nanoshell work)

2. Hajitou A, Pasqualini R, Arap W. Vascular targeting: Recent advances and therapeutic perspectives. Trends Cardiovasc Med 16:80-8, 2006.

3. Sergeeva A, Kolonin MG, Molldrem JJ, Pasqualini R, Arap W. Display technologies: application for the discovery of drug and gene delivery agents. Adv Drug Deliv Rev 58:1622-54, 2006.

4. J. L. West, R. A. Drezek, and N. J. Halas, "Nanotechnology Provides New Tools for Biomedical Optics," in *Chapter 25* (CRC press, 2006), pp. 1-24.

5. Christianson DR, Ozawa MG, Arap W, Pasqualini R. Techniques to decipher molecular diversity by phage display. Methods Mol Biol 357:385-406, 2006.

6. S. Lal, S. E. Clare and Naomi J. Halas, "Nanoshell-enabled cancer therapy: impending clinical impact", Accounts of Chemical Research, 41 (12), 1842-1851 ,2008.

Book Chapters

1. J. Chen, A. Lin, C. Loo, K. Hsu, J. West, N. Halas, and R. Drezek "Optical Technologies for Noninvasive Functional and Molecular Imaging," in *Advanced Therapy of Breast Disease*, edited by S. Singletary, G. Robb, and G. Hortobagyi, BC Decker: 859-868 (2004).

2. C. Loo, A. Lin, L. Hirsch, M. Lee, J. Barton, N. Halas, J. West, and R. Drezek, "Chapter12: Diagnostic and Therapeutic Applications of Metal Nanoshells," in *Nanofabrication for Biomedical Applications*. Wiley, pp. 327-342 (2005).

3. L. Hirsch, A. Lowery, R. Drezek, N. Halas, and J. West, "Biomedical Applications of Nanoshells," in Encyclopedia of BioMEMs and Bionanotechnology, edited by Tejal Desai and Sangeeta Bhatia, Kluwer, in press (2005).

4. J. L. West, R. A. Drezek, N. J. Halas, Nanotechnology Provides New Tools for Biomedical Optics. In Chapter 25, CRC press, pp 1-24, (2006).

Conference Proceedings

1. Lee, MH, West, J., Halas, N. and Drezek, R. "Nanoengineered Optical Contrast Agents," Nanosummit. Houston, TX. July 2004.

2. Loo, C., Hirsch, L., Halas, N., West, J., and Drezek, R., "Towards Molecular Imaging Using Gold Nanoshells," Biomaterials 2004. Sydney, Australia. May 2004.

3. Loo, C., Hirsch, L., Halas, N., West, J., and Drezek, R., "Cancer Imaging Using Gold Nanoshells," OSA Biomedical Topical Meeting 2004. Miami, Fl. April 2004.

4. Lin, A., West, J., Halas, N., and Drezek, R. Monte Carlo Investigation of Optical Signal Changes in Tissue After Nanoshell Application. Houston Society for Engineering in Medicine and Biology Annual Meeting. Podium presentation. Houston, TX. February 2004.

5. Fu, K., Halas, N. and Drezek R. Automated Goniometer for Polarized Angular Light Scattering Measurements. Houston Society for Engineering in Medicine and Biology Annual Meeting. Houston, TX. February 2004.

6. Lee, MH., West, J., Halas, N., and Drezek, R. Nanoshells as Contrast Agents for Optical Coherence Tomography. Houston Society for Engineering in Medicine and Biology Annual Meeting. Houston, TX. February 2004.

7. Loo, C., West, J., and Drezek, R. Nanoshell-Enabled Molecular Imaging. 21st Annual Houston Society for Engineering in Medicine and Biology Annual Meeting. Houston, TX. February 2004.

8. Loo, C., West, J., Halas, N., and Drezek, R. Targeted Breast Cancer Imaging Using Scattering Nanoshells. Nanodays. Poster presentation. Houston, TX. October 2003.

9. Lin, A., West, J., Halas, N., and Drezek, R. Nanoengineered Contrast Agents for Biophotonics. Nanodays. Houston, TX. October 2003.

10. Lin, A., Halas, N., West, J. and Drezek, R. Nanoengineered Contrast Agents for Biophotonics. Advances in Optical Technologies for Lasers, Medicine, and Surgery. Banff, Canada. August 2003.

11. Loo, C., Halas, N., West, J., and Drezek, R. Molecular Specific Imaging Using Scattering Nanoshells. Advances in Optical Technologies for Lasers, Medicine, and Surgery. Banff, Canada. August 2003.

12. Loo, C., West, J., Halas, N., and <u>Drezek, R.</u> Imaging Applications of Metal Nanoshells. Nanosummit 2003. Houston, TX. July 2003.

13. Lowery, A.; O'Neal, P.; Loo, C.; Hirsch, L. R.; Stafford, J.; Hazle, J.; Halas, N. J.; Drezek, R.; West, J. L. "Photothermal Tumor Therapy with Metallic Nanoshells," World Biomaterials Congress, Sydney, Australia, May 2004.

14. Gobin, A. M.; O'Neal, P.; Halas, N. J.; Drezek, R.; West, J. L. "Nanoshells as Near Infrared Absorbers to Enhance Laser Tissue Welding," World Biomaterials Congress, Sydney, Australia, May 2004.

15. Loo, C.; Hirsch, L.; Halas, N.; West, J.; and Drezek, R. "Towards Molecular Imaging Using Gold Nanoshells," World Biomaterials Congress, Sydney, Australia, May 2004.

16. Loo, C.; Lowery, A.; West, J. L.; Halas, N. J.; Drezek, R. "Molecular Imaging of Breast Cancer using Gold Nanoshells," World Biomaterials Congress, Sydney, Australia, May 2004.

17. Drezek, R.; Halas, N.; West, J. "Nanotechnology in Breast Cancer Imaging," Fifth Annual CAMD Workshop: Nanotechnology in Bioscience, Biotechnology, and Medicine, New Orleans, LA, June 2004.

18. Drezek, R.; Halas, N.; West, J, "Towards Nanotechnology-Enabled Breast Cancer Imaging," NanoSummit, Houston, TX, July 2004.

19. Lee, M.; West, J.; Halas, N.; and Drezek, R. "Nanoengineered Optical Contrast Agents," NanoSummit. Houston, TX, July 2004.

20. Halas, N. J. "Nanoshells: Optimizing Nanophotonic Properties for Probing Living Systems," Abstracts of papers, 229th ACS National Meeting. San Diego, CA, March 2005.

21. Agrawal, A.; Huang, S.; Pfefer, P.; Lee, M.; and Drezek, R. "Quantitative Evaluation of Nanoshells as a Contrast Agent for 1300 nm OCT," Conference on Lasers and Electro-Optics (CLEO). Baltimore, MD, 2005.

22. Agrawal, A.; Huang, S.; Pfefer, P.; Lee, M.; and Drezek, R. "Quantitative Evaluation of Nanoshells as a Contrast Agents for OCT," OSA European Conference on Biomedical Optics (ECBO). Munich, Germany, 2005.

23. Loo, C., West, J., Halas, N., and Drezek, R. Nanoshells for Real-Time NIR RCM-Based Molecular Imaging. Biomedical Engineering Society Annual Meeting. Baltimore, MD. October 2005.

24. Loo, C., West, J., Halas, N., and Drezek R. Nanoshell-Based Molecular Imaging of Breast Tissue. MSTP Annual Symposium. Houston, TX. 2005.

25. O'Neal, P.; Gobin, A.; Bayazitoglu, Y.; Halas, N.; Drezek, R.; and West, J. "Nanoshells as an Exogenous Absorber for Laser Tissue Welding," Photonics Therapeutics and Diagnostics. Biophotonics West. San Jose, CA. January 2005. Proceedings to SPIE The International Society for Optical Engineering, (2005).

26. Lin, A.; Loo, C.; Hirsch, L.; Halas. N.; West, J.; and Drezek, R. Nanoshells for Cancer Imaging and Therapy. Optics East. Philadelphia, PA. October 2004. Proceedings to SPIE-The International Society for Optical Engineering, in press, 2005.

27. Lowery A., Gobin A.M., Day E., Shah K., Halas N., Drezek R., West J. "Antibody-Conjugated Metal Nanoshells for Tumor Specific Photothermal Therapy" Society for Biomaterials, Pittsburgh, PA, April 2006

28. Lowery A., Loo C., O'Neal P., Hirsch L., Halas N., Drezek R., West J. "Antibody-Conjugated Metal Nanoshells for Tumor Specific Photothermal Therapy" Society For Biomaterials, Memphis, TN, April 2005

29. Lowery A., O'Neal P., Hirsch L., Halas N., Drezek R., West J."Antibody-conjugated Metal Nanoshells for Selective Photothermal Therapy" Rice University Institute of Biosciences and Bioengineering Graduate Training Programs Annual Retreat. Rice University, Houston, TX, March 2005

30. Lowery A., Loo C., O'Neal P., Hirsch L., Halas N., Drezek R., West J."Antibody-conjugated Metal Nanoshells for Selective Photothermal Therapy" Houston Society for Engineering in Medicine. University of Houston, Houston, TX, Feb 2005

31. Lowery A., Gobin A.M., Day E., Shah K., Halas N., Drezek R., West J. "Antibody-Conjugated Metal Nanoshells for Tumor Specific Photothermal Therapy" (oral) Society for Biomaterials, Pittsburgh, PA, April (2006).

32. A.M. Gobin, M. Lee, N. Halas, R. Drezek1 & J. West. Nanoshells for Integrated Cancer Imaging and Therapy. *Poster*, American Association of Cancer Research: Molecular Diagnostics in Cancer Therapeutic Development, Chicago, IL, September 12-15, 2006

33. Fu, K., Halas, N., West J,and Drezek, R. "A Scatter-Based Method for Quantifying Nanoparticle Binding to Targeted Cells" SPIE Photonics West. Oral presentation (2007).

34. Fu, K., Halas, N., West J,and Drezek, R. "A Scatter-Based Method for Quantifying Nanoparticle Binding to Surface Markers" RQI Annual Symposium (2006).

Poster Presentations

1. Lowery A., Gobin A.M., Day E., Shah K., Halas N., West J. "Immunonanoshells for Selective Photothermal Therapy" American Association of Cancer Research: Molecular Targets and Cancer Theraputics, Philadelphia, PA, Nov. 2005

2. Lowery A., Gobin A.M., Day E., Shah K., Halas N., West J. "Immunonanoshells for Selective Photothermal Therapy" (poster) Nanotech Initiative. Rice University. Houston, TX, Oct. 2005

3. Lowery A., Gobin A.M., Halas N., West J. "Immunonanoshell laser-assisted therapy targets and ablates tumor cells" (poster) San Antonio Breast Cancer Symposium, San Antonio, TX, Dec. 2006

4. Lowery A., Gobin A.M., Halas N., West J. "Selective Photothermal Tumor Ablation using Immunonanoshells" (poster) Biomedical Engineering Society 2006, Chicago, IL, Oct. 2006

5. Lowery A., Gobin A.M., Halas N., West J. "Vascular targeting of nanoshells for photothermal cancer therapy" (poster) American Association of Cancer Research: Molecular Diagnostics in Cancer Therapeutic Development, Chicago, IL, Sept. 2006

Invited talks

1. Breast Imaging Applications of Nanoshell Bioconjugates. Optics East. Bionanotechnology Symposium. Philadelphia, PA. October 2004.

2. Nanoshell-Enabled Optical Molecular Imaging. NCI Symposium on Imaging and Advanced Technologies. Washington DC. October 2004.

3. Nanoshells for Breast Cancer Imaging. SPRING 2004. Dallas, TX. November 2004.

4. Towards Nanotechnology-Enabled Breast Cancer Imaging. NanoSummit 2004. Houston, TX. July 2004.

5. Nanotechnology in Cancer Imaging. Fifth Annual CAMD Workshop: Nanotechnology in Bioscience, Biotechnology, and Medicine. New Orleans, LA. June 2004.

6. Nanoshells for Imaging. University of Arizona. Department of Biomedical Engineering Seminar Series. Tucson, AZ. March 2004.

7. Optical Imaging for Minimally Invasive Medical Diagnosis. University of Pennsylvania. Department of Biomedical Engineering Seminar Series. Philadelphia, PA. January 2004.

8. Biophotonics Applications of Nanotechnology. Department of Radiology Seminar Series. Southwestern. Dallas, TX. January 2004.

9. Nanoengineered Contrast Agents for Biophotonics. SPIE Biophotonics West. San Jose,CA. January 2004.

10. Optical Molecular Imaging at Rice University. Texas/United Kingdom Collaborative Research Initiative Molecular Imaging Workshop. Houston, TX. November 2003.

11. Translational Biophotonics Research at Rice, Third Annual Biotechnology/Bioscience Innovation Forum, Rice Alliance, Rice University, Houston, TX, November 2003.

12. Biomolecular Optical Imaging, Computer and Information Technology Institute Seminar Series, Rice University, Houston, TX, October 2003.

13. Optical Spectroscopy for Minimally Invasive Medical Diagnosis, Harvard/MIT Division of Health Sciences and Technology/Department of Electrical and Computer Engineering, Boston, MA, April 2003.

14. Optical Spectroscopy for In Vivo Assessment of Tissue Pathology, Society of Surgical Oncologists Annual Meeting, Los Angeles, CA, March 2003.

15. Optical Imaging for Minimally Invasive Medical Diagnosis. Department seminar. Princeton University. April 2005.

16. Nanoshell Bioconjugates in Cancer Imaging. MD Anderson Grand Rounds. Houston, TX. April 2005.

17. Nanoshells for Imaging. University of Arizona. Department of Biomedical Engineering Seminar Series. Tucson, AZ. December 2004.

18. Diagnostic Applications of Nanoshells. Optics East. Bionanotechnology Symposium. Philadelphia, PA. October 2004.

19. Sensing Cancer Specific Signatures Using Nanoshell Bioconjugates. Rice-UK Conference on Sensing and Imaging Using Nanomaterials. October 2004.

20. Nanoparticle-Enabled Optical Molecular Imaging. NCI Symposium on Imaging and Advanced Technologies. Washington DC. October 2004.

21. Nanoshell Cancer Imaging and Therapy. NCI Scientific Advisory Board Meeting. Washington, DC. July 2004.

22. Towards Nanotechnology-Enabled Breast Cancer Imaging. NanoSummit 2004. Houston, TX. July 2004.

23. Nanotechnology in Cancer Imaging. Fifth Annual CAMD Workshop: Nanotechnology in Bioscience, Biotechnology, and Medicine. New Orleans, LA. June 2004.

24. Nanotechnology Academy for High School AP/IB and Honors Teachers. Faculty speaker on nanoshells in medicine. Summer 2004.

25. Rice University YES College Preparatory Intern Program. Faculty speaker on nanoshells. Summer 2004.

26. "Nanoshells: using Nanotechnology to harvest light for Biomedicine," Benson Lecturer, Physics Department, Miami University, April 2004. Prof. Naomi Halas.

27. Nanoshells: applications of Plasmonic Nanostructures in Biomedicine," NIH/NIAID Workshop, Gaithersburg, MD, June 2004. Naomi Halas, Ph.D.

28. "Nanoshells: from plasmon physics to cancer therapy," Research Seminar, Chalmers University, Goteborg, Sweden, June 2004. Naomi Halas, Ph.D.

29. Nanotechnology in Cancer Imaging," Fifth Annual CAMD Workshop: Nanotechnology in Bioscience, Biotechnology, and Medicine. New Orleans, LA. June 2004. Rebekah Drezek, Ph.D.

30. "Towards Nanotechnology-Enabled Breast Cancer Imaging," NanoSummit 2004. Houston, TX. July 2004. Rebekah Drezek, Ph.D.

31. "Truth and Beauty at the Nanoscale: Texas-Sized Molecules and Cancer Therapy," Houston Philosophical Society, September 2004. Naomi Halas, Ph.D.

32. "Breast Imaging Applications of Nanoshell Bioconjugates," Optics East.

33. Bionanotechnology Symposium. Philadelphia, PA. October 2004. Rebekah Drezek,

34. "Nanoshell-Enabled Optical Molecular Imaging," NCI Symposium on Imaging and Advanced Technologies. Washington DC. October 2004. Rebekah Drezek, Ph.D.

35. "Nanoshells in Biomedical Applications," U. T. M. D. Anderson Imaging Physics Research Seminar, Houston, TX, November 2004. Naomi Halas, Ph.D.

36. "Nanoshells for Breast Cancer Imaging," SPRING 2004. Dallas, TX. November 2004. Rebekah Drezek, Ph.D.

37. "Nanoshells: manipulating light at nanoscale dimensions for biomedicine," University of Texas Center for Biomedical Engineering Annual Conference, Westin, Galleria, Houston,TX, December 2004. Naomi Halas.

38. "Nanoshells in Biomedicine," AIChE Regional Meeting, Beaumont, TX, February 2005.

39. Drezek, R., West, J., and Halas, N. Nanoshells for Imaging and Therapy of Breast Cancer. DOD Era of Hope Meeting. 2006.

40. Design and Implementation of a Standalone Raman-based All-optical Nanosensor", Quantum Electronics and Laser Science Conference (QELS), Baltimore, May 2005. Naomi Halas.

41. "Nanoshells: applying Nanotechnology to harvest light for biomedicine" at "Minds without Borders: Frontiers in Medical Research", Medical Sciences Graduate Student Association, University of Calgary, Calgary, Alberta, Canada, May 2005. Naomi Halas.

42. "Nanoshells: Seamless Integration of Cancer Imaging and Therapy", Era of Hope Conference, Philadelphia, PA, June 2005. Naomi Halas.

43. "Nanoshells: using Nanotechnology to harvest light for biomedicine", The 2005 Landsdowne Lecturer in Chemistry and Electrical Engineering, University of Victoria, CA, September, 2005 (popular lecture) Naomi Halas.

44. "Nanoshells: from plasmon physics to cancer therapy", Distinguished Speaker Series, Center for Nano and Molecular Science and Technology, University of Texas, February 2005. Naomi Halas.

45. "Nanoshells: from Plasmon physics to cancer therapy", Invited speaker series, Department of Chemistry, University of Utah, February 13, 2006. Naomi Halas.

46. "Designing Nanotools for Biomedicine", 28th Annual Symposium of the Burnham Institute, La Jolla, CA, April 2006. Naomi Halas.

47. "Designing Optical Nanotools for Biomedicine", The Dorothy J. Killam Lecture, Montreal Neurological Society, McGill University, May 2006. Naomi Halas.

48. " Nanoshells: from plasmon physics to cancer therapy" and "Nanoengineered Plasmonic substrates for surface enhanced spectroscopies", Colloquium and Tutorial, Kavli Nanoscience Institute Distinguished Speaker Series, Caltech, May 2006. Naomi Halas.

49. "Beyond Drugs, Cancer, and Fear: The promise of nanotechnology in biomedicine", Perspectives on the Future of Science and Technology Conference, U. S. Department of State sponsorship, Lake Como, IT, May 2006. Naomi Halas.

50. "Taking the (Nano) device approach: applications of nanotechnology in the diagnosis and treatment of cancer and other diseases," Gordon Research Conference in Molecular Therapeutics of Cancer, Oxford, UK, July 2006. Naomi Halas.

51. "An all-optical SERS-based pH nanosensor," SPIE (Society for Photo-optical Instrumentation Engineers) Annual Meeting, San Diego, CA, August 2006. Naomi Halas.

52. "Taking the (Nano) device approach: applications of nanotechnology in the diagnosis and treatment of cancer and other diseases," Gordon Research Conference in Molecular Therapeutics of Cancer, Oxford, UK, July 2006. Naomi Halas.

53. "Plasmonic Nanostructures: artificial molecules enabling nanoscale spectroscopies and nanophotonics-based biomedical applications," Gordon Research Conference in Plasmonics – Optics at the Nanoscale, Keene, NH, July 2006. Naomi Halas.

54. "Plasmonic Nanostructures: artificial molecules enabling nanoscale spectroscopies and nanoparticle-based biomedical applications", Invited talk, European Union Research Raining Network HYTEC, Annual Meeting, Heraklion, Crete, July 2006. Naomi Halas.

55. "Plasmonic Nanostructures: Artificial Molecules," Plenary Talk, SPIE (Society for Photo-optical Instrumentation Engineers) Annual Meeting, San Diego, CA, August 2006. Naomi Halas.

56. "An all-optical SERS-based pH nanosensor," SPIE (Society for Photo-optical Instrumentation Engineers) Annual Meeting, San Diego, CA, August 2006. Naomi Halas.

57. "Plasmonic Nanostructures: artificial molecules enabling nanoscale spectroscopies and nanoparticle-based biomedical applications", Nano 2006 Conference, San Sebastian, Spain, September 2006. Naomi Halas.

58. "Plasmonic Nanoparticles: Molecular Orbitals writ large", Chemistry Department Colloquium, Case Western Reserve University, Cleveland, OH, September 2006. Naomi Halas.

59. "Plasmonic Nanostructures: molecular orbitals writ large" and "Nanoengineered Plasmonic substrates for surface enhanced spectroscopies", Annual Nanowire Symposium, Division of Solid State Physics and the Nanometer Consortium, Lund University, Sweden, October 2006. Naomi Halas.

60. "When plasmons interact, worlds collide", Kirkpatrick Lecture, Illinois Institute of Technology, Chicago, IL, September 2006. Naomi Halas.

61. "Plasmon Hybridization: molecular orbitals writ large", Physical Chemistry Seminar, U. C. Berkeley, October 2006. Naomi Halas.

62. A Nanoscale all-optical pH meter", IEEE-LEOS Annual Meeting, Montreal, Canada, November 2006. Naomi Halas.

63. "Plasmonics", Ecole Polytechnique de Monteal, Montreal, CA, November 2006. Naomi Halas.

64. "Taming surface enhanced spectroscopies with tailored plasmonic nanoparticle substrates", Chemistry Research Seminar, University of California, Santa Barbara October 2006.

65. Plasmonic Nanoparticles: Molecular Orbitals writ large" ECE Departmental Seminar, Georgia Tech, Atlanta GA, November 2006. Naomi Halas.

66. "Plasmonic Nanoparticles: Molecular Orbitals writ large" Invited talk, Chemistry Department, Georgia Tech, Atlanta, GA, November 2006.

67. "Plasmonic Nanostructures: Molecular Orbitals writ large" Invited talk, Nanoscience Speaker Series, University of Pittsburgh, December 2006.

68. "Plasmonic Design" Invited talk, Physics of Quantum Electronics Conference, Snowbird, UT, January 2007.

69. "Nanophotonics: the next Big Thing", Invited talk, CINT Annual Workshop, Los Alamos National Laboratory/Sandia National Laboratory.

70. "Plasmonic Nanoparticles: Molecular Orbitals writ large" Annual Invited Lecturer, Institute for Materials Research, University of Connecticut, February 2007.

71. "Designing optical Nanotools for Biomedicene" Keynote Speaker, Peachey Conference, Purdue, University, Lafayette, IN, February 2007.

72. "Plasmonic Nanoparticles: Molecular Orbitals writ large" Invited talk, University of Utah, February 2007.

73. "Plasmonic coupling and nanophotonics" Invited speaker, ICAM Workshop, Santa Fe, NM March 2007.

74. "Designing optical Nanotools for Biomedicene" Plenary Speaker, IOP Annual Meeting in Nanoscale Physics and Technology, Southhampton, UK, March 2007.

75. "Nanophotonics: from Plasmon Physics to Cancer Therapy" Invited talk, TAMEST meeting, Austin, TX, April 2007.

76. "Plasmonic Nanoparticles: Molecular Orbitals writ large" Invited talk, Physics Department, University of Pittsburgh, April 2007.

77. "Plasmonic Nanomaterials: Enabling Solutions in Pursuit of Challenges" Invited talk, Fundamentals of Nanoscience Conference, Snowbird, UT, April 2007.

78. "An Enabling Technology for Nanoscience and Defense Applications" Invited talk, "Nanotechnology for Defense Applications", San Diego, April 2007.

79. "Plasmonic Nanoparticles: Molecular Orbitals writ large" Invited talk, University of California Davis, Applied Physics Department, April 2007.

80. "Plasmon-based Nanoparticle Probes for Multifunctional Diagnostics and Therapeutics" Invited talk, Spring MRS meeting, San Francisco, CA, April 2007.

81. Invited talk, Spring MRS meeting, San Francisco, CA, April 2007.

82. "Using Nanotechnology to Harvest Light for Nanomedicene" WINS Lecturer, University of Western Ontario, May 2007 (popular lecture).

83. Nanotechnology in Cancer Imaging. MRS Annual Meeting. Materials/Biology Interface. Boston, MA. November 2007.

84. Nanotechnology-Enabled Optical Molecular Imaging of Cancer. Rice University Workshop on Translational Optical Imaging. May 2007.

85. Nanotechnology for Point of Care Diagnostics. World Health Symposium. April 2007.

86. Optical Imaging for Minimally Invasive Medical Diagnosis. MD Anderson Cancer Center Pediatrics Grand Rounds. April 2007.

87. Nanotechnology in Medical Imaging. MD Anderson Cancer Phase I Clinical Trial Lecture Series. February 2007.

88. Towards Point-of-Care Optical Technologies for Early Cancer Detection. Department of Electrical and Computer Engineering Corporate Affiliates Meeting. Rice University. September 2006.

89. Activatable Nanoparticles for Cancer Imaging. Gordon Research Conference on Lasers in Medicine and Surgery. July 2006.

90. Nanotechnology and Cancer. American Association for Cancer Research Annual Meeting. Washington, DC. April 2006.

91. Optical Molecular Cancer Imaging. IEEE International Symposium on Biomedical Imaging: Nano to Marco. Washington, DC. April 2006.

92. Speaker, 4th Annual Angiogenesis & Vascular Targeting Agents Drug Discovery & Development World Summit, Boston, MA, 09/06

93. Speaker, Diagnosis and Therapeutic Discovery in Neuro-Oncology Conference, Houston, TX, 10/06

94. Speaker, Clontech, Mountain View, CA, 10/06

95. Speaker, A.C. Camargo/Sister Institution, Extramural Program, Sao Paulo, Brazil, 10/06

96. Speaker, Biogen, Boston, MA, 11/06

97. Speaker, 18th EORTC-NCI-AACR Symposium, Prague, Czech Republic, 11/06

98. Speaker, 6th Edition of Amazon Project Conference on Cancer, Palermo, Italy, 11/06

99. Speaker, San Rafaelle Hospital, Milan, Italy, 11/06

100. Speaker, Arap/Pasqualini Program Retreat, San Francisco, CA, 12/06

101. Speaker, University of Texas M. D. Anderson Cancer Center, Grand Rounds, Houston, TX, 01/07

102. Speaker, Nano Medicine Annual Symposium, Helsinki, Finland, 01/07

103. Speaker, International Symposium on Polymer Therapeutics (ISPT 07), Berlin, Germany,02/07

104. Speaker, 2007 Advances in Oncology: Emerging Trends, Targets, and Approaches to Solid Tumors Symposium, Houston, TX, 3/07

105. Speaker, Memorial-Sloan Kettering Cancer Center, Molecular Pharmacology & Chemistry Seminar, New York, NY, 3/07

106. Speaker, Massachusetts General Hospital, Boston, MA, 04/07

107. Speaker, Stanford University, Palo Alto, CA, 4/07

108. Speaker, McGill Cancer Centre, Montreal, Canada, 4/07

109. Scientific Program Committee for the 6th Annual Joint Molecular Imaging Conference Providence, RI, 07/07

110. Michale E. Keeling Center for Comparative Medicine and Research, Department of Veterinary Sciences, Bastrop, TX, 07/20/07-07/24/07

111. 13th Annual International Congress of Immunology, Rio de Janeiro, Brazil, 08/20/07-08/25/07

112. U.S. Army Institute of Surgical Research, Fort Sam Houston, San Antonio, TX 08/28/07

113. USC Grand Rounds, USC Norris Cancer Center, Los Angeles, CA 09/10/07-09/11/07

114. Conway Institute, University College of Dublin, Dublin, Ireland 09/24/07-09/28/07

115. 2007 Prostate Cancer Foundation Scientific Retreat, Lake Tahoe, NV, 10/11/07-10/13/07

116. 2nd Annual France – USA Science & Technology Workshop, Rice University, Houston, TX, 10/15/07

117. TATRC's Integrated Research Team (IRT) Meeting, Nanotechnology Solutions for Long-term Implantable Devices, The University of Texas Health Science Center, Houston, TX, 10/24/07

118. Organizing Committee, Session Co-Chair, International Society of Biological Therapy of Cancer 22nd Annual Meeting, Seaport World Trade Center, Boston, MA, 11/02/07

119. International Symposium "Mechanisms of Tumor Control", São Paulo, Brazil, 11/07

120. First Annual Cullen Trust for Higher Education Symposium on Translational Research, UT M. D. Anderson Cancer Center, Houston, TX, 01/11/08

121. Grand Rounds at the Camargo Cancer Hospital, (Sister Institution to The University of Texas M. D. Anderson Cancer Center), Sao Paulo, Brazil, 02/21/08-02/28/08

122. Texas-United Kingdom Collaborative Co-hosted with the Alliance for Nanohealth and UK Science & Innovation, British Consulate-General Houston, Baker Institute for Public Policy, "Ligand-directed vascular targeting and molecular imaging," Rice University, Houston, TX, 03/17/08

123. PRBB-CRG Seminar of the Barcelona Biomedical Research Park (PRBB), "Ligand-directed vascular targeting and molecular imaging," Barcelona, Spain, 04/12/08-04/15/08

124. 4th Annual PEGS, Cambridge Healthtech Institute's conference, InterContinental-Boston, "Ligand-directed vascular targeting and molecular imaging," Boston, MA, 04/28/08-04/29/08

125. Institute of Biosciences and Technology Information Exchange Seminar, "Therapeutic implications of combinatorial vascular targeting," Texas A&M Health Science Center, Institute of Biosciences and Technology, Houston, TX, 05/15/08

126. BRP Renewal Meeting, Rice University, Houston, TX, 06/02/08

127. The Marcus Foundation, David M. Eisenberg, M.D. Site Visit, "Molecular Targeting Using Vascular Zip Codes," The University of Texas M. D. Anderson Cancer Center, Houston, TX, 07/14/08

128. Controlled Release Society 35th Annual Meeting and Exposition, "Ligand-directed targeting and molecular genetic imaging in diseases with an angiogenesis component," New York, NY, 07/15/08

129. Imperial College London, "Ligand-directed targeting and molecular imaging in cancer and obesity," London, Heathrow, 07/24/08

130. Edinburgh International Phage Conference, Vaccines, gene therapy and drug delivery vehicles, "Ligand-directed vascular targeting and molecular imaging," Edinburgh, United Kingdom, 07/27/08

Continuing Education Courses

1.   Rice Alumni College. Nanotechnology in Medicine lecture, Spring 2005.

2.   The Year's Best: Nanotechnology. Rice Teaching Award Winners Continuing Studies. Lecture Series, Spring 2005.

3.   Nanotechnology-Enabled Medical Imaging. School of Continuing Studies. Nanoscience:

4.   The Science of the Very Small. Lecture Series, Fall 2004.

5.   Nanotechnology in Imaging. School of Continuing Studies Nanotechnology Academy.

6.   Rice University. Houston, TX, July 2004.

Patents:

West, J., Drezek, R, Sershen, S., and Halas, N. "Optically-absorbing Nanoparticles for Enhanced Tissue Healing." U.S Patent No. 6,685,730.

Conclusions

The team from Rice University and M D Anderson has successfully demonstrated, and reached out beyond the key technologies outlined in our original proposal. We have optimized nanoshell sizes so that we can synthesize a single multifunctional nanoshell to combine optical diagnostic imaging with subsequent photothermal ablation of the tumor. We have demonstrated the above paradigm *in vivo* in a mouse tumor model. Mice receiving the nanoshell + near IR laser treatment showed a long term survival rate of 83 %.

Beyond the initial proposal, the research from this grant has stimulated research in many other laboratories around the country. Beyond the imaging modalities explored within this grant numerous other imaging techniques using nanoshells as contrast agents have been reported. Nanoshell based treatment of cancer as an adjunct to standard existing clinical treatment options has been reported. Some of these have been reviewed in the Accounts of Chemical Research invited article.[1]

The photothermal ablation of solid tumors using NIR nanoshells technology is being expanded towards clinical trials by a local company; Nanospectra Biosciences. They have received FDA approval for initial clinical trials.

References

1. S. Lal, S. E. Clare, and N. J. Halas, "Nanoshell-Enabled Photothermal Cancer Therapy: Impending Clinical Impact," Accounts of Chemical Research (special issue on Nanoscience) **41**, 1842-1851 (2008).

2. A. R. Lowery, A. M. Gobin, E. S. Day, N. J. Halas, and J. L. West, "Immunonanoshells for targeted photothermal ablation of tumor cells," International Journal of Nanomedicine **1**(2)(2006).

3. G. R. Souza, D. R. Christianson, F. I. Staquicini, M. G. Ozawa, E. Y. Snyder, R. L. Sidman, J. H. Miller, W. Arap, and R. Pasqualini, "Networks of gold nanoparticles and bacteriophage as biological sensors and cell-targeting agents," Proc. Natl. Acad. Soc. **103**(5), 1215–1220 (2006).

4. G. R. Souza, C. S. Levin, A. Hajitou, R. Pasqualini, W. Arap, and J. H. Miller, "In Vivo Detection of Gold-Imidazole Self-Assembly Complexes: NIR-SERS Signal Reporters," Anal. Chem. (2006).

5. A. W. H. Lin, N. A. Lewinski, M.-H. Lee, and R. A. Drezek, "Reflectance spectroscopy of gold nanoshells: computational predictions and experimental measurements," Journal of Nanoparticle Research (2006).

6. C. Loo, L. Hirsch, J. Barton, N. Halas, J. West, and R. Drezek, "Nanoshell-Enabled Photonics-Based Cancer Imaging and Therapy," Technology in Cancer Research and Treatment **3**, 33-40 (2004).

7. C. Loo, L. Hirsch, M.-H. Lee, E. Chang, J. West, N. Halas, and R. Drezek, "Gold nanoshell bioconjugates for molecular imaging in living cells," Optics Letters **30**(9), 1012-1014 (2005).

8. V. Nammalvar, A. Wang, and R. Drezek, "Enhanced gold nanoshell scattering contrast using angled fiber probes," J. Nanophoton **1**, 013510 (2007).

9. A. M. Gobin, M. H. Lee, N. J. Halas, W. D. James, R. A. Drezek, and J. L. West, "Near-Infrared Resonant Nanoshells for Combined Optical Imaging and Photothermal Cancer Therapy," Nano Lett. (2007).

10. C. S. Levin, S. W. Bishnoi, N. K. Grady, and N. J. Halas, "Determining the Conformation of Thiolated Poly(ethylene glycol) on Au Nanoshells by Surface-Enhanced Raman Scattering Spectroscopic Assay," Anal. Chem. **78**, 3277-3281 (2006).

11. K. Smallbone, D. J. Gavaghan, R. A. Gatenby, and P. K. Maini, "The role of acidity in solid tumour growth and invasion," Journal of Theoretical Biology **235**, 476–484 (2005).

12. S. W. Bishnoi, C. J. Rozell, C. S. Levin, M. K. Gheith, B. R. Johnson, D. H. Johnson, and N. J. Halas, "An all-optical nanoscale pH meter," Nano Lett. **6**(8), 1687-1692 (2006).

13. L. R. Hirsch, Andre M. Gobin, A. R. Lowery, R. A. Drezek, N. J. Halas, and J. L. West, "Metal Nanoshells," Annal. Biomed. Eng. **34**(1), 15–22 (2006).

14. D. P. O'Neal, L. R. Hirsch, N. J. Halas, J. D. Payne, and J. L. West, "Photo-Thermal Tumor Ablation in Mice Using Near Infrared-Absorbing Nanoparticles," Cancer Letters **209**(2), 171-176 (2004).

15. D. P. O'Neal, L. R. Hirsch, N. J. Halas, J. D. Payne, and J. L. West, "Photo-thermal cancer therapy using intravenously injected near infrared-absorbing nanoparticles," Proceedings of SPIE **5689**, 149-157 (2005).

16. C. Loo, A. Lowery, N. J. Halas, J. L. West, and R. Drezek, ""Immunotargeted Nanoshells for Integrated Cancer Imaging and Therapy," Nano Letters **5**(4), 709-711 (2005).

Appendices:

Published articles attached.

Nanoshells for Integrated Diagnosis and Therapy of Cancer

Alex W.H. Lin[1], Christopher H. Loo[1], Leon R. Hirsch[1], Jennifer K. Barton[3], Min-Ho Lee[1]
Naomi J. Halas[2], Jennifer L. West[1], Rebekah A. Drezek[1]

[1]Dept. of Bioengineering, Rice University, MS-142, Houston, TX 77251-1892
[2]Dept. of Electrical & Computer Engineering, Rice University, MS-336, Houston, TX 77251-1892
[3]Dept. of Biomedical Engineering, The University of Arizona, Tucson, AZ 85721-0104

ABSTRACT

Metal nanoshells are a novel type of composite nanoparticle consisting of a dielectric core covered by a thin metallic shell which is typically gold. Nanoshells possess highly favorable optical and chemical properties for biomedical imaging and therapeutic applications. By varying the relative the dimensions of the core and the shell, the optical resonance of these nanoparticles can be precisely and systematically varied over a broad wavelength region ranging from the near-UV to the mid-infrared. This range includes the near-infrared (NIR) region where tissue transmissivity peaks. In addition, nanoshells offer other advantages over conventional organic dye imaging agents, including improved optical properties and reduced susceptibility to chemical/thermal denaturation. Furthermore, the same conjugation protocols used to bind biomolecules to gold colloid are easily modified for nanoshells. We first review the synthesis of gold nanoshells and illustrate how the core/shell ratio and overall size of a nanoshell influences its scattering and absorption properties. We then describe several examples of nanoshell-based diagnostic and therapeutic approaches including the development of nanoshell bioconjugates for molecular imaging, the use of scattering nanoshells as contrast agents for optical coherence tomography (OCT), and the use of absorbing nanoshells in NIR thermal therapy of tumors.

Keywords: Nanoshells, Nanoparticles, Contrast agents, Molecular imaging, Photothermal therapy, Optical Coherence Tomography, Cancer, Nanotechnology.

1. INTRODUCTION

Figure 1: Visual demonstration of the tunability of metal nanoshells. Different size parameters give rise to different optical effects.

There is a significant clinical need for novel methods for detection and treatment of cancer which offer improved sensitivity, specificity, and cost-effectiveness. In recent years, photonics-based technologies have shown tremendous improvements in addressing this need. Optical technologies promise high resolution, noninvasive functional imaging of biological tissues. However, in many cases, these technologies are limited by the inherently weak optical signatures of endogenous chromophores and the subtle differences between normal and diseased tissue. Over the past several years, there has been increasing interest in combining emerging optical technologies with the development of novel exogenous contrast agents, designed to probe the molecular specific signatures of cancer, to improve the detection limits and clinical effectiveness of optical imaging. Sokolov *et al.*[1] recently demonstrated the use of gold colloid conjugated to antibodies to the epidermal growth factor receptor (EGFR) as scattering contrast agents for biomolecular optical imaging of cervical cancer cells and tissue specimens. In addition, optical imaging applications of nanocrystal bioconjugates have been described by multiple groups including Bruchez *et al.*[2], Chan and Nie[3], and Akerman *et al.*[4] More recently, interest has developed in the creation of nanotechnology-based technologies which

couple molecular specific early detection strategies with appropriate therapeutic intervention and monitoring capabilities.

Metal nanoshells are a new type of nanoparticle composed of a dielectric core (silica) such and an ultrathin metallic layer (gold). Gold nanoshells possess physical properties similar to gold colloid, in particular, a strong optical absorption due to the collective electronic response of the metal to light. The optical absorption of gold colloid yields a brilliant red color which has been of considerable utility in consumer related medical products, such as home pregnancy tests. In contrast, the optical response of gold nanoshells depends on the relative size of the nanoparticle core and the thickness of the gold shell. By varying the relative core and shell thicknesses, the optical resonance gold nanoshells can be varied across the visible and the near infrared spectral regions (Figure 1).[5,6] Gold nanoshells can be made to either preferentially absorb or scatter light by varying the size of the particle relative to the wavelength of the light at their optical resonance. In Figure 2, the Mie extinction plot of the plasmon resonance shift as a function of the gold nanoshell dimensions for the case of a 60 nm radius silica core is depicted. In this figure, the core and shell sizes are shown to relative scale beneath their corresponding optical resonances. In Figure 3, a plot of the core/shell ratio versus resonance wavelength for a silica core/gold shell nanoparticle is displayed.[6] The extremely agile "tunability" of the optical resonance is a property unique to nanoshells: in no other molecular or nanoparticle structure can the resonance of the optical properties be so systematically designed.
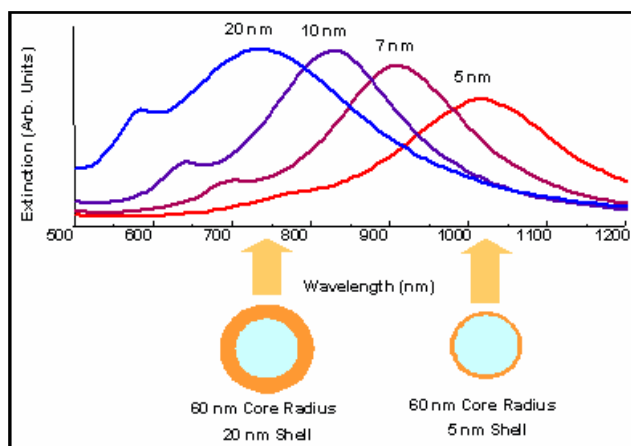

Figure 2: Optical resonances of gold shell-silica core nanoshells as a function of their core/shell ratio. Respective spectra correspond to the nanoparticles depicted beneath.
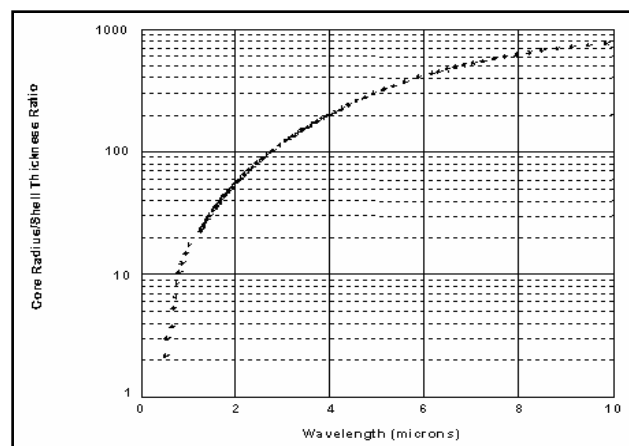
Figure 3: Core/shell ratio as a function of resonance wavelength for gold/silica nanoshells.

Halas and colleagues have completed a comprehensive investigation of the optical properties of metal nanoshells.[7] Experimental observations of gold nanoshell resonances were shown to closely match Mie theory and can be fabricated with nanoscale tolerances with adequate predictability and reproducibility.[6] The approach has been successfully used to grow various types of metal shells onto silica nanoparticles. Various stages in the growth of a gold metallic shell onto a functionalized silica nanoparticle are shown in Figure 4. Based on the core/shell ratios that can be achieved with this protocol, gold nanoshells with optical resonances extending from the visible region and well into the infrared can currently be fabricated. This spectral region includes the 800-1300 nm "water window" of the near infrared, a region of high physiological transmissivity, which has been demonstrated as the spectral region best suited for optical bio-imaging and biosensing applications. The optical properties of gold nanoshells, when coupled with their biocompatibility and their ease of bioconjugation, render these nanoparticles highly suitable for targeted bioimaging and therapeutics applications. By controlling the physical parameters of the nanoshells, it is possible to engineer nanoshells which primarily scatter light as would be desired for many imaging applications, or alternatively, nanoshells which are strong absorbers permitting photothermal-based therapy applications. The tailoring of scattering and absorption cross-sections is demonstrated in Figure 5 which shows sample spectra for two nanoshell configurations, one designed to scatter light and the other to preferentially absorb light with the peak at the same wavelength.
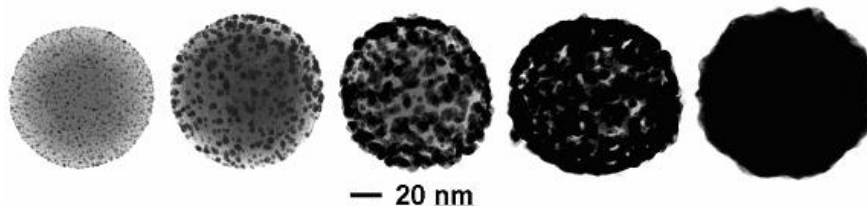
Figure 4: Transmission electron microscope images of gold/silica nanoshells during shell growth.
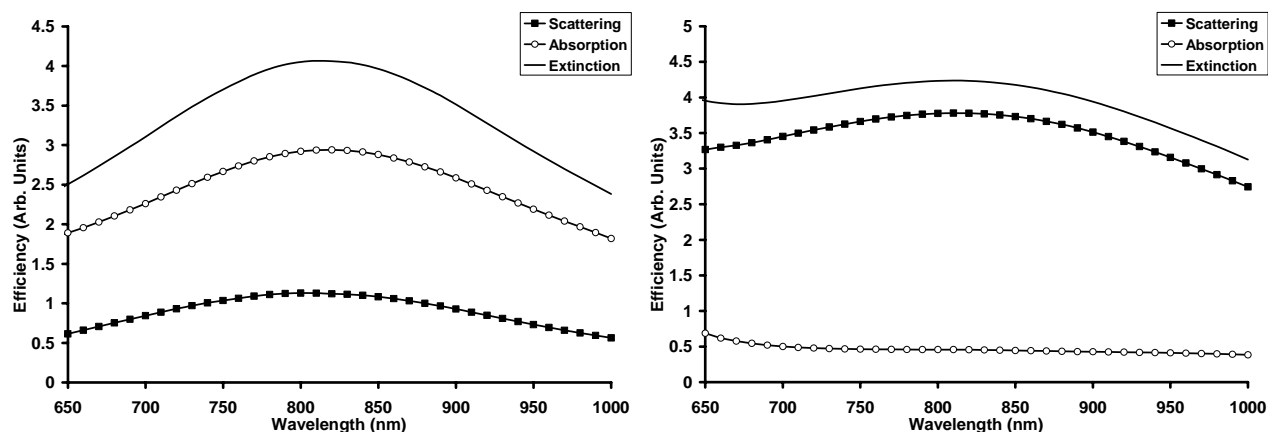

Figure 5: Nanoshells may be designed to be predominantly scattering or absorbing by tailoring the core and shell fabrication materials. To demonstrate this concept, the predicted scattering efficiency, absorption efficiency, and extinction are shown for two nanoshells: (left) an absorbing configuration (core radius = 50nm; shell thickness = 10nm) and (right) a scattering configuration (core radius = 50nm; shell thickness = 10nm).

Because the metal layer of gold nanoshells is grown using the same chemical reaction as gold colloid synthesis, the surfaces of gold nanoshells are virtually chemically identical to the surfaces of the gold nanoparticles universally used in bioconjugate applications. The use of gold colloid in biological applications began in 1971 when Faulk and Taylor invented the immunogold staining procedure.[8] Since that time, the labeling of targeting molecules, especially proteins, with gold nanoparticles has revolutionized the visualization of cellular or tissue components by electron microscopy. The optical and electron beam contrast qualities of gold colloid have provided excellent detection qualities for such techniques as immunoblotting, flow cytometry, and hybridization assays. Conjugation methods exist for the labeling of a broad range of biomolecules with gold colloid, such as protein A, avidin, streptavidin, glucose oxidase, horseradish peroxidase, and IgG. Successful gold nanoshell conjugation with enzymes and antiobodies has previously been demonstrated. In this article, we present data demonstrating the potential of nanoshells for several biomedical applications including the use of nanoshell bioconjugates as biological labels for optical imaging, the development of nanoshell-based scattering contrast agents for optical coherence tomography, and the use of absorbing nanoshells for photothermal therapy of tumors.

2. METHODS AND MATERIALS

2.1 Gold nanoshell fabrication: Cores of silica nanoparticles were fabricated as described by Stober *et al.*[9] in which tetraethylorthosilicate was reduced in NH_4OH in ethanol. Particles were sized with scanning electron microscopy (SEM) and a polydispersity of <10% was considered acceptable. The particle surface was then terminated with amine groups with aminopropylethoxysilane in ethanol. Small gold colloid (1-3 nm) were grown as outlined by Duff *et al.*[10], was adsorbed onto the aminated silica nanoparticle surface. More gold was then reduced onto these colloid nucleation sites using $HAuCl_4$ in the presence of formaldehyde. Gold nanoshell formation and dimensions were assessed with a UV-VIS spectrophotometer and SEM. The nanoshells used in the darkfield scattering imaging studies described consisted of a 120 nm silica core radius with a 35 nm thick gold shell. Nanoshells used in the OCT imaging consisted of a 100 nm core radius and a 20 nm thick shell, which was chosen to predominantly scattering in the NIR. The nanoshells used in the therapy application described used a 60 nm core radius and a 10 nm thick shell which absorb light with an absorption peak at ~815 nm.

2.2 Antibody conjugation: Ortho-pyridyl-disulfide-*n*-hydroxysuccinimide polyethylene glycol polymer (OPSS-PEG-NHS, MW=2000) was used to tether antibodies onto the surfaces of gold nanoshells. Using $NaHCO_3$ (100 mM, pH 8.5) OPSS-PEG-NHS was re-suspended to a volume equal to that of either HER2 (specific) or IgG (non-specific) antibodies. At this concentration, the concentration of polymer was in molar excess to the amount of HER2 or IgG antibody used. The reaction was allowed to proceed on ice overnight. Excess, unbound polymer was removed by membrane dialysis (MWCO=10,000). PEGylated antibody (0.67 mg/mL) was added to nanoshells (~10^9 nanoshells/mL) for 1 hr to facilitate targeting. Unbound antibody was removed by centrifugation at 650 G, supernatant removal, and resuspension in potassium carbonate (2 mM). Following antibody conjugation, nanoshells surfaces were further modified with PEG-thiol (MW=5000, 1 µM) to block non-specific adsorption sites and to enhance biocompatibility.

2.3 Cell culture: HER2-positive SKBr3 human mammary adenocarcinoma cells were cultured in McCoy's 5A modified medium supplemented with 10% fetal bovine serum (FBS) and antibiotics. HER2-negative MCF7 human mammary adenocarcinoma cells were cultured in Eagle's minimum essential medium supplemented with 10% FBS and 0.01 mg/ml of bovine insulin. Cells were maintained at 37°C and 5% CO_2.

2.4 Molecular imaging, cytotoxicity, and silver staining: SKBr3 cells were exposed to 8 µg/mL of bioconjugated nanoshells for 1 hr, washed with phosphate-buffered saline, and observed under darkfield microscopy. The calcein-AM live stain (Molecular Probes, 1 µM) was used to assess cell viability after nanoshell targeting. A silver enhancement stain, a qualitative stain capable of detecting the presence of metals such as gold on cell surfaces, was used to assess cellular-nanoshell binding. Cells incubated with targeted nanoshells were fixed with 2.5% glutaraldehyde, and exposed to silver stain for 15 minutes. Silver growth was monitored under phase-contrast microscopy, with further silver enhancement blocked by immersion in 2.5% sodium thiosulfate. Darkfield and silver stain images were taken with a Zeiss Axioskop 2 plus microscope equipped with a black-white CCD camera. All images were taken at 40X magnification under the same lighting conditions.

2.5 Optical coherence tomograhy (OCT): Optical coherent tomography (OCT) is a state-of-the-art imaging technique which produces high resolution (typically 10-15 µm), real-time, cross-sectional images through biological tissues. The method is often described as an optical analog to ultrasound. OCT detects the reflections of a low coherence light source directed into a tissue and determines at what depth the reflections occurred. By employing a heterodyne optical detection scheme, OCT is able to detect very faint reflections relative to the incident power delivered to the tissue. In OCT imaging out of focus light is strongly rejected due to the coherence gating inherent to the approach. This permits deeper imaging using OCT than is possible using alternative methods such as reflectance confocal microscopy where the out of focus rejection achievable is far lower. In the OCT experiments described in this paper, a conventional OCT system with a superluminescent diode with a center wavelength of 830nm was used to obtain m-scans of the cuvette (images with time as the x-axis and depth as the y-axis, no lateral scanning). The axial and lateral resolution of the OCT system was 14 µm (in air) and 15 µm, respectively. Each image required approximately 20 seconds to acquire. System parameters remained the same throughout the experiment.

2.6 *In vitro* photothermal nanoshell therapy: SKBr3 breast cancer cells were cultured in 24-well plates until fully confluent. Cells were then divided into two treatment groups: nanoshells + NIR-laser and NIR-laser alone. Cells exposed to nanoshells alone or cells receiving neither nanoshells nor laser were used as controls. Nanoshells were prepared in FBS-free medium (~2 x 10^9 nanoshells/mL). Cells were then irradiated under a laser emitting light at 820 nm at a power density of ~35 W/cm^2 for 7 minutes with or without nanoshells. After NIR-light exposure, cells were replenished with FBS-containing media and were incubated for an additional hour at 37°C. Cells were then exposed to the calcein-AM live stain for 45 minutes in order to measure cell viability. The calcein dye causes viable cells to fluoresce green. Fluorescence was visualized with a Zeiss Axiovert 135 fluorescence microscope equipped with a filter set specific for excitation and emission wavelengths at 480 and 535 nm, respectively. Membrane damage was assessed using an aldehyde-fixable fluorescein dextran dye. Cells were incubated for 30 min with the fluorescent dextran, rinsed, and immediately fixed with 5% glutaraldehyde. Photothermal destruction of cells was attributed to hyperthermia induced via nanoshell absorption of NIR light.

3. RESULTS

As an initial demonstration of the potential of nanoshells in cancer imaging and therapy, we designed and fabricated nanoshells suitable for both scattering and absorption-based photonics applications. For proof-of-principle imaging studies, we fabricated nanoshells with a 120 nm radius and 35 nm shell thickness. It should be noted that nanoshells over a broad range of sizes can be fabricated for scattering based imaging applications. This permits the same nanoshells to be used in light-based microscopy studies employing silicon CCDs and in NIR tissue imaging studies using reflectance confocal microscopy and OCT. We also fabricated nanoshells with a 100 nm radius and 20 nm shell thickness for OCT imaging. These nanoshells have very similar scattering and absorption spectra to the larger nanoshells; however, the scattering and absorption cross-sections are smaller due largely to the smaller particle size. In addition, smaller 60 nm radius nanoshells with a 10 nm shell were fabricated for photothermal therapy applications. Figure 6 shows SEM images of the nanoshells fabricated at all three sizes.
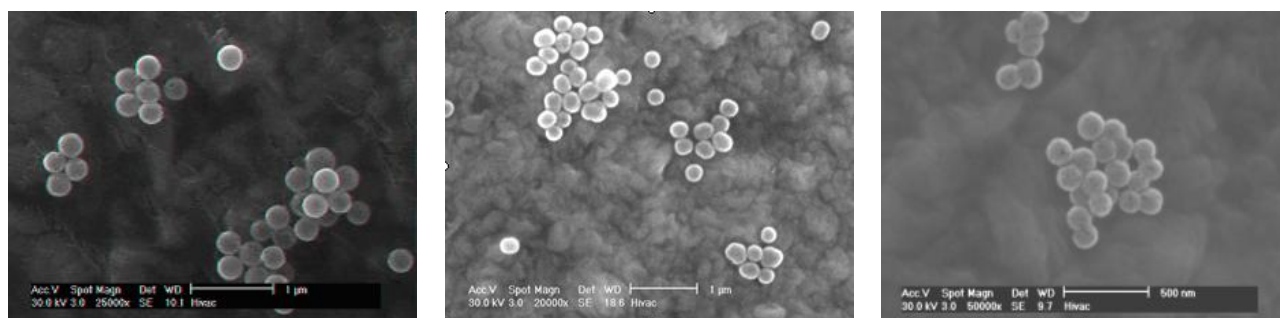

Figure 6: SEM micrographs of nanoshells used in the described studies. The left image shows the larger diameter nanoshells used in the darkfield imaging experiments. The center image shows the nanoshells used in the OCT experiments. The right image shows the smaller diameter nanoshells used for photothermal therapy applications. The scale bars in the left and center images are 1 μm while the scale bar in right image is 500 nm.

3.1 Molecular Imaging of HER2 receptor: As an initial demonstration of the molecular imaging potential of nanoshell bioconjugates, we imaged carcinoma cells which overexpress HER2, a clinically significant molecular marker of breast cancer. Under darkfield microscopy, significantly increased optical contrast due to HER2 expression was observed in HER2-positive SKBr3 breast cancer cells targeted with HER2-labeled nanoshells compared to cells targeted by nanoshells non-specifically labeled with IgG (Figure 7). In addition, greater silver staining intensity was seen in cells exposed to HER2-targeted nanoshells than cells exposed to IgG-targeted nanoshells, providing additional evidence that the increased contrast seen under darkfield may be specifically attributable to nanoshell targeting of the HER2 receptor. No differences were observed under darkfield or silver stain in HER2 and IgG-targeted nanoshells using the HER2-negative MCF7 breast cancer cell line (data not shown).
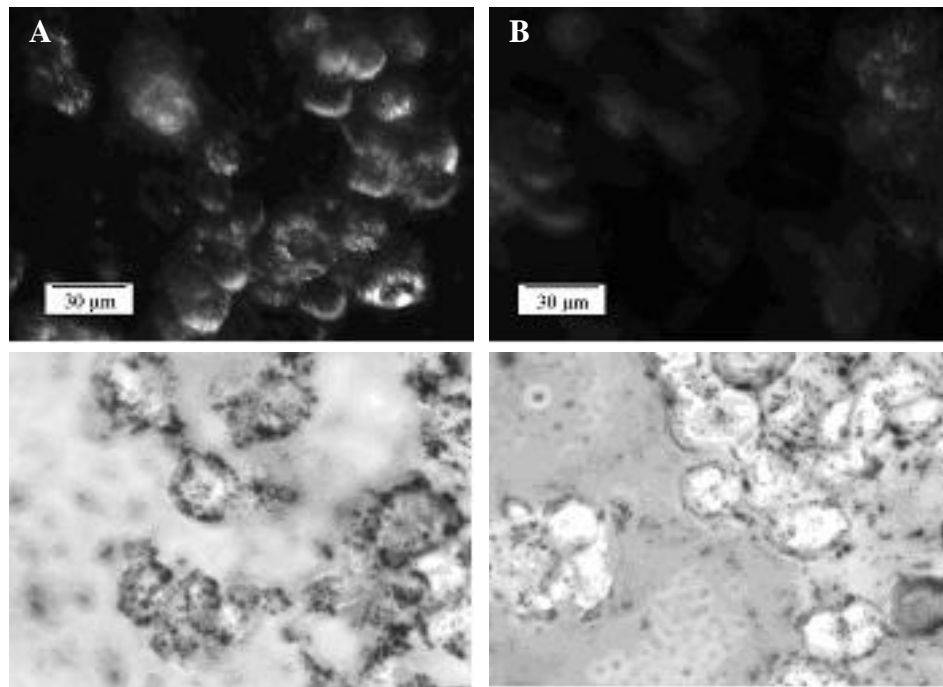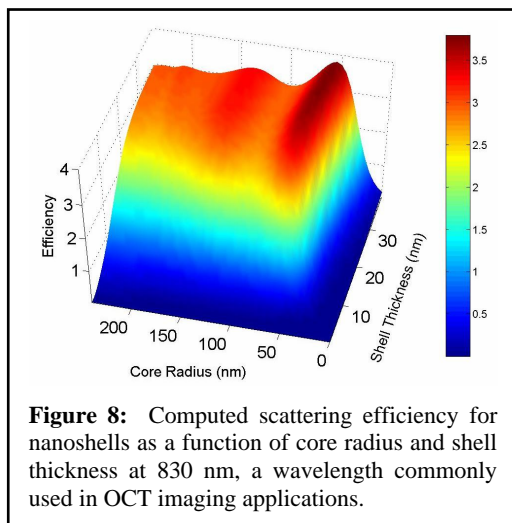
Figure 7: Darkfield (top row) and silver stain (bottom row) images of HER2-positive SKBR3 breast cancer cells exposed to nanoshells conjugated with either (A) HER2 (specific) or (B) IgG (non-specific) antibodies. As demonstrated here, it is possible to exploit the optical properties of predominantly-scattering nanoshells to image overexpressed HER2 in living cells. Similar scattering intensities were observed when comparing cells exposed to IgG-targeted nanoshells and cells not exposed to nanoshell bioconjugates.

3.2 Optical Coherence Tomography: Although darkfield microscopy is suitable for *in vitro* cell level imaging experiments, *in vivo* imaging applications will require the use of appropriate scattering-based imaging technologies such as optical coherence tomography (OCT). To assess the suitability of nanoshells for OCT applications, we computed the scattering efficiencies of gold nanoshells (in saline) over a range of core radii and shell thicknesses at 830 nm as shown in Figure 8. The promising scattering cross-sections (approximately several times the geometric cross-sections) computed for nanoshells based on physical parameters which could be readily fabricated encouraged further experimental investigation. To provide a basis for comparison of scattering efficiencies, a 150 nm diameter polystytene sphere in saline at 830 nm has a scattering efficiecy of 0.009; a 300 nm polystyrene sphere has an efficiency of 0.09. As a visual demonstration of the potential of nanoshells for OCT imaging applications, we imaged a 1 mm pathlength cuvette containing one of three solutions: saline, a microsphere-based scattering solution, or a solution of scattering nanoshells in water (Figure 9). The microsphere mixture was 0.1% solids by volume of 2 µm polystyrene spheres in saline at a concentration which provided a scattering coefficient, $\mu_s = 16$ cm^{-1} and an anisotropy factor, g = 0.96. mimicing a weakly scattering tissue. The nanoshell (100 nm radius/20 nm shell) concentration was ~10^9/cc. Figure 9 shows OCT images of the cuvette with saline, microspheres and nanoshells. The images consist of one hundred scans in the same lateral location. The average grayscale value inside the cuvette walls was calculated using the NIH Image Analysis Program. The OCT intensity is based on a log scale where black (0) corresponds to the noise floor of -102 dB and white (255) to –30 dB. To provide an approximate comparison of measured scattered intensity, the average grayscale

Figure 8: Computed scattering efficiency for nanoshells as a function of core radius and shell thickness at 830 nm, a wavelength commonly used in OCT imaging applications.

intensity for saline was 8 while the average intensity within the cuvette walls containing nanoshells the intensity was 95. It has already been further demonstrated that the potential of nanoshells as contrast agents for OCT can enhance *in vivo* imaging studies of mice after direct injection of scattering nanoshells into the vasculature via a tail vein catheter.[11]
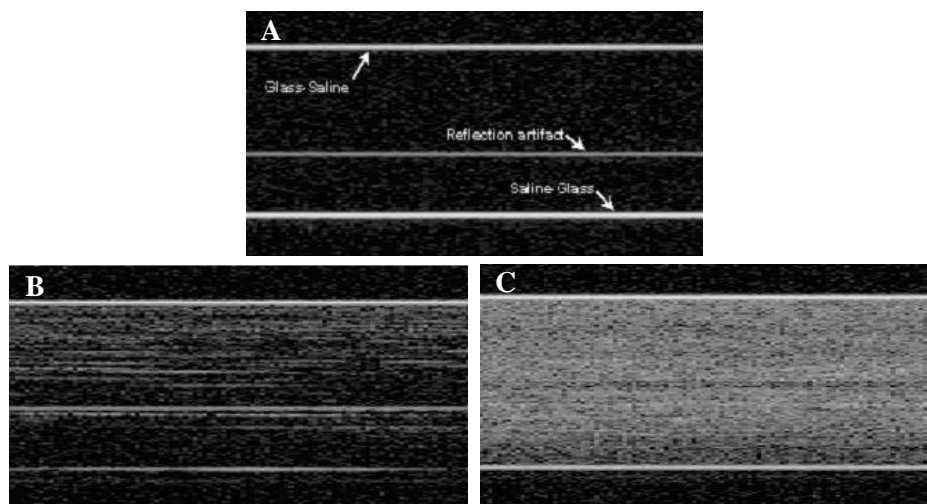

Figure 9: OCT (830 nm) images of a cuvette filled with saline (A), cuvette containing microspheres to approximate a scattering coefficient of 16 cm^{-1} (B), and cuvette containing nanoshells at a concentration of ~10^9/ml (C).

4. DISCUSSION

Future efforts will be directed towards coupling nanoshell-based molecular imaging technologies to some form of activated therapeutic intervention. Recent studies have considered a novel approach to cancer therapy based on the use of metal nanoshells as near-infrared (NIR) absorbers.[12] In biological tissue, photon transmissivity is highest in the NIR range due to low inherent scattering and absorption properties within the region. As an example of the intense absorption possible using nanoshells, the coventional NIR dye indocyanine green has an absorption cross-section of ~10^{-20} m^2 at ~800 nm while the cross-section of the absorbing nanoshells described in this article is ~4 x 10^{-14} m^2, an approximate millionfold increase in absorption cross-section.[12] By combining NIR absorbing nanoshells with an appropriate light source, it is possible to selectively induce photothermal destruction of cells and tumors treated with gold nanoshells. Nanoshell-mediated photothermal destruction of carcinoma cells is demonstrated in Figure 10. After laser exposure of 35 W/cm^2 for 7 minutes, all cells within the laser spot underwent photothermal destruction as assessed using calcein AM viability staining, an effect that was not observed in cells exposed to either nanoshells alone or NIR light alone. In addition, evidence of irreversible cell membra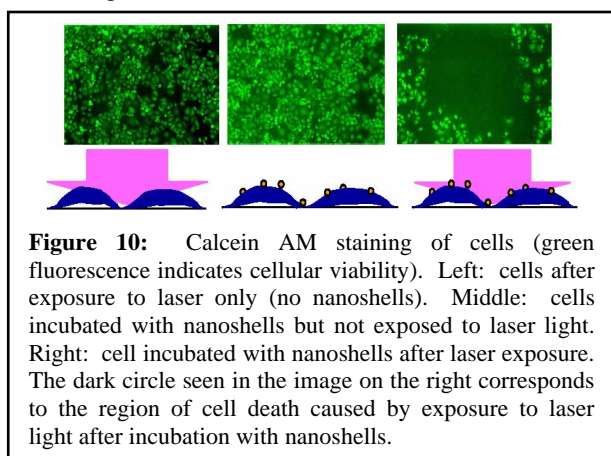ne damage was noted in the cells within the laser spot via imaging of fluorescent dextran dye (data not shown). This dye is normally impermeable to healthy cells. The dye was found in the intracellular space of cells exposed to both NIR nanoshells and the laser but was not observed in cells exposed to either the NIR nanoshells or the laser alone. The calcein AM stain and the fluorescent dextran stain can be used to indicate that the cells are not viable and that membrane damage has occurred but do not determine the underlying cause of cell death.

Figure 10: Calcein AM staining of cells (green fluorescence indicates cellular viability). Left: cells after exposure to laser only (no nanoshells). Middle: cells incubated with nanoshells but not exposed to laser light. Right: cell incubated with nanoshells after laser exposure. The dark circle seen in the image on the right corresponds to the region of cell death caused by exposure to laser light after incubation with nanoshells.

In the animal study by Hirsch and colleagues[12], absorbing nanoshells (~10^9/ml, 20-50 μl) were injected interstially (~5 mm) into solid tumors (~1 cm) in female SCID mice. Within thirty minutes of injection, tumor sites were exposed to NIR light (820 nm, 4 W/cm^2, 5 mm spot diameter, <6

min). Temperatures were monitored via phase-sensitive, phase-spoiled gradient-echo MRI. Magnetic resonance temperature imaging (MRTI) demonstrated that tumors reached temperatures which caused irreversible tumor damage ($\Delta T = 37.4 \pm 6.6°C$) within 4-6 minutes. Controls which were exposed to a saline injection rather than nanoshells experienced significantly reduced average temperatures after exposure to the same NIR light levels ($\Delta T < 10°C$). These average temperatures were obtained at a depth of ~2.5 mm below the surface. The MRTI findings demonstrated good agreement with gross pathology indications of tissue damage. Histological indications of thermal damage including coagulation, cell shrinkage, and loss of nuclear staining were noted in nanoshell-treated tumors; no such changes were found in control tissue. Silver enhancement staining provided further evidence of nanoshells in regions with thermal damage. The work described here established nanoshell and laser dosages which provided effective nanoshell-mediated photothermal therapy. Based on the parameters identified through these investigations, further survival studies have shown that mice with tumors treated with gold nanoshells and laser irradiation appeared healthy and tumor free for more than 90 days. Control animals were euthanized when tumors continued growing to a predetermined size.[13] Future work will also consider nanoshells conjugated to surface markers overexpressed within tumors.

5. CONCLUSIONS

Combining advances in biophotonics and nanotechnology offers the opportunity to significantly impact future strategies towards the detection and therapy of cancer. Currently, cancer is typically diagnosed after the discovery of either a palpable mass or based on relatively low resolution imaging of smaller, but still significantly sized tumors. In the future, it is likely that contrast agents targeted to molecular markers of disease will routinely provide information that enables characterization of disease susceptibility long before pathologic changes occur at the anatomic level. Currently, our ability to develop contrast agents is partly constrained by limitations in our understanding of the earliest molecular signatures of specific cancers. Although the process of identifying appropriate targets for detection and therapy is ongoing, there is a strong need to develop the technologies which will allow us to image these molecular targets *in vivo* as they are elucidated. In this article, we describe the optical properties and several emerging clinical applications of nanoshells, one class of nanostructures which is an attractive candidate for specific *in vivo* imaging and therapy applications. We have reviewed our preliminary work towards the development of nanoshell bioconjugates for molecular imaging applications and described an important new approach to photothermal cancer therapy. More extensive *in vivo* animal studies for both cancer imaging and therapy applications are currently underway in order to more thoroughly investigate both the potential and any limitations of nanoshell technologies. Additional studies are in progress to more thoroughly assess the biodistribution and biocompatibility of nanoshells. We believe there is tremendous potential for synergy between the rapidly developing fields of biophotonics and nanotechnology. Combining the tools of both fields – together with the latest advances in understanding the molecular origins of cancer – may provide a fundamentally new approach to detection and treatment of cancer, a disease responsible for over one quarter of all deaths in the United States today.

ACKNOWLEDGEMENTS

REFERENCES

1.   Sokolov, K., Follen, M., Aaron, J., Pavlova, I., Malpica, A., Lotan, R., and Richards-Kortum, R., "Real-time vital optical imaging of precancer using anti-epidermal growth factor receptor antibodies conjugated to gold nanoparticles", *Cancer Research.* **63**, 1999-2004 (2003).
2.   Bruchez, M., Moronne, M, Gin, P, Weiss, S, and Alivisatos, A.P., "Semiconductor labels as fluorescent biological labels" *Science.* **281**, 2013-2016 (1998).
3.   Chan, W.C.W. and Nie, S., "Quantum dot bioconjugates for ultrasensitive nonisotopic detection", *Science.* 281, 2016-2018 (1998).
4.   Akerman, M.E., Chan, W., Laakkonen, P., Bhatia, S.N., and Ruoslahti, E., "Nanocrystal targeting in vivo", *PNAS.* **99**, 12617-12621 (2002).

5.   Brongersma, M.L., "Nanoshells: gifts in a gold wrapper", *Nature Materials.* **2**, 296-297 (2003).
6.   Oldenburg, S.J., Averitt, R.D., Westcott, S.L., and Halas, N.J., "Nanoengineering of optical resonances", *Chemical Physics Letters.* **288**, 243-247 (1998).
7.   Averitt R.D., Sarkar D., and Halas N.J., "Plasmon resonance shifts of Au-coated Au2S nanoshells: insights into multicomponent nanoparticles growth", *Phys Rev Letters.* **78**, 4217-4220 (1997).
8.   Faulk, W.T., and Taylor G., "An immunocolloid method for the electron microscope", *Immunochemistry.* **8**, 1081-1083 (1971).
9.   Stober, W., Fink, A., and Bohn, E., "Controlled growth of monodisperse silica spheres in the micron size range" *Journal of Colloid and Interface Science.* **26**, 62-69 (1968).
10.   Duff, D.G., Baiker, A., and Edwards, P.P., "A new hydrosol of gold clusters. 1. formation and particle size variation", *Langmuir.* **9**, 2301-2309 (1993).
11.   Barton, J., Halas, N.J., West, J.K., and Drezek, R., "Nanoshells as an OCT contrast agent" *Proc. SPIE Int. Soc. Opt. Eng.* **5316**, 99 (2004).
12.   Hirsch, L.R., Stafford, R.J., Bankson, J.A., Sershen, S.R., Rivera, B., Price, R.E., Hazle, J.D., Halas, N.J., and West, J.L., "Nanoshell-mediated near-infrared thermal therapy of tumors under magnetic resonance guidance", *PNAS.* **100**, 13549-13554 (2003).
13.   O'Neal. D.P., Hirsch, L.R., Halas, N.J., Payne, J.D., West, J.L., "Photo-thermal tumor ablation in mice using near infrared-absorbing nanoparticles", *Cancer Lett.* **209**(2), 171-6 (2004).

Nanoshell-Enabled Photonics-Based Imaging and Therapy of Cancer

www.tcrt.org

Christopher Loo, B.S.[1]
Alex Lin, B.S.[1]
Leon Hirsch, B.S.[1]
Min-Ho Lee, M.S.[1]
Jennifer Barton, Ph.D.[2]
Naomi Halas, Ph.D.[3]
Jennifer West, Ph.D.[1]
Rebekah Drezek, Ph.D.[1,*]

[1]Department of Bioengineering
Rice University
P.O. Box 1892, MS-142
Houston, TX 77030

[2]Biomedical Engineering Program
University of Arizona
1501 N. Campbell
P.O. Box 245084
Tucson, Arizona 85724

[3]Departments of Electrical and
Computer Engineering
Rice University
P.O. Box 1892, MS-366
Houston, TX 77030

Metal nanoshells are a novel type of composite spherical nanoparticle consisting of a dielectric core covered by a thin metallic shell which is typically gold. Nanoshells possess highly favorable optical and chemical properties for biomedical imaging and therapeutic applications. By varying the relative the dimensions of the core and the shell, the optical resonance of these nanoparticles can be precisely and systematically varied over a broad region ranging from the near-UV to the mid-infrared. This range includes the near-infrared (NIR) wavelength region where tissue transmissivity peaks. In addition to spectral tunability, nanoshells offer other advantages over conventional organic dyes including improved optical properties and reduced susceptibility to chemical/thermal denaturation. Furthermore, the same conjugation protocols used to bind biomolecules to gold colloid are easily modified for nanoshells. In this article, we first review the synthesis of gold nanoshells and illustrate how the core/shell ratio and overall size of a nanoshell influences its scattering and absorption properties. We then describe several examples of nanoshell-based diagnostic and therapeutic approaches including the development of nanoshell bioconjugates for molecular imaging, the use of scattering nanoshells as contrast agents for optical coherence tomography (OCT), and the use of absorbing nanoshells in NIR thermal therapy of tumors.

Key words: Biophotonics, Contrast agents, Photothermal therapy, Nanotechnology.

Introduction

There is a significant clinical need for novel methods for detection and treatment of cancer which offer improved sensitivity, specificity, and cost-effectiveness. In recent years, a number of groups have demonstrated that photonics-based technologies are valuable in addressing this need. Optical technologies promise high resolution, noninvasive functional imaging of tissue at competitive costs. However, in many cases, these technologies are limited by the inherently weak optical signals of endogenous chromophores and the subtle spectral differences of normal and diseased tissue. Over the past several years, there has been increasing interest in combining emerging optical technologies with the development of novel exogenous contrast agents, designed to probe the molecular specific signatures of cancer, to improve the detection limits and clinical effectiveness of optical imaging. For instance, Sokolov *et al.* (1) recently demonstrated the use of gold colloid conjugated to antibodies to the epidermal growth factor receptor (EGFR) as scattering contrast agents for biomolecular optical imaging of cervical cancer cells and tissue specimens. In addition, optical imaging applications of nanocrystal bioconjugates have been described by multiple groups including Bruchez *et al.* (2), Chan and Nie (3), and Akerman *et al.* (4). More

* Corresponding Author:
Rebekah Drezek, Ph.D.
Email: drezek@rice.edu

Abbreviations: Near infrared (NIR), Optical coherence tomography (OCT), Polyethylene glycol (PEG)

recently, interest has developed in the creation of nanotechnology-based platform technologies which couple molecular specific early detection strategies with appropriate therapeutic intervention and monitoring capabilities.

Figure 1: Visual demonstration of the tunability of metal nanoshells.

Metal nanoshells are a new type of nanoparticle composed of a dielectric core such as silica coated with an ultrathin metallic layer, which is typically gold. Gold nanoshells possess physical properties similar to gold colloid, in particular, a strong optical absorption due to the collective electronic response of the metal to light. The optical absorption of gold colloid yields a brilliant red color which has been of considerable utility in consumer-related medical products, such as home pregnancy tests. In contrast, the optical response of gold nanoshells depends dramatically on the relative size of the nanoparticle core and the thickness of the gold shell. By varying the relative core and shell thicknesses, the color of gold nanoshells can be varied across a broad range of the optical spectrum that spans the visible and the near infrared spectral regions (Figure 1) (5, 6). Gold nanoshells can be made to either preferentially absorb or scatter light by varying the size of the particle relative to the wavelength of the light at their optical resonance. In Figure 2, a Mie scattering plot of the nanoshell plasmon resonance wavelength shift as a function of nanoshell composition for the case of a 60 nm
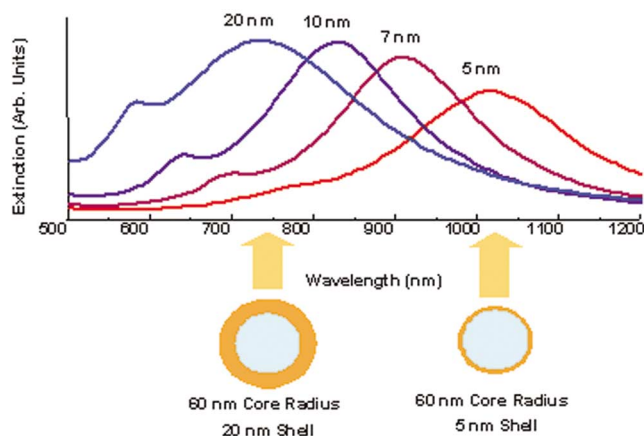

Figure 2: Optical resonances of gold shell-silica core nanoshells as a function of their core/shell ratio. Respective spectra correspond to the nanoparticles depicted beneath.

core gold/silica nanoshell is depicted. In this figure, the core and shell of the nanoparticles are shown to relative scale directly beneath their corresponding optical resonances. In Figure 3, a plot of the core/shell ratio versus resonance wavelength for a silica core/gold shell nanoparticle is displayed (6). The extremely agile "tunability" of the optical resonance is a property unique to nanoshells: in no other molecular or nanoparticle structure can the resonance of the optical absorption properties be so systematically "designed."
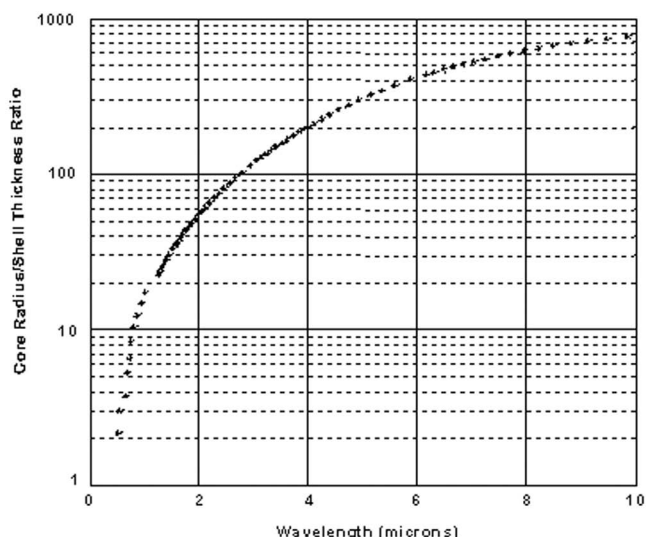

Figure 3: Core/shell ratio as a function of resonance wavelength for gold/silica nanoshells.

Halas and colleagues have completed a comprehensive investigation of the optical properties of metal nanoshells (7). Quantitative agreement between Mie scattering theory and the experimentally observed optical resonant properties has been achieved. Based on this success, it is now possible to predictively design gold nanoshells with the desired optical resonant properties and fabricate the nanoshell with the dimensions and nanoscale tolerances necessary to achieve these properties (6). The synthetic protocol developed for the fabrication of gold nanoshells is very simple in concept:

I.   grow or obtain silica nanoparticles dispersed in solution,

II. attach very small (1-2 nm) metal "seed" colloid to the surface of the nanoparticles via molecular linkages; these seed colloids cover the dielectric nanoparticle surfaces with a discontinuous metal colloid layer,

III. grow additional metal onto the "seed" metal colloid adsorbates via chemical reduction in solution.

This approach has been successfully used to grow both gold and silver metallic shells onto silica nanoparticles. Various stages in the growth of a gold metallic shell onto a function-

alized silica nanoparticle are shown in Figure 4. Figure 5 shows the optical signature of shell coalescence and growth for two different nanoshell core diameters.
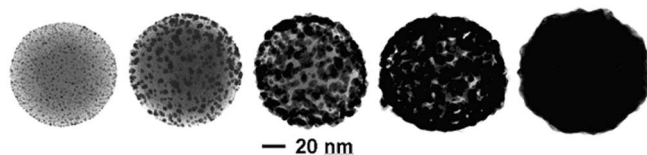

Figure 4: Transmission electron microscope images of gold/silica nanoshells during shell growth.
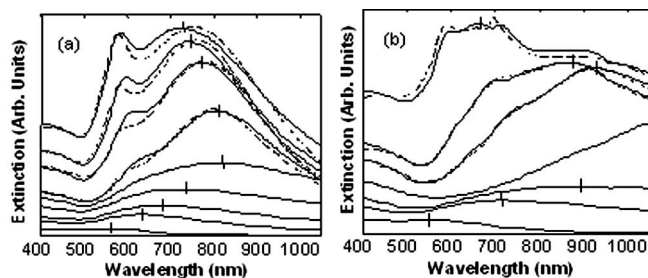

Figure 5: (**a**) Growth of gold shell on 120 nm diameter silica nanoparticle. The lower spectral curves follow the evolution of the optical absorption as coalescence of the gold layer progresses. Once the shell is complete, the peak absorbance is shifted to shorter wavelengths. Corresponding theoretical peaks are plotted with dashed lines. (**b**) Growth of gold shell on 340 nm diameter silica nanoparticles. Here the peak shifts are more pronounced with only the shoulder of the middle curve visible in our instrument range.

Based on the core/shell ratios that can be achieved with this protocol, gold nanoshells with optical resonances extending from the visible region to approximately 3 μm in the infrared can currently be fabricated. This spectral region includes the 800-1300 nm "water window" of the near infrared, a region of high physiological transmissivity which has been demonstrated as the spectral region best suited for optical bioimaging and biosensing applications. The optical properties of gold nanoshells, when coupled with their biocompatibility and their ease of bioconjugation, render these nanoparticles highly suitable for targeted bioimaging and therapeutic applications. By controlling the physical parameters of the nanoshells, it is possible to engineer nanoshells which primarily scatter light as would be desired for many imaging applications, or alternatively, to design nanoshells which are strong absorbers permitting photothermal-based therapy applications. The tailoring of scattering and absorption cross-sections is demonstrated in Figure 6 which shows sample spectra for two nanoshell configurations, one designed to scatter light and the other to preferentially absorb light.

Because the metal layer of gold nanoshells is grown using the same chemical reaction as gold colloid synthesis, the surfaces of gold nanoshells are virtually chemically identical to the surfaces of the gold nanoparticles universally used in bioconjugate applications. The use of gold colloid in bio-
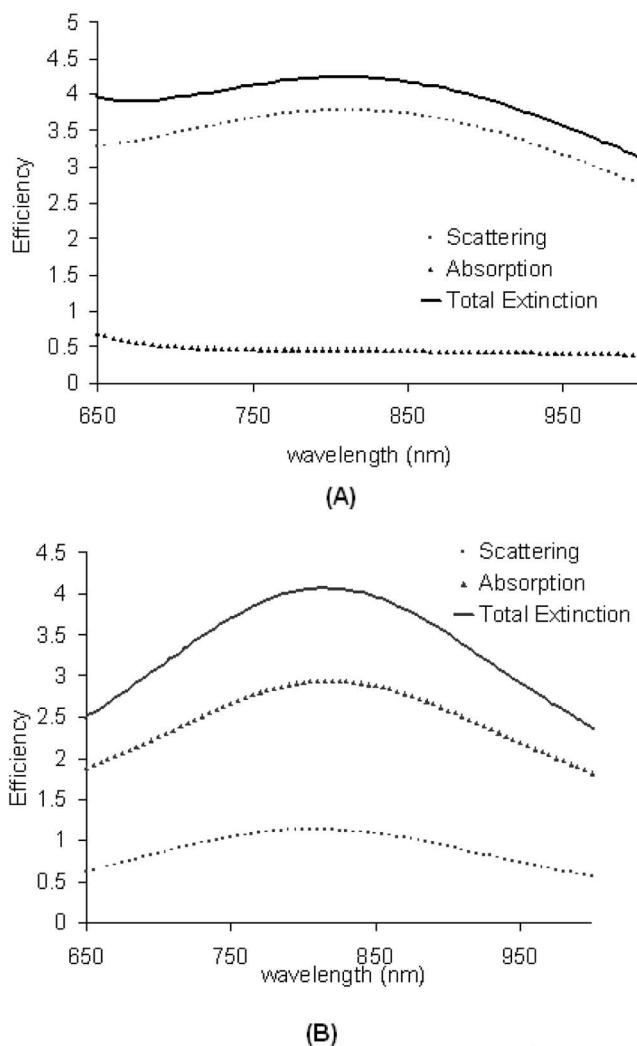

Figure 6: Nanoshells may be designed to be predominantly scattering or absorbing by tailoring the core and shell fabrication materials. To demonstrate this concept, the predicted scattering efficiency, absorption efficiency, and extinction are shown for two nanoshells: (**A**) a scattering configuration (core radius = 40 nm; shell thickness = 20 nm) (5) and (**B**) an absorbing configuration (core radius = 50 nm; shell thickness = 10 nm).

logical applications began in 1971 when Faulk and Taylor invented the immunogold staining procedure (8). Since that time, the labeling of targeting molecules, especially proteins, with gold nanoparticles has revolutionized the visualization of cellular or tissue components by electron microscopy. The optical and electron beam contrast qualities of gold colloid have provided excellent detection qualities for such techniques as immunoblotting, flow cytometry, and hybridization assays. Conjugation protocols exist for the labeling of a broad range of biomolecules with gold colloid, such as protein A, avidin, streptavidin, glucose oxidase, horseradish peroxidase, and IgG. Successful gold nanoshell conjugation with enzymes and antibodies has previously been demonstrated.

In this article, we present data demonstrating the potential of nanoshells for several biomedical applications including the use of nanoshell bioconjugates as biological labels for optical imaging, the development of nanoshell-based scattering contrast agents for optical coherence tomography, and the use of absorbing nanoshells for photothermal therapy of tumors.

Methods and Materials

Gold Nanoshell Fabrication

Cores of silica nanoparticles were fabricated as described by Stober *et al.* (9) in which tetraethyl orthosilicate was reduced in NH_4OH in ethanol Particles were sized with a Philips XL30 scanning electron microscope. Polydispersity of <10% was considered acceptable. Next, the silica surface was aminated by reaction with aminopropyltriethoxysilane in ethanol. Gold shells were grown using the method of Duff *et al.* (10). Briefly, small gold colloid (1-3 nm) was adsorbed onto the aminated silica nanoparticle surface. More gold was then reduced onto these colloid nucleation sites using potassium carbonate and $HAuCl_4$ in the presence of formaldehyde. Gold nanoshell formation and dimensions were assessed with a UV-VIS spectrophotometer and scanning electron microscopy (SEM). The nanoshells used in the darkfield scattering imaging studies described consisted of a 120 nm silica core radius with a 35 nm thick gold shell. The nanoshells used in the OCT imaging consisted of a 100 nm core radius and 20 nm thick shell. The nanoshells used in the therapy application described used a 60 nm core radius and a 10 nm thick shell which absorb light with an absorption peak at ~815 nm. The reader is referred to (6) for a detailed description of nanoshell synthesis procedures.

Antibody Conjugation

Ortho-pyridyl-disulfide-*n*-hydroxysuccinimide polyethylene glycol polymer (OPSS-PEG-NHS, MW=2000) was used to tether antibodies onto the surfaces of gold nanoshells. Using $NaHCO_3$ (100 mM, pH 8.5) OPSS-PEG-NHS was re-suspended to a volume equal to that of either HER2 (specific) or IgG (non-specific) antibodies. At this concentration, the concentration of polymer was in molar excess to the amount of HER2 or IgG antibody used. The reaction was allowed to proceed on ice overnight. Excess, unbound polymer was removed by membrane dialysis (MWCO = 10,000). PEGylated antibody (0.67 mg/mL) was added to nanoshells (~10^9 nanoshells/mL) for 1 hr to facilitate targeting. Unbound antibody was removed by centrifugation at 650 G, supernatant removal, and resuspension in potassium carbonate (2 mM). Following antibody conjugation, nanoshells surfaces were further modified with PEG-thiol (MW=5000, 1 μM) to block non-specific adsorption sites and to enhance biocompatibility.

Cell Culture

HER2-positive SKBr3 human mammary adenocarcinoma cells were cultured in McCoy's 5A modified medium supplemented with 10% FBS and antibiotics. Cells were maintained at 37° C and 5% CO_2.

Molecular Imaging, Cytotoxicity, and Silver Staining

SKBR3 cells were exposed to 8 μg/mL of bioconjugated nanoshells for 1 hr, washed with phosphate-buffered saline, and observed under darkfield microscopy, a form of microscopy sensitive only to scattered light. The calcein-AM live stain (Molecular Probes, 1 μM) was used to assess cell viability after nanoshell targeting. A silver enhancement stain (Amersham Pharmacia), a qualitative stain capable of detecting the presence of gold on cell surfaces, was used to assess cellular nanoshell binding. Cells incubated with targeted nanoshells were fixed with 2.5% glutaraldehyde, and exposed to silver stain for 15 minutes. Silver growth was monitored under phase-contrast, with further silver enhancement blocked by immersion in 2.5% sodium thiosulfate. Darkfield and silver stain images were taken with a Zeiss Axioskop 2 plus microscope equipped with a black-white CCD camera. All images were taken at 40X magnification under the same lighting conditions.

Optical Coherence Tomograhy (OCT)

Optical coherent tomography (OCT) is a state-of-the-art imaging technique which produces high resolution (typically 10-15 μm), real-time, cross-sectional images through biological tissues. The method is often described as an optical analog to ultrasound. OCT detects the reflections of a low coherence light source directed into a tissue and determines at what depth the reflections occurred. By employing a heterodyne optical detection scheme, OCT is able to detect very faint reflections relative to the incident power delivered to the tissue. In OCT imaging out of focus light is strongly rejected due to the coherence gating inherent to the approach. This permits deeper imaging using OCT than is possible using alternative methods such as reflectance confocal microscopy where the out of focus rejection achievable is far lower. In the OCT experiments described in this paper, a conventional OCT system with an 830 nm superluminescent diode was used to obtain m-scans of the cuvette (images with time as the x-axis and depth as the y-axis). The axial and lateral resolution of the OCT system were 16 μm and 12 μm, respectively. Each image required approximately 20 seconds to acquire. System parameters remained the same throughout the experiment.

In Vitro Photothermal Nanoshell Therapy

SKBr3 breast cancer cells were cultured in 24-well plates until fully confluent. Cells were then divided into two treat-

ment groups: nanoshells + NIR-laser and NIR-laser alone. Cells exposed to nanoshells alone or cells receiving neither nanoshells nor laser were used as controls. Nanoshells were prepared in FBS-free medium (2×10^9 nanoshells/mL). Cells were then irradiated under a laser emitting light at 820 nm at a power density of ~35 W/cm^2 for 7 minutes with or without nanoshells. After NIR-light exposure, cells were replenished with FBS-containing media and were incubated for an additional hour at 37° C. Cells were then exposed to the calcein-AM live stain for 45 minutes in order to measure cell viability. The calcein dye causes viable cells to fluoresce green. Fluorescence was visualized with a Zeiss Axiovert 135 fluorescence microscope equipped with a filter set specific for excitation and emission wavelengths at 480 and 535 nm, respectively. Membrane damage was assessed using an aldehyde-fixable fluorescein dextran dye. Cells were incubated for 30 min with the fluorescent dextran, rinsed, and immediately fixed with 5% glutaraldehyde. Photothermal destruction of cells was attributed to hyperthermia induced via nanoshell absorption of NIR light.

Results and Discussion

As an initial demonstration of the potential of nanoshells in cancer imaging and therapy, we designed and fabricated nanoshells suitable for both scattering and absorption-based photonics applications. For proof-of-principle imaging studies, we fabricated nanoshells with a 120 nm radius and 35 nm shell thickness. It should be noted that nanoshells over a broad range of sizes can be fabricated for scattering based imaging applications. Figure 7 displays the predicted scattering and absorption spectra for these nanoshells obtained using software extensively verifed against Mie theory which numerically computes optical spectra for gold nanoshells.
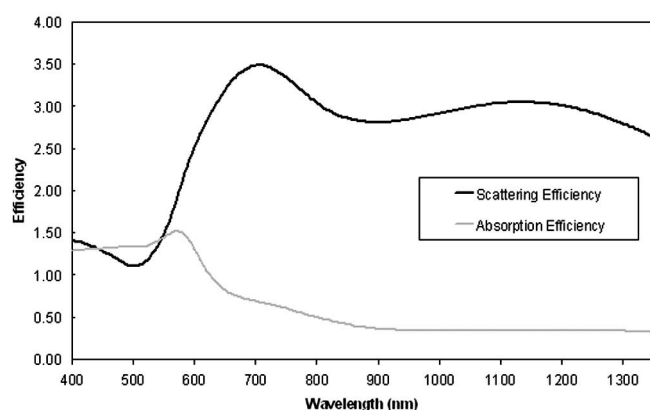

Figure 7: Scattering and absorbing properties of nanoshells with a 120 nm silica core radius and a 35 nm thick gold shell predicted analytically. Scattering maximum (705-710 nm) is 2.5-times greater than absorption maximum (570 nm) and extends into the NIR region. Nanoshell dimensions were assessed using scanning electron microscopy (SEM). Shell thickness was mathematically corroborated by matching experimental measurements to scattering theory and confirmed with SEM.

As Figure 7 demonstrates, these nanoshells scatter light strongly throughout the visible and near-infrared regions. This permits the same nanoshells to be used in light-based microscopy studies employing silicon CCDs and in NIR tissue imaging studies using reflectance confocal microscopy and OCT. We also fabricated nanoshells with a 100 nm radius and 20 nm shell thickness for OCT imaging. These nanoshells have very similar scattering and absorption spectra to the larger nanoshells; however, the scattering and absorption cross-sections are smaller due largely to the smaller particle size. In addition, smaller 60 nm radius
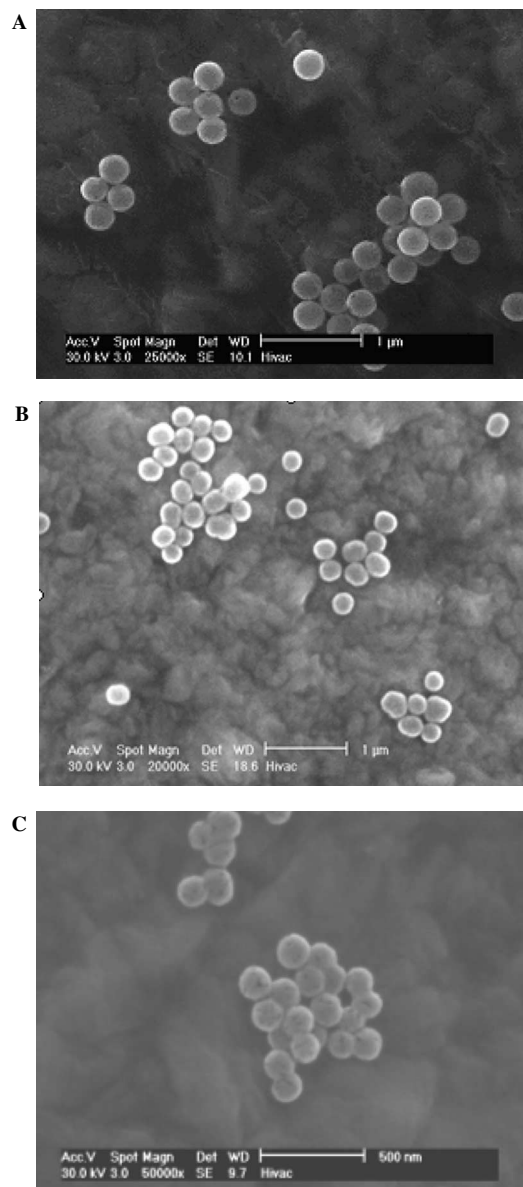

Figure 8: SEM images of nanoshells used in the described studies. The top image (**A**) shows the larger diameter nanoshells used in the darkfield imaging experiments. The middle image (**B**) shows the nanoshells used in the OCT experiments. The bottom image (**C**) show the smaller diameter nanoshells used for photothermal therapy applications. The scale bars in (**A**) and (**B**) are 1 μm while the scale bar in (**C**) is 500 nm.

nanoshells with a 10 nm shell were fabricated for photothermal therapy applications. Figure 8 shows SEM images of the nanoshells fabricated at all three sizes.

As an initial demonstration of the molecular imaging potential of nanoshell bioconjugates, we imaged carcinoma cells which overexpress HER2, a clinically significant molecular marker of breast cancer. Under darkfield microscopy, a form of microscopy sensitive only to scattered light, significantly increased optical contrast due to HER2 expression was observed in HER2-positive SKBR3 breast cancer cells targeted with HER2-labeled nanoshells compared to cells targeted by nanoshells non-specifically labelled with IgG (Figure 9). In addition, greater silver staining intensity was seen in cells exposed to HER2-targeted nanoshells than cells exposed to IgG-targeted nanoshells, providing additional evidence that the increased contrast seen under darkfield may be specifically attributable to nanoshell targeting of the HER2 receptor. No differences were observed under darkfield or silver stain in HER2 and IgG-targeted nanoshells using the HER2-negative MCF7 breast cancer cell line (data not shown). More extensive descriptions of imaging experiments using nanoshell bioconjugates are described in (11).

Although darkfield microscopy is suitable for *in vitro* cell level imaging experiments, *in vivo* imaging applications will require the use of appropriate scattering-based imaging technologies such as optical coherence tomography (OCT). To assess the suitability of nanoshells for OCT applications, we computed the scattering efficiencies of gold nanoshells (in

saline) over a range of core radii and shell thicknesses at 830 nm as shown in Figure 10. The promising scattering cross-sections (approximately several times the geometric cross-sections) computed for nanoshells based on physical parameters which could be readily fabricated encouraged further experimental investigation. To provide a basis for comparison of scattering efficiencies, a 150 nm diameter polystytene sphere in saline at 830 nm has a scattering efficiecy of 0.009; a 300 nm polystyrene sphere has an efficiency of 0.09. As a visual demonstration of the potential of nanoshells for OCT imaging applications, we imaged a 1 mm pathlength cuvette containing one of three solutions: saline, a microsphere-based scattering solution, or a solution of scattering nanoshells in water (Figure 10). The microsphere mixture was 0.1% solids by volume of 2 μm polystyrene spheres in saline at a concentration which provided a scattering coefficient, $\mu_{s,}$ = 16 cm^{-1} and an anisotropy factor, g = 0.96. The nanoshell (100 nm radius/20 nm shell) concentration was approximately 10^9/mL. Figure 10 shows OCT images of the cuvette with saline, microspheres and nanoshells. The images consist of one hundred scans in the same lateral location. The average grayscale value inside the cuvette walls was calculated using the NIH Image Analysis Program. The OCT intensity is based on a log scale where black (255) corresponds to the noise floor of -100 dB and white (0) to -40 dB. The average grayscale intensity for saline was 247 while the average intensity within the cuvette walls containing nanoshells the intensity was 160. Current efforts are more carefully exploring the potential of nanoshells as contrast agents for OCT through *in vivo* imaging studies of mice after direct injection of scattering nanoshells into the vasculature via a tail vein catheter (12).

Currently, our efforts are directed towards coupling our nanoshell-based molecular imaging technologies to some form of triggerable therapeutic intervention. Recent studies have considered a novel approach to cancer therapy based on the use of metal nanoshells as near-infrared (NIR) absorbers (13). In biological tissue, tissue transmissivity is highest in the NIR spectral range due to low inherent scattering and absorption properties within the region. Figure 7 demonstrates that nanoshells can be developed to highly scatter within this spectral regions; alternatively, nanoshells may be engineered to function as highly effective NIR absorbers as well. As an example of the intense absorption possible using nanoshells, the coventional NIR dye indocyanine green has an absorption cross-section of ~10^{-20} m^2 at ~800 nm while the cross-section of the absorbing nanoshells described in this article is ~4 × 10^{-14} m^2, an approximately millionfold increase in absorption cross-section (13). By combining NIR absorbing nanoshells with an appropri-
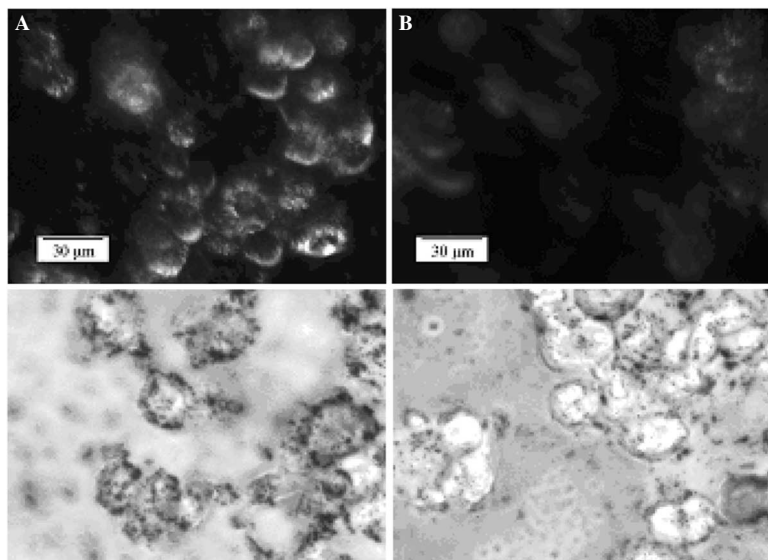

Figure 9: Darkfield (**top row**) and silver stain (**bottom row**) images of HER2-positive SKBR3 breast cancer cells exposed to nanoshells conjugated with either (**A**) HER2 (specific) or (**B**) IgG (non-specific) antibodies. As demonstrated here, it is possible to exploit the optical properties of predominantly-scattering nanoshells to image overexpressed HER2 in living cells. Similar scattering intensities were observed when comparing cells exposed to IgG-targeted nanoshells and cells not exposed to nanoshell bioconjugates.
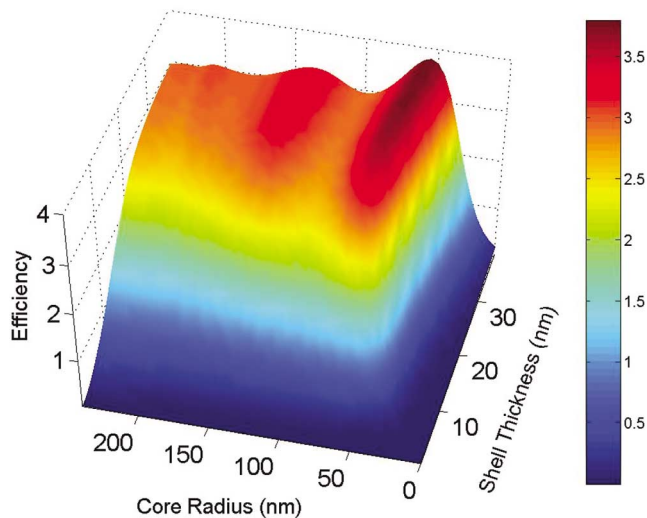
Figure 10: Computed scattering efficiency for nanoshells as a function of core radius and shell thickness at 830 nm, a wavelength commonly used in OCT imaging applications.

ate light source, it is possible to selectively induce photothermal destruction of cells and tumors treated with gold nanoshells. Nanoshell-mediated photothermal destruction of carcinoma cells is demonstrated in Figure 12. After laser exposure of 35 W/cm^2 for 7 minutes, all cells within the laser spot underwent photothermal destruction as assessed using calcein AM viability staining, an effect that was not observed in cells exposed to either nanoshells alone or NIR light alone. In addition, evidence of irreversible cell membrane damage was noted via imaging of the fluorescent dextran dye (date not shown). This dye is normally impermeable to healthy cells. However, the dye was found in the intracellular space of cells exposed to both NIR nanoshells and the laser but was not observed in cells exposed to either the NIR nanoshells or the laser alone. The calcein AM stain and the fluorescent dextran stain can be used to indicate that the cells are not viable and that membrane damage has occurred but do not determine the underlying cause of cell death.

In an animal study described in (13), absorbing nanoshells (10^9/ml, 20-50 µl) were injected interstially (~5 mm) into solid tumors (~1 cm) in female SCID mice. Within thirty minutes of injection, tumor sites were exposed to NIR light (820 nm, 4 W/cm^2, 5 mm spot diameter, <6 min). Temperatures were monitored via phase-sensitive, phase-spoiled gradient-echo MRI. Magnetic resonance temperature imaging (MRTI) demonstrated that tumors reached temperatures which caused irreversible tumor damage ($\Delta T = 37.4 \pm 6.6°$ C) within 4-6 minutes. Controls which were exposed to a saline injection rather than nanoshells experienced significantly reduced average temperatures after exposure to the same NIR light levels ($\Delta T < 10°$ C). These average temperatures were obtained at a depth of ~2.5 mm below the surface. The MRTI findings demonstrated good agree-
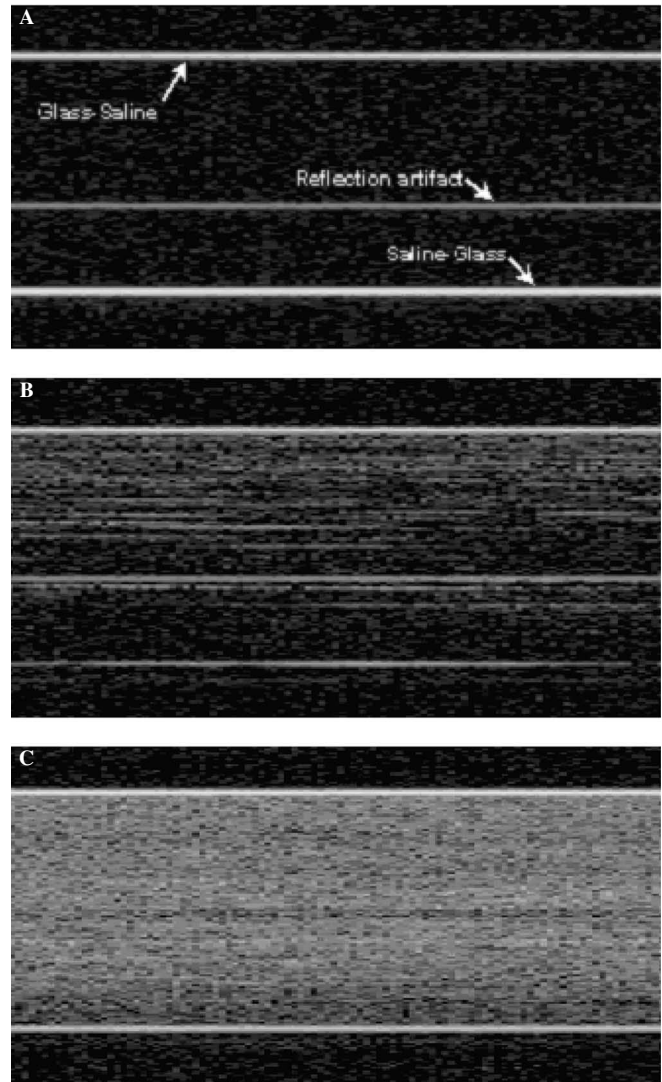

Figure 11: OCT (830 nm) images of a cuvette filled with saline (**A**), cuvette containing microspheres to approximate a scattering coefficient of 16 cm^{-1} (**B**), and cuvette containing nanoshells at a concentration of ~10^9/ml (**C**).

ment with gross pathology indications of tissue damage. Histological indications of thermal damage including coagulation, cell shrinkage, and loss of nuclear staining were noted in nanoshell-treated tumors; no such changes were found in
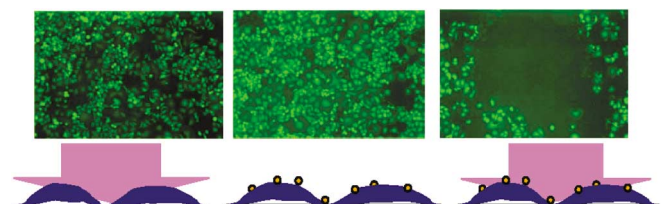
Figure 12: Calcein AM staining of cells (green fluorescence indiciates cellular viability). **Left:** cells after exposure to laser only (no nanoshells). **Middle:** cells incubated with nanoshells but not exposed to laser light. **Right:** cell incubated with nanoshells after laser exposure. The dark circle seen in the image on the right corresponds to the region of cell death caused by exposure to laser light after incubation with nanoshells.

control tissue. Silver enhancement staining provided further evidence of nanoshells in regions with thermal damage. The intial work described here established nanoshell and laser dosages which provided effective nanoshell-mediated photothermal therapy. Based on the parameters identified through these intial investigations, survival studies are now underway. Future work will also consider nanoshells conjugated to surface markers overexpressed within tumors.

Conclusions

Combining advances in biophotonics and nanotechnology offers the opportunity to significantly impact future strategies towards the detection and therapy of cancer. Today, cancer is typically diagnosed many years after it has developed usually after the discovery of either a palpable mass or based on relatively low resolution imaging of smaller but still significant masses. In the future, it is likely that contrast agents targeted to molecular markers of disease will routinely provide molecular information that enables characterization of disease susceptibility long before pathologic changes occur at the anatomic level. Currently, our ability to develop molecular contrast agents is at times constrained by limitations in our understanding of the earliest molecular signatures of specific cancers. Although the process of identifying appropriate targets for detection and therapy is ongoing, there is a strong need to develop the technologies which will allow us to image these molecular targets *in vivo* as they are elucidated. In this article, we describe the optical properties and several emerging clinical applications of nanoshells, one class of nanostructures which may provide an attractive candidate for specific *in vivo* imaging and therapy applications. We have reviewed our preliminary work towards the development of nanoshell bioconjugates for molecular imaging applications and described an important new approach to photothermal cancer therapy. More extensive *in vivo* animal studies for both cancer imaging and therapy applications are currently underway in order to investigate both the potential and limitations of nanoshell technologies. Additional studies are in progress to more thoroughly assess the biodistribution and biocompatibility of nanoshells used in *in vivo* imaging and therapy applications. We believe there is tremendous potential for synergy between the rapidly developing fields of biophotonics and nanotechnology. Combining the tools of both fields – together with the latest advances in understanding the molecular origins of cancer – may provide a fundamentally new approach to detection and treatment of cancer, a disease responsible for over one quarter of all deaths in the United States today.

Acknowledgements

References

1. Sokolov, K., Follen, M., Aaron, J., Pavlova, I., Malpica, A., Lotan, R., and Richards-Kortum, R. Real-time Vital Optical Imaging of Precancer Using Anti-epidermal Growth Factor Receptor Antibodies Conjugated to Gold Nanoparticles. *Cancer Research 63*, 1999-2004 (2003).
2. Bruchez, M, Moronne, M, Gin, P, Weiss, S, and Alivisatos, A. P. Semiconductor Labels as Fluorescent Biological Labels. *Science 281*, 2013-2016 (1998).
3. Chan, W. C. W. and Nie, S. Quantum Dot Bioconjugates for Ultrasensitive Nonisotopic Detection. *Science 281*, 2016-2018 (1998).
4. Akerman, M. E., Chan, W., Laakkonen, P., Bhatia, S. N., and Ruoslahti, E. Nanocrystal Targeting *In Vivo*. *PNAS. 99*, 12617-12621 (2002).
5. Brongersma, M. L. Nanoshells: Gifts in a Gold Wrapper. *Nature Materials 2*, 296-297 (2003).
6. Oldenburg, S. J., Averitt, R. D., Westcott, S. L., and Halas, N. J. Nanoengineering of Optical Resonances. *Chemical Physics Letters 288*, 243-247 (1998).
7. Averitt R. D., Sarkar D., and Halas N. J. Plasmon Resonance Shifts of Au-coated Au2S Nanoshells: Insights into Multicomponent Banoparticles Growth. *Phys. Rev. Letters 78*, 4217-4220 (1997).
8. Faulk, W. T., and Taylor G. An Immunocolloid Method for the Electron Microscope. *Immunochemistry 8*, 1081-1083 (1971).
9. Stober, W., Fink, A., and Bohn, E. Controlled Growth of Monodisperse Silica Spheres in the Micron Size Range. *Journal of Colloid and Interface Science 26*, 62-69 (1968).
10. Duff, D. G., Baiker, A., and Edwards, P. P. A New Hydrosol of Gold Clusters. 1. Formation and Particle Size Variation. *Langmuir 9*, 2301-2309 (1993).
11. Loo, C. H., Hirsch, L. R, West, J. L., Halas, N. J. & Drezek, R. A. Molecular Imaging in Living Cells Using Nanoshell Bionconjugates. *Nanoletters*. In review (2004).
12. Barton, J., Romanowski, M., Halas, N., and Drezek, R. Nanoshells as an OCT Contrast Agent. *Proceedings of SPIE 5316*. In press (2004).
13. Hirsch, L. R., Stafford, R. J., Bankson, J. A., Sershen, S. R., Rivera, B., Price, R. E., Hazle, J. D., Halas, N. J., and West, J. L. Nanoshell-mediated Near-infrared Thermal Therapy of Tumors Under Magnetic Resonance Guidance. *PNAS. 100*, 13549-13554 (2003).

Date Received: December 22, 2003

ELSEVIER

Photo-thermal tumor ablation in mice using near infrared-absorbing nanoparticles

D. Patrick O'Neal[a], Leon R. Hirsch[b], Naomi J. Halas[c],
J. Donald Payne[a], Jennifer L. West[b,*]

[a]Nanospectra Biosciences, Inc., 8285 El Rio Suite #130, Houston, TX 77054, USA
[b]Department of Bioengineering, Rice University, P.O. Box 1892, MS-142, Houston, TX 77251-1892, USA
[c]Department of Electrical and Computer Engineering, Rice University, P.O. Box. 1892, MS-366 77251-1892 USA

Abstract

The following study examines the feasibility of nanoshell-assisted photo-thermal therapy (NAPT). This technique takes advantage of the strong near infrared (NIR) absorption of nanoshells, a new class of gold nanoparticles with tunable optical absorptivities that can undergo passive extravasation from the abnormal tumor vasculature due to their nanoscale size. Tumors were grown in immune-competent mice by subcutaneous injection of murine colon carcinoma cells (CT26.WT). Polyethylene glycol (PEG) coated nanoshells ($\approx$ 130 nm diameter) with peak optical absorption in the NIR were intravenously injected and allowed to circulate for 6 h. Tumors were then illuminated with a diode laser (808 nm, 4 W/cm^2, 3 min). All such treated tumors abated and treated mice appeared healthy and tumor free > 90 days later. Control animals and additional sham-treatment animals (laser treatment without nanoshell injection) were euthanized when tumors grew to a predetermined size, which occurred 6–19 days post-treatment. This simple, non-invasive procedure shows great promise as a technique for selective photo-thermal tumor ablation.
© 2004 Elsevier Ltd. All rights reserved.

Keywords: Hyperthermia; Nanotechnology; Nanoshell; Near infrared; Laser; Minimally invasive therapy

1. Introduction

The destruction of solid tumors using hyperthermia has been under investigation for some time. Previously investigated thermal therapies have employed a variety of heat sources including laser light, [1–4] focused ultrasound, [5] and microwaves [6–8].

The benefits of thermal therapeutics over conventional resection are numerous; most approaches are minimally or non-invasive, relatively simple to perform, and have the potential of treating embedded tumors in vital regions where surgical resection is not feasible. However, in order to reach underlying tumors or to treat large tumors, the activating energy source must sufficiently penetrate healthy tissues. Unfortunately, simple heating techniques have trouble discriminating between tumors and surrounding healthy tissues, and often heat intervening tissue

* Corresponding author. Tel.: +1-713-348-5955; fax: +1-713-348-5877.
E-mail address: jwest@rice.edu (J.L. West).

between the source and the target site. Several groups have investigated treatment of tumors via hyperthermia using deep penetrating near infrared (NIR) lasers with or without contrast enhancing agents (indocyanine green); however, success with current systems has been modest [1,9,10].

This study introduces a new laser-induced thermal therapy employing systemically delivered, NIR absorbing nanoparticles called nanoshells. Nanoshells are a new class of optically tunable nanoparticles composed of a dielectric core (silica) coated with an ultrathin metallic layer (gold) [11]. By adjusting the relative core and shell thickness, nanoshells can be manufactured to absorb or scatter light at a desired wavelength across visible and NIR wavelengths. This optical tunability permits the fabrication of nanoshells with a peak optical absorption in the NIR, a region of light where optical penetration through tissue is optimal [12]. Furthermore, the metal shell of the nanoshell converts absorbed light to heat with an efficacy and stability that far exceeds that of conventional dyes investigated earlier. Nanoshells possess absorption cross sections that are six orders of magnitude larger than indocyanine green, making this material a much stronger NIR absorber, and therefore a more effective photothermal coupling agent [13]. In addition, a nanoshell's absorption properties are dependent upon the material's rigid metallic structure rather than the more labile molecular orbital electronic transitions of conventional dyes. This makes nanoshells less susceptible to photobleaching, a problem commonly associated with dyes. The efficacy of nanoshells as a NIR absorber has already been demonstrated in a series of in vivo magnetic resonance thermal imaging (MRTI) studies examining temperature profiles of nanoshell-loaded tumors irradiated with NIR light. These studies found nanoshells absorb NIR light and generate increased temperatures sufficient to produce irreversible photo-thermal damage to subcutaneous tumors [14].

As a biomaterial, nanoshells are composed of elements generally understood to be biocompatible. The metal surface of the nanoshells employed here consists of gold, an inert metal well known for its biocompatibility. To further improve biocompatibility, 'stealthing' polymers like poly(ethylene glycol) (PEG) can be grafted to nanoshell surfaces using simple molecular self assembly techniques [15]. It has been demonstrated that stealthing liposomes as well as other biomolecules and materials with PEG suppresses immunogenic responses, improving blood circulation times and overall material/implant performance [16,17].

Substantial prior research has investigated the delivery of macromolecules and small particles through the tumor vasculature. It has been demonstrated that macromolecules and small particles in the 60–400 nm size range will extravasate and accumulate in tumors [18–22] via a passive mechanism referred to as the 'enhanced permeability and retention' (EPR) effect [23,24]. This behavior has been attributed to the leaky nature of tumor vessels, which contain wide interendothelial junctions, an incomplete or absent basement membrane, a dysfunctional lymphatic system, and large numbers of transendothelial channels [19,25]. NIR absorbing nanoshells can be manufactured within size ranges that should demonstrate the same preferential, size-dependent accumulation in tumors via the EPR effect.

This report describes a new technique that exploits the optical, chemical and physical properties of nanoshells in conjunction with the deep penetrating properties of NIR light for a targeted, minimally invasive photothermal therapy. The principle goal of this project was to determine the efficacy of NAPT using nanoshells fabricated of an appropriate size for extravasation into tumors with optical absorption in the NIR. Subcutaneous tumors were grown in mice, solutions of PEG-coated (or 'PEGylated') nanoshells were injected intravenously, and accumulation within the tumor was monitored. Nanoshell-treated tumors and nanoshell-free shams were then exposed to NIR light. Resultant heating and therapeutic efficacy was assessed via surface temperature measurements, monitoring of tumor growth/regression, and animal survival times.

2. Materials and methods

2.1. Synthesis of thiolated polyethylene glycol (PEG-SH)

PEG with a terminal thiol group (PEG-SH) was synthesized by reacting PEG-amine (MW 5000, chromatographically pure, Nektar) with

2-iminothiolane (Sigma) for 1 hour. The product was then dialyzed (MWCO 3500 dialysis cassette, Pierce) against deionized (DI) H_2O for 6–8 hours to remove excess reagent. The PEG-SH yield was determined colorimetrically at 412 nm after reaction with Ellman's Reagent (5,5′-Dithio-bis(2-Nitrobenzoic Acid), Sigma). The product was stored in aliquots at −20 °C.

2.2. Gold-silica nanoshell fabrication

Nanoshells were fabricated as previously described [26]. Briefly, 110 nm diameter silica nanoparticles were obtained (MP-1040, Nissan Chemical America Corporation) and suspended in ethanol. The particle surface was then terminated with amine groups by reaction with 3-aminopropyltriethoxysilane (APTES, 97 + %, Avocado Research Chemicals, Ltd). Very small gold colloid (1–3 nm dia.) was grown using the method of Duff, et al. [27]. This colloid was aged for 4–14 days at 6 °C and then concentrated using a rotary evaporator. The aminated silica particles were then added to the gold colloid suspension. Gold colloid adsorbs to the amine groups on the silica surface resulting in a silica nanoparticle covered with islands of gold colloid. Gold-silica nanoshells were then grown by reacting $HAuCl_4$ (Sigma-Aldrich) with the silica-colloid particles in the presence of formaldehyde. This process reduces additional gold onto the colloid adsorbed the silica particle surface. These colloidal islands serve as nucleation sites, causing the surface colloid to grow, eventually coalescing with neighboring colloid, to form a complete metal shell. Nanoshell optical properties were assessed using a UV–Vis spectrophotometer (Genesys 5, Spectronic, Inc.). The resulting nanoshell solutions possessed an 8–10 nm thick gold shell, generating a peak optical absorption at 805–810 nm. Nanoshell surfaces were coated with PEG by combining PEG-SH (25 μM final concentration) with nanoshells (8×10^9 nanoshells/ml) in DI water for 1 hr, followed by centrifugation to remove residual PEG-SH from the nanoshell formulation. Prior to injection, PEGylated nanoshells were resuspended at 2.0×10^{11} nanoshells/ml concentration in sterile 0.9% saline solution and sterilized using a 0.22 μm syringe filter.

2.3. Tumor inoculation

All animals were handled and cared for in accordance with the 'Guide for the Care and Use of Laboratory Animals' [28] 25 female albino BALB/cAnNHsd mice (5–6 weeks age, 15–20 g, Harlan Sprague–Dawley, Indianapolis, IN) were obtained. Each was shaved on the right dorsal flank prior to subcutaneous inoculation with 1.5×10^5 (50 μl injection volume) CT26.WT murine colon carcinoma tumor cells (ATCC) [29].

2.4. Nanoshell injection and laser treatment

Mice were selected for treatment when the subcutaneous tumors reached 3–5.5 mm diameter as measured with a digital caliper (8–16 days post-inoculation). A 5.5 mm tumor diameter was selected as the maximum possible treatment size due to the spot size of the collimated laser. Seven of the mice had two tumors, and 17 had one. These were randomly distributed between 3 groups. Prior to each nanoshell injection, each mouse was anesthetized via intraperitoneal avertin injection (120 mg/kg, or 20 μl/g body weight, 1.2% solution). 100 μl of the 2.4×10^{11} nanoshells/ml solution was then injected via the tail vein for mice in the treatment group. For the sham treatment group, a 100 μl 0.9% sterile saline injection was substituted for the nanoshells suspension. The control group received no intravenous injections or subsequent laser treatment. Laser treatments on the nanoshell treatment and sham treatment groups were performed 6 h after injection to allow the systemically delivered nanoshells time to accumulate in the tumors. The skin at the tumor site was swabbed with polyethylene glycol (Aldrich) as an index matching agent to maximize penetration of light into the tissue. Tumors in the nanoshell and sham treatment groups were exposed to NIR light (808 nm diode laser, 800 mW, Power Technologies, Alexander, AR; 600 μm fiber optic patch cable to a collimating lens, 1:1 Optical Imaging Accessory, Coherent, Inc., Santa Clara, CA) at 4 W/cm^2 for 3 min. An additional laser treatment was performed on one mouse in the nanoshell treatment group at a spot 3 mm away from the tumor to determine if abnormal heating occurred in nearby normal tissue where nanoshells should not have accumulated.
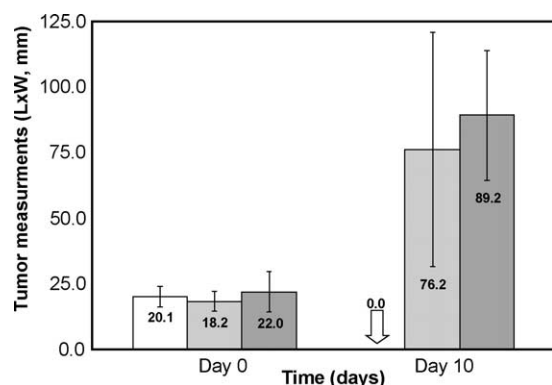
Fig. 1. Mean tumor size measured on treatment day and 10 days later for 25 tumors. All tumors which were treated using NAPT showed complete necrosis by day 10. One standard deviation is shown. NAPT treatment group ($n = 7$), sham treatment group ($n = 8$), untreated controls ($n = 9$).

During the NIR treatments, the cutaneous temperature was measured with a handheld infrared thermometer (Omegascope OS530L-CF, Omega Engineering, Stamford, CT) which integrates thermal measurements across a 5 mm diameter spot. Post-treatment tumor size measurements were taken daily using a digital caliper. Survival time was also monitored, and animals were euthanized via trifluoroethane asphyxiation when tumor diameter reached 10 mm.

Statistical analysis was performed on the three groups by comparing the means of the tumor sizes at day 0 and day 10 post-treatment and computing the level of significant difference as measured by the p value. Similarly, p values were computed to compare the mean surface temperatures measured for the treatment and sham treatment groups. The survival time comparison for the three groups was augmented with a Kaplan-Meier survival analysis which generates confidence intervals for survival times.

3. Results and discussion

Surface temperature measurements were obtained during each NIR laser treatment for the 15 mice in the nanoshell and sham treatment groups as described. The surface temperature is a surrogate for temperatures achieved within the tumors of the NAPT treatment group as well as a measurement of thermal absorption by skin and tissue in both laser treated groups. By 30 s, the mean temperature of

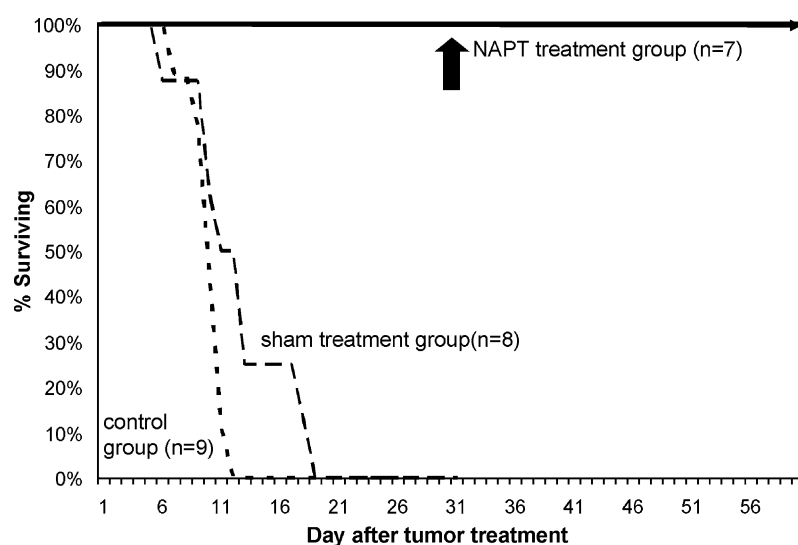Fig. 2. A survival time plot for the three groups for the first 60 days. The mean survival time for the control group was 10.1 days with a 95% confidence interval of 9.2–11.1 days. The mean survival time for the sham group was 12.5 days with a 95% confidence interval of 9.5–15.5 days. By 18 days the mean survival time of the treatment group was significantly higher ($P < 0.001$) compared to either the control or the sham group.

the laser/nanoshell treated tumors ($\sim 50\,^{\circ}$C) was significantly higher than NIR treated but nanoshell-free controls ($P < 0.0001$). For comparison, a NIR treatment was applied to a healthy skin area several mm away from the tumor site on a nanoshell treated animal. In this non-tumor location, thermal responses were identical to those observed in animals that had not received a nanoshell treatment. This suggested that a preferential accumulation of nanoshells via the EPR effect was sufficient to generate a therapeutic result at the tumor site but not sufficient to affect damage to surrounding healthy tissues.

Tumor size and animal survival were monitored for 90 days following treatment. Within 10 days of nanoshell treatment, complete resorption of the tumor was observed. At $90 +$ days post-treatment, all mice remained healthy and free of tumors. Meanwhile, tumors in both the sham and control groups continued to grow rapidly (Fig. 1). Mice were euthanized when tumor diameter exceeded 10 mm (corresponding to $>5\%$ body weight). All control mice were euthanized by day 12 (mean survival time 10.1 days) and all mice in the sham group were euthanized by day 19 (mean survival time 12.5 days) (Fig. 2).

The goals of this study were to determine if nanoshell-assisted photo-thermal ablation would arrest the growth of tumors grown in mice. NAPT-treated tumors displayed complete regression and these mice remained healthy and tumor-free >90 days following treatment. Further research is ongoing to optimize treatment parameters and to investigate the mechanisms involved in tumor regression following NAPT treatment. These studies will include analysis of nanoshell biodistribution and histological assessment of tissue damage.

References

[1] W.R. Chen, R.L. Adams, R. Carubelli, R.E. Nordquist, Laser-photosensitizer assisted immunotherapy: a novel modality for cancer treatment, Cancer Lett. 115 (1997) 25–30.

[2] M. Castren-Persons, T. Schroder, O.J. Ramo, P. Puolakkainen, E. Lehtonen, Contact Nd:YAG laser potentiates the tumor cell killing effect of hyperthermia, Lasers Surg. Med. 11 (1991) 595–600.

[3] S.M. Waldow, P.R. Morrison, L.I. Grossweiner, Nd:YAG laser-induced hyperthermia in a mouse tumor model, Lasers Surg. Med. 8 (1988) 510–514.

[4] C.M. Philipp, E. Rohde, H.P. Berlien, Nd:YAG laser procedures in tumor treatment, Semin. Surg. Oncol. 11 (1995) 290–298.

[5] F.A. Jolesz, K. Hynynen, Magnetic resonance image-guided focused ultrasound surgery, Cancer J. 8 (suppl. 1) (2002) S100–S12.

[6] G.S. Gazelle, S.N. Goldberg, L. Solbiati, T. Livraghi, Tumor ablation with radio-frequency energy, Radiology 217 (2000) 633–646.

[7] A.N. Mirza, B.D. Fornage, N. Sneige, H.M. Kuerer, L.A. Newman, F.C. Ames, S.E. Singletary, Radiofrequency ablation of solid tumors, Cancer J. 7 (2001) 95–102.

[8] T. Seki, M. Wakabayashi, T. Nakagawa, M. Imamura, T. Tamai, A. Nishimura, et al., Percutaneous microwave coagulation therapy for patients with small hepatocellular carcinoma: comparison with percutaneous ethanol injection therapy, Cancer 85 (1999) 1694–1702.

[9] M. Prudhomme, J. Tang, S. Rouy, G. Delacretaz, R.P. Salathe, G. Godlewski, Interstitial diode laser hyperthermia in the treatment of subcutaneous tumor, Lasers Surg. Med. 19 (1996) 445–450.

[10] W.R. Chen, R.L. Adams, A.K. Higgins, K.E. Bartels, R.E. Nordquist, Photothermal effects on murine mammary tumors using indocyanine green and an 808-nm diode laser: an in vivo efficacy study, Cancer Lett. 98 (1996) 169–173.

[11] S.J. Oldenburg, J.B. Jackson, S.L. Westcott, N.J. Halas, Infrared extinction properties of gold nanoshells, Appl. Phys. Lett. 111 (1999) 2897.

[12] R. Weissleder, A clearer vision for in vivo imaging, Nat. Biotechnol. 19 (2001) 316–317.

[13] M.L.J. Landsman, G. Kwant, G.A. Mook, W.G. Zijlstra, Light-absorbing properties, stability, and spectral stabilization of indocyanine green, J. Appl. Physiol. 40 (1976) 575–583.

[14] L.R. Hirsch, R.J. Stafford, J.A. Bankson, S.R. Sershen, B. Rivera, R.E. Price, Nanoshell-mediated near infrared thermal therapy of tumors under MR guidance, Proc. Natl Acad. Sci. 100 (23) (2003) 13549–13554.

[15] L.R. Hirsch, J.B. Jackson, A. Lee, N.J. Halas, J.L. West, A whole blood immunoassay using gold nanoshells, Anal. Chem. 75 (2003) 2377–2381.

[16] A.M. Chen, M.D. Scott, Current and future applications of immunological attenuation via pegylation of cells and tissue, BioDrugs 15 (2001) 833–847.

[17] J.M. Harris, N.E. Martin, M. Modi, Pegylation: a novel process for modifying pharmacokinetics, Clin. Pharmacokinet. 40 (2001) 539–551.

[18] G. Kong, R.D. Braun, M.W. Dewhirst, Hyperthermia enables tumor-specific nanoparticle delivery: effect of particle size, Cancer Res. 60 (2000) 4440–4445.

[19] O. Ishida, K. Maruyama, K. Sasaki, M. Iwatsuru, Size-dependent extravasation and interstitial localization of polyethyleneglycol liposomes in solid tumor-bearing mice, Int. J. Pharm. 190 (1999) 49–56.

[20] D.C. Litzinger, A.M. Buiting, N. van Rooijen, L. Huang, Effect of liposome size on the circulation time and intraorgan distribution of amphipathic poly(ethylene glycol)-containing liposomes, Biochim. Biophys. Acta 1190 (1994) 99–107.

[21] F. Yuan, M. Leunig, S.K. Huang, D.A. Berk, D. Papahadjo-poulos, R.K. Jain, Microvascular permeability and interstitial penetration of sterically stabilized (stealth) lipo-somes in a human tumor xenograft, Cancer Res. 54 (1994) 3352–3356.

[22] S.K. Hobbs, W.L. Monsky, F. Yuan, W.G. Roberts, L. Griffith, V.P. Torchilin, R.K. Jain, Regulation of transport pathways in tumor vessels: role of tumor type and microenvironment, Proc. Natl Acad. Sci. USA 95 (1998) 4607–4612.

[23] H. Maeda, The enhanced permeability and retention (EPR) effect in tumor vasculature: the key role of tumor-selective macromolecular drug targeting, Adv. Enzyme Regul. 41 (2001) 189–207.

[24] H. Maeda, J. Fang, T. Inutsuka, Y. Kitamoto, Vascular permeability enhancement in solid tumor: various factors, mechanisms involved and its implications, Int. Immunophar-macol. 3 (2003) 319–328.

[25] H.F. Dvorak, J.A. Nagy, J.T. Dvorak, A.M. Dvorak, Identification and characterization of the blood vessels of solid tumors that are leaky to circulating macromolecules, Am. J. Pathol. 133 (1988) 95–109.

[26] S.J. Oldenberg, R.D. Averitt, S.L. Westcott, N.J. Halas, Nanoengineering of Optical Resonances, Chem. Phys. Lett. 28 (1998) 243–247.

[27] D.G. Duff, A. Baiker, A new hydrosol of gold clusters. 1. Formation and particle size variation, Langmuir 9 (1993) 2301.

[28] National Research Council, Guide for the Care and Use of Laboratory Animals, National Academy Press, Washington, DC, 1996.

[29] M. Wang, V. Bronte, P.W. Chen, L. Gritz, D. Panicali, S.A. Rosenberg, N.P. Restifo, Active immunotherapy of cancer with a nonreplicating recombinant fowlpox virus encoding a model tumor-associated antigen, J. Immunol. 154 (1995) 4685–4692.

Optically tunable nanoparticle contrast agents for early cancer detection: model-based analysis of gold nanoshells

Alex W. H. Lin
Nastassja A. Lewinski
Jennifer L. West
Rice University
Department of Bioengineering
PO Box 1892-MS 142
Houston, Texas 77251

Naomi J. Halas
Rice University
Department of Electrical and Computer Engineering
Houston, Texas 77251

Rebekah A. Drezek
Rice University
Department of Bioengineering
PO Box 1892-MS 142
Houston, Texas 77251
E-mail: drezek@rice.edu

Abstract. Many optical diagnostic approaches rely on changes in scattering and absorption properties to generate optical contrast between normal and diseased tissue. Recently, there has been increasing interest in using exogenous agents to enhance this intrinsic contrast with particular emphasis on the development for targeting specific molecular features of disease. Gold nanoshells are a class of core-shell nanoparticles with an extremely tunable peak optical resonance ranging from the near-UV to the mid-IR wavelengths. Using current chemistries, nanoshells of a wide variety of core and shell sizes can easily be fabricated to scatter and/or absorb light with optical cross sections often several times larger than the geometric cross section. Using gold nanoshells of different size and optical parameters, we employ Monte Carlo models to predict the effect of varying concentrations of nanoshells on tissue reflectance. The models demonstrate the importance of absorption from the nanoshells on remitted signals even when the optical extinction is dominated by scattering. Furthermore, because of the strong optical response of nanoshells, a considerable change in reflectance is observed with only a very small concentration of nanoshells. Characterizing the optical behavior of gold nanoshells in tissue will aid in developing nanoshells as contrast agents for optical diagnostics. © *2005 Society of Photo-Optical Instrumentation Engineers.* [DOI: 10.1117/1.2141825]

Keywords: nanoshells; nanoparticles; nanotechnology; Monte Carlo; contrast agents.

1 Introduction

Optical technologies promise high-resolution, noninvasive functional imaging of tissue with improved sensitivity, specificity, and cost effectiveness relative to current approaches. Numerous studies over the past decade have shown the viability of scattering-based optical approaches, including spectroscopy,[1–3] confocal microscopy,[4–6] and optical coherence tomography[7–9] (OCT) in addressing some of the limitations associated with current methods of cancer detection and have generated promise in differentiating normal from diseased tissue. Confocal microscopy is a rapidly developing optical technology that can noninvasively image several hundred micrometers into tissue with micrometer resolution,[10] and the capability to detect subcellular morphological changes that are potentially useful for monitoring epithelial precancers.[6] OCT is another optical method that can provide both real-time and *in situ* imaging without the necessity for removal and processing of biological samples for biopsies and histopathological assessment. The images captured are 10 to 100 times finer in detail compared to conventional imaging techniques such as magnetic resonance imaging and ultrasound and axial resolutions as fine as 1 to 2 μm have been recently demonstrated.[11] Optical coherence microscopy (OCM) is another scattering-based optical method that combines the advantages of both confocal and OCT imaging, demonstrating significant promise for epithelial cancer detection.[12] Subcellular changes that alter scattering signals, such as increased nuclear size and change in refractive index, are useful indicators of dysplasia.[13] However, many other valuable molecular indicators of early precancers may not generate obvious intrinsic optical contrast. In these cases, targeted contrast agents are desirable.

As optical imaging is still an emerging field in medical diagnostics, the application of optical contrast agents to enhance contrast of the signatures of disease is not routine. Chemical agents such as dilute acetic acid,[10,14] toluidine blue,[15,16] and Lugol's iodine[17,18] have been shown to enhance visualization of dysplasia by augmenting the overall optical properties of dysplastic tissue relative to normal surrounding tissue.[19] Acetic acid causes selective whitening of tissue and it is suggested that it alters the refractive index of the cell nucleus, causing an increased scattering effect. This effect is

Address all correspondence to Rebekah A. Drezek, Rice University, Department of Bioengineering, PO Box 1892–MS 142, Houston, Texas 77251. Tel.: 713–348–3011; Fax: 713–348–5877; E-mail: drezek@rice.edu

more pronounced in dysplastic regions with greater nuclear size and density. Toluidine blue is a dye that stains acidic components of cells such as the DNA and RNA. The higher level of nucleic acids present in enlarged nuclei of dysplastic cells enables the dye to enhance differentiation between normal and abnormal tissue. Lugol's iodine reacts with glycogen, present in normal epithelial tissue, while dysplastic cells and carcinomas remain comparatively unstained or lightly stained, as they contain very little tissue glycogen. Other contrast agents such as indocyanine green have been widely investigated for use in enhancing imaging and detection of cancers via fluorescence.[20,21] The dye has excitation and emission peaks near 780 and 830 nm, respectively, and this spectral region lies within the "water window" of the near IR (NIR), where photon absorption in biological tissue is at a minimum. This is most useful for detecting cancers in optical applications such as diffuse optical tomography.[22] Particle-based technologies have also generated much interest for use to enhance contrast for optical imaging and microscopy due to its optical capabilities and ease of adding surface modifications. Lee et al.[23] developed oil-filled encapsulating protein microspheres that can incorporate various particles such as gold and carbon to alter backscattering optical signatures for OCT. This can be used as a contrast agent and the enhancement was demonstrated by imaging a mouse liver with intravenously injected gold-shelled microspheres. Similarly, the use of intravenously injected polystyrene microspheres was shown to enhance imaging of skin and microcirculation under confocal reflectance microscopy.[24]

To achieve more precise and accurate diagnosis and detection of cancer, it is desirable for optical contrast agents that can target molecule specific signatures of interest. Specific targeting by therapeutic and diagnostic agents through antibody binding of tumor cell surface molecules or tumor-specific peptides has been used extensively. For example, a commercial product for the detection of prostate cancer (ProstaScint) is an antibody conjugated against prostate-specific membrane antigen also conjugated to a scintigraphic target.[25] It is also possible to achieve similar targeting efficiencies with small tumor-specific peptides.[26,27] Nanoengineered technologies and molecular targeting strategies provide an exciting nexus for further development in detection, monitoring, and biosensing of biomolecules. Technologies such as nanoprobes can be used for optical sensing of biomolecular activity in single cells, while preserving vital cellular processes.[28,29] Surfaces of nanoparticles are easily modified with antibodies, peptides, and other cell-specific moieties and can be used for applications such as glucose sensing[30] and immunoassays.[31,32] Hirsch et al. devised a simple and rapid immunoassay by successfully measuring spectral changes using gold nanoshells to target very small quantities of analytes.[31] Nanoparticles have also generated considerable interest for use as a target-specific contrast agent to enhance optical detection, diagnosis, and therapy of cancers.[33] Recent work by Sokolov et al.[34] demonstrated that the detection of precancerous cells using confocal reflectance imaging can be enhanced with gold nanoparticles bioconjugated with molecule-specific markers bound to their targets. Other nanoparticles, such as semiconductor quantum dots, also show similar potential for use as target-specific biological probes.[35,36] Quantum dots, such as ZnS-capped CdSe, are emissive at wavelengths ranging from
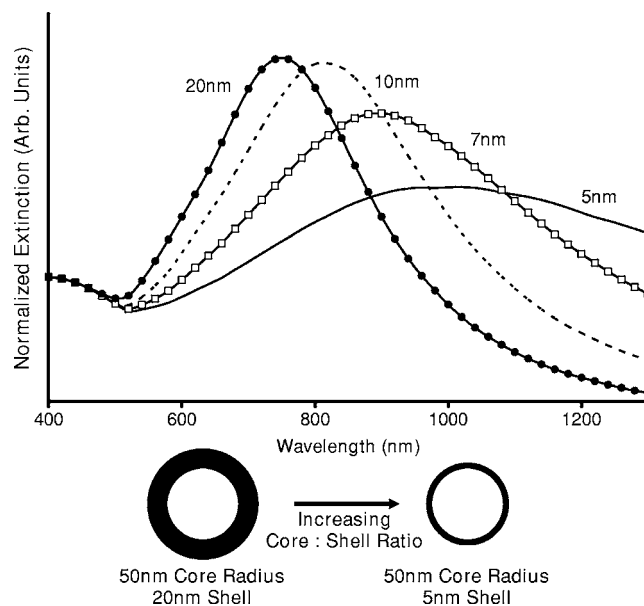

Fig. 1 By increasing the core radius to shell thickness ratio, the peak extinction resonance can be shifted well into the NIR. For gold nanoshells with a core (silica) radius of 50 nm and a decreasing gold shell thickness, the peak resonance shifts to longer wavelengths.

the near-UV to the NIR by changing the size and composition. Their surfaces are also highly modifiable for bioconjugation of target-specific peptides, and it has been shown that it is possible to use such nanoparticles to bind to specific targets *in vivo* using a tumor rat model, enhancing visualization under fluorescence or confocal microscopy.[35]

In this paper, we consider the use of metal nanoshells as exogenous contrast agents. Metal nanoshells are composed of a dielectric core (e.g., silica) coated with an ultrathin metallic layer (e.g., gold). Gold nanoshells possess physical properties similar to gold colloid and exhibit strong scattering and absorption effects due to the strong plasmon resonance of the metallic-dielectric concentric spherical configuration.[37,38] In particular, the optical behavior of gold nanoshells in the NIR shows scattering and/or absorption cross sections often several times the particle geometric cross section. This is not seen with comparable nanoparticles such as gold colloidal nanoparticles, which show weak optical activity in the NIR spectrum region.[38,39] By varying the relative core size and shell thickness, the peak resonance of gold nanoshells can be dramatically varied across a broad range of the optical spectrum that spans the visible and the NIR spectral regions.[40] The "tunability" of the optical resonance is a property unique to metal nanoshells. Figure 1 shows Mie extinctions plots with a 50-nm-radius silica core. By increasing the core radius-shell thickness ratio, it is possible to shift the peak plasmon resonance of the nanoshell well into the NIR and to wavelengths greater than 2 μm. Furthermore, gold nanoshells can also be tuned to show the same peak optical resonance with different size parameters.[41] Under current laboratory methods, it is also possible to fabricate gold nanoshells of varying sizes with experimental observations of gold nanoshell resonances closely matching Mie theory. The fabrication method uses a combination of molecular self-assembly and colloid chemistry

in aqueous solution and is well described in literature.[31,37]

The large optical efficiencies of nanoshells in the NIR are especially useful for biological applications. Moreover, gold nanoshells can be used for bioconjugating applications as their surfaces are virtually chemically identical to gold colloid, universally used in numerous bioconjugate applications.[42] By using nonbioconjugated gold nanoshells, Hirsch et al.[43] and O'Neal et al.[44] showed that gold nanoshells can be used as an agent for photothermal therapy of cancers. By further functionalizing gold nanoshell surfaces with target-specific antibodies, Loo et al. showed enhanced visualization using gold nanoshells targeted to HER2-positive breast cancer cells under brightfield and darkfield microscopy.[45] The targeted cancer cells can subsequently be selectively destroyed through photothermal therapy,[46] paving way for an integrated imaging and therapy of cancer. Although gold nanoshells have already shown success for cancer imaging and therapy, the optical effect of adding nanoshells to tissue has not yet been elucidated. It is important to predict how gold nanoshells affect tissue reflectance for scattering-based optical methods, so that optimal parameters for its use as an optical contrast agent can be fully realized. We evaluate gold nanoshells as an optical contrast agent with computational tools. We first use analytical electromagnetic methods to calculate optical properties of various nanoshells with a wide variety of scattering and absorbing capabilities. As the optical response of nanoshells are typically described by the optical extinction,[37,38,40] it is critical for our studies to consider the optical effect of scattering and absorption. We then employ the use of Monte Carlo methods to evaluate the effect of adding varying concentrations of gold nanoshells in tissue on photon reflectance. We also consider how the combination of scattering and absorption properties of nanoshells with different size parameters affect remitted signals. In our work, the Monte Carlo models suggest that even as the optical extinction is strongly dominated by scattering, absorption from the nanoshells cannot be neglected in predicting tissue reflectance. Furthermore, because of the strong optical behavior of nanoshells, a considerable change in reflectance was observed with only a very small concentration of nanoshells.

2 Methods

2.1 Optical Properties of Gold Nanoshells

The optical response of gold nanoshells can be described by using computed solutions of Mie theory for concentric spherical shells at the boundaries between different mediums.[38] For use in the Monte Carlo studies described later, Mie solutions of gold nanoshells were computed with an excitation wavelength of 830 nm, within the region of optimal physiological transmissivity best suited for optical bioimaging and biosensing applications. Typically, optical resonances of gold nanoshells are calculated with air ($n=1.0$) or water ($n=1.33$) as the embedding medium.[37,40] However, it is important that the optical properties of gold nanoshells are calculated with $n=1.4$, simulating the embedding medium as a physiological environment, as the Monte Carlo studies will use tissue models embedded with nanoshells. Table 1 shows the optical properties of the R75/115 nanoshell with $n=1.0$, 1.33, and 1.4. The differences in optical properties must be

Table 1 Optical properties calculated from Mie solutions of various particles at a 830-nm excitation wavelength.

Particle	Extinction Eff.	Sca/Abs Ratio	Sca XS/Vol	Abs XS/Vol
R10-Au	0.00511	0.122	4.18×10^4	3.41×10^5
R40/45	1.614	0.059	1.50×10^6	2.54×10^7
R50/60	4.047	0.380	1.39×10^7	3.67×10^7
R40/55	2.620	0.701	1.47×10^7	2.10×10^7
R55/80	4.414	3.199	3.15×10^7	9.85×10^6
R40/80	3.738	6.270	3.02×10^7	4.82×10^6
R75/115	3.700	8.980	2.17×10^7	2.42×10^6
R75/115*	3.82	9.23	2.25×10^7	2.43×10^6
R75/115#	2.97	8.25	1.73×10^7	2.09×10^6

R40/45 represents a nanoshell with a 40-nm core radius with a 5-nm-thick gold shell. Extinction efficiencies, scattering-to-absorption efficiency ratio (Sca/Abs ratio), and the volume-normalized scattering and absorption cross sections are shown. The units for the volume-normalized cross-sections are inverse meters. Properties of the 10-nm-radius gold nanoparticle (R10-Au), a commonly used agent for biological interrogation, are included for comparison. The values shown are calculated with an embedding medium index of refraction, $n=1.4$, simulating a physiological medium. Also shown as an example, are optical property values of the R75/115 nanoshell in water (*) and air (#) with index of refraction, $n=1.33$ and $n=1.0$, respectively. The differences in the values show the importance of using the medium that more accurately mimics physiological conditions.

taken into account as it would subsequently affect the optical properties calculated and used in the Monte Carlo studies.

To choose different nanoshells with varying optical properties, we first assume independent scattering of the nanoshell particles for simplification. Under independent scattering, the optical cross section per unit volume of the particle becomes more appropriate than the optical efficiency for subsequent calculations of scattering and absorption coefficients[47,48] for use in the Monte Carlo studies. Core radius-to-shell thickness space-maps [see Figs. 2(a) and 2(b)] of volume-normalized optical cross sections are used to select the nanoshells, with a range of sizes and optical properties. The space-maps were computed with an excitation wavelength of 830 nm, including sizes that can be fabricated with current laboratory methods. As gold nanoshells possess not just scattering, but also absorbing properties, nanoshells with a variety different scattering and absorbing proportions are also considered for the Monte Carlo studies. A simple relation—the scattering-to-absorption efficiency ratio (Sca/Abs ratio)—can be used to compare how much more scattering a nanoshell is compared to its absorption ability [see Fig. 2(c)].

2.2 Monte Carlo Modeling

Monte Carlo modeling of photon transport in multilayered tissues by Wang et al.,[49] a computational tool written in Standard C, has been widely used to simulate random walk of photons through turbid media and is useful for investigating light propagation in tissue. The fraction of remitted and absorbed photons can be predicted from Monte Carlo computations, and the fraction changes accordingly as the optical pa-
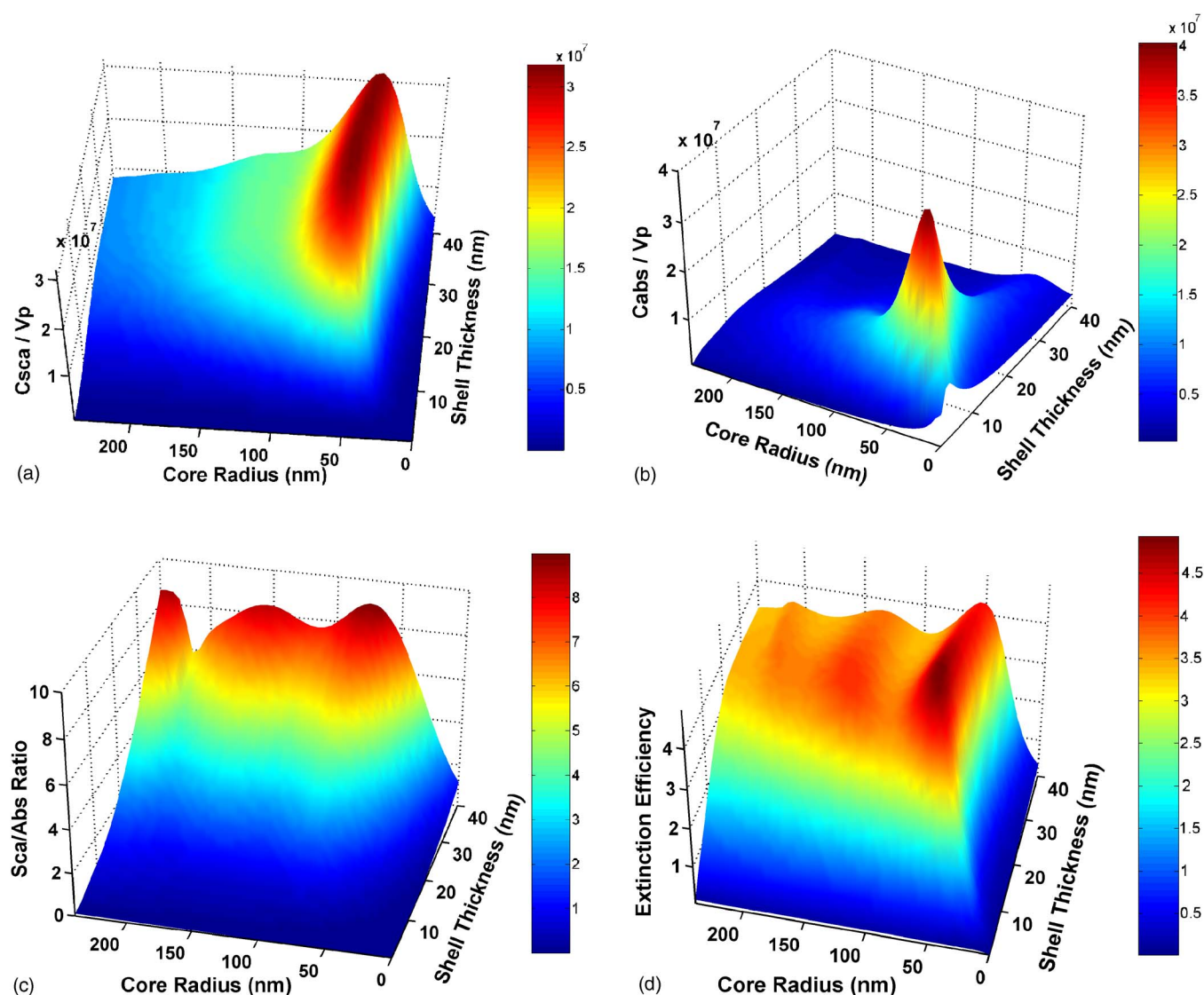
Fig. 2 Computed optical properties of gold nanoshells as a function of the core radius and the shell thickness (both in nanometers) at an excitation wavelength of 830 nm. These diagrams can aid in selecting specific nanoshells with desired optical properties. The graphs describe (a) volume-normalized scattering cross section (C_{sca}/V_p), (b) volume-normalized absorption cross section (C_{abs}/V_p), (c) scattering-to-absorption efficiency ratio (Sca/Abs), and (d) extinction efficiency. These space-maps can aid in determining the desired size and optical properties to be used in subsequent studies.

rameters of the medium are changed. The theories behind Monte Carlo methods are well described in literature and are not be repeated here.[49] Simulations were performed on two models (A and B) that will each be differentiated into two sets: a bulk tissue model (models A-1 and A-2) and a multi-layered tissue model (models B-1 and B-2). The description of the two sets is provided later. The bulk tissue model was assumed to be an infinitely thick precancerous tissue layer with uniform homogeneous optical properties. The base optical properties before the addition of nanoshells of this precancerous layer was set with the absorption coefficient at $\mu_{abs(c)}=0.05$ cm^{-1}, and the scattering coefficient, $\mu_{sca(c)}=50$ cm^{-1}, both within cited literature[50–52] values in the NIR. The tissue properties of this layer are then changed, simulating an increasing concentration of nanoparticles added to the tissue.

A three-layered model (models B-1 and B-2) used in our studies (see Fig. 3) is similar to the theoretical model used by Quan and Ramanujam,[53] which mimics the basic structure of epithelial and stromal tissue. The first layer represents normal surface epithelium with a thickness of $d_1=175$ μm, and optical parameters were kept constant at $\mu_{sca(1)}=50$ cm^{-1} and $\mu_{abs(1)}=1.5$ cm^{-1}. The second precancerous layer ($d_2=175$ μm), originates from the basal membrane, occupying space between the stroma and the normal epithelium of the top layer. As the epithelium consists of the most superficial tissue layers, hemoglobin content is negligible. The absorption coefficients of the epithelial layers represent absorption by tissue chromophores such as lipid, water and cytochrome oxidase.[54–56] Similar to model A, increasing concentrations of nanoshells were added to this representative precancerous
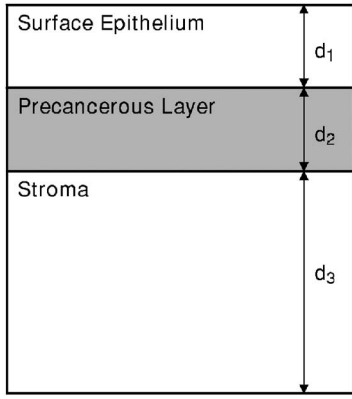
Fig. 3 Schematic showing the multilayered tissue model used in the Monte Carlo studies. The depths of the parameters shown are: normal surface epithelium, $d_1 = 175 \ \mu m$; precancerous layer, $d_1 = 175 \ \mu m$; and stromal layer (semi-infinitely thick), $d_3 = 1.0 \times 10^8$ cm. The optical parameters of the layers were set as, normal surface epithelium, $\mu_{sca(1)} = 50$ cm^{-1} and $\mu_{abs(1)} = 1.5$ cm^{-1}, and the stromal layer optical properties of $\mu_{sca(3)} = 250$ cm^{-1} and $\mu_{abs(3)} = 1.5$ cm^{-1}. The concentration of nanoparticles was incremented in the precancerous layer, with base optical properties of $\mu_{sca(c)} = 50$ cm^{-1} and $\mu_{abs(c)} = 0.05$ cm^{-1}.

layer and the optical properties of this second layer without any nanoshells was the same as the bulk tissue, where $\mu_{sca(c)} = 50$ cm^{-1} and $\mu_{abs(c)} = 0.05$ cm^{-1}. The stromal layer was modeled as a semi-infinitely thick $(d_3 = 1.0 \times 10^8$ cm) layer with $\mu_{sca(3)} = 250$ cm^{-1} and $\mu_{abs(3)} = 1.5$ cm^{-1}. The following properties were kept constant for all simulations: the anisotropy factor (g) was kept constant at 0.9 and $n = 1.4$ for the tissue refractive index.

The overall scattering $[\mu_{sca(t)}]$ and absorption coefficient $[\mu_{abs(t)}]$ of the tissue is altered by the optical properties of the particles added to the models. As a basis of comparison, gold nanoparticles (10 nm radius) commonly used for biological interrogation such as biomolecular analysis, interactions, and imaging[34,57,58] were used in place of the gold nanoshells. To account for interparticle effects by the nanoparticles on photon scattering, a correction factor is required for volume fractions higher[59,60] than $\sim$1%, when the diameter of the particles are much less than the wavelength to account for the reduction of bulk optical cross section as a result of non-independent scattering among subwavelength spheres. As mentioned, for these studies, we impose a limit on the density and size of nanoshells added to the precancerous layers to ensure independent scattering. Each type of nanoparticles is then added separately, so that only one type of particle is added to the models at one time. Using well established light scattering theory, the change in the optical coefficient $[\Delta\mu_{(p)}]$ due to particles in a medium, is related to the scattering or absorption cross section (C) and the number of particles per unit volume[48] (N):

$$\Delta\mu_{(p)} = N \times C.$$

This can then be related to the volume fraction (V_f) of nanoparticles added to the models, and also the scattering (C_{sca}) or absorption cross section (C_{abs}) normalized by the volume of the particle used (V_p),
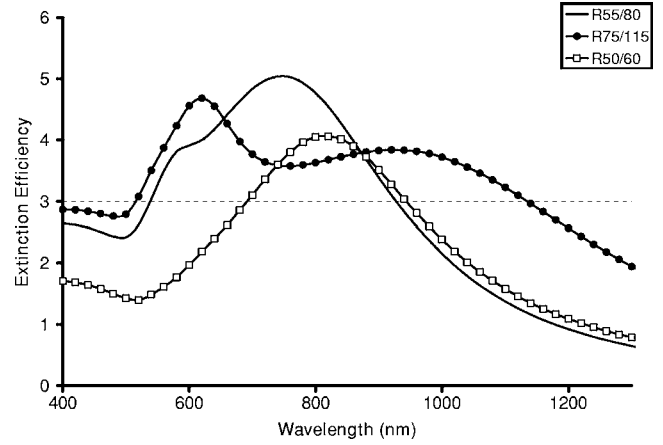

Fig. 4 Representative extinction efficiencies of three different nanoshells, R75/115, R50/60, and R55/80, used in the Monte Carlo experiments. The different extinction profiles are plotted against a broad wavelength range, showing optical activity well into the NIR. Nanoshells of different sizes produce unique and different optical responses.

$$\Delta\mu_{sca,abs(p)} = \frac{C_{sca,abs}}{V_p} V_f.$$

The change in scattering or absorption coefficient $[\Delta\mu_{(p)}]$ can be due to the scattering or absorption of the particle added. To evaluate the overall effect adding particles with a variety of physical and optical parameters, the studies are separated into two sets for both the bulk (model A) and multilayered (model B) models. As gold nanoshells can be fabricated to be far more scattering than absorbing, for example, the R75/115 (representing a core radius of 75 nm and an overall radius of 115 nm) gold nanoshell shows almost 90% of the extinction as scattering, we access if such highly scattering particles can be simply considered as a scatterer while neglecting its absorption properties. Thus, the studies will be further separated into two sets, one considering only the scattering properties of the particles and neglecting the absorption. The other will take
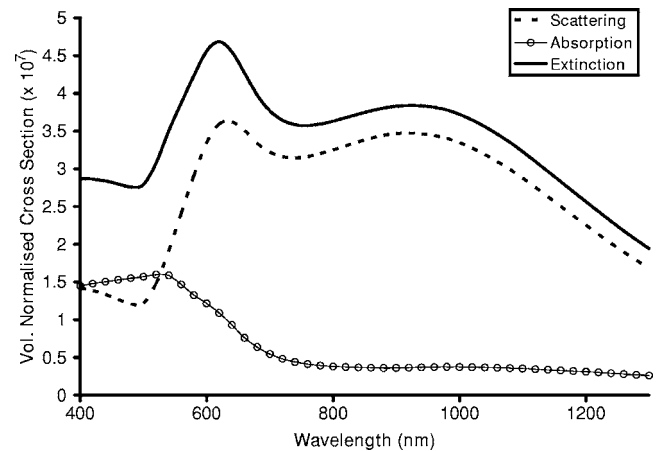

Fig. 5 Volume normalized cross sections of the R75/115 gold nanoshell $(n=1.4)$. Although the scattering property of the nanoshell generally dominates the absorption, it is expected that the diffuse reflectance of tissue with nanoshells will decrease across wavelength.
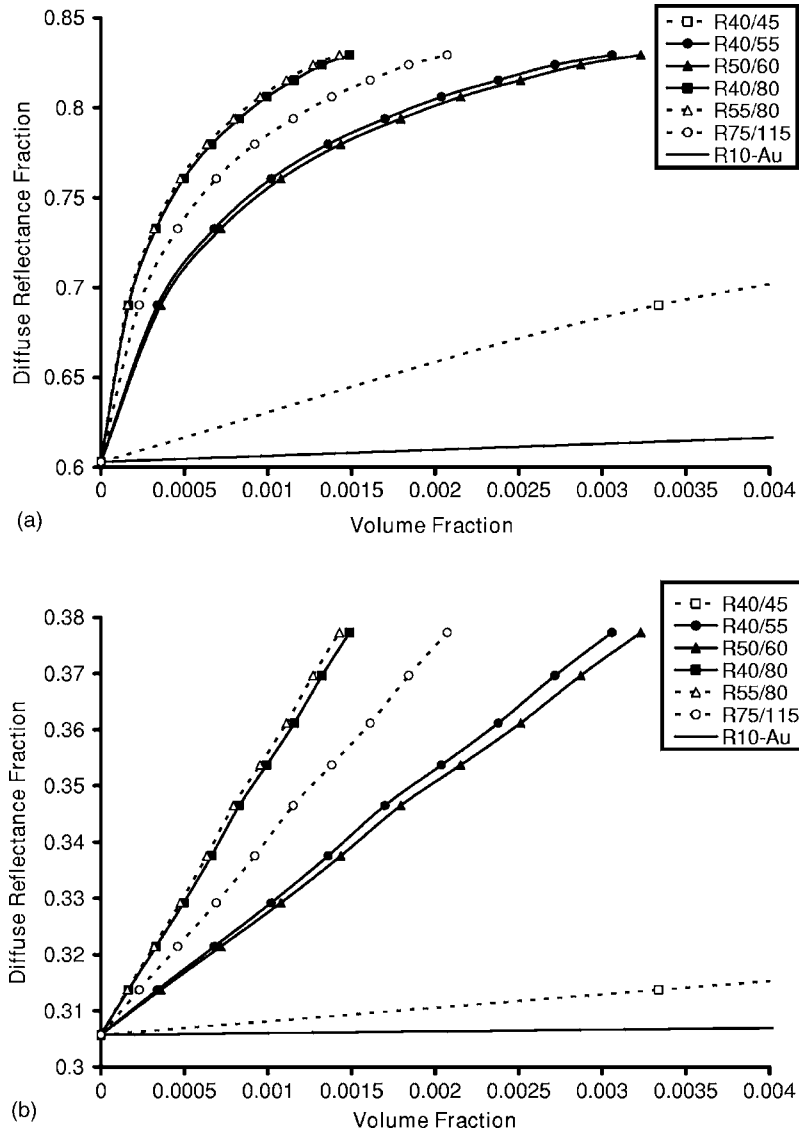
Fig. 6 Diffuse reflectance from the (a) bulk (model A-1) and (b) multilayered (model B-1) models with $\mu_{\text{abs}(c)}=0.05$ cm^{-1}, using different types of nanoparticles. The higher the volume-normalized scattering cross section, the more the diffuse reflectance increases with the same volume fraction of nanoshells added. The results show the studies that neglected absorption from the nanoparticles, assuming the particles as simple scatterers.

into account both the scattering and absorption properties of the particles. For the first set (models A-1 and B-1), as only the scattering effect by the nanoparticles $[\Delta\mu_{\text{sca}(p)}]$ is considered for the change of the overall scattering properties of the tissue $[\mu_{\text{sca}(t)}]$, the tissue absorption therefore does not change and remains at the base level $[\mu_{\text{abs}(c)}=0.05$ cm$^{-1}]$. The overall scattering $[\mu_{\text{sca}(t)}]$ and absorption coefficient $[\Delta\mu_{\text{abs}(p)}]$ of set 1 can be related through

$$\mu_{\text{abs}(t)} = \mu_{\text{abs}(c)},$$

$$\mu_{\text{sca}(t)} = \mu_{\text{sca}(c)} + \Delta\mu_{\text{sca}(p)}.$$

In the second set (models A-2 and B-2), the combination of both scattering and absorption by the nanoparticles are taken into consideration. The respective change in absorption coefficient $[\Delta\mu_{\text{abs}(p)}]$ can then also be calculated using a similar

relation. Both the overall scattering $[\mu_{\text{sca}(t)}]$ and absorption coefficients $[\mu_{\text{abs}(t)}]$ of tissue are consequently altered by the optical response of the nanoshells. Thus the overall change in optical properties of the precancerous layer is,

$$\mu_{\text{abs}(t)} = \mu_{\text{abs}(c)} + \Delta\mu_{\text{abs}(p)},$$

$$\mu_{\text{sca}(t)} = \mu_{\text{sca}(c)} + \Delta\mu_{\text{sca}(p)}.$$

From this set of Monte Carlo studies, we evaluate the effect of absorption from nanoshells on tissue reflectance with absorption and/or scattering dominated gold nanoshells, and compare this to the results from set 1.
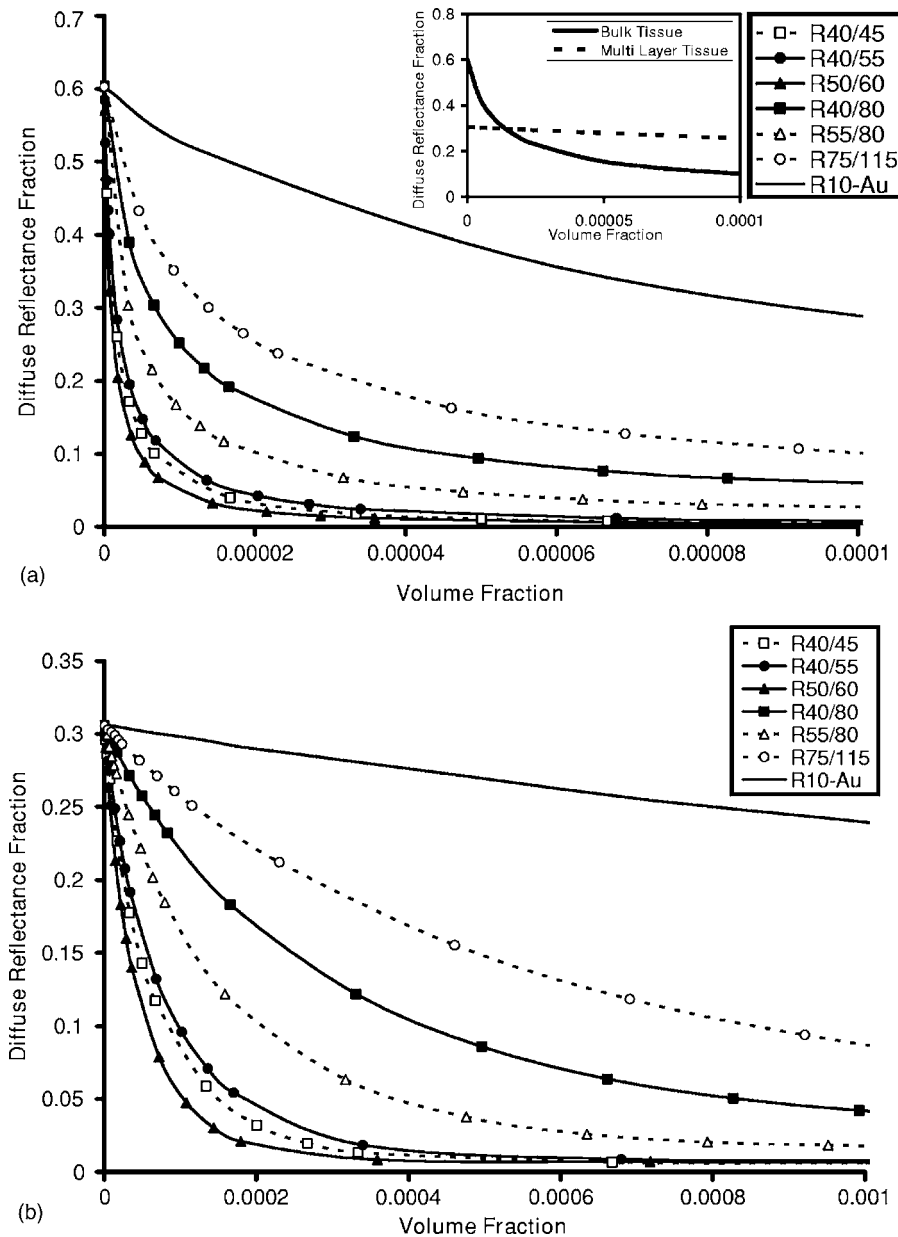
Fig. 7 Diffuse reflectance from the (a) bulk (model A-2) and (b) multilayered (model B-2) tissue when both scattering and absorption from the nanoparticles were considered. As the volume-normalized absorption cross section of the particle increases, the reflectance decreases. Model B-2 shows a more gradual decrease in reflectance compared to model A-2, and eventually shows higher reflectance as more particles were added, even though model A-2 showed higher reflectance before any nanoparticles were added. To describe this, the insert shown in (a) shows comparison of the diffuse reflectance fraction from the bulk (solid line) and multilayered (dotted line) models with increasing volume fractions of the R75/115 nanoshell.

3 Results and Discussion

3.1 Gold Nanoshells

Figures 2(a)–2(d) shows various optical properties of gold nanoshells compared to core radius and shell thicknesses up to an overall radius of 280 nm at an excitation wavelength of 830 nm. The figures show the volume normalized scattering cross section [Fig. 2(a)], volume normalized absorption cross section [Fig. 2(b)], and the scattering-to-absorption efficiency ratio [Fig. 2(c)]. Figure 2(d) shows the extinction efficiency of the nanoshells. Using these space-maps of optical properties, nanoshells of different sizes and properties (also see Table 1)

were chosen and their effect on tissue diffuse reflectance investigated. The table shows that the particles with the highest scattering and absorption efficiencies do not necessarily show the highest optical cross sections per unit volume of the particle, and this becomes important and are described later. To further describe the optical versatility of gold nanoshells, Fig. 4 shows representative optical extinction profiles of some of the nanoshells (R75/115, R50/60, and R55/80) used in these studies showing very different responses across wavelengths. Figure 5 shows volume-normalized absorption, scattering and extinction of the R75/115 nanoshell.

3.2 Monte Carlo Studies

The Monte Carlo studies show that the addition of gold nanoshells to tissue causes a significant change in tissue reflectance. It is also possible to detect the change in reflectance due to a buried layer of tissue containing nanoshells. Between Monte Carlo modeling sets 1 and 2, the absorption properties of nanoshells are an important factor for predicting the tissue reflectance and cannot be neglected, even if the optical properties of the particle is dominated by scattering. The gold nanoshells were observed to scatter or absorb light far more efficiently than the gold nanoparticles. A large change in reflectance was observed with only a very small amount of nanoshells, while the gold nanoparticle caused little change in reflectance.

In set 1 of the Monte Carlo studies, the diffuse reflectance generally increased as the amount of nanoshells added increased. Figures 6(a) and 6(b) shows the diffuse reflectance results from the bulk (model A-1) and multilayered (model B-1) tissue models after gold nanoshells of a variety of scattering properties and the 10-nm gold nanoparticles were added to the tissue with increasing concentration. The reflectance increases after the addition of gold nanoshells, while the results from the gold colloid particle remain relatively unchanged. The photon reflectance, before adding any nanoparticles, is approximately 0.6 from model A-1 and 0.3 from model B-1. With the same concentration of particles added, the particle with the greater volume-normalized scattering cross sections shows higher reflectance. For example, the R55/80 nanoshell exhibits the highest reflectance, while the R40/45 shows the lowest of all the nanoshells. This corresponds to the volume-normalized scattering cross-section values as shown in Table 1. The R55/80 nanoshell exhibits the highest volume-normalized scattering cross section (Abs XS/Vol$=3.15 \times 10^7$ m^{-1}) and the R40/45 nanoshell had the lowest value among the gold nanoshells used, with Abs XS/Vol$=1.50 \times 10^6$ m^{-1}. The 10 nm radius gold colloid particle (R10-Au) with the lowest volume-normalized scattering cross section correspondingly shows very little change in both models A-1 and B-1.

In set 2, the results, when absorption from gold nanoshells and gold colloid $[\Delta \mu_{\text{abs}(p)}]$ was considered together with the scattering, are shown in Figs. 7(a) and 7(b). The results also show an immediate decrease in reflectance after the nanoparticles were included. When the concentration of the particles was increased, the diffuse reflectance decreased, and this occurred for all the particle configurations used in the simulations. Furthermore, the diffuse reflectance from model A-2 decreases more rapidly compared to model B-2 and eventually shows higher reflectance for the same amount of nanoshells added, as shown in the inset of Fig. 7(a). The graph shows that at a volume fraction of 0.00005, the reflectance with the R75/115 gold nanoshell is approximately 0.15 in model A-2, and about 0.28 from model B-2. Compared to when no particles were added to the tissue, the reflectances are approximately 0.3 (model B-2) and 0.6 (model A-2). Further increases in concentration diminish the reflectance close to zero. The uniform change in the optical properties of the bulk model (model A-2), leads to a higher probability that photons will be absorbed in the topmost regions, whereas in model B-2, as the precancerous layer is buried away from the
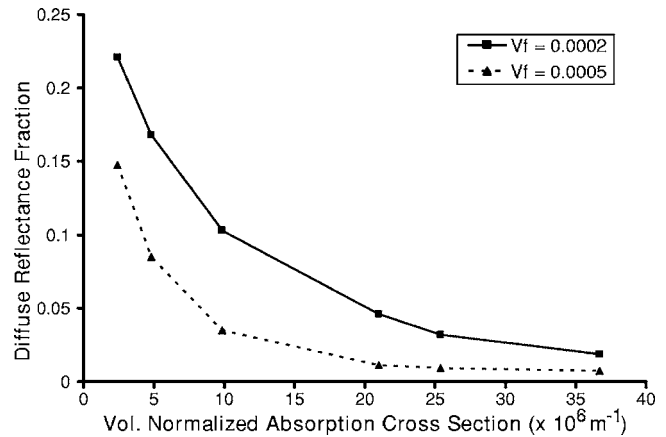

Fig. 8 The diffuse reflectance as a function of the volume normalized absorption cross section of different gold nanoshells used in the multilayered Monte Carlo studies (refer to Table 1). As the volume normalized absorption increases, the reflectance correspondingly decreases. Volume fractions (V_f) of 0.0002 and 0.0005 are shown, within the constraints for independent scattering.

surface, there are greater chances of scattering when the photons first travel through the surface epithelium.

Even as it is useful to use the scattering-to-absorption ratio (Abs/Sca ratio) of the optical properties to describe how much more scattering the particle is compared to absorption, the volume-normalized absorption cross section of the particles is a more adequate description of how the optical properties of the particles influences tissue reflectance in our studies. The comparison of the scattering and absorbing properties of each particle is shown in Table 1 under Abs/Sca Ratio. For example, the R75/115 nanoshell shows a scattering cross section of almost 9 times over the absorption cross section, while the scattering of the R40/45 nanoshell is about 5.9% that of its absorption. Comparing this to the reflectance, the R75/115 and R40/45 nanoshells, however, do not show the highest and lowest reflectances, respectively. Thus, we can infer that absorption from the particles has a far greater effect on reflectance and cannot be neglected, even if the particle possess scattering cross section several times larger than its absorption. When we consider only scattering from the nanoparticles in models A-1 and B-1, it is obvious that higher scattering cross section per unit volume of the particle shows higher reflectance with the limitation of independent scattering. However, with different configurations of scattering and absorption from the gold nanoshells, the reflectance is more dependent on the volume-normalized absorption cross section than the combination of scattering and absorption. Figure 8 shows the relationship between diffuse reflectance and volume-normalized absorption cross sections of gold nanoshells. The diffuse reflectance decreases correspondingly (volume fraction, $V_f=0.0002$ and 0.0005) as the absorption of gold nanoshells increase. This reemphasizes the importance of absorption from the particles and suggests that gold nanoshells can more efficiently lower the photon reflectance compared to gold colloid. This can be potentially useful for enhancing reflectance signatures through absorption for spectroscopic detection modalities. Furthermore, only a very small number of nanoshells are required to produce an observable

change in the remitted signal. The volume-normalized absorption cross section of the R75/115 nanoshell shown in Fig. 5 range from 1.6×10^7 m^{-1} at 520 nm to 3.74×10^6 m^{-1} at 1000 nm ($n=1.4$). As spectroscopic methods typically use a range of wavelengths, comparing these values to the R10-Au gold nanoparticle, these values are still considerably larger. Thus, when comparing normal tissue and nanoshell targeted tissue, the spectra of the diseased tissue would likely show a much reduced spectral intensity with the presence of nanoshells, which would provide an indication of the presence of targeted cells.

Throughout the Monte Carlo simulations, the anisotropy (g) of the tissue was assumed to remain constant with the addition of the particles. From Mie solutions of the gold nanoshells, the g values for the nanoshells can be calculated, and the overall effect on the anisotropy of the tissue is related by,

$$g_{\text{overall}} = (g_{\text{tissue}})(1 - V_f) + (g_{\text{nanoshell}})(V_f),$$

where V_f is the volume fraction of the nanoshells as described before, and $1 - V_f$ is the volume fraction of the tissue not occupied by the nanoshells. With such a low-volume fraction of nanoshells, the overall change in the anisotropy of the tissue is very small and can be assumed as negligible. For instance, the R40/80 nanoshell has a g value of approximately -0.033 at an excitation wavelength of 830 nm in physiological media ($n=1.4$). At a volume fraction of $V_f=0.0005$, the change in the g value of the tissue ($g=0.9$) is less than 0.0005, not enough to significantly alter the reflectance.

4   Conclusions

Gold nanoshells possess unique and tunable optical signatures, in particular, strong optical responses in the NIR, desirable for biological applications. Gold nanoshells are easily fabricated for size and desired optical response under current chemistries. The absorption of gold nanoshells is critical in predicting the macroscopic behavior of light transport through turbid media embedded with nanoshells. The large scattering cross section of gold nanoshells in the NIR has already been exploited and demonstrated[61] to enhance contrast for imaging in OCT. In addition, the strong absorption capabilities has been used in new imaging technologies such as photoacoustic tomography on the rat brain *in vivo*,[62] further underlining the cross-platform potential of gold nanoshells for integrated imaging, diagnosis, and therapy of cancers. By exploring gold nanoshells with different physical parameters, we can continue to investigate the effects of changing nanoshell properties, possibly optimizing nanoshells with parameters best suited for different imaging and spectroscopic modalities. The studies reported in this paper strongly suggest that the strong optical responses of gold nanoshells can be utilized to alter signatures for scattering-based optical diagnostic methods.

References

1. H. Zeng, M. Petek, M. T. Zorman, A. McWilliams, B. Palcic, and S. Lam, "Integrated endoscopy system for simultaneous imaging and spectroscopy for early lung cancer detection," *Opt. Lett.* **29**(6), 587–589 (2004).
2. A. Amelink, H. J. C. M. Sterenborg, M. P. L. Bard, and S. A. Burgers, "*In vivo* measurement of the local optical properties of tissue by use of differential path-length spectroscopy," *Opt. Lett.* **29**(10), 1087–1089 (2004).
3. K. Sokolov, L. T. Nieman, A. Myakov, and A. Gillenwater, "Polarized reflectance spectroscopy for pre-cancer detection," *Technol. Cancer Res. Treat.* **3**(1), 1–14 (2004).
4. C. Liang, K. B. Sung, R. R. Richards-Kortum, and M. R. Descour, "Design of a high-numerical-aperture miniature microscope objective for an endoscopic fiber confocal reflectance microscope," *Appl. Opt.* **41**(22), 4603–4610 (2002).
5. K. B. Sung, C. Liang, M. Descour, T. Collier, M. Follen, and R. Richards-Kortum, "Fiber-optic confocal reflectance microscope with miniature objective for *in vivo* imaging of human tissue," *IEEE Trans. Biomed. Eng.* **49**(10), 1168–1172 (2002).
6. T. Collier, A. Lacy, R. Richards-Kortum, A. Malpica, and M. Follen, "Near real-time confocal microscopy of amelanotic tissue," *Acad. Radiol.* **9**(5), 504–512 (2002).
7. T. Q. Xie, M. L. Zeidel, and Y. T. Pan, "Detection of tumorigenesis in urinary bladder with optical coherence tomography: optical characterization of morphological changes," *Opt. Express* **10**, 1431–1443 (2002).
8. J. G. Fujimoto, "Optical coherence tomography for ultrahigh resolution *in vivo* imaging," *Nat. Biotechnol.* **21**(11), 1361–1367 (2003).
9. E. S. Matheny, N. M. Hanna, W. G. Jung, Z. Chen, P. Wilder-Simth, R. Mina-Araghi, and M. Brenner, "Optical Coherence Tomography of malignancy in hamster cheek pouces," *J. Biomed. Opt.* **9**(5), 978–981 (2004).
10. R. A. Drezek, T. Collier, C. K. Brookner, A. Malpica, R. Lotan, R. R. Richards-Kortum, and M. Follen, "Laser scanning confocal microscopy of cervical tissue before and after application of acetic acid," *Am. J. Obstet. Gynecol.* **182**, 1135–1139 (2000).
11. W. Drexler, U. Morgner, F. X. Kartner, C. Pitris, S. A. Boppart, X. D. Li, E. P. Ippen, and J. G. Fujimoto, "*In vivo* ultrahigh resolution optical coherence tomography," *Opt. Lett.* **24**, 1221–1223 (1999).
12. A. L. Clark, A. Gillenwater, R. Alizadeh-Naderi, A. K. El-Naggar, and R. Richards-Kortum, "Detection and diagnosis of oral neoplasia with an optical coherence microscope," *J. Biomed. Opt.* **9**(6), 1271–1280 (2004).
13. R. Drezek, T. Collier, C. MacAulay, M. Follen, and R. Richards-Kortum, "Light scattering from cervical cells throughout neoplastic progression: influence of nuclear size, DNA content, and chromatin texture," *J. Biomed. Opt.* **8**, 7–16 (2003).
14. T. Collier, P. Shen, B. de Pradier, K. B. Sung, R. Richards-Kortum, A. Malpica, and M. Follen, "Near real time confocal microscopy of amelanotic tissue: dynamics of aceto-whitening enable nuclear segmentation," *Opt. Express* **6**(2), 40–48 (2000).
15. M. A. Onofre, M. R. Sposto, and C. M. Navarro, "Reliability of toluidine blue application in the detection of oral epithelial dysplasia and in situ and invasive squamous cell carcinomas," *Oral Surg. Oral Med. Oral Pathol. Oral Radiol. Endod.* **91**(5), 535–540 (2001).
16. I. C. Martin, C. J. Kerawala, and M. Reed, "The application of toluidine blue as a diagnostic adjunct in the detection of epithelial dysplasiam," *Oral Surg. Oral Med. Oral Pathol. Oral Radiol. Endod.* **85**(4), 444–446 (1998).
17. A. J. Tincani, N. Brandalise, A. Altemani, R. C. Scanavini, J. B. M. Valerio, H. T. Lage, G. Molina, and A. S. Martins, "Diagnosis of superficial esophageal cancer and dysplasia using endoscopic screening with a 2% Lugol dye solution in patients with head and neck cancer," *Head Neck* **22**(2), 170–174 (2000).
18. Y. Nakanishi, A. Ochiai, K. Yoshimura, H. Kato, T. Shimoda, H. Yamaguchi, Y. Tachimori, H. Watanabe, and S. Hirohashi, "The clinicopathologic significance of small areas unstained by Lugol's iodine in the mucosa surrounding resected esophageal carcinoma," *Cancer* **82**(8), 1454–1459 (1998).

19. A. F. Zuluaga, R. Drezek, T. Collier, R. Lotan, M. Follen, and R. Richards-Kortum, "Contrast agents for confocal images of normal and cancer cells in suspension," *J. Biomed. Opt.* **7**(3), 398–403 (2002).

20. E. M. Sevick-Muraca, J. P. Houston, and M. Gurfinkel, "Fluorescence-enhanced, near infrared diagnostic imaging with contrast agents," *Curr. Opin. Chem. Biol.* **6**, 642–650 (2002).

21. A. Godavarty, A. B. Thompson, R. Roy, M. Gurfinkel, M. J. Eppstein, C. Zhang, and E. M. Sevick-Muraca, "Diagnostic imaging of breast cancer using fluorescence-enhanced optical tomography," *J. Biomed. Opt.* **9**(3), 488–496 (2004).

22. V. Ntziachristos, A. G. Todh, M. Schnall, and B. Chance, "Concurrent MRI and diffuse optical tomography of breast after indocyanine green enhancement," *Proc. Natl. Acad. Sci. U.S.A.* **97**(6), 2767–2772 (2000).

23. T. M. Lee, F. J. Toublan, S. Sitafalwalla, A. L. Oldenburg, K. S. Suslick, and S. A. Boppart, "Engineered microsphere contrast agents for optical coherence tomography," *Opt. Lett.* **28**(17), 1546–1548 (2003).

24. M. Rajadhyaksha, S. Gonzalez, and J. M. Zavislan, "Detectability of contrast agents for confocal reflectance imaging of skin and microcirculation," *J. Biomed. Opt.* **9**(2), 323–331 (2004).

25. A. K. Gregorakis, E. H. Holmes, and G. P. Murphy, "Prostate-specific membrane antigen: current and future utility," *Semin Urol. Oncol.* **16**(1), 2–12 (1998).

26. M. Kolonin, R. Pasqualini, and W. Arap, "Molecular addresses in blood vessels as targets for therapy," *Curr. Opin. Chem. Biol.* **5**(3), 308–313 (2001).

27. U. Mahmood, C. H. Tung, A. Bogdanov, Jr., and R. Weissleder, "Near-infrared optical imaging of protease activity for tumor detection," *Radiology* **213**(3), 866–870 (1999).

28. P. M. Kasili, J. M. Song, and T. Vo-Dinh, "Optical sensor for the detection of caspase-9 activity in a single cell," *J. Am. Chem. Soc.* **126**(9), 2799–2806 (2004).

29. J. M. Song, P. M. Kasili, and T. Vo-Dinh, "Detection of cytochrome *c* in a single cell using and optical nanobiosensor," *Anal. Chem.* **76**(9), 2591–2594 (2004).

30. K. Aslan, J. R. Lackowicz, and C. D. Geddes, "Nanogold-plasmon-resonance-based glucose sensing," *Anal. Biochem.* **330**(1), 145–155 (2004).

31. L. R. Hirsch, J. B. Jackson, A. Lee, N. J. Halas, and J. L. West, "A whole blood immunoassay using gold nanoshells," *Anal. Chem.* **75**, 2377–2381 (2003).

32. J. R. Lakowicz, J. Malicka, J. Huang, Z. Gryczynski, and I. Gryczynski, "Ultrabright fluorescein-labeled antibodies near silver metallic surfaces," *Biopolymers* **74**, 467–475 (2004).

33. I. Brigger, C. Dubernet, and P. Couvreur, "Nanoparticles in cancer therapy and diagnosis," *Adv. Drug Delivery Rev.* **54**, 631–651 (2002).

34. K. Sokolov, M. Follen, J. Aaron, I. Pavlova, A. Malpica, R. Lotan, and R. Richards-Kortum, "Real-time vital optical imaging of precancer using anti-epidermal growth factor receptor antibodies conjugated to gold nanoparticles," *Cancer Res.* **63**, 1999–2004 (2003).

35. M. E. Akerman, W. C. W. Chan, P. Laakkonen, S. N. Bhatia, and E. Ruoslahti, "Nanocrystal targeting *in vivo*," *Proc. Natl. Acad. Sci. U.S.A.* **99**(20), 12617–12621 (2002).

36. W. C. W. Chan, D. J. Maxwell, X. Gao, R. E. Bailey, M. Y. Han, and S. Nie, "Luminescent quantum dots for multiplexed biological detection and imaging," *Curr. Opin. Biotechnol.* **13**, 40–46 (2002).

37. S. J. Oldenburg, R. D. Averitt, S. L. Westcott, and N. J. Halas, "Nanoengineering of optical resonance," *Chem. Phys. Lett.* **288**, 243–247 (1998).

38. R. D. Averitt, S. L. Westcott, and N. J. Halas, "Linear optical properties of gold nanoshells," *J. Opt. Soc. Am. B* **16**(10), 1824–1832 (1999).

39. U. Kreibig and M. Vollmer, *Optical Properties of Metal Clusters*, Springer-Verlag, Berlin (1995).

40. S. J. Oldenburg, J. B. Jackson, S. L. Westcott, and N. J. Halas, "Infrared extinction properties of gold nanoshells," *Appl. Phys. Lett.* **75**(19), 2897–2899 (1999).

41. C. Loo, A. Lin, L. Hirsch, M. Lee, J. Barton, N. Halas, J. West, and R. Drezek, "Nanoshell-enabled photonics-based imaging and therapy

42. W. T. Faulk and G. Taylor, "An immunocolloid method for the electron microscope," *Immunochemistry* **8**(11), 1081–1083 (1971).

43. L. R. Hirsch, R. J. Stafford, J. A. Bankson, S. R. Sershen, B. Rivera, R. E. Price, J. D. Hazle, N. J. Halas, and J. L. West, "Nanoshell-mediated near-infrared thermal therapy of tumors under magnetic resonance guidance," *Proc. Natl. Acad. Sci. U.S.A.* **23**, 13549–13554 (2003).

44. D. P. O'Neal, L. R. Hirsch, N. J. Halas, J. D. Payne, J. L. West, "Photo-thermal tumor ablation in mice using near infrared-absorbing nanoparticles," *Cancer Lett.* **109**, 181–176 (2004).

45. C. Loo, L. Hirsch, M. Lee, E. Chang, J. West, N. Halas, and R. Drezek, "Gold nanoshell bioconjugates for molecular imaging in living cells," *Opt. Lett.* **30**(9), 1012–1014 (2004).

46. C. Loo, A. Lowery, N. Halas, J. West, and R. Drezek, "Immunotargeted nanoshells for integrated cancer imaging and therapy," *Nano Lett.* **5**(4), 709–711 (2005).

47. G. Zaccanti, S. Del Bianco, and F. Martelli, "Measurements of optical properties of high-density media," *Appl. Opt.* **42**(19), 4023–4030 (2003).

48. H. C. van der Hulst, *Light Scattering by Small Particles*, Dover Press, New York (1981).

49. L. H. Wang, S. L. Jacques, and L. Q. Zheng, "MCML—Monte Carlo modeling of photon transport in multi-layered tissues," *Comput. Methods Programs Biomed.* **47**, 131–146 (1995).

50. R. Hornung, T. H. Pham, K. A. Keefe, M. W. Berns, Y. Tadir, and B. J. Tromberg, "Quantitative near-infrared spectroscopy of cervical dysplasia *in vivo*," *Hum. Reprod.* **14**(11), 2908–2916 (1999).

51. A. Toricelli, A. Pifferi, P. Taroni, E. Giambattistelli, and R. Cubeddu, "*In vivo* optical characterization of human tissues from 610–1010 nm by time-resolved reflectance spectroscopy," *Phys. Med. Biol.* **46**, 2227–2237 (2001).

52. R. M. P. Doornbos, R. Lang, M. C. Aalders, F. W. Cross, and H. J. C. M. Sterenborg, "The determination of *in vivo* human tissue optical properties and absolute chromophore concentrations using spatially resolved steady-state diffuse reflectance spectroscopy," *Phys. Med. Biol.* **44**, 967–981 (1999).

53. L. Quan and N. Ramanujam, "Relationship between depth of a target in a turbid medium and fluorescence measured by a variable-aperture method," *Opt. Lett.* **27**(2), 104–106 (2002).

54. R. L. P. van Veen, H. J. C. M. Sterenborg, A. Pifferi, A. Torricelli, and R. Cubeddu, "Determination of VIS-NIR absorption coefficients of mammalian fat, with time- and spatially resolved diffuse reflectance and transmission spectroscopy," in *Proc. Biomedical Topical Meetings*, on CD-ROM, Paper SF5, Optical Society of America, Washington, DC (2004).

55. A. Akin, "Functional imaging using near infrared light," in *Proc. of ISIK2000 Workshop on Biomedical Information Engineering*, pp. 209–212, Istanbul, Turkey (2000).

56. B. Chance, M. Cope, E. Gratton, N. Ramanujam, and B. Tromberg, "Phase measurement of light absorption and scatter in human tissue," *Rev. Sci. Instrum.* **69**(10), 3457–3481 (1998).

57. N. T. K. Thanh and Z. Rosenberg, "Development of an aggregation-based immunoassay for anti-protein A using gold nanoparticles," *Anal. Chem.* **74**, 1624–1628 (2002).

58. C. H. Teng, K. C. Ho, Y. S. Lin, and Y. C. Chen, "Gold nanoparticles as selective and concentrating probes for samples in MALDI MS analysis," *Anal. Chem.* **76**, 4337–4342 (2004).

59. A. Ishimaru and Y. Kuga, "Attenuation constant of a coherent field in a dense distribution of particles," *J. Opt. Soc. Am.* **72**, 1317–1320 (1982).

60. J. M. Schmitt and G. Kumar, "Optical scattering properties of soft tissue: a discrete particle model," *Appl. Opt.* **37**(3), 2788–2797 (1998).

61. J. K. Barton, N. J. Halas, J. L. West, and R. A. Drezek, "Nanoshells as an optical coherence tomography contrast agent," *Proc. SPIE* **5316**, 99–106 (2004).

62. Y. Wang, X. Xie, X. Wang, G. Ku, K. L. Gill, D. P. O'Neal, G. Stoica, and L. V. Wang, "Photoacoustic tomography of a nanoshell contrast agent in the in vivo rat brain," *Nano Lett.* **4**(9), 1689–1692 (2004).

Gold nanoshell bioconjugates for molecular imaging in living cells

Christopher Loo, Leon Hirsch, Min-Ho Lee, Emmanuel Chang, Jennifer West, Naomi Halas, and Rebekah Drezek

Department of Bioengineering, Rice University, MS-142, P.O. Box 1892, Houston, Texas 77251-1892

Advances in scattering-based optical imaging technologies offer a new approach to noninvasive point-of-care detection, diagnosis, and monitoring of cancer. Emerging photonics technologies provide a cost-effective means to image tissue *in vivo* with high resolution in real time. Advancing the clinical potential of these imaging strategies requires the development of optical contrast agents targeted to specific molecular signatures of disease. We describe the use of a novel class of contrast agents based on nanoshell bioconjugates for molecular imaging in living cells. Nanoshells offer significant advantages over conventional imaging probes including continuous and broad wavelength tunability, far greater scattering and absorption coefficients, increased chemical stability, and improved biocompatibility. We show that nanoshell bioconjugates can be used to effectively target and image human epidermal growth factor receptor 2 (HER2), a clinically relevant biomarker, in live human breast carcinoma cells. © 2005 Optical Society of America

OCIS codes: 170.0170, 170.3880, 290.5850.

Optical imaging tools such as reflectance confocal microscopy (RCM) and optical coherence tomography (OCT) offer the potential for noninvasive, high-resolution *in vivo* imaging at competitive costs relative to current imaging modalities. Scattering-based optical technologies rely on inherent changes in indices of refraction for image contrast.[1] Strategies that depend on only the intrinsic optical contrast within tissue have proved clinically valuable in many screening applications including early cancer detection; however, such techniques are not sensitive enough to resolve an image based solely on the presence of biomarkers of disease. In cases of cancer, when early detection is critical to reducing morbidity and mortality, the use of molecular-specific contrast agents provides the capacity to optically sense and image abnormalities long before pathologic changes occur at the anatomic level. In addition, imaging based on molecular-specific targets allows real-time *in vivo* monitoring of the treatment course and can provide fundamental insights into cancer biology.[2] A recent demonstration of scattering-based optical molecular imaging used gold colloid conjugates to antibodies to the epidermal growth factor receptor as a contrast agent in imaging cervical cancer cells and biopsy samples.[3] Although gold colloid conjugates are highly valuable as contrast agents for detecting superficial epithelial cancers with visible light, there is particular need for contrast agents in the near-infrared (NIR) region of the spectrum. This is the spectral region in which tissue is most optically transparent,[4] allowing imaging of deeper tissue structures. The NIR region is also the region already exploited by RCM and OCT; thus contrast agents would provide greatly needed enhancement wherever these imaging modalities are utilized.

Over the years, the expanding availability of a variety of nanostructures with highly controllable optical properties has provided a series of new contrast agents for optical imaging. The use of a variety of nanomaterials such as quantum dots, gold nanoparticles, and their bioconjugates in biological imaging has been described in recent literature.[5,6] Typically, nanostructures have many properties far superior to molecular species such as Indocyanine Green. Advantages include higher quantum efficiencies, greater scattering and absorbance cross sections, optical activities over more biocompatible wavelengths, and significantly increased chemical or photochemical stability. Compared with Indocyanine Green, nanoshells provide a millionfold enhancement in optical extinction.[7] Nanostructures can also be targeted to specific molecular signatures of interest. Therefore the systematic control of nanostructure properties that can be obtained by particular size variations is in direct contrast with molecular probes, whose properties vary nonsystematically between molecular species.

Nanoshells are a novel class of nanoparticles composed of a dielectric silica core surrounded by a thin metallic shell, which is typically made of gold. Nanoshells have a strong optical resonance whose wavelength can be tuned across much of the visible and infrared region of the spectrum by varying the relative size of the core and shell layer.[8] Varying the absolute nanoparticle size allows the relative contributions of scattering and absorption at a given wavelength of interest to be controlled.[9] This extremely agile tunability of the optical resonance is completely unique to nanoshells. Gold nanoshells are capable of scattering light in the NIR and provide appealing optical properties for use in conjunction with reflectance-based optical imaging methods. Additionally, the gold surface is biologically inert and allows proteins to be readily conjugated, facilitating *in vivo* use.[10]

Nanoshells have demonstrated promise in a variety of biomedical applications ranging from substrates for whole-blood immunoassays[11] to photothermal cancer therapy. By use of magnetic resonance thermal guidance, *in vitro* cancer cells were successfully ablated with gold nanoshells tuned to absorb

NIR light.[12] Similar use of nanoshells for photothermal ablation of tumors in mice further showed complete regression of tumors with the mice remaining healthy compared with controls.[13] In contrast with therapeutic NIR-absorbing nanoshells, we fabricate highly scattering NIR nanoshells for optical imaging. We then demonstrate the feasibility of using these targeted nanoshell bioconjugates as contrast agents to image human epidermal growth factor receptor 2 (HER2) expression in living human breast carcinoma cells.

HER2-positive SKBr3 human breast cancer cells were cultured in McCoy's 5A modified medium supplemented with 10% fetal bovine serum and antibiotics. HER2-negative MCF7 human breast cancer cells were cultured in Eagle's minimum essential medium supplemented with 10% fetal bovine serum, 0.01 mg/ml of bovine insulin, and antibiotics. Cells were maintained at 37°C and 5% CO_2.

The synthetic protocol developed for the fabrication of gold nanoshells is based on the principles of molecular self-assembly and colloid chemistry in aqueous solution. On the basis of the Stöber method,[14] we fabricated silica nanoparticle cores by reducing tetraethylorthosilicate in ammonium hydroxide and ethanol. Particle surfaces were terminated with amine groups by reaction with aminopropyltriethoxysilane. Small gold colloid was grown with the method of Duff and Baiker.[15] Gold–silica nanoshells were then grown by reacting gold salt ($HAuCl_4$) with the silica–colloid particles in the presence of formaldehyde. Nanoshell formation was assessed with an UV–Vis spectrophotometer and scanning electron microscopy. Nanoshell dimensions were mathematically assessed with Mie scattering theory with good agreement with scattering electron microscopy and UV–Vis spectra.

Either anti-HER2 (specific) or anti-immunoglobulin G (anti-IgG) (nonspecific) antibodies were attached to a polyethyleneglycol (PEG) linker [orthopyridyldisulfide-polyethyleneglycol-N-hydroxysuccinimide (OPSS-PEG-NHS), molecular weight of 2000] through a hydroxysuccinimide group (NHS). The antibody–PEG linker complex was then attached to the nanoshell surface through a sulfur-containing group located at the distal end of the PEG linker. By use of $NaHCO_3$ (100 mM, pH of 8.5), OPSS-PEG-NHS was resuspended to a volume equal to that of the antibody. The reaction was allowed to proceed on ice overnight. Excess unbound polymer was removed by membrane dialysis (molecular weight cutoff of 10,000). PEG-ylated antibody (0.67 mg/ml) was added to nanoshells (2×10^9 nanoshells/ml) to facilitate targeting. After antibody conjugation, nanoshell surfaces were coated with PEG-thiol (PEG-SH, molecular weight of 5000, 25 mM) to block nonspecific adsorption sites.

HER2-expressing SKBr3 cells were exposed to bioconjugated nanoshells (8 μg/mL) and observed under dark-field microscopy, a form of microscopy sensitive only to scattered light. Images were taken with a Zeiss Axioskop 2 plus microscope equipped with a black-and-white CCD camera under the same magnification and lighting conditions. Optical contrast was quantified with the Scion image analysis program. Average intensity values were obtained in each dark-field image. Normality of intensity data was established through a Shapiro Wilk test before using a paired Student's t-test (two tailed) to test for significance.

Figure 1 shows the optical properties for nanoshells with a 120-nm silica core radius and 35-nm-thick shell that were used in this study. Nanoshells with these dimensions generate a scattering spectrum beginning at 700 nm and extending far into the NIR region; thus nanoshells with these spectral characteristics are capable of facilitating imaging in both the visible and the NIR regions, allowing the nanoshell conjugates to be used as contrast agents for RCM and OCT.

As shown in Fig. 2, significantly increased optical contrast under dark-field conditions caused by HER2 expression was observed in HER2-positive cells targeted with anti-HER2-labeled nanoshells (right column) compared with cells targeted by either anti-IgG-labeled nanoshells (middle column) or cells not exposed to nanoshell conjugates (left column). Images in Figs. 2(a)–2(c) are cross-sectional slices of cells taken at the mid-focal plane at $40\times$ magnification. A series of dark-field images [Figs. 2(d)–2(f)] taken at a lower magnification ($10\times$) is included to demonstrate nanoshell targeting and coating of cell surfaces [Fig. 2(f)].

Histogram analysis of dark-field images shows that nanoshell targeting of the HER2 receptor resulted in significantly ($p < 0.05$) greater average contrast values in the anti-HER2 group (142 ± 16) compared with controls (anti-IgG 48 ± 12, no nanoshells 26 ± 4) (Fig. 3). Significantly less contrast was measured in HER2-negative cells exposed to anti-HER2-labeled nanoshells (34 ± 5) compared with HER2-positive cells (142 ± 16), providing additional evidence that the increased contrast seen under dark-field conditions may be specifically attributable to nanoshell targeting of the HER2 receptor. No significant differences were found between control groups.

Knowledge of potential molecular targets for diagnosis and therapy of disease continues to expand at a
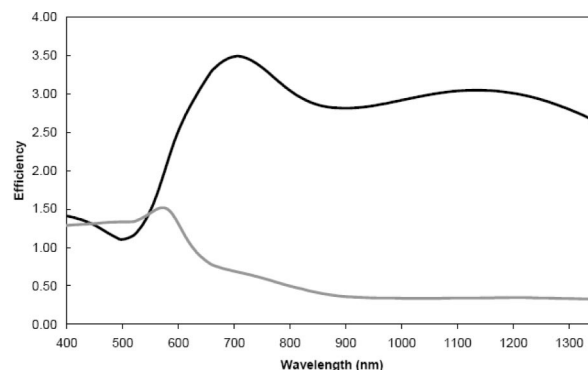

Fig. 1. Mie scattering theory predictions of the scattering (black) and absorption (gray) efficiencies for nanoshells with the 120-nm silica core radius and 35-nm-thick shell that were used in this study.
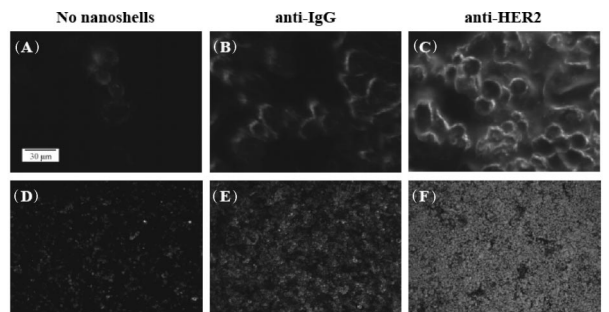
Fig. 2. (a)–(c) High-magnification dark-field images of HER2-positive SKBr3 breast cancer cells exposed to no nanoshells (left-hand column), anti-IgG-labeled nanoshells (middle column), or anti-HER2-labeled nanoshells (right-hand column). Cross-sectional images were taken at $40\times$ magnification at the mid-focal plane. (d)–(f) Dark-field images of HER2-positive cells taken at lower magnification $(10\times)$ demonstrating nanoshell targeting and coating of the cell surface.
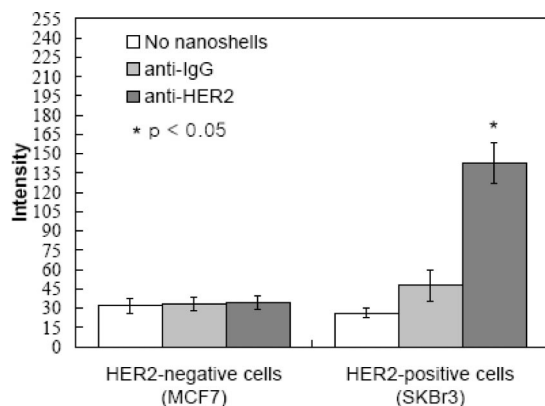

Fig. 3. Quantitative analysis of optical contrast owing to HER2-expression. Contrast was quantified by obtaining average histogram intensity values of dark-field images. Contrast data quantified with a HER2-negative MCF7 cell line are shown for comparison purposes. Intensity values range from 0 (black) to 255 (white), with higher values corresponding to greater contrast. Differences in mean scattered intensity between the anti-HER2 group and all other cell groups are statistically significant ($p < 0.05$).

rapid rate. However, translating knowledge of potential targets into new diagnostic and therapeutic techniques requires the development of methods to image molecular targets or the effects of therapeutic interventions on these targets *in vivo*, in real time, and in a cost-effective manner. Nanoshell-based molecular contrast agents offer unique advantages, including NIR tunability, size flexibility, and systematic control of optical properties. In this study we demonstrated that nanoshell bioconjugates can provide molecular optical contrast enhancement both qualitatively and quantitatively. Our findings collectively show that gold nanoshells can be used to target specific cancer

markers and allow *in vitro* cell-level molecular imaging with a scattering-based optical approach. A dark-field microscope was used in this study to demonstrate the feasibility of nanoshell bioconjugates for molecular imaging in living cells. Although dark-field microscopy is appropriate for *in vitro* imaging applications, use of nanoshell conjugates *in vivo* will require more sophisticated imaging techniques. Our current results encourage future work assessing nanoshell-based contrast agents *in vivo* with RCM and OCT. The combination of targeted nanoshells and the field of biophotonics have the potential to play a vital role in the future of cancer screening and diagnosis, in designing and monitoring therapeutic interventions, and in fundamental studies of carcinogenesis.

References

1. G. J. Tearney, M. E. Brezinski, B. E. Bouma, S. A. Boppart, C. Pitris, J. F. Southern, and J. G. Fujimoto, Science **276**, 2037 (1996).
2. R. Weissleder and U. Mahmood, Radiology **219**, 316 (2001).
3. K. Sokolov, M. Follen, J. Aaron, I. Pavlova, A. Malpica, R. Lotan, and R. Richards-Kortum, Cancer Res. **63**, 1999 (2003).
4. R. Weissleder, Nat. Biotechnol. **19**, 316 (2001).
5. M. E. Akerman, W. Chan, P. Laakkonen, S. N. Bhatia, and E. Ruoslahti, Proc. Natl. Acad. Sci. USA **99**, 12617 (2002).
6. X. Gao, Y. Cui, R. M. Levenson, L. W. Chung, and S. Nie, Nat. Biotechnol. **22**, 969 (2004).
7. M. Landsman, G. Kwant, G. Mook, and W. Zijlstra, J. Appl. Physiol. **40**, 575 (1976).
8. S. J. Oldenburg, J. B. Jackson, S. L. Westcott, and N. J. Halas, Appl. Phys. Lett. **75**, 2897 (1999).
9. S. J. Oldenburg, G. D. Hale, J. B. Jackson, and N. J. Halas, Appl. Phys. Lett. **75**, 1063 (1999).
10. L. Tang, L. Liu, and H. Elwing, J. Colloid Interface Sci. **41**, 333 (1998).
11. L. R. Hirsch, J. B. Jackson, A. Lee, N. J. Halas, and J. L. West, Anal. Chem. **75**, 2377 (2003).
12. L. R. Hirsch, R. J. Stafford, J. A. Bankson, S. R. Sershen, B. Rivera, R. E. Price, J. D. Hazle, N. J. Halas, and J. L. West, Proc. Natl. Acad. Sci. USA **100**, 13549 (2003).
13. D. P. O'Neal, L. R. Hirsch, N. J. Halas, J. D. Payne, and J. L. West, Cancer Lett. (Shannon, Irel.) **209**, 171 (2004).
14. W. Stober, and A. Fink, J. Colloid Interface Sci. **26**, 62 (1968).
15. D. G. Duff and A. Baiker, Langmuir **9**, 2301 (1993).

Immunotargeted Nanoshells for Integrated Cancer Imaging and Therapy

Christopher Loo,[†,‡] Amanda Lowery,[†,‡] Naomi Halas,[§] Jennifer West,[†,‡] and Rebekah Drezek*,[†,‡]

Departments of Bioengineering and Electrical and Computer Engineering, Rice University, P.O. Box 1892, Houston, Texas 77251-1892

ABSTRACT

Nanoshells are a novel class of optically tunable nanoparticles that consist of a dielectric core surrounded by a thin gold shell. Based on the relative dimensions of the shell thickness and core radius, nanoshells may be designed to scatter and/or absorb light over a broad spectral range including the near-infrared (NIR), a wavelength region that provides maximal penetration of light through tissue. The ability to control both wavelength-dependent scattering and absorption of nanoshells offers the opportunity to design nanoshells which provide, in a single nanoparticle, both diagnostic and therapeutic capabilities. Here, we demonstrate a novel nanoshell-based all-optical platform technology for integrating cancer imaging and therapy applications. Immunotargeted nanoshells are engineered to both scatter light in the NIR enabling optical molecular cancer imaging and to absorb light, allowing selective destruction of targeted carcinoma cells through photothermal therapy. In a proof of principle experiment, dual imaging/therapy immunotargeted nanoshells are used to detect and destroy breast carcinoma cells that overexpress HER2, a clinically relevant cancer biomarker.

Background. Nanoshells are composed of a dielectric silica core covered by a thin metal shell which is typically gold. Based on the relative dimensions of the core radius and shell thickness, nanoshell optical resonances may be continuously tuned through wavelengths ranging from the ultraviolet to the infrared,[1] including the NIR region where tissue transmissivity is highest due to low scattering and absorption from intrinsic chromophores.[2] Gold nanoshells offer appealing properties for biomedical sensing and therapeutic applications including large optical cross-sections exceeding conventional NIR dyes, such as indocyanine green, by many orders of magnitude as well as significantly improved photostability resulting from the rigid metallic structure of a nanoshell.[3] Furthermore, antibodies and other targeting moieties can be readily conjugated to the gold surface of nanoshells.[4] Although the gold surfaces of nanoshells are generally considered to be biocompatible, stealthing polymers such as poly(ethylene glycol) (PEG) may be attached to nanoshell surfaces to further enhance biocompatibility and improve blood circulation times.[5]

Nanoshells designed to have a high scattering optical cross-section are potentially valuable contrast agents for photonics-based imaging modalities such as reflectance confocal microscopy (RCM)[6] and optical coherence tomography (OCT),[7] which offer high-resolution approaches to early cancer detection. To image deeper tumors, other methods such as frequency-domain photon migration may be used to enable optical visualization of scatter-based contrast.[8] Alternatively, nanoshells can be designed to strongly absorb NIR light providing a novel means to mediate photothermal ablation of cancer cells.[9,10] Of particular interest is the possibility of engineering nanoshells with optical properties suitable for combined imaging and therapy. Past attempts to develop combined approaches to imaging and therapy have relied on methods such as the use of radio-immunoconjugates[11] whose clinical effectiveness is limited by factors including low tumor uptake, dose-limiting toxicity, and the necessity to expose patients to ionizing radiation.[12] Nanoshells provide an alternative means to enable dual imaging/therapy applications as they can be engineered to simultaneously provide both scattering and absorption properties at specific frequencies. Selective accumulation of nanoshells may be achieved via passive extravasation based on the enhanced permeability and retention (EPR) of small particles (<400 nm) associated with the leaky tumor vasculature,[13] with further targeting possible using antibodies targeted against oncoproteins overexpressed on cell surfaces. In principle, upon accumulation within tumors, nanoshells may provide both molecular-specific image contrast and, when clinically indicated, mediate cancer treatment based on NIR thermal ablation therapy. Here we provide an in vitro demonstration of the dual imaging/therapy approach, first detecting and then thermally ablating human breast cancer cells that overexpress HER2 using immunotargeted nanoshells that have been designed to both scatter and absorb light within the NIR.

---

* Corresponding author. E-mail: drezek@rice.edu; phone (713) 348-3011; fax (713) 348-5877.
† These authors contributed equally to this work.
‡ Department of Bioengineering.
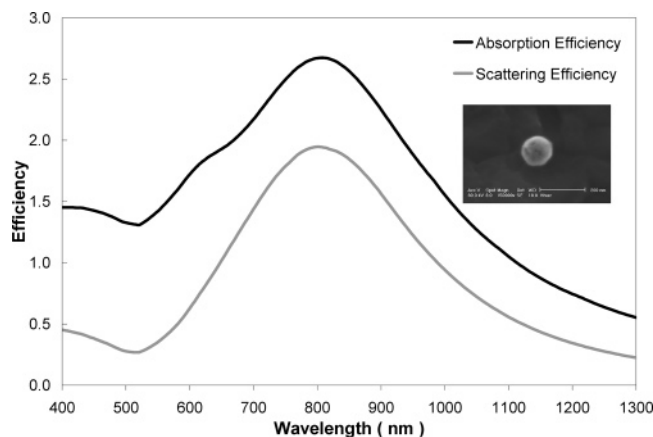§ Department of Electrical and Computer Engineering.

Figure 1. Spectral characteristics and SEM image of NIR scattering/absorbing nanoshells. Spectrum obtained by Mie scattering theory shows the dual scattering/absorbing NIR nature (~800 nm) of nanoshells with dimensions consisting of a 120 nm diameter silica core and 10 nm thick shell. Predicted optical extinction, the sum of the combined contributions of absorption and scattering, was confirmed with a UV−vis spectrophotometer (data not shown). SEM image of nanoshells with an overall diameter of 140 nm is included. Scale bar = 200 nm.

Nanoshell Fabrication. Nanoshells with dimensions providing peak optical scattering and absorption efficiencies in the NIR (~800 nm) were designed and fabricated as described in previous studies.[14] Using the Stöber method,[15] 120 nm diameter silica nanoparticles were fabricated. The particle surface was then terminated with amine groups by reaction with (aminopropyl)triethoxysilane (APTES). Small gold colloid was grown using the method of Duff[16] and then adsorbed onto the aminated silica nanoparticle surface. More gold was reduced onto these colloid nucleation sites using potassium carbonate and $HAuCl_4$ in the presence of formaldehyde. Gold nanoshell formation was assessed with a UV−vis spectrophotometer. Nanoshell dimensions were assessed using scanning electron microscopy (SEM). Shell thickness was mathematically corroborated by Mie scattering theory with good agreement with SEM. Figure 1 shows the spectral characteristics and an SEM image of nanoshells possessing a 10 nm thick shell that were used in this study.

Antibody Conjugation. Either anti-HER2 or a nonspecific antibody (anti-IgG) was first attached to a PEG linker (OPSS-PEG-NHS, MW = 2 K) through an amidohydroxysuccinimide group (NHS). The antibody-PEG linker complex was then attached to the nanoshell surface through a sulfur-containing group located at the distal end of the PEG linker. The antibody-PEG complex was reacted with nanoshells for 1 h. Additional PEG-thiol (MW = 5 K, 50 nM) was later added to the nanoshell suspension in order to block non-specific adsorption sites. Nanoshells were centrifuged to remove excess PEG and antibody and resuspended in water at a final concentration of 3×10^9 nanoshells/mL.

Cell Culture and Incubation of Nanoshell Bioconjugates with Cells. HER2-positive SKBr3 breast adenocarcinoma cells were grown in McCoy's 5A growth media containing 10% FBS and 1% antibiotics at 37 °C and 5% CO_2. Concentrated 10× McCoy's media (free of FBS and

antibiotics to eliminate nonspecific interactions with nanoshells) was quickly added to the nanoshells at a volumetric ratio of 1:9. Next, 500 μL of this McCoy's nanoshell suspension was placed on cells, followed by 1 h incubation. McCoy's media containing FBS and antibiotics was added following rinsing of unbound nanoshells.

Molecular Imaging of HER2 Expression and in Vitro Photothermal Therapy. Cells were imaged under a darkfield microscope sensitive to scattered light. Images were taken with a Zeiss Axioscope2 microscope equipped with a black/white CCD camera. All images were taken at the same magnification under the same lighting conditions. Immediately following imaging, cells were exposed to NIR irradiation (820 nm, 0.008 W/m^2 for 7 min). The overlap of peak nanoshell absorbance with the emission wavelength of the laser source promoted optimal laser-induced nanoshell heating. Cells were stained for viability using calcein AM. Stained cells were examined under fluorescence and phase contrast microscopy with a Zeiss Axiovert 135 microscope. Silver staining was then performed to assess the presence of nanoshell binding on cell surfaces.

Results. Figure 2 presents results from combined imaging and therapy of SKBr3 breast cancer cells using nanoshells targeted against HER2 (right column). In addition, control images of cells taken without nanoshells (left column) and of cells incubated with nonspecifically labeled nanoshells (middle column) are presented. Significantly increased scatter-based optical contrast due to nanoshell binding was observed in cells incubated with anti-HER2 nanoshells (top row, right column) as compared to the two control cell groups (top row, left and middle columns). After photothermal therapy, cell death was observed only in cells treated with NIR laser following exposure to anti-HER2 nanoshells (middle row, right column). This effect was not observed in cells treated with either nanoshells conjugated to a nonspecific antibody or NIR light alone (middle row, left and middle columns). Greater silver staining intensity was seen in cells exposed to anti-HER2 nanoshells (bottom row, right column) compared to controls (bottom row, left and middle columns), suggesting enhanced nanoshell binding to cell surfaces overexpressing HER2. To establish that anti-HER2 nanoshells alone do not induce cytotoxicity, we incubated SKBr3 cells with anti-HER2 nanoshells over a range of concentrations and incubation times. Figure 3 shows calcein fluorescence of SKBr3 cells that were exposed to HER2-targeted nanoshells (3×10^9 nanoshells/mL). In statistical analysis comparing cells incubated with nanoshells and control cells not exposed to nanoshells, no differences in viability were observed.

Discussion. Currently, distinct diagnostic and therapeutic modalities are employed for the diagnosis and treatment of cancer. Furthermore, in most cases, standard of care treatment requires invasive surgical procedures or other therapies associated with significant side effect profiles, high cost, and poor clinical outcome. A single technology providing both diagnostic and therapeutic capabilities would potentially yield significant savings in time, cost, and patient discomfort associated with diagnosing and treating many cancers today. Nanoshells offer unique properties that facilitate an integrated
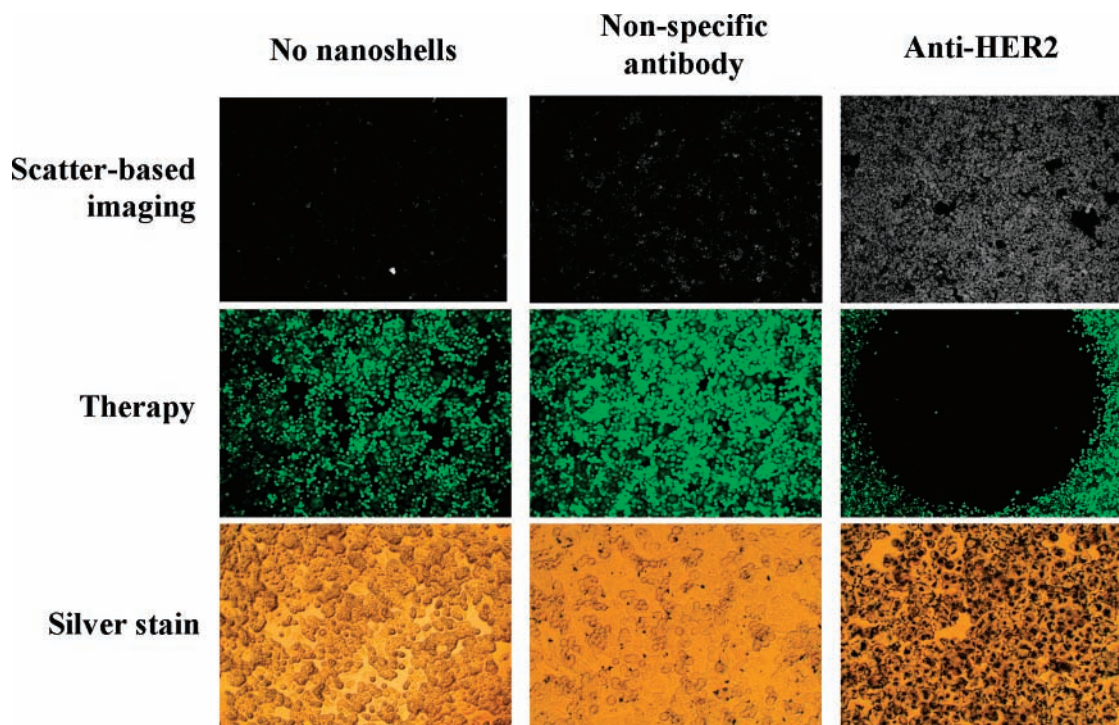
Figure 2. Combined imaging and therapy of SKBr3 breast cancer cells using HER2-targeted nanoshells. Scatter-based darkfield imaging of HER2 expression (top row), cell viability assessed via calcein staining (middle row), and silver stain assessment of nanoshell binding (bottom row). Cytotoxicity was observed in cells treated with a NIR-emitting laser following exposure and imaging of cells targeted with anti-HER2 nanoshells only. Note increased contrast (top row, right column) and cytotoxicity (dark spot) in cells treated with a NIR-emitting laser following nanoshell exposure (middle row, right column) compared to controls (left and middle columns).
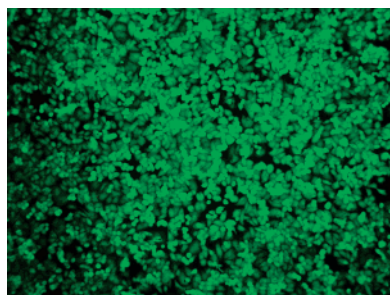

Figure 3. Calcein fluorescence of HER2-positive SKBr3 cells incubated with anti-HER2 nanoshells without NIR photothermal therapy. No cytotoxicity is observed.

imaging/therapy approach including systematic control of both optical scattering and absorption, tunability throughout the NIR where tissue penetration is highest, and a particle size conducive to passive extravasation from the tumor vasculature. We showed that immunotargeted nanoshells can provide scattering contrast for imaging while also exhibiting sufficient absorption to enable effective photothermal therapy. This is the first demonstration of coupling a bioimaging application to a cancer therapy application using nanoshells targeted against a clinically relevant biomarker. Future studies will extend the in vitro concept demonstrated here to in vivo animal experiments.

References

(1) Oldenburg, S. J.; Jackson, J. B.; Westcott, S. L.; Halas, N. J. *Appl. Phys. Lett.* **1999**, *111*, 2897−2899.
(2) Weissleder, R. *Nat. Biotechnol.* **2001**, *19*, 316−317.
(3) Landsman, M. L. J.; Kwant, G.; Mook, G. A.; Zijlstra W. G. *J. Appl. Physiol.* **1976**, *40*, 575−583.
(4) Tang, L.; Liu, L.; Elwing, H. *J. Colloid Interface Sci.* **1998**, *41*, 333−340.
(5) Chen, A. M.; Scott, M. D. *BioDrugs* **2001**, *15*, 833−847.
(6) Smithpeter, C. L.; Dunn, A. K.; Welch, A. J.; Richards-Kortum, R. *Appl. Opt.* **1998**, *37*, 2749−2754.
(7) Tearney, G. J.; Brezinski, M. E.; Bouma, B. E.; Boppart, S. A.; Pitris, C.; Southern, J. F.; Fujimoto, J. G. *Science* **1997**, *276*, 2037−2039.
(8) Ntziachristos, V.; Bremer, C.; Weissleder, R. *Eur. Radiol.* **2003**, *13*, 195−208.
(9) Hirsch, L. R.; Stafford, R. J.; Bankson, J. A.; Sershen, S. R.; Rivera, B.; Price, R. E.; Hazle, J. D.; Halas, N. J.; West, J. L. *Proc. Natl. Acad. Sci.* **2003**, *100*, 13549−13554.
(10) O'Neal, D. P.; Hirsch, L. R.; Halas, N. J.; Payne, J. D.; West, J. L. *Cancer Lett.* **2004**, *209*, 171−176.
(11) Li, W. P.; Lewis, J. S.; Kim, J.; Bugaj, J. E.; Johnson, M. A.; Erion, J. L.; Anderson, C. J. *Bioconjugate Chem.* **2002**, *13*, 721−728.
(12) Goldenberg, D. M. *Am. J. Med.* **1993**, *94*, 297−312.
(13) Maeda, H.; Fang, J.; Inutsuka, T.; Kitamoto, Y. *Int. Immunopharmacol.* **2003**, *3*, 319−328.
(14) Oldenburg, S. J.; Averitt, R. D.; Westcott, S. L.; Halas, N. J. *Chem. Phys. Lett.* **1998**, *288*, 243−247.
(15) Stöber, W.; Fink, A. *J. Colloid Interface Sci.* **1968**, *26*, 62−69.
(16) Duff, D. G.; Baiker, A. *Langmuir* **1993**, *9*, 2301−2309.

NL050127S

Photo-thermal cancer therapy using intravenously injected near infrared-absorbing nanoparticles

D. Patrick O'Neal[a*], Leon R. Hirsch[b], Naomi J. Halas[c], J. Donald Payne[a], Jennifer L. West[b]

[a]Nanospectra Biosciences, Inc., 8285 El Rio Suite #130, Houston, TX 77054, USA
[b]Department of Bioengineering, Rice University, P.O. Box 1892, MS-142, Houston, TX 77251 USA
[c]Department of Electrical and Computer Engineering, Rice University, P.O. Box. 1892, MS-366, Houston, TX 77251 USA

ABSTRACT

This report focuses on the treatment parameters leading to successful nanoshell-assisted photo-thermal therapy (NAPT). NAPT takes advantage of the strong near infrared (NIR) absorption of gold-silica nanoshells, a new class of nanoparticles with tunable optical absorptivities that are capable of passive extravasation from the abnormal tumor vasculature due to their nanoscale size. Under controlled conditions nanoshells accumulate in tumors with superior efficiency compared to surrounding tissues. For this treatment: (1) tumors were inoculated in immune-competent mice by subcutaneous injection, (2) polyethylene glycol coated nanoshells ($\approx$150 nm diameter) with peak optical absorption in the NIR were intravenously injected and allowed to circulate for 6 – 48 hours, and (3) tumors were then extracorporeally illuminated with a collimated diode laser (808 nm, 2-6 W/cm2, 2-4 min). Nanoshell accumulations were quantitatively assessed in tumors and surrounding tissues using *neutron activation analysis* for gold. In order to assess temperature elevation, laser therapies were monitored in real-time using a mid-infrared thermal sensor. NAPT resulted in complete tumor regression in >90% of the subjects. This simple, non-invasive procedure shows great promise as a technique for selective photo-thermal tumor treatment.

Keywords: Hyperthermia, nanotechnology, nanoshell, near infrared, laser, minimally invasive therapy

1. INTRODUCTION

Nanoshells are a new class of nanoparticles being utilized in development of therapies for the photo-thermal treatment of solid tumors, as a contrast agent for use in photo-acoustic tomography, for laser tissue welding, and for biosensing applications. This research demonstrates the potential of this nanoshell-based therapy to provide a significant new method for the minimally invasive treatment of cancer. The potential benefits of this new therapeutic technique include: (i) a rapid complete or partial response detectable by the physician within days; (ii) the treatment of early regional metastatic disease before clinical detection; (iii) low-to-no systemic toxicity, resulting in a superior side effect profile compared to traditional and targeted chemotherapeutic agents; (iv) the ability to repeat therapy as desired (including prophylactic treatment) because there is no thermal "tissue memory", unlike radiation, and low-to-no toxicity; and (v) compatibility with, and potential enhancements of, standard chemotherapy and radiation treatment modalities.

Nanoshells are a novel class of materials consisting of a metallic shell and a dielectric core. These nanoparticles can be designed and constructed to absorb or scatter light at desired wavelengths, including ranges where human tissue is minimally absorptive. This "tunability" is achieved by altering the ratio of the thickness of the metal shell to the non-conducting core. Nanoshells for most applications range from 90 to 300 nanometers in diameter.[1]

---

*Correspondence: Email: poneal@nanospectra.com; Telephone: (713) 842-2720

For life science applications, the shells are comprised of gold, which has a long history of use *in vivo* in a particulate form or as a coating. The non-conducting core is generally silica, but can be any biocompatible dielectric material. For therapeutic applications, Nanoshells can be designed to absorb infrared light at wavelengths where light is not significantly absorbed by human tissue. Human tissue is minimally absorptive in the ranges from 750 nm to 1100 nm, often referred to as the "water window" or "tissue optical window". While solid gold particles absorb light at wavelengths also absorbed by tissue, gold-coated Nanoshells can be designed to absorb or scatter light within this "tissue optical window", enabling new *in vivo* applications.

2. EXPERIMENTAL METHODS

Synthesis of Thiolated Polyethylene Glycol (PEG-SH)

PEG-SH was synthesized by reacting PEG-Amine (MW 5,000, chromatographically pure, Nektar) with 2-iminothiolane (Sigma) for 1 hour. This size PEG was selected after a review of studies investigating the dependence of PEG chain length on liposome half-life in the blood supply. The product was then dialyzed (MWCO 3,500 dialysis cassette, Pierce) against 18 M•ohm-cm deionized (DI) H_2O for 6-8 hours to remove excess reagent. The SH-PEG yield was determined colorimetrically at 412 nm after reacting with Ellman's Reagent (5,5'-Dithio-bis(2-Nitrobenzoic Acid), Sigma). Product was stored in aliquots at –20 ºC.

Gold-Silica Nanoshell Fabrication

Nanoshells were fabricated as previously described.[2] Briefly, ≈120nm dia. silica nanoparticles were obtained (MP-1040, Nissan Chemical America Corporation) and transferred to pure ethanol. The particle surface was then terminated with amine groups by reaction with 3-aminopropyltriethoxysilane (APTES, 97+%, Avocado Research Chemicals, Ltd.). Very small gold colloid (1 –3 nm) was grown using the method of Duff, et. al.[3] This colloid was aged for 4-14 days at 6 ºC and then concentrated 15-20X using a rotary evaporator. The amineated silica particles were then added to the gold colloid suspension. Gold colloid adsorbs to the amine groups on the silica surface resulting in a silica nanoparticle covered with islands of gold colloid. Gold-silica nanoshells were then grown by reacting $HAuCl_4$ with the silica-colloid particles in the presence of formaldehyde. This process reduces additional gold onto the colloid adsorbed the silica particle surface. These colloidal islands serve as nucleation sites, causing the surface colloid to grow eventually coalescing neighboring colloid, forming a complete metal shell. Nanoshell formation was assessed using a UV-Vis spectrophotometer (Genesys 5, Spectronic, Inc.) and TEM when available. The resulting nanoshell solutions possessed a ≈14 nm thick gold shell, generating a peak optical absorption at 805 – 810 nm. PEG-SH was then assembled onto nanoshell surfaces by combining PEG-SH (25 μM final concentration) with refrigerated nanoshells ($4.5x10^9$ nanoshells/mL) in DI water for 1 hr followed by gentle centrifugation. Prior to injection, nanoshells were resuspended at $110x10^9$ nanoshells/mL concentration in a sterile 0.9% sodium chloride solution. Nanoshell stability in saline, which suggests an adequate PEG coverage of the gold surface, was monitored separately via spectrophotometric analysis at the nanoparticles' peak absorbance. The concentration of nanoshells injected was verified with *neutron activation analysis* (NAA), which is capable of quantifying picogram quantities of gold in solution or tissue (see below).

Animal and Tumor Model

All animals were handled and cared for in accordance with the "Guide for the Care and Use of Laboratory Animals".[4] 25 female albino BALB/cAnNHsd (Harlan Sprague Dawley, Indianapolis, IN) mice were obtained at 5-6 weeks (15-20g body weight) of age. Each was subcutaneously inoculated with $1.5x10^5$ (50μL injected) CT26.WT (ATCC) murine colon carcinoma tumor cells.(22)

When necessary, mice were anesthetized with a 20mg/mL Avertin solution at 100μL/5 grams body weight. Stock Avertin was prepared by mixing 25g 2,2,2-tribromoethanol (TCI) with 15.5 mL tert-Amyl alcohol (TCI America) for 12 hours in a dark bottle. A working solution was prepared by mixing 0.5 mL Avertin stock with 39.5 ml 0.9% saline in a dark container, then filter sterilized (0.22μM) and stored in aliquots at 6

°C. This product can become toxic as it is subject to photo-degradation, and was stored and handled accordingly.

Other products employed during the study included a depilatory (Surgicream, Ardell International) used in conjunction with a small electric razor to remove hair at the treatment site. Liquid PEG (600 MW, Sigma-aldrich) was manually applied to the skin at the treatment site which acted as a both an ointment to reduce irritation after hair removal and as an index matching agent prior to laser treatment.

Biodistribution Analysis and Tumor Accumlation of Nanoshells

NAA for gold content was chosen to assess the location and/or accumulation of nanoshells in the murine model. NAA was performed under the direction of William Dennis James, Ph.D. and Michael Raulerson at the Center for Chemical Characterization and Control, Texas A&M University, using a 1 M•watt TRIGA reactor. Briefly, tissue sample vials were loaded into cans near (1) vials containing NIST gold standards as well as (2) nanoshell standards representing the precise quantity of each injected dose. The cans were lowered into close proximity of the 1 MW 96-rod ^{235}U fission reactor core (neutron flux $> 10^{12}$ cm^{-2}s^{-1}) for 4 – 14 hr. After activation, samples were "cooled" to allow radioactive decay of short life isotopes (Na, Cl) for several days. Gamma rays (1.3 keV) from samples and controls were then quantified with germanium detectors.

Nanoshell distribution in tissue and accumulation in tumors were evaluated separately, the results of which are described in abbreviated form here to specifically address the challenge of optimizing tumor treatment parameters. Briefly, female albino BALB/c mice (as described above) were anesthetized (2-4 % isoflurane) and injected via tail vein with 100 μL of PEGylated nanoshells (11.0 x 10^9/mL, A^{800} = 1.8 @ 25x dilution) suspended in 0.9 % NaCl. For biodistrbution, mice were revived and nanoshells were allowed to circulate between 4 hours and 28 days (n = 4 at each of 6 time points), at which point mice were exsanguinated via cardiac stick then sacrificed. Blood, liver, lung, spleen, muscle (quadricep), kidney, bone (femur), and brain were excised and placed into polyethylene sample vials (preweighed and etched in acid to remove residual gold). For tumor accumulation analysis, separate mice with tumors (as above) were sacrificed and tissues harvested at 1, 4, 24, and 48 hours (n=3 for each time point). In both cases wet tissue weight of each sample was recorded before being frozen at -80 ^{0}C and then lyophilized. Dry tissue weights were then recorded and vials were then sealed for nuclear activation analysis (NAA) as described below.

3. RESULTS AND DISCUSSION

NAA Analysis of Nanoshell Concentration

The chart below (Fig 1) illustrates the measured gold content in parts per million of the blood, muscle and tumor from each animal. Error bars represent one standard deviation. Based on NAA analysis of blood content, the circulation half life of the injected dose of nanoshells may be estimated at 3.7 hours (Fig 2). This is substantially higher than the 1 to 3 minute half-life of unPEGylated gold colloid. The following chart illustrates this calculation (error bars represent one standard deviation).

Laser Dosimetry Studies

Using an 808-nm laser diode selected to maximize penetration depth and minimize optically induced thermal damage to superfluous tissue, experiments were performed on a small number (n=5) of BALB/cAnNHsd mice (>6 weeks age, 15 g) to determine the maximum non-damaging laser dose. These experiments were performed while the animal was anesthetized. It was determined that 4W/cm^2 (spot < 6mm diameter) could be delivered to healthy epidermis for 3 minutes resulting in surface temperature increases of < 20°C (T$_{max}$ = 48 ºC) and no visible damage. Subsequent observation and analysis of these treatment sites indicated no evidence of thermal damage – scarring, epidermal loss, etc.

Female albino BALB/cAnNHsd mice (>6 weeks age, 15 g) were obtained and inoculated with CT26.WT murine colon carcinoma tumor cells (ATCC) as previously described. Tumors were allowed to reach a burden of ~0.5 cm diameter. The laser dose of $4W/cm^2$ was tested on these tumors. During laser exposure, temperatures were quantified with an infrared thermal thermometer. It should be noted that there is some question about the accuracy of temperature measurements estimated in this manner, but in any case the measurements were precise and repeatable. The increase ($T_{max} = 52$ ºC) was still observed to remain below the damage threshold. Minimal skin irritation was observed following treatment in the stretched skin covering flank tumors at this dose, but this irritation healed in 2 to 3 days time.

These measurements were repeated for verification in additional animals that became part of the survivability study, with the additional goal of estimating damage to healthy skin in animals which had received nanoshell injections Surface temperature measurements were taken and analyzed during laser treatment on the first 16 mice that later became part of the greater survivability study (temperature readings on subsequently treated mice were consistent with these initial readings). These measurements, using an infrared thermal sensor, were taken at the location of the laser spot on NAPT treated tumors (n=8), healthy areas surrounding the NAPT treated tumors (n=6), and tumors on animals which received laser treatments but no nanoshell injection (n=8). As indicated in Figure 3, temperature changes in areas where there was no nanoshell accumulation were significantly lower. Also, for mice injected with nanoshells, there were smaller temperature changes in areas away form the tumor when these areas were exposed to laser. This implies that significant nanoshell accumulations were necessary to achieve a damage threshold.

Preliminary Accumulation time and Nanoshell Dose Studies

Feasibility experiments were performed to determine a range of nanoshell doses and accumulation times that worked in practice. BALB/cAnNHsd mice (>6 weeks age, 15 g) inoculated with the CT26.WT cell line were utilized in these studies. Nanoshell doses between $0.3 – 3 \times 10^9$ nanoshells/g were injected intravenously with accumulation times between 3 and 24 hours. No statistically significant difference, in terms of measured temperature or survivability, was noted when varying treatment times at (n=2 at each timepoint) at t = 3 hr, 6 hr, 9 hr, or 24 hr. When the nanoshell dose was varied from 0.3 to 3×10^9 nanoshells/g body weight, measured differences were seen with surface temperature measurements from 51 ºC to 68 ºC increasing concomitant with the dose. All mice with $\geq 1 \times 10^9$ nanoshells/g showed complete remission (n=5), with those mice receiving less than 1×10^9 nanoshells/g showing a 50% response rate (n=6). From this initial set of experiments, the "standard" dose of 1×10^9 nanoshells/g was selected for use in survivability experiments. A treatment timepoint of 6 hours after injection was chosen for expediency. No unusual symptoms or adverse physiological effects were noted in any mice due to the effects of the nanoshell injections.

Survival Study

In a formal survival study involving 44 mice, tumor size and animal survival were monitored for 60 days following treatment. Complete tumor resorption was observed in 91% of the treatment mice, with the remaining mice exhibiting tumors with significantly arrested growth, while tumors in both the sham (laser only, no nanoshells) and control groups continued to grow rapidly (Fig 4).

BALB/cAnNHsd mice (>6 weeks age, 15 g) were inoculated with the CT26.WT cell line as previously noted. Mice were selected for treatment when the subcutaneous tumors reached 3-5.5 mm diameter as measured with a digital caliper (8-16 days post-inoculation). A 5.5 mm tumor diameter was selected as the maximum possible treatment size due to the spot size of the collimated laser available. Seventeen of the mice had two tumors, and 27 had one. These were randomly distributed between 3 groups. Prior to each nanoshell injection, each mouse was anesthetized via intraperitoneal avertin injection (120 mg/kg, or 20μL/g body weight, 1.2% solution). 100 μL of the 1.1×10^{11} nanoshells/mL solution was then injected via the tail vein for mice in the treatment group. For the sham treatment group, a 100 μL 0.9% sterile saline injection was substituted for the nanoshell suspension. The control group received no intravenous injections or subsequent laser treatment. Laser treatments on the nanoshell treatment and sham treatment groups were performed 6 hours after injection to allow the systemically delivered nanoshells time to

accumulate in the tumors. The skin at the tumor site was swabbed with polyethylene glycol (Aldrich) as an index matching agent to maximize penetration of light into the tissue. Tumors in the nanoshell and sham treatment groups were exposed to NIR light (808 nm diode laser, 800 mW; 600μm fiber optic patch cable to a collimating lens) at 4 W/cm^2 for 3 minutes. During the NIR treatments, the cutaneous temperature was measured with a handheld infrared thermometer as previously noted (Fig 3). Post-treatment tumor size measurements were taken daily using a digital caliper. Survival time was also monitored, and animals were euthanized via trifluoroethane asphyxiation when tumor diameter reached 10 mm.

Statistical analysis was performed on the three groups by comparing the means of the tumor sizes at day 0 and day 10 post-treatment and computing the level of significant difference as measured by the p value. Similarly, p values were computed to compare the mean surface temperatures measured for the treatment and sham treatment groups. The survival time comparison for the three groups was augmented with a Kaplan-Meier survival analysis which generates confidence intervals for survival times (Fig 4).

4. CONCLUSION

The goals of the survivability study were to determine if nanoshell-assisted photo-thermal ablation would arrest the growth of tumors grown in mice. NAPT-treated tumors displayed complete regression in 91% of the mice, and these mice remained healthy and tumor-free >180 days following treatment. No mice under observation grew new tumors at a later date. Retreatment of the mouse experiencing a partial response was a viable option; however this was beyond the scope of this study. Further research is ongoing to optimize treatment parameters and to investigate the mechanisms involved in tumor regression following NAPT treatment.

ACKNOWLEDGEMENTS

[1] S. J. Oldenberg, R. D. Averitt, S. L. Westcott, and N. J. Halas, Nanoengineering of Optical Resonances, Chem Phys Lett, vol. 28, pp. 243-247, 1998.
[2] D. P. O'Neal, L. R. Hirsch, N. J. Halas, J. D. Payne, J. L. West, Photo-thermal tumor ablation in mice using near infrared-absorbing nanoparticles, Cancer Letters, 209(2), pp. 171-176, 2004.
[3] D. G. Duff and A. Baiker, A new hydrosol of gold clusters. 1. Formation and particle size variation, Langmuir, vol. 9, pp. 2301, 1993.
[4] National Research Council, Guide for the Care and Use of Laboratory Animals. Washington, D.C.: National Academy Press, 1996.
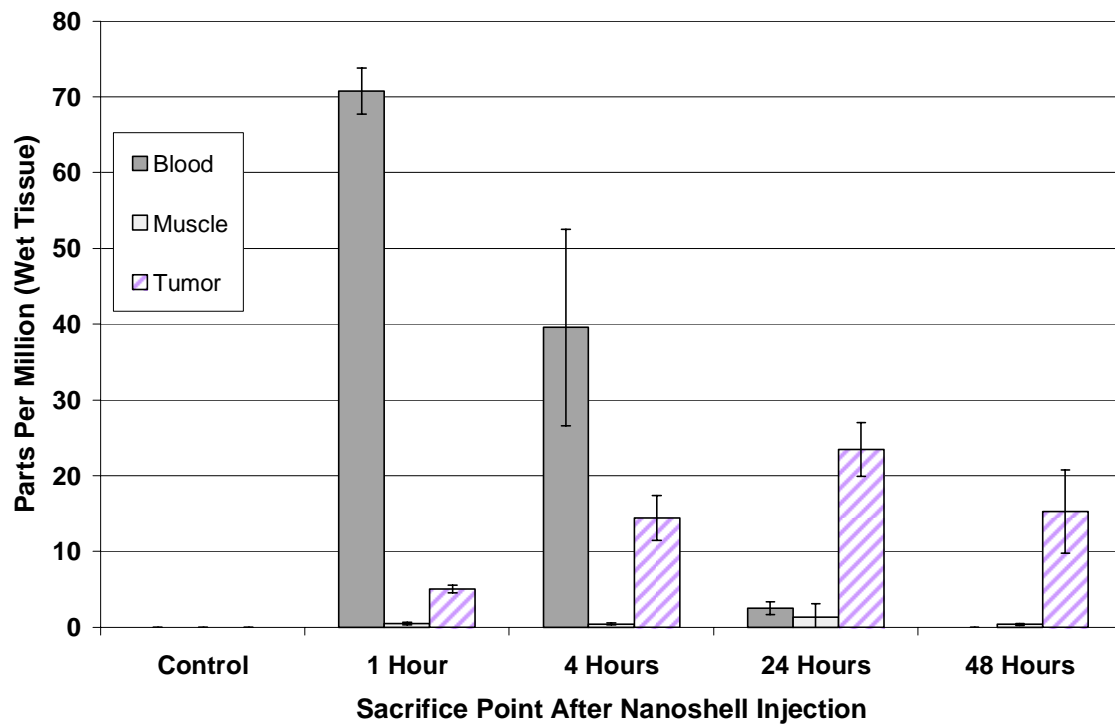
Figure 1. Gold content measured by neutron activation analysis (in parts per million) of blood, tumor and muscle samples at four timepoints after nanoshell injection. (n=15, 3 at each time point)

$$y = 102.12e^{-0.1856x}$$
$$R^2 = 0.9852$$
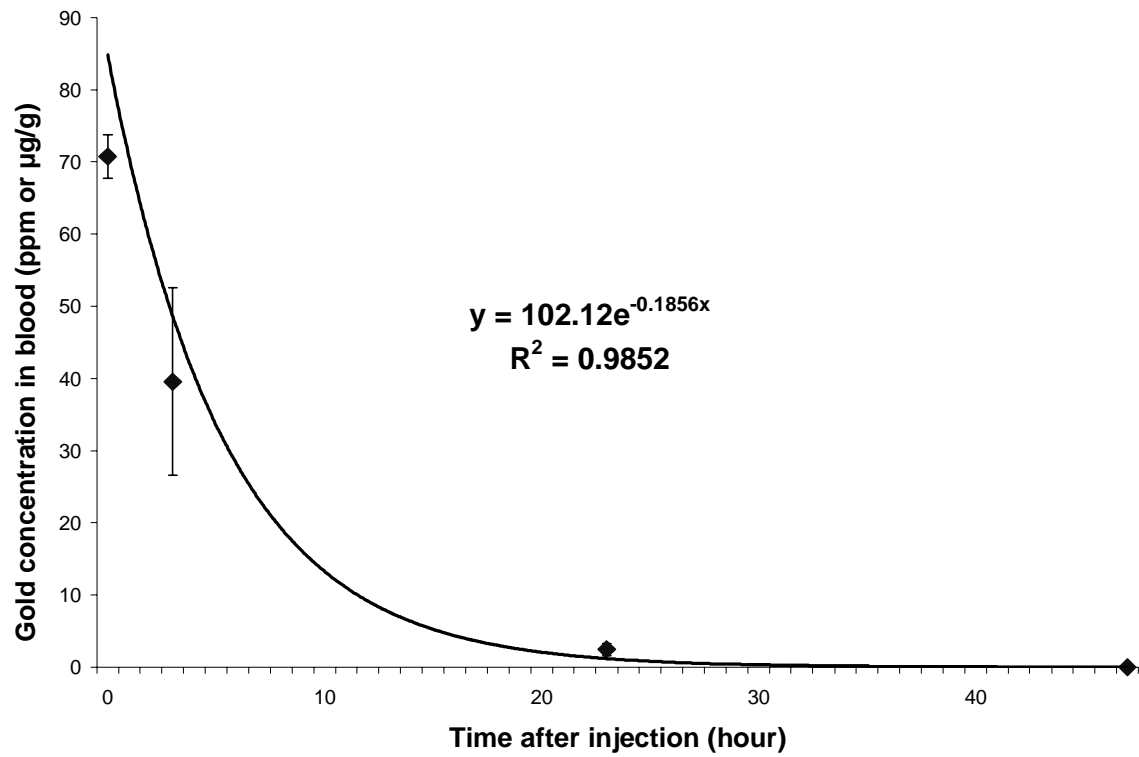
Figure 2: Estimate of circulating half-life of nanoshells after injection using gold content in blood (as measured by neutron activation analysis). Half-life is estimated at 3.7 hours using this technique (n=12, 3 at each time point).
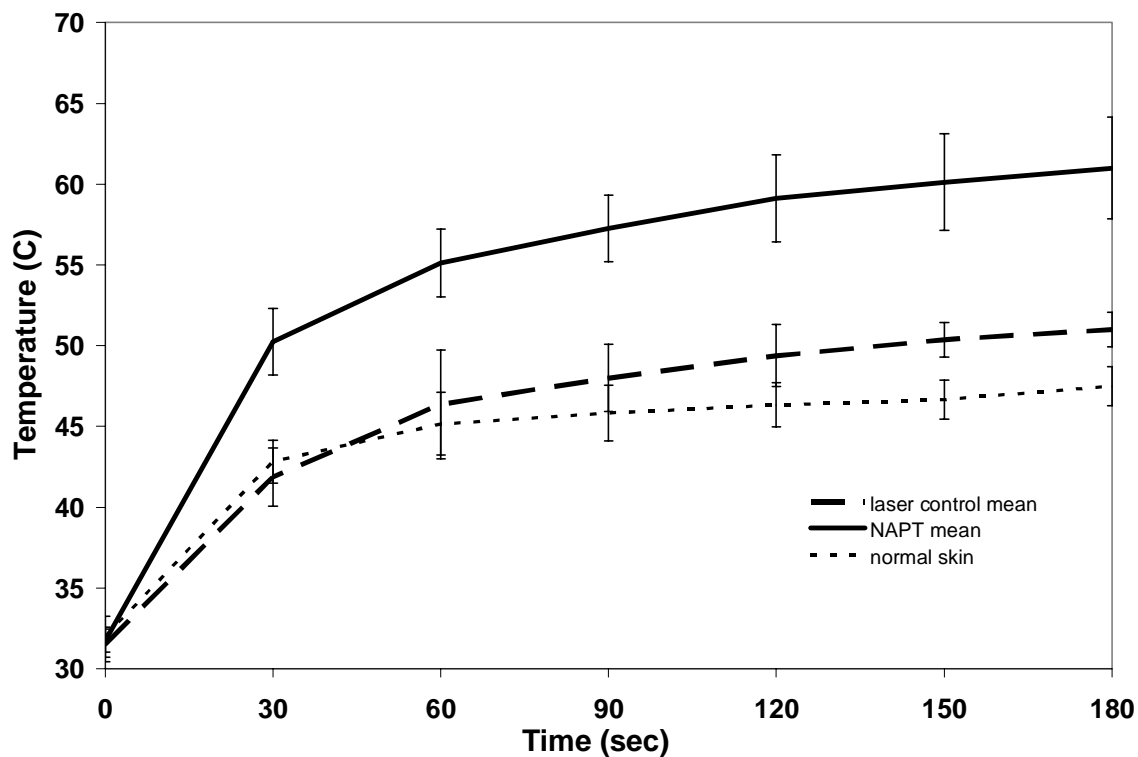
Figure 3. Surface temperature measurements via mid-infrared thermal imaging. These measurements were taken during laser treatment on the first 16 mice that later became part of the greater survivability study. These measurements, which must be considered with a knowledge of the limitations of a mid-infrared thermal sensor, were taken at the location of the laser spot on NAPT treated tumors (n=8), healthy areas surrounding the NAPT treated tumors (n=6), and tumors on animals which received laser treatments but no nanoshell injection (n=8).
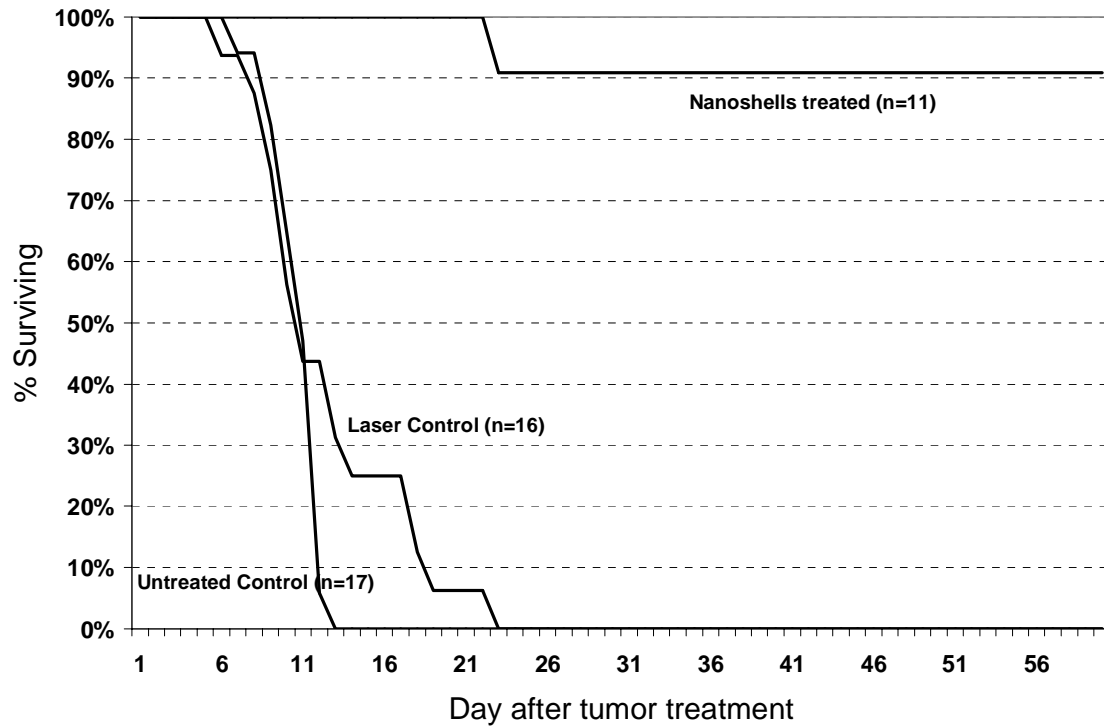
Figure 4. A survival time plot for the three groups. The mean survival time for the control group was 10.9 days with a 95% confidence interval of 10.2 to 11.6 days. The mean survival time for the laser control (sham treatment) group was 12.6 days with a 95% confidence interval of 10.3 to 14.9 days. The NAPT treatment mouse which did not survive had a survival time of 23 days.

All-Optical Nanoscale pH Meter

**Sandra W. Bishnoi,[†,‡] Christopher J. Rozell,[‡] Carly S. Levin,[§]
Muhammed K. Gheith,[‡] Bruce R. Johnson,[§] Don H. Johnson,[‡] and
Naomi J. Halas*[,‡,§]**

*Department of Electrical and Computer Engineering, Department of Chemistry, and
the Laboratory for Nanophotonics, Rice University, P.O. Box 1892,
Houston, Texas 77251-1892*

Received April 18, 2006; Revised Manuscript Received June 12, 2006

ABSTRACT

We show that an Au nanoshell with a pH-sensitive molecular adsorbate functions as a standalone, all-optical nanoscale pH meter that monitors its local environment through the pH-dependent surface-enhanced Raman scattering (SERS) spectra of the adsorbate molecules. Moreover, we also show how the performance of such a functional nanodevice can be assessed quantitatively. The complex spectral output is reduced to a simple device characteristic by application of a locally linear manifold approximation algorithm. The average accuracy of the nano-"meter" was found to be ±0.10 pH units across its operating range.

The development of active nanostructures, capable of performing a function or executing a specific task, is currently a major focus of research efforts in nanotechnology. One already highly successful nanodevice paradigm is the nanosensor: a designed nanostructure, which, when addressed either optically or electrically, responds by providing information about its local environment through its optical or electrical response. All-optical nanosensors hold exceptional promise as embeddable nanodevices that could potentially be used to probe a variety of exceedingly complex environments, such as individual living cells or the human body, in a virtually noninvasive manner. Early examples of optically addressable nanosensors are quantum dots and fluorescent nanoparticles, which have been used as passive, beaconlike reporters for marking specific biological structures in imaging applications that can potentially assist medical procedures.[1,2] Metallic nanoparticles, such as nanoshells,[3,4] nanocubes,[5] and nanorods,[6] have also been successfully demonstrated as contrast agents in bioimaging. When designed to elicit an optical resonant response at near-infrared wavelengths, the spectral region of greatest physiological transmissivity, they provide image contrast by increasing the scattered light from their immediate location without the strong absorption and fluorescence encountered when using visible light. Metallic nanoparticles have also been shown to provide a highly localized photothermal heating response sufficient to induce cell death and to induce complete, long-term tumor remission in animal studies.[7]

In addition to passive and active functions, there is a third, "informative" role, for which metallic nanoparticles are particularly well suited, and which enables nanosensor development. Metal nanostructures, when excited on their plasmon resonance, give rise to high-intensity electromagnetic fields at their surfaces, which can be harnessed for chemically specific sensing functionalities. Metallic nanoparticles can be designed to enhance the spectroscopic response of molecules bound to, or in close proximity of, their surfaces, an effect known as surface-enhanced Raman scattering (SERS).[8,9] Detailed local chemical information can be retrieved from the spectrum of the inelastically scattered light from the nanoparticle complex.[10] A more general all-optical nanosensing device can be envisioned based on a plasmon-resonant nanoparticle and a physically or chemically responsive layer of adsorbate molecules, where the local environment of the nanodevice is probed by incident light and the device output is the spectrum of Raman scattered light.

Here we report an all-optical nanosensor capable of measuring pH in its local vicinity continuously over the range of 5.80 to 7.60 pH units. The device consists of an Au nanoshell designed to elicit a high-enhancement SERS response as a standalone nanostructure from a layer of adsorbate molecules[11,12] at near-infrared wavelengths. The molecular adsorbate layer consists of *para*-mercaptobenzoic acid (pMBA), previously shown to be a molecule with a pH-sensitive SERS response.[13−15] Here we exploit the fact that the SERS signal of an individual adsorbate-coated nanoshell can be of the same order of magnitude intensity as the SERS signal from an individual nanosphere junction, or "hot spot"[16] so that individual nanostructures can function as standalone
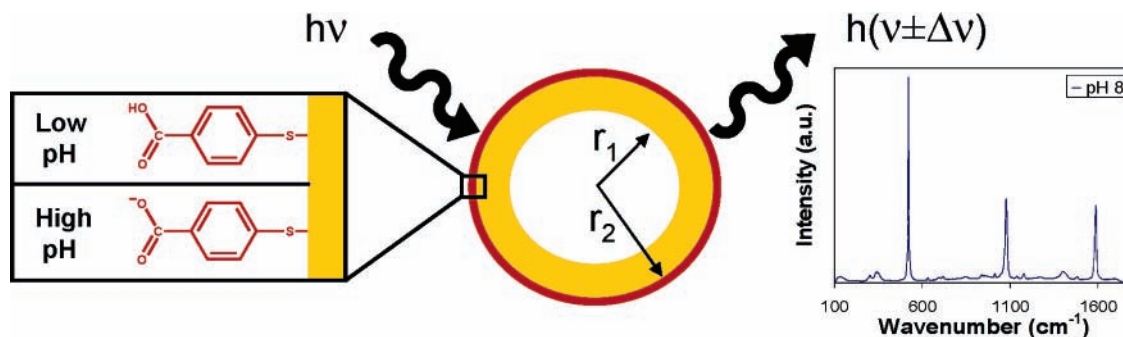
Figure 1. Schematic diagram of the Au nanoshell pH sensor, consisting of nanoshells with core radius $r_1 = 55$ nm, total nanoparticle radius $r_2 = 71$ nm, and an adsorbed monolayer of *para*-mercaptobenzoic acid. The pMBA molecules yield a pH-dependent SERS spectrum.

nanosensors. We show that the structure we have designed can function as an optically addressable, robust nanodevice, providing complex yet highly reproducible pH-dependent SERS spectra as the optical output. Because the nanosensor is designed for optimal use with near-infrared excitation and Raman-emission wavelengths, the input and output optical signals of this nanosensor are transmissible through blood and tissue and enabling their potential use in diagnostic applications in living systems. By comparison, pH-sensitive dyes, which also have been pursued as optical sensors, require excitation and emission wavelengths in the visible region of the spectrum greatly restricting their use in living systems, exhibit cell leakage and diffusion which prevents their use for local nanoscale pH measurements, and are unable to provide a continuous signal across a broad pH range.[17] We develop a highly practical and general method for converting the complex pH-dependent SERS spectral output into a streamlined pH readout while maximally preserving its information content, and thereby the resolution and accuracy, of the nanodevice. By adapting an approach from statistical learning theory (which infers simple statistical structure from large and complex data sets)[18] that reduces the dimensionality of the multispectral data set to a simple device characteristic, we can assess the accuracy and resolution of the nanoscale pH "meter". We obtain an average accuracy of ± 0.10 pH units across the working pH range of the device. In the study reported here, both the working nanodevice and its performance analysis illustrate general approaches that should be broadly applicable in the development of other SERS-based functional nanodevices and in evaluating SERS-based device performance relative to an analogous micro- or macroscopic device.

The nanosensor is illustrated in Figure 1. To construct this device, Au nanoshells were fabricated according to protocols reported previously.[3] The nanoshell core and shell dimensions were adjusted so that the plasmon resonance provided a far-field absorbance maximum near 785 nm in H_2O, $[r_1, r_2] = [55, 71]$ nm, to provide surface-enhanced Raman scattering enhancement at the 785 nm pump laser wavelength. Au nanoshells were immobilized by depositing a drop of aqueous nanoshells solution onto 3-aminopropyltriethoxy silane-(APTES, Aldrich) coated silicon wafer supports (Addison Engineering, Inc.) and allowing the water to evaporate. The electrostatic interaction between the nanoshells and the amine group resulted in dispersed nanoshells bound to the

silicon substrate. The anchored nanoshells were exposed to solutions of pMBA (Sigma-Aldrich) presolubilized in ethanol then diluted in Milli-Q water (Millipore) for 1 h, then thoroughly rinsed with Milli-Q water. To measure the pH response, SERS spectra were measured from acidic to basic pH levels. Before acquiring Raman spectra at each pH, the sample was immersed in phosphate-buffered saline (PBS) of pH adjusted to the desired value for 10 min. A Fisher Scientific accumet AP63 portable pH meter was used to adjust the pH of the buffer to an accuracy of 0.01 pH units. Raman spectra were then recorded while the entire substrate was immersed in ambient buffer solution using a Renishaw inVia Raman microscope (Renishaw, U.K.) with 785 nm wavelength excitation and 55 μW power at the sample. Backscattered light was collected using a 63x water immersion lens (Leica, Germany), and high-resolution spectra were acquired using a 30-s integration time. Scans were collected from various spots on each silicon wafer, at each pH value. Between the Raman scans at different pH levels, samples were rinsed with Milli-Q water and incubated, for 10 min, in fresh buffer at the new pH.

Figure 2a shows the SERS spectra of the nanosensor as a function of pH, ranging from pH 4.0 to 9.0. The most prominent features in the SERS spectra are the Stokes features appearing at 1077 and 1590 cm^{-1}, assigned to the ring breathing and axial deformation modes of pMBA, respectively.[13] As the pH of the nanoenvironment is changed from pH 4.0 to 9.0, highly reproducible spectral changes are observed in the SERS spectra. The most significant of these changes occurs at 1702 and 1394 cm^{-1}, attributable to the C=O and COO$^-$ stretching modes of pMBA, respectively. By monitoring the ratio of these two peaks, we illustrate that this nanodevice can be cycled repeatedly from pH 4 to 9, where the ratio of the 1702 and 1394 cm^{-1} peaks provides a simple optical readout for low-resolution changes in local pH (Figure 2b).

The highly complex changes in the SERS spectrum of this molecule that occur over this large pH range not only provide a great deal of information that can be used in assessing the device resolution but are themselves of intrinsic fundamental interest. pMBA is a weak acid,[19,20] and because a reduction in the pK_a of acid molecules typically occurs upon covalent attachment to metal surfaces,[21,22] it is expected that pMBA may still be partially protonated under significantly acidic conditions. The presence of dissociated carboxylate groups
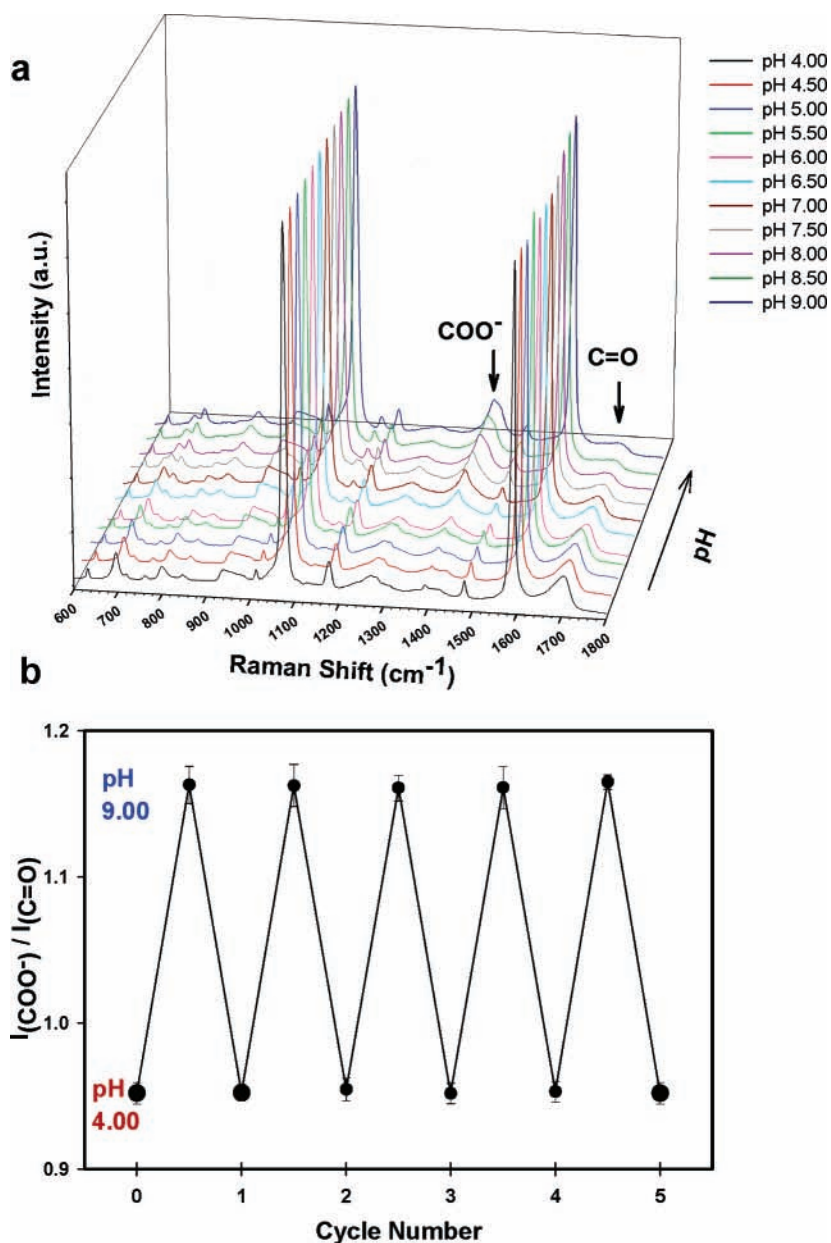
Figure 2. (a) SERS spectra of pMBA on nanoshells at various pH values ranging from pH 4.0 to pH 9.0 in steps of 0.50 pH units. (b) Repetitive cycling of the Raman pH nanosensor measured by monitoring the change in the $I_{(COO-)}/I_{(C=O)}$ (1702 cm^{-1}/1393 cm^{-1}) Stokes modes. The intensities were measured with respect to that of the 1077 cm^{-1} band to which spectra (at each pH) were normalized. Error bars represent the standard deviation for the measurements.

at low pH is indicated by the appearance of the broad COO$^-$ band at 1393 cm^{-1}, appearing much weaker than the C=O band at 1702 cm^{-1}. With increasing pH, the number of dissociated carboxylate groups increases, enhancing the vibrational stretching mode of COO$^-$, resulting in an increase in mode intensity and a shift of the 1393 cm^{-1} mode to higher wavenumbers. However, even at pH 9, the COO$^-$ band remains broad, suggesting that some pMBA molecules may still be involved in hydrogen bonding in addition to the possible interaction between COO$^-$ groups and the ring hydrogens. The low-energy shoulder of the carbonyl mode at 1702 cm^{-1}, occurring most strongly at low pH, indicates that some pMBA molecules might be participating in intramonolayer hydrogen bonding between adjacent pMBA molecules and/or between pMBA and the solution ambient.

Multiple overlapping features in the broad 1393 cm^{-1} COO$^-$ band are evident at low pH, which may possibly be attributable to hydrogen bonding between protonated and deprotonated carboxylate groups.[23] From Gaussian calculations (DFT/B3LYP level), it can be inferred that such broadening could be caused by possible interactions between the carboxylate groups and the ring hydrogens. Interactions involving the COO$^-$, COOH, and the ring hydrogens may be responsible for altering the COO$^-$ and C=O modes, resulting in the spectral broadening of this mode observed at acidic pH.[24] Other spectral features in the pMBA SERS spectrum that also show pH-dependency include the nominally 1137 cm^{-1} Stokes mode, predicted to be a CH in-plane bending mode, which undergoes noticeable spectral changes in intensity with increasing pH.[25] The intensity of this weak

mode increases with increasing pH, as does the mode appearing at 845 cm^{-1}. This latter spectral feature is assigned to COO$^-$ bending,[13,25] and its spectral behavior closely resembles that of the COO$^-$ stretching mode at 1393 cm^{-1}. The spectral features at 696, 718, and 800 cm^{-1} also show pH-dependent changes in intensity. With increasing pH, the intensity of the 696 cm^{-1} band gradually decreases and that of the 718 cm^{-1} band increases. The 696 cm^{-1} mode was assigned in neutral pMBA (acidic limit) to a mixture of OCO bending, in-plane ring compression, and C–S stretching. The mode at 718 cm^{-1} was assigned to out-of-plane ring hydrogen wagging. In the basic limit, the deprotonated pMBA anion was found to have corresponding modes, only reversed in energy from the case of the protonated molecule. The 800 cm^{-1} band appears to have a mixed vibrational nature of in-plane ring deformation motion, C–COOH stretching, and COO$^-$ bending, decreasing with increasing pH. Because the intensity of in-plane ring vibrational modes, such as that of the 1137 cm^{-1} and 718 cm^{-1} bands, was seen to increase with increasing pH, it is proposed that the 800 cm^{-1} band is dominated mainly by the C–COOH stretching vibration.[14,26] Because the 696, 718, and 1137 cm^{-1} features are all related to the benzene ring of the pMBA molecule, the pH-dependent change in the intensity of these bands may be related to the orientation of pMBA on the Au nanoshell surface.[27] However, because saturation coverage of pMBA was present on the nanoshells, it is expected that the pMBA molecules are packed densely on the nanoshell surface in an upright configuration and undergo only minor reorientations with respect to surface normal over the pH range investigated.

Transforming a complex data set of pH-dependent SERS spectra into a device whose accuracy can be assessed quantitatively presents an interesting challenge. Clearly, the accuracy of the nanodevice will depend critically on how much pH-dependent information inherently available in the SERS spectra can be accommodated in device analysis. The data displayed in Figure 2a demonstrates a large pH range (4.00–9.00) in increments of 0.5 units where the SERS signal is clearly dependent on local pH. However, to test the validity and accuracy of the nanodevice, a finer data set was collected in increments of 0.2 pH units over a narrower pH range (5.80–7.60). This pH range was chosen because of its biological relevance; for example, within this pH range a distinction can be made between acidic cancer cells and healthy tissue.[28] A simple ratio of pH-dependent SERS peaks extracted from the spectral output of the nanodevice (Figure 2b) may be used to monitor large changes in pH, but in order to determine the usefulness of such a nanodevice in real applications, it is crucial to obtain a quantitative understanding of the accuracy of its pH measurements across the working pH range of the device.

We begin by observing that the changes in pH elicit smooth changes in the measured SERS spectrum over this pH range. Each measured spectrum is considered as a point in an N-dimensional space (R^N), where N is the number of discrete points taken to acquire each SERS spectrum. Each axis in this abstract space indicates Raman frequency, with

the value along each axis expressing the spectral energy at that frequency. Varying pH induces spectral changes that trace out a well behaved one-dimensional trajectory in R^N (parametrized by the pH value) that defines the relationship between the pH and the SERS spectra (Figure 3a). If we could exactly parametrize this pH-dependent Raman curve (more generally known as a manifold), then for a given test sample we could estimate the pH by simply finding the point on the curve closest to the test sample's spectrum. It is very difficult to exactly characterize manifolds in high-dimensional spaces using limited data. Instead, we built a locally linear approximation to the pH-Raman manifold by finding the best collection of straight line segments to fit a collection of training data samples (similar to the locally linear embedding algorithm[29]).

A series of pH-dependent SERS spectra serves as our "training" data with which we test this parametrization. Each spectrum in this figure was constructed from an average of five SERS spectra taken at the same pH and at different regions on the wafer sample. Because the analysis depends only on the relative intensity at many different Raman frequencies ranging from 600 to 1800 cm^{-1}, we normalized each SERS spectrum to its value at a specific frequency (1400 cm^{-1}). Because the relative changes in peak heights is being examined, it does not matter where the baseline is chosen as long as there is no known contributing signal from the molecule or possible contribution from the silicon substrate. To model the pH-Raman manifold, we then found the piecewise linear curve in R^N with k segments that minimizes the mean-squared error over this collection of training data. The ($k - 1$) breakpoints were found by exhaustively searching all possible gaps between the training data pH values to find the breakpoints that produce the minimum mean-squared error fit. The best-fitting linear segments were found using a standard least-squares method applied in R^N. For this device output, a two-segment piecewise linear curve was found to fit the pH manifold with high accuracy and minimal complexity. We then used cross-validation[30] to judge the variation of our estimation procedure by testing each SERS spectrum against the parametrized manifold (Figure 3b). This was accomplished by constructing the pH-Raman manifold model using four of the five available spectra at each pH and testing the variation between the fifth spectrum and the parametrized model. This procedure was repeated five times (leaving each scan out once), and the resulting pH estimates were used to judge the accuracy and precision of the procedure. The magnitude of the average error over the pH range of the device was obtained in this manner (Figure 3c). The average error magnitude across the working pH range is 0.10. As we can see, however, this varies significantly across the pH range of the device, with a much larger error occurring around pH 6.0 than elsewhere in the pH range being evaluated. The increased error in this specific range is due to an observed increase in spectral fluctuations for the SERS spectra for this specific pH, which is likely to be near the effective pK_a of the pMBA adsorbate molecules. It is quite possible that molecular fluctuations occurring at this pH due to protona-
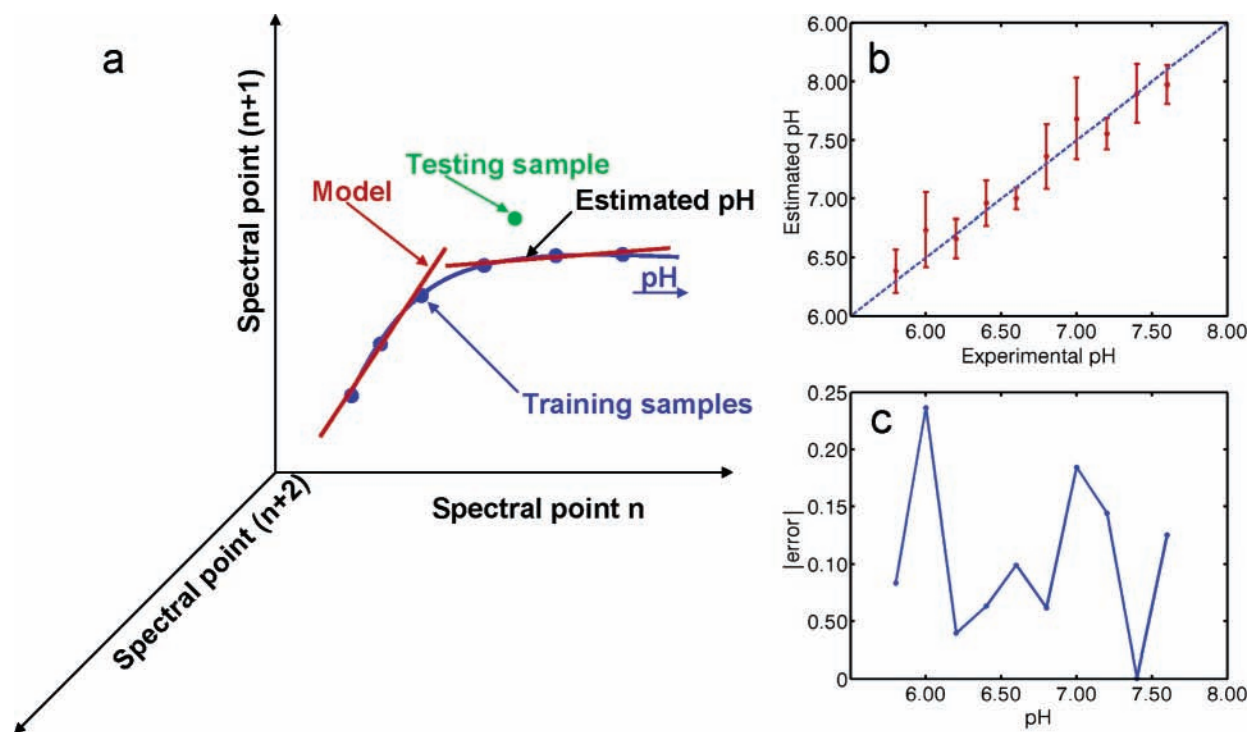
Figure 3. (a) Spectral changes form a manifold (one-dimensional curve) in R^N that is indexed by pH, where N is the number of spectral bands measured. The best piecewise linear fit to the training samples is found using two segments, and that local linear approximation forms a model of the pH manifold. (b) The spectrum of a testing sample is projected onto the model described in a to find the point on the manifold that is closest to the spectrum of the test data. The index of this projected point forms the pH estimate. Cross validation was used to judge the quality of the model (leave one scan out of the model building and then estimate using that scan). The points are the average of the cross validation estimates, and the error bars represent one standard deviation in the cross validation estimates. (c) Magnitude of the average error of the cross validation estimation procedure shown in b. The average error magnitude across the pH range of the device is 0.10 pH.

tion−deprotonation dynamics may give rise to the increased spectral noise observed, which translate to a lower accuracy for our nanodevice at this specific region of its pH range.

The ultimate resolving power of this nanosensor depends partially on the resolution of the training data used to model the pH-Raman manifold. To further explore the resolving power of the nanosensor built with training data at 0.20 pH intervals, we used our manifold approximation technique to estimate the pH of two test samples taken between the training data pH values (having pH values of 6.10 and 7.15). The nanosensor estimated the pH values of these test samples to be 6.47 and 7.01, respectively. For the pH 6.10 test sample, we see an error slightly larger than that predicted by the cross-validation study. As we saw with the training data, the larger error appears in the pH range where increased SERS spectral fluctuations are observed.

The all-optical nanoscale pH "meter" reported here is likely to be highly useful in a wide range of applications within biology and biomedicine where such a probe may prove to be a useful new tool for research, diagnosis, or monitoring. Embedding the pH sensor inside plant or animal cells or tissues would allow a new way to monitor the complex changes that can occur within living systems at the single-cell or subcellular level. Examples may include studying the response of plant cells to stress, early-stage monitoring of transplant rejection, or the "optical biopsy" of possibly cancerous lesions or tumors.[31] The analysis

method demonstrated here to assess the accuracy of the nanodevices may also be broadly applicable across a family of chemically functional, SERS-based nanodevices that, in principle, could be fabricated on a ever-increasing variety of plasmon-resonant nanoparticle substrates with large local field enhancements at their surfaces.

References

(1) Clark, H. A.; Barker, S. L. R.; Brasuel, M.; Miller, M. T.; Monson, E.; Parus, S.; Shi, Z.-Y.; Song, A.; Thorsrud, B.; Kopelman, R.; Ade, A.; Meixner, W.; Athey, B.; Hoyer, M.; Hill, D.; Lightle, R.; Philbert, M. A. *Sens. Actuators, B* **1998**, *51*, 12−16.

(2) Michalet, X.; Pinaud, F. F.; Bentolila, L. A.; Tsay, J. M.; Doose, S.; Li, J. J.; Sundaresan, G.; Wu, A. M.; Gambhir, S. S.; Weiss, S. *Science* **2005**, *307*, 538−544.

(3) Oldenberg, S. J.; Averitt, R. D.; Westcott, S. L.; Halas, N. J. *Chem. Phys. Lett.* **1998**, *288*, 243−247.

(4) Prodan, E.; Radloff, C.; Halas, N. J.; Nordlander, P. *Science* **2003**, *302*, 419−422.

(5) Chen, J.; Saeki, F.; Wiley, B. J.; Cang, H.; Cobb, M. J.; Li, Z.-Y.; Au, L.; Zhang, H.; Kimmey, M. B.; Li, X. D.; Xia, Y. *Nano Lett.* **2005**, *5*, 473−477.

(6) Huang, X. H.; El-Sayed, I. H.; Qian, W.; El-Sayed, M. A. *J. Am. Chem. Soc.* **2006**, *128*, 2115−2120.

(7) O'Neal, D. P.; Hirsch, L. R.; Halas, N. J.; Payne, J. D.; West, J. L. *Cancer Lett.* **2004**, *209*, 171−176.

(8) Jeanmarie, D. L.; Van Duyne, R. P. *J. Electroanal. Chem.* **1977**, *84*, 1−20.

(9) Moskovits, M. *Rev. Mod. Phys.* **1985**, *57*, 783−826.

(10) Xu, S.; Ji, X.; Xu, W.; Zhao, B.; Dou, X.; Bai, Y.; Ozaki, Y. *J. Biomed. Opt.* **2005**, *10*, 031112.

(11) Jackson, J. B.; Halas, N. J. *Proc. Natl. Acad. Sci.* **2004**, *101*, 17930−17935.

(12) Jackson, J. B.; Westcott, S. L.; Hirsch, L. R.; West, J. L.; Halas, N. J. *Appl. Phys. Lett.* **2003**, *82*, 257−259.

(13) Michota, A.; Bukowska, J. *J. Raman Spectrosc.* **2003**, *34*, 21−25.

(14) Lee, S. B.; Kim, K.; Kim, M. S. *J. Raman Spectrosc.* **1991**, *22*, 811−817.

(15) Talley, C. E.; Jusinski, L.; Hollars, C. W.; Lane, S. M.; Huser, T. *Anal. Chem.* **2004**, *76*, 7064−7068.

(16) Talley, C. E.; Jackson, J. B.; Oubre, C.; Grady, N.; Huser, T.; Hollars, C.; Lane, S.; Nordlander, P.; Halas, N. J. *Nano Lett.* **2005**, *5*, 18218−18222.

(17) Clark, H. A.; Hoyer, M.; Philbert, M. A.; Kopelman, R. *Anal. Chem.* **1999**, *71*, 4831−4836.

(18) Burges, C. J. C. Geometric Methods for Feature Extraction and Dimensional Reduction. In *Data Mining and Knowledge Discovery Handbook: A Complete Guide for Practitioners and Researchers*; Rokach, L., Maimon, O. S., Eds.; Springer Science & Business Media: New York, 2005; pp 59−92.

(19) Ramakrishna, R. S.; Fernandopulle, M. E. *J. Inorg. Nucl. Chem.* **1971**, *33*, 1940−1942.

(20) Martell, A. E.; Smith, R. M. In *Critical Stability Constants*; Plenum Press: New York, 1977.

(21) Joo, T. H.; Kim, K.; Kim, M. S. *J. Phys. Chem.* **1986**, *90*, 5816−5819.

(22) Moskovits, M.; Suh, J. S. *J. Phys. Chem.* **1984**, *88*, 1293−1298.

(23) Wells, M.; Dermody, D. L.; Yang, H. C.; Kim, T.; Crooks, R. M.; Ricco, A. J. *Langmuir* **1996**, *12*, 1989−1996.

(24) Gao, P.; Weaver, M. J. *J. Phys. Chem.* **1985**, *89*, 5040−5046.

(25) Kwon, Y. J.; Son, D. H.; Ahn, S. J.; Kim, M. S.; Kim, K. *J. Phys. Chem.* **1994**, *98*, 8481−8487.

(26) Varsanyi, G. *Assignments for Vibrational Spectra of Seven Hundred Benzene Derivatives*; Wiley: New York, 1974.

(27) Osawa, M.; Matsuda, N.; Yoshii, K.; Uchida, I. *J. Phys. Chem.* **1994**, *98*, 12702−12707.

(28) Smallbone, K.; Gavaghan, D. J.; Gatenby, R. A.; Maini, P. K. *J. Theor. Biol.* **2005**, *235*, 476−484.

(29) Roweis, S. T.; Saul, L. K. *Science* **2000**, *290*, 2323−2326.

(30) Hardle, W. *Applied Nonparametric Regression*; Cambridge University Press: Cambridge, U.K., 1990.

(31) Vaupel, P.; Kallinowski, F.; Okunieff, P. *Cancer Res.* **1989**, *49*, 6449−6465.

Resource

A Hybrid Vector for Ligand-Directed Tumor Targeting and Molecular Imaging

Amin Hajitou,[1] Martin Trepel,[5,6] Caroline E. Lilley,[7] Suren Soghomonyan,[2] Mian M. Alauddin,[2] Frank C. Marini, III,[3] Bradley H. Restel,[1] Michael G. Ozawa,[1] Catherine A. Moya,[1] Roberto Rangel,[1] Yan Sun,[1] Karim Zaoui,[5,6] Manfred Schmidt,[5,6] Christof von Kalle,[5,6] Matthew D. Weitzman,[7] Juri G. Gelovani,[2] Renata Pasqualini,[1,4,*] and Wadih Arap[1,4,*]

[1] Department of Genitourinary Medical Oncology
[2] Department of Experimental Diagnostic Imaging
[3] Department of Bone Marrow Transplantation
[4] Department of Cancer Biology
The University of Texas M.D. Anderson Cancer Center, 1515 Holcombe Boulevard, Houston, TX 77030, USA
[5] Department of Hematology and Oncology
[6] Institute for Molecular Medicine and Cell Research
University of Freiburg Medical Center, Hugstetter Strasse 55, D-79106 Freiburg, Germany
[7] The Salk Institute, 10010 North Torrey Pines Road, La Jolla, CA 92037, USA
*Contact: rpasqual@mdanderson.org (R.P.); warap@mdanderson.org (W.A.)
DOI 10.1016/j.cell.2006.02.042

SUMMARY

Merging tumor targeting and molecular-genetic imaging into an integrated platform is limited by lack of strategies to enable systemic yet ligand-directed delivery and imaging of specific transgenes. Many eukaryotic viruses serve for transgene delivery but require elimination of native tropism for mammalian cells; in contrast, prokaryotic viruses can be adapted to bind to mammalian receptors but are otherwise poor vehicles. Here we introduce a system containing *cis*-elements from adeno-associated virus (AAV) and single-stranded bacteriophage. Our AAV/phage (AAVP) prototype targets an integrin. We show that AAVP provides superior tumor transduction over phage and that incorporation of inverted terminal repeats is associated with improved fate of the delivered transgene. Moreover, we show that the temporal dynamics and spatial heterogeneity of gene expression mediated by targeted AAVP can be monitored by positron emission tomography. This new class of targeted hybrid viral particles will enable a wide range of applications in biology and medicine.

INTRODUCTION

Integration of tumor targeting and imaging technologies into a single discipline has the potential to improve the practice of medicine. Noninvasive molecular-genetic imaging of temporal dynamics and spatial heterogeneity of transgene expression can provide the means for the assessment of specificity of targeting and for monitoring the efficacy of genetic transfer (Blasberg and Tjuvajev, 2003; Gross and Piwnica-Worms, 2005a; Medintz et al., 2005; Tai and Laforest, 2005). However, this emerging field depends on development of ligand-directed particles to enable systemic targeted delivery and molecular imaging of reporter trangenes.

Currently, eukaryotic viruses unquestionably provide superior transgene delivery and transduction (Kootstra and Verma, 2003), but ligand-directed targeting of such vectors requires ablation of their native tropism for mammalian cell-membrane receptors (Müller et al., 2003; Mizuguchi and Hayakawa, 2004). In contrast, prokaryotic viruses such as bacteriophage (phage) are considered poor vehicles for mammalian cell transduction. However, despite their inherent shortcomings as "eukaryotic" viruses, phage particles have no tropism for mammalian cells (Barrow and Soothill, 1997; Barbas et al., 2001) and have even been adapted to transduce such cells (Ivanenkov et al., 1999; Larocca et al., 1999; Poul and Marks, 1999; Piersanti et al., 2004), albeit at low efficiency. Phage display-based technology allows direct ligand-directed selection of homing peptides to corresponding receptors selectively expressed in normal or tumor tissues (Hajitou et al., 2006). We hypothesized that combining the favorable biological attributes of eukaryotic viruses to those of prokaryotic viruses might yield chimeric particles with potential as targeted delivery tools for molecular imaging. Since the genomes of recombinant adeno-associated virus (AAV) and single-stranded phage consist of compatible DNA, we generated novel chimeras between AAV and fd-tet (Zacher et al., 1980), an M13-derived filamentous phage, displaying short peptides (Smith and Scott, 1993) and evaluated them for tumor targeting and molecular imaging of *Herpes simplex virus thymidine kinase* (*HSVtk*)

gene expression with [18F]FEAU and positron emission tomography (PET) in preclinical tumor models.

RESULTS AND DISCUSSION

Ligand-Directed Particles Are Functional in Mammalian Cells

As a proof of concept, we constructed a targeted chimeric virus comprised of recombinant AAV and an fd-tet phage clone displaying the double-cyclic peptide CDCRGDCFC (termed RGD-4C) phage (Pasqualini et al., 1997; Arap et al., 1998; Ellerby et al., 1999). The RGD-4C peptide binds to αv integrins, a cell-surface receptor overexpressed in both tumor and endothelial cells (Arap et al., 1998; Hood et al., 2002). To obtain chimeric viruses (hereafter referred to as AAV/phage; AAVP), we inserted an eukaryotic gene cassette from AAV in an intergenomic region of RGD-4C phage (RGD-4C AAVP); insertless phage (nontargeted AAVP); or phage displaying control peptides, such as scrambled RGD-4C AAVP or D→E mutant (termed RGE-4C) AAVP, and packaged it with the phage DNA into the phage capsid (see Figure S1 in the Supplemental Data available with this article online). In order to show that the *cis*-elements of the resulting targeted chimeric virus remain functional, we evaluated the ligand properties of the RGD-4C peptide and the rescuing properties of the inverted terminal repeats (ITRs) in the context of AAVP. First, to evaluate peptide specificity, we show that RGD-4C AAVP binds to mammalian cells expressing αv integrins, in contrast to the nontargeted AAVP or AAVP displaying negative control peptides such as RGE-4C or various scrambled versions of the RGD-4C sequence (Figure 1A), which neither bind to nor infect mammalian cells. We also demonstrate that RGD-4C AAVP carrying reporter genes can mediate ligand-directed internalization (Figure 1B) and transduction of mammalian cells (Figure 1C) relative to controls. For cell internalization experiments, negative controls included nontargeted AAVP, various scrambled RGD-4C AAVP, or RGE-4C AAVP (Figure 1B); for cell transduction experiments, nontargeted AAVP (Figure 1C), scrambled RGD-4C AAVP, or RGE-4C AAVP (data not shown) served as negative controls. Consistent with these results, we have previously demonstrated that the synthetic RGD-4C peptide specifically inhibits cell binding and internalization of various targeted RGD-4C phage-based constructs (Giordano et al., 2001; Chen et al., 2004; unpublished data). Finally, we show that mammalian cell transduction can also be specifically competed by the synthetic RGD-4C peptide relative to negative controls such as nontargeted AAVP (Figure 1D), scrambled RGD-4C, or RGE-4C (data not shown). To rule out the possibility that some of these results (Figures 1A and 1B) could represent an artifact resulting from selective failure of the glycine (low pH) wash step to remove AAVP from cell membranes, we performed ice-cold control experiments (Giordano et al., 2001), in which we observed cell binding but not internalization mediated by

RGD-4C AAVP (data not shown), thus supporting our interpretation.

Next, to evaluate whether the ITRs are still functional in the AAVP particle, we performed rescue experiments. We show that functional recombinant AAV particles are generated from mammalian cells transduced with the RGD-4C AAVP only but not from the cells transduced with negative control constructs (Figure 1E). These data establish that the genetic chimerization resulting in an RGD-4C AAVP particle does not fundamentally alter (1) the peptide targeting properties of the ligand-directed RGD-4C phage or (2) the ability to rescue recombinant AAV particles from mammalian cells transduced by RGD-4C AAVP. A side-by-side time course of a reporter transgene expression revealed that RGD-4C AAVP transduction was detectable for much longer compared to that of the RGD-4C phage (Table S1).

Molecular Mechanisms of Transgene Expression

To gain an insight into the molecular mechanisms of transgene expression mediated by AAVP, we investigated the fate of the transduced genome in mammalian cells. First, we generated stably transduced cell lines by using *GFPneo*-expressing AAVP to allow for the selection of individual transduced cell clones. Either RGD-4C AAVP-*GFPneo* or RGD-4C phage-*GFPneo* lacking AAV ITRs were used to transduce αv integrin-expressing 293 cells, and clones were isolated under G418 selection. Rescue experiments showed functional recombinant AAV-*GFPneo* generated from all of the RGD-4C AAVP-*GFPneo* 293 cell clones, but none generated from the RGD-4C phage-*GFPneo* clones (data not shown), thus confirming that the chimeric individual clones contain functional ITRs. Although cells transduced with the nonchimeric RGD-4C phage-*GFPneo* retained G418 resistance, GFP expression was generally weaker than that of the RGD-4C AAVP-*GFPneo* clones (Figure 2A). We then set out to determine the fate of the *GFPneo* transgene cassette in stably transduced clones by a comprehensive restriction-enzyme digestion of genomic DNA followed by Southern blotting and PCR analysis (Figure 2; Figure S2 and Table S2). To prove persistence of the transgene cassette, genomic DNA was digested with AflII and XhoI to detect the release of full-length transgene cassettes prior to the analysis. We observed such release in 100% of the clones transduced by RGD-4C AAVP (n = 9 of 9 clones), compared to only in 33% of the clones (n = 3 of 9 clones) transduced by the nonchimeric RGD-4C phage construct (Figure 2B). We next designed another restriction digest of genomic DNA to detect potential concatemeric forms of the transgene cassette (Lieber et al., 1999; Hsiao et al., 2001). We detected the presence of head-to-tail concatemers of the transgene cassette in 67% of the clones transduced by RGD-4C AAVP (n = 6 of 9 clones), while no such concatemers were detected in clones transduced by the nonchimeric RGD-4C phage construct (Figure 2C). To identify possible additional concatemeric forms of the transgene cassette, we performed a multiplex PCR by
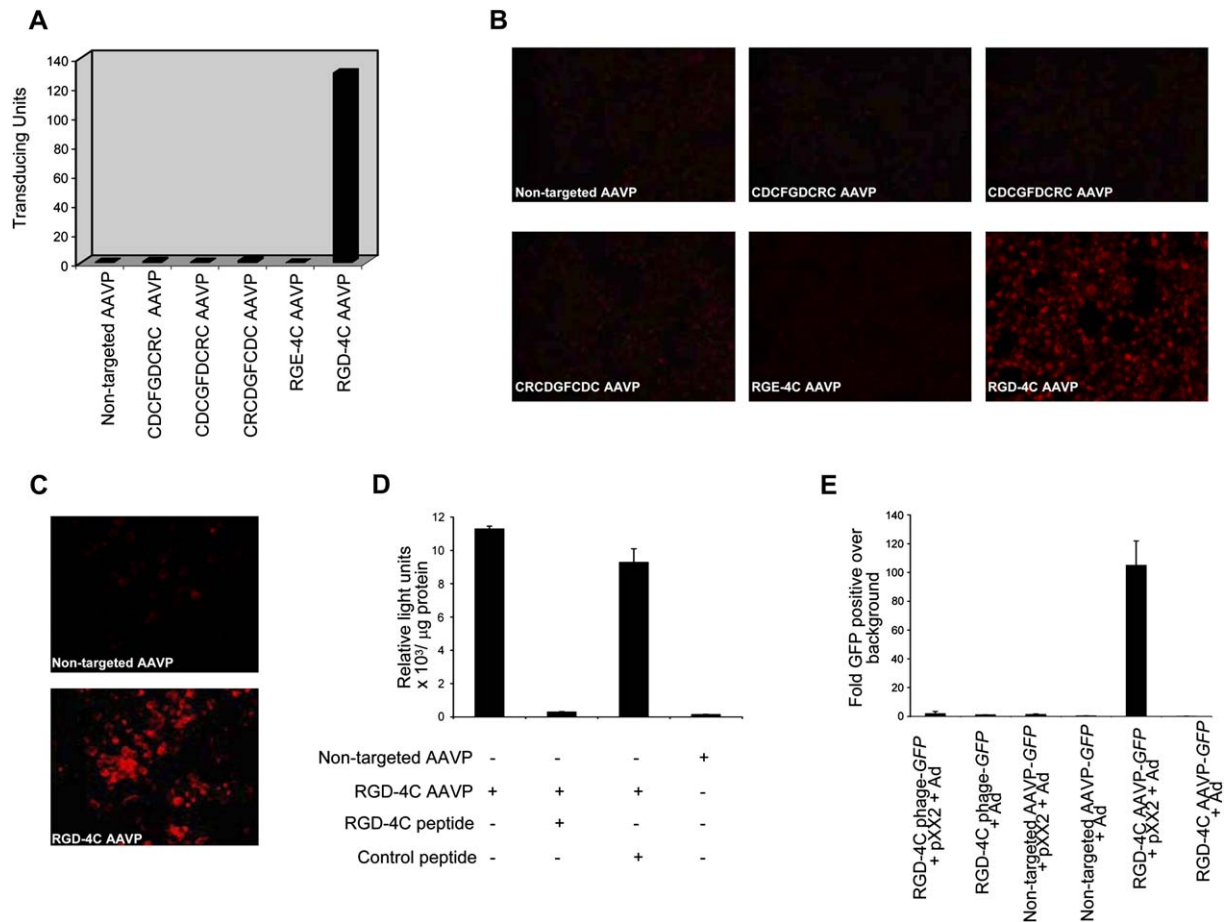
Figure 1. Ligand-Directed RGD-4C AAVP Transduction of αv Integrin-Expressing Cells and Rescue of Recombinant AAV

(A and B) Phage binding and internalization in KS1767 cells were performed with RGD-4C AAVP or negative AAVP controls (nontargeted, scrambled, or mutated) as indicated.

(C) Targeted gene transfer mediated by RGD-4C AAVP-β-*gal* to KS1767 cells.

(D) Inhibition of transduction by the synthetic RGD-4C peptide but not by an unrelated control peptide; nonspecific transduction levels were determined by using nontargeted AAVP. An anti-β-gal antibody was used for staining, and gene expression was detected by immunofluorescence. Error bars indicate standard error of the mean (SEM) obtained from duplicate wells.

(E) Rescue of recombinant AAV from cells infected with RGD-4C AAVP. Human 293 cells were incubated with targeted RGD-4C AAVP-*GFP* (10^6 TU/cell) or negative controls (targeted nonchimera RGD-4C phage-*GFP*, nontargeted AAVP-*GFP*). Four days postinfection, cells were transfected with an AAV *rep*- and *cap*-expressing plasmid (pXX2; Xiao et al., 1998) and superinfected with wild-type adenovirus type 5 (Ad). Cells were harvested 72 hr post adenoviral infection, and supernatants were then used to infect new 293 cells. GFP expression was FACS analyzed 48 hr later. Shown are mean increases in recombinant AAV-*GFP* produced over background after rescue from each construct. Data presented are the mean of triplicate transfections, and error bars represent the standard deviation (SD) from the mean.

using primers flanking the 5′ and 3′ ends of the constructs. Again, we found no concatemers in clones transduced by nonchimeric RGD-4C phage construct, whereas 100% of clones transduced by RGD-4C AAVP contained concatemeric forms (n = 9 of 9 clones), all of them found in head-to-tail orientation (Figure S2B). Moreover, topo cloning of smaller PCR products revealed the head-to-tail orientation of the transgene cassette with ITR deletions (Figure S2C) (Yang et al., 1997). Finally, although the large PCR products could not be sequenced, their sizes suggest the presence of concatemers with intact ITRs at

the junction site. An individual analysis of DNA for each single clone is also detailed in Table S2. These data suggest that AAVP may bestow an advantage in gene expression by means of an altered fate of the transgene cassette through maintenance of the entire mammalian transgene cassette, better persistence of episomal DNA, formation of concatemers of the transgene cassette, or perhaps a combination of these non-mutually exclusive mechanisms. These observations are consistent with recent developments in the understanding of AAV (McCarty et al., 2004).
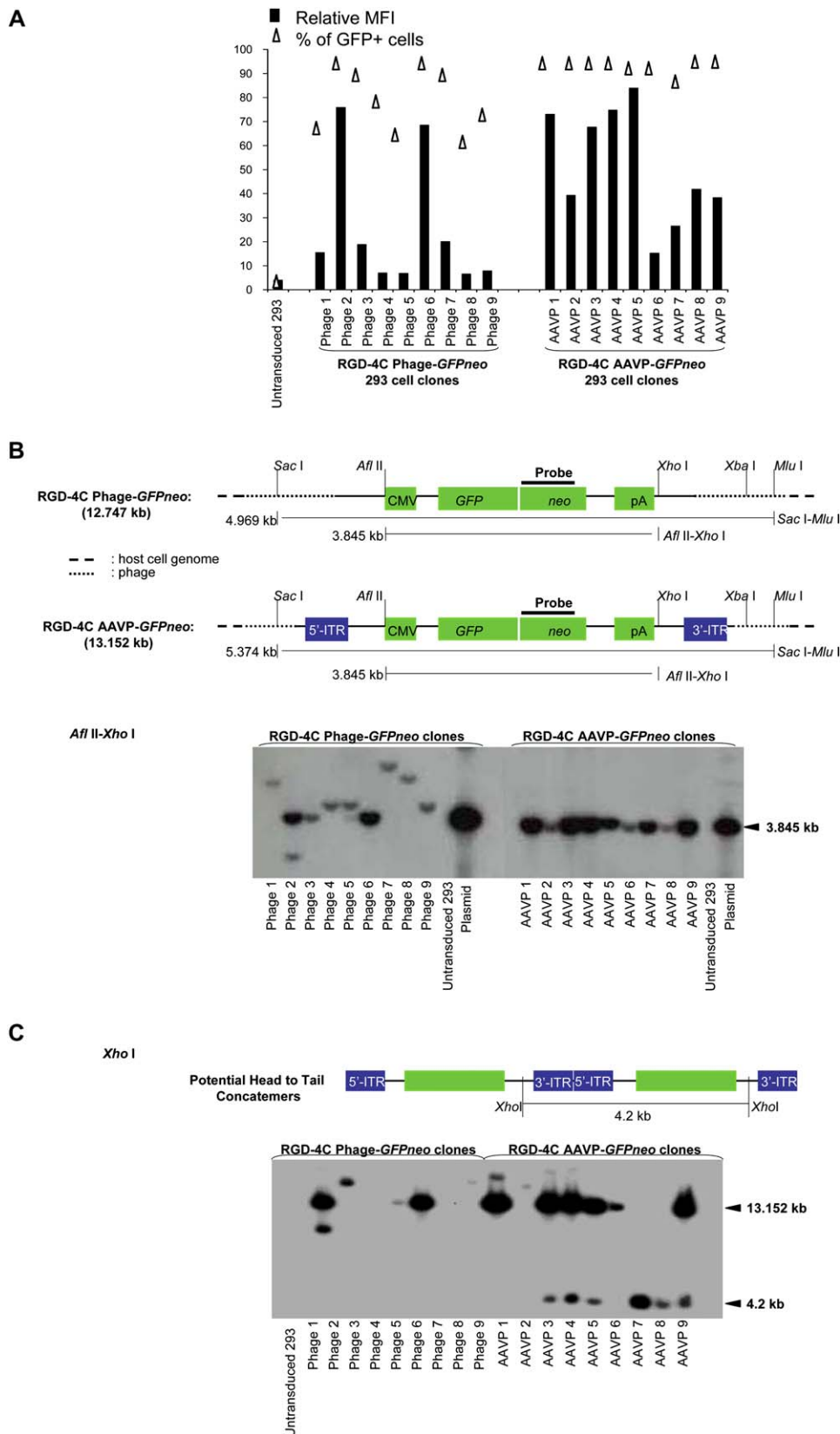
Tumor Targeting In Vivo and
Molecular-Genetic Imaging

After demonstrating that the central elements of the targeted chimeric viral particle (i.e., the RGD-4C peptide and the AAV ITRs) are intact and functional and after elucidating the molecular mechanisms of AAVP-mediate gene expression in mammalian cells, we evaluated the specificity and efficacy of gene delivery into tumors after systemic administration of AAVP. As an initial preclinical model, we used nude mice bearing subcutaneous tumor xenografts derived from human Kaposi sarcoma KS1767 cells (Arap et al., 1998; Ellerby et al., 1999). First, to verify that the viral construct targets to KS1767-derived xenografts in mice, we intravenously administered either RGD-4C AAVP or one of several negative controls (nontargeted AAVP, scrambled RGD-4C AAVP, or RGE-4C AAVP). After a 3–5 min circulation time, a strong anti-AAVP staining in tumor vasculature was observed in mice that received RGD-4C AAVP but not in control mice (Figure 3A). We next used an RGD-4C AAVP variant encoding the *GFP* gene as a reporter to determine, by using in situ immunofluorescence microscopic imaging, whether this vector (RGD-4C AAVP-*GFP*) could transduce KS1767-derived xenografts. We performed immunostaining against GFP in tumors and in different organs 7 days after systemic administration of either RGD-4C AAVP-*GFP* or negative control constructs into tumor-bearing mice. Immunofluorescence revealed GFP expression largely in tumor blood vessels and surrounding tumor cells in mice that received RGD-4C AAVP-*GFP*. In contrast, no GFP staining was detected in tumors from control mice that received nontargeted, scrambled, or mutant AAVP-*GFP* (Figure 3B). This staining pattern suggests that ligand-directed transduction is mediated by targeting of αv integrins in the vascular endothelium of tumors. Consistently, several nontarget control organs (brain, liver, pancreas, and kidney) lacked tissue expression of GFP (Figure S3). These results indicate that RGD-4C AAVP particles can specifically target tumor xenografts by a ligand-directed mechanism and transduce them after systemic administration in vivo.

Next, we assessed the efficacy of preclinical bioluminescence imaging (BLI) and clinically applicable molecular-genetic PET imaging with [^{18}F]FEAU for noninvasive monitoring of temporal dynamics and spatial heterogeneity of the firefly *luciferase* (*Luc*) and the *HSVtk* reporter-gene expression, respectively, in living tumor-bearing mice following systemic administration of the RGD-4C

AAVP. These molecular-genetic imaging studies were conducted in a preclinical model of human prostate cancer since this particularly prevalent tumor remains a challenge to properly image in patients. We first used a standard experimental setup for in vivo imaging of the *Luc* transgene reporters in tumor-bearing mice (Figure 4A). We selected BLI of Luc expression because it is a very sensitive method for reporter-gene imaging in mice and has virtually no nonspecific background activity in the images (Gross and Piwnica-Worms, 2005a; Gelovani Tjuvajev and Blasberg, 2003). Tumor-specific expression of *Luc* was observed in DU145 tumors in mice receiving RGD-4C AAVP-*Luc*. In contrast, tumor-associated bioluminescence signals could not be observed in control mice receiving the nontargeted AAVP-*Luc* or scrambled RGD-4C AAVP-*Luc*. No bioluminescence was observed in normal organs with any AAVP tested. These data confirm the tumor specificity of RGD-4C AAVP-mediated targeting and transgene expression observed with immunofluorescence microscopy imaging studies with RGD-4C AAVP-*GFP*. Consistent with previous results presented here (Figure S3), the kinetics of distribution suggests that, despite the nonspecific hepatic clearance of phage particles (Geier et al., 1973), such a phenomenon does not result in an undesirable gene transduction of the liver. These observations are in sharp contrast with the well-documented nonspecific transduction of normal organs (such as liver) by the mammalian viral gene delivery vectors. By using BLI in vivo, *Luc* reporter-transgene expression within tumors was clearly detectable at day 3 after AAVP administration and increased gradually to reach maximal levels by day 10. Repetitive two-dimensional BLI of *Luc* reporter-gene expression was performed every other day and provided an initial cost-effective strategy to study the specificity, temporal dynamics, and spatial heterogeneity of reporter-transgene expression mediated by AAVP.

However, because BLI of *Luc* reporter-gene expression is not clinically applicable, we next introduced into the AAVP vector the *HSVtk* gene, which can serve as both a "suicide" gene (when combined with ganciclovir [GCV]) and a reporter transgene for clinically applicable PET imaging with *HSVtk*-specific radiolabeled nucleoside analogs ([^{124}I]FIAU, [^{18}F]FHBG, [^{18}F]FEAU). Previous studies established that PET imaging of *HSVtk* expression provides the ability to define the location, magnitude, and duration of transgene expression (Tjuvajev et al., 1998, 1999; Ray et al., 2001; Massoud and Gambhir,

Figure 2. Analysis of the Fate of Genomes from RGD-4C AAVP-*GFPneo* or from RGD-4C Phage-*GFPneo* upon Transduction

We generated 293 stable clonal cell lines (n = 9 per each group) that were then analyzed. Individual clones were termed AAVP 1–9 or phage 1–9. Nontransduced 293 parental cells served as a negative control.

(A) Histogram shows a summary of flow cytometric analyses of 293 clones stably transduced with either AAVP-*GFPneo* (n = 9) or phage-*GFPneo* (n = 9). Open triangles indicate percentages of GFP-positive cells; black bars represent GFP expression levels (mean fluorescent intensity; MFI).

(B) Southern blot analysis of the persistence of the transgene cassette in clonal cell lines transduced with RGD-4C AAVP-*GFPneo* or RGD-4C phage-*GFPneo*. Total cellular DNA from nontransduced 293 parental cells or each of the transduced cell clones (1–9 for each group) was double digested with AflII-XhoI (one restriction site per enzyme within the construct DNA flanking the transgene cassette).

(C) Analysis of potential head-to-tail concatemers of the transgene cassette by Southern blot. Total cellular DNA was digested with XhoI (single restriction site within the transgene cassette next to the 3′ITR) prior to Southern blotting.
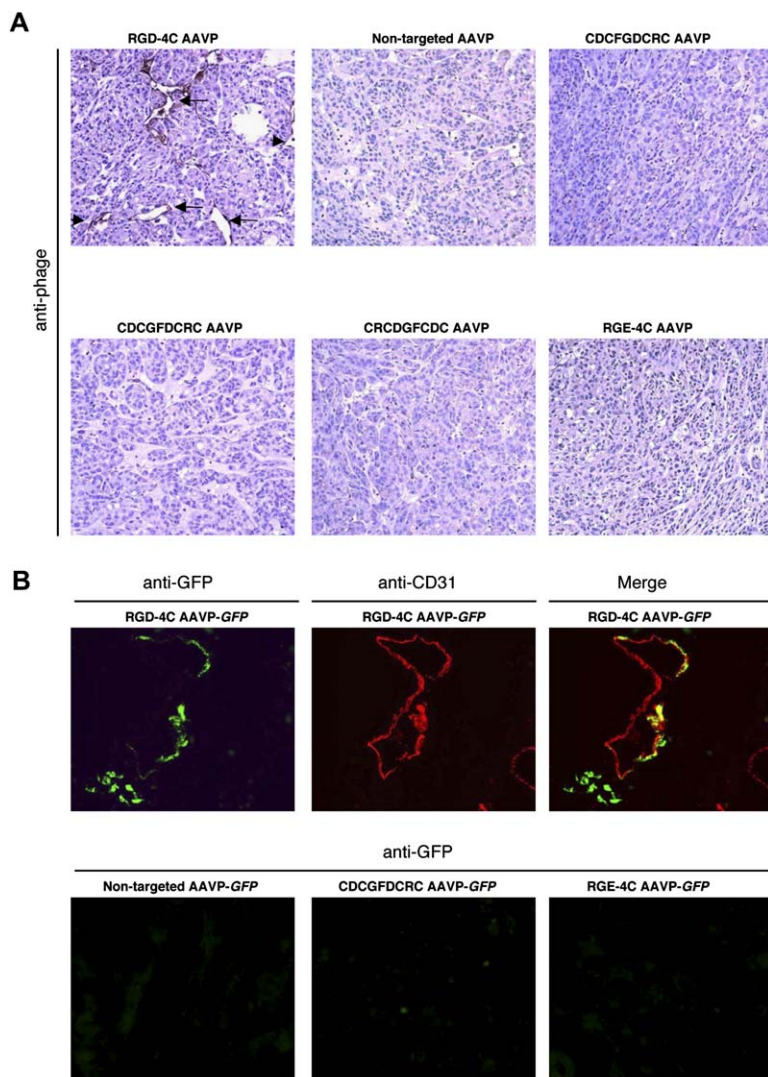
Figure 3. RGD-4C AAVP-Mediated Specific Gene Delivery to Tumors

(A) Immunohistochemical staining against phage in KS1767-derived xenografts after intravenous administration of RGD-4C AAVP (5×10^{10} TU) or negative controls (nontargeted AAVP, scrambled RGD-4C AAVP, or RGE-4C AAVP) into nude mice bearing KS1767-derived tumor xenografts. AAVP constructs were allowed to circulate for 5 min, followed by perfusion and surgical removal of tumors. Arrows point to phage staining in tumor blood vessels. (B) Immunofluorescence analysis of GFP expression in KS1767-derived xenografts at day 7 after systemic administration of either RGD-4C AAVP-*GFP* or negative controls (nontargeted, scrambled, or mutant) as indicated.

2003). It has also been previously determined that the magnitude of accumulated radiolabeled tracers in *HSVtk*-transduced cell lines and tumors in vivo correlates with the level of *HSVtk* expression (Blasberg and Tjuvajev, 2003; Gross and Piwnica-Worms, 2005a; Tai and Laforest, 2005). In the studies presented here, we selected, synthesized, and used the radiolabeled nucleoside analog 2′-[^{18}F]-fluoro-2′-deoxy-1-β-D-arabino-furanosyl-5-ethyl-uracil ([^{18}F]FEAU), which is a better radiolabeled substrate for the HSVtk enzyme than other nucleoside analogs, especially from pharmacokinetic considerations (a very low background activity in all normal organs and tissues) (Kang et al., 2005). By using repetitive PET imaging with [^{18}F]FEAU (on days 0, 3, 5, 10, and 16), we have visualized and quantitated the temporal dynamics and spatial heterogeneity of *HSVtk* gene expression after a single systemic administration of RGD-4C AAVP-*HSVtk* or nontargeted AAVP-*HSVtk* in DU145-derived tumor xenografts and other organs and tissues in nude mice (Figure 4B). Tu-

mor xenograft sizes (∼150 mm^3) before, as well as tumor growth rates after, administration of either RGD4C AAVP-*HSVtk* or nontargeted AAVP-*HSVtk* were similar in both cohorts of mice (Figure 4C). PET imaging with [^{18}F]FEAU revealed a gradual increase in the level of *HSVtk* transgene expression in tumors (increase in % administered intravenous dose per gram) during the initial 5 days after administration of RGD-4C AAVP-*HSVtk*, followed by gradual stabilization of *HSVtk* expression levels toward day 10 post vector administration. In contrast, in control tumor-bearing mice receiving nontargeted AAVP-*HSVtk*, only a minor increase in tumor accumulation of [^{18}F]FEAU was observed at day 3, which rapidly decreased to background level (Figure 4D). Consistent with preceding BLI experiments, no [^{18}F]FEAU PET-detectable *HSVtk* expression was observed in nontarget organs or tissues (Figure 4B). Indeed, low-level heterogeneous activity in the PET images (blue color) represents normal background activity, which was intentionally intensified in the
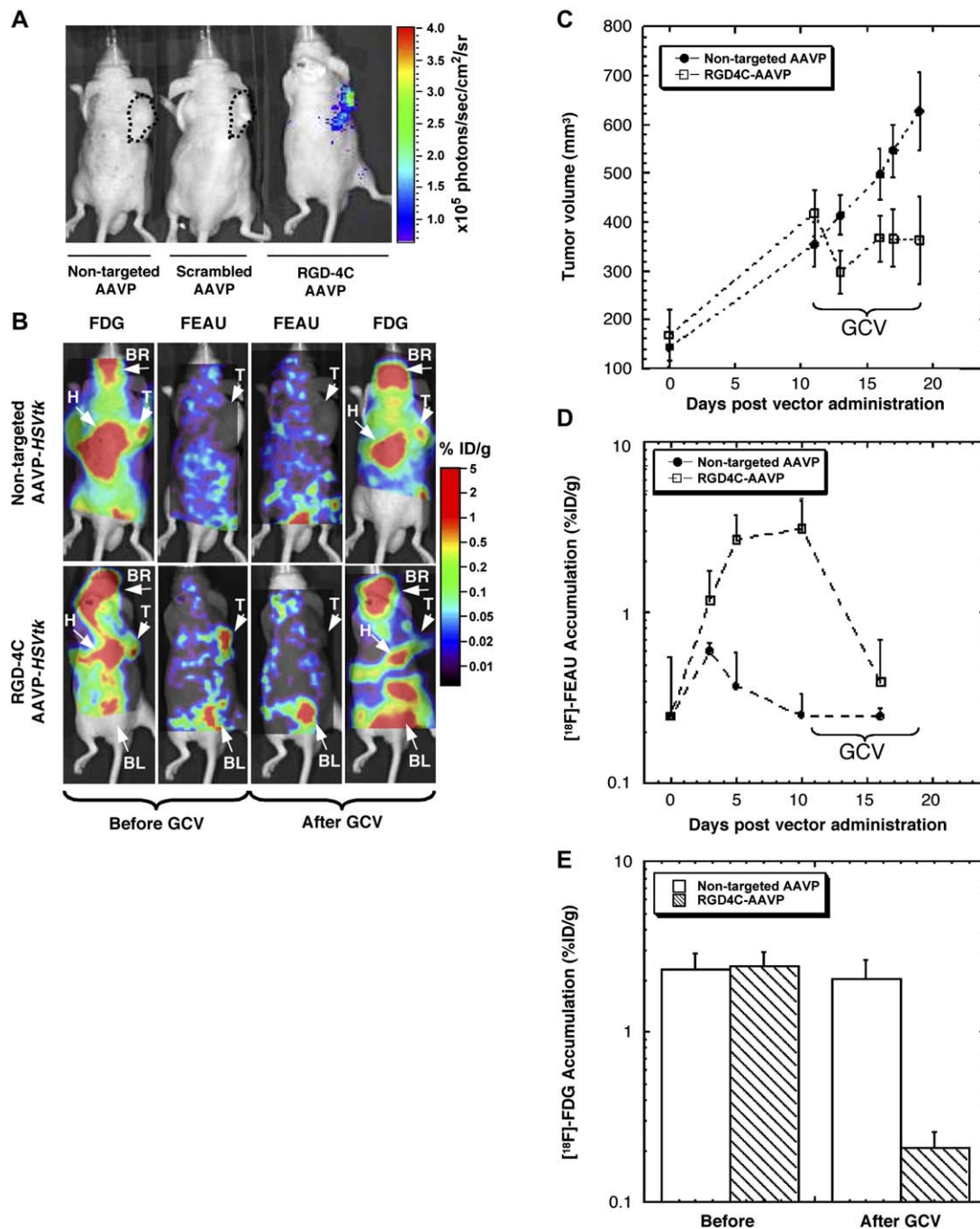
Figure 4. Targeted AAVP-Mediated Molecular Imaging of Tumor-Bearing Mice

(A) In vivo bioluminescent imaging (BLI) of luciferase expression after systemic AAVP delivery. Nude mice bearing DU145-derived tumor xenografts received an intravenous single dose of either RGD-4C AAVP-*Luc* (5×10^{11} TU) or controls (nontargeted AAVP-*Luc* or scrambled RGD-4C AAVP-*Luc*). Ten days later, BLI of tumor-bearing mice was performed.

(B) Multitracer PET imaging in tumor-bearing mice after systemic delivery of RGD-4C AAVP-*HSVtk*. Nude mice bearing DU145-derived tumor xenografts (n = 9 tumor-bearing mice per cohort) received an intravenous single dose (5×10^{11} TU) of RGD-4C AAVP-*HSVtk* or nontargeted AAVP-*HSVtk*. PET images with [^{18}F]FDG and [^{18}F]FEAU obtained before and after GCV treatment are presented. T, tumor; H, heart; BR, brain; BL, bladder. Calibration scales are provided in (A) and (B). Superimposition of PET on photographic images of representative tumor-bearing mice was performed to simplify the interpretation of [^{18}F]FDG and [^{18}F]FEAU biodistribution.

(C) Growth curves of individual tumor xenografts after AAVP administration.

(D) Temporal dynamics of *HSVtk* gene expression as assessed by repetitive PET imaging with [^{18}F]FEAU at different days post AAVP administration.

(E) Changes in tumor viability before and after GCV therapy as assessed with [^{18}F]FDG PET. Error bars in (C)–(E) represent standard deviations (SD).
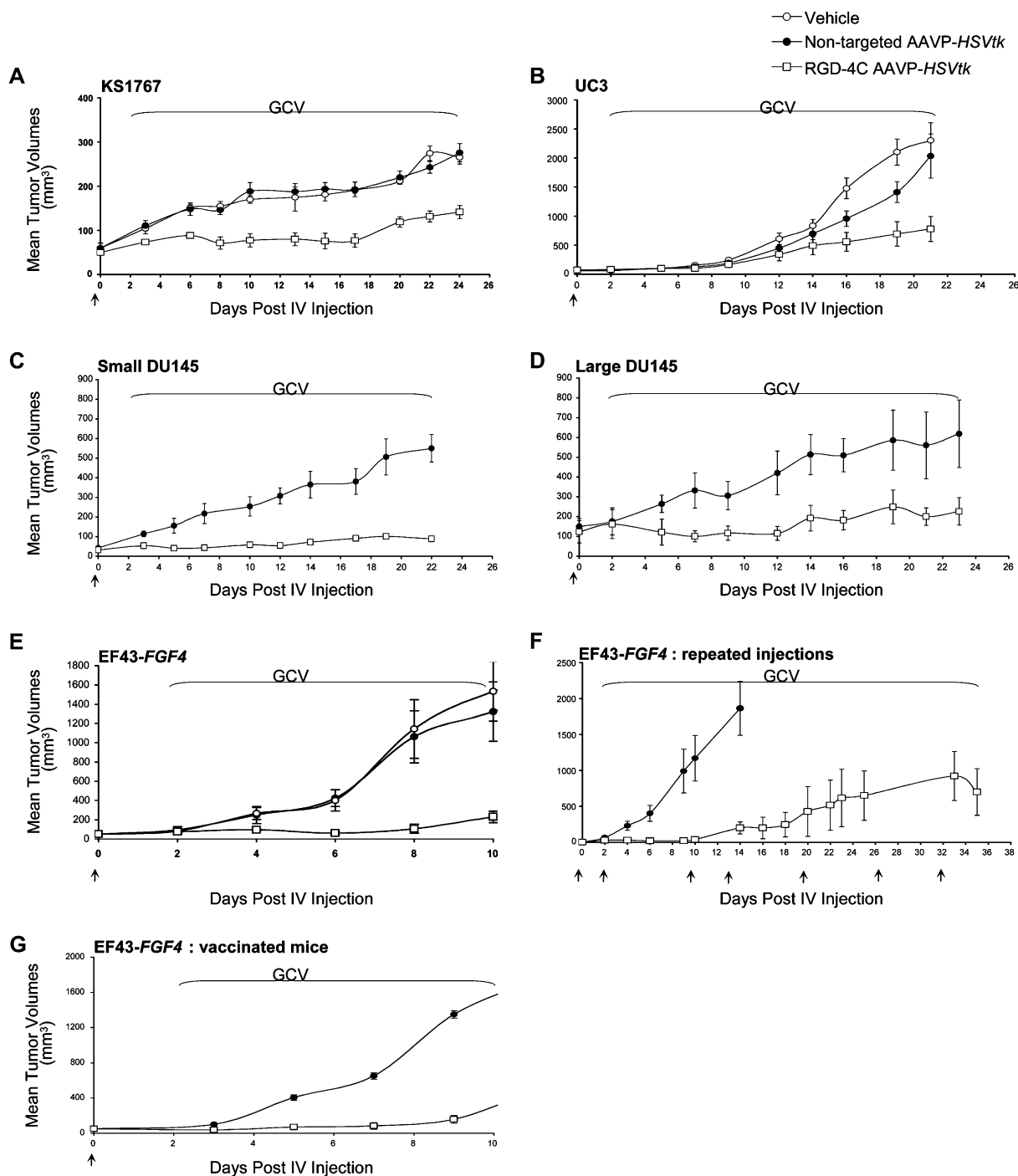
Figure 5. Tumor Growth Suppression by RGD-4C AAVP-*HSVtk* Transduction plus Ganciclovir

(A–C) Cohorts of immunodeficient nude mice with established human xenografts (∼50 mm³) derived from KS1767 cells (A), bladder UC3 carcinoma cells (B), or prostate DU145 carcinoma cells (C) received a single intravenous administration (5 × 10¹⁰ TU) of RGD-4C AAVP-*HSVtk* or controls (non-targeted AAVP-*HSVtk*, RGD-4C AAVP-*GFP*, or vehicle alone). GCV was administered to mice from posttreatment day 2 until the end of the experiments. All mice received GCV except for a control group treated with RGD-4C AAVP-*HSVtk* and no GCV afterwards. Shown are the mean tumor volumes ± standard deviations (SD).

(D) Growth inhibition of large DU145-derived xenografts (at ∼150 mm³) by a single intravenous dose (5 × 10¹⁰ TU) of RGD-4C AAVP-*HSVtk*.

(E) Inhibition of tumor growth of EF43-*FGF4* mouse mammary carcinoma (∼50 mm³) in immunocompetent BALB/c mice by a single intravenous dose (5 × 10¹⁰ TU) of RGD-4C AAVP-*HSVtk*.

images presented to demonstrate that no truncation of low levels of radioactivity was made to artificially "improve" the specificity of *HSVtk* expression in tumors versus nontarget tissues. When tumors grew to reliably palpable sizes ($\sim$350–400 mm^3) and a plateau of *HSVtk* expression was achieved in tumors, treatment with GCV was initiated in all cohorts of animals (Figure 4C). PET imaging with [^{18}F]fluorodeoxyglucose ([^{18}F]FDG) served to monitor glucose metabolism and GCV-induced changes in tumor viability. Two days before initiation of GCV therapy (day 9 post vector administration), the DU145 tumors in both groups of mice were viable and actively accumulated [^{18}F]FDG (Figure 4E). After GCV therapy, the volume of tumors in mice that received RGD-4C AAVP-*HSVtk* was significantly smaller than in mice that received nontargeted AAVP-*HSVtk* (p < 0.05; Figure 4C). Moreover, tumor xenografts were also metabolically suppressed, as evidenced by a decrease in accumulation of [^{18}F]FDG (Figure 4E). The levels of *HSVtk* expression in tumors of mice administered with RGD-4C AAVP-*HSVtk* were also significantly decreased after GCV therapy, as evidenced by a sharp decrease in [^{18}F]FEAU accumulation in PET images (Figure 4D), which were obtained 24 hr after the last GCV dose (to avoid competition with FEAU). These studies confirm the specificity of tumor targeting by RGD-4C AAVP and demonstrate that the level of *HSVtk* transgene expression is adequately high for effective prodrug activation of GCV.

In order to evaluate efficacy horizontally in other preclinical models, we assembled a panel of tumor cell lines from different species and histological origins and generated tumors in immunosuppressed or immunocompetent mice. Cohorts of Kaposi sarcoma (KS1767) derived tumor-bearing mice systemically received a single intravenous dose of either the RGD-4C AAVP-*HSVtk* or nontargeted AAVP-*HSVtk* (control), followed by GCV treatment in all groups. Marked tumor growth suppression was observed in tumor-bearing mice receiving RGD-4C AAVP-*HSVtk* as compared to mice treated with vehicle or mice that received nontargeted AAVP (Figure 5A). Similar tumor growth-suppressive effects were observed in UC3-derived bladder carcinomas (Figure 5B) and DU145-derived prostate carcinomas (Figure 5C) in nude mice, even if larger tumor xenografts were treated (Figure 5D) and consistent with the imaging results presented (Figure 4).

To rule out the possibility that the observed antitumor effects were either species specific or xenograft specific, we sought to analyze the efficacy of the RGD-4C AAVP-*HSVtk* on a standard mouse tumor model. We chose an isogenic tumor in which EF43-*FGF4* mouse mammary cells are administered subcutaneously to induce rapid growth of highly vascularized tumors in immunocompetent mice (Hajitou et al., 2001). First, we established the ligand-directed homing of RGD-4C AAVP to EF43-*FGF4*-derived tumors by anti-phage immunostaining (Figure S4). Either RGD-4C AAVP-*GFP* or nontargeted AAVP-*GFP* was administered intravenously to mice bearing isogenic mammary tumors for a 3–5 min circulation time. Unlike the nontargeted AAVP-*GFP*, RGD-4C AAVP-*GFP* produced a strong anti-phage staining in tumors (Figure S4A). Next, we performed immunofluorescence with an anti-GFP antibody at 7 days after intravenous administration to reveal strong GFP expression in the tumors in mice that received RGD-4C AAVP-*GFP*; in contrast, no GFP staining was detected in tumors from mice that received nontargeted AAVP-*GFP*; consistently, an anti-αv integrin antibody detected strong expression in EF43-*FGF4* tumors (Figure S4B). Again, a single systemic dose of RGD-4C AAVP-*HSVtk* followed by GCV markedly inhibited the growth of EF43-*FGF-4* tumors (Figures 5E–5G and Figure 6). Moreover, when tumors grew back after termination of therapy, repeated administrations of RGD-4C AAVP-*HSVtk* again inhibited EF43-*FGF4* tumor growth and improved survival of tumor-bearing mice (Figure 5F). Phage-based particles are known to be immunogenic, but this feature can be modulated through targeting itself (Trepel et al., 2001). In fact, RGD-4C AAVP-*HSVtk* plus GCV remained surprisingly effective on phage-vaccinated immunocompetent mice despite very high titers of circulating anti-phage IgG (Figure 5G). In selective experiments, a comprehensive panel of negative experimental controls including vehicle alone, vehicle plus GCV, nontargeted AAVP, nontargeted AAVP plus GCV, targeted RGD-4C AAVP, targeted RGD-4C AAVP-*GFP*, and targeted RGD-4C AAVP-*GFP* plus GCV (mock transduction) were used (Figure 6A and data not shown).

To check for posttreatment effects, we obtained detailed histopathological analysis of EF43-*FGF4* tumors recovered 7 days after therapy. We noted extensive tumor destruction caused by the single systemic dose of RGD-4C AAVP-*HSVtk* plus GCV. Specifically, hematoxylin and eosin (H&E) staining revealed uniform destruction of the central area of the tumor and only a small viable outer rim; in contrast, nontargeted AAVP-*HSVtk* had no such effect (Figure 6B). Staining with an anti-CD31 antibody confirmed both disrupted tumor blood vessels within the tumor central region and preserved vasculature toward the outer rim, whereas no damage was observed in the

(F) Long-term efficiency of RGD-4C AAVP-*HSVtk* and GCV by repeated intravenous doses of AAVP (5 × 10^{10} TU per dose) to immunocompetent BALB/c mice bearing isogenic EF43-*FGF4* tumors. Therapy results were consistently observed in independent experiments with tumor-bearing mice cohorts (n = 10 mice per treatment group). Arrows indicate times of AAVP administration.
(G) Effect of humoral immune response against phage on therapy with RGD-4C AAVP-*HSVtk*. BALB/c immunocompetent mice (n = 7 mice per group) were first "vaccinated" with RGD-4C AAVP-*GFP* (10^{10} TU per week for 3 weeks, intravenous) and then implanted with EF43-*FGF4* cells. Tumor-bearing mice received a single systemic dose of RGD-4C AAVP-*HSVtk* or nontargeted AAVP-*HSVtk* followed by GCV maintenance (started at day 2 post AAVP administration). Vaccination did not affect the antitumor effects, despite high anti-phage antibody titers (up to $\sim$1:10,000). Error bars in (D)–(G) represent standard deviations (SD).
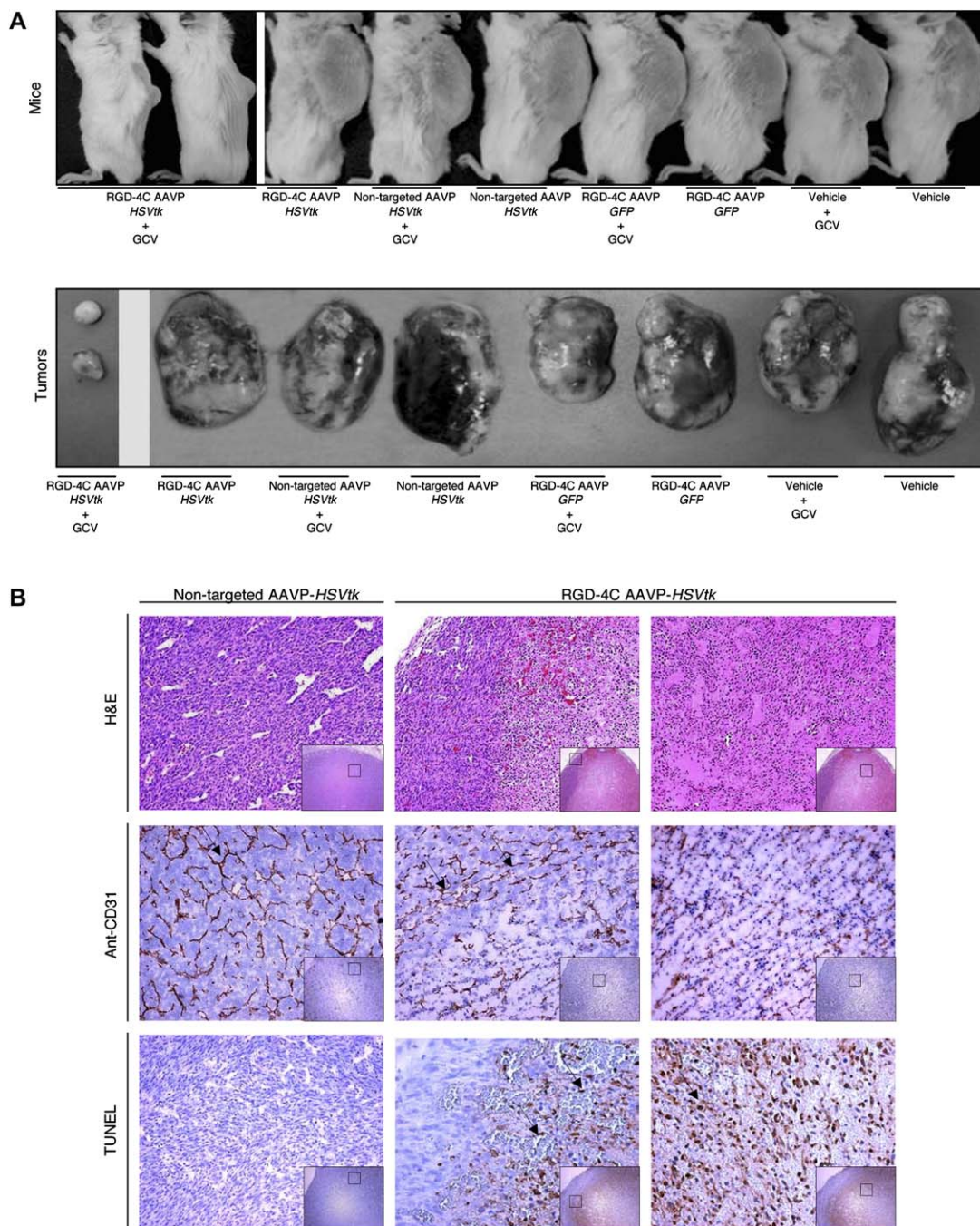
Figure 6. Histological Analysis of Representative Experiments

(A) Tumor-bearing mice (upper panel) and corresponding surgically removed tumors (lower panel) from all the experimental groups of therapy (EF43-*FGF4* mammary tumors in BALB/c immunocompetent mice).

(B) Histopathologic analysis of EF43-*FGF4* treated tumors. Nontargeted AAVP-*HSVtk*-treated tumors (left panels), the border between the outer rims and central tumor areas (middle panels), and central tumor areas of RGD-4C AAVP-*HSVtk*-treated tumors (right panels) are shown as high-magnification views from the low-magnification inserts of serial tumor sections. Hematoxylin and eosin (H&E) staining, CD31 immunostaining (arrows, tumor blood vessels), and TUNEL staining (arrows, apoptotic cells) are shown.

tumors treated with nontargeted AAVP-*HSVtk* (Figure 6B). We also evaluated the tumors for terminal deoxynucleo-tidyl-transferase-mediated dUTP-biotin nick end labeling

(TUNEL) staining, which marks apoptotic cells, because the HSVtk/GCV strategy is associated with apoptotic death of cells. In tumors treated with RGD-4C AAVP-*HSVtk*

and GCV, TUNEL staining detected apoptosis in the tumor central region but not within the outer rim, while no apoptosis was observed in tumors from mice that received nontargeted AAVP-*HSVtk* chimera (Figure 6B). Control organs removed from tumor-bearing mice treated by the same experimental protocol revealed no histopathologic abnormalities (Figure S5). Together, these results show that a single systemic dose of RGD-4C AAVP-*HSVtk* plus GCV maintenance can suppress tumor growth.

Some of our results merit further discussion. First, the relative contribution of targeting each tumor compartment (i.e., tumor cells versus tumor vascular endothelium and/ or stroma) will depend on the ligand-receptor system and on the experimental model (or models) used. For instance, the expression of the membrane target (i.e., αv integrins) in tumor cells will vary from low (EF43-*FGF4*) to strong (KS1767). Moreover, aside from the specific optimal dose for transduction of each model (and application) used, there is also an optimal time to examine transgene expression. In other words, the stoichiometry of reporter-gene expression depends not only on levels and patterns of reporter expression in individual cells but also on the relative number of proliferating transgene-expressing cells versus dying transgene-expressing cells. Thus, while we used fixed parameters for the experiments presented here, further determination of targeted AAVP optimal doses and timeframes on a case-by-case basis still apply. Future translational studies will need to be conducted to determine what doses are clinically meaningful and how an AAVP-based system can be optimized for therapy of patients by using clinically applicable molecular-genetic imaging with PET.

Finally, one might speculate that a broad range of currently intractable biological questions well beyond molecular oncology will be addressed by using targeted AAVP, especially in combination with different preclinical and clinical molecular-genetic imaging settings. For example, the systemic ligand-directed delivery of constructs with tissue- and/or disease-specific promoters (instead of a CMV promoter) to target sites will allow monitoring expression of their corresponding native genes in vivo; such promoter-driven transcription of reporter activity will allow the study of cell trafficking and engraftment. Several noninvasive imaging applications such as experimental monitoring of substrate-specific degradation, protein-protein interactions, and other molecular events via reporter transactivation, complementation, or reconstitution strategies in cells and in whole animals (Luker et al., 2004; De and Gambhir, 2005; Gross and Piwnica-Worms 2005b) will likely follow. In fact, we have recently described networks of gold nanoparticles and bacteriophage as biological sensors and cell targeting agents (Souza et al., 2006); such technology can be combined with ligand-directed AAVP to further improve molecular-genetic imaging. On another note, AAVP itself may provide suitable reagents to study the mechanistic role of ITR structures in transgene persistence and chromosomal integration since (in contrast to AAV vectors) phage-based

constructs with no ITRs can serve as negative experimental controls. In translational terms, the results presented here bode well with an existing framework leading to direct AAVP-based random peptide library screening in patients (Arap et al., 2002; Pentz et al., 2005) and may form the basis for the discovery of new or unrecognized human ligand receptors. Thus, many other systemic targeting and imaging applications in tandem will become possible in a relatively short time frame.

Conclusions

Ligand-directed AAVP combines desirable properties from two unrelated genetic systems to yield a targeted particle for molecular imaging. Attractive features include a cheap and high yield of production in host bacteria and no requirements for helper viruses or *trans*-acting factors. Moreover, the native tropism of AAV for mammalian cells is eliminated since there is no AAV capsid formation and the displayed ligand peptides allow homing to tissue-specific receptors. In the prototype presented here, the ligand-directed AAVP sustains no loss of systemic phage targeting properties and even acquires some posttargeting patterns associated with AAV. We have previously proposed that molecular imaging of marker genes would have the potential to assess therapeutic levels of expression and markedly improve our ability to predict response to therapies in which target genes are known. The introduction of ligand-directed AAVP for systemic targeting and molecular-genetic imaging, rationally designed along the lines described here, is a major step in that direction. Finally, one might speculate that (1) in addition to ligand-directed targeting, further platform refinements such as transcriptional targeting will certainly be possible by incorporation of specific promoters and (2) other hybrid viruses containing prokaryotic and eukaryotic elements (such as, for instance, chimeras between adenovirus and double-stranded lambda phage) may also be envisioned for systemically targeted imaging of reporters. Based on this comprehensive analysis, it seems that the translation of our prototype particle may lead to realistic imaging of gene expression in cancer patients. In a larger context, given the favorable tissue-targeting and molecular-imaging profiles, ligand-directed AAVP is likely to be a useful tool in dissecting other relevant biological questions.

EXPERIMENTAL PROCEDURES

Design, Construction, and Generation of Targeted AAVP Particles

RGD-4C phage and RGD-4C AAVP were engineered in a two-step process: generation of an intermediate (RGD-4C fUSE5-MCS) and subsequent production of RGD-4C phage construct and RGD-4C AAVP. RGD-4C fUSE5-MCS contained the oligonucleotide insert encoding the specific targeting peptide RGD-4C and a fragment of the fMCS plasmid that had a multicloning site (MCS) for insertion of the eukaryotic expression cassette. RGD-4C phage-derived fUSE5 DNA and phage-derived fMCS DNA were purified from lysates of *E. coli* (MC1061). We obtained the intermediate RGD-4C fUSE5-MCS by ligating a 5.4 kb BamHI/SacII fragment of the RGD-4C FUSE5 plasmid to the 4.1 kb BamHI/SacII fragment of the fMCS plasmid. Next, we

created a targeted AAVP-*GFP* by cloning the PacI fragment (2.8 kb) of pAAV-*eGFP* plasmid (enhanced GFP; Stratagene) from ITR to ITR into the PstI site of RGD-4C fUSE5-MSC. Briefly, pAAV was digested with PacI to release a 2.8 kb fragment, which was blunted with DNA polymerase and cloned into the blunted PstI site of RGD-4C fUSE5-MSC. To generate the targeted phage constructs without ITRs, a 2.3 kb fragment located between the ITRs of pAAV-*eGFP* and containing pCMV-*GFP* and SV40 poly A was released by EcoRI digestion, blunted, and cloned into the MCS of RGD-4C fUSE5-MSC. To select cells expressing GFP, the BamHI-SacI fragment of the pQBI phosphoglycerate kinase-1 (QBIOgene) promoter containing a *GFPneo* fusion sequence was cloned in the NotI site of AAVP or control phage constructs to ensure that cells expressing GFP were G418- resistant. The *GFPneo* fragment of pQBI PGK was released by BamHI and SacI digestion and blunted with DNA polymerase; then, phosphorylated linkers to NotI were added. After NotI digestion, the 1.57 kb *GFPneo* fragment was cloned into the NotI site of AAVP or nonchimeric phage construct. Finally, to generate a targeted AAVP particle carrying the gene for *HSVtk* or *Luc*, the BamHI-NotI fragment containing *HSVtk* or *Luc* was subcloned into the BamHI-NotI site of pAAV plasmid to replace *GFP*. The ITR-*HSVtk*-ITR or ITR-*Luc*-ITR fragments were removed from pAAV-*HSVtk* and pAAV-*Luc* was then inserted into RGD-4C fUSE5-MSC. Constructs were verified by DNA sequencing and restriction analysis, purified from the culture supernatant of host *E. coli* (MC1061), resuspended in PBS, and recentrifuged. Resulting supernatants were titrated in *E. coli* (k91Kan). Serial dilutions were plated on Luria-Bertani (LB) agar plates containing tetracycline and kanamycin, and transducing units (TU) were determined by colony counting.

Mammalian Cell-Surface Binding and Internalization Assays

We used the biopanning and rapid analysis of selective interactive ligands (termed BRASIL) method (Giordano et al., 2001) to evaluate phage binding to intact cells. In brief, KS1767 cells were detached by EDTA and resuspended in Dulbecco's modified Eagle's medium (DMEM) containing 1% BSA at 4×10^6 cells/ml. The cell suspension (50 μl) was incubated with 10^9 TU of either RGD-4C AAVP or AAVP clones displaying scrambled versions of RGD-4C (CDCFGDCRC, CDCGFDCRC, CRCDGFCDC), mutant RGE-4C peptide, or nontargeted control. After 2 hr, the AAVP/cell mixture (aqueous phase) was transferred to the top of a nonmiscible organic phase (200 μl solution in a 400 μl Eppendorf tube) consisting of dibutyl phthalate:cyclohexane (9:1 [v/v], D = 1.03 g/ml) and centrifuged at 10,000 $\times$ g for 10 min at 4°C. The tube was snap frozen in liquid nitrogen, the bottom of the tube was sliced off, the pellet was isolated, and membrane bound AAVP was recovered.

For cell internalization, KS1767 cells were grown in tissue chamber slides, washed with PBS, incubated with 10^9 TU of RGD-4C AAVP or control AAVP displaying scrambled versions of RGD-4C or RGE-4C in DMEM containing 1% BSA at 37°C, and washed with PBS to remove unbound AAVP after 4 hr incubation. Cell membrane bound clones were eluted by 20 mM glycine. Next, cells were washed three times with PBS, fixed with PBS containing 4% PFA at RT for 15 min, washed with PBS, permeabilized with 0.2% Triton X-100, washed with PBS, and blocked with PBS containing 1% BSA. Cells were then incubated with a 1:200 dilution of the primary anti-M13 phage antibody (Amersham) in PBS containing 1% BSA at RT for 2 hr, washed with PBS, and incubated with a 1:200 dilution of a Cy3-conjugated anti-rabbit secondary antibody in PBS containing 1% BSA for 1 hr at RT. Finally, cells were washed with PBS, fixed with PBS containing 4% PFA, mounted, and visualized in an optical fluorescence microscope.

Recombinant AAV Rescue Assay

Human 293 cells were infected with AAVP or phage. Four days after infection, cells were transfected with pXX2, an AAV *rep-* and *cap-* expressing plasmid (Xiao et al., 1998), and superinfected with adenovirus type 5. Cells were harvested 72 hr post adenoviral infection, and

supernatants were used to infect new 293 cells. GFP expression was FACS analyzed 48 hr later.

Generation of Clonal Cell Lines

Human 293 cells were infected with RGD-4C AAVP-*GFPneo* or RGD-4C phage-*GFPneo* (at 10^6 TU per cell in each case). Single clones (n = 9 per group) were isolated under G418 selection and FACS analyzed for GFP expression at 12 weeks after selection. Stable clones were termed phage clones #1–9 for phage-*GFPneo* and AAVP clones #1–9 for AAVP-*GFPneo*.

Tumor Models

Tumor-bearing mice were established and tumor volumes were calculated as described (Hajitou et al., 2001; Arap et al., 2004; Marchiò et al., 2004). Mice were anesthetized by intraperitoneal administration of Avertin or by gas (2% isoflurane and 98% oxygen) inhalation. Tumor cells were trypsinized, counted, centrifuged, and resuspended in serum-free medium. A total of 10^6 cells from Kaposi sarcoma (KS1767), bladder carcinoma (UC3), or prostate carcinoma (DU145) lines were implanted subcutaneously into 6-week-old immunodeficient nude mice. The EF43-*FGF4* mouse mammary tumor cells (5 $\times$ 10^4) were implanted subcutaneously into 6-week-old female BALB/c immunocompetent mice. When tumors reached a volume of $\sim$50 mm^3 (deemed small) or $\sim$150 mm^3 (deemed large) DU145-derived xenografts (day 0), tumor-bearing mice received a single intravenous dose of RGD-4C AAVP-*HSVtk* or controls. GCV (80 mg/kg per day, intraperitoneal) was started 2 days later in cohorts of size-matched tumor-bearing mice.

Molecular-Genetic Imaging in Tumor-Bearing Mice

For noninvasive molecular imaging, we used a model of prostate cancer based on the human cell line DU145 in which male nude mice bearing tumor xenografts in the subcutaneous area of the right shoulder were used. To image *Luc* gene expression, tumor-bearing mice received a single dose (150 mg/kg, intraperitoneal) of the substrate D-luciferin (Xenogen). Photonic emission was imaged with the In Vivo Imaging System 200 (IVIS200; Xenogen) after tail-vein administration of targeted RGD-4C AAVP carrying the *Luc* gene or controls (nontargeted AAVP-*Luc* or scrambled RGD-4C AAVP-*Luc*). Imaging parameters were image acquisition time, 1 min; binning, 2; no filter; f/stop, 1; field of view, 10 cm. Regions of interest (roi) were defined manually over the tumors for measuring signal intensities, expressed as photons/sec/cm^2/sr.

While BLI can assess transgene-expressing cell viability in experimental systems, it is not clinically applicable. Thus, to assess the viability of the established tumor xenografts, mice were imaged with a microPET scanner (Concorde Microsystems) at 2 hr post intravenous administration of [^{18}F]FDG 100 μCi/mouse. [^{18}F]FDG was obtained commercially (PETNet). To image *HSVtk* gene expression, PET imaging was performed at 1–2 hr after intravenous administration of the radiolabeled nucleoside analog [^{18}F]FEAU. PET imaging was performed using a microPET R4 (Concorde Microsystems) equipped with a computer-controlled positioning bed. It has a 10.8 cm transaxial and 8 cm axial field of view (fov) without a septa and operates in a three-dimensional list mode. Fully three-dimensional list mode data were collected using an energy window of 350–750 kiloelectron volts and a time window of 6 ns. All raw data were first sorted into three-dimensional sinograms, followed by Fourier rebinning and OSEM image reconstruction using ASIPRO VM software (Concord Microsystems). Image pixel size was $\sim$1 mm transaxially with a 1.2 mm slice thickness.

Radiolabeled [^{18}F]FEAU was synthesized to radiochemical purity greater than 99% by using 5-ethyluracil-2,5-bis-trimethylsilyl ether as the pyrimidine base for condensation with 1-bromo-2-deoxy-2-[^{18}F]fluoro-3,5-di-O-benzoyl-α-D-arabinofuranose (Alauddin et al., 2003). To quantitate the [^{18}F]FEAU or [^{18}F]FDG-derived radioactivity concentration in tumors and other organs and tissues, regions of interest were drawn on images and the measured values converted from

nCi/mm³ into % injected dose per gram (%ID/g; Tjuvajev et al., 1998). Repetitive [18F]FEAU PET imaging was performed at days 0, 3, 5, 10, and 16 post administration of targeted AAVP carrying the *HSVtk* gene or control nontargeted AAVP; GCV treatment was administered between days 11 and 19. Of note, PET imaging at day 16 was performed at 24 hr after GCV dosing to allow for sufficient elimination of GCV, which would otherwise compete with FEAU for phosphorylation by the HSVtk enzyme. PET imaging with [18F]FDG was repeated at day 17 after AAVP administration to assess the viability of residual tumor, if any.

Immunohistochemistry

Anesthetized mice were killed and perfused with PBS containing 4% PFA. Tumor vascularization was assessed on frozen sections by using a rat anti-mouse CD31 antibody (BD Biosciences). Apoptosis analysis was performed on paraffin-embedded sections with a TUNEL kit (Promega). For phage immunodetection, paraffin sections were incubated with a rabbit anti-phage antibody (Sigma) followed by a peroxidase-conjugated anti-rabbit secondary antibody (Dako). For GFP immunostaining, tissues were fixed for 2 hr in PBS containing 2% PFA and equilibrated for 48 hr in PBS containing 15% sucrose. Cryosections were postfixed in PBS containing 4% PFA for 20 min and blocked with 5% goat serum in PBS containing 1% BSA and 0.1% Triton X-100. Tissue sections were incubated with a rabbit affinity-purified GFP antibody (Molecular Probes) in 2% goat serum and 1% BSA. Sections were then stained with the secondary antibody AlexaFluor 488-conjugated goat anti-rabbit (Molecular Probes). αv integrin immunostainings were performed on acetone-fixed frozen sections of tumors removed from PBS-perfused animals. Sections were incubated for 1 hr with a rat anti-integrin αv monoclonal antibody (Chemicon), followed by a secondary Cy3-conjugated goat anti-rat antibody (Jackson ImmunoResearch).

Supplemental Data

Supplemental Data include five figures and two tables and can be found with this article online at http://www.cell.com/cgi/content/full/125/2/385/DC1/.

REFERENCES

Alauddin, M.M., Fissekis, J.D., and Conti, P.S. (2003). A general synthesis of 2′-deoxy-2′-([18F]fluoro-5-methyl-1-β-D-arabinofuranosyluracil and its 5-substituted nucleosides. J. Labelled Comp. Radiopharm. *46*, 285–289.

Arap, W., Pasqualini, R., and Ruoslahti, E. (1998). Cancer treatment by targeted drug delivery to tumor vasculature in a mouse model. Science *279*, 377–380.

Arap, W., Kolonin, M.G., Trepel, M., Lahdenranta, J., Cardó-Vila, M., Giordano, R.J., Mintz, P.J., Ardelt, P.U., Yao, V.J., Vidal, C.I., et al.

(2002). Steps toward mapping the human vasculature by phage display. Nat. Med. *8*, 121–127.

Arap, M.A., Lahdenranta, J., Mintz, P.J., Hajitou, A., Sarkis, A.S., Arap, W., and Pasqualini, R. (2004). Cell surface expression of the stress response chaperone GRP78 enables tumor targeting by circulating ligands. Cancer Cell *6*, 275–284.

Barbas, C.F., III, Burton, D.R., Scott, J.K., and Silverman, G.J. (2001). Phage Display: A Laboratory Manual (New York: Cold Spring Harbor Press).

Barrow, P.A., and Soothill, J.S. (1997). Bacteriophage therapy and prophylaxis: rediscovery and renewed assessment of potential. Trends Microbiol. *5*, 268–271.

Blasberg, R.G., and Tjuvajev, J.G. (2003). Molecular-genetic imaging: current and future perspectives. J. Clin. Invest. *111*, 1620–1629.

Chen, L., Zurita, A.J., Ardelt, P.U., Giordano, R.J., Arap, W., and Pasqualini, R. (2004). Design and validation of a bifunctional ligand display system for receptor targeting. Chem. Biol. *11*, 1081–1091.

De, A., and Gambhir, S.S. (2005). Noninvasive imaging of protein-protein interactions from live cells and living subjects using bioluminescence resonance energy transfer. FASEB J. *19*, 2017–2019.

Ellerby, H.M., Arap, W., Ellerby, L.M., Kain, R., Andrusiak, R., Rio, G.D., Krajewski, S., Lombardo, C.R., Rao, R., Ruoslahti, E., et al. (1999). Anti-cancer activity of targeted pro-apoptotic peptides. Nat. Med. *5*, 1032–1038.

Geier, M.R., Trigg, M.E., and Merill, C.R. (1973). Fate of bacteriophage lambda in non-immune germ-free mice. Nature *246*, 221–223.

Gelovani Tjuvajev, J., and Blasberg, R.G. (2003). *In vivo* imaging of molecular-genetic targets for cancer therapy. Cancer Cell *3*, 327–332.

Giordano, R.J., Cardó-Vila, M., Lahdenranta, J., Pasqualini, R., and Arap, W. (2001). Biopanning and rapid analysis of selective interactive ligands. Nat. Med. *11*, 1249–1253.

Gross, S., and Piwnica-Worms, D. (2005a). Spying on cancer: molecular imaging in vivo with genetically encoded reporters. Cancer Cell *7*, 5–15.

Gross, S., and Piwnica-Worms, D. (2005b). Monitoring proteasome activity in cellulo and in living animals by bioluminescent imaging: technical considerations for design and use of genetically encoded reporters. Methods Enzymol. *399*, 512–530.

Hajitou, A., Sounni, N.E., Devy, L., Grignet-Debrus, C., Lewalle, J.M., Li, H., Deroanne, C.F., Lu, H., Colige, A., Nusgens, B.V., et al. (2001). Down-regulation of vascular endothelial growth factor by tissue inhibitor of metalloproteinase-2: effect on in vivo mammary tumor growth and angiogenesis. Cancer Res. *61*, 3450–3457.

Hajitou, A., Pasqualini, R., and Arap, W. (2006). Vascular targeting: recent advances and therapeutic perspectives. Trends Cardiovasc. Med. *16*, 80–88.

Hood, J.D., Bednarski, M., Frausto, R., Guccione, S., Reisfeld, R.A., Xiang, R., and Cheresh, D.A. (2002). Tumor regression by targeted gene delivery to the neovasculature. Science *296*, 2404–2407.

Hsiao, C.D., Hsieh, F.J., and Tsai, H.J. (2001). Enhanced expression and stable transmission of transgenes flanked by inverted terminal repeats from adeno-associated virus in zebrafish. Dev. Dyn. *220*, 323–336.

Ivanenkov, V.V., Felici, F., and Menon, A.G. (1999). Targeted delivery of multivalent phage display vectors into mammalian cells. Biochim. Biophys. Acta *1448*, 463–472.

Kang, K.W., Min, J.J., Chen, X., and Gambhir, S.S. (2005). Comparison of [14C]FMAU, [3H]FEAU, [14C]FIAU, and [3H]PCV for monitoring reporter gene expression of wild type and mutant *Herpes simplex* virus type 1 thymidine kinase in cell culture. Mol. Imaging Biol. *7*, 296–303.

Kootstra, N.A., and Verma, I.M. (2003). Gene therapy with viral vectors. Annu. Rev. Pharmacol. Toxicol. *43*, 413–439.

Larocca, D., Kassner, P.D., Witte, A., Ladner, R.C., Pierce, G.F., and Baird, A. (1999). Gene transfer to mammalian cells using genetically targeted filamentous bacteriophage. FASEB J. *13*, 727–734.

Lieber, A., Steinwaerder, D.S., Carlson, C.A., and Kay, M.A. (1999). Integrating adenovirus-adeno-associated virus hybrid vectors devoid of all viral genes. J. Virol. *73*, 9314–9324.

Luker, K.E., Smith, M.C., Luker, G.D., Gammon, S.T., Piwnica-Worms, H., and Piwnica-Worms, D. (2004). Kinetics of regulated protein-protein interactions revealed with firefly luciferase complementation imaging in cells and living animals. Proc. Natl. Acad. Sci. USA *101*, 12288–12293.

Marchiò, S., Lahdenranta, J., Schlingemann, R.O., Valdembri, D., Wesseling, P., Arap, M.A., Hajitou, A., Ozawa, M.G., Trepel, M., Giordano, R.J., et al. (2004). Aminopeptidase A is a functional target in angiogenic blood vessels. Cancer Cell *5*, 151–162.

Massoud, T.F., and Gambhir, S.S. (2003). Molecular imaging in living subjects: seeing fundamental biological processes in a new light. Genes Dev. *17*, 545–580.

McCarty, D.M., Young, S.M., Jr., and Samulski, R.J. (2004). Integration of adeno-associated virus (AAV) and recombinant AAV vectors. Annu. Rev. Genet. *38*, 819–845.

Medintz, I.L., Uyeda, H.T., Goldman, E.R., and Mattoussi, H. (2005). Quantum dot bioconjugates for imaging, labelling and sensing. Nat. Mater. *6*, 435–446.

Mizuguchi, H., and Hayakawa, T. (2004). Targeted adenovirus vectors. Hum. Gene Ther. *15*, 1034–1044.

Müller, O.J., Kaul, F., Weitzman, M.D., Pasqualini, R., Arap, W., Kleinschmidt, J.A., and Trepel, M. (2003). Random peptide libraries displayed on adeno-associated virus to select for targeted gene therapy vectors. Nat. Biotechnol. *21*, 1040–1046.

Pasqualini, R., Koivunen, E., and Ruoslahti, E. (1997). Alpha v integrins as receptors for tumor targeting by circulating ligands. Nat. Biotechnol. *15*, 542–546.

Pentz, R.D., Cohen, C.B., Wicclair, M., Devita, M.A., Flamm, A.L., Youngner, S.J., Hamric, A.B., McCabe, M.S., Glover, J.J., Kittiko, W.J., et al. (2005). Ethics guidelines for research with the recently dead. Nat. Med. *11*, 1145–1149.

Piersanti, S., Cherubini, G., Martina, Y., Salone, B., Avitabile, D., Grosso, F., Cundari, E., Di Zenzo, G., and Saggio, I. (2004). Mammalian cell transduction and internalization properties of lambda phages displaying the full-length adenoviral penton base or its central domain. J. Mol. Med. *82*, 467–476.

Poul, M.A., and Marks, J.D. (1999). Targeted gene delivery to mammalian cells by filamentous bacteriophage. J. Mol. Biol. *288*, 203–211.

Ray, P., Bauer, E., Iyer, M., Barrio, J.R., Satyamurthy, N., Phelps, M.E., Herschman, H.R., and Gambhir, S.S. (2001). Monitoring gene therapy with reporter gene imaging. Semin. Nucleic Med. *31*, 312–320.

Smith, G.P., and Scott, J.K. (1993). Libraries of peptides and proteins displayed on filamentous phage. Methods Enzymol. *217*, 228–257.

Souza, G.R., Christianson, D.R., Staquicini, F.I., Ozawa, M.G., Snyder, E.Y., Sidman, R.L., Miller, H.L., Arap, W., and Pasqualini, R. (2006). Networks of gold nanoparticles and bacteriophage as biological sensors and cell targeting agents. Proc. Natl. Acad. Sci. USA *103*, 1215–1220.

Tai, Y.C., and Laforest, R. (2005). Instrumentation aspects of animal PET. Annu. Rev. Biomed. Eng. *7*, 255–285.

Tjuvajev, J.G., Avril, N., Oku, T., Sasajima, T., Miyagawa, T., Joshi, R., Safer, M., Beattie, B., DiResta, G., Daghighian, F., et al. (1998). Imaging herpes virus thymidine kinase gene transfer and expression by positron emission tomography. Cancer Res. *58*, 4333–4341.

Tjuvajev, J.G., Chen, S.H., Joshi, A., Joshi, R., Guo, Z.S., Balatoni, J., Ballon, D., Koutcher, J., Finn, R., Woo, S.L., et al. (1999). Imaging adenoviral-mediated herpes virus thymidine kinase gene transfer and expression in vivo. Cancer Res. *59*, 5186–5193.

Trepel, M., Arap, W., and Pasqualini, R. (2001). Modulation of the immune response by systemic targeting of antigens to lymph nodes. Cancer Res. *61*, 8110–8112.

Xiao, X., Li, J., and Samulski, R.J. (1998). Production of high-titer recombinant adeno-associated virus vectors in the absence of helper adenovirus. J. Virol. *72*, 2224–2232.

Yang, C.C., Xiao, X., Zhu, X., Ansardi, D.C., Epstein, N.D., Frey, M.R., Matera, A.G., and Samulski, R.J. (1997). Cellular recombination pathways and viral terminal repeat hairpin structures are sufficient for adeno-associated virus integration in vivo and in vitro. J. Virol. *71*, 9231–9247.

Zacher, A.N., III, Stock, C.A., Golden, J.W., II, and Smith, G.P. (1980). A new filamentous phage cloning vector: fd-tet. Gene *9*, 127–140.

Metal Nanoshells

Leon R. Hirsch,[1] Andre M. Gobin,[1] Amanda R. Lowery,[1] Felicia Tam,[2] Rebekah A. Drezek,[1] Naomi J. Halas,[2] and Jennifer L. West [1]

[1]Rice University, Department of Bioengineering, Box 1892, MS 144, Houston, TX 77251-1892, USA and [2]Department of Electrical and Computer Engineering, Box 1892, MS 366, Houston, TX 77251-1892, USA

Abstract—Metal nanoshells are a new class of nanoparticles with highly tunable optical properties. Metal nanoshells consist of a dielectric core nanoparticle such as silica surrounded by an ultra-thin metal shell, often composed of gold for biomedical applications. Depending on the size and composition of each layer of the nanoshell, particles can be designed to either absorb or scatter light over much of the visible and infrared regions of the electromagnetic spectrum, including the near infrared region where penetration of light through tissue is maximal. These particles are also effective substrates for surface-enhanced Raman scattering (SERS) and are easily conjugated to antibodies and other biomolecules. One can envision a myriad of potential applications of such tunable particles. Several potential biomedical applications are under development, including immunoassays, modulated drug delivery, photothermal cancer therapy, and imaging contrast agents.

Keywords—Nanotechnology, immunoassay, controlled release, optical imaging, cancer.

WHAT IS A METAL NANOSHELL?

Medieval alchemists were some of the first to discover the plasmon resonance phenomenon when they successfully reduced gold from a salt solution into its reddish colloidal form. The reddish color arises from the metal colloid's extinction at approximately 520 nm, which results from optical resonances of surface plasmons (or oscillating conducting electrons) in the metal induced by the incident light. Many bulk metals (i.e., Au, Ag, Ni, Pt) demonstrate a plasmon resonance with each metal having a characteristic peak within a defined region of the visible spectrum.[5] Plasmon resonance phenomena of metal colloids have enabled several biomedical applications, but these have been limited by the fact that the plasmon resonances of conventionally available materials fall within the visible range of the spectrum where penetration of light through blood and tissue is low.

Nanoshells are a new class of nanoparticles with tunable plasmon resonance, allowing materials to be specifically

designed to match the wavelength required for a particular application, for instance to fall within near infrared (NIR) regions where light penetration through tissue is optimal. Conceived of over 50 years ago[1] but not realized until the 1990's,[3,26,50] a metal nanoshell consists of a spherical dielectric nanoparticle surrounded by an ultrathin, conductive, metallic layer. By varying the composition and dimensions of the layers of the nanoparticles, nanoshells can be designed and fabricated with plasmon resonances from the visible to infrared regions of the spectrum.[27] For a given composition of core and metal shell, the plasmon resonances of the nanoparticle, which determines the particle's optical absorption and scattering, may be tuned by changing the ratio of the nanoparticle's core size to its shell thickness (Fig. 1).

Experimentally, the first metal nanoshell, developed by Zhou *et al.*,[50] consisted of an Au_2S dielectric core surrounded by a gold shell. Depending upon the size of the nanoparticles, it was possible to shift the plasmon resonance to longer wavelengths of light, ranging from the standard gold colloid peak of ∼520 out to ∼900 nm. Gold-gold sulfide (Au–Au_2S) nanoshells have limits to their size (≤40 nm) and plasmon tunability due their synthesis chemistry. These nanoparticles are grown in a one step process where chloroauric acid ($HAuCl_4$) and sodium sulfide (Na_2S) are mixed. Depending upon the ratios of $HAuCl_4$ and Na_2S added (with an excess of Au), Au–Au_2S nanoshells are grown with different core and shell thicknesses. Due to the kinetics of the core and shell growth[3,4] this synthesis lacks the facility for independent control over nanoparticle core and shell dimensions. Additionally, large amounts of gold colloid are formed as a secondary product of this synthesis scheme, generating an additional absorption peak at ∼520 nm.

Oldenburg *et al.* developed a new nanoparticle, a silica-gold core-shell nanoshell, which overcame many of the limitations of the Au–Au_2S particles.[26] To synthesize these particles, a dielectric silica core is grown by the Stöber method,[42] where tetraethylorthosilicate is reduced in ethanol under basic conditions resulting in the nucleation
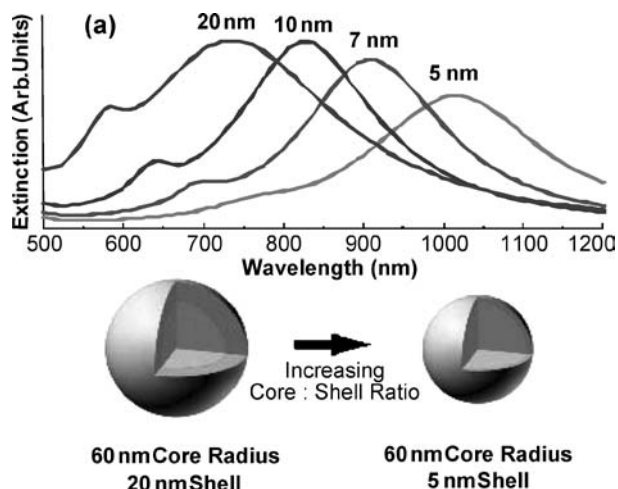
FIGURE 1. Optical tunability is demonstrated for nanoshells with a 60 nm silica core radius and gold shells 5, 7, 10, and 20 nm thick. Observe that the plasmon resonance (extinction) of the particles red shifts with decreasing thickness of the gold shell (or an increasing core:shell ratio). Nanoshells are easily fabricated with resonance in the NIR. Greater tunability can be achieved by also altering the core size, changing the composition of the core and shell, and forming multilayered structures.

FIGURE 2. Series of TEM images showing gold colloid growth into a complete shell on silica core particle surface. Beginning form the upper left, the gold colloid (dark dots) serve as nucleation sites for additional electroless plating of gold. As additional gold is deposited onto the gold islands, the gold grows until coalescing with neighboring colloid, finally forming a complete metal shell (bottom right).

and growth of highly monodisperse and spherical silica colloid. Particle diameters ranging from 50 to 500 nm can be synthesized by this method. The surfaces of the silica core particles are then functionalized with amine groups by reaction with aminopropyltriethoxysilane (APTES). Small gold colloid (1–2 nm) is then adsorbed onto their aminated surfaces. This disperse surface Au colloid layer serves as nucleation sites for further reduction of gold onto the silica nanoparticle core by reduction of Au in a $HAuCl_4$ solution. As more gold is reduced, the surface coating grows and coalesces into a complete gold shell (Fig. 2). The amount of $HAuCl_4$ added determines the final thickness of the gold shell, which can typically range between 5 and 30 nm. By changing the ratio of the core diameter to shell thickness, the plasmon resonance peak may be placed anywhere within the visible to mid-infrared region of light. More recently, this geometry has been extended into multilayered, concentric nanoshells, producing more complex hybridized resonances whose spectral profiles span the infrared spectrum to thermal wavelengths.[31]

Additionally, metal nanoshells have demonstrated strong surface-enhanced Raman scattering (SERS)—at least 10^{10} enhancements are possible.[18,19,26] Metal films and nanoparticles have been investigated by many groups as substrates for SERS. The tremendous enhancement in Raman scattering for molecules close to such metal surfaces is believed to be due to the local enhanced electromagnetic field at the surface due to the excitation of surface plasmons.[24] Thus, optimal SERS is observed at the plasmon resonance of the substrate material; the tunability of the plasmon resonance of nanoshells is exciting as it may enable one to design a

substrate to match the wavelength desired for a given application and to work in the NIR to potentially enable *in vivo* applications of SERS. A NIR SERS nanosensor may be possible for assays performed in whole blood, intracellular spectroscopy, or *in vivo* diagnostics.

Gold nanoshells are particularly attractive for use in biological applications due to the fact that their outer shell is composed of reduced gold. This noble metal is resistant to corrosion, demonstrates low toxicity, and is a popular material for medical applications such as dental prosthetics, which utilize its inert chemical properties and conformational flexibility.[6,9,29] Biomedical applications also use gold in electrodes for amperometric detection of analytes (i.e., O_2, H_2O_2, urea, glucose) in long term sensing applications.[14,21,34] Additionally, gold facilitates easy conjugation of proteins onto its surface. Proteins spontaneously chemisorb to gold surfaces when incubated with the metal at or slightly basic to their isoelectric point. This technique is commonly used for immunogold labeling techniques.[15] However, most current methods prefer a more irreversible, if not covalent, method of molecule immobilization onto gold surfaces. Proteins and other thiol/disulfide-possessing molecules are capable of spontaneously self-assembling into dense networks on gold surfaces. This strong dative interaction between the sulfur and gold is reversible, but strongly favors binding in the forward direction with a bond enthalpy of 126–146 kJ/mol—a strength approaching that of other covalent bonds.[25] Proteins and other synthetic molecules are easily functionalized with these sulfhydryl moieties to create a robust, simple method of tailoring the gold nanoshell surface chemistry, and concomitantly, its bioreactivty/inertness for biosensing or therapeutic applications. Using this type of chemistry, metal nanoshells can be chemically modified with either hydrophobic or hydrophilic species. This provides the advantage of using nanoshells in solution-based systems

without compromising solubility or colloidal stability in either organic or aqueous environments. For *in vivo* applications, nanoshells can be immoblized within "stealthing" polymers or microencapsulated to provide steric stabilization and reduce the risk of opsonization.[12,13]

BIOMEDICAL APPLICATIONS OF METAL NANOSHELLS

Optical methods for diagnosis and treatment in medicine and biology are attractive due to their potential for non-invasive and minimally-invasive applications. NIR light between 700–1100 nm is particularly interesting due to the absence of significant absorption from either biological chromophores or water within this region, permitting deep optical penetration into biological samples such as tissue or whole blood.[48] Numerous diagnostic systems employing NIR optical probes are under investigation. Tomographic techniques, such as optical coherence tomography (OCT), use backscattered light to reconstruct high-resolution images (≤ 10 μm) of tissue morphology.[17] While OCT has been used most extensively in ophthalmology, it has also examined features such as intimal thickening in human aortae.[7] On a larger scale, tomographic reconstructions of whole brain specimens have been made with NIR light. Although this technique does not approach the spatial resolution of conventional methods (i.e., MRI, CT), it does contain spectral information as well; NIR spectroscopy in conjunction with tomography may provide both space- and time-resolved information about cerebral oxygenation, which is of particular interest in neonates.[16] Some other NIR applications worth mentioning are confocal imaging, iridotomy, and photothermal coagulation—all of which take advantage of tissue's increased transparency within this region.[33,44] As discussed above, metal nanoshells can be easily tuned to have strong scattering or absorption properties in the NIR, enabling many new biomedical applications in this interesting spectral region.

Nanoshells for Immunoassays

Immunoassays utilize antibody-antigen interactions to detect a specific antigen within a complex mixture. The Sandwich-Type Enzyme Linked Immunosorbant Assay (ELISA) is the most widely used immunoassay. Although ELISAs are very effective at detecting small amounts of analyte, they suffer a few limitations. These systems rely upon either fluorescence or a colorimetric change in solution to determine antigen concentrations, making it necessary to use purified, cell-free specimens and perform multiple rinsing steps in order to minimize optical interference and obtain a pure signal. For the analysis of a blood specimen, these additional purification steps may lengthen the time necessary to complete an assay (4–24 h). In addition, these assays are performed on a solid, macroscopic substrate,

limiting the application to *in vitro* use only. The ELISA's dependence upon enzymatic activity for detection is another problem, due to its dependence upon temperature, denaturation, pH, and other factors. To overcome these issues, a new immunoassay technique has been developed utilizing antibody conjugated, NIR resonant nanoshells. This assay can be performed in whole blood and provides results within several minutes with sensitivity similar to an ELISA.[12,13]

The underlying mechanism behind the nanoshell-based immunoassay is similar to that of conventional latex agglutination (LA) and sol particle immunoassays (Singer and Plotz, 1956, Leuvering *et al.*, 1980). When antibody conjugated particles are exposed to a multivalent analyte, multiple particles will bind to the analyte, forming particle dimers and higher order assemblies of particles. Unfortunately, LA and sol particle assays are difficult to perform in whole blood due to blood's high turbidity and strong visible extinction. The aggregation of nanoshells gives rise to additional optical resonances at longer wavelengths for the aggregate structure since the plasmon resonant spectral response of nanoparticle masses differs significantly from that of isolated, dispersed plasmon resonant nanoparticles.[32] Nanoshell dimers and larger aggregates produce a significantly red-shifted plasmon resonance. The red-shifted plasmon from aggregation is simultaneously accompanied by a decrease in the amplitude of the single nanoshell plasmon resonance in the overall spectral response.[32] This appears in the optical signal as a net shift in the nanoshell resonance to longer wavelengths in the NIR extinction spectrum. This provides a straightforward method for detecting nanoshell-bioconjugate aggregation via monitoring of the decrease in extinction at the original nanoshell plasmon resonance peak, as shown in Fig. 3.[12,13]
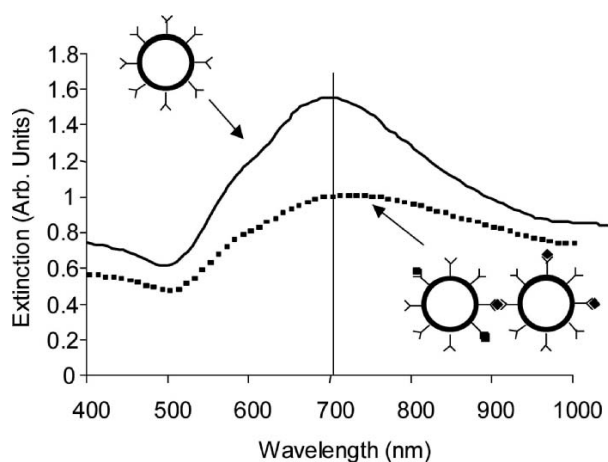
FIGURE 3. The principle of the nanoshell immunoassay. Nanoshells conjugated with antibody specific for a particular analyte are well dispersed in an analyte free environment (–), and possess a spectrum with a resonance in the near infrared. In the presence of analyte, however, antibody-antigen interactions cause nanoshell agglutination, a phenomenon that is easily detected by a reduction in the nanoshell suspension's original peak resonance (–).

The performance of the nanoshell-based immunoassay has been evaluated in saline, serum, and blood samples for a variety of analytes.[12,13] For these assays, antibodies are conjugated to nanoshells via a polyethylene glycol (PEG) linker that is derivatized with thiol groups. Quantitative analyte detection could be achieved over the concentration range of 0.4–400 ng/ml, with completion of the assay in 10 min. The availability of this type of rapid, *in situ*, whole blood assay with the capacity to detect a variety of analytes would greatly benefit point-of-care or public health applications where there is a strong demand for rapid screening of blood-borne species such as bacteria, viruses, or proteins.

Optically-Responsive Nanoshell-Hydrogel Composites

Over the past several decades, the field of controlled drug delivery has faced two major challenges; sustained zero-order release of a therapeutic agent and pulsatile delivery of a therapeutic agent. The first goal has been largely addressed by a variety of delivery systems, including osmotically driven pumps and biodegradable matrices (reviewed in).[40] The second goal, controlled modulation of drug delivery, has proved more difficult. Thermally responsive hydrogels and membranes have been extensively evaluated as platforms for the pulsatile delivery of drugs. One of the characteristics of temperature-responsive hydrogels is the presence of a lower critical solution temperature (LCST), a temperature at which the hydrogel material will undergo a dramatic phase change. The driving force for this phase change is based on the interactions between the polymer and the surrounding water.[35,43] Below the LCST, the most thermodynamically stable configuration is for the water molecules to remain clustered around the polymer chains. Above the LCST, the polymer chains collapse upon each other and minimize interaction with water. Due to this phase change, a macroscopic hydrogel will undergo a drastic change in dimensions, collapsing as the temperature exceeds the LCST, with expulsion of water (and dissolved drug) from the matrix.

N-isopropylacrylamide (NIPAAm) is a commonly used thermoresponsive polymer, and copolymers of NIPAAm and acrylamide form hydrogel materials with LCSTs ranging from 32–60°C, depending on the composition of the copolymer.[30] Pulsatile delivery of a variety of drugs has been demonstrated from NIPAAm-co-acrylamide hydrogels by subjecting the materials to changes in temperature.[30,49] While very nice results have been achieved with this system, the practical implementation of the system has been difficult due to issues with inducing temperature changes in implanted materials. In order to develop NIR responsive materials that might be more easily manipulated implants for modulated drug delivery, composite hydrogels formed from NIPAAm-co-acrylamide and NIR-absorbing nanoshells have been developed.[39] The compos-
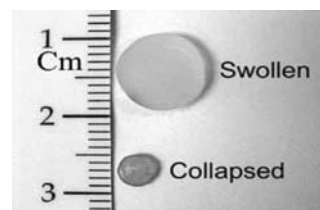
FIGURE 4. Nanoshells entrapped within the NIPAAm-co-acrylamide hydrogels absorb near infrared light to drive the phase change of the thermally responsive polymer. Exceeding the LCST caused collapse of the hydrogel material, due to expulsion of water and collapse of the polymer chains.

ites were fabricated by mixing nanoshells into the monomer mixture. After polymerization, the nanoshells were physically entrapped in the hydrogel matrix. As shown in Fig. 4, the composite hydrogels undergo a pronounced collapse in response to NIR light; the nanoshells absorb the light, generating heat within the composite to exceed the LCST of the copolymer, thus inducing the phase change.[37]

The collapse of the hydrogel material is completely reversible. When the temperature falls below the LCST, the polymer chains extend and interact with water, causing the material to swell. The reversible nature of this phenomenon allows one to partially collapse the material, re-swell it, cycling above and below the LCST repeatedly. If a drug has been incorporated into the hydrogel matrix, each time the hydrogel collapses, a burst of drug will be expelled from the material, as demonstrated in Fig. 5.[39] Because of the deep penetration of NIR light through tissue, the composite hydrogels may be implanted subcutaneously, with the phase change behavior easily manipulated by externally applied NIR light.

Recently, these optically responsive composites have been utilized as valves within a microfluidics device.[40] In this case, it is desirable to have independent optical
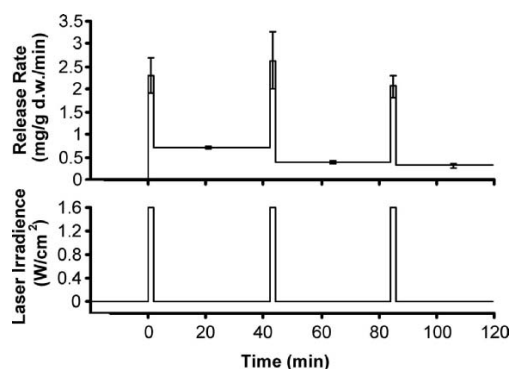
FIGURE 5. Pulsatile release of protein (top panel) from nanoshell composite NIPAAm-co-AAm hydrogels was achieved through pulsatile near infrared irradiation (bottom panel).
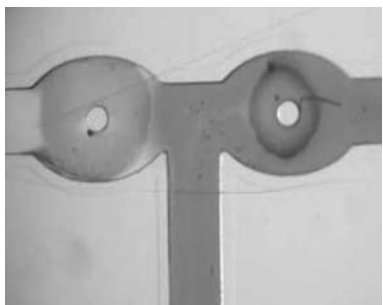
FIGURE 6. Nanoparticle-containing NIPAAm-co-AAm hydrogels were photopolymerized within microfluidics devices to form optically-controlled valves. By changing the optical absorption of the nanoshells within a particular valve, one can determine what wavelengths of light will cause valve opening. In this case, two valves were formed at a T-junction, one that responded to green light while the other responded to NIR light. Independent control of the two valves was obtained. Blue dextran was used to visualize flow patterns.

control over multiple valve structures within a single device, allowing one to control complex flow patterns through a device simply by changing the wavelength of light used for illumination. In such an application, the broad tunability of nanoshells is advantageous. In a preliminary study, independent control over two separate valves at a T-junction has been demonstrated, one opening in response to 532 nm illumination while the other opened upon exposure to light at 832 nm (Fig. 6).[40]

Photothermal Ablation

As discussed above, nanoshells can be designed to strongly absorb NIR light and thus generate localized heating, potentially enabling nanoshell-mediated thermal ablation therapies for applications such as cancer treatment. Thermal ablation therapies can provide a minimally invasive alternative to surgical excision of tumors and are particularly attractive for situations where surgery is not possible. Thermal delivery methods under investigation for local tissue ablation include lasers,[2,45] microwave and radio frequency energy,[8,36] magnetic thermal ablation,[11] and focused ultrasound.[20] The goal of thermal ablation is to conform a lethal dose of heat to a prescribed tissue volume with as little damage to intervening and surrounding normal tissue as possible, which has been difficult with the majority of techniques currently under investigation. Due to the lack of absorption of NIR light by tissue components, use of this type of light source, with nanoshells localized within the tumor site, should minimize collateral tissue damage. *In vitro* studies with nanoshells bound to breast carcinoma cells have demonstrated effective destruction of the cancerous cells upon exposure to near infrared light,[12,13] with cell damage limited to the laser treatment spot (Fig. 7).

The efficacy of nanoshell-mediated photothermal ablation has also been assessed in several *in vivo* studies. Initial studies involved directly injecting nanoshell suspensions into tumor sites and utilizing MRI thermal imaging to monitor temperature profiles during NIR-induced heating.[12,13] These studies demonstrated rapid heating of nanoshell-laden tissues upon exposure to the near infrared light. Evaluation of the gross pathology and histology demonstrated marked tissue damage at the treatment sites, with little or no damage to surrounding tissue. This initial work also provided information about the relationships between nanoshell dosages, light intensity, and duration of illumination with the ultimate thermal profile and resultant tissue damage. However, for the majority of applications, direct injection into the tumor site may not be feasible.

An alternative approach is to inject nanoshells intravenously, allowing them to circulate and accumulate at the tumor site before NIR treatment. The size of nanoshells is critical to the success of this type of approach. Substantial prior research has investigated the delivery of macromolecules and small particles through the tumor vasculature. These efforts have demonstrated that particles in the 60–400 nm size range will extravasate and accumulate in many tumor types via a passive mechanism referred to as the "enhanced permeability and retention" (EPR) effect.[23] This effect has been attributed to the highly proliferative vasculature within neoplastic tumors. During rapid angiogenesis, defects in the vascular architecture are often present, resulting in leaky vessels. Nanoshells fall within the range applicable for the EPR effect, and thus should accumulate in most tumor types following intravenous injection. The efficacy of photothermal ablation following systemic delivery of nanoshells has been evaluated in a mouse model.[28] Complete regression of tumors was observed within 10 days following treatment with nanoshells and near infrared light, with no tumor re-growth over at least 60 days. Survival times for mice with the nanoshell treatment in this study were significantly improved compared to untreated mice or those receiving laser treatment alone. Additionally, it is possible to conjugate nanoshells to antibodies to oncoproteins or endothelial markers, which may improve the accumulation of nanoshells in the tumor tissue and further localize nanoshells to targeted cells at the treatment site.

Nanoshell Contrast Agents in Imaging

The drug delivery and thermal ablation applications described in the preceding sections used nanoshells designed to strongly absorb light in the NIR spectral region. By fabricating nanoshells designed to preferentially scatter rather than absorb light, nanoshells can serve as strong optical contrast agents for a variety of biomedical optical imaging applications. Photonics-based imaging technologies offer
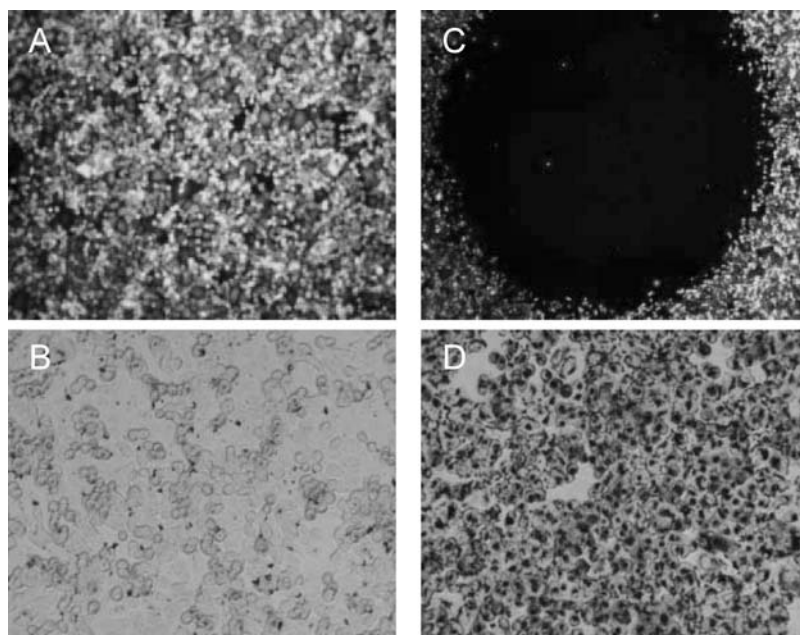
FIGURE 7. HER2-positive breast carcinoma cells were treated with nanoshells conjugated with either a control anti-IgG (panels A and B) or anti-HER2 (panels C and D). Upon NIR laser treatment, cells exposed to anti-HER2 nanoshells were effectively destroyed, as demonstrated by the circular region corresponding to the laser spot that lacks staining with a fluorescent viability marker (C), while the nanoshells bound to the control antibody did not produce this effect. Silver staining was then performed to visualize nanoshell binding to cells. Nanoshells only bound to the breast carcinoma cells when conjugated to the anti-HER2 antibody (control = B, anti-HER2 = D).

the potential for non-invasive, high-resolution *in vivo* imaging. However, the clinical utility of optical imaging strategies has been significantly constrained both by the limited variety of endogenous chromophores present in tissue and by relatively low levels of optical contrast between normal and diseased tissue. Furthermore, in the case of cancer, where early detection is critical to reducing morbidity and mortality, it is often desirable to image specific molecular biomarkers which are present long before pathologic changes occur at the anatomic level. Imaging biomarkers of interest requires development of targetable optical contrast agents. A recent demonstration of scattering-based molecular imaging used gold colloid conjugated to antibodies to the epidermal growth factor receptor (EGFR) as an optical contrast agent for imaging early cervical pre-cancers.[41] While gold colloid bioconjugates are valuable as contrast agents for detecting superficial epithelial cancers with visible light, a primary challenge in optical contrast agent development has been the need for optical contrast agents at the multiple laser wavelengths within in the NIR spectral region commonly used in optical imaging applications. The facile tunability of nanoshells facilitates their use as NIR contrast agents. In addition, nanoshells offer other advantages relative to conventional imaging agents including more favorable optical scattering properties, enhanced biocompatibility, and reduced susceptibility to chemical/thermal denaturation. Furthermore, as described above,

nanoshells are readily conjugated to antibodies or other targeting moieties of interest, enabling molecular specific imaging.

Initial *in vitro* studies were conducted to demonstrate the potential of nanoshell bioconjugates for molecular imaging applications. These experiments used nanoshell designed to strongly scatter light throughout the NIR "optical window" of 700–1200 nm. To enable molecular targeting, antibodies were conjugated onto nanoshell surfaces using a PEG linker. Cells incubated with scattering nanoshell bioconjugates were viewed under darkfield microscopy, a form of microscopy sensitive only to scattered light. Significantly increased optical contrast due to expression of HER2, a clinically relevant cancer biomarker, was observed in HER2-positive breast carcinoma cells targeted with HER2-labeled nanoshells compared to the contrast observed in cells targeted by either nanoshells non-specifically labeled with IgG or control cells which were not exposed to nanoshell conjugates (Fig. 8). Recently, it has also been demonstrated that nanoshells designed to have both scattering and absorption components to their extinction can be used for integrated imaging and therapy.[22]

Nanoshells have also been utilized as contrast agents in a very different type of imaging modality—photoacoustic tomography.[46] Photoacoustic tomography (PAT) is a hybrid imaging modality that uses light to rapidly heat elements
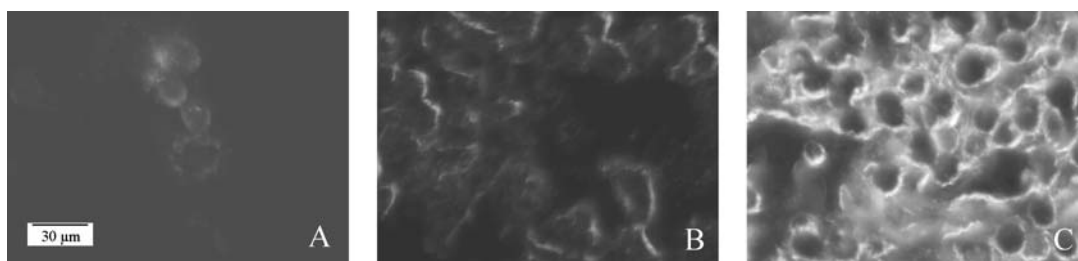
FIGURE 8. Dark field images of HER2-positive breast carcinoma cells A: untreated, B: treated with non-specific anti-IgG conjugated nanoshells or C: treated with anti-HER2-conjugated nanoshells. The nanoshells were designed to be strongly scattering, thus generating bright images of targeted cells observed via dark field microscopy. Length bar = 30 μm.

within tissue; the resultant thermoelastic expansion generates photoacoustic waves that are then detected with an ultrasonic transducer. The use of NIR-absorbing agents, such as metal nanoshells, should generate greater contrast in images due to the more substantial differences in optical absorption and thus in generation of photoacoustic waves than is possible based on endogenous tissue chromophores. In an *in vivo* brain imaging study, PEG-coated, NIR-absorbing gold nanoshells were injected intravenously, then PAT was used to image the cerebral vasculature.[46] Nanoshell injection increased optical absorption in the brain tissue by more than 60%. Moreover, due to the long circulation time of PEG-coated nanoshells, images could be taken for many hours without decreased contrast.[46]

REFERENCES

[1] Aden, A. L., and M. Kerker. *J. Appl. Phys.* 22:1242–1246, 1951.

[2] Amin, Z., W. Thurrell, G. M. Spencer, S. A. Harries, W. E. Grant, S. G. Bown, W. R. Lees. *Invest. Radiol.* 28:1148–1154, 1993.

[3] Averitt, R. D., D. Sarkar, and N. J. Halas. *Phys. Rev. Lett.* 78:4217–4220, 1997.

[4] Averitt, R. D., S. L. Westcott, and N. J. Halas. *J. Opt. Soc. Am. B* 16:1824–1832, 1999.

[5] Bohren, C. F., and D. R. Huffman. In *Absorption and Scattering of Light by Small Particles*, Wiley-Interscience, New York, pp. 379, 1983.

[6] Eichner, K. *Int. Dent. J.* 33:1–10, 1983.

[7] Fujimoto, J. G., M. E. Brezinski, B. J. Tearney, S. A. Boppart, B. Bouma, M. R. Hee, J. F. Southern, and E. A. Swanson. *Nat. Med.* 1:970–972, 1995.

[8] Gazelle, G. S., S. N. Goldberg, L. Solbiati, and T. Livraghi. *Radiology* 217:633–646, 2000.

[9] Hagman, H. *Dent. Lab. Rev.* 54:28–30, 1979.

[10] Hilger, I., R. Hiergeist, R. Hergt, K. Winnefeld, H. Schubert, and W. A. Kaiser. *Invest. Radiol.* 37:580–586, 2002.

[11] Hirsch, L. R., J. B. Jackson, A. Lee, N. J. Halas, and J. L. West. *Analyt. Chem.* 75:2377–2381, 2003.

[12] Hirsch, L. R., R. J. Stafford, J. A. Bankson, S. R. Sershen, B. Rivera, R. E. Price, J. D. Hazle, N. J. Halas, and J. L. West. *Proc. Natl. Acad. Sci. USA* 100:13549–13554, 2003.

[13] Holstrum, N., P. Nilsson, J. Carlsten, and S. Bowland. *Biosensors and Bioelectronics* 13:1287–1295, 1998.

[14] Horisberger, M., and J. Rosset. *J. Histochem. Cytochem.* 25:295–305, 1977.

[15] Houten, J. V., D. Benaron, S. Spilman, and D. K. Stevenson. *Ped. Res.* 39:470–476, 1996.

[16] Huang, D., E. A. Swanson, C. P. Lin, J. S. Schuman, W. G. Stinson, W. Chang, M. R. Hee, T. Flotte, K. Gregory, C. A. Puliafito, and J. G. Fujimoto. *Science* 254:1178–1181, 1991.

[17] Jackson, J. B., S. L. Westcott, L. R. Hirsch, J. L. West, and N. J. Halas. *Appl. Phys. Lett.* 82:257–259, 2003.

[18] Jackson, J. B., and N. J. Halas. *Proc. Natl. Acad. Sci. USA* 101:17930–17935, 2004.

[19] Jolesz, F. A., and K. Hynynen. *Cancer J.* S1:100–112, 2002.

[20] Leuvering J. H., Thal P. J., van der Waart M., Schuurs A. H. *J. Immunoassay*, 1:77–91, 1980.

[21] Lindholm-Sethson, B., J. C. Gonzalez, and G. Puu. *Langmuir* 14:6705–6708, 1998.

[22] Loo, C., A. Lowery, N. Halas, J. West, and R. Drezek. *NanoLett.* 5:709–711, 2005.

[23] Maeda, H., T. Sawa, and T. Konno. *J. Control. Rel.* 74:46–61, 2001.

[24] Maher, R. C., L. F. Cohen, P. Etchegoin, H. J. N. Hartigan, R. J. C. Brown, and M. J. T. Milton. *J. Chem. Phys.* 120:11746–11753, 2004.

[25] Nuzzo, R. G., F. A. Fusco, and D. L. Allara. *J. Am. Chem. Soc.* 109:2358–2368, 1987.

[26] Oldenburg, S. J., R. D. Averitt, S. L. Westcott, and N. J. Halas. *Chem. Phys. Lett.* 28:243–247, 1998.

[27] Oldenburg, S. J., S. L. Westcott, R. D. Averitt, and N. J. Halas. *J. Chem. Phys.* 111:4729–4735, 1999.

[28] O'Neal, D. P., L. R. Hirsch, N. J. Halas, J. D. Payne, and J. L. West. *Cancer Lett.*, In Press, 2004.

[29] Pourbaix, M. *Biomaterials* 5:122–134, 1984.

[30] Priest, J. H., S. L. Murray, R. J. Nelson, and A. S. Hoffman. *Revers. Polym. Gels Relat. Syst.* 350:255–264, 1987.

[31] Prodan, E., C. Radloff, N. Halas, and P. Nordlander, *Science* 302:419–422, 2003.

[32] Quinten, M. *Appl. Phys. B* 73:317–326, 2001.

[33] Rajadhyaksha, M., S. González, J. M. Zavislan, R. R. Anderson, and R. H. Webb. *J. Invest. Dermatol.* 113:203–303, 1999.

[34] Ruan, C., R. Yang, X. Chen, and J. Deng. *J. Electroanal. Chem.* 455:121–125, 1998.

[35] Sasaki, S., H. Kawasaki, and H. Maeda. *Macromolecules* 30:1847–1848, 1997.

[36] Seki, T., M. Wakabayashi, T. Nakagawa, M. Imamura, T. Tamai, A. Nishimura, N. Yamashiki, A. Okamura, and K. Inoue. *Cancer* 85:1694–1702, 1999.

[37] Singer J. M. and Plotz, C. M. *Am. J. Med.* 21:888–892, 1956.

[38] Sershen, S., and J. West. *Adv. Drug Del. Rev.* 54:1225–1235, 2002.

[39.] Sershen, S. R., J. L. Westcott, J. L. West, and N. J. Halas. *Appl. Phys. B* 73:379–381, 2001.

[40.] Sershen S.R., Mensing G. A., Ng M., Halas N.J., Beebe D. J. West J. L. *Adv. Mat.*, 17:1366–1368, 2005.

[41.] Sershen, S. R., S. L. Westcott, N. J. Halas, and J. L. West. *J. Biomed. Mater. Res.* 51:293–298, 2000.

[42.] Sershen, S. R., S. L. Westcott, N. J. Halas, and J. L. West. *Appl. Phys. Lett.* 80:4609–4611, 2002.

[43.] Sokolov, K., M. Follen, I. Pavolva, A. Malpica, R. Lotan, and R. Richards-Kortum. *Cancer Res.* 63:1999–2004, 2003.

[44.] Stober, W., and A. Fink. *J. Colloid. Interf. Sci.* 26:62–69, 1968.

[45.] Tanaka, N., S. Matsukawa, H. Kuroso, and I. Ando. *Polymer* 39:4703–4706, 1998.

[46.] Vogel, A. *Phys. Med. Biol.* 42:895–912, 1997.

[47.] Vogl, T. J., M. G. Mack, R. Straub, K. Engelmann, S. Zangos, and K. Eichler. *Radiologe* 39:764–771, 1999.

[48.] Wang, Y., X. Xie, X. Wang, G. Ku, K. L. Gill, D. P. O'Neal, G. Stoica, and L. V. Wang. *NanoLett.* 4:1689–1692, 2004.

[49.] Weissleder, R. *Nat. Biotech.* 19:316–317, 2001.

[50.] Welch, A., and M. van Gemert (Eds). *Optical-Thermal Response of Laser-Irradiated Tissue*, Plenum Press, New York, 1995.

[51.] Yoshida, R., K. Sakai, T. Okano, and Y. Sakurai. *J. Biomat. Sci. Polym. Ed.* 6:585–598, 1994.

[52.] Zhou, H. S., I. Honma, and H. Komiyama. *Phys. Rev. B* 50:12052–12056, 1994.

Ligand-Directed Surface Profiling of Human Cancer Cells with Combinatorial Peptide Libraries

Mikhail G. Kolonin,[1] Laura Bover,[1] Jessica Sun,[1] Amado J. Zurita,[1] Kim-Anh Do,[1]
Johanna Lahdenranta,[1] Marina Cardó-Vila,[1] Ricardo J. Giordano,[1] Diana E. Jaalouk,[1]
Michael G. Ozawa,[1] Catherine A. Moya,[1] Glauco R. Souza,[1] Fernanda I. Staquicini,[1]
Akihiko Kunyiasu,[1] Dominic A. Scudiero,[2] Susan L. Holbeck,[2] Edward A. Sausville,[2]
Wadih Arap,[1] and Renata Pasqualini[1]

[1]The University of Texas M.D. Anderson Cancer Center, Houston, Texas; and [2]Developmental Therapeutics Program,
Division of Cancer Treatment and Diagnosis, National Cancer Institute, NIH, Bethesda, Maryland

Abstract

A collection of 60 cell lines derived from human tumors (NCI-60) has been widely explored as a tool for anticancer drug discovery. Here, we profiled the cell surface of the NCI-60 by high-throughput screening of a phage-displayed random peptide library and classified the cell lines according to the binding selectivity of 26,031 recovered tripeptide motifs. By analyzing selected cell-homing peptide motifs and their NCI-60 recognition patterns, we established that some of these motifs (*a*) are similar to domains of human proteins known as ligands for tumor cell receptors and (*b*) segregate among the NCI-60 in a pattern correlating with expression profiles of the corresponding receptors. We biochemically validated some of the motifs as mimic peptides of native ligands for the epidermal growth factor receptor. Our results indicate that ligand-directed profiling of tumor cell lines can select functional peptides from combinatorial libraries based on the expression of tumor cell surface molecules, which in turn could be exploited as "druggable" receptors in specific types of cancer. (Cancer Res 2006; 66(1): 34-40)

Introduction

The National Cancer Institute panel of human cancer cell lines from different histologic origins and grades (NCI-60) has been extensively used to screen compounds for anticancer activity (1, 2). The NCI-60 includes carcinomas of several origins (kidney, breast, colon, lung, prostate, and ovarian), tumors of the central nervous system, malignant melanomas, leukemias, and lymphomas. Gene expression determined by high-throughput microarrays has been used to survey the variation in abundance of thousands of distinct transcripts in the NCI-60; such data provided functional insights about the corresponding gene products in tumor cell transformation (2–4). This information-intensive genomic approach has yielded candidate diagnostic tumor markers to be validated at the protein level in prospective studies (4). Moreover, systematic proteomic studies based on two-dimensional PAGE (5) and protein microarrays (4) have also been implemented. Finally, in parallel with the NCI-60 transcriptome and proteome initiatives, pharmacologic sensitivity of the cells to $>10^5$ different chemical compounds has been registered (1, 2). Indeed, for some genes, correlation of expression data to drug sensitivity profiles has uncovered the mechanistic basis for the drug activity (3, 6–10). Thus, conventional genomic and proteomic approaches have identified several potential tumor markers and drug targets. However, despite such advances, correlation between drug activity and gene expression profiles has not as yet been established for most of the compounds tested (9, 11, 12). This suggests the likely existence of unknown factors and the need to develop alternative methodology to discover "druggable" molecular targets.

Over the past few years, it has been proposed that (*a*) characterization of molecular diversity at the tumor cell surface level (represented primarily by membrane-associated proteins that are often modified by lipids and carbohydrates) is required for the development of ligand-directed anticancer therapies, and that (*b*) peptides binding to surface receptors preferentially expressed on tumor cells may be used to ligand-direct therapeutics to sites of disease with potential for increased therapeutic windows (13, 14). It has become increasingly clear that selective cell surface features can be mapped by screening libraries of peptides (14–17). In fact, combinatorial peptide libraries displayed from pIII protein of an M13-derived phage have now been successfully screened on intact cells and *in vivo* (13–15). Peptide ligands selected from unbiased screens without any predetermined notions about the nature of the cellular receptor repertoire have been used for the subsequent identification of the corresponding target cell surface receptors (16–21). In addition, novel techniques, such as the biopanning and rapid analysis of selective interactive ligands (BRASIL), have enabled high-throughput phage library screening on cells (16). Here, we used the BRASIL method to systematically screen combinatorial libraries on tumor cells of the NCI-60 panel. Results of this feasibility study suggest that tumor cells can be grouped by profiles of their peptide ligands directed to differentially expressed cell surface receptors. Our data support the notion that many tumor cell surface-exposed receptors are expressed irrespective of tumor origin, thus suggesting they could be developed as broad tumor targets. Integration of ligand-directed surface profiling with other approaches related to the NCI-60 may uncover functional ligand-receptor pairs for the targeted drug delivery.

Materials and Methods

Combinatorial library screening on cells. All the NCI-60 cell lines (1), except MDA-N (unavailable), were grown in RPMI 1640 supplemented with 5% fetal bovine serum (FBS) and 5 mmol/L L-glutamine. A phage display

random peptide library based on the vector fUSE5 displaying the insert CX_7C was screened by using BRASIL as described (16). Exponentially growing cells were harvested with 0.5 mmol/L EDTA, 0.4 g/L KCl, 8 g/L NaCl, and 1 g/L dextrose, washed once with phosphate buffer saline (PBS), and resuspended in RPMI containing 1% bovine serum albumin (BSA) and 1 mmol/L HEPES. Cells ($\sim 10^6$) were incubated for 2 hours on ice with 10^9 transduction units of CX_7C phage in 200-μL suspension, transferred to the top of a nonmiscible organic lower phase (dibutyl phtalate/cyclohexane, 9:1), and centrifuged at $10,000 \times g$ for 10 minutes. The phage-bound cell pellet was incubated with 200 μL of K91 bacterial culture, and the bound phages were amplified and used in the following round. To prevent preferential isolation of peptides containing the RGD motif, which is selected on tissue-cultured cells due to expression of cell adhesion molecules binding to vitronectin, library screening was done in the presence of 1 mg/mL of the synthetic peptide RGD-4C (AnaSpec, San Diego, CA) in each round. After three rounds of selection, phage peptide-encoding inserts were sequenced as described (15, 17, 21).

Hierarchical cluster analysis of peptide motif/cell line association. We created an interactive sequence management database of all peptide sequences isolated in the screen. Calculation of tripeptide motif frequencies in CX_7C peptides (in both directions) was done by using a character pattern recognition program based on SAS (version 8.1.2, SAS Institute, Cary, NC) and Perl (version 5.6.1) as described (17). To identify the most closely related tripeptides and cell lines, we generated clustered image maps (CIM) by using online software CIMminer available at http://discover.nci.nih.gov/tools.jsp. Data were centered (mean subtracted and divided by SD) on both cell lines and tripeptide motifs; correlation coefficient metric with average linkage algorithm was used as distance measurement. The tripeptide motif frequencies across the NCI-60 cell lines formed a two-dimensional data matrix that was used to correlate motif enrichment with groups of cell lines. To evaluate whether CIMMiner algorithm is appropriate for clustering analysis of peptide frequency data, we devised a simulation test assuming that the frequencies of tripeptide motifs in a given data set follow an independent Poisson distribution. We simulated a random $3,280 \times 59$ data matrix of the dimension identical to that of tripeptide motif frequency data matrix (corresponding to the set of 3,280 tripeptides and 59 cell lines). These simulated data were centered the same way as the experimental data by transforming to mean of 0, variance of 1. For CIM in Fig. 1, tripeptides selected on all but one cell line of common origin (17) were used. Specificity of five tripeptides selectively overrepresented or underrepresented in lung tumor cell binding peptides for the 11 boxed cell lines (against the other 48 cell lines) was evaluated by using the R Package, version 2.0.0 (http://www.r-project.org) by performing two-sample t test (one tailed), as well as using Wilcoxon rank sum test (one tailed) and Fisher exact test (one tailed) as described (17).

Identification of candidate targeted receptors. To identify lead receptors targeted by tripeptide motifs, we screened the Molecular Target Database (http://www.dtp.nci.nih.gov) to identify proteins, expression levels of which in individual cell lines of the NCI-60 correlated with frequencies of individual tripeptides from Fig. 1 in the corresponding cell lines. We used the COMPARE software (http://dtp.nci.nih.gov/docs/compare/compare.html) to calculate pairwise Pearson correlations between tripeptide frequencies in cell lines and the protein expression patterns in the database. Minimum Pearson correlation coefficient of 0.2 served as cutoff for the selection of lead receptors, as it provided a reasonable number of candidate molecular targets for which NCI-60 expression profiles and tripeptide frequency distribution profiles correlated. To initially restrict the candidate targets analyzed to broad-specificity receptors, we included only putative cell surface molecules (Table 1), expression of which in the NCI-60 was found to correlate with the frequency profile of at least 25% of the tripeptides.

Protein database screening for peptide motif similarity. To identify natural prototype ligands of candidate receptors that are mimicked by selected peptides, we screened all 7-mer peptides selected in the screen by using online ClustalW software (http://www.ebi.ac.uk/clustalw/) to identify extended (four or longer amino acids) motifs shared between multiple peptides containing the broad-specificity tripeptides (Fig. 1). Nonredundant

databases of human proteins were searched by the BLAST software (http://www.ncbi.nlm.nih.gov/BLAST/) for proteins containing the cell-targeting 4-mers under the condition that at least the tripeptide part of the motif is identical to the part of the BLAST match.

Validation of epidermal growth factor receptor as one of the peptide targets. To isolate peptides binding to epidermal growth factor receptor (EGFR), phage clones selected on SKOV3 in rounds 2 and 3 of the screening were individually amplified and pooled, and 10^9 transduction units of the mixed phage were incubated overnight at $4°C$ with 10 μg of purified human EGFR (Sigma, St. Louis, MO), or BSA control immobilized on plastic. Unbound phages were extensively washed off with PBS, and then the bound phages were recovered by infecting host K91 *Escherichia coli* directly on the plate, and tetracycline-resistant clones were selected/quantified and sequenced. To identify EGFR ligand-matching motifs among phage-displayed SKOV3-binding peptides, custom-designed Perl 5.8.1–based software was used to run peptide sequences against biological EGFR ligand sequences. Each 7-mer peptide sequence was aligned in each orientation against the EGFR ligand sequences from the NH_2 to COOH terminus in one-amino-acid shifts. The peptide/protein similarity scores for each residue were calculated based on a BLOSUM62 matrix modified to identify peptide matches of at least three amino acids in any position being identical and one being similar to the corresponding amino acid positions in the EGFR ligands (Fig. 2*A*).

Results

Isolation of peptides binding to surface of the NCI-60 cancer cells. As an initial attempt to profile cell surface of the tumor cell panel, we screened a large (2×10^8 unique sequences) cyclic random peptide library with the basic structure CX_7C (C, cysteine; X, any residue) on every cell line of the NCI-60. Phage selection was done in the excess of a competing Arg-Gly-Asp (RGD) synthetic integrin-binding peptide (13) to minimize the recovery of RGD-containing peptides. This strategy was designed to facilitate the recovery of ligands binding to nonintegrin families of cell surface receptors because RGD tends to become dominant in the screening due to the high levels of integrin expression in adherent cells.[3] Preferential cell binding of specific cell-targeting peptides results in enrichment, defined by the increased recovery frequency of these peptide motifs in each subsequent round of the screen (14, 21). Thus, we set out to profile the expression of nonintegrin cell surface molecules among the cell lines of the NCI-60 according to the differential selection of motifs enriched in the screen.

Hierarchical cluster analysis of peptides binding to the NCI-60 cells. To analyze the spectrum of the peptides resulting from the screening and compare those among different cell lines of the panel, we adopted a combinatorial statistical approach based on the premise that three residue motifs (tripeptides) provide a sufficient structure for protein-peptide interactions in the context of phage display (17). For each NCI-60 cell line, we sequenced CX_7C peptide-encoding DNA inserts from 96 phage clones recovered after three rounds of selection. We did a computer-assisted survey of all tripeptides within the library-derived sequences selected on each cell line by analyzing a database of 26,031 tripeptides contained within the 5,270 CX_7C-encoded 7-mer peptides isolated (an average of eighty-nine 7-mer peptide sequences analyzed per each NCI-60 cell line). Thus, each cell line was assigned a unique set of tripeptides that was identified during the selection for cell surface binders, and the frequencies of each motif among all peptides for a given cell line were calculated.

---

[3] Unpublished observations.
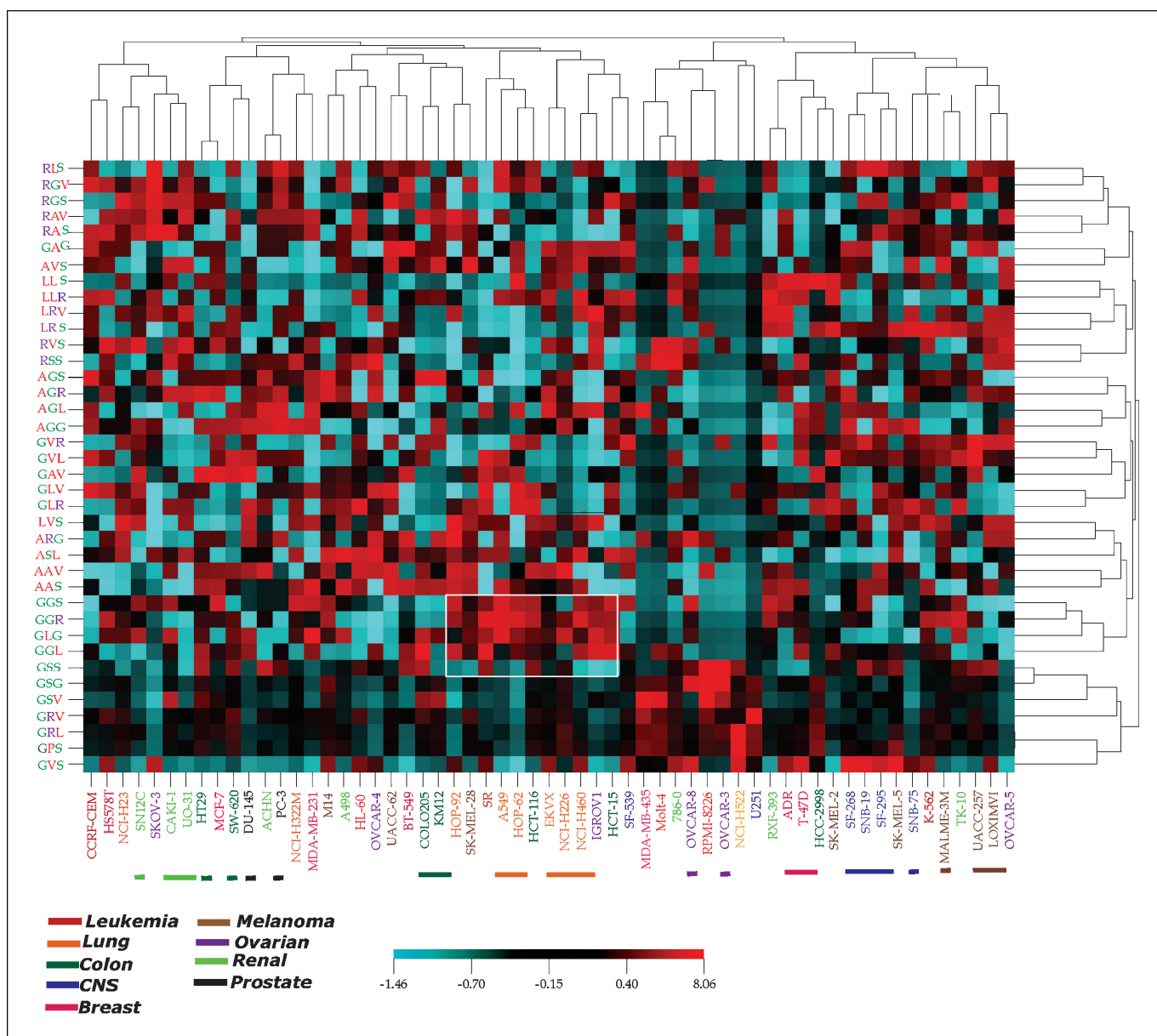
Figure 1. Selectivity of broad-specificity tripeptides for clusters of NCI-60 cell lines. Two-dimensional hierarchical clustering was applied to the frequencies of 38 tripeptides (*rows*) encountered in CX$_7$C peptides selected on NCI-60 cell lines (*columns*). Tripeptides selected on all but one cell line of common origin were clustered based on their correlations with cell lines; cell lines were clustered based on their correlations with the tripeptides. Tripeptide frequencies were mean subtracted and average linkage clustered with correlation metric. Amino acid color code: *red,* hydrophobic; *green,* neutral and polar; *purple,* basic. The color in each CIM segment ranges from blue (negative correlation) to red (positive correlation), as indicated by the scale bar. Cell lines are color-coded based on previously defined histologic tumor origin (1, 2). *Bars underneath dendrogram,* clusters of cells of similar tumor tissue origin (one exception allowed). *Boxed,* cluster of lung cancer–derived cell lines and associated/dissociated tripeptides.

To classify cell lines according to their association with particular motifs, which might provide inference on the targeted surface molecules, we did a hierarchical clustering analysis of the 3,280 nonredundant tripeptides based on the frequency of association with the NCI-60 cell lines. For the construction of a CIM, we adapted a hierarchical clustering algorithm and a pseudo-color visualization matrix initially designed to address differential gene expression among the cells of the panel (3, 6–8). CIMMiner (2) was used for inference of the variation in peptide binding specificity across the cell lines by comparing relative frequencies of tripeptides found in 7-mer peptides binding to each cell (see Materials and Methods). Clustering of peptide motifs with similar

cell selectivity revealed that the peptide distribution of the combinatorial library within the NCI-60 set was nonrandom (Supplementary Fig. S1*A*). Computer simulations of the permutated data set show that the observed pattern could not be generated by random chance (Supplementary Fig. S1*B*), thus indicating that the discontinuous tripeptide frequency data is applicable for cluster analysis.

The selective spectra of peptide motifs interacting with the clustered cell lines suggest the existence of shared targeted surface receptor(s) expressed in these lines. In this study, we chose to focus on putative peptide-targeted receptors with broad cell line specificity, which would be more informative for an initial peptide

binding/receptor expression correlation analysis. We therefore excluded from the data set motifs selected only on a single or few cell lines. Instead, we focused on 38 tripeptides that showed a semiubiquitous distribution among the NCI-60 lines (Fig. 1). A CIM constructed according to the isolation frequency of these broader-specificity tripeptides from each cell line revealed several apparent

clusters of cell lines that displayed distinct profiles of association with certain classes of peptide motifs. For example, the majority of lung cancer–derived cell lines segregated as a separate group, suggesting that some of the receptors targeted may be conserved among cell lines derived from a common origin (Fig. 1). Thus, although we severely restricted our analysis by limiting it

Table 1. Candidate ligand-receptor interactions mimicked by NCI-60-binding tripeptides

Motif	Candidate peptide motif receptors				Candidate peptide-mimicked receptor ligands
RLS	ErbB2, ErbB4	FGF2,4			EGF-TM7
RGV					
RGS	ErbB4	FGF2		EphA2,A3,A4,A8,B1	EGF-TM7, FGF-12b, FGF-5, NGF-beta
RAV	ErbB2				MEGF7, NGF-beta. NTF 6 alpha
RAS			TRKA		FGF-20, NRG-3
GAG	EGFR	FGF1,2,3			MEGF4. FGF6, NGF-beta
AVS	EGFR, ErbB2, ErbB4	FGF1	TRKB,C	EphA2,A3,A4,A7,B1,B2,B3,B5	TRK1
LLS					amphiregulin
LLR			TRKA		Eph A4
LRV	EGFR, ErbB2, ErbB4	FGF3	TRKA, B, C	EphA2,A3,A7	FGF-12b, Eph-B3
LRS	ErbB3				MEGF4, MEGF5, MEGF8, NRG-3, NGF-beta
RVS	EGFR, ErbB2, ErbB4	FGF1,2	TRKB	EphA7	MEGF10, amphiregulin
RSS		FGF3	TRKA	EphA5	EGF-TM7, FGF-5, NRG-3
AGS	EGFR		TRKA		MEGF6, brain NGF
AGR					MEGF2, MEGF4, FGF6, NTF-5, NTF-6
AGL	EGFR, ErbB2, ErbB3	FGF1,3		EphA5,A6,A8	MEGF12
AGG				EphA5	HB-EGF, Ephr-B3
GVR	EGFR, ErbB2, ErbB4	FGF1,2	TRKB	EphA7	MEGF4, MEGF6 MEGF8, FGF-5, bFGF, brain NGF
GVL		FGF1,2		EphA2,A3,A5,A6,B3	NGF2, Ephrin-B3,
GAV					MEGF5, MEGF6, NGF-beta
GLV	ErbB4	FGF4		EphA5	EGF-TM7, betacellulin, NTF 3, Eph-B3,
GLR	ErbB4				MEGF5, EGFL5, FGF-12b, FGF-16, NRG-3
LVS		FGF1,4		EphA5,A6	EGFL5. FGF23, GDNF, Eph-B3
ARG	ErbB2	FGF2,4	TRKA	EphA1	FGF-12b, FGF23, NGF-beta. GDNF. NTF 6
ASL		FGF1,2	TRKC		EGF-TM7, FGFR1
AAV			TRKB	EphA2,A3,A4,A7,B3,B5	-
AAS		FGF1,2	TRKC		-
GGS				EphA5	Eph-B3, Eph A4
GGR	EGFR,ErbB2	FGF2			EGF-TM7, HB-EGF, FGF23, Ephrin-B3
GLG	ErbB2, ErbB3	FGF2,3,4		EphA1,A6	heparin binding growth factor 8
GGL	ErbB2				HB-EGF, MEGF5, EGFL5, NRG-3
GSS	EGFR, ErbB2	FGF3	TRKA,C	EphA5	MEGF5
GSG	EGFR			EphA5	-
GSV	EGFR, ErbB2, ErbB4	FGF4	TRKB	EphA7,B2	MEGF5, NRG-3, Ephrin-B3
GRV	EGFR				MEGF8, EGF-TM7, FGF23, NTF5
GRL	EGFR,ErbB2			EphA5,B1,B2,B4	betacellulin, EGFL5, NGF2, NTF5, EphB3, EphA4
GPS	EGFR, ErbB2, ErbB4	FGF3	TRKB	EphA2,A3,A4,A7,B2,B5	MEGF5, EGFL5, EGF-like EMR3, SPGF
GVS	EGFR	FGF4	TRKA		MEGF-1, MEGF5, NRG-3, NTF-6, NTF-5

NOTE: Candidate peptide motif receptors are the human cell surface proteins (identified by COMPARE) expressed in profiles correlating with the selectivity of the corresponding tripeptides. Candidate peptide-mimicked receptor ligands are human proteins (identified by automated BLAST) that contained the corresponding tripeptides. Tripeptides in the column are ordered as in Fig. 1. Receptors of the same family and their corresponding candidate biological ligands identified based on tripeptide similarity are coded by the same color [EGFR, blue; FGFR, green; TRK receptor (NGFR), purple; ephrin receptor, red]. Tripeptides that both have a selectivity correlating with EGFR family receptor expression and are found within EGFR ligands (boldface). Tripeptides that were confirmed to reside within EGFR-binding SKOV3-slected peptides (Fig. 2; blue). See Supplementary Materials and Methods for Genbank accession nos. of BLAST-identified proteins.

to semiubiquitous tripeptides, clustering of some of them (predominantly with cell lines derived from the same tumor type) is consistent with their relative tissue specificity. To evaluate individual motifs for selectivity, we identified a distinct cluster of five tripeptides associated with lung tumor–derived cell lines (Fig. 1, *boxed*). We compared tripeptide frequencies for the 11 cell lines within this cluster with their frequencies for the rest of NCI-60 lines by using statistical tests (Fisher exact, Wilcoxon rank-sum, and t test). Consistently, we observed that motif GGS was isolated for the clustered lines significantly ($P < 0.05$) more frequently than for the other NCI-60 cell lines (Supplementary Table S1).

Notably, the distribution of cell lines in the dendrogram (Fig. 1) was partially consistent with the reported association of cells derived from tumors with common tissue origin (3, 4). This suggests that some of the receptors, such as the one presumably recognized by the lung tumor–specific tripeptide GGS (Fig. 1; Supplementary Table S1), may be up-regulated only in certain cancer origins. However, the tumor cell phylogeny was recapitulated only to an extent; the majority of the observed clusters contained cell lines derived from unrelated tumor types (Fig. 1). The limited grouping of lines derived from tumors of common origin is perhaps not surprising: the relationship between different cell lines in our study is based on peptide binding to putative cell surface molecules, many of which may be tumor induced rather than characteristic of the tissue of origin. If so, our analysis of broad-specificity motif distribution may be well suitable for identification of specific surface molecules that are generally up-regulated by tumors and thus may constitute broad drug targets against cancer.

Identification of candidate receptor targets for peptide motifs. We next attempted to identify the targets for the 38 broad-specificity tripeptides, most of which presumably bind to receptors expressed by multiple NCI-60 cell lines. We used the NCI Molecular Targets Database that contains detailed information on the expression and activity of 1,218 human proteins measured by nonarray methods (22). By using the COMPARE algorithm (6), we correlated the selectivity profiles of the 38 tripeptide motifs with the expression profiles of the characterized molecular targets. We observed that several of the qualifying proteins, expression of which correlated with enrichment profiles of certain motifs, represented tyrosine kinase receptors, such as those for ligands belonging to families of EGFs, fibroblast growth factors (FGF), nerve growth factors (NGF), and ephrins (Table 1). When transferred to molecular target correlation data, the order of the 38-tripeptide motif set in the dendrogram (Fig. 1) revealed clusters of tripeptides for which cell line association profile correlated with expression profiles of EGF, FGF, NGF, or ephrin receptors (Table 1).

The peptide distribution-correlating tyrosine kinase receptors, belonging to EGFR, FGFR, NGFR, and ephrin receptor families (Table 1), are often up-regulated in many types of cancer (23). To determine if the cell-binding peptides may target these tyrosine kinases, we employed the notion that receptor-binding peptide motifs often mimic natural ligands for these receptors (16, 17, 19). Thus, we tested whether the selected motifs mimic ligands for the candidate tyrosine kinases by determining whether tripeptides listed in Table 1 are embedded into longer peptides that may be responsible for cell surface binding. We analyzed the CX_7C phage inserts containing the 38 tripeptides by using the ClustalW software and compiled extended motifs containing the tripeptides shared among multiple peptides selected during the screen (data not shown). To identify candidate prototype human ligands, epitopes of which could be mimicked, we screened each of the

ClustalW-extended motifs against the nonredundant database of human proteins by using the BLAST software (National Center for Biotechnology Information). As a result of this analysis, we found the motifs containing 34 of 38 tripeptides (89%) to be identical or very similar to segments of proven or putative ligands for the tyrosine kinase receptors listed (Table 1).

A

EGF

```
MLLTLIILLPVVSKFSFVSLSAPQHWSCPEGTLAGNGNSTCVGPAPFLIFSHGNSIFRID
TEGTNYEQLVVDAGVSVIMDFHYNEKRIYWVDLERQLLQRVFLNGSRQERVCNIEKNVSG
        ATLDGVS                                          RRHSVSG
MAINWINEEVIWSNQQEGIITVTDMKGNNSHILLSALKYPANVAVDPVERFIFWSSEVAG
                                                         SGWFAG
SLYRADLDGVGVKALLETSEKITAVSLDVLDKRLFWIQYNREGSNSLICSCDYDGGSVHI
S                                                       GSVSH
SKHPTQHNLFAMSLFGDRIFYSTWKMKTIWIANKHTGKDMVRINLHSSFVPLGELKVVHP
RR
LAQPKAEDDTWEPEQKLCKLRKGNCSSTVCGQDLQSHLCMCAEGYALSRDRKYCEDVNEC
AFWNHGCTLGCKNTPGSYYCTCPVGFVLLPDGKRCHQLVSCPRNVSECSHDCVLTSEGPL
CFCPEGSVLERDGKTCSGCSSPDNGGCSQLCVPLSPVSWECDCFPGYDLQLDEKSCAASG
      GSVLPVL
PQPFLLFANSQDIRHMHFDGTDYGTLLSQQMGMVYALDHDPVENKIYFAHTALKWIERAN
MDGSQRERLIEEGVDVPEGLAVDWIGRRFYWTDRGKSLIGRSDLNGKRSKIITKENISQP
RGIAVHPMAKRLFWTDTGINPRIESSSLQGLGRLVIASSDLIWPSGITIDFLTDKLYWCD
AKQSVIEMANLDGSKRRRLTQNDVGHPFAVAVFEDYVWFSDWAMPSVIRVNKRTGKDRVR
LQGSMLKPSSLVVVHPLAKPGADPCLYQNGGCEHICKKRLGTAWCSCREGFMKASDGKTC
LALDGHQLLAGGEVDLKNQVTPLDILSKTRVSEDNITESQHMLVAEIMVSDQDDCAPVGC
                                RSGRVSN
SMYARCISEGEDATCQCLKGFAGDGKLCSDIDECEMGVPVCPPASSKCINTEGGYVCRCS
EGYQGDGIHCLDIDECQLGVHSCGENASCTNTEGGYTCMCAGRLSEPGLICPDSTPPPHL
REDDHHYSVRNSDSECPLSHDGYCLHDGVCMYIEALDKYACNCVVGYIGERCQYRDLKWW
       NSVRGSR
ELRHAGHGQQQKVIVVAVCVVVLVMLLLLSLWGAHYYRTQKLLSKNPKNPYEESSRDVRS
RRPADTEDGMSSCPQPWFVVIKEHQDLKNGGQPVAGEDGQAADGSMQPTSWRQEPQLCGM
GTEQGCWIPVSSDKGSCPQVMERSFHMPSYGTQTLEGGVEKPHSLLSANPLWQQRALDPP
HQMELTQ
```

Amphiregulin

```
RAPLLPPAPVVLSLLILGSGHYAAGLDLNDTYSGKREPFSGDHSADGFEVTSRSEMSSGS
                     SAAGLAR                           SPSSGT
EISPVSEMPSSSEPSSGADYDYSEEYDNEPQIPGYIVDDSVRVEQVVKPPQNKTESENTS
Y                SPSSGTY                  NSVRGSR
                 SGAFWGS
DKPKRKKKGGKNGKNRRNRKKKNPCNAEFQNFCIHGECKYIEHLEAVTCKCQQEYFGERC
GEKSMKTHSMIDSSLSKIALAAIAAFMSAVILTAVAVITVQLRRQYVRKYEGEAEERKKL
RQENGNVHAIA
```

Heparin-binding EGF-like growth factor (HB-EGF)

```
MKLLPSVVLKLFLAAVLSALVTGESLERLRRGLAAGTSNPDPPTVSTDQLLPLGGGRDRK
                                                     GGRHWVR
                                                     IGGRWVR
VRDLQEADLDLLRVTLSSKPQALATPNKEEHGKRKKKGKGLGKKRDPCLRKYKDFCIHGE
CKYVKELRAPSCICHPGYHGERCHGLSLPVENRLYTYDHTTILAVVAVVLSSVCLLVIVG
LLMFRYHRRGGYDVENEEKVKLGMTNSH
    RVWHRGG
     VVWRGGI
```

Epiregulin

```
MTAGRRMEMLCAGRVPALLLCLGFHLLQAVLSTTVIPSCIPGESSDNCTALVQTEDNPRV
AQVSITKCSSDMNGYCLHGQCIYLVDMSQNYCRCEVGYTGVRCEHFFLTVHQPLSKEYVA
                                    FAGAGVR
LTVILIILFLITVVGSTYYFCRWYRNRKSKEPKKEYERVTSGDPELPQV
```

B

[Bar chart showing Transducing Units ($\times 10^4$) on the y-axis (0–6). Two groups labeled "Round I" and "Round II," each comparing EGFR (filled bars) versus BSA (open bars).]

Figure 2. Identification of peptides mimicking EGFR ligands. *A,* EGFR-binding peptide sequences isolated from the SKOV3-selected phage pool were matched in each orientation to protein sequences of biological human EGFR ligands (leader peptide sequence underlined). Matches displayed are peptides with three or more amino acids being identical (*red*) and one or more being from the same class (*green*) as the correspondingly positioned protein amino acids. Tripeptides listed in Table 1 (*yellow*). *B,* isolation of peptides targeting EGFR. Binding of SKOV3-selected phage pool to immobilized EGFR compared with BSA in rounds 1 and 2 of biopanning of SKOV3-selected phage pool on immobilized human EGFR.

Validation of EGFR as a targeted receptor. To show that the approach taken can lead to actual targetable tumor cell surface proteins, we chose to test if the EGFR is bound by any of the tripeptide motifs distributed in the panel in a profile correlating with EGFR expression. Consistently, 24 of 38 tripeptides surveyed displayed NCI-60 cell line association pattern consistent with that of EGFR expression (Table 1). Of these tripeptides, 22 were isolated in the screens on ovarian cancer cell lines SKOV3 and OVCAR4 (data not shown). Because EGFR is well known to be associated with ovarian cancer (23), we deemed these cell lines to be likely expressers of targetable EGFR, which would account for the selection of EGFR ligand-mimicking motifs. To validate EGFR binding by the selected motifs, we screened the SKOV3-binding phage sublibrary (pooled clones recovered in rounds 2 and 3) on immobilized human EGFR. After two rounds of selection, we analyzed phage displaying the EGFR-binding peptides: the majority were comprised by different 7-mer peptides (Fig. 2*A*) that contained 17 of 22 SKOV3-selected tripeptide motifs distributed in the panel in a profile correlating with EGFR expression (Table 1). Phage displaying these peptides had specific affinity to EGFR, as determined by subjecting the same sublibrary to immobilized BSA control binding (Fig. 2*B*). Remarkably, computer-assisted analysis of sequences (Fig. 2*A*) revealed that 12 of the 7-mer EGFR-binding peptides contained amino acid motifs similar to those present in some of the biological EGFR ligands (23). These peptides, containing eight of the candidate tripeptides (RVS, AGS, AGL, GVR, GGR, GGL, GSV, and GVS), were found highly similar to fragments of EGF, amphiregulin, heparin-binding EGF-like growth factor, and epiregulin (Fig. 2*A*). Similarity search using the same algorithm on the same twelve 7-mers did not reveal any matches to two other EGFR ligands, transforming growth factor-α and β-cellulin, or randomly chosen control ligands of tyrosine kinase receptors from the three other candidate families listed in Table 1: ephrin A, NGF-β, and FGF6 (data not shown). Taken together, these data suggest that at least some of the peptides selected on the NCI-60 cells target EGFR, whereas others may bind to different tyrosine kinases, possibly including those from TRK, ephrin, or FGF receptor families.

Discussion

Expression profiles of the candidate receptor targets for peptides identified in the screen illustrate the concept that in cancer, at least some tumor-associated cell surface molecules seem up-regulated regardless of cancer tissue origin. As such, this is the case for the EGFR and other tyrosine kinases possibly targeted by peptide ligands selected on the NCI-60 cell panel. This may also be the case for many other receptors with a role in tumorigenesis, expression profiles of which may not correlate with the overall proteomic profile of the original tumor tissue. In fact, these observations may account for the relatively limited success in correlating drug toxicity profiles with the genomic and/or proteomic profiles of the NCI-60 panel (12). On the other hand, some of the receptors, such as EphA5 presumably targeted by GGS tripeptide and its derivatives predominantly selective for lung tumor-derived cell lines (Fig. 1), seem to be at least partially specific for the progenitor cancer type.

The candidate ligand-receptor leads identified in this study can be characterized further for the development of targeted agents selective for tumors. Moreover, the peptides identified by the approach described here may map receptor interaction domains of biological (native) ligands. Similarity of peptides to the corresponding receptor-binding ligands has already been used for validation of the IL-11Rα receptor as a target of an interleukin-11 mimic peptide homing to blood vessels in the prostate (17, 24). We and others have modeled the usage of peptides homing to receptors expressed by tumors (18) or nonmalignant tissues (19, 20) for directing the delivery of cytotoxics, proapoptotic peptides, metalloprotease inhibitors, cytokines, fluorophores, and genes (13, 14). Thus, our approach provides a straightforward way to identify drug-accessible tumor cell surface receptors and to discover peptide ligands that can serve as mimetic prototype drugs. Unlike genomic or proteomic-based approaches that rely on differential expression levels of transcripts or protein products, this discovery platform directly addresses functional protein-protein interactions at the level of physical binding. In contrast to protein array systems, it is possible to select binding peptides even if the ligand-receptor interaction is mediated by conformational (rather than linear) epitopes. In summary, ligand-directed screening of combinatorial libraries on tumor cell surfaces may lead to improved selection of functionally relevant peptides that can be developed for targeting "druggable" molecular targets.

Acknowledgments

References

1. Monks A, Scudiero D, Skehan P, et al. Feasibility of a high-flux anticancer drug screen using a diverse panel of cultured human tumor cell lines. J Natl Cancer Inst 1991; 83:757–66.
2. Weinstein JN, Myers TG, O'Connor PM, et al. An information-intensive approach to the molecular pharmacology of cancer. Science 1997;275:343–9.
3. Scherf U, Ross DT, Waltham M, et al. A gene expression database for the molecular pharmacology of cancer. Nat Genet 2000;24:236–44.
4. Nishizuka S, Charboneau L, Young L, et al. Proteomic profiling of the NCI-60 cancer cell lines using new high-density reverse-phase lysate microarrays. Proc Natl Acad Sci U S A 2003;100:14229–34.
5. Myers TG, Anderson NL, Waltham M, et al. A protein expression database for the molecular pharmacology of cancer. Electrophoresis 1997;18:647–53.
6. Zaharevitz DW, Holbeck SL, Bowerman C, Svetlik PA. COMPARE: a web accessible tool for investigating mechanisms of cell growth inhibition. J Mol Graph Model 2002;20:297–303.
7. Blower PE, Yang C, Fligner MA, et al. Pharmacogenomic analysis: correlating molecular substructure classes with microarray gene expression data. Pharmacogenomics J 2002;2:259–71.
8. Rabow AA, Shoemaker RH, Sausville EA, Covell DG. Mining the National Cancer Institute's tumor-screening database: identification of compounds with similar cellular activities. J Med Chem 2002; 45:818–40.
9. Wallqvist A, Rabow AA, Shoemaker RH, Sausville EA, Covell DG. Establishing connections between microarray expression data and chemotherapeutic cancer pharmacology. Mol Cancer Ther 2002;1:311–20.
10. Szakacs G, Annereau JP, Lababidi S, et al. Predicting drug sensitivity and resistance: profiling ABC transporter genes in cancer cells. Cancer Cell 2004;6:129–37.
11. Brown JM. NCI's anticancer drug screening program may not be selecting for clinically active compounds. Oncol Res 1997;9:213–5.

12. Wallqvist A, Rabow AA, Shoemaker RH, Sausville EA, Covell DG. Linking the growth inhibition response from the National Cancer Institute's anticancer screen to gene expression levels and other molecular target data. Bioinformatics 2003;19:2212–24.

13. Arap W, Pasqualini R, Ruoslahti E. Cancer treatment by targeted drug delivery to tumor vasculature in a mouse model. Science 1998;279:377–80.

14. Kolonin MG, Pasqualini R, Arap W. Molecular addresses in blood vessels as targets for therapy. Curr Opin Chem Biol 2001;5:308–13.

15. Pasqualini R, Ruoslahti E. Organ targeting *in vivo* using phage display peptide libraries. Nature 1996;380: 364–6.

16. Giordano RJ, Cardo-Vila M, Lahdenranta J, Pasqualini R, Arap W. Biopanning and rapid analysis of selective interactive ligands. Nat Med 2001;7: 1249–53.

17. Arap W, Kolonin MG, Trepel M, et al. Steps toward mapping the human vasculature by phage display. Nat Med 2002;8:121–7.

18. Pasqualini R, Koivunen E, Kain R, et al. Aminopeptidase N is a receptor for tumor-homing peptides and a target for inhibiting angiogenesis. Cancer Res 2000;60: 722–7.

19. Kolonin MG, Pasqualini R, Arap W. Teratogenicity induced by targeting a placental immunoglobulin transporter. Proc Natl Acad Sci U S A 2002;99: 13055–60.

20. Kolonin MG, Saha PK, Chan L, Pasqualini R, Arap W. Reversal of obesity by targeted ablation of adipose tissue. Nat Med 2004;10:625–32.

21. Pasqualini R, Arap W, Rajotte D, Ruoslahti E. *In vivo* selection of phage-display libraries. In: Barbas C, Burton D, Silverman G, Scott J, editors. Phage display: a laboratory manual. New York (NY): Cold Spring Harbor Laboratory Press; 2001. p. 22.1–4.

22. Holbeck SL. Update on NCI *in vitro* drug screen utilities. Eur J Cancer 2004;40:785–93.

23. Vogelstein B, Kinzler KW. Cancer genes and the pathways they control. Nat Med 2004;10:789–99.

24. Zurita AJ, Troncoso P, Cardo-Vila M, et al. Combinatorial screenings in patients: the interleukin-11 receptor α as a candidate target in the progression of human prostate cancer. Cancer Res 2004;64:435–9.

Synchronous selection of homing peptides for multiple tissues by *in vivo* phage display

Mikhail G. Kolonin, * **Jessica Sun,** * **Kim-Anh Do,**‡ **Claudia I. Vidal,** * **Yuan Ji,**‡
Keith A. Baggerly,‡ **Renata Pasqualini,** *†,1 **and Wadih Arap** *†,1

*Department of Genitourinary Medical Oncology, †Department of Cancer Biology, and ‡Department of Biostatistics, The University of Texas M. D. Anderson Cancer, Houston, Texas, USA

To read the full text of this article, go to http://www.fasebj.org/cgi/doi/10.1096/fj.05–5186fje

SPECIFIC AIMS

The aim of the study was to streamline the procedure for mapping vascular ligand-receptor pairs in patients with in vivo phage display. Specifically, we tested the approach for simultaneous screening of multiple organs with combinatorial phage display libraries in the mouse model.

PRINCIPAL FINDINGS

1. A platform strategy combining advanced molecular biology, biostatistics, and biochemistry has been established that allows to quickly and efficiently identify vascular ligand-receptor pairs in multiple organs

Selectivity of tissue expression for surface molecules of cells lining the vasculature has been uncovered in disease and during normal development. Systematic profiling of selectively expressed "vascular addresses" has revealed prospective molecular targets that may be used to direct therapies to specific tissues. *In vivo* phage display is a technology used to reveal organ-specific vascular ligand-receptor systems in animal models and, recently, in patients, and to validate them as potential therapy targets. Because a single biopanning round of a phage library may not always sufficiently enrich for organ-homing peptides, until now, phage display screens have encompassed recovery of phage from the organ of interest in three to four rounds of library selection, utilizing one subject per each round. Thus, systematic characterization of the vasculature by using this "conventional" *in vivo* phage display screen setup has been rate-limited by the need to separately perform individual multiround screens for motifs homing to each tissue studied. To screen phage libraries in patients more efficiently, we have initiated attempts to isolate tissue-homing peptides for several tissues in a single screen. Here, we integrated a comprehensive strategy to simultaneously screen phage display libraries

for peptides homing to any number of tissues without the need for an individual subject for each target tissue.

2. We isolated peptides independently homing to six different mouse organs: pancreas, muscle, bowel, uterus, kidney, and brain
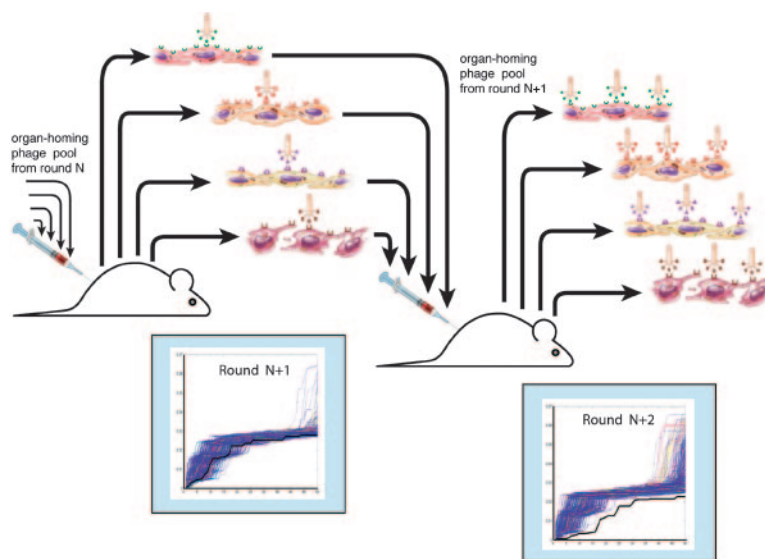
To establish the experimental framework for selection of peptides independently homing to different organs, we performed a synchronous *in vivo* screen of a phage-displayed cyclic random peptide library on six mouse organs: muscle, bowel, uterus, kidney, pancreas, and brain. Three rounds of library selection were done without the step of whole-body perfusion of the vasculature, which was skipped in order to simulate screening conditions to be used in patients. In each round, peptide-displaying phage were isolated from target organs, amplified, and pooled for the next round of selection. To identify organ-homing motifs, we sequenced the DNA corresponding to peptide inserts from phage clones recovered after each of the three rounds of selection for each of the six organs and analyzed the sequences. Preferential cell binding of specifically homing peptides to differentially expressed receptors results in enrichment, defined by the increased frequency of the peptide recovery in each subsequent round of the screen. Thus, we set out to profile the differential distribution of library-encoded peptides among the six organs, which could be used for the subsequent identification of their targets.

3. Novel statistical algorithms have been integrated into the library screening procedure that enable the identification of peptide motifs enriched throughout the successive rounds of the screening

Based on the premise that three residue motifs (tri-peptides) provide a sufficient structure for peptide-

Figure 1. Schematic description of synchronous in vivo phage display screening. In every selection round, phage are intravenously (i.v.) administered and simultaneously recovered from *N* target tissues, amplified, pooled, and used for the next selection round. Increased recovery of phage transforming units (TU) in the third round reflects the selection of peptides preferentially homing to the target organ.

protein interactions, we performed a computer-assisted analysis of the 7489 tripeptides contained in each direction within the phage-displayed peptides (2620 from the first round; 2554 from the second round; and 2315 from the third round). First, we evaluated the increase in recovery frequency for individual tripeptides in the three consecutive rounds of selection by using the Bayesian Beta/Binomial model and for each organ found a number of tripeptides progressively enriched, thus suggesting their superior affinity and/or specificity. Next, we assessed the significance of motif representation increase on selection by using the Fisher exact test and identified within the enriched motifs those with terminal frequencies higher than those present in the phage library prior to selection. We adapted the Monte Carlo algorithm to confirm that the statistical cutoff for the Fisher exact test was set appropriately and to demonstrate a progressive accumulation of tripeptides isolated with lower *P* values from the first to the third round, consistent with enrichment of the corresponding motifs. Finally, we adapted the Fisher exact test to analyze the motifs recovered from the third selection round for specificity of tissue homing by identifying tripeptides that were enriched in one of the six organs, but not in the rest of the organs studied.

4. We implemented a concept of performing a systematic "retro-basic local alignment search tool (BLAST)" analysis of the homing peptide sequences against the prototype biological ligands of the candidate peptide-bound receptors in order to validate the targeted receptors and to map sites of ligands involved in receptor interaction

To identify candidate biological ligands mimicked by homing peptides, we chose an approach based on the previous notion that peptide motifs binding to cell surface receptors often mimic native ligands of these receptors. We used the online ClustalW software to determine extended tripeptide-containing motifs re-

sponsible for organ homing and searched a nonredundant database of mouse proteins to identify regions of similarity within proteins potentially mimicked by the motifs using the NCBI BLAST. This revealed 19 motifs as segments of extracellular signaling factors that had been reported to regulate organ-dependent vascular growth or homeostasis and, in some cases, identified several motifs that homed to the same organ and that matched different domains within the same protein. For some of the organs, BLAST identified matches of homing tripeptides to different ligands that share a receptor with a functional role in vascular biology in the target organ, which strongly suggests such a receptor as a vascular zip code.

To demonstrate the possibility of efficient characterization of circulation-accessible receptors by synchronous biopanning, as a proof-of-principle, we chose to validate the PRL receptor (PRLR) as a peptide target in the pancreas. PL-I and PLP-M identified by BLAST analysis to contain pancreas-targeted peptide sequences (ASVL, WSGL, and SWSG) belong to the conserved family of PRL-like peptidic hormones that have been shown to function in the pancreas during pregnancy. Because PRLR is the only known receptor for these proteins, we proposed that the selected peptide motifs target PRLR *in vivo* by mimicking PRL family hormones. To validate a biochemical interaction of pancreas-homing motifs with PRLR, we screened pancreas-homing phage (pooled clones recovered in rounds 2 and 3) against recombinant PRLR, as well as against PRLR expressed on the surface of COS-1 cells. As a result, we selected seven dominating phage-peptides that bound to PRLR but not to control proteins. Remarkably, computer-assisted "retro-BLAST" analysis of sequences revealed that all of the selected peptides contained amino acid motifs similar to those present in proteins of PRL family. The cluster of matches identified around one of the hormone domains that had been shown to mediate receptor interaction supports

our conclusion that the peptides selected mimic the PRLR-binding domain of placental lactogens.

5. To demonstrate the efficiency of the approach, we validated prolactin receptor (PRLR) as a target of pancreas-homing peptides mimicking prolactin-like hormones and as a previously unrecognized vascular marker

As a test case for the biochemical validation of PRLR as a pancreatic vascular marker, we chose CRVASVLPC: the peptide that contained a pancreas-enriched SVL tripeptide and was also recovered as a PRLR-binding prolactin mimic. To demonstrate direct physical interaction between CRVASVLPC and PRLR, we tested binding of CRVASVLPC-phage to COS-1 cells transfected with PRLR and found it to be 9-fold higher than its nonspecific binding to nontransfected COS-1 cells that served as a negative control. The CRVASVLPC motifs bound to PRLR in both forward and reverse orientation in the context of phage, and alanine-scanning mutagenesis demonstrated that all of the residues within the RVASVLP sequence were important for PRLR binding. To further demonstrate the specific affinity of the CRVASVLPC motif for its receptor, we showed that the PRL mimic specifically bound to cells expressing PRLR by using immunofluorescence: phage displaying either CRVASVLPC or CPLVSAVRC were found bound and internalized specifically by cells expressing PRLR, but not by nonexpressing control cells, whereas none of the CRVASVLPC mutants displayed detectable PRLR-expressing cell binding and internalization. Finally, since the SVL tripeptide found within the PRL mimic CRVASVLPC was isolated from the pancreas, we evaluated weather the motif homes to PRLR in the pancreatic blood vessels. We showed that the previously reported pancreatic expression of mouse PRLR protein in the vasculature and in the islets closely resembles the in vivo distribution of phage displaying the CRVASVLPC motif. Taken together, these data indicate that the peptide CRVASVLPC binds to PRLR and suggests that it targets vasculature-exposed PRLR in the pancreas.

CONCLUSIONS AND SIGNIFICANCE

An important aspect of experimental biology is the identification of molecular targets and the design of methods for their functional validation. Here, we tested the approach for synchronous biopanning in mice by selecting homing peptide ligands for six different organs in a single screen and prioritizing them by using software compiled for statistical validation of peptide biodistribution specificity. Both Bayesian and frequentist statistics have led to the identification of largely overlapping populations of peptide sequences enriched in the target organs, thus reinforcing the validity of the identified homing motifs. Based on similarity of the selected peptide motifs to mouse proteins, we identified a number of motif-containing biological candidates for ligands binding to organ-selective receptors. To demonstrate that this methodology can lead to targetable ligand-receptor systems, we validated one of the pancreas-homing peptides as a mimic peptide of natural prolactin receptor ligands. A concept to systematically "retro-BLAST" the receptor-binding peptides onto prototype ligands in order to map sites of ligands involved in receptor interaction allowed us to identify multiple additional PRL mimics. The successful validation of PRLR as a PRL-mimicking peptide target establishes this receptor as a previously unrecognized vascular marker and demonstrates the viability of our approach.

The high-throughput targeting strategy bestowed by the synchronous biopanning reported in this study will open new possibilities for rapid and efficient identification and validation of vascular receptors and their ligand-directed targeting. This approach for screening phage libraries in vivo enables highly efficient isolation of organ-homing ligands from combinatorial libraries and may streamline vascular mapping efforts, thus leading to a better understanding of the functional protein–protein interactions in the vasculature. The synchronous approach to in vivo phage display provides an advantage over the conventional approach because multiple organs internally control for organ selectivity of each other in the successive rounds of selection. Direct combinatorial screenings recently initiated in patients have opened the possibility for systematic isolation of peptide ligands for therapeutic targeting. Synchronous selection of homing peptides for multiple tissues will accelerate the process of phage display-based vascular mapping in vivo and may prove particularly relevant for patient studies, allowing efficient high-throughput selection of targeting ligands for multiple organs in a single screening. In the future, the use of peptide libraries for probing the vasculature in individual patients for diagnostic and therapeutic purposes may become a reality. In summary, the combinatorial methodological platform optimized here for identification of differentially expressed vascular ligand-receptor pairs will greatly advance the initiative in human vasculature mapping. [Fj]

Synchronous selection of homing peptides for multiple tissues by *in vivo* phage display

Mikhail G. Kolonin, * **Jessica Sun,** * **Kim-Anh Do,** ‡ **Claudia I. Vidal,** * **Yuan Ji,** ‡
Keith A. Baggerly, ‡ **Renata Pasqualini,** *,†,1 **and Wadih Arap** *,†,1

*Department of Genitourinary Medical Oncology, †Department of Cancer Biology, and ‡Department of Biostatistics, The University of Texas M. D. Anderson Cancer, Houston, Texas, USA

ABSTRACT   *In vivo* **phage display is a technology used to reveal organ-specific vascular ligand-receptor systems in animal models and, recently, in patients, and to validate them as potential therapy targets. Here, we devised an efficient approach to simultaneously screen phage display libraries for peptides homing to any number of tissues without the need for an individual subject for each target tissue. We tested this approach in mice by selecting homing peptides for six different organs in a single screen and prioritizing them by using software compiled for statistical validation of peptide biodistribution specificity. We identified a number of motif-containing biological candidates for ligands binding to organ-selective receptors based on similarity of the selected peptide motifs to mouse proteins. To demonstrate that this methodology can lead to targetable ligand-receptor systems, we validated one of the pancreas-homing peptides as a mimic peptide of natural prolactin receptor ligands. This new comprehensive strategy for screening phage libraries in vivo provides an advantage over the conventional approach because multiple organs internally control for organ selectivity of each other in the successive rounds of selection. It may prove particularly relevant for patient studies, allowing efficient high-throughput selection of targeting ligands for multiple organs in a single screen.— Kolonin, M. G., Sun, J., Do, K.-A., Vidal, C. I., Ji, Y., Baggerly, K. A., Pasqualini, R., Arap, W. Synchronous selection of homing peptides for multiple tissues by in vivo phage display. *FASEB J.* 20, E99–E107 (2006)**

Key Words: vascular · receptor · ligand · combinatorial peptide library · phage display

SELECTIVITY OF TISSUE expression for surface molecules of cells lining the vasculature has been uncovered in disease and during normal development (1–3). Systematic profiling of selectively expressed "vascular addresses" has revealed prospective molecular targets that may be used to direct therapies to specific tissues (1, 4). Vascular mapping by in vivo phage display is based on the preferential ability of short peptide ligands from combinatorial libraries (displayed on the pIII protein of an M13-derived phage vector) (5) to home to a specific organ after systemic administration

(1, 2, 4, 6). Peptides targeting several tissues and disease states isolated in mouse models (1, 2, 7–9) and patients (10, 11) have led to the identification of the corresponding vascular receptors (7–12).

Because a single biopanning round of a large (~10^9 unique combinatorial sequences) phage library may not always sufficiently enrich for organ-homing peptides, until now, phage display screens have encompassed recovery of phage from the organ of interest in three to four rounds of library selection, utilizing one subject per each round (2, 4, 6). Thus, systematic characterization of the vasculature by using this "conventional" in vivo phage display screen setup has been rate-limited by the need to separately perform individual multiround screens for motifs homing to each tissue studied. To screen phage libraries in patients more efficiently, we have initiated attempts to isolate tissue-homing peptides for several tissues in a single screen (10). The proof-of-principle screen involved only one round of selection and, therefore, required statistical analysis of very large numbers of phage clones (thousands, as opposed to hundreds in a conventional screen) in order to identify homing peptide motifs. Although this effort yielded a prostate vasculature-selective ligand-receptor pair (10, 12, 13), for future systematic vascular mapping, there are practical limitations to the number of phage clones that can be routinely processed, thus requiring further optimization of the methodology.

To meet such challenge of the setting where maximal information recovery is critical, here we integrated a comprehensive strategy to use phage display for synchronous identification of organ-homing peptides for multiple tissues in a single screen. This strategy allows us to analyze an order of magnitude fewer peptide sequences than those surveyed for the initial single-round multi-organ screen (10). We evaluated our approach in the mouse model by performing a screen to

---

[1] Correspondence: Wadih Arap and Renata Pasqualini, 1515 Holcombe, Blvd, Houston, TX 77030-4095, USA. E-mail: warap@mdanderson.org; rpasqual@mdanderson.org
    doi: 10.1096/fj.05-5186fje

isolate peptides independently segregating to six different organs and developed a statistical analysis platform for identification of motifs selectively enriched in targeted tissues. Finally, to demonstrate the efficiency of this approach, we biochemically validated one of the identified pancreas-homing peptides as a mimic of peptide hormones that bind to prolactin receptor (PRLR).

MATERIALS AND METHODS

Synchronous screening of phage libraries in vivo

C57Bl/6 female mice were injected intravenously (i.v.) with 10^{10} transducing units (TU) of previously described (6) library CX_7C (round 1) or a mixture (10^9 TU per organ) of amplified phage recovered from each of the organs studied (rounds 2 and 3). For each round, phages were allowed to circulate for 15 min prior to organ recovery (without heart perfusion). After each round of selection, phage peptide-coding inserts were sequenced as described (6), amplified for each organ individually, and subsequently pooled for the next round of in vivo selection.

Statistical analysis of selected peptide motifs

Calculation of tripeptide motif frequencies in CX_7C peptides encountered in each target tissue (in both directions) was done by using a character pattern recognition program based on SAS (version 8.1.2, SAS Institute) and Perl (version 5.8.1), as described (10). To identify tripeptides progressively enriched from round 1 to round 3 of panning, a Bayesian Beta/Binomial model was implemented by estimation of the posterior probability distribution for each tripeptide (14, 15); posterior distributions for the proportion of each tripeptide in rounds 1 through 3 were calculated by using Splus (version 6). To determine the selectivity of tripeptide motif distribution in tissues, we used Fisher's exact test (one-tailed) and calculated the P values for the count of each tripeptide in a target tissue, as compared with its count within the 2210 tripeptides of the unselected library (**Table 1**, middle column) or the combined tripeptides from the other five tissues (Table 1, right column). Statistical uncertainty was further assessed by Monte Carlo simulations based on an established algorithm (16, 17). Using MATLAB, all tripeptide sequences (unselected library and selected for each organ) were pooled, and the combined tripeptide pool was distributed in 1000 simulations into permutated groups corresponding in size to those analyzed in Table 1 for each organ and the preselection library. For each round, Fisher's exact test was performed on the 1000 scrambled datasets, and distributions of the 50 lowest P values generated in each simulated test were compared with the distribution of 50 lowest P values from the actual experimental data (the most significant of which are shown in Table 1, middle column).

High-throughput identification of peptide-mimicked proteins

To facilitate large-scale peptide sequence analysis, we constructed an interactive peptide sequence management database based on MySQL. We developed a web-based peptide sequence retrieval and management software based on Common Gateway Interface (CGI) and Perl, and integrated it with the statistical analysis software. To identify candidate cellular proteins mimicked by selected peptides, we consolidated our database with on-line ClustlW software (http://www.ebi.ac.uk/clustalw/) to identify extended (4–7 residue long) motifs shared among multiple peptides homing to a specific tissue. Basic local alignment search tool (BLAST) (http://www.ncbi.nlm.nih.gov/basic local alignment search tool/) was used to identify proteins mimicked by the extended homing motifs by screening batches of ClustlW-identified peptide motifs against sequences contained in on-line nonredundant databases of mouse proteins. To identify PRLR ligand-matching motifs among phage-displayed pancreas-homing peptides binding to PRLR, a software was codified in Perl 5.8.1 and run against ClustlW-aligned protein sequences for sheep PL (oPL), and mouse mPL-I and mPRL. Each seven-mer peptide sequence was aligned in each orientation against the protein sequences from N- to C-terminus in one-residue shifts. The peptide-protein similarity scores for each residue were calculated based on a BLOSUM62 matrix modified to identify peptide matches of four or more residues in any position being identical to the corresponding amino acid positions in any of the three PRL homologues aligned.

Phage-peptide binding to PRLR

To identify peptides binding to PRLR, phage clones isolated from the pancreas in rounds 2 and 3 of the screening were individually amplified and pooled. For panning on immobilized PRLR, 10^9 TU of the mixed phage clones were incubated overnight at 4°C with 10 μg of purified recombinant rabbit PRLR (Protein Laboratories Rehovot, Israel), or BSA control, immobilized on plastic. Unbound phage were extensively washed off with PBS, and then the bound phage were recovered by infecting host K91 *E. coli* directly on the plate. For panning on cell surface-expressed PRLR, COS-1 cells from American Type Culture Collection (ATCC, Manassas, VA) were transiently transfected with pECE-PRLR as described (18) and subjected to biopanning with the amplified pancreas-isolated phage using the BRASIL protocol (19). In each biopanning, bound phage were selected for tetracycline resistance, quantified by infecting host K91 *E. coli* and sequenced. Single amino acid substitutions and reversal of the PRL-matching motif displayed on phage was performed by polymerase chain reaction (PCR)-directed mutagenesis of the peptide-coding insert (TGTCGCGTGGCGAGCGTGCTGC-CGTGT) and cloning it into the fUSE5 vector (5). Phage displaying forward (CRVASVLPC), reverse CPLVSAVRC, and the alanine point mutants were titered inparallel with insert-less fd-tet phage and tested for binding to COS-1 cells transfected with PRLR by using the BRASIL method (19). COS-1 cells not transfected with PRLR served as a negative control.

Immunolocalization

Immunofluorescent detection of PRLR expression in COS-1 cells was performed by using anti-PRLR antibody (Ab) MA1–610 (Affinity Bioreagents) diluted to 20 μg/ml and a secondary FITC-conjugated goat anti-mouse Ab F-0257 (Sigma) at 1:100 dilution. For validating phage binding and internalization into COS-1 cells transfected with PRLR, 10^9 TU of phage displaying PRLR-binding or mutant peptides were subjected to cell binding and internalization as described (12). Immunodetection of cell-associated phage was performed with anti-fd Ab B-7786 (Sigma) at 1:500 dilution and a secondary Cy3-conjugated donkey anti-rabbit Ab 711–165-152 (Jackson)

TABLE 1. *Peptide motifs homing to n different tissues*[a]

Tripeptides progressively enriched in Rounds 1–3				Tripeptides selected (vs. unselected library)			Tripeptides specific (vs. other organs)		
	Motif frequency (%)			Posterior		Motif			Motif	
Target organ/motif	Round 1	Round 2	Round 3	probability fold over baseline	Target organ/motif	frequency (%)	P value	Target organ/motif	frequency (%)	P value
Muscle					**Muscle**			**Muscle**		
RSG	2.2	2.4	5.6	10.0	RSG	5.6	0.0301	RSG	5.6	0.0351
SGA	0.0	1.2	5.6	7.0	SGA	5.6	0.0301	SGA	5.6	0.0132
AIG	0.0	0.0	4.4	5.0	AIG	4.4	0.0006	AIG	4.4	0.0242
IGS	0.0	1.2	5.6	7.0	IGS	5.6	0.0037	IGS	5.6	0.0010
GSF	0.0	1.2	5.6	7.0	GSF	5.6	0.0072	GSF	5.6	0.0030
AGG	1.1	1.2	4.4	7.0	AGG	4.4	0.0261	APA	2.2	0.0333
ASR	0.0	0.0	3.3	4.0	APA	2.2	0.0253	DFS	4.4	0.0121
DFS	0.0	0.0	4.4	5.0	DFS	4.4	0.0028	GDT	3.3	0.0210
DGT	0.0	0.0	3.3	4.0	GDT	3.3	0.0040	GGT	5.6	0.0010
DTG	0.0	0.0	3.3	4.0	GGT	5.6	0.0201	IAY	4.4	0.0011
FRS	0.0	1.2	3.3	5.0	IAY	4.4	0.0006			
GDT	0.0	1.2	3.3	5.0						
GGT	0.0	0.0	5.6	6.0						
GWS	0.0	0.0	3.3	4.0						
IAY	0.0	0.0	4.4	5.0						
RRS	0.0	1.2	3.3	5.0						
SGV	0.0	1.2	3.3	5.0						
Pancreas					**Pancreas**			**Pancreas**		
SVL	1.1	3.3	4.8	9.0	SVL	4.8	0.0022	VSS	7.1	0.0012
VSS	1.1	0.0	7.1	8.0	VSS	7.1	0.0006	WSG	6.0	0.0021
WSG	1.1	0.0	6.0	7.0	WSG	6.0	0.0012	FGV	3.6	0.0371
GWR	0.0	1.1	3.6	5.0	FGV	3.6	0.0033	GYN	3.6	0.0169
GYN	0.0	0.0	3.6	4.0	GYN	3.6	0.0033	LTR	3.6	0.0048
LTR	0.0	1.1	3.6	5.0	LTR	3.6	0.0118	TLV	3.6	0.0371
TLV	0.0	0.0	3.6	4.0	TLV	3.6	0.0033			
Brain					**Brain**			**Brain**		
LGG	1.1	0.0	5.8	8.0	LGG	5.8	0.0204	LGG	5.8	0.0427
RGF	0.0	0.0	3.5	4.0	RGF	3.5	0.0337	RGF	3.5	0.0250
ALG	2.1	0.0	3.5	6.0	DSY	2.3	0.0174	DSY	2.3	0.0215
LLS	1.1	0.0	3.5	5.0	GFS	2.3	0.0174	GIW	2.3	0.0215
					GIW	2.3	0.0174	HGL	2.3	0.0215
					HGL	2.3	0.0477	ALG	3.5	0.0446
								LLS	3.5	0.0446
Kidney					**Kidney**			**Kidney**		
LGS	1.1	2.3	4.4	8.0	SLS	4.4	0.0004	SLS	4.4	0.0030
SLS	1.1	1.1	4.4	7.0	DRG	3.3	0.0239	DRG	3.3	0.0151
DRG	0.0	0.0	3.3	4.0	RRV	3.3	0.0239	FLS	2.2	0.0265
RRV	0.0	0.0	3.3	4.0	SRV	4.4	0.0186			
DSG	0.0	1.1	3.3	5.0	FLS	2.2	0.0208			
LRV	0.0	1.1	3.3	5.0						
SRV	1.1	1.1	4.4	7.0						
Uterus					**Uterus**			**Uterus**		
GSS	1.2	0.0	4.9	6.0	GSS	4.9	0.0456	GPS	3.7	0.0157
LLG	1.2	0.0	4.9	6.0	LLG	4.9	0.0308	GAA	4.9	0.0322
GAA	0.0	1.1	4.9	6.0	GAA	4.9	0.0109			
GLL	1.2	0.0	4.9	6.0	GPS	3.7	0.0246			
ARG	1.2	3.2	3.7	8.0						
GAS	0.0	1.1	3.7	5.0						
GGL	2.4	1.1	4.9	8.0						
GPS	0.0	0.0	3.7	4.0						
Bowel					**Bowel**			**Bowel**		
AGV	0.0	0.0	4.7	5.0	AGV	4.7	0.0719	AGV	4.7	0.0344
WRD	0.0	0.0	4.7	5.0	WRD	4.7	0.0023	WRD	4.7	0.0098
FGG	0.0	0.0	4.7	5.0	FGG	4.7	0.0005	FGG	4.7	0.0199
GGR	1.1	0.0	7.1	8.0	RWS	3.5	0.0275	RWS	3.5	0.0179
GRV	0.0	1.2	3.5	5.0	VGV	3.5	0.0124			
RWS	0.0	0.0	3.5	4.0	GVG	3.5	0.0488			
VGV	0.0	0.0	3.5	4.0						

Left column: using the Bayesian Beta/Binomial model, we ranked tripeptides according to posterior mean. Shown are tripeptides with posterior probability fold change of x3 or more over baseline (posterior probability for tripeptides not isolated in any of the three rounds). *Middle column*: tripeptide motifs contained in CX_7C peptides isolated in round 3 from target organs with frequency significantly higher than that observed in the unselected phage library (Fisher Exact test, one-tailed; $P<0.05$). *Right column*: tripeptide motifs occurring in CX_7C peptides enriched in round 3 in a specific organ but not in other target organs analyzed (Fisher Exact test, one-tailed; $P<0.05$).

at 3 μg/ml. For phage-peptide immunolocalization in situ, 10^{10} TU of iv-injected phage were let circulate for 5 min. Immunohistochemistry on formalin-fixed, paraffin-embedded mouse tissue sections was performed as described (6, 10) by using anti-fd Ab B-7786 at 1:1,000 dilution and the LSAB+ peroxidase kit (DAKO).

RESULTS

Synchronous phage library screening in vivo

We reasoned that peptide-displaying phage clones of systemically administered library would segregate in the bloodstream irrespective of each other and, thus, target individual organs independently. If this hypothesis is correct, independent enrichment of phage-peptides targeting any number of organs should take place on successive rounds of selection. To establish the experimental framework for synchronous selection of peptides independently homing to different organs, we screened a phage-displayed cyclic random peptide library CX_7C (C, cysteine; X, any residue). Six organs were targeted in mice: muscle, bowel, uterus, kidney, pancreas, and brain (**Fig. 1**). Three rounds of library selection were performed based on previously described methodology (6), but without the step of whole-body perfusion of the vasculature, which was skipped in order to simulate screening conditions used in patients (10). In each round, peptide-displaying phage were isolated from target organs, amplified, and pooled for the next round of selection. To identify organ-homing motifs, we sequenced the DNA corresponding to peptide inserts from 96 recovered phage clones after each of the three rounds of selection for each of the six organs and analyzed the sequences. Preferential cell binding of specifically homing peptides to differentially-expressed receptors results in enrichment, defined by the increased frequency of the peptide recovery in each subsequent round of the screen (4, 6). Thus, we set out to profile the differential distribution of library-encoded peptides among the six organs, which could be used for the subsequent identification of their targets.

To analyze the spectrum of the peptides resulting from the screening and to compare those among different organs, we adopted a combinatorial statistical approach based on the premise that three residue motifs (tripeptides) provide a sufficient structure for peptide-protein interactions in the context of phage display (10). Since a tripeptide within a CX_7C sequence may be responsible for receptor targeting in either orientation, we performed a computer-assisted analysis of the 7489 tripeptides contained in each direction within the CX_7C inserts (2620 from the first round; 2554 from the second round; and 2315 from the third round) successfully sequenced for the organ-recovered clones. First, we evaluated the increase in recovery frequency for individual tripeptides in the three consecutive rounds of selection by using the Bayesian Beta/Binomial model (14, 15). For each organ, we found a number of tripeptides progressively enriched (Table 1, left column), thus, suggesting their superior affinity and/or specificity. Next, we surveyed the 2315 motifs recovered from the third round of selection to identify motifs with terminal frequencies higher than those present in the phage library prior to selection. The significance of motif representation increase on selection was assessed by the Fisher exact test (Table 1, middle column). To show that the P value of 0.05 for establishment of selected tripeptides was chosen appropriately, we adapted the Monte Carlo algorithm (16), and confirmed in the third selection round that the P values of the actual data were smaller than at least 95% of the simulated P values (**Fig. 2**). Of note, Monte Carlo simulations showed a progressive accumulation of tripeptides isolated with lower P values from the first to the third round (Fig. 2), consistent with enrichment of the corresponding motifs identified by the Bayesian Beta/Binomial model (Table 1, left column). Finally, we used the Fisher exact test to analyze the motifs recovered from the third selection round for specificity of tissue homing by identifying tripeptides that were enriched in one of the six organs, but not in the rest of the organs studied (Table 1, right column).

Identification of candidate biological ligands mimicked by homing peptides

The majority of peptide motifs identified by statistical analysis enriched during the screen also showed specificity of association with the organ from which they were recovered (Table 1). For validation of potentially

Figure 1. Schematic description of synchronous in vivo phage display screening. In every selection round, phage are i.v. administered and simultaneously recovered from n target tissues, amplified, pooled, and used for the next selection round. Increased recovery of phage transforming units (TU) in the third round reflects the selection of peptides preferentially homing to the target organ.
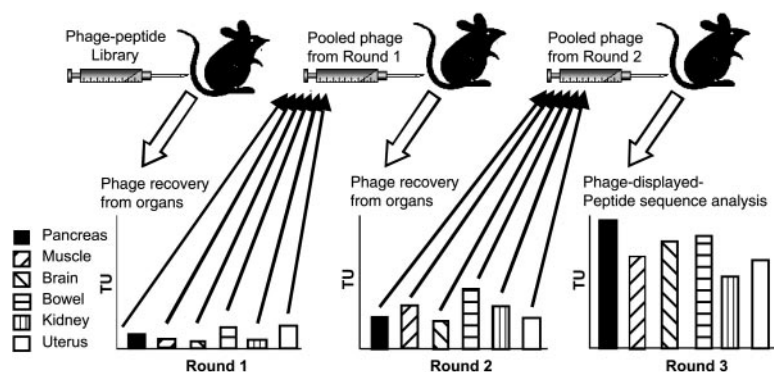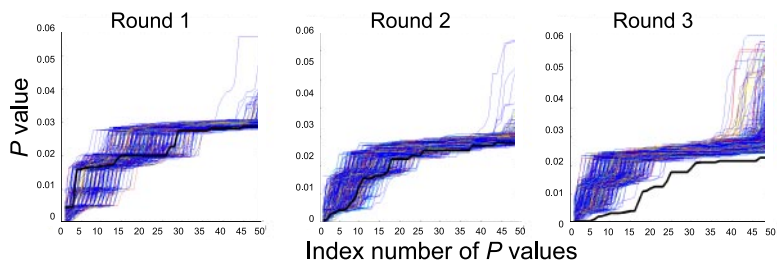
Figure 2. Monte Carlo simulations to assess tripeptide motif tissue homing. For each selection round, the plot of 50 smallest P values (black line) determined by Fisher's exact test for enriched tripeptides (Table 1, middle column), was compared with the corresponding simulated dataset plots (colored lines). To generate simulated datasets, all tripeptides isolated from the target organs were pooled with tripeptides isolated from the unselected CX_7C library, and Fisher's exact test was performed on 1000 random permutations. For every permutation, the pool of tripeptides was randomly distributed into groups corresponding to numbers of peptide sequences analyzed for each tissue (Table 1, middle column). Plotted are the 50 smallest P values (index number of P values 1 through 50, ascending order) generated in each of the 1000 permutations.

specific organ-homing motifs, we chose to focus on tripeptides that fulfilled the criteria of the statistical tests applied (Table 1). Since peptide motifs binding to cell surface receptors have been previously found to mimic native ligands for these receptors (7, 10, 19), the ClustalW software was used to determine whether the tripeptides represented parts of longer motifs responsible for organ homing, which would facilitate peptide/protein similarity search. For some of the tripeptides, this analysis identified extended (four to seven residue) motifs shared among multiple CX_7C peptides isolated from the given organ (**Fig. 3**). Each of these extended motifs was screened by using the BLAST algorithm against a nonredundant database of mouse proteins to identify regions of similarity within proteins potentially mimicked by the motifs (**Table 2**).

We systematically analyzed the BLAST output for selected motif similarities to extracellular signaling factors that had been reported to regulate organ-dependent vascular growth or homeostasis. This revealed 19 motifs as segments of such proteins and, in some cases, identified several motifs that homed to the same organ and that matched different domains within the same protein (Table 2). For example, muscle-homing motifs GRSG+R and SGASAV, matched to two different domains of the Jagged2-like protein (Table 2) that belongs to a family of ligands for Notch receptors known to regulate vascular development and function (20, 21). Similarly, pancreas-homing motifs ASVL (in the reverse orientation) and WSGL showed close similarity to different domains of a placental lactogen (22). Interestingly, for muscle and pancreas, we also matched homing tripeptides to different ligands that share a receptor with a functional role in vascular biology in the target organ (Table 2). Among skeletal muscle-homing motifs, tripeptides FSG and SGI were partially overlapping in the extended DFSGIA+ region of similarity to disintegrin family metalloproteinases ADAM and Spi 12, respectively, which cleave Notch receptors (23). In the pancreas, motif SWSG matched to prolactin (PRL)-like protein M (PLP-M), which belongs to the same family as the placental lactogen PL-I (containing the reverse ASVL and WSGL) and also binds to the PRL receptor (22,24).

Biochemical validation of PRLR as the target for pancreas-homing peptides

To demonstrate the possibility of efficient characterization of circulation-accessible receptors by synchronous biopanning, as a proof-of-principle, we chose to validate the PRL receptor (PRLR) as a peptide target in the pancreas. PL-I and PLP-M identified by BLAST analysis belong to the conserved family of PRL-like peptidic hormones that have been shown to function in the pancreas during pregnancy (22, 25). Because PRLR is the only known receptor for these proteins (22, 24), we proposed that the ASVL, WSGL, and SWSG motifs target PRLR in vivo by mimicking PRL family hormones.

To test this hypothesis, we attempted to reveal a biochemical interaction of pancreas-homing motifs with PRLR. We used the BRASIL (biopanning and rapid analysis of selective interactive ligands) method (19) to screen a pancreas-homing phage sublibrary (pooled clones recovered in rounds 2 and 3) against PRLR expressed on the surface of COS-1 cells (18). In parallel, we screened the same sublibrary on purified recombinant PRLR (26). A single round of each selec-
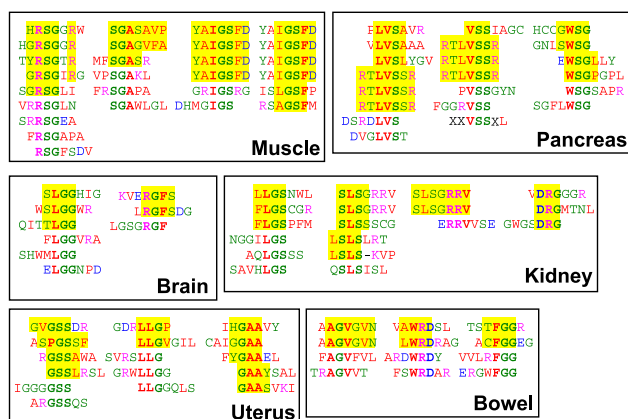

Figure 3. Identification of extended motifs homing to mouse tissues. Peptide sequences containing tripeptides enriched in a given tissue (Table 1) were aligned in clusters by using the ClustalW software to obtain longer motifs shared among different peptides from each cluster. Similarity between peptides at the concentration of amino acid class is color-coded: red, hydrophobic; green, neutral and polar; purple, basic; blue, acidic. Original tripeptides are depicted in bold; extended motifs are highlighted in yellow.

TABLE 2. *Candidate mouse proteins mimicked by synchronously selected peptides[a]*

Extended motif	Mouse protein containing motif	Protein description	Accession #
Muscle			
DFSGIA+; DF**SGI**A+	ADAM 10; Spi12	Notch Interactor; Serine protease inhibitor (serpin)	NP_031425; NP_035584
G**RSG**+R; **SGA**SAV	Syndactylism, Jagged 2-similar	Notch ligand	XP_192739
SG+GVF	DPP IV	Dipeptidylpeptidase active in muscle vasculature	NP_034204
A**GSF**	Fibrillin-1	Extracellular matrix protein, TGFβ interactor	XP_192917
SL**GSF**P	SPARC-related protein	Extracellular matrix calcium-binding protein	NP_071711
Pancreas			
LVSA; **WSG**L	Placental lactogen-I α (PL-I)	Pancreas-signaling peptide hormone	AAN39710.1
G**WSG**	PRL-like protein M	Pancreas-signaling peptide hormone	NP_064375
+**SVL**TR	Ecgf1, gliostatin	Endothelial cell growth factor	NP_612175.1
Brain			
SLGG	NGF-alpha; kallikrein K22	Nerve growth factor; NGF endopeptidase	NP_035045; P15948
Kidney			
G**SLS**	Endothelin-converting enzyme	Processing of peptidic vasoconstricting hormones	XP_131743.2
L**SLS**L	Thrombospondin	Anti-angiogenic ECM protein, TGFβ activator	AAA50611.1
Uterus			
+P**GSS**F	Pregnancy zone protein; α1 м	Differentially expressed endometrial LRP subunit	NP_031402.1
GSS+WA	Fractalkine; neurotactin	Chemokine; small inducible cytokine	NP_033168
P**GLL**	Luteinizing hormone β	Pregnancy peptide hormone	NP_032523
Bowel			
A**GV**GV	Fibrillin-2	Extracellular matrix protein, TGFβ interactor	AAA74908
+C**FGG**+	Prepronatriodilatin	Atrial natriuretic factor: intestinal paracrine effector	P05125

For sequence similarity search to mouse proteins, tripeptide-containing motifs (in either orientation) identified in Fig. 3 were screened using BLAST (NCBI). Examples of candidate proteins potentially mimicked by the peptides homing to mouse tissues are listed. Sequences correspond to the regions of 100% identity between the peptide selected and the candidate protein. Conserved amino acid substitutions are indicated as (+). Tripeptides shown in Table 1 are highlighted.

tion for PRLR-binding phage-peptides resulted in over 90% of the clones sequenced comprised by seven different peptides, five of which were enriched on both immobilized and cell surface-expressed PRLR (**Fig. 4***A*). Phage displaying these peptides had specific affinity to PRLR, as determined by subjecting the same sublibrary to binding of an immobilized BSA control (Fig. 4*B*). Remarkably, computer-assisted analysis of sequences revealed that all of the selected peptides contained amino acid motifs similar to those present in proteins of PRL family (Fig. 4*A*). Furthermore, a clear cluster of matches was identified around one of the hormone domains that had been shown (27) to mediate receptor interaction (Fig. 4*A*). As a negative control, the same similarity search algorithm did not reveal such matches for the selected sequences to unrelated proteins such as insulin, IL-11 and bZIP (data not shown).

Peptide motif CRVASVLPC recovered as a PRLR-binding prolactin mimic (Fig. 4) contained a tripeptide, SVL, also identified as one of those enriched in the pancreas during the screen (Table 1). The CRVAS-VLPC motif matched one of the PL-I sites involved in PRLR interaction (27), as it had amino acids identical to those found in one or more of the three aligned PRL homologues in four out of seven positions (Fig. 4*A*). Similarity of this peptide in reverse orientation to a part of PL-I (Fig. 4*A*), initially identified by the BLAST analysis (Table 2), was found by RasMol-assisted analysis of 3D protein structure to reside within the domain exposed on the surface of PRL family proteins (data not shown). To demonstrate direct physical interaction between CRVASVLPC and PRLR, we tested binding of CRVASVLPC-phage to COS-1 cells transfected with PRLR and found it to be 9-fold higher than its nonspecific binding to nontransfected COS-1 cells that served as a negative control (**Fig. 5***A*). To address the issue of
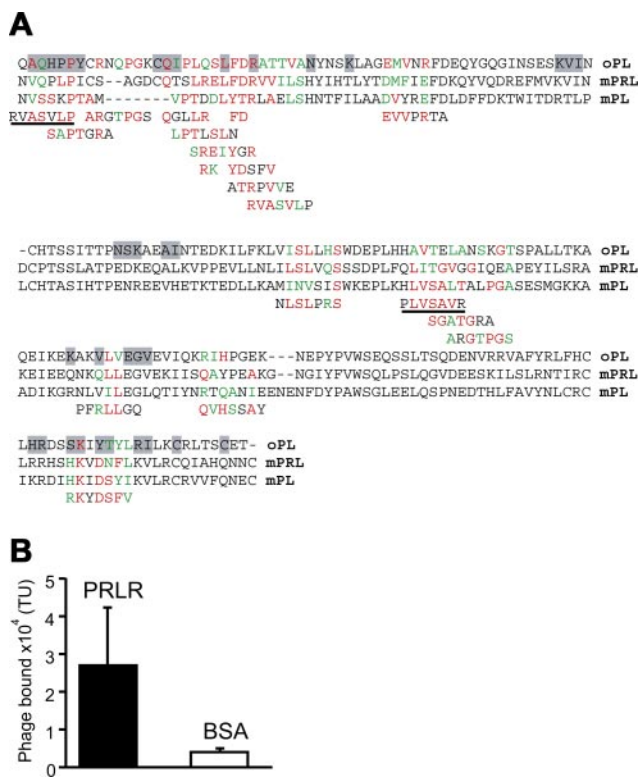
Figure 4. Retro-BLAST analysis to identify PRLR ligand-matching motifs. *A)* Peptide sequences isolated from the pancreas-homing phage pool as those binding to PRLR were matched in each orientation to mature sheep (oPL) and mouse (mPL-I and mPRL) protein sequences (leader peptide sequence not included). Peptide matches of four or more residues in any position being identical to the corresponding amino acid positions in any of the three PRL homologues are displayed. Shaded protein sequences: published PRLR binding sites. Peptide amino acid colors are coded according to their relationship to the corresponding amino acid positions of one or more of the three aligned PRLR ligands: red, identity; green, similarity. Motifs SGATGRA, SGPTGRA, QVHSSAY, VFSDYKR, and LPTLSLN were isolated by biopanning on both: in vitro immobilized and cell-surface expressed PRLR. Forward and reverse matches of the validated RVAS-VLP motif are underlined. *B)* Binding of pancreas-homing phage-peptides (recovered from synchronous biopanning rounds 2 and 3) to recombinant rabbit PRLR, as compared to their binding to BSA control. TU: transforming units.

a possible importance of the motif orientation for PRLR binding, we constructed phage displaying CPLVSAVRC, the PRL-mimicking motif in the opposite orientation. Reversal of the motif did not significantly decrease its binding to PRLR on the expressing cells (Fig. 5*B*). However, disruption of the motif by alanine-scanning mutagenesis of any amino acid significantly decreased binding to PRLR-expressing cells (Fig. 5*A*), thus indicating cooperation of the RVASVLP residues comprising the motif in the receptor recognition. To further demonstrate the specific affinity of the CRVAS-VLPC motif for its receptor, we showed that the PRL mimic specifically bound to cells expressing PRLR by using immunofluorescence (Fig. 5*C*). Phage displaying either CRVASVLPC or CPLVSAVRC were found bound and internalized specifically by cells expressing PRLR,

but not by nonexpressing control cells, whereas none of the CRVASVLPC mutants displayed detectable PRLR-expressing cell binding and internalization (Figs. 5*C–D* and data not shown).

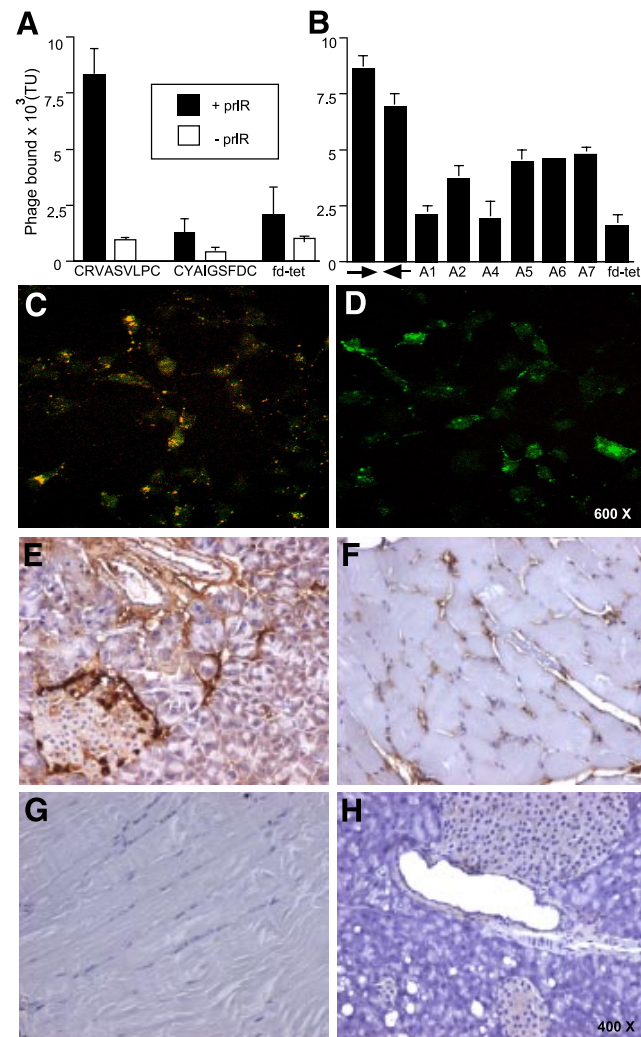Finally, since the SVL tripeptide found within the

Figure 5. Validation of PRLR as a candidate receptor for a PRLR ligand mimic CRVASVLPC. *A)* Specific binding of the CRVASVLPC-phage, but not of the control phage (CYAIGS-FDC-displaying or insertless fd-tet) to COS-1 cells transfected with pECE-PRLR. Phage binding to COS-1 PRLR-transfected cells (as compared to control nontransfected cells) was determined by BRASIL (10, 19). *B)* Binding of phage displaying forward SVL-containing CRVASVLPC motif (right arrow), as well as the reverse CPLVSAVRC motif (left arrow), to PRLR-transfected COS-1 cells, as compared to biding of the six alanine-scan motif mutants (A1:CAVASVLPC, A2:CRAASV-LPC, A3:CRVAAVLPC, A4:CRVASALPC, A5:CRVASVAPC, and A6:CRVASVLAC). *C–D)* Specific binding to and internalization of CRVASVLPC-phage (*C*) and an alanine-scan mutant A4 (*D*) into COS-1 PRLR-transfected cells, detected by co-immunolocalization of CRVASVLPC-phage (red) with PRLR-expression (green), resulting in overlapping yellow signal (*C*). *E–H)* Antiphage immunohistochemistry (brown) in paraffin sections of formalin-fixed pancreas (*E, H*) or skeletal muscle (*F, G*) from mice i.v. injected with CRVASV-LPC-phage (*E, G*), or control muscle-homing CYAIGSFDC-phage (*F, H*). Hematoxylin counterstaining is shown in blue.

PRL mimetope CRVASVLPC was isolated from the pancreas, we evaluated weather the motif homes to PRLR in the pancreatic blood vessels. We showed that the previously reported pancreatic expression of mouse PRLR protein in the vasculature and in the islets (28) closely resembles the in vivo distribution of phage displaying the CRVASVLPC motif (Fig. 5*E–H*). Immunohistochemistry of mouse tissues on i.v. CRVASVLPC-phage administration revealed localization of the CRVASVLPC motif to pancreatic blood vessels and the pancreatic islet cells (Fig. 5*E*), but not to skeletal muscle (Fig. 5*F*). In contrast, a control in vivo–administered phage clone displaying CYAIGSFDC sequence homing to the skeletal muscle was found predominantly in the vasculature of the skeletal muscle, but not in the pancreas (Fig. 5*H*). Taken together, these data indicate that the peptide CRVASVLPC binds to PRLR and suggests that it targets vasculature-exposed PRLR in the pancreas.

DISCUSSION

Here, we present an advance in the in vivo phage display methodology: simultaneous screening of peptide libraries on multiple organs. Parallel analysis of fewer sequences (hundreds) in multiple biopanning rounds performed here, as opposed to thousands of sequences required for the identification of homing motifs in a single round, as reported preciously (10), provides control over the progressive organ-specific enrichment of individual motifs throughout the consecutive screening rounds. Our approach enables highly efficient isolation of organ-homing ligands from combinatorial libraries and may streamline vascular mapping efforts, thus leading to a better understanding of the functional protein–protein interactions in the vasculature.

Both Bayesian and frequentist statistics have led to the identification of largely overlapping populations of peptide motifs enriched in the target organs, thus reinforcing the validity of the identified homing motifs. Organ-homing peptides were prioritized for further validation based on their sequence similarity to domains of mouse proteins. Protein-peptide similarity-based survey failed to identify prototype proteins for some of the homing tripeptides. This is not surprising, as the approach does not reveal peptide motifs that mimic conformationally defined interacting sites within proteins. Moreover, it is certainly not a given that every similarity-based lead will ultimately yield a biologically significant interaction. Nevertheless, this strategy has proven effective in the identification of receptor-ligand leads that might subsequently be validated directly by using binding assays (12, 19).

As an example, we validated a pancreas-homing motif CRVASVLPC as a peptide mimic of natural ligands of PRLR, which include PL, PRL, and a number of other hormones from the same family. A concept implemented here is the ability to systematically "retro-

BLAST" the receptor-binding peptides onto prototype ligands in order to map sites of ligands involved in receptor interaction. By such retro-targeting of the receptor ligands with peptides derived from in vivo selections, we were able to identify multiple apparent PRL mimics, many of which had been missed in the statistical survey of selected tripeptides. We show that one of the PRL mimics, CRVASVLPC, specifically binds to PRLR in the context of phage coat pIII protein, and that the precise amino acid sequence of the motif appears to be essential for binding. We demonstrate that the CRVASVLPC motifs binds to PRLR in both forward and reverse orientation, however it should be noted that such orientation independence may not be a general feature that is applicable to every ligand-receptor pair interaction. We also show that the CRVASVLPC peptide homes to pancreatic vasculature in vivo, consistent with vascular PRLR expression and with the established function of placental lactogens in the pancreas during pregnancy (22, 24, 25, 28–30). These findings are also consistent with reported PRLR expression in other organs, as neither VSL, nor other motifs apparently mimicking biological PRLR ligands, qualified the statistical test of organ-specific motif distribution (Table 1, right column).

In summary, synchronous selection of homing peptides for multiple tissues accelerates the process of phage display-based vascular mapping in vivo. Direct combinatorial screenings in patients (10, 11, 13) have opened the possibility of systematic isolation of peptide ligands for therapeutic targeting. In the future, the use of peptide libraries for probing the vasculature in individual patients for diagnostic and therapeutic purposes may become a reality. The high-throughput targeting strategy bestowed by the synchronous biopanning reported here will open new possibilities for rapid and efficient identification and validation of vascular receptors and their ligand-directed targeting. [FJ]

REFERENCES

1. Arap, W., Pasqualini, R., and Ruoslahti, E. (1998) Cancer treatment by targeted drug delivery to tumor vasculature in a mouse model. *Science* **279,** 377–380
2. Pasqualini, R., and Ruoslahti, E. (1996) Organ targeting in vivo using phage display peptide libraries. *Nature* **380,** 364–366
3. Rajotte, D., Arap, W., Hagedorn, M., Koivunen, E., Pasqualini, R., and Ruoslahti, E. (1998) Molecular heterogeneity of the vascular endothelium revealed by in vivo phage display. *J. Clin. Invest.* **102,** 430–437
4. Kolonin, M. G., Pasqualini, R., and Arap, W. (2001) Molecular addresses in blood vessels as targets for therapy. *Curr. Opin. Chem. Biol.* **5,** 308–313
5. Smith, G. P., and Scott, J. K. (1993) Libraries of peptides and proteins displayed on filamentous phage. *Methods Enzymol.* **217,** 228–257

6. Pasqualini, R., Arap, W., Rajotte, D., and Ruoslahti, E. (2001) In Vivo Selection of Phage-display Libraries. In *Phage Display: A Laboratory Manual* (Barbas, C., Burton, D., Silverman, G., and Scott, J., eds) pp. 22.21–22.24, Cold Spring Harbor Laboratory Press, New York, NY

7. Kolonin, M. G., Pasqualini, R., and Arap, W. (2002) Teratogenicity induced by targeting a placental immunoglobulin transporter. *Proc. Natl. Acad. Sci. U. S. A.* **99,** 13055–13060

8. Pasqualini, R., Koivunen, E., Kain, R., Lahdenranta, J., Sakamoto, M., Stryhn, A., Ashmun, R. A., Shapiro, L. H., Arap, W., and Ruoslahti, E. (2000) Aminopeptidase N is a receptor for tumor-homing peptides and a target for inhibiting angiogenesis. *Cancer Res.* **60,** 722–727

9. Kolonin, M. G., Saha, P. K., Chan, L., Pasqualini, R., and Arap, W. (2004) Reversal of obesity by targeted ablation of adipose tissue. *Nature Med.* **10,** 625–632

10. Arap, W., Kolonin, M. G., Trepel, M., Lahdenranta, J., Cardó-Vila, M., Giordano, R. J., Mintz, P. J., Ardelt, P. U., Yao, V. J., Vidal, C. I., Chen, L., Flamm, A., Valtanen, H., Weavind, L. M., Hicks, M. E., Pollock, R. E., Botz, G. H., Bucana, C. D., Koivunen, E., Cahill, D., Troncoso, P., Baggerly, K. A., Pentz, R. D., Do, K. A., Logothetis, C. J., and Pasqualini, R. (2002) Steps toward mapping the human vasculature by phage display. *Nature Med.* **8,** 121–127

11. Kolonin, M. G., Pasqualini, R., and Arap, W. (2003) Mapping human vascular heterogeneity by in vivo phage display. In *Genetics of Angiogenesis* (Hoying, J. B., ed), BIOS Scientific Publishers Ltd., Oxford

12. Zurita, A. J., Troncoso, P., Cardó-Vila, M., Logothetis, C. J., Pasqualini, R., and Arap, W. (2004) Combinatorial screenings in patients: the interleukin-11 receptor alpha as a candidate target in the progression of human prostate cancer. *Cancer Res.* **64,** 435–439

13. Pentz, R. D., Flamm, A. L., Pasqualini, R., Logothetis, C. J., and Arap, W. (2003) Revisiting ethical guidelines for research with terminal wean and brain-dead participants. *Hastings Cent. Rep.* **33,** 20–26

14. Lee, K. E., Sha, N., Dougherty, E. R., Vannucci, M., and Mallick, B. K. (2003) Gene selection: a Bayesian variable selection approach. *Bioinformatics* **19,** 90–97

15. Carlin, B. P., and Sargent, D. J. (1996) Robust Bayesian approaches for clinical trial monitoring. *Stat. Med.* **15,** 1093–1106

16. Gelman, A., and Rubin, D. B. (1996) Markov chain Monte Carlo methods in biostatistics. *Stat. Methods Med. Res.* **5,** 339–355

17. Zhang, L., Zhou, W., Velculescu, V. E., Kern, S. E., Hruban, R. H., Hamilton, S. R., Vogelstein, B., and Kinzler, K. W. (1997) Gene expression profiles in normal and cancer cells. *Science* **276,** 1268–1272

18. Wang, Y., O'Neal, K. D., and Yu-Lee, L. (1997) Multiple prolactin (PRL) receptor cytoplasmic residues and Stat1 mediate PRL signaling to the interferon regulatory factor-1 promoter. *Mol. Endocrinol.* **11,** 1353–1364

19. Giordano, R. J., Cardó-Vila, M., Lahdenranta, J., Pasqualini, R., and Arap, W. (2001) Biopanning and rapid analysis of selective interactive ligands. *Nature Med.* **7,** 1249–1253

20. Lindner, V., Booth, C., Prudovsky, I., Small, D., Maciag, T., and Liaw, L. (2001) Members of the Jagged/Notch gene families are expressed in injured arteries and regulate cell phenotype via alterations in cell matrix and cell-cell interaction. *Am. J. Pathol.* **159,** 875–883

21. Krebs, L. T., Xue, Y., Norton, C. R., Shutter, J. R., Maguire, M., Sundberg, J. P., Gallahan, D., Closson, V., Kitajewski, J., Callahan, R., Smith, G. H., Stark, K. L., and Gridley, T. (2000) Notch signaling is essential for vascular morphogenesis in mice. *Genes Dev.* **14,** 1343–1352

22. Wiemers, D. O., Shao, L. J., Ain, R., Dai, G., and Soares, M. J. (2003) The mouse prolactin gene family locus. *Endocrinology* **144,** 313–325

23. Brou, C., Logeat, F., Gupta, N., Bessia, C., LeBail, O., Doedens, J. R., Cumano, A., Roux, P., Black, R. A., and Israel, A. (2000) A novel proteolytic cleavage involved in Notch signaling: the role of the disintegrin-metalloprotease TACE. *Mol. Cell* **5,** 207–216

24. Goffin, V., Binart, N., Touraine, P., and Kelly, P. A. (2002) Prolactin: the new biology of an old hormone. *Annu. Rev. Physiol.* **64,** 47–67

25. Freemark, M., Avril, I., Fleenor, D., Driscoll, P., Petro, A., Opara, E., Kendall, W., Oden, J., Bridges, S., Binart, N., Breant, B., and Kelly, P. A. (2002) Targeted deletion of the PRL receptor: effects on islet development, insulin production, and glucose tolerance. *Endocrinology* **143,** 1378–1385

26. Bignon, C., Sakal, E., Belair, L., Chapnik-Cohen, N., Djiane, J., and Gertler, A. (1994) Preparation of the extracellular domain of the rabbit prolactin receptor expressed in *Escherichia coli* and its interaction with lactogenic hormones. *J. Biol. Chem.* **269,** 3318–3324

27. Elkins, P. A., Christinger, H. W., Sandowski, Y., Sakal, E., Gertler, A., de Vos, A. M., and Kossiakoff, A. A. (2000) Ternary complex between placental lactogen and the extracellular domain of the prolactin receptor. *Nature Struct. Biol.* **7,** 808–815

28. Brelje, T. C., Svensson, A. M., Stout, L. E., Bhagroo, N. V., and Sorenson, R. L. (2002) An immunohistochemical approach to monitor the prolactin-induced activation of the JAK2/STAT5 pathway in pancreatic islets of Langerhans. *J. Histochem. Cytochem.* **50,** 365–383

29. Brelje, T. C., Scharp, D. W., Lacy, P. E., Ogren, L., Talamantes, F., Robertson, M., Friesen, H. G., and Sorenson, R. L. (1993) Effect of homologous placental lactogens, prolactins, and growth hormones on islet B-cell division and insulin secretion in rat, mouse, and human islets: implication for placental lactogen regulation of islet function during pregnancy. *Endocrinology* **132,** 879–887

30. Vasavada, R. C., Garcia-Ocana, A., Zawalich, W. S., Sorenson, R. L., Dann, P., Syed, M., Ogren, L., Talamantes, F., and Stewart, A. F. (2000) Targeted expression of placental lactogen in the beta cells of transgenic mice results in beta cell proliferation, islet mass augmentation, and hypoglycemia. *J. Biol. Chem.* **275,** 15399–15406

Immunonanoshells for targeted photothermal ablation of tumor cells

Amanda R Lowery[1]
André M Gobin[1]
Emily S Day[1]
Naomi J Halas[2]
Jennifer L West[1]

[1]Department of Bioengineering,
[2]Department of Electrical and
Computer Engineering, Rice
University, Houston, TX, USA

Abstract: Photothermal cancer therapy using immunonanoshells yields targeted cell death. Consisting of a silica core surrounded by a thin gold shell, nanoshells possess an optical tunability that spans the visible to the near infrared (NIR) region, a region where light penetrates tissues deeply. Conjugated with tumor-specific antibodies, NIR-absorbing immunonanoshells can preferentially bind to tumor cells. NIR light then heats the bound nanoshells, thus destroying the targeted cells. Antibodies can be consistently bound to the nanoshells via a bifunctional polyethylene glycol (PEG) linker at a density of ~150 antibodies per nanoshell. In vitro studies have confirmed the ability to selectively induce cell death with the photothermal interaction of immunonanoshells and NIR light. Prior to incubation with anti-human epidermal growth factor receptor (HER2) immunonanoshells, HER2-expressing SK-BR-3 breast carcinoma cells were seeded alone or adjacent to human dermal fibroblasts (HDFs). Anti-HER2 immunonanoshells bound to HER2-expressing cells resulted in the death of SK-BR-3 cells after NIR exposure only within the irradiated area, while HDFs remained viable after similar treatment since the immunonanoshells did not bind to these cells at high levels. Control nanoshells, conjugated with nonspecific anti-IgG or PEG, did not bind to either cell type, and cells continued to be viable after treatment with these control nanoshells and NIR irradiation.

Keywords: nanoshells, immunonanoshells, photothermal, antibody, targeting, cancer

Introduction

Metal nanoshells are optically tunable nanoparticles, consisting of a spherical dielectric core encapsulated by a thin metal shell. The overall particle size as well as the ratio of core radius to shell thickness dictates the scattering and absorbing properties of the particle. For a given core radius, decreasing the shell thickness (increasing the core: shell ratio) shifts the peak plasmon resonance to longer wavelengths (Oldenburg et al 1998; Averitt et al 1999). The resonance tunablity spans the visible and infrared spectrum (Averitt et al 1999). By placing the peak absorption properties in the near infrared (NIR) region where tissue absorption is at a minimum (Welch and van Gemert 1995; Weissleder 2001), nanoshells within tissue can preferentially absorb NIR light energy.

Nanoshell photothermal cancer therapy works through the preferential accumulation of nanoshells in a tumor and absorption of NIR light by those particles to locally generate heat at the tumor site. Nanoshells have been shown to passively accumulate in tumors after intravenous injection (O'Neal et al 2004) as a result of the leaky vasculature characteristic of neoplastic tumors (Hashizume et al 2000). After systemic injection and accumulation at the tumor site, NIR light is applied over the tumor region. The absorbed energy causes the nanoshells to heat, allowing local destruction of the tumor tissue. In a mouse model, nanoshell-treated tumors completely regressed after NIR illumination without tumor regrowth (O'Neal et al 2004). The tumors receiving

Correspondence: Jennifer L West
Rice University, MS 142, 6100 Main Street,
Houston, TX 77005, USA
Tel +1 713 348 5955
Fax +1 713 348 5154
Email jwest@rice.edu

the nanoshell therapy experienced rapid temperature rises sufficient to cause irreversible tissue damage, while laser application to nearby healthy tissue or to tumors not treated with nanoshells did not induce a significant temperature increase (Hirsch et al 2003).

Molecularly targeting nanoshells to tumors via antibodies against cell surface markers may further enhance the accumulation of nanoshells in tumors, prolong their presence in tumors, and potentially allow the use of lower nanoshell dosages. Many tumors have increased expression of specific cell surface markers. Several markers have been investigated for targeting, including human epidermal growth factor receptor (HER2) (Wu et al 2003), α_v integrin (Arap et al 1998; Anderson et al 2000; Reynolds et al 2003), and CD44 (Verel et al 2002). These targets have been used to deliver genes (Reynolds et al 2003), chemotherapeutics (Backer and Backer 2001), and nanoparticles (Anderson et al 2000; Wu et al 2003). Antibody targeting of nanoparticles and drugs to tumors has shown increased delivery of therapeutic agents (Tarli et al 1999; Cortez-Retamozo et al 2002; Reynolds et al 2003). Specifically, the human epidermal growth factor receptor HER2 has been used to target breast cancer cells because of its stable overexpression on ~30% of breast cancers (Slamon et al 1989; McDermont et al 2002; Kämmerer et al 2003; Carlsson et al 2004). Using HER2 targeted immunoliposomes, the uptake of the chemotherapeutic drug doxorubicin was increased 700-fold (Park et al 2001, 2002; Noble et al 2004). In the current studies, antibody conjugation to nanoshells has been evaluated, and nanoshells conjugated with anti-HER2 are investigated for targeting nanoshell binding to HER2-expressing breast carcinoma cells.

Materials and Methods
Synthesis of polyethylene (PEG) thiol (PEG-SH)

PEG-SH was synthesized by reacting PEG-amine (M_r 5000, Nektar, Huntsville, AL, USA) with 2-iminothiolane (Sigma-Aldrich, St Louis, MO, USA) for 1 hour. The product was dialyzed (molecular weight cutoff of 500 Da; Spectrum Laboratories, Rancho Domingo, CA, USA) against deionized (DI) water for at least 4 hours to remove excess reagents. The PEG-SH yield was determined colorimetrically at 412 nm after reacting with Ellman's reagent, 5,5'-dithio-bis(2-nitrobenzoic acid) (Sigma-Aldrich). PEG-SH was stored at –20°C.

Antibody PEG conjugation

Orthopyridyl-disulfide-poly(ethylene glycol)-N-hydroxysuccinimide ester (OPSS-PEG-NHS, 2000MW) was obtained from Nektar (San Carlos, CA, USA) in lyophilized form. C-erbB-2/HER2/neu Ab-4 (clone N12) (anti-HER2) was obtained from NeoMarkers (Fremont, CA, USA). A 81 μmol/L (0.16 mg/mL) solution of OPSS-PEG-NHS was mixed with 5.4 μmol/L (1mg/mL) anti-HER2 at a volumetric ratio of 1:9 and reacted at 4°C overnight.

Nanoshell synthesis

Nanoshells were synthesized as previously described (Oldenburg et al 1998; Averitt et al 1999). Briefly, silica nanoparticles were fabricated by the Stöber method (Stöber et al 1968) in which tetraethyl orthosilicate is reduced in basic ethanol. The surfaces of the silica particles were reacted with aminopropyl triethoxysilane, terminating the surface with amine groups. Small gold colloid (~3 nm), prepared by the method of Duff et al (1993), was then adsorbed onto the nanoparticle surface. The adsorbed colloid was used as nucleation sites for reduction of additional gold onto the surface to generate a contiguous shell of gold. Nanoshells were evaluated by their optical absorption profiles using a Cary 50 BIO UV Vis spectrophotometer and size distribution under scanning electron microscopy (XL30, Philips Electron Optics, Netherlands). The nanoshells used in the following study had a 110 nm core diameter with an 11 nm thick gold shell and peak extinction at ~820 nm.

Nanoshell anti-HER2 conjugation

PEG-conjugated anti-HER2/neu (0.9 mg/mL) was added to 8.8×10^8 nanoparticles/ml (absorption=1.5 at 800 nm at 1 cm path length) to obtain a final antibody concentration of 7.5 μg/mL. The suspension was reacted at 4°C overnight. A 0.05 mM PEG-SH solution was added to the nanoshells at a volume ratio of 9 parts nanoshells:1 part PEG-SH and reacted at 4°C overnight. Immunonanoshells were divided as 1 mL aliquots into 2.0 mL eppendorf tubes (Sigma-Aldrich). The aliquots were centrifuged at 500 g for 5 min (Eppendorf Centrifuge 5415C). Immediately, the supernatant was removed and aliquots were resuspended in McCoy's 5a medium supplemented with 10% fetal bovine serum (FBS), 1.8 mM L-glutamine, 90 units/mL penicillin, and 0.9 μg/mL streptomycin to obtain a final nanoshell concentration of 2.9×10^9 particles/mL (absorption=5 at 800 nm at a 1 cm path length).

Quantification of the number of antibodies per nanoshell (ELISA)

Immunonanoshells were incubated with horseradish peroxidase-labeled (HRP) anti-mouse IgG (Sigma-Aldrich, A3682) for 1 hour. Nonspecific reaction sites were blocked with a 3% solution of bovine serum albumin (BSA). Nanoshells were rinsed to remove any unbound IgG. The HRP bound to the immunonanoshells was developed with 3,3',5,5'-tetramethylbenzidine and compared with a HRP anti-mouse IgG standard curve ranging from $7x10^{-6}$ to $7x10^{-9}$ g/ml. Results were read using a spectrophotometer (Cary BIO 50, Varian, CA, USA) at 450 nm.

Imaging of antibodies bound to nanoshells

Immunonanoshells, prepared as described above, were incubated with gold-labeled anti-mouse IgG (Molecular Probes, Eugene, OR, USA) for 1 hour. Nonspecific reaction sites were blocked with a 3% solution of BSA. Nanoshells were rinsed to remove any unbound IgG. Samples were mounted on copper grids and imaged with a JEOL 2010 transmission electron microscope (TEM, JEOL Ltd., Japan).

Cell maintenance

Chemicals were obtained from Sigma-Aldrich unless otherwise stated. SK-BR-3 breast carcinoma cells were obtained from American Type Culture Collection (ATCC, Manassas, VA, USA). Cells were maintained in McCoy's 5a medium supplemented with 10% FBS, 1.8 mM L-glutamine, 90 units/mL penicillin, and 0.9 μg/mL streptomycin. MCF-7 breast carcinoma cells were obtained from ATCC and maintained in Eagle's Minimal Essential Medium supplemented with 10% FBS, 1.8 mM L-glutamine, 90 units/mL penicillin, 0.9 μg/mL streptomycin, and 0.01 mg/mL bovine insulin. Human dermal fibroblasts (HDFs) were obtained from ATCC and maintained in Dulbecco's Modified Eagle's Medium (DMEM) supplemented with 10% FBS, 1.8 mM L-glutamine, 90 units/ml penicillin, and 0.9 μg/ml streptomycin. Cells were incubated at 37°C in a 5% CO_2 environment. For monoculture experiments, cell were seeded into 24-well trays at $1x10^4$ cells/cm^2 and cultured to near confluency. For side-by-side co-culture experiments, where 2 cell types were located adjacent to one another, each cell type was grown separately on glass cover slips coated in 1% gelatin. Immediately prior to nanoshell incubation, 2 cover slips containing different cell types were aligned such that the cover slips set side-by-side on a glass-chambered slide without a gap separating them.

Photothermal destruction of cells incubated with immunonanoshells

Cells were rinsed 3 times in phosphate buffered saline (PBS, pH 7.4). Nanoshells were mixed with 10x McCoy's 5A medium without FBS at a ratio of 9:1. 500 μl of nanoshell suspension was added to the cell cultures. Cells were returned to the 37°C incubator for 45 minutes. Following incubation, cells were rinsed 3 times in PBS and then covered in McCoy's 5A medium. Cells were exposed to NIR laser irradiation (Coherent, 820 nm, 0.8 W/m^2 for 7 min) and then returned to the 37°C incubator overnight.

Silver staining to evaluate nanoshell binding

Cells were fixed with a 2.5% formalin solution for 10 minutes then rinsed 3 times with DI water. A silver staining kit (Amersham Biosciences, Piscataway, NJ, USA) was used to stain cells, depositing silver onto the gold nanoshell surfaces, to allow visualization of nanoshell binding to cells via light microscopy.

Viability staining

A Live/Dead Stain Kit (calcein AM and ethidium homodimer, Molecular Probes, CA, USA) was used to evaluate cell viability after NIR treatment. Cells were then examined by fluorescence microscopy (Ziess Axiovert 135, Thornwood, NY, USA).

Results

Quantification and imaging of antibodies on nanoshells

The anti-HER2 conjugated nanoshells bound a significant number of antibodies compared with PEG-coated nanoshells (p<0.05). Each immunonanoshell was conjugated with 152±128 anti-HER2 antibodies. The ELISA-style assay confirmed that no antibodies were present on the nanoshells coated with PEG only (–16±19 antibodies/nanoshell). In the TEM image of the nanoshell (Figure 1), the binding of the gold colloid-labeled secondary antibody can be clearly seen. Additionally, the visualization of antibody conjugation is in good agreement with the quantification achieved using the ELISA-style assay.
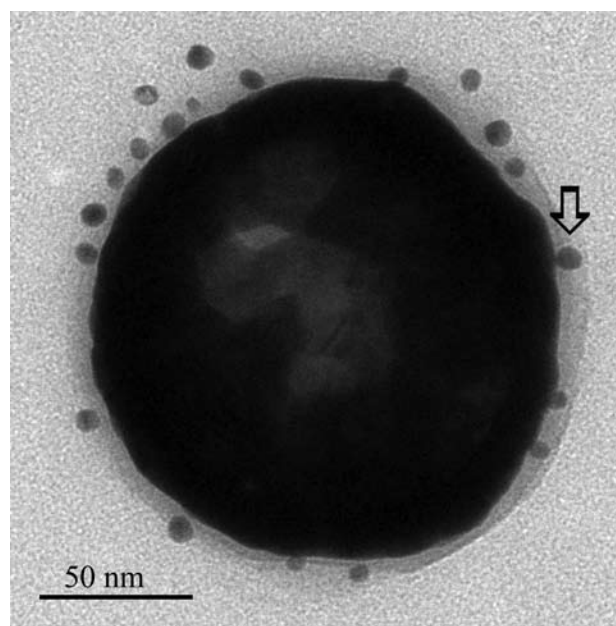
Figure 1 Transmission electron micrograph of an immunonanoshell with gold-labeled antibodies (example indicated by arrow) shows several antibodies bound to the nanoshell surface within the hazy polyethylene glycol (PEG) layer.

Photothermal destruction of mono-cultured cells incubated with immunonanoshells

Anti-HER2 conjugated nanoshells associated specifically with HER2 expressing cells at sufficient concentrations such that the combination of nanoshells and NIR light-induced cell death. Anti-HER2 conjugated nanoshells bound to the SK-BR-3 cell surface, as seen in the silver stain image (Figure 2f), and induced cell death within the laser exposure area, as seen in the viability stain (Figure 2c). Incubation of SK-BR-3 cells with nanoshells conjugated with a non-specific anti-IgG (Figure 2a, d) or with PEG alone (Figure 2b, e) did not facilitate the binding of the nanoshells to the cell surface. Anti-HER2 conjugated nanoshells did not bind to MCF-7 cells, which do not express HER2.

Photothermal destruction of targeted cells in co-culture

In Figure 3, where the two cell types were adjacent to one another, only cells within the laser spot and of the targeted cell type were destroyed by the treatment. The HDFs, also exposed to the NIR light, did not die. When co-cultures were incubated with PEG-coated nanoshells (Figure 3b), both cell types remained viable after laser irradiation. Only the HER2-expressing SK-BR-3 cells bound with anti-HER2 immunonanoshells and irradiated with NIR laser died.

Discussion

The anti-HER2 conjugated nanoshells bound a significant number of antibodies. The density of ~152 anti-HER2 antibodies per immunonanoshell exceeded that obtained on immunoliposomes of similar size, where 30–50 antibodies per liposome were achieved (Cerletti et al 2000; Park et al 2002). The ELISA-style data are supported by the TEM images (Figure 1) where the gold-labeled secondary antibody bound to the anti-HER2 antibody speckles the outer surface of the conjugated nanoshell. TEM imaging and the ELISA
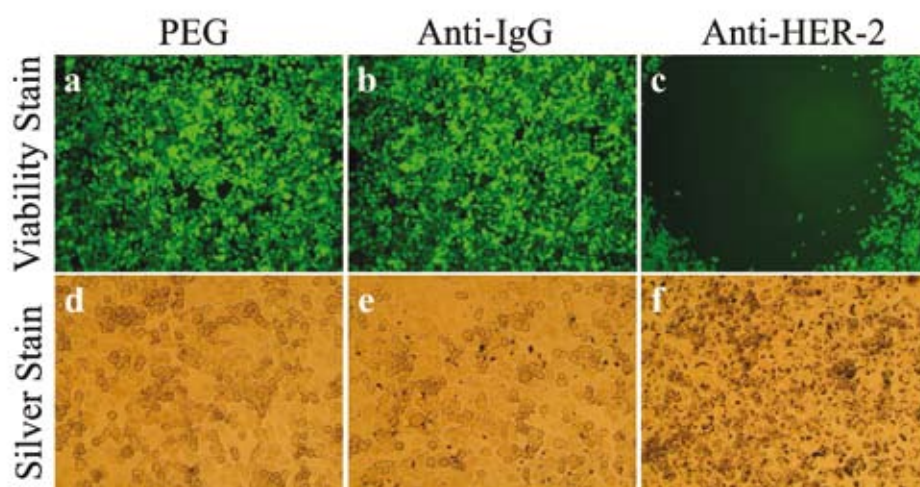

Figure 2 Antibody conjugated nanoshells bound to cells when the appropriate antigen was present. SK-BR-3 cells were incubated with PEG-coated nanoshells (a, d), anti-IgG conjugated nanoshells (b, e), and anti-HER2 conjugated nanoshells (c, f). Following laser exposure, a region of cell death corresponding to the laser spot resulted in groups incubated with anti-HER2 conjugated nanoshells (c). Cells incubated with PEGylated or anti-IgG conjugated nanoshells continued to live. Silver staining (d–f) showed maximal binding of anti-HER2 conjugated nanoshells to the SK-BR-3 cells (f).

Abbreviations: HER2, epidermal growth factor receptor; PEG, polyethylene glycol.
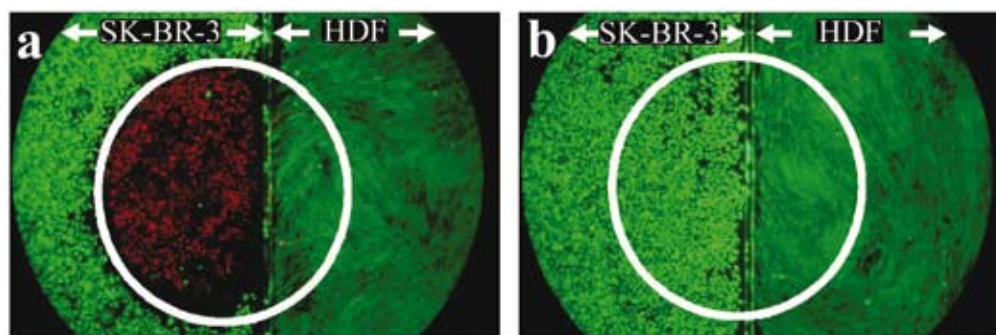
Figure 3 Two cell types, SK-BR-3 (left side of a and b) and HDF (right side of a and b) cells, were grown on glass cover slip and aligned as shown prior to the experiment. (a) Anti-HER2 immunonanoshells bound to the HER2 expressing SK-BR-3 cells resulted in targeted cell death after laser irradiation. The laser area is outlined in white. (b) Nanoshells coated in PEG only did not bind cells and laser irradiation produced no area of cell death.

Abbreviations: HDF, human dermal fibroblasts; HER2, epidermal growth factor receptor; PEG, polyethylene glycol.

assay confirmed that no antibodies were present on the nanoshells coated with PEG only.

Anti-HER2 conjugated immunonanoshells bound to the SK-BR-3 cell surface and induced cell death within the laser exposure area. Anti-HER2 nanoshells did not bind to MCF-7 cells, which do not express HER2. Incubation of SK-BR-3 cells with nanoshells conjugated with a nonspecific anti-IgG or with PEG alone did not facilitate the binding of the nanoshells to the cell surface. As previously seen, cell death requires the simultaneous exposure of cells to both nanoshells and NIR light (Hirsch et al 2003; Loo et al 2004, 2005). Nonspecific anti-IgG nanoshells and PEG nanoshells, not bound to cell surfaces, were rinsed away during washing thus preventing cell death after NIR irradiation.

The cellular specificity of the nanoshell treatment achieved through the addition of the antibody was verified in the co-culture experiments. In Figure 3, where the SK-BR-3 cells and HDFs were adjacent to one another, only cells within the laser spot and of the targeted cell type died. NIR light was applied to the co-culture overlapping both cell types simultaneously. An area of cell death resulted only on the targeted SK-BR-3 cells incubated with anti-HER2 immunonanoshells. When co-cultures were incubated with PEG-coated nanoshells, both cell types continued to live after laser irradiation. Only the HER2-expressing cells bound with anti-HER2 immunonanoshells and irradiated with the NIR laser died, even when they were in close proximity to nontargeted healthy cells.

The in vitro studies detailed here demonstrate the ability of the immunonanoshells to bind specifically and to facilitate the thermal therapy locally on an individual cell level. Within tumors, the active binding of nanoshells will increase the accumulation by promoting longer retention times in the tumor. The incorporation of an antibody onto the nanoshell surface should increase the uptake within targeted tissues in vivo.

Conclusions

The addition of a tumor-specific antibody should increase the specificity of the nanoshell therapy, as indicated by these initial in vitro results. Immunonanoshells bind to targeted cells whether the cells are alone or adjacent to healthy cells. Upon laser irradiation, the cells bound by nanoshells are killed, leaving the healthy cells unharmed. Successful treatments not only require the laser and nanoshells to be present simultaneously, but in order for nanoshells to be present in vitro, they must actively bind to the targeted cell type. In vivo, the accumulation of immunonanoshells within a tumor will not simply rely on the enhanced permeability of tumors as previously demonstrated (O'Neal et al 2004). In addition to utilizing the elevated permeability of tumors, the ability of immunonanoshells to bind tumor cells should further promote the localization of nanoshells within the tumor. The increased specificity by the antibodies has tailored the immunonanoshell for higher accumulations at targeted tissues and thus improved the nanoshell therapeutic efficiency.

Acknowledgments

References

Anderson SA, Rader RK, Westlin WF, et al. 2000. Magnetic resonance contrast enhancement of neovasculature with $_{v}3$-targeted nanoparticles. *Magn Reson Med*, 44:433–9.

Arap W, Pasqualini R, Ruoslahti E. 1998. Cancer treatment by targeted drug delivery to tumor vasculature in a mouse model. *Science Magazine*, 16:377–80.

Averitt RD, Westcott SL, Halas NJ. 1999. Linear optical properties of gold nanoshells. *J Opt Soc Am B*, 16:1824–32.

Backer MV, Backer JM. 2001. Targeting endothelial cells overexpressing VEGFR-2: Selective toxicity of shiga-like toxin-VEGF fusion proteins. *Bioconjug Chem*, 12:1066–73.

Carlsson J, Nordgren H, Sjostrom J, et al. 2004. HER2 expression in breast cancer primary tumours and corresponding metastases. Original data and literature review. *Br J Cancer*, 90:2344–8.

Cerletti A, Drewe J, Fricker G, et al. 2000. Endocytosis and transcytosis of an immunoliposome-based brain drug delivery system. *J Drug Target*, 8:435–46.

Cortez-Retamozo V, Lauwereys M, Hassanzadeh G, et al. 2002. Efficient tumor targeting by single-domain antibody fragments of camels. *Int J Cancer*, 98:456–62.

Duff DG, Baiker A, Edwards P. 1993. A new hydrosol of gold clusters. 1. Formation and particle size variation. *Langmuir*, 9:2301–9.

Hashizume H, Baluk P, Morikawa S, et al. 2000. Openings between defective endothelial cells explain tumor vessel leakiness. *Am J Pathol*, 156:1363–80.

Hirsch LR, Stafford RJ, Bankson JA, et al. 2003. Nanoshell-mediated near-infrared thermal therapy of tumors under magnetic resonance guidance. *Proc Natl Acad Sci U S A*, 100:13549–54.

Kämmerer U, Thanner F, Kapp M, et al. 2003. Expression of tumor markers on breast and ovarian cancer cell lines. *Anticancer Res*, 23:1051–6.

Loo C, Lin A, Hirsch L, et al. 2004. Nanoshell-enabled photonics-based imaging and therapy of cancer. *Technol Cancer Res Treat*, 3:33–40.

Loo C, Lowery A, Halas N, et al. 2005. Immunotargeted nanoshells for integrated cancer imaging and therapy. *Nano Lett*, 5:709–11.

McDermont RS, Beuvon F, Pauly M, et al. 2002–03. Tumor antigens and antigen-presenting capacity in breast cancer. *Pathobiology*, 70:324–32.

Noble CO, Kirpotin DB, Hayes ME, et al. 2004. Development of ligand-targeted liposomes for cancer therapy. *Expert Opin Ther Targets*, 8:335–53.

Oldenburg SJ, Averitt RD, Westcott SL, et al. 1998. Nanoengineering of optical resonances. *Chem Phys Lett*, 288:243–7.

O'Neal DP, Hirsch LR, Halas NJ, et al. 2004. Photo-thermal tumor ablation in mice using near infrared-absorbing nanoparticles. *Cancer Lett*, 209:171–6.

Park JW, Hong K, Kirpotin DB, et al. 2002. Anti-HER2 immunoliposomes: enhanced efficacy attributable to targeted delivery. *Clin Cancer Res*, 8:1172–81.

Park JW, Kirpotin DB, Hong K, et al. 2001. Tumor targeting using anti-her2 immunoliposomes. *J Control Release*, 74:95–113.

Reynolds AR, Moghimi SM, Hodivala-Dilke K. 2003. Nanoparticle-mediated gene delivery to tumor neovasculature. *Trend Mol Med*, 9:2–4.

Slamon DJ, Godolphin W, Jones LA, et al. 1989. Studies of the HER-2/neu proto-oncogene in human breast and ovarian cancer. *Science*, 244:707–12.

Stöber W, Fink A, Bohn E. 1968. Controlled growth of monodisperse silica spheres in the micron size range. *J Colloid Interface Sci*, 26:62–9.

Tarli L, Balza E, Viti F, et al. 1999. A high affinity human antibody that targets tumoral blood vessels. *Blood*, 94:192–8.

Verel I, Heider K-H, Siegmund M, et al. 2002. Tumor targeting properties of monoclonal antibodies with different affinity for target antigen CD44V6 in nude mice bearing head-and-neck cancer xenografts. *Int J Cancer*, 99:396–402.

Weissleder HB. 2001. A clearer vision for *in vivo* imaging. *Nat Biotechnol*, 19:316–7.

Welch A, van Gemert M (eds). 1995. Optical-thermal response of laser-irradiated tissues. New York: Plenum Press.

Wu X, Liu H, Liu J, et al. 2003. Immunofluorescent labeling of cancer marker Her2 and other cellular targets with semiconductor quantum dots. *Nat Biotechnol*, 21:41–6.

Networks of gold nanoparticles and bacteriophage as biological sensors and cell-targeting agents

Glauco R. Souza*, Dawn R. Christianson*, Fernanda I. Staquicini*, Michael G. Ozawa*, Evan Y. Snyder†, Richard L. Sidman‡§, J. Houston Miller¶, Wadih Arap*§, and Renata Pasqualini*§

*University of Texas M. D. Anderson Cancer Center, 1515 Holcombe Boulevard, Houston, TX 77030; †Burnham Institute, 10901 North Torrey Pines Road, La Jolla, CA 92037; ¶Department of Chemistry, George Washington University, 725 21st Street NW, Washington, DC 20052; and ‡Harvard Medical School and Department of Neurology, Beth Israel Deaconess Medical Center, Harvard Institutes of Medicine, 77 Avenue Louis Pasteur, Boston, MA 02115

Biological molecular assemblies are excellent models for the development of nanoengineered systems with desirable biomedical properties. Here we report an approach for fabrication of spontaneous, biologically active molecular networks consisting of bacteriophage (phage) directly assembled with gold (Au) nanoparticles (termed Au–phage). We show that when the phage are engineered so that each phage particle displays a peptide, such networks preserve the cell surface receptor binding and internalization attributes of the displayed peptide. The spontaneous organization of these targeted networks can be manipulated further by incorporation of imidazole (Au–phage–imid), which induces changes in fractal structure and near-infrared optical properties. The networks can be used as labels for enhanced fluorescence and dark-field microscopy, surface-enhanced Raman scattering detection, and near-infrared photon-to-heat conversion. Together, the physical and biological features within these targeted networks offer convenient multifunctional integration within a single entity with potential for nanotechnology-based biomedical applications.

target | fractal | hydrogel | stem cell | assembly

In nature, the assembly of molecules and particles is often directed by hydrophobic, van der Walls, and/or electrostatic interactions (1, 2). Biological systems in particular are driven toward energetically favorable structures that have molecular selectivity and recognition and thus serve as models for nanoscale engineering-based molecular assembly. Given that filamentous bacteriophage (phage) (3–6) are resistant to harsh conditions such as high salt concentration, acidic pH, chaotropic agents, and prolonged storage (6), they are suitable candidate building blocks to meet the challenges of bottom-up nanofabrication (1, 2). Moreover, the pIII minor capsid protein of the phage can be easily engineered genetically to display ligand peptides that will bind to and modify the behavior of target cells in selected tissues (3, 4, 6–8). Thus, the tactic of integrating phage display technology with tailored nanoparticle assembly processes offers opportunities for reaching specific nanoengineering and biomedical goals (1–4, 6, 8–10).

In this work, we show that such networks are biocompatible and preserve the cell-targeting and internalization attributes mediated by a displayed peptide and that spontaneous organization (without genetic manipulation of the pVIII major capsid protein), and optical properties can be manipulated by changing assembly conditions. By taking advantage of gold (Au) optical properties (11–16), we generated Au–phage networks that, in addition to targeting cells, can function as signal reporters for fluorescence and dark-field microscopy and near-infrared (NIR) surface-enhanced Raman scattering (SERS) spectroscopy. Notably, this strategy maintains the low-cost, high-yield production of complex polymer units (phage) in host bacteria and bypasses many of the challenges in developing cell/peptide detection tools, such as complex synthesis and coupling chemistry, poor solubility of peptides, the presence of organic solvents, and weak detection signals. We also show that, despite the evident structural contrast between the Au–phage fractal networks and the usual geometrically symmetrical nanostructures (17, 18), these networks can effectively integrate the unique signal reporting properties of Au nanoparticles while preserving the biological properties of phage.

Results and Discussion

Design, Synthesis, and Characterization of Au–Phage Networks. We hypothesized that spontaneous assembly of Au nanoparticles onto phage occurs without genetic modification of the pVIII major capsid proteins or complex conjugation chemistry (Fig. 1a). To test that hypothesis, we generated biologically active networks of directly assembled Au–phage complexes by optimizing the phage concentration required to convert Au colloidal solutions into hydrogels, which is the precursor for generating network suspension (Fig. 1b). We first tested the biocompatibility and cytotoxicity of these networks by showing that C17.2 murine neural stem cells widely infiltrate the Au–phage hydrogel network structure indicated by the stretched Au–phage fibers (Fig. 1 c and d) and continue to proliferate (data not shown). Next, we found that the surface plasmon absorption wavelengths of the Au–phage complexes can be modulated by changes in phage input and the presence of imidazole (imid). TEM, elastic light scattering, visible/NIR absorption and NIR SERS confirmed Au–phage assembly. Data on these findings are presented in the following paragraphs.

We used two strategies to generate biologically active networks: with or without the metal-binding molecule imid (Fig. 1a) (11, 19). The different assemblies yielded distinct network organizations, as revealed by transmission electron microscopy (TEM) (Fig. 1e). Au nanoparticles appear as black dots connecting long, white, filamentous phage structures. Once assembled, the phage in these networks still maintained their ability to infect bacteria (Fig. 1f) and showed distinctive physical characteristics such as fractal structure and NIR optical properties. Because fractal patterns are often observed in naturally occurring assembly processes (19, 20), we evaluated whether the spontaneously assembled structures would show fractal traits and whether this feature could distinguish the structural differences between the networks. The fractal dimension (Df) analysis of the two-dimensional TEM images (Au–phage, 1.32 ± 0.12; Au–phage–imid, 1.78 ± 0.14; t test, $P < 0.0001$) correlated with the apparent aggregation of Au nanoparticles within each network. The lower Df for Au–phage indicated looser, more dispersed structures observed by TEM (Fig. 1e Upper); in comparison, the higher Df for the Au–phage–imid reflected the denser networks as a result of imidazole-induced aggregation
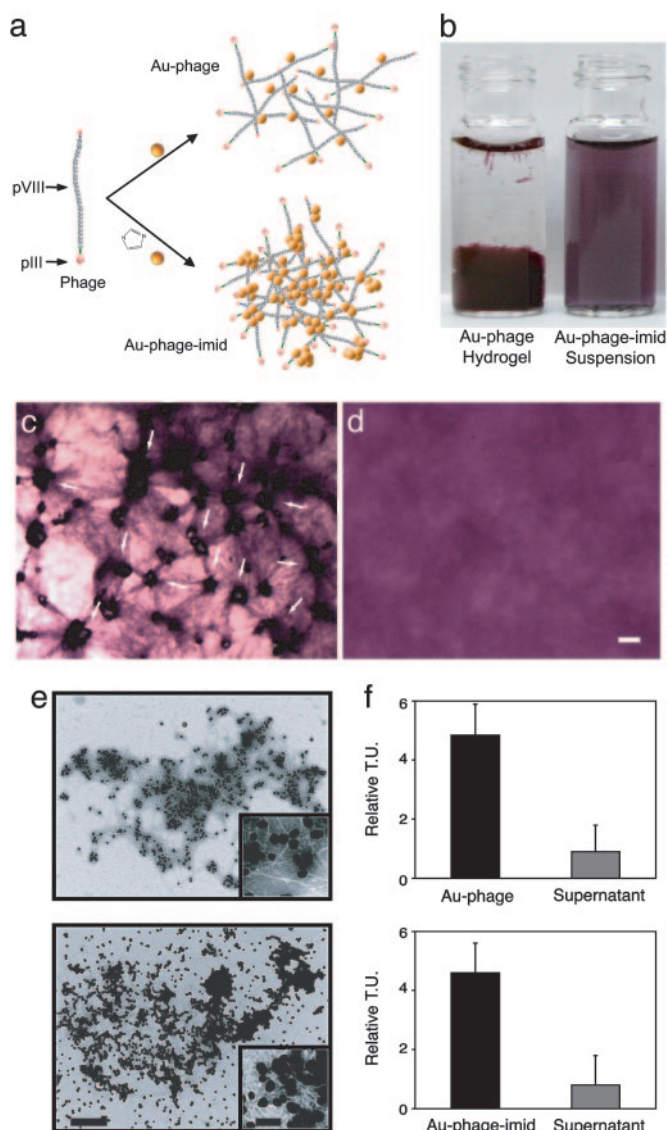

CHEMISTRY

BIOCHEMISTRY

Fig. 1. Concept and biological/structural characterization of Au–phage and Au–phage–imid networks. (*a*) Strategy for Au assembly onto phage nanoparticles. Imid and the yellow spheres [Au nanoparticles (not drawn to scale); the Au particles have a diameter of 44 ± 9 nm, and the pVIII capsid peptide has a thickness of ≈ 6 nm]. (*b*) Vials of nanoparticle solutions: Au–phage hydrogel (*Left*) and suspension of purified Au–phage–imid (*Right*; suspended from hydrogels precursor). (*c* and *d*) Hydrogel formed with RGD-4C-displaying phage. (Scale bar, 20 μm.) (*c*) C17.2 murine neural stem cells cultured within hydrogel for 24 h. Cell accumulation followed by cell-induced network displacement is shown (arrows point to cells within the network). (*d*) Control hydrogel (no cells). (*e*) TEM of purified networks: Au–phage (*Upper*) and Au–phage–imid (*Lower*). (Scale bar, 500 nm; inset scale bar, 100 nm.) (*f*) Bacterial infection with purified Au–phage (*Upper*) and Au–phage–imid (*Lower*) networks; TU are shown for purified and functional Au–phage and Au–phage–imid solution and for unbound phage present in the supernatant from centrifuged network solutions.

(Au–imid) of Au nanoparticles (Fig. 1*e Lower*). Consistently, angle-dependent elastic light-scattering Df analysis (based on Rayleigh–Debye–Gans scattering theory) (21, 22) revealed the same Df trend for the networks in solution (data not shown) as that obtained from the TEM image analysis. The characteristic high-surface area of fractal networks (23) can improve accessibility to binding sites, which is a central feature for fabricating cell-targeting systems.
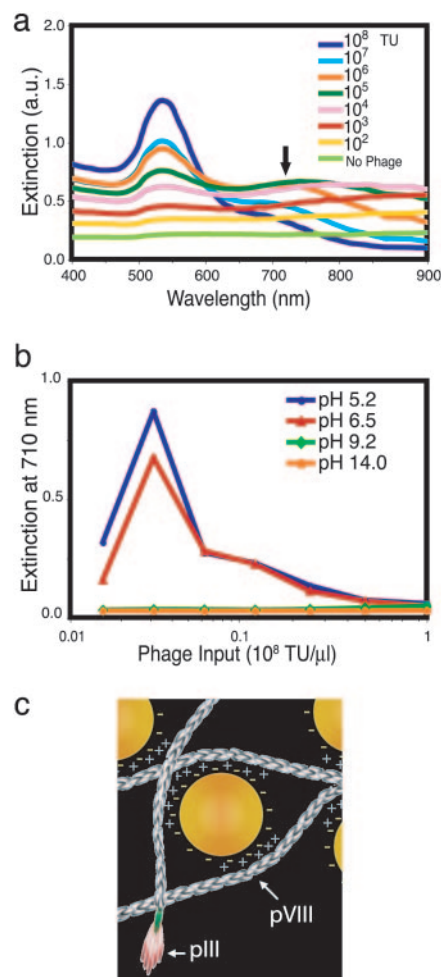

Fig. 2. Mechanism of assembly for Au–phage networks. (*a*) Light-absorption spectrum at various phage input (indicated in the legend) in the presence of 0.25 M NaCl (no phage, bottom curve). (*b*) Light extinction at 710 nm for Au–phage solutions as a function of phage input at various pH levels (10 mM boric acid, pH 5.2; 10 mM sodium borate buffer, pH 6.5; 10 mM sodium borate, pH 9.2; or 10 mM NaOH, pH 14.0). (*c*) Cartoon illustrating electrostatic interaction of Au (yellow spheres) with phage [elongated structures (not drawn to scale)]. Arrows point to pVIII major capsid protein and pIII minor capsid protein.

Next, we evaluated network formation by monitoring the shift in surface plasmon absorption into the NIR spectral region when phage concentration was increased [Fig. 2 *a* (spectra red shift indicated with an arrow) and *b*]. The red shift, which generally occurs when the distance between Au nanoparticles (d_{Au}) is less than the average particle diameter ($2r_{Au}$; $d_{Au} < 2r_{Au}$), is usually a good diagnostic for Au–Au interactions because of particle agglomeration (14–16).

It is our hypothesis that the native pVIII major capsid proteins function as the binding sites for the Au–phage network assembly (Fig. 1*a*). Given the absence of typical metal-binding amino acid residues (such as Cys and His) on the pVIII protein, the direct assembly of Au nanoparticles onto phage should be largely directed by electrostatic interactions (14–16, 24–29). It is well known that Au nanoparticles can be made to agglomerate by varying solution ionic conditions (specifically, agglomeration shows a dependence on ionic strength). In solution, Au nanoparticles are coated with a layer of adsorbed citrate anions (citrate from Au nanoparticle synthesis procedure) (14–16, 30). Attraction between like-charged particles can occur because of
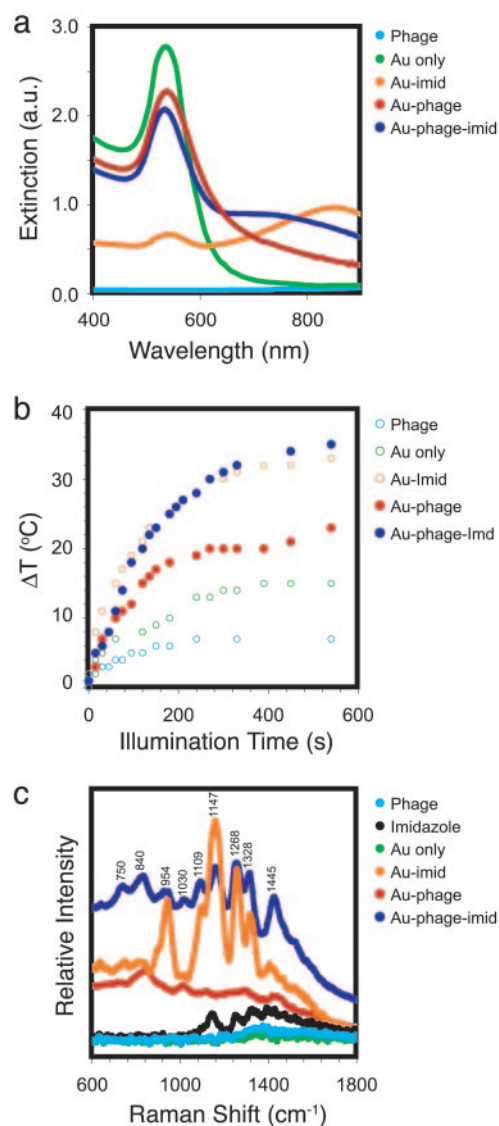
Fig. 3. Optical and physical characterization of Au–phage networks. (*a*) Light-absorption spectrum of purified and suspended Au–phage–imid (dark blue) and Au–phage (red). (*b*) Temperature as a function of illumination (785-nm laser light) time of Au–phage–imid (blue) and Au–phage (red) solutions; the controls (○) are the solutions of Au (green), Au–imid (orange), and phage (cyan). The concentrations of all solutions carrying Au were normalized according to the area under the absorption region of the spectra (>475 nm). The solution temperature was measured with a digital temperature probe (Teflon-coated cables of type-K beaded sensor coupled to a Fisher traceable double thermometer with computer output from Fisher Scientific) immersed in 300 μl of solution and 5 mm away from the laser focal point. (*c*) SERS of Au–phage–imid (blue) and Au–phage (red) measured in water.

correlated fluctuations in the surrounding ion clouds. Thus, the presence of ions can be used to mediate the agglomeration. For example, Au nanoparticles agglomerate in the presence of salt as indicated by a broadening and shift to longer wavelength in the surface plasmon absorption peak (Fig. 2*a*, no phage, green spectrum). It has been reported that phage particles (both fd and M13) also act as polyanionic particles in solution with several negative surface charges associated with each of the ≈2,700 copies of the major capsid protein (fd is more anionic than M13 because of the replacement of Asn-12 with Asp-12) (26–29). In addition, bundles of phage form from like-charge attraction (26–29), and analogous to the mediation of Au nanoparticle

agglomeration, solubilization of such bundles depends on solution ionic strength. We found that Au agglomeration induced by 0.25 M NaCl (Fig. 2*a*, no phage, green spectrum) could be minimized by Au–phage interactions (indicated by the small red shift) when phage input increased, which suggests a similar physical interpretation for binding in the mixed phage/Au systems as that found in the Au–Au and phage–phage binding. These findings indicate a greater stability of the Au–phage networks in the presence of salt.

To explore further the role of electrostatics in the assembly mechanism, we monitored network formation at a series of solution pH levels (Fig. 2*b*). Under all tested conditions, phage have an overall negative charge, but we observed formation of the Au–phage networks only at a pH level well below the calculated pI (9.4) of the individual pVIII proteins (31). For solutions in which networks did form (as indicated by the extinction at 710 nm attributable to Au aggregation), lower pH levels led to increased extinction. These results imply that the pVIII positive charge at pH≤7 mediates the mechanism of assembly through opposite-charge interaction (Fig. 2*c*) between the citrate-adsorbed Au nanoparticles and the thin and long phage surface (6 × 1,000 nm) (26–29). Finally, the data in Fig. 2*b* show that at a low phage input level, the aggregation falls off because of titration of phage-binding sites in the solution.

Next, we compared the optical properties of the purified Au–phage and Au–phage–imid network solutions. The more compact Au–phage–imid complexes had a relatively larger red shift in the extinction spectrum with increased absorptivity in the NIR wavelength region (700–900 nm; Fig. 3*a*) (16, 32). To support the assertion that NIR photons were also being absorbed instead of only scattered by the larger agglomerates, we measured the temperature change for the two network solutions as a direct function of illumination time by using NIR incident laser light (785 nm; Fig. 3*b*). There was a substantial temperature change for both the Au–phage and Au–phage–imid networks from the efficient photon-to-heat conversion, which demonstrates that the NIR photons are being absorbed as a result of the surface plasmon absorption red shift.

Finally, we used NIR SERS spectroscopy to characterize the interactions among Au, phage, and imid (Fig. 3*c* and Table 1). Differences between the spectra of Au–phage and Au–phage–imid seem to arise from the distinct chemical environments in the vicinity of the Au nanoparticles. Signature bands for phage and Au interaction emerged by identifying common attributes when comparing NIR SERS spectra intrinsic with each of the networks (33, 34) and controls. First, from an analysis of control experiments without phage (Au–imid, Fig. 3*c*, orange curve), the 1,030-cm^{-1} band is a SERS feature that is detected only in the networks spectra (33–35) and could be assigned to Tyr, Phe, and/or Met (pVIII major capsid protein). Second, the mode at 1,445 cm^{-1} is likely attributed to Trp and/or Met (33–35). A third peak was seen only in the Au–phage spectrum (the broad and low intensity peak centered at 840 cm^{-1}), which has been assigned to Tyr residues present within the pVIII (33, 34). Several other peaks (750, 840, 954, 1,109, 1,169, and 1,268 cm^{-1}) present in the Au–phage–imid spectrum have been observed in systems in which imidazole is adsorbed onto Au (36) or silver (37) electrodes. Additional peaks in the Au–phage spectrum might be attributable to exposed residues on the major capsid. For example, strong SERS signals near 1,147 and 1,301 cm^{-1} have been observed in systems of both Lys and Met with Au nanoparticles (the last three amino acids of the exposed N-terminal end of the pVIII capsid are Lys-Lys-Met) (35).

Targeted and Fluorescence-Enhanced Cell Detection. To evaluate whether Au–phage-based networks could be efficiently used to study peptide ligand binding to receptors on the cell surface as well as receptor-mediated properties such as phage internalization, we

CHEMISTRY

BIOCHEMISTRY

Table 1. Assignment of Raman bands and amino acids in the SERS spectra shown in Fig. 3c

Au–phage, cm⁻¹	Au–phage–imid, cm⁻¹	Au–imid, cm⁻¹	Imid, cm⁻¹	Side chain or imid designation	Vibrational assignment*	Ref(s).
	670	650		Imid	γ_{ring} (628 cm⁻¹, Raman)	36 and 37
	750	764		Imid	γ_{ring} (743 cm⁻¹, SERS)	36
	840	838		Imid	γ_{ring} (832 cm⁻¹, SERS)	37
854				Tyr, Ile, and/or Met	γ_{ring} (853 cm⁻¹, Raman), γ(CC) (874 cm⁻¹, Raman and SERS)	34 and 35
	954	954	931	Imid	γ(NH) + δ_{ring} (950 cm⁻¹, SERS)	36 and 37
1,030	1,030			Tyr, Phe, and/or Met	γ(CH) (1,033 cm⁻¹, SERS), ν(CC, CN, CO) (1,031 cm⁻¹, Raman)	33
	1,109	1,109		Imid	δ(CH) + ν_{ring} (1,097 cm⁻¹, SERS)	36 and 37
1,147				Met and Lys	ν(CC) (1,158 cm⁻¹, Raman)	33
	1,169	1,169	1,160	Imid	δ_{ring} (1,164 cm⁻¹, SERS)	36 and 37
	1,268	1,268	1,263	Imid	δ(CH) (1,265 cm⁻¹, SERS)	36 and 37
1,301				Amide III, Tyr, Ala, Lys, Ile, Val, Ser, Gly, Trp, and pVIII main chain	δ(CH) and ν(CC) (1,300 cm⁻¹, Raman)	33–35
	1,328	1,328		Imid	ν_{ring} (1,329 cm⁻¹, SERS)	36 and 37
1,445	1,436	1,415	1,436	Trp and Imid	ν_{ring} (1,449 cm⁻¹, Raman)	36 and 37

*δ, in-plane bending; γ, out-of-plane bending; ν, stretching.

performed immunofluorescence-staining assays with antibodies directed to the phage capsid. Melanoma cells were chosen because they express high levels of α_v integrins (38), the cell surface receptor for a well characterized phage displaying the peptide CDCRGD-CFC (termed RGD-4C) (39). Here we show that the targeting and receptor-mediated internalization capabilities of the RGD-4C peptide remained intact within the Au–RGD-4C networks (Fig. 4a). Accordingly, internalization was inhibited (40) in a dose-dependent manner when cells were preincubated with the RGD-4C synthetic peptide before incubation with Au–RGD-4C networks (Fig. 4b). The likely synergy between the receptor-mediated phage internalization and electromagnetically induced surface enhancement of the Au nanoparticles (41) resulted in an increase in the enhanced fluorescence for the targeted Au–RGD-4C networks (Fig. 4a) relative to those observed for the RGD-4C phage alone (Fig. 4c). Negative controls show only background signal (Fig. 4 d–f).

Confocal Fluorescence Image Analysis. We reasoned that, when examined by confocal microscopy, Au–phage networks could serve as sensitive reporters to localize and evaluate ligand binding and receptor-mediated internalization events (Fig. 5). It seems that differences in the structure of the targeting networks result in distinct kinetics of the internalization event that follows ligand–receptor binding. By incorporating imid into the nanoarchitecture of the networks, we were able to influence the localization of the Au–phage networks to either the cell surface or cytoplasm. More compact networks with a higher Df (Au–RGD-4C-imid) preferentially localized at the cell surface, whereas those with a lower Df (Au–RGD-4C) were internalized (Fig. 5). Dynamic examination of confocal image stacks from different cell planes is consistent with this interpretation (data not shown). These results lead us to hypothesize the existence of an aggregate morphology dependence (as measured by Df) for receptor-mediated internalization, in which network changes from more to less compact structures might favor
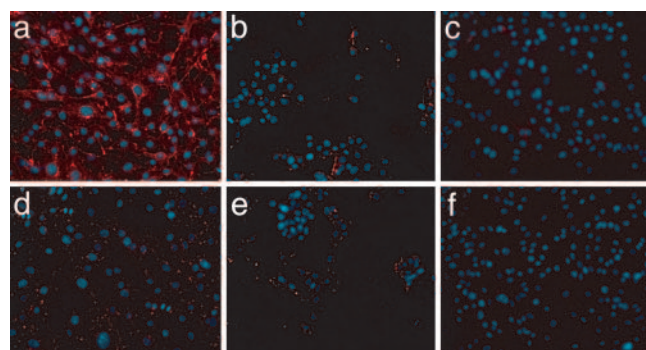

Fig. 4. Immunofluorescence-based phage binding and internalization assay with cultured melanoma cells. The red color represents fluorescence related to the RGD-4C peptide, and the blue color shows fluorescence of DAPI-stained cell nuclei. Cells were incubated with different phage preparations, all carrying a phage input of 1.0×10^7 TU. (a) Au–RGD-4C-displaying phage. (b) Cells preincubated with the RGD-4C synthetic peptide (1.0×10^{-3} nM for 30 min) followed by addition of Au–RGD-4C. (c) RGD-4C phage (no Au). (d) Au–fd-tet (negative control). (e) Cells preincubated with the RGD-4C synthetic peptide (1.0×10^{-3} nM) followed by addition of Au–fd-tet (negative control). (f) fd-tet phage (negative control).
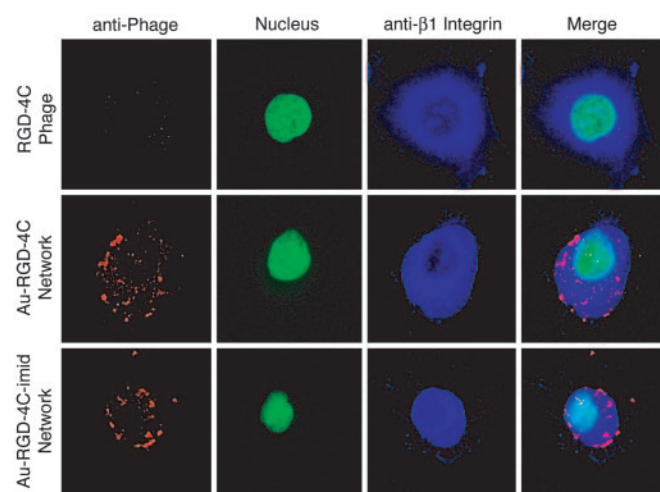
Fig. 5. Confocal fluorescence. Shown are KS1767 cells incubated with phage preparations (input of 1.0×10^7 TU) and labeled with anti-fd bacteriophage antibody (red, first column), SYTOX green nucleic acid stain (green, second column), and an anti-β_1 integrin antibody demarking the cell surface (blue, third column). The fourth column shows merged images: RGD-4C phage, Au–RGD-4C networks, and Au–RGD-4C-imid networks (controls for each of the respective RGD-4C phage preparations are shown in Fig. 8, which is published as supporting information on the PNAS web site). (Scale bar, 10 μm.)
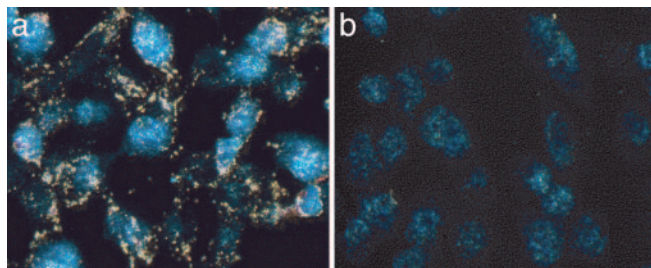
Fig. 6. Dark-field images (real color) of cell-bound Au–phage networks using light from a microscope mercury lamp. Confluent KS1767 cells incubated with phage preparations (input of 1.0×10^7 TU): Au–RGD-4C (gold color) (*a*) and Au–fd-tet (control insertless phage) networks (*b*). The blue color shows residual fluorescence from DAPI-stained cell nuclei.

cell internalization over surface binding. These findings suggest that the control of network morphology through titration with a nanoparticle complexing agent such as imid may be used to modulate their ligand-directed cell-targeting ability to match a desired application.

**Elastic Light Scattering and SERS Detection of Cells with Targeted Networks.** To extend the light-scattering attributes of the networks into analytical applications, we used dark-field microscopy to generate a single-step, fast, sensitive imaging system that does not require staining (Fig. 6). Dark-field microscopy detects scattered light, and the large scattering cross section of the Au nanoparticles (11–13) makes them ideal contrast agents. The Au–RGD-4C-targeted networks (Fig. 6*a*) when compared with RGD-4C phage without Au (data not shown) or networks formed by untargeted nanoparticles (Fig. 6*b*) showed markedly increased signal.

We next evaluated the potential of Au–phage–imid networks as cell nanosensors by integrating their unique Raman spectrum to their biological activity (Fig. 7). We measured the SERS spectra of suspended cells incubated with Au–phage–imid by using a fiber-optic probe to deliver 785-nm laser light and to collect the Raman signal into a spectrometer (Fig. 7*a*). We obtained the NIR-SERS spectra of mammalian cells incubated with Au–phage–imid networks (Fig. 7*b*). The high signal intensity (blue spectrum, Au–RGD-4C–imid) directly correlated with the level of cell binding and internalization by the networks carrying phage directed at α_v integrin receptors on the surface of target cells. Cells treated with
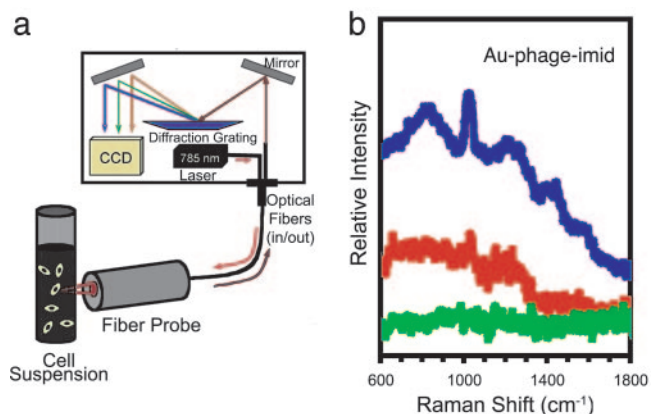

Fig. 7. Targeted cell detection by using SERS. (*a*) Cell-suspension scheme for SERS detection. Light from a laser diode (785 nm) was delivered through a fiber-optic probe to a suspension of KS1767 cells; the same fiber-optic probe collected and delivered the Raman signal. (*b*) SERS and spectra of cells incubated with Au–phage: Au–RGD-4C-imid (blue line), Au–fd-tet-imid (red line), and RGD-4C phage (green line; control, no Au) in suspension.

RGD-4C phage alone could not be differentiated from untreated cells. The sensitive detection and distinct SERS spectra for the cells treated with Au–phage–imid showed that phage, Au nanoparticles, and imid (or imid-like molecules) can be combined to form distinct Raman signal signatures as reporters for receptor-mediated targeting in cells or tissues. Peak-intensity differences in SERS spectra between the cell-free (Fig. 3*c*) and bound Au–RGD-4C–imid (Fig. 7*b*) are likely the result of cell binding and internalization events.

Because of the very high chemical selectivity and sensitivity of NIR SERS spectroscopy (42), the Raman labeling strategy described here can provide SERS-based labels for high-throughput molecular and biological detection schemes.

Materials and Methods

Au–Phage Synthesis and Quantitation. Insertless phage (fd-tet) and phage displaying the targeting peptide RGD-4C on the surface of its pIII protein were amplified in host bacteria and purified (6). The 44 ± 9-nm Au nanoparticle solution, verified by TEM image analysis, was prepared following the common citrate-reduction (30) procedure [mass ratio of 0.8 sodium citrate: 1 Au(III) chloride]. Au(III) chloride ($\geq 99.99\%$) was purchased from Sigma-Aldrich. Assembly of Au–phage complexes began with eight serial dilutions of 10^7 transducing units (TU) of phage in 200 μl of nanopure water (>18.0 MΩ). An equal volume of Au solution (200 μl), first normalized to 4.2 a.u. (extinction measured at 530 nm), was added to each dilution without mixing and allowed to stand for 12 h at room temperature (here, hydrogel formation takes place). Preparations then were mixed together in sequential order beginning with the least concentrated. Au–phage–imid networks were produced by mixing equal volumes of 10^9 TU/μl of phage and 1.0 M imid, followed by the addition of an equal volume of Au solution (4.2 a.u., extinction measured at 530 nm). Finally, the networks were purified by three consecutive centrifugation cycles ($20,800 \times g$, relative centrifugal force for 30 min) in glass sterile tubes (Becton Dickinson). Extinction of the Au–phage was measured at 530 nm and adjusted to between 1.2 and 1.5 a.u. by either diluting with water or concentrating by centrifugation. The fd-tet phage was used as a negative control to evaluate background under all of the experimental conditions. Standard bacterial infection was used to determine phage titers as described in ref. 19.

Hydrogel Biocompatibility and Cytotoxicity. Assembly of Au–phage hydrogel was achieved by adding 150 μl of Au nanoparticles (1.2 a.u for extinction at 530 nm) to 150 μl of aqueous solution of RGD-4C-displaying phage (0.14 a.u. for extinction at 270 nm) under sterile conditions in a 96-microwell plate. Hydrogels were allowed to form overnight at 4°C. After hydrogel formation, solution was exchanged by removing the supernatant, while avoiding disturbing the hydrogel structure, and then adding an equal volume of medium (10% FCS in DMEM high glucose with sodium pyruvate/2 mM glutamine/penicillin and streptomycin). C17.2 murine neural stem cells (1.0×10^4 cells per well) (43) were added and allowed to grow for several days at 37°C. Photomicrographs were taken 12 h after cell addition.

TEM Imaging. Nickel mesh grids previously coated with Formvar and evaporated with carbon were floated on drops of 0.1% poly-L-lysine (Sigma Diagnostics) on parafilm for 5 min. Excess solution was removed from the grid by carefully touching the edge of the grid onto filter paper. The grids were not allowed to dry completely in any of the following steps. The grids were floated on drops of sample on parafilm for 1 h. Excess fluid was removed as described above, and the grids then were floated on drops of 1% ammonium molybdate in 0.02% BSA in distilled water (pH 7.0) for 60 sec. Excess fluid was removed, and the grids were allowed to dry overnight. TEM images were captured by a transmission electron microscope (JEM-1010, JEOL) fitted with an AMT Advantage

(Deben UK Limited, Suffolk, U.K.) digital charge-coupled device camera system. Au nanoparticle size (44 ± 9 nm) was determined by averaging particle sizes within representative TEM fields. Df analysis of the two-dimensional TEM images was performed with the box-counting method (IMAGEJ 1.33 software). Df measurements were averaged from 10 separate TEM images of three different samples.

Cell-Targeting and Peptide-Inhibition Assay. B-16 malignant melanoma cells were seeded on 16-chamber culture slides (BD Falcon, Bedford, MA) at a density of 5×10^4 cells per well and grown overnight at $37°C$ in RPMI (GIBCO/BRL) containing 10% FBS, antibiotics, and 1% L-glutamine. The next day, each well was blocked with RPMI 30% FBS for 1 h at $37°C$ and incubated with different concentrations of RGD-4C synthetic peptide (from 10^{-3} to 10^{-10} nM) for 30 min. Suspended and purified Au–phage (10^7 TU) solutions then were added to the wells. After 12 h, fluorescence phage staining was performed as described in *Fluorescence Imaging*.

Fluorescence Imaging. After the cell-targeting assay, cells were washed and fixed with PBS containing 4% paraformaldehyde. The cells then were permeabilized with 0.2% Triton X-100, washed, and blocked with PBS containing 1% BSA, and the cells were incubated with rabbit anti-fd bacteriophage antibody (Sigma) for 2 h at room temperature followed by a 1-h incubation with Cy3-labeled anti-rabbit IgG antibody (Jackson Immuno-Research). Finally, cells again were fixed with PBS containing 4% paraformaldehyde and mounted in the presence of DAPI (nuclear staining dye, Vectashield, Vector Laboratories). Images were acquired with an Olympus fluorescence microscope equipped with an Hg lamp and a band-pass excitation filter (530–555 nm) in the fluorescence excitation path and a long-pass dichroic filter (570 nm) and long-pass filter (590 nm) in the emission path.

Confocal Fluorescence Imaging. After the cell-targeting assay, cells were incubated with rabbit anti-fd bacteriophage antibody and mouse anti-β_1 integrin antibody in PBS/1% BSA for 2 h at room temperature followed by a 1-h incubation with Cy3-labeled anti-rabbit IgG antibody and Cy5-labeled anti-mouse IgG antibody diluted in PBS containing 1% BSA (Jackson Immuno-Research). SYTOX green nucleic acid stain (Molecular Probes) was then incubated with the cells for 10 min. Confocal images were acquired with a Zeiss LSM510 laser scanning confocal microscope by using krypton-argon and helium-neon lasers. Image analysis and stack projections were created with the Zeiss LSM 3.2 software package.

Dark-Field Imaging. Dark-field images were acquired before the permeabilization step and antibody incubations described in the cell-targeting assay procedure with an Olympus fluorescence microscope equipped with a dark-field condenser.

SERS Detection of Cells. KS1767 cells (2×10^5) were incubated in 1.0 ml of Eagle's minimal essential medium (MEM) containing 2% FBS with phage (10^9 TU) or Au–phage–imid (10^6 TU) for 18 h at $37°C$. Negative controls included cells alone and fd-tet phage, Au–fd-tet, Au–fd-tet–imid, and Au only. Each tube was washed with a glycine buffer (50 mM glycine/150 mM NaCl, pH 2.8) followed by several PBS washes. Cells then were counted and normalized to the lowest cell count. SERS measurements of suspended cells were gathered by using an R2001 Raman spectrometer (Ocean Optics, Dunedin, FL) equipped with a fiber-optic probe to deliver 785-nm laser light and to collect the Raman-scattered light.

1. Dutta, J. & Hofmann, H. (2003) in *Encyclopedia of Nanoscience and Nanotechnology*, ed. Nalwa, H. S. (American Scientific Publishers, Stevenson Ranch, CA), Vol. 10, pp. 1–23.
2. Leite, E. R. (2004) in *Encyclopedia of Nanoscience and Nanotechnology*, ed. Nalwa, H. S. (American Scientific Publishers, Stevenson Ranch, CA), Vol. 6, pp. 537–554.
3. Giordano, R. J., Cardo-Vila, M., Lahdenranta, J., Pasqualini, R. & Arap, W. (2001) *Nat. Med.* **7,** 1249–1253.
4. Trepel, M., Arap, W. & Pasqualini, R. (2002) *Curr. Opin. Chem. Biol.* **6,** 399–404.
5. Pasqualini, R. & Arap, W. (2002) in *Encyclopedia of Cancer*, ed. Bertino, J. R. (Academic, San Diego), Vol. 4, pp. 501–507.
6. Barbas, C. F., III, Burton, D. R., Scott, J. K. & Silverman, G. J. (2001) *Phage Display, A Laboratory Manual* (Cold Spring Harbor Lab. Press, Woodbury, NY).
7. Kolonin, M. G., Saha, P. K., Chan, L., Pasqualini, R. & Arap, W. (2004) *Nat. Med.* **10,** 625–632.
8. Arap, W., Kolonin, M. G., Trepel, M., Lahdenranta, J., Cardó-Vila, M., Giordano, R. J., Mintz, P. J., Ardelt, P. U., Yao, V. J., Vidal, C. I., *et al.* (2002) *Nat. Med.* **8,** 121–127.
9. Langer, R. & Tirrell, D. A. (2004) *Nature* **428,** 487–492.
10. LaVan, D. A., Lynn, D. M. & Langer, R. (2002) *Nat. Rev. Drug. Discov.* **1,** 77–84.
11. Souza, G. R. & Miller, J. H. (2001) *J. Am. Chem. Soc.* **123,** 6734–6735.
12. Yguerabide, J. & Yguerabide, E. E. (1998) *Anal. Biochem.* **262,** 137–156.
13. Yguerabide, J. & Yguerabide, E. E. (1998) *Anal. Biochem.* **262,** 157–176.
14. Mirkin, C. A., Letsinger, R. L., Mucic, R. C. & Storhoff, J. J. (1996) *Nature* **382,** 607–609.
15. Shipway, A. N., Lahav, M., Gabai, R. & Willner, I. (2000) *Langmuir* **16,** 8789–8795.
16. Weisbecker, C. S., Merritt, M. V. & Whitesides, G. M. (1996) *Langmuir* **12,** 3763–3772.
17. Bai, J., Virovets Alexander, V. & Scheer, M. (2003) *Science* **300,** 781–783.
18. Pham, T., Jackson, J., Halas, N. & Lee, T. R. (2002) *Langmuir* **18,** 4915–4920.
19. Dewey, T. G. (1997) *Fractals in Molecular Biophysics* (Oxford Univ. Press, New York).
20. Mandelbrot, B. B. (1982) *The Fractal Geometry of Nature* (Freeman, San Francisco).
21. Avnir, D., Farin, D. & Pfeifer, P. (1984) *Nature* **308,** 261–263.
22. Farias, T. L., Koylu, U. O. & Carvalho, M. G. (1996) *Appl. Opt.* **35,** 6560–6567.
23. West, G. B., Brown, J. H. & Enquist, B. J. (1999) *Science* **284,** 1677–1679.
24. Reches, M. & Gazit, E. (2003) *Science* **300,** 625–627.
25. Dujardin, E., Peet, C., Stubbs, G., Culver, J. N. & Mann, S. (2003) *Nano Lett.* **3,** 413–417.
26. Purdy, K. R. & Fraden, S. (2004) *Phys. Rev. E Stat. Phys. Plasmas Fluids Relat. Interdiscip. Top.* **70,** 161703-1–161703-8.
27. Marvin, D. A. (1998) *Curr. Opin. Chem. Biol.* **8,** 150–158.
28. Tang, J. X., Janmey, P. A., Lyubartsev, A. & Nordenskio, L. (2002) *Biophys. J.* **83,** 566–581.
29. Zimmermann, K., Hagedorn, H., Heuck, C. C., Hinrichsen, M. & Ludwig, H. (1986) *J. Biol. Chem.* **261,** 1653–1655.
30. Handley, D. A. (1989) in *Colloidal Gold: Principles, Methods, and Applications*, ed. Hayat, M. A. (Academic, San Diego), Vol. 1, pp. 23–27.
31. Gasteiger, E., Hoogland, C., Gattiker, A., Duvaud, S., Wilkins, M. R., Appel, R. D. & Bairoch, A. (2005) in *The Proteomics Protocols Handbook*, ed. Walker, J. M. (Humana, Totowa, NJ), pp. 571–608.
32. Elghanian, R., Storhoff, J. J., Mucic, R. C., Letsinger, R. L. & Mirkin, C. A. (1997) *Science* **277,** 1078–1081.
33. Aubrey, K. L. & Thomas, G. J., Jr. (1991) *Biophys. J.* **60,** 1337–1349.
34. Overman, S. A. & Thomas, G. J., Jr. (1999) *Biochemistry* **38,** 4018–4027.
35. Schwartzberg, A. M., Grant, C. D., Wolcott, A., Talley, C. E., Huser, T. R., Bogomolni, R. & Zhang, J. Z. (2004) *J. Phys. Chem. B* **108,** 19191–19197.
36. Holze, R. (1993) *Electrochim. Acta* **38,** 947–956.
37. Cao, P., Gu, R. & Tian, Z. (2003) *J. Phys. Chem. B* **107,** 769–777.
38. Albelda, S. M., Mette, S. A., Elder, D. E., Stewart, R., Damjanovich, L., Herlyn, M. & Buck, C. A. (1990) *Cancer Res.* **50,** 6757–6764.
39. Arap, W., Pasqualini, R. & Ruoslahti, E. (1998) *Science* **279,** 377–380.
40. Chen, L., Zurita, A. J., Ardelt, P. U., Giordano, R. J., Arap, W. & Pasqualini, R. (2004) *Chem. Biol.* **11,** 1081–1091.
41. Kneipp, K., Kneipp, H., Itzkan, I., Dasari, R. R. & Feld, M. S. (1999) *Chem. Rev.* **99,** 2957–2976.
42. Cao, Y. C., Jin, R. & Mirkin, C. A. (2002) *Science* **297,** 1536–1540.
43. Snyder, E. Y., Deitcher, D. L., Walsh, C., Arnold-Aldea, S., Hartweig, E. A. & Cepko, C. L. (1992) *Cell* **68,** 33–51.

In Vivo Detection of Gold−Imidazole Self-Assembly Complexes: NIR-SERS Signal Reporters

Glauco R. Souza,[†,‡] Carly S. Levin,[†] Amin Hajitou,[‡] Renata Pasqualini,[‡] Wadih Arap,[‡] and J. Houston Miller*,[†]

Department of Chemistry, The George Washington University, Washington, D.C. 20052, and The University of Texas M. D. Anderson Cancer Center, 1515 Holcombe Boulevard, Houston, Texas 77030

Here we report in vitro and in vivo detection of self-assembled Au−imidazole by using near-infrared surface-enhanced Raman scattering (NIR-SERS). In vivo, the Au−imidazole structures were administered into tumor-bearing mice and detected noninvasively. The self-assembled Au−imidazole complexes were generated by the adsorption of imidazole molecules onto Au nanoparticles (NP) and were then characterized as aqueous suspensions by using NIR-SERS, angle-dependent light scattering with fractal dimension analysis, and visible extinction spectroscopy. The structure and optical activity was sensitive to imidazole concentration and Au NP size. Specifically, the Au−imidazole assemblies formed at lower imidazole concentrations had the lowest fractal dimension ($D_f = 1.2$) and the largest Raman enhancement factors for the dominant NIR-SERS feature, a ring-breathing vibrational mode at 954 cm^{-1}. Changes in elastic scattering intensity, fractal dimension, and surface plasmon absorption were observed with increasing imidazole concentration. The Raman enhancement factor was also found to range between 10^6 and 10^9 with different primary Au nanoparticle sizes. For the higher enhancement factor systems, NIR-SERS detection of Au−imidazole was performed with data acquisitions time of only 5 s. The largest enhancement was observed for the 954-cm^{-1} feature at an imidazole concentration of 1.9 μM when coupled to 54-nm-diameter Au NPs (the largest NP tested). Finally, we show the first demonstration of in vivo, noninvasive, and real-time SERS detection.

Development of signal reporters based on near-infrared surface-enhanced Raman scattering (NIR-SERS) is required for application of this technology in biomolecular imaging.[1−3] Biological tissues show minimal NIR radiation (700−900 nm) absorption, thus allowing efficient light penetration for imaging and phototherapy applications in vivo.[4−6] We have coupled Au nanoparticles (NPs) with imidazole (Au−imidazole) into self-assembled NPs, which can be used for real-time, in vivo NIR-SERS detection. The strong affinity between imidazole and Au induces the aggregation of the Au NPs, which results in a shift in the surface plasmon resonance absorption into the NIR wavelengths along with changes in fractal structure and optical properties. All of these attributes are desirable for noninvasive, detection in tissue.

Here we present proof of principle for the use of NIR-SERS in noninvasive, in vivo, and real-time detection of self-assembled nanoparticle complexes. We show the optical and structural characterization of these assemblies by using SERS, UV−visible extinction, and angle-dependent light scattering (ADLS) coupled with fractal dimension analysis. We also show detection in vivo by using a fiber-optic probe to deliver and collect light through the skin of tumor-bearing mice injected with Au−imidazole complexes.

Imidazole has been the target of several prior SERS studies using Ag NPs and electrodes.[7−10] Holze[11] reported the only prior study of SERS for imidazole on gold, specifically on the surface of an Au electrode. The two nitrogens[12] of imidazole (Scheme 1a), the position 1 nitrogen (sp^3 as in pyrrole, pK_a 6.5), and the position 3 nitrogen (sp^2 as in pyridine, pK_a 14.0)[11] play a role in bridging metal particles[7] (Scheme 1b). Because the in vitro work was performed at pH 8.0, one would expect electrostatic interaction between the cationic form of imidazole (Scheme 1a, right) and the negatively charged Au NP (resulting from adsorbed citrate ions from Au synthesis). Imidazole and its derivatives are associated with corrosion prevention and serve as precursors for the adsorption of other molecules onto metal surfaces.[7−10,13,14] The

(1) Souza, G. R.; Christianson, D. R.; Staquicini, F. I.; Ozawa, M. G.; Snyder, E. Y.; Sidman, R. L.; Miller, J. H.; Arap, W.; Pasqualini, R. *Proc. Natl. Acad. Sci. U.S.A.* **2006**, *103*, 1215−1220.
(2) Kneipp, J.; Kneipp, H.; Rice, W. L.; Kneipp, K. *Anal. Chem.* **2005**, *77*, 2381−2385.
(3) Schwartzberg, A. M.; Grant, C. D.; Wolcott, A.; Talley, C. E.; Huser, T. R.; Bogomolni, R.; Zhang, J. Z. *J. Phys. Chem. B* **2004**, *108*, 19191−19197.
(4) Kneipp, K.; Kneipp, H.; Itzkan, I.; Dasari, R. R.; Feld, M. S. *Chem. Rev.* **1999**, *99*, 2957−2976.
(5) Kerker, M.; Wang, D. S.; Chew, H. *Appl. Opt.* **1980**, *19*, 3373−3388.
(6) Broderick, J. B.; Natan, M. J.; O'Halloran, T. V.; Van Duyne, R. P. *Biochemistry* **1993**, *32*, 13771−13776.
(7) Xue, G.; Dai, Q.; Jiang, S. *J. Am. Chem. Soc.* **1988**, *110*, 2393−2395.
(8) Cao, P.; Gu, R.; Tian, Z. *J. Phys. Chem. B* **2003**, *107*, 769−777.
(9) Wang, G.; Shi, J.; Yang, H.; Wu, X.; Zhang, Z.; Gu, R.; Cao, P. *J. Raman Spectrosc.* **2002**, *33*, 125−130.
(10) Carter, D. A.; Pemberton, J. E. *Langmuir* **1992**, *8*, 1218−1225.
(11) Holze, R. *Electrochim. Acta* **1993**, *38*, 947−956.
(12) Davis, K. L.; McGlashen, M. L.; Morris, M. D. *Langmuir* **1992**, *8*, 1654−1658.
(13) Carter, D. A.; Pemberton, J. E.; Woelfel, K. *J. Phys. Chem. B* **1998**, *102*, 9870−9880.

Scheme 1. (a) Imidazole Neutral and Ionic Forms. (b) Au−Imidazole Assembly Interaction
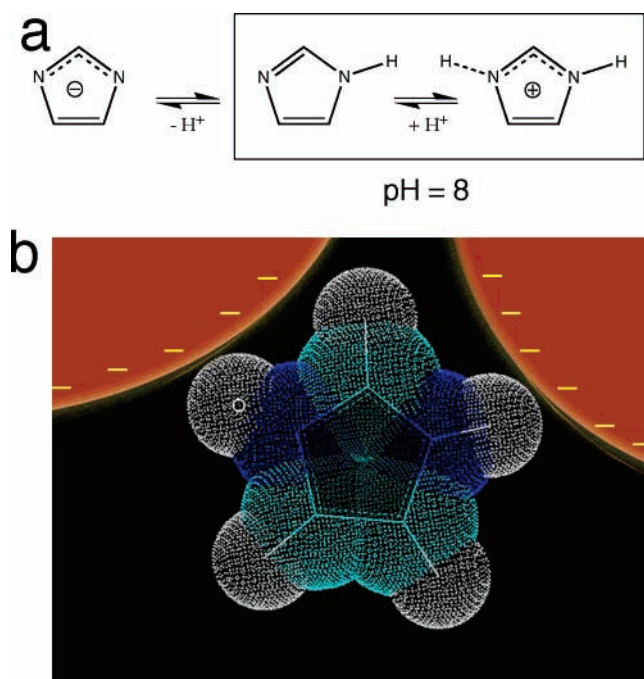
interaction between imidazole and metals is also of biological relevance,[15−19] as it is the functional moiety of several biomolecules, such as nucleic acids, histidine, and histamine. With the growing interest in combining NPs for detection of biomolecules,[1,20−23] biological imaging, and targeted drug delivery,[1,24,25] it is central to understand the interaction of molecules, such as imidazole, with dispersed metal NPs in aqueous environments. Essentially, this work provides the basis for application of imidazole (an inexpensive, soluble, and relatively nontoxic molecule) as a practical and sensitive NIR-SERS signal reporter.

EXPERIMENTAL SECTION

Gold Nanoparticle Self-Assembly Preparation. Samples consisted of 500 μL of Nanopure water, 500 μL of 100 mM borate buffer at pH 8.0, 3 μL of imidazole solution at 99.5% (Fluka), with 500 μL of 0.32 nM Au solution added last. To ensure that the system had reached equilibrium, all measurements were made 12 h after sample preparation. Samples were vigorously mixed to guarantee homogeneity before each measurement. Imidazole solutions consisted of 12 separate dilutions (in Nanopure water)

(14) Carter, D. A.; Pemberton, J. E. *J. Raman Spectrosc.* **1997**, *28*, 939−946.
(15) Kendall, P. A.; Barnard, E. A. *Biochim. Biophys. Acta* **1969**, *188*, 10−24.
(16) Caswell, D. S.; Spiro, T. G. *J. Am. Chem. Soc.* **1986**, *108*, 6470−6477.
(17) Salama, S.; Spiro, T. G. *J. Am. Chem. Soc.* **1978**, *100*, 1105−1111.
(18) Yoshida, C. M.; Freedman, T. B.; Loehr, T. M. *J. Am. Chem. Soc.* **1975**, *97*, 1028−1032.
(19) Pack, D. W.; Putnam, D.; Langer, R. *Biotechnol. Bioeng.* **2000**, *67*, 217−223.
(20) Mirkin, C. A.; Letsinger, R. L.; Mucic, R. C.; Storhoff, J. J. *Nature* **1996**, *382*, 607−611.
(21) Souza, G. R.; Miller, J. H. *J. Am. Chem. Soc.* **2001**, *123*, 6734−6735.
(22) Natan, M. J. *J. Phys. Chem.* **1998**, *102*, 9404−9413.
(23) Hirsch, L. R.; Jackson, J. B.; Lee, A.; Halas, N. J.; West, J. L. *Anal. Chem.* **2003**, *75*, 2377−2381.
(24) Sershen, S. R.; Westcott, S. L.; Halas, N. J.; West, J. L. *J. Biomed. Mater. Res.* **2000**, *51*, 293−298.
(25) Shen, W. C. *Biochim. Biophys. Acta* **1990**, *1034*, 122−124.

ranging from 0.24 to 500 μM. The Au NPs were prepared by the standard method of citrate reduction of gold(III) chloride[26] (99.99+% from Aldrich) in which different sizes were obtained by varying gold(III) chloride and citrate molar ratios. Resulting particle sizes were determined through extinction and transmission electron microscope (TEM) measurements. For all measurements reported below, there was a constant molar concentration of gold atoms, which results in a variable concentration of Au NP in solutions. For 17-nm particles, molar extinction at 520 nm indicated a concentration of 1.96×10^{14} particles/L.

Spectroscopy Measurements. The NIR-SERS measurements were obtained using a Raman Systems R2001 spectrophotometer equipped with a 785-nm laser coupled to a fiber-optic probe. The incident laser power was maintained at 250 mW and was operated in a continuous wave mode. The integration time of each SERS spectrum varied from 5 to 60 s. Extinction measurements were obtained in a diode array spectrophotometer (Hewlett-Packard 8452A). The scattering measurements were obtained using a custom-made ADLS apparatus[27] equipped with a CCD detector and a 5-mW, 532-nm laser. Nanopure water served as the blank in all three types of measurements for the purpose of background subtraction.

TEM Measurements. Nickel mesh grids previously coated with Formvar and evaporated with carbon were floated on drops of 0.1% poly(L-lysine) (Sigma Diagnostics) on Parafilm for 5 min. Excess solution was removed from the grid by carefully touching the edge of the grid onto filter paper. The grids were not allowed to dry completely in any of the following steps. The grids were floated on drops of sample on Parafilm for 1 h. Excess fluid was removed as above, and the grids were then floated on drops of 1% ammonium molybdate in 0.02% BSA in distilled water, pH 7.0 for 60 s. Excess fluid was removed, and the grids were allowed to dry overnight. TEM images were captured by a transmission electron microscope (JEOL JEM-1010) fitted with an AMT Advantage digital CCD camera system. Au NP size was determined by averaging a population of primary particle sizes (and aspect ratios) for representative TEM images using the ImageJ software.[28]

RESULTS AND DISCUSSION

NIR-SERS, UV−Visible, and ADLS of Au−Imidazole Assemblies. Figure 1 shows quantitatively and qualitatively the optical characteristics of Au−imidazole complexes. Figure 1a compares the NIR-SERS from a mixture of 3.9×10^{-6} M imidazole and 17-nm Au NPs (blue spectrum), with the normal Raman spectrum of 0.33 M imidazole aqueous solution (red spectrum). The prominent feature at 954 cm^{-1} in the SERS spectrum is assignable to the $\gamma(NH) + \delta_{ring}$ vibration observed weakly at 931 cm^{-1} in the unenhanced Raman spectrum of imidazole in aqueous solutions[8] (Table 1). A comparison of the intensity of the SERS signal with the normal Raman serves to estimate an enhancement factor of 2×10^6 for this sample. We defined the Raman signal enhancement for a given feature as the ratio of Raman intensities

(26) Geoghegan, W. D.; Ackerman, G. A. *J. Histochem. Cytochem.* **1977**, *25*, 1187−1200.
(27) Souza, G. R.; Miller, J. H. In *Annual Reviews in Plasmonics*; Geddes, C., Ed.; Kluwer Academic/Plenum Publishers: New York, Vol. 2006. In press.
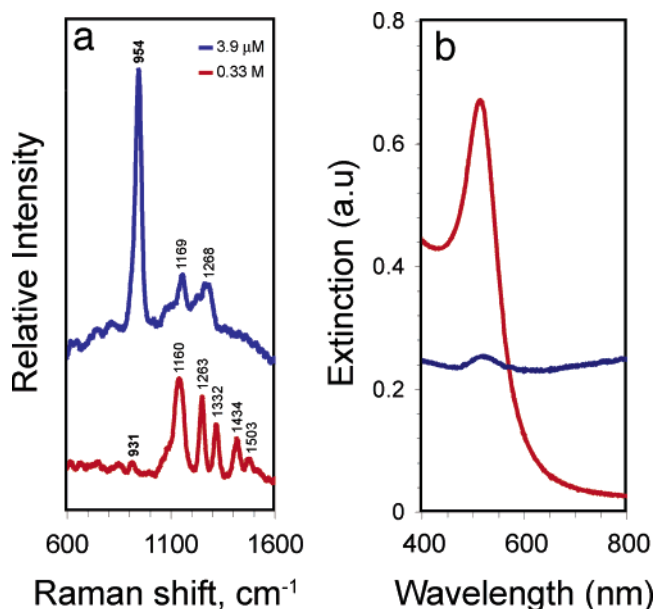(28) Rasband, W. S. ImageJ, U.S. National Institutes of Health, Bethesda, MD, 1997−2006.

Figure 1. (a) Raman signal of 3.9 μM imidazole in 0.33 mM borate buffer pH 8.0 (borate buffer) enhanced by interaction with 17-nm Au NPs (blue spectrum, 60-s integration) and Raman spectrum of 0.3 M imidazole in borate buffer (red spectrum). Plots are offset for clarity. (b) UV–visible absorption spectra of a mixture of 3.9 μM imidazole in borate buffer with 17-nm Au NPs (blue spectrum) and 17-nm Au in borate buffer (red spectrum).

Table 1. Assignment of Raman and SERS Modes of Imidazole

this work Au−imidazole (cm^{-1})	imidazole (cm^{-1})	imidazole SERS[8,11] (cm^{-1})	vibrational assignment[8,11a]
650		628	A$_2$[d]δ_{ring}
764		743	A$_1$ δ_{ring}
838		832	A$_1$ δ_{ring}
954	931	950	A$_2$ δ(NH) + A$_1$ δ_{ring}
1109		1097	A$_1$ δ(CH) + A$_1$ ν_{ring}
1169	1160	1164	A$_1$ δ_{ring}
1268	1263	1265	A$_1$ δ(CH)
1328		1329	A$_1$ ν_{ring}

[a] δ, in-plane bending; γ, out-of-plane bending; ν, stretching.

Figure 2. (a) Surface enhancement of 954-cm^{-1} mode relative to the imidazole concentration; (b) light extinction by the sample measured by light absorption at 520 nm; and (c) dissymmetry ratio of light scattering signal of Au NPs as a function of imidazole concentration.

normalized by imidazole concentration in samples with and without gold present, as follows:

$$E_{SERS} = \frac{I_{SERS}}{C_{SERS}} \frac{C_{Neat}}{I_{Neat}}$$

where C_{SERS} is the concentration of imidazole in solution with Au NPs and C_{Neat} is the concentration of imidazole aqueous solution without any Au NP. Of note, this estimation is only applicable for features observed in both normal and enhanced Raman spectra.

Color change from red to gray-blue occurred after mixing Au nanoparticles with imidazole solution (Figure 1b). To explore these optical changes, visible extinction spectra and angle-dependent light scattering data were collected for each sample. Figure 1b shows extinction spectra of Au solutions with and without imidazole, clearly showing a red shift in the surface plasmon absorption wavelength from 520 nm for the dispersed, isolated particles (red spectrum) to longer wavelengths for the imidazole-containing solutions (blue spectrum). As a red shift in Au surface plasmon is indicative of Au NP aggregation,[29,30] this observation implicates participation of imidazole in the NP assembly process. Often, excitation at a surface plasmon resonance of metal NPs is associated with the SERS signal from adsorbed molecules.[4,31]

The dependence of several experimental observables on the concentration of imidazole were performed using 17-nm Au Nps (Figure 2). The surface enhancement in the SERS signal at 954 cm^{-1} is shown, in which largest enhancement of $\sim$3 × 10^6 was observed for an imidazole concentration of 1.9 μM (Figure 2a). The magnitude of the extinction feature at 520 nm, characteristic

(29) Bohren, C. F.; Huffman, D. R. *Absorption and Scattering of Light by Small Particles*; John Wiley and Sons: New York, 1983.
(30) Weisbecker, C. S.; Merritt, M. V.; Whitesides, G. M. *Langmuir* **1996**, *12*, 3763−3772.
(31) Wang, H.; Levin, C. S.; Halas, N. J. *J. Am. Chem. Soc.* **2005**, *127*, 14992−14993.

of dispersed Au NPs, also changed as a function of imidazole concentration (Figure 2b). Further, the dissymmetry ratio analysis (the ratio between intensities for forward scattering at 30° and backscattering at 140°) of the scattering data are shown in (Figure 2c). The dissymmetry ratio provides a qualitative measure of the relative size of NP aggregates,[32] with larger aggregates possessing a larger dissymmetry ratio.

All three experiments indicate "threshold" behavior when imidazole concentrations are in the range of 1.9−15.6 μM (Figure 2). In order of appearance with increasing imidazole concentration, maximum Raman enhancement precedes the sharp decrease in extinction at 520 nm, which in turn precedes the sharp increase in the dissymmetry ratio. Notably, the maximum enhancement factor is observed at a concentration (1.9 μM) where change in 520-nm SP extinction is not significant (Figure 2b). Moreover, large changes in surface plasmon absorbance, resulting from increase in NP aggregation at higher imidazole concentrations ($\geq$3.9 μM), did not provide additional signal enhancement. Together, these data suggest that the SERS signal originates from small aggregates consisting of the assembly of relatively few cross-linked primary Au NP.

The surface coverage of imidazole on the Au NP can be estimated by comparing the available imidazole in solution with the number of molecules required for monolayer coverage. For the latter, we first estimated the surface area of 17-nm particles (assuming spherical symmetry) and divided this number by the footprint of imidazole by assuming edge-on adsorption. Imidazole size was estimated from a semiempirical structure optimization by using Hyperchem 7.0. Essentially, the results of these calculations suggest that 1 μM imidazole represents coverage of $\sim$1−2 monolayers, assuming that all of the imidazole in solution has been adsorbed. It has been postulated[33,34] that the greatest Raman enhancement will occur near the contact point of metallic NPs where the plasmon field is the greatest. In an evenly distributed monolayer coverage, only a fraction of adsorbed molecules would be at these contact points, suggesting that the actual enhancement may be much greater than that estimated above.

Fractal Dimension Analysis of Au−Imidazole Assemblies. There has been recent interest in understanding the relationship between large enhancements and fractal dimension characteristics of metal surfaces and metal NP assemblies.[4,35−37] Here we used fractal dimension analysis of the ADLS signal (Figure 3a) to structurally characterize and correlate D_f structure with the observed surface enhancement of self-assembled Au−imidazole complexes.

Fractal theory[27,38−41] postulates that the relationship between the number of primary particles (N) in a fractal aggregate follows the relationship, $N = k(R_g/a)^{D_f}$. The angle-dependent light scattering signal is related to the fractal dimension of an aggregate
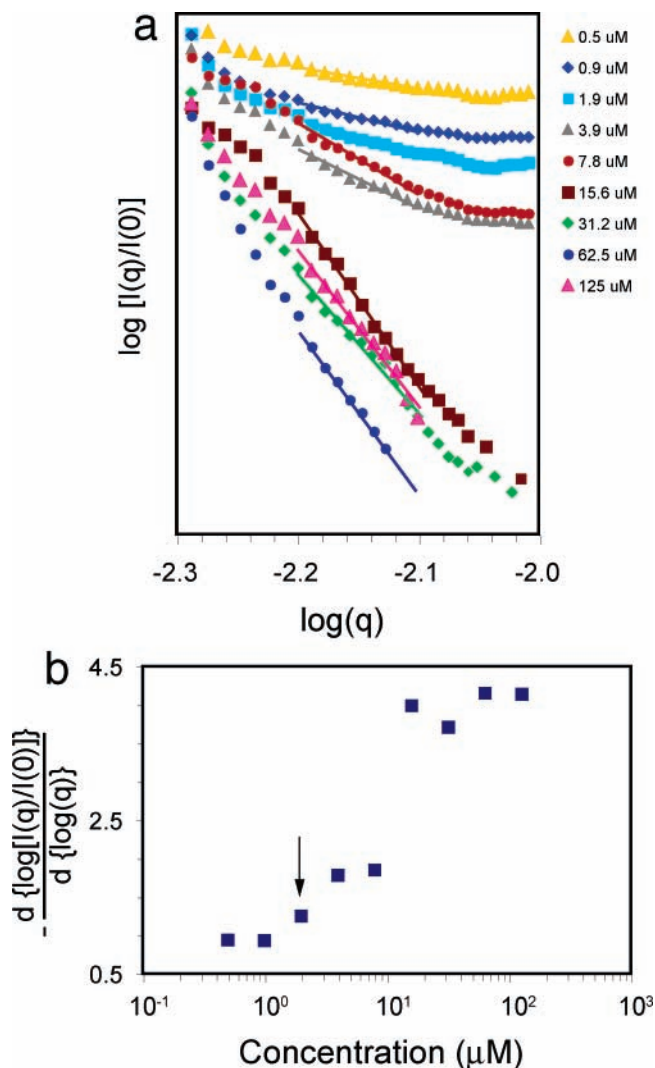
(32) Hunter, R. J. *Introduction to Modern Colloid Science*; Oxford Science Publications: New York, 1993.
(33) Jiang, J.; Bosnick, K.; Maillard, M.; Brus, L. *J. Phys. Chem. B* **2003**, *107*, 9964−9972.
(34) Li, K.; Stockman, M. I.; Bergman, D. J. *Phys. Rev. Lett.* **2003**, *91*, 227402.
(35) Micic, M.; Klymyshyn, N.; Lu, H. P. *J. Phys. Chem. B* **2004**, *108*, 2939−2947.
(36) Kneipp, K.; Kneipp, H.; Dresselhaus Mildred, S.; Lefrant, S. *Philos. Trans., Ser. A* **2004**, *362*, 2361−2373.
(37) Garcia-Ramos, J. V.; Sanchez-Gil, J. A. *Proc. SPIE* **1999**, *3572*, 461−464.
(38) Avnir, D.; Farin, D.; Pfeifer, P. *Nature* **1984**, *308*, 261−263.
(39) Farias, T. L.; Koylu, U. O.; Carvalho, M. G. *Appl. Opt.* **1996**, *35*, 6560.

Figure 3. (a) Angle-dependent light scattering signal from Au agglomerates formed from 17-nm Au in the presence of different imidazole concentrations. (b) Fractal dimension analysis resulting from the measurement of the slope of the curves in (a) between −2.2 < log(q) < −2.1.

according to $I(q) \propto q(\theta)^{-D_f}$, where $I(q)$ is the angle-dependent scattered light intensity, $q(\theta)$ is the scattering wavevector, which is a function of the scattering angle (θ) and wavelength of incident light (λ), and D_f is the fractal dimension of the scattering aggregate, which is the negative of the slope of the curves in Figure 3a. This relationship results from the interference between the scattered electromagnetic waves from individual particles forming the fractal aggregates. Numerical results for the fractal dimension analysis of the ADLS signal shown in Figure 3a are plotted in Figure 3b, where $((d\{\log [(I(q)/I(0))]\})/(d\{\log (q)\}))$ is the slope of the scattering curves in Figure 3a. The data in Figure 3 indicate that the morphology of the aggregates is a strong function of imidazole concentration. These results also show that the fractal dimension of these assemblies also follow a threshold-type behavior shown in Figure 2, where the slope increases

(40) Mandelbrot, B. B. *The Fractal Geometry of Nature*; Freeman: San Francisco, 1982.
(41) Dewey, T. G. *Fractals in Molecular Biophysics*; Oxford University Press: New York, 1997.
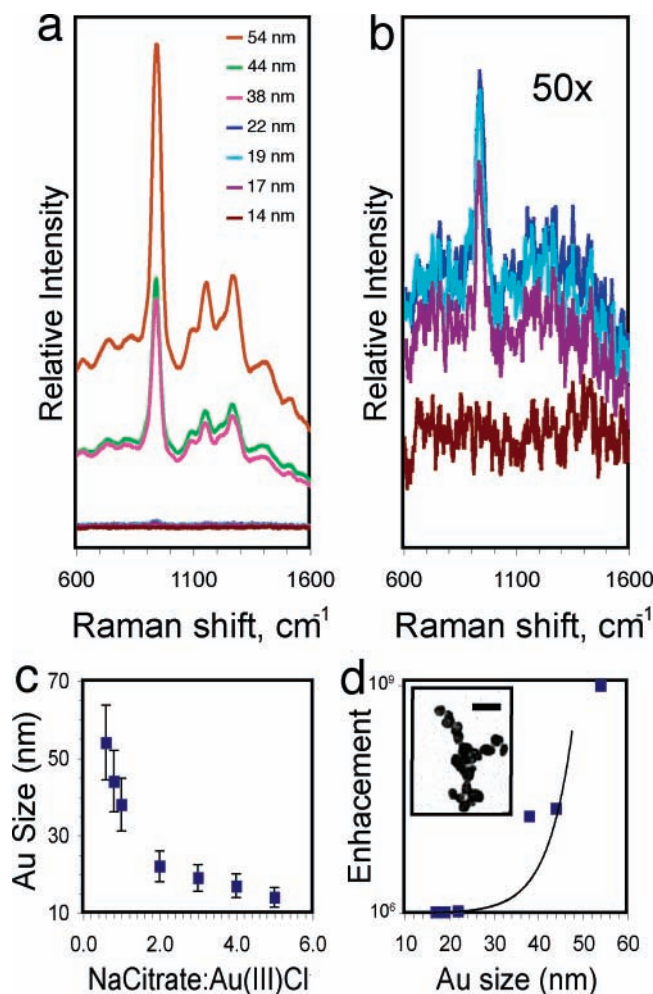
Figure 4. (a) NIR-SERS spectra from imidazole in the presence of different Au sizes (5-s integration time). (b) Magnified spectra (50-fold) of (a) for imidazole solutions prepared with 14-, 17-, 19-, and 22-nm Au NP sizes. (c) Au NP size as a function of sodium citrate to Au^{III}Cl$^-$ ratio during Au NP synthesis. (d) Surface enhancement of 954-cm^{-1} mode relative to Au size (inset, TEM of representative Au−imidazole clusters formed with 54-nm Au at 1.9 μM imidazole; 100 μm, scale bar).

sharply between 7.8 and 15.6 μM imidazole indicating structural transition from predominantly fractal aggregates ($\leq$7.8 μM imidazole) to more homogeneous[41] and compact particle assemblies ($\geq$15.6 μM of imidazole; slope $\geq$3).

Notably, the largest Raman enhancement factor was observed with systems with low fractal dimension (Figure 3b, D_f of 1.2 for 1.9 μM imidazole). Recent reports have shown that surface enhancement is greatest in NP clusters containing only a few primary particles (dimers and trimers),[42,43] systems expected to have near-unity fractal dimensions. These results have implications for the use of NP assemblies as biomolecular labels. The characteristic high surface area of low-dimension fractal aggregates[1,44] provides improved coupling efficiency and accessibility to binding sites, both of which are relevant for fabricating tissue-targeting image systems.

(42) Hao, E.; Schatz, G. C. *J. Chem. Phys.* **2004**, *120*, 357−366.
(43) Talley, C. E.; Jackson, J. B.; Oubre, C.; Grady, N. K.; Hollars, C. W.; Lane, S. M.; Huser, T. R.; Nordlander, P.; Halas, N. J. *Nano Lett.* **2005**, *5*, 1569−1574.
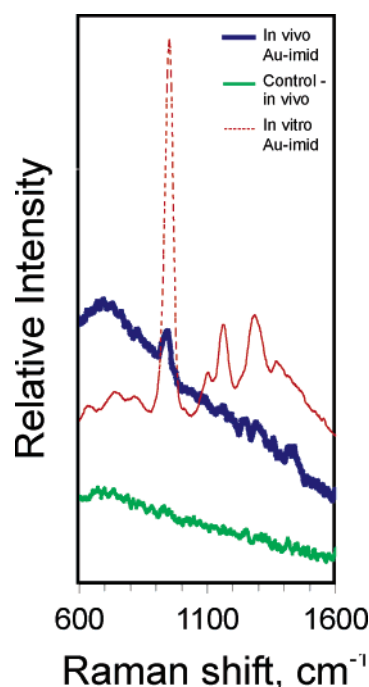(44) West, G. B.; Brown, J. H.; Enquist, B. J. *Science* **1999**, *284*, 1677−1679.

Figure 5. Noninvasive NIR-SERS detection across skin in a tumor-bearing mouse that received 300 μL of Au−imidazole clusters (7.8 μM imidazole) administered locally in the tumor xenograft. SERS spectra description: the blue curve (in vivo) is the spectrum generated by the Au−imidazole assemblies inside the tumor with 15-s integration; red curve (in vivo) is the spectrum from tumor prior to administration of Au−imidazole assemblies injection with 15-s integration; and green (in vitro) is the spectrum from Au−imidazole complexes in solution measured in a glass cuvette with 5-s integration.

Enhancement as a Function of Au Size. Panels a and b in Figure 4 show the NIR-SERS from Au−imidazole clusters as a function of Au NP size for an imidazole concentration of 1.9 μM (indicated by the arrow in Figures 2 and 3b). As stated above, particle size is related to the ratio of sodium citrate to Au^{III}Cl$^-$ salt in the Au synthesis procedure (Figure 4c). Surface enhancement increased sharply with NP size (Figure 4d); an enhancement on the order of 10^9 was observed for Au NP of 54 nm. Large enhancements for Au NPs of >40 nm have been reported previously.[45] The pronounced SERS signal from assemblies formed with 38-, 44-, and 54-nm Au NP are obtained with data acquisition time of only 5 s. Such strong enhancements indicate that these assemblies would provide desirable characteristics required for targeted biological imaging and detection,[1] such as reduced data acquisition time and laser light exposure.

In Vivo NIR-SERS Detection. To demonstrate the feasibility of using NIR-SERS for noninvasive detection of Au−imidazole assemblies in vivo, 300 μL of a solution of Au−imidazole clusters (7.8 μM imidazole in H$_2$O) were injected into the tumors of tumor-bearing mice. Specifically, six tumor-bearing mice were tested. Of this group, three were injected with Au−imidazole solutions and the other three were injected with water as a control population. Then, a fiber-optic probe with a focal length of 7 mm was positioned 3 mm above the tumor to deliver and collect light through the exposed skin (i.e., the fur had been shaved off). Figure 5 compares the in vitro spectrum of Au−imidazole clusters

(45) Lee, C. R.; Kim, S. I.; Yoon, C. J.; Gong, M. S.; Choi, B. K.; Kim, K.; Joo, S. W. *J. Colloid Interface Sci.* **2004**, *271*, 41−46.

with the in vivo spectrum, clearly showing the 954-cm^{-1} ring-breathing mode of imidazole. Only the three mice injected with Au−imidazole presented this SERS spectral feature. Although the 3-mm standoff distance resulted in the best signal, it has been our experience that this distance can be varied by ∼ ±2 mm without significant degradation in the signal. Finally, the instrumentation used in this demonstration study was not designed for in vivo detection; thus, it is likely that further instrument optimization will markedly improve these initial results.

CONCLUSION

We report NIR-SERS signals resulting from nanoparticle self-assembly triggered by the imidazole adsorption onto Au nano-particles. The ADLS and UV−visible extinction serve to monitor the assembly and optical properties of the Au nanoparticle aggregates as they interact with imidazole. Enhancements of up to 10^9, measured in solution, are observed for a ring-breathing vibrational mode of imidazole for low fractal dimension aggregates of 54-nm primary particle size. The onset of the enhancement in Raman scattering at lower imidazole concentrations preceded the onset of marked changes in elastic scattering, indicating that the largest surface enhancement results from small Au nanoparticles assemblies. Finally, we have shown the in vivo detection of these assemblies in a preclinical tumor-bearing mouse model. We have

for the first time demonstrated that optics, spectroscopy, and Au−imidazole signal reporting can be effectively combined to observe intratissue NIR-SERS signals in vivo. While direct injection was used as proof of concept, the long-term goal is to use systemic delivery of targeted nanoparticles, such as was demonstrated for "nanoshuttles", assemblies of gold nanoparticles, and bacteriophage.[1] The use of such nanostructures has the potential to overcome many of the difficulties associated with in vivo detection by allowing faster data acquisition time and reduced laser power in a biologically transparent wavelength region.

A Previously Unrecognized Protein-Protein Interaction between TWEAK and CD163: Potential Biological Implications[1]

Laura C. Bover,[2,3]* Marina Cardó-Vila,[2]* Akihiko Kuniyasu,[§] Jessica Sun,* Roberto Rangel,* Motohiro Takeya,[¶] Bharat B. Aggarwal,[‡] Wadih Arap,[4]*[†] and Renata Pasqualini[4]*[†]

TWEAK (TNF-like weak inducer of apoptosis) is a TNF superfamily member implicated in several mechanisms. Although fibroblast growth factor inducible 14 (Fn14)/TweakR has been reported as its receptor, an as yet unrecognized surface molecule(s) might modulate TWEAK function(s). Thus, we set out to identify TWEAK-binding proteins by screening a combinatorial peptide library. Cyclic peptides containing a consensus motif (WXDDG) bound to TWEAK specifically. These peptides were similar to CD163, a scavenger receptor cysteine-rich domain family member, restricted to the monocyte/ macrophage lineage and responsible for the uptake of circulating haptoglobin-hemoglobin (Hp-Hb) complexes. Sequence profile analysis suggested that TWEAK mimicked the CD163 natural ligand (Hp-Hb). Consistently, we show dose-dependent TWEAK binding to CD163 and blockade by an anti-CD163 Ab. In a competition assay, both soluble CD163 and Fn14/ TweakR were able to compete off TWEAK binding to coated Fn14/TweakR or CD163, respectively. Flow-cytometry and immunofluorescence assays showed that human monocytes (Fn14/TweakR negative and CD163 positive) bind TWEAK, thus blocking the recognition of CD163 and reducing the activation mediated by a specific mAb in these cells. We demonstrate that monocytes can sequester TWEAK from supernatants, thus preventing tumor cell apoptosis; this effect was reverted by preincubation with the peptide mimicking CD163 or with a mAb anti-CD163, indicating specificity. Finally, we show that recombinant human TWEAK binding to CD163-transfected Chinese hamster ovary cells is inhibited by the presence of either unlabeled TWEAK or the Hp-Hb complex. Together, these data are consistent with the hypothesis that CD163 either acts as a TWEAK scavenger in pathological conditions or serves as an alternate receptor for TWEAK in cells lacking Fn14/TweakR. *The Journal of Immunology,* **2007, 178: 8183–8194.**

The TNF and TNFR superfamilies play important roles in the development and regulation of the immune system and are implicated in diverse physiologic processes such as apoptosis, cell proliferation, and bone remodeling (1–3). TWEAK (TNFS12) is a "TNF-like weak inducer" of apoptosis (hence its name) through a non-death domain-dependent mecha-

nism (Refs. 2 and 4; see also HBNC Gene Family Nomenclature; http://www.gene.ucl.ac.uk/nomenclature/genefamily/tnftop.html). It also mediates angiogenesis (5, 6) and inflammation (7, 8). In particular, interactions between TWEAK and monocytes have been reported (9, 10).

However, despite this relatively extensive literature, the complete biological effects of TWEAK remain largely unknown because cells lacking the corresponding receptor (11–13) have also been shown to be TWEAK sensitive. Death receptor 3 (DR3; TNFRS12), a member of the TNFR family containing an intracellular death domain, was initially suggested as a TWEAK-binding molecule (14, 15), but subsequent studies opposed these results (12). More recently, fibroblast growth factor inducible 14 (Fn14)/ TweakR has been reported to control TWEAK-associated proliferation of endothelial cells and angiogenesis (16). Supporting these findings, Nakayama et al. have shown that Fn14/TweakR mediates TWEAK-induced programmed cell death (17). However, because Fn14/TweakR lacks the cytoplasmic death domain, the ligand-receptor structural basis is still unclear. Finally, Polek et al. (18) have demonstrated that TWEAK mediates signal transduction and linear differentiation of monocyte/macrophage cells lacking Fn14/ TweakR, suggesting that such cells contain an alternative TWEAK receptor, TweakR2. Interestingly, TweakR2 and Fn14/TweakR induce a differential activation of signaling pathways (18). Nevertheless, the identification of such a putative receptor remains elusive.

In this study, we report the screening of a random combinatorial peptide library (19–23) on TWEAK to identify new TWEAK-binding proteins. We show that TWEAK binds specifically to several consensus peptide motifs that are homologous to the scavenger receptor

cysteine-rich (SRCR)[5] CD163 protein (also called M130 and RM3/1; Refs. 24–28). Consistently, TWEAK binding to purified CD163 was dose dependent and blocked by either the peptide motif mimicking CD163 or by an anti-CD163 mAb. Interestingly, in competition assays TWEAK binding to Fn14/TweakR is competed out by preincubation with soluble CD163 and vice versa. Next, we used cells sensitive to TWEAK but Fn14/TweakR deficient (CD14-positive human monocytes) to demonstrate that TWEAK interacts with CD163 expressed on the cell surface. This association can partially inhibit the activation of monocytes by an anti-CD163 Ab. Then, we show that TWEAK-mediated apoptosis in IFN-γ-treated HT29 cells (12) can be prevented when TWEAK is preincubated with monocytes but not when an anti-CD163 mAb or the peptide that mimics CD163 is added to the culture medium. Finally, we demonstrate that CD163-transfected Chinese hamster ovary (CHO) cells bind ^{125}I-labeled recombinant human TWEAK (^{125}I-rHuTWEAK), but other SRCR members (CD5 and CD6) do not. This process is reverted in a dose-dependent manner by the addition of unlabeled TWEAK; haptoglobin (Hp) and hemoglobin (Hb) complex (Hp-Hb); peptide mimicking CD163 and anti-CD163 Ab. Together, these findings indicate a possible functional link between TWEAK and CD163.

Materials and Methods

Reagents

rHuTWEAK and the goat polyclonal anti-human TWEAK Ab were purchased from Peprotech. CD163 was purified from solubilized human spleen membranes as described (29). Anti-CD163 Abs were obtained as follows: clone GHI/61 from BD Biosciences, clone Ki-M8 from BMA Biomedicals, clone10D6 from Vector Laboratories, and clone AM-3K as described (30). Secondary Abs used were HRP-conjugated anti-goat IgG from Sigma-Aldrich and HRP-conjugated anti-mouse IgG from Bio-Rad. FITC-conjugated anti-human CD14 was purchased from Miltenyi Biotec, purified and PE-conjugated anti-Fn14/TweakR (PE-ITEM-4) and anti-human CD5 (clone UCHT2) Abs were purchased from eBiosciences, and Cyanine 3 (Cy3)-conjugated AffiniPure F(ab')$_2$ donkey anti-goat IgG (H+L) was purchased from Jackson ImmunoResearch Laboratories. Isotype controls (PE-mIgG1/k, PE-mIgG2b/k, and FITC-mIgG2a) and the anti-human CD6 Ab (clone M-T605) were purchased from BD Pharmingen. CWDDGWSFC (CD163-like peptide) and CRKFRDEATC (used as a control peptide) were purchased from Genemed Synthesis. Human epidermal growth factor (EGF), human IL-2, and human IL-11 and their correspondent Abs (goat anti-human) were from R&D Systems. Human Hb and Hp phenotype 2-2 were from Sigma-Aldrich. FuGENE (Roche) was used for transfection procedures. Na^{125}I (3.7 GBq/ml) was purchased from GE Healthcare Bioscience. Human CD163 (transcript variant 1)-pCMV6-XL4, Fn14-pCMV6-XL5, and human CD5 full-length cDNA clones were purchased from OriGene Technologies, and human CD6 was from Invitrogen Life Technologies.

Phage display screening and phage binding assays

A phage display random peptide library based on the vector fUSE5 displaying the insert CX$_7$C (where C is cysteine and X is any residue) (23) was used in the screening (31, 32); phage input was 2.5 × 10^9 transforming units (TU). The TWEAK-GST recombinant fusion protein (18) was coated on microtiter wells (Linbro; ICN Pharmaceuticals) as described (21) at 4.5 μg per 50 μl of PBS. The original cyclic phage peptide inserts of seven amino acid residues were analyzed by multiple sequence alignment by using the Clustal W software (European Molecular Biology Laboratory; 32, 33). The selected motifs were then searched against protein databases (National Center for Biotechnology Information (NCBI); www.ncbi. nlm.nih.gov/BLAST/) to search for similarity to known human proteins. Phage binding assays on rHuTWEAK, TWEAK-GST, GST, and BSA (Fraction V, Sigma-Aldrich) were conducted as described (21). Briefly, proteins were immobilized on microtiter wells overnight at 4°C at decreas-
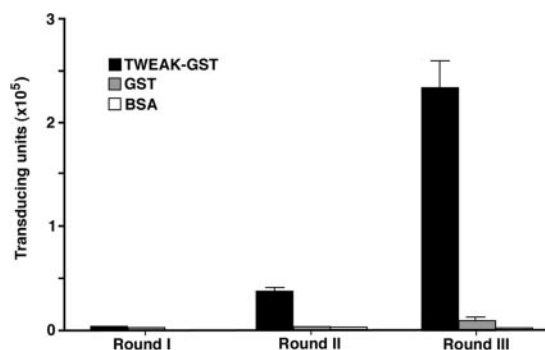
FIGURE 1. In vitro screening for peptides targeting TWEAK from a random phage display library. Microtiter plates coated with TWEAK-GST fusion protein were incubated with 2.5 × 10^9 TU of a CX$_7$C phage display random peptide library. Bound phage was recovered and amplified for the subsequent second and third rounds of selection on TWEAK-GST, GST, and BSA. Bound phage was quantified by counting TU plated in serial dilutions. Bars, mean ± SEM from duplicate wells.

ing concentrations (from 5.0 to 0.5 μg/well). Wells were washed twice with PBS, blocked with PBS plus 3% BSA for 2 h at room temperature, and incubated with 10^9 TU of CWDDGWSFC, CLWTDDGYC, CYWG-DDGFC, CWWFDDGYC, and CRWADDGFC phage clones or insertless fd-tet phage in 50 μl PBS containing 2% BSA. After 1 h at room temperature, the wells were washed 10 times with PBS and bound phage was recovered by bacterial infection. Goat polyclonal anti-human TWEAK Ab (Peprotech) at 2 μg/ml was used to evaluate the inhibition of phage binding for 90 min at room temperature. In an alternative experimental design, either CWDDGWSFC phage or fd-tet was coincubated with mouse anti-human CD163 mAb (clone GHI/61; 10 μg/ml) or a mouse IgG1 control isotype and then added to rHuTWEAK or BSA-coated wells.

Protein-protein interaction assays

CD163 or Fn14/TweakR was coated onto a 96-well plate at 2 μg/ml and rHuTWEAK was added at 2 μg/ml. VEGF and BSA were used as coating negative controls. After 2 h, the binding of TWEAK to CD163 or Fn14/TweakR was detected by ELISA with an anti-TWEAK Ab (diluted at 1/1,000). Parallel ELISAs were performed by using a 1/150 dilution of an anti-CD163 Ab followed by an HRP-conjugated anti-mouse IgG to confirm CD163 coating or by adding EGF, IL-2 or IL-11 as alternate ligands for CD163 and recognizing the cytokines with the corresponding Abs. Bound proteins were analyzed by ELISA on an automated reader at 450 nm (Bio-Tek Instruments). For experiments showing dose-dependent TWEAK binding to CD163 or Fn14/TweakR, increasing concentrations of rHuTWEAK were added to the wells (3, 10, 30, 100, 300 and 1,000 ng/ml). In competition experiments, soluble CD163 or soluble Fn14/TweakR (at a range from 0.05 μM to 15 μM) was preincubated with rHuTWEAK for 30 min and then added to the coated Fn14/TweakR or CD163, respectively. To test inhibition of TWEAK binding to CD163 by anti-CD163 Abs, CD163 protein was coated, blocked with PBS containing 2% BSA, and incubated with anti-CD163 Abs (clones Ki-M8, GHI/61, and 10D6) at 200 ng/ml for 30 min at room temperature. Control IgGs were used at same conditions. Then, rHuTWEAK was added onto the wells for 2 h and developed with anti-TWEAK (1/1,000 dilution). TWEAK binding to CD163 was evaluated by preincubation of rHuTWEAK with CWWDGWSFC or control peptides added at 0, 3, 6, 10, 30, 60, 100, and 300 μM).

PBMCs and monocyte purification

Fresh human PBMCs were isolated from 50–60 ml of buffy coat from normal volunteer blood donors (Gulf Coast Blood Bank, Houston, TX) by using Ficoll-Paque (Pharmacia Biotech) density gradients. Monocytes were isolated from the PBMC population by positive selection using a CD14-positive magnetic bead separation system (Miltenyi Biotec). Cells were used immediately for flow cytometry or cultured in AIM-V medium (Invitrogen Life Technologies) for other assays.

Flow cytometric analysis for CD163 expression and other SRCR expression

CD14-positive monocytes were incubated on ice for 1 h with PE-labeled mouse anti-human-CD163 (clone GHI/61), FITC-conjugated anti-human

---

[5] Abbreviations used in this paper: SRCR, scavenger receptor cystein rich; CHO, Chinese hamster ovary; Cy3, cyanine 3; EGF, epidermal growth factor; Fn14, fibroblast growth factor inducible 14; Hb, hemoglobin; Hp, haptoglobin; rHuTWEAK, recombinant human TWEAK; ^{125}I-rHuTWEAK, ^{125}I-labeled rHuTWEAK; TU, transforming unit.

Sequences	n=158	(Frequency%)
RWADDGF	8	(5.1)
FWADDGF	2	(1.3)
YWADDGF	1	(0.6)
YWGDDGF	3	(1.9)
SWGDDGY	4	(2.5)
RWGDDGY	1	(0.6)
FWGDDGW	1	(0.6)
RWEDDGF	4	(2.5)
VWEDDGF	3	(1.9)
WWFDDGY	4	(2.5)
LWTDDGY	2	(1.3)
HWTDDGY	2	(1.3)
EWRDDGW	1	(0.6)
WRDDGWS	1	(0.6)
FWRDDGW	1	(0.6)
WWRDDGF	1	(0.6)
LWYDDGW	2	(1.3)
FWVDDGY	1	(0.6)
RWQDDGL	1	(0.6)
W-DDGWWD	2	(1.3)
W-DDGWSF	1	(0.6)
W-DDGFYP	2	(1.3)
WFDDGF	1	(0.6)
WEED-LDV	6	(3.8)
W-EDTLDW	2	(1.3)
W-EDWLDK	1	(0.6)
W-EDTLDH	1	(0.6)
W-EDTLDM	1	(0.6)
WDWDGWT	1	(0.6)
WDWDGWP	1	(0.6)
SWDGWVI	1	(0.6)
FWDGWGT	2	(1.3)
YWDGWGT	1	(0.6)
FWDGWGV	1	(0.6)
FWDGWDL	2	(1.3)
FWDGWSL	1	(0.6)
YWDGWLD	2	(1.3)
DPHWDGW	1	(0.6)
YPHWDGW	1	(0.6)
WLEWDGW	1	(0.6)
WGGWDGW	1	(0.6)
WWGWDGW	1	(0.6)
NFWDGLG	2	(1.3)
LHWDGYG	1	(0.6)
WPEWDGL	1	(0.6)
W-EDGWYA	2	(1.3)
W-EDGIFF	2	(1.3)
W-EDGICL	1	(0.6)
W-EDGLWQ	1	(0.6)
W-EDGWYA	2	(1.3)
RWLEDGY	1	(0.6)
RWKEDGK	1	(0.6)
SWGEDGY	1	(0.6)
YWGEDGY	1	(0.6)
EFREDGW	1	(0.6)
FYREDGW	1	(0.6)
Total	95	(60.0)
Others	63	(40.0)

FIGURE 2. Phage sequences isolated by selection on TWEAK-GST.

FIGURE 3. Binding of selected peptides to TWEAK. *A*, Phage clones displaying individual peptide sequences or negative control phage (insert-less Fd-tet) were incubated on microtiter wells (10^9 TU per well) coated with TWEAK-GST, GST, or BSA. *B*, Binding inhibition of CWDDGWSFC phage to TWEAK by an anti-TWEAK polyclonal Ab. Microtiter wells coated with rHuTWEAK were incubated with goat anti-human anti-TWEAK Ab. CWDDGWSFC phage was added (10^9 TU) and incubated for additional 2 h. Shown is mean ± SEM of a representative experiment. The experiments were repeated three times with similar results.

CD14, PE-anti-mouse and human Fn14/TweakR (PE-ITEM-4), or the respective isotype controls (PE-mIgG1/k, PE-mIgG2b/k, and FITC-mIgG2a). For inhibition assays, monocytes were incubated with either 200 ng/ml rHuTWEAK or PBS at 4°C. Cells were then washed and left not fixed or fixed in PBS containing 2% paraformaldehyde and then treated with PE-anti-human CD163. After processing, cells were fixed in PBS containing 2% paraformaldehyde and subjected to flow cytometry analysis by using a FACScan flow cytometer (BD Biosciences) with CellQuest software. To analyze the cell surface expression of SRCR or Fn14 on the CHO cells, CD163-, CD5-, CD6-, or Fn14-transient transfectant or wild-type CHO cells (10^6 cells/200 μl) were incubated with a mouse mAb against CD163, CD5, CD6, Fn14, or control mouse IgG at 4°C for 1 h followed by FITC-labeled secondary Ab to at 4°C for 30 min and then subjected to flow cytometry analysis.

Confocal immunofluorescence microscopy

CD14-positive monocytes plated overnight in the LabTek II chamber slide system (2.5×10^5 cells/well) were incubated with 200 ng/ml rHuTWEAK or PBS for 30 min at 4°C to prevent or minimize receptor internalization. After three washes with ice-cold PBS, cells were incubated with an polyclonal goat-anti-human TWEAK Ab. A Cy3-conjugated AffiniPure F(ab')$_2$ donkey anti-goat IgG (H+L) was used as a secondary Ab. Fixed slides mounted with fluorescent mounting medium (DakoCytomation) were examined in a confocal microscope (Olympus FV500).

Monocyte activation assay

Monocyte activation was measured by quantifying the ability of cells to metabolize the tetrazolium salt WST-1 to formazan (Roche) at 37°C (34). CD14-positive monocytes were plated in 96-well plates (30,000 cells/well) and incubated for 42 h with or without dexamethasone (10 ng/ml; Sigma-Aldrich), rHuTWEAK (1 μg/ml) and anti-CD163 GHI/61 (1.25 μg/ml). WST-1 was added for 4 h after finishing the incubation period. Absorbance was determined at 440 nm in an optical reader (Bio-Tek Instruments).

TWEAK-depleted supernatants

Freshly isolated human monocytes preincubated with or without anti-CD163 Ab for 30 min were treated with increasing concentrations of

CD163

```
              Extracytoplasmic Domain              TM    Cytoplasmic
                       1043aa                      24aa     88aa
```

```
   1 MVLLEDSGSADFRRHFVNLSPFTITVVLLLSACFVTSSLGGTDKELRLVDGENKCSGRVE
  61 VKVQEEWGTVCNNGWSMEAVSVICNQLGCPTAIKAPGWANSSAGSGRIWMDHVSCRGNES
 121 ALWDCKHDGWGKHSNCTHQQDAGVTCSDGSNLEMRLTRGGNMCSGRIEIKFQGRWGTVCD
 181 DNFNIDHASVICRQLECGSAVSFSGSSNFGEGSGPIWFDDLICNGNESALWNCKHQGWGK
 241 HNCDHAEDAGVICSKGADLSLRLVDGVTECSGRLEVRFQGEWGTICDDGWDSYDAAVACK
 301 QLGCPTAVTAIGRVNASKGFGHIWLDSVSCQGHEPAVWQCKHHEWGKHYCNHNEDAGVTC
 361 SDGSDLELRLRGGGSRCAGTVEVEIQRLLGKVCDRGWGLKEADVVCRQLGCGSALKTSYQ
 421 VYSKIQATNTWLFLSSCNGNETSLWDCKNWQWGGLTCDHYEEAKITCSAHREPRLVGGDI
 481 PCSGRVEVKHGDTWGSICDSDFSLEAASVLCRELQCGTVVSILGGAHFGEGNGQIWAEEF
 541 QCEGHESHLSLCPVAPRPEGTCSHSRDVVSRYTEIRLVNGKTPCEGRVELKTLGAWG
 601 SLCNSHWDIEDAHVLCQQLKCGVALSTPGGARFGKGNGQIWRHMFHCTGTEQHMGDCPVT
 661 ALGASLCPSEQVASVICSGNQSQTLSSCNSSSLGPTRPTIPEESAVACIESGQLRLVNGG
 721 GRCAGRVEIYHEGSWGTICDDSWDLSDAHVVCRQLGCGEAINATGSAHFGEGTGPIWLDE
 781 MKCNGKESRIWQCHSHGWGQQNCRHKEDAGVICSEFMSLRLTSEASREACAGRLEVFYNG
 841 AWGTVGKSSMSETTVGVVCRQLGCADKGKINPASLDKAMSIPMWVDNVQCPKGPDTLWQC
 901 PSSPWEKRLASPSEETWITCDNKIRLQEGPTSCSGRVEIWHGGSWGTVCDDSWDLDDAQV
 961 VCQQLGCGPALKAFKEAEFGQGTGPIWLNEVKCKGNESSLWDCPARRWGHSECGHKEDAA
1021 VNCTDISVQKTPQKATTGRSSRQSSFIAVGILGVVLLAIFVALFFLTKKRRQRQRLAVSS
1081 RGENLVHQIQYREMNSCLNADDLDLMNSSGLWVLGGSIAQGFRSVAAVEAQTFYFDKQLK
1141 KSKNVIGSLDAYNGQE
```

```
CD163    17   VNLSPFTITV    26      CD163    597   GA-WGSLCNSHW      607
Peptide       CIVN--PFR--VC         Peptide        CWGAEW-------WLC

CD163    34   FVTSSL        39      CD163    657   CPVTAL            662
Peptide       CVVFVLMSL             Peptide        CPRPALDMC

CD163    49   VDGENKCSG     57      CD163    723   CAGRVEIYHEGSWGTIC 739
Peptide       CWVDG--WC-GC          Peptide        CAGR-------S-GSIC

CD163    123  WDCKHDGW      130     CD163    735   WGTICDDSW         743
Peptide       CWD---DGWSFC          Peptide        CW----DDGWSFC

CD163    174  RWGTVCDD      181     CD163    777   WLDEM             781
Peptide       CRWG---DDGC           Peptide        CDESWLD-MC

CD163    192  CRQLE         196     CD163    803   CRHKED            808
Peptide       CRWLEDGYC             Peptide        CRWKEDGKC

CD163    217  WFDD          220     CD163    890   CPKGPDTL-WQC      900
Peptide       CWWFDDGYC             Peptide        CW--EDTLDW-C

CD163    236  QGWG          239     CD163    940   WHGGSWGT          947
Peptide       CWQGWGCKC             Peptide        CFWDG--WGTC

CD163    282  WGTICDDGW     290     CD163    940   WHGGSWGTV         948
Peptide       CW----DDGWSFC         Peptide        CFWDG---WG-VC

CD163    320  FGHIWLDSVSC   330     CD163    949   C-DDSW            953
Peptide       CFES-WLD-L-C          Peptide        CWDDGWSFC

CD163    450  WQWGGL        455     CD163    954   DLDDAQV           960
Peptide       CRWQDDGLC             Peptide        CWEEDLD---VC
```
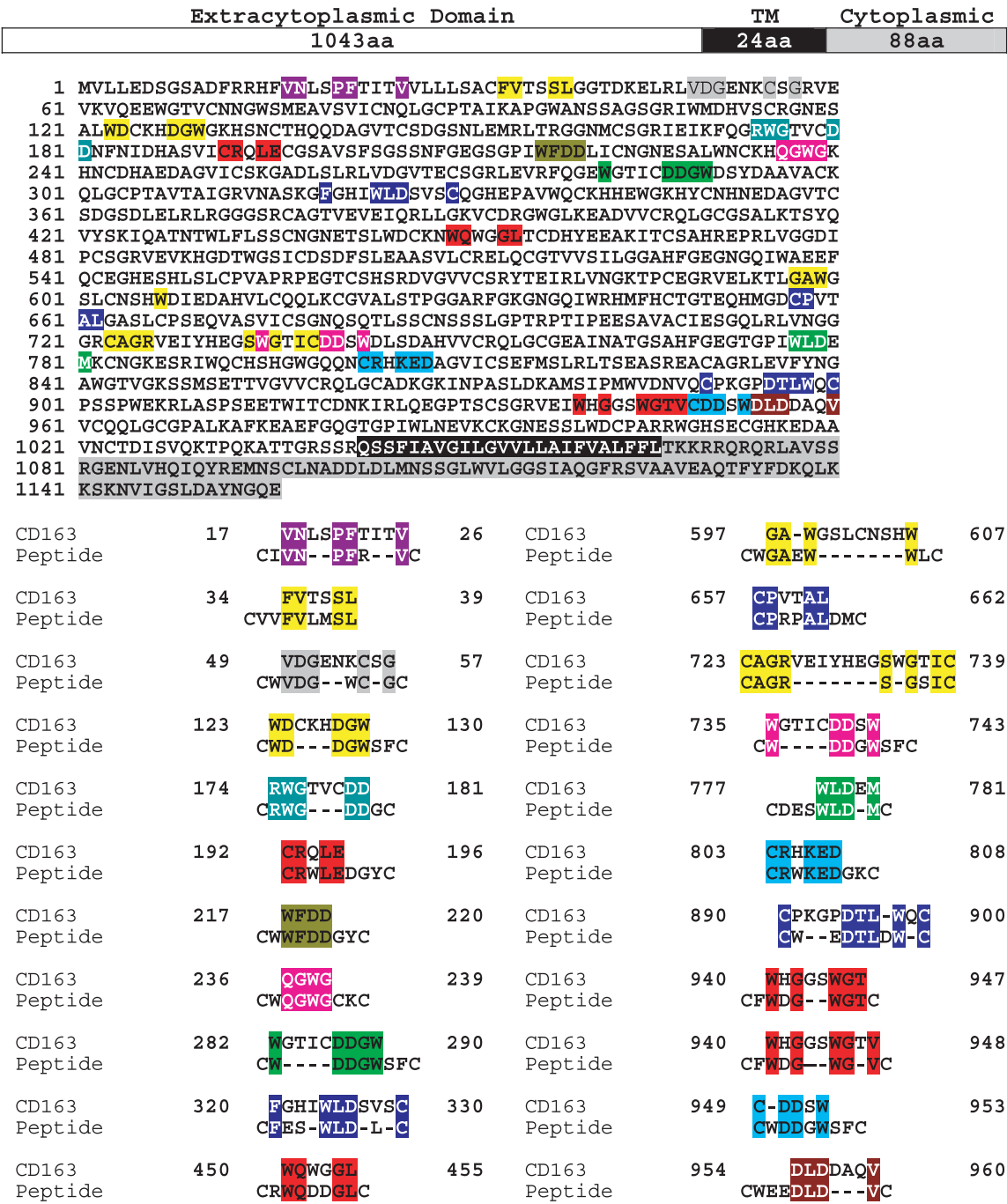
FIGURE 4. Alignment of peptide sequences isolated from in vitro selection on TWEAK and CD163 SRCR protein.

rHuTWEAK (0, 10, 50, and 100 ng/ml) for 1 h at 4°C or 24 h at 37°C. After that, monocytes were decanted by centrifugation and supernatants were frozen at −80°C until additional experiments were performed. Additional time points were also obtained by treating monocytes for 30 min and 2 h (data not shown). Alternatively, rHuTWEAK was preincubated with CWDDGWSFC or the control peptide (30 and 100 μM) for 30 min before admixture into the monocyte culture.

Cell viability on TWEAK-sensitive cells

Human colon adenocarcinoma HT-29 cells were obtained from American Type Culture Collection and cultured with modified RPMI 1640 containing 10% FBS, 100 μg/ml streptomycin and penicillin, and 2 mM glutamine. Cells were plated in 96-microtiter well plates (20,000 cells/well) and pretreated with IFN-γ (20 ng/ml; R&D Systems) for 12 h.

Then, cells were incubated with or without rHuTWEAK as indicated. After 36 h of culture, cell proliferation was assessed. To evaluate the ability of monocytes to deplete TWEAK from the medium, supernatants from monocyte cultures (as described above) were added to IFN-γ-treated HT29 cells and a cell viability assay was performed under the same conditions. To rule out the possibility of TWEAK degradation by monocyte-secreted proteins, parallel experiments were performed by using a conditioned medium of cultured monocytes incubated with or without same amounts of rHuTWEAK, and a cell viability assay was conducted (data not shown).

Transient expression of huCD163 in CHO cells

The open reading frames of CD5 and CD6 were directionally cloned in the eukaryotic vector pCMV and confirmed by DNA sequencing. Plasmids
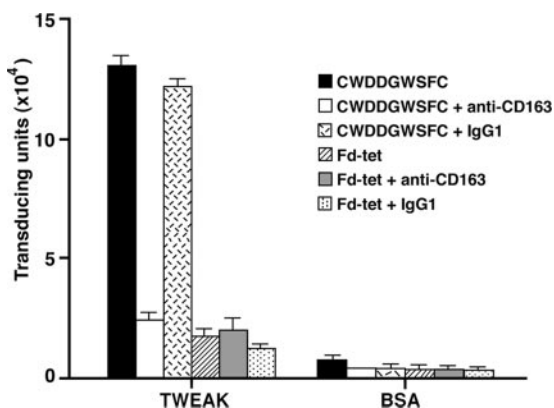
FIGURE 5. Binding inhibition of CWDDGWSFC phage to TWEAK by an anti-human CD163 mAb. Either CWDDGWSFC phage or insertless phage at 10^9 TU was incubated with 10 μg/ml anti-human CD163 mouse mAb. A control isotype Ab was used as a negative control. Afterward, each solution was transferred to microtiter wells coated with rHuTWEAK or BSA and incubated for an additional 2 h. Shown is mean ± SEM of a representative experiment. Three experiments were performed with similar results.

were prepared by using the GenElute HP Endotoxin-free kit (Sigma-Aldrich) for cell transfection. CHO cells were maintained with RPMI 1640 medium containing 5% FBS and no antibiotics. Cells were seeded at 30% confluence into 24-well plates and transfected at a ratio of 6 μl of FuGENE per 1 μg of DNA with the plasmids encoding human SRCR or Fn14. Twenty-four hours after transfection, the cells were washed once with PBS and fresh medium containing the adequate ligands was added. Cell surface expression of the transfectants was analyzed by the flow assay cytometry described above.

Preparation of ^{125}I-rHuTWEAK and Hp-Hb complexes

^{125}I-rHuTWEAK was prepared by using an Iodogen coating tube (Pierce) as described (35). Briefly, 200 μg of rHuTWEAK was incubated with Na^{125}I (0.925 MBq) in 200 μl of 0.5 M sodium phosphate buffer (pH 7.4) for 20 min at 37°C, and then dialyzed against PBS. Complexes were pre-pared by mixing equimolar concentrations of Hb and Hp in PBS as de-scribed (30).

Cellular binding of ^{125}I-rHuTWEAK by CD163-CHO cells

Cellular binding of ^{125}I-rHuTWEAK was performed in accordance to that of advanced glycated end product-modified BSA by CD36 as described previously (35). For cell binding assay, cells were incubated with 100 ng/ml ^{125}I-rHuTWEAK at 4°C in RPMI 1640 containing 3% BSA for 3 h. After incubation, cells were washed three times with ice-cold PBS and lysed with 0.1 M NaOH. Radioactivity and protein concentration of whole cell lysates were determined by using a gamma well counter and a BCA protein assay kit (Pierce). For inhibition assays, cells were also incubated with or without the indicated ligands (1 or 10 μg/ml rHuTWEAK or Hp-Hb complexes, 100 μM CWDDGWSFC or control peptide CRKFRDEATC, and 10 μg/ml AM-3K anti-CD163 Ab or control mouse IgG).

Results

Identification of TWEAK-binding peptides

We isolated TWEAK-binding peptides by screening a CX$_7$C phage library (22, 23) on a recombinant TWEAK-GST fusion protein (Fig. 1). A marked enrichment in phage binding to TWEAK-GST relative to the negative controls GST (30-fold) or BSA (2,000-fold) was observed after three rounds of selection.

Analysis of peptide sequences and specificity of binding to TWEAK

Forty-nine of 158 (31%) of clones obtained from the screening displayed a WXDDG motif or some variation of it; X was pref-erentially a nonpolar or polar uncharged residue (Fig. 2). Phage clones displaying the peptide sequences CWDDGWSFC, CLWTD DGYC, CYWGDDGFC, CWWFDDGYC, and CRWADDGFC were used for additional experiments. Such sequences were chosen because they were enriched or because they showed homology to candidate binding proteins. The relative binding of these peptide se-quences to TWEAK in regard to negative controls was then individ-ually determined (Fig. 3A). Selected peptides showed an enhanced binding to TWEAK relative to GST (mean 26-fold; range 7- to 48-fold). Phage clones displaying the peptide CWDDGWSFC had the

FIGURE 6. Protein sequence align-ment of TWEAK and haptoglobin and hemoglobin.

A. Alignment of human TWEAK (NP_003800) with human haptoglobin (NP_005134)

```
TWEAK        117   PGQDGAQAG-VDGTVSGW-EEARINSSSPLRY  146
Haptoglobin  268   PSKDYAEVGRV-GYVSGWGRNANFKFTDHLKY  298
```

B. Alignment of human TWEAK (NP_003800) with hemoglobin b-chain (P02023)

```
TWEAK            154   IVTRAGLYY-LYCQVHFDE-G   172
Hemoglobin β-chain  11   AVT-A-LWGKVN--V--DEVG    25
```

C. Human TWEAK protein sequence matching with haptoglobin and hemoglobin residues

```
TWEAK isoform 1 (NP_003800)

  1  MAARRSQRRRGRRGEPGTALLVPLALGLGLALACLGLLLAVVSLGSRASLSAQEPAQEEL
 61  VAEEDQDPSELNPQTEESQDPAPFLNRLVRPRRSAPKGRKTRARRAIAAHYEVHPRPGQD
121  GAQAGVDGTVSGWEEARINSSSPLRYNRQIGEFIVTRAGLYYLYCQVHFDEGKAVYLKLD
181  LLVDGVLALRCLEEFSATAASSLGPQLRLCQVSGLLALRPGSSLRIRTLPWAHLKAAPFL
241  TYFGLFQVH
```

```
S  Cleavage site
PGQ…LRY =Hp homologue region
IVT…DEG =Hb homologue region
```

D. Alignment of phage clones that bind TWEAK with the heavy chain CDR3 of a mAb raised against the Hp-Hb complex

```
CDR3        EDTTDWY-FDV
Clone 15   CWEDTLDWC
Clone 17     CWYLFDEPC
```
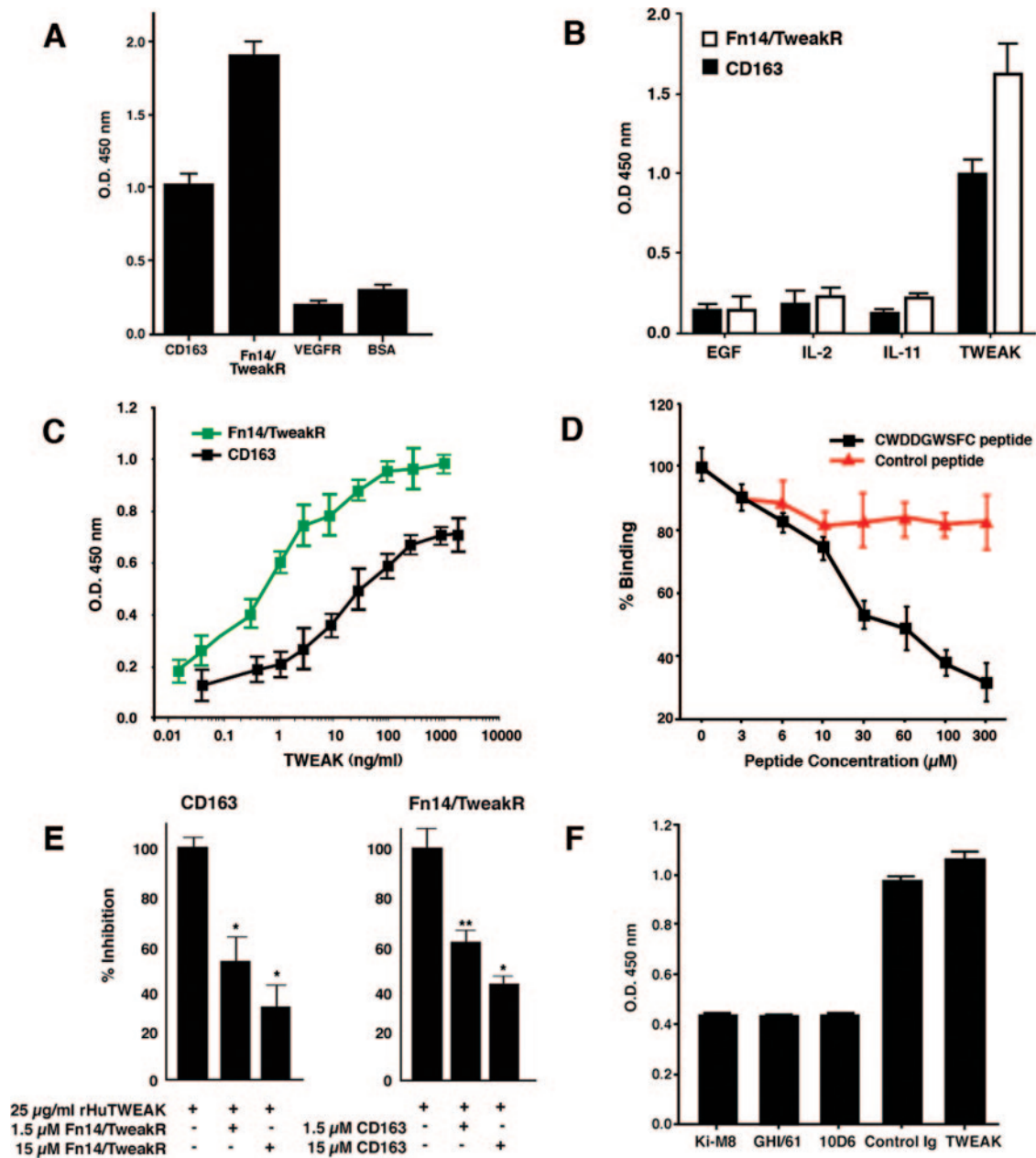
FIGURE 7. Dose-dependent and inhibitable binding of TWEAK to CD163. *A*, rHuTWEAK binding to CD163. TWEAK was added (50 μl of 500 ng/ml) to the CD163-coated well. Vascular endothelial growth factor receptor (VEGFR) and BSA served as coated negative controls. Bound protein was measured by ELISA. *B*, Interactions of soluble cytokines with CD163. CD163 (filled bars) or Fn14/TweakR (open bars) proteins (1 μg/ml) were coated onto 96-microtiter well plates and incubated with 500 ng/ml EGF or IL-11 or 100 ng/ml IL-2. Cytokine binding was detected with anti-EGF, anti-IL-11, and anti-IL-2 Abs. *C*, Dose-dependent binding of TWEAK to CD163. CD163 was coated onto a 96-microtiter well plate and incubated with increasing amounts of rHuTWEAK. *D*, Dose-dependent inhibition of TWEAK-CD163 interaction by the CWDDGWSFC peptide was measured by ELISA. *E*, Inhibition of TWEAK-receptor binding by soluble receptor. rHuTWEAK preincubated with Fn14/TweakR for 30 min at room temperature was added to CD163 coated plate (*left panel*). rHuTWEAK preincubated with CD163 for 30 min at room temperature was added to Fn14/TweakR coated plate (right panel) (*t* test; *, $p < 0.001$; **, $p < 0.004$). *F*, Inhibition of TWEAK-CD163 interaction by CD163 Abs. CD163 protein was coated onto 96-microtiter well plates. Anti-CD163 Abs (clones Ki-M8, GHI/61, and 10D6) were added into wells for 30 min at room temperature before adding rHuTWEAK. Isotype IgG was used as a negative control. Coated rHuTWEAK with no Abs added served as a positive control. Results from two representative experiments are shown.

highest relative binding to TWEAK (10-fold for GST and 900-fold for BSA) and bound over 800-fold more than binding of the insertless control phage. Similar results were also obtained with the purified rHuTWEAK protein. To evaluate the specificity of the interaction between CWDDGWSFC and TWEAK, we tested whether CWDDGWSFC-phage binding to TWEAK was inhibited when immobilized rHuTWEAK was preincubated with an anti-TWEAK Ab. CWDDGWSFC-displaying phage binding (but not binding of the

control phage) was inhibited (Fig. 3*B*). Together, these data indicate that the CWDDGWSFC interacts specifically with TWEAK.

Mapping of peptide sequences to CD163

Peptide sequences obtained from the phage selection ($n = 158$) were analyzed for similarity to known human proteins by using the NCBI BLAST software. Of these sequences, 41 (26%) matched motifs found within the CD163 protein (NCBI protein
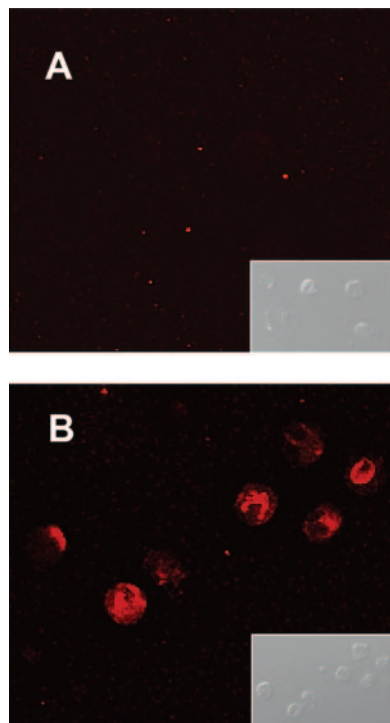
FIGURE 8. In situ detection of TWEAK binding to a subset of CD14-positive monocytes. Human CD14-positive monocytes plated overnight in AIM-V medium were incubated with rHuTWEAK or PBS for 30 min at 4°C. After washing, cells were fixed and incubated with goat anti-human TWEAK and a secondary Ab conjugated to Cy3. Cells were examined under a confocal microscope. *A*, PBS. *B*, rHuTWEAK. *Insets*, The corresponding contrast phase images. Original magnification, ×400.

FIGURE 9. Expression of CD14, CD163, and Fn14/TweakR surface molecules on freshly isolated CD14-positive monocytes. CD14-positive monocytes were labeled with anti-CD14-FITC, anti-CD163-PE, an Ab against Fn14/TweakR, or their respective control isotype Abs. *A*, Cells incubated with anti Fn14/TweakR-PE or control isotype. *B*, Cells incubated with anti-human-CD14-FITC and anti-human-CD163-PE. *C*, Cells were preincubated with 200 ng/ml rHuTWEAK (blue) or PBS (red) for 30 min at 4°C and then incubated with anti-human CD163-PE. Incubation with isotype control (black) was included. A representative experiment is shown.

database accession no. NP_004235). CD163 is a member of the SRCR superfamily and is expressed on the human monocyte and macrophage lineage. An alignment of a subset of peptide sequences isolated from panning on TWEAK with the protein sequence of CD163 was assembled (Fig. 4). Because the CWDDGWSFC peptide aligned to different sites of the CD163 sequence (data not shown), we estimate a total of 44 putative interacting sites between TWEAK and CD163. As predicted, all sites located to the extracellular domain containing the SRCR of the CD163 protein.

CWDDGWSFC mimics CD163

Based on these observations, we hypothesized that the selected TWEAK-binding phage clones mimic CD163. To test this hypothesis, we evaluated the specific recognition of the CWDDGWSFC-phage by an anti-CD163 mAb raised against the N-terminal domain of the protein (which includes the cysteine-rich domain). We next performed a binding experiment in vitro in which the CWDDGWSFC-phage or the control phage was preincubated with anti-CD163 mAb or an isotype control. The anti-CD163 mAb inhibited the binding of the CWDDGWSFC-phage to immobilized rHuTWEAK, whereas the isotype control did not exert any detectable blocking effect (Fig. 5). This result suggests that the CWDDGWSFC peptide mimics, at least partially, the epitope recognized by the anti-CD163 mAb.

TWEAK exhibits similarity to a native CD163 ligand

The SRCR CD163 was identified as a specific Hb scavenger receptor that mediates the uptake of Hb in complex with Hp (i.e., the Hp-Hb complex; Refs. 29 and 36). A search for sim-
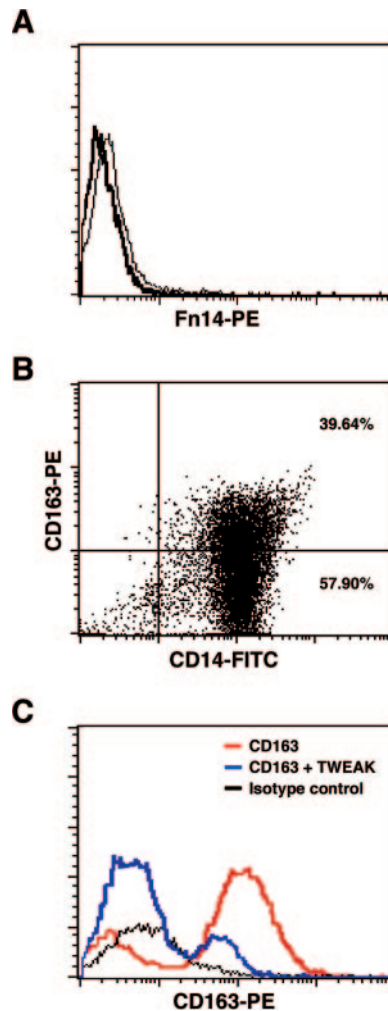
ilarities in the protein sequences of TWEAK, Hp, and Hb led to several observations. First, TWEAK (NCBI protein database accession no. NP_003800) and Hp (NCBI protein database accession no. NP_005134) each contained a region consisting of a 31-residue motif with 13 identical amino acids and six amino acids with the same hydropathic profile (Fig. 6A). This region represents 19% of secreted TWEAK (residues 95–249) and 12% of the Hp β-chain (residues 162–406). We also observed that the residues 11–25 in the Hb β-chain (NCBI protein database accession no. P02023), which are also implicated in Hp-Hb complex formation (37), matched a region comprising amino acids 154–172 in TWEAK (Fig. 6B). This segment in TWEAK is separated by only seven residues from the domain homologous to Hp (Fig. 6C). Finally, the CDR3 of a Fab Ab (10 residues; sequence EDTTDWYFDV) that blocks the binding of Hp-Hb complex to CD163 (38) revealed >50% homology with the CWEDTLDWC peptide (Fig. 4) and ~40% homology with the CWYLFDEPC peptide (Figs. 6D and 2) of the screening.
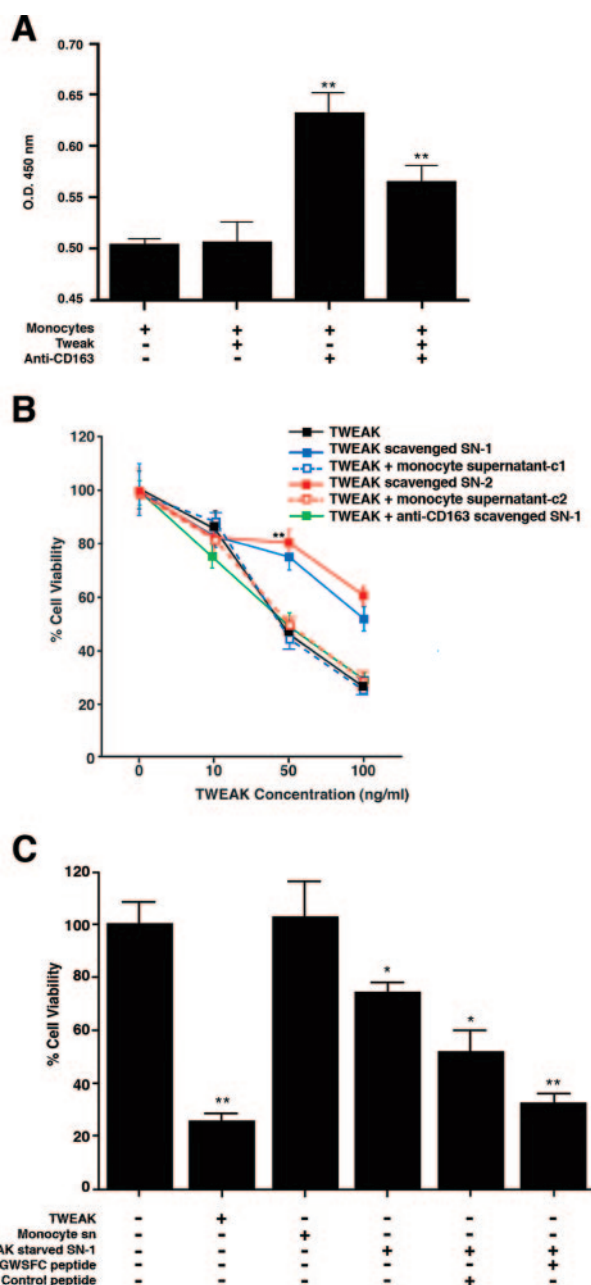
FIGURE 10. Interaction between TWEAK and CD163 in human monocytes. *A*, Effects of anti-CD163 mAb and TWEAK on monocyte activation. CD14-positive monocytes were plated in 96-well plates (30,000 cells/well). After 4 h of plating, rHuTWEAK (1 μg/ml) and anti-CD163 mAb GHI/61 (1.25 μg/ml) were added. Cells were incubated for 42 h and pulsed for 4 h with WST-1. Absorbances were measured at 450 nm. An isotype control had no detectable effect (data not shown). Shown are the means ± SEM of a representative experiment (*t* test; ∗, *p* < 0.005; ∗∗, *p* < 0.001). *B*, TWEAK-mediated programmed cell death can be inhibited by preincubation of TWEAK with monocytes, but not in the presence of an anti-CD163 Ab. HT-29 cells (20,000 cells/well) in the presence of IFN-γ (20 ng/ml; black line) were cultured with the indicated concentrations of rHuTWEAK or with supernatants from TWEAK-treated (1 h) monocytes (blue line, SN1 (supernatant from freshly isolated monocytes); red line, SN-2 (supernatant from 24 h cultured monocytes)). After 36 h in culture, cell viability was assessed by the WST-1 assay. Data are represented as the mean ± SEM of triplicate samples. Similar results were obtained in three independent experiments. *C*, Inhibition of TWEAK-mediated programmed cell death by the CWDDGWSFC peptide. IFN-γ treated HT29 cells were cultured with supernatants from freshly isolated monocytes containing 100

TWEAK binds to CD163

To support our hypothesis, we evaluated the binding of rHu TWEAK to CD163. We show that TWEAK binds specifically to CD163 in a dose-dependent manner (Fig. 7, *A* and *C*). As controls, binding to Fn14/TweakR but not to an unrelated receptor (variable endothelial growth factor receptor) or BSA are shown (Fig. 7*A*). Human EGF, IL-2, and IL-11 also failed to bind to CD163 (Fig. 7*B*). Next, we showed that TWEAK binding to CD163 is inhibited by a CWDDGWSFC synthetic peptide in a dose-dependent manner; a control peptide with an unrelated sequence had no effect (Fig. 7*D*). We sought to determine whether the addition of the soluble receptor would interfere with the TWEAK binding. Soluble CD163 preincubated with rHuTWEAK was able to inhibit the binding to Fn14/TweakR (Fig. 7*E*, *left panel*). In contrast, Fn14/ TweakR preincubated with rHuTWEAK also inhibited TWEAK binding to CD163 (Fig. 7*E*, *right panel*) suggesting a competition between both receptors. Recently, Madsen et al. (39) described ligand-binding properties of the membrane-associated CD163 protein and identified the SRCR domains involved in Hp-Hb and Ab binding. Thus, we next evaluated whether preincubation with three different clones of anti-CD163 Abs (Ki-M8, GHI-61, and 10D6) could inhibit TWEAK binding to CD163. Consistent with our findings, all the three Abs inhibited TWEAK binding to CD163 (Fig. 7*F*).

Fn14/TweakR-negative/CD163-positive human monocytes specifically bind TWEAK

Because TWEAK is not present at detectable levels on the surface of freshly isolated monocytes (9), we asked whether monocytes would bind TWEAK. CD14-positive monocytes, selected because this subset of cells displays the highest expression of CD163 among monocytes (26), did not show expression of TWEAK on the surface after 18 h in culture (Fig. 8*A*); however, we detected TWEAK binding at the cell surface after incubation with rHuTWEAK (Fig. 8*B*). To further investigate the protein responsible for TWEAK binding in CD14-positive human monocytes, we first evaluated the expression of Fn14/TweakR and that of CD163. Flow cytometry revealed no expression of the recently identified receptor of TWEAK (Fn14/TweakR; Refs. 16 and 17), suggesting the presence of another TWEAK-binding protein on CD14-positive human monocytes. In contrast and in agreement with previous reports (26), we found a high expression of CD163 in 40% of CD14-positive monocytes, (Fig. 9, *A* and *B*). To determine whether TWEAK and CD163 interact specifically at the surface of human monocytes, we analyzed the expression of CD163 after the preincubation of freshly isolated CD14-positive cells with TWEAK. We found that the detection of CD163 with an anti-CD163 mAb was inhibited in the presence of TWEAK, but no effect was noted when the cells were preincubated with PBS alone (Fig. 9*C*). Collectively, these data are consistent with a specific interaction between TWEAK and CD163 on the cell surface of Fn14/ TweakR-negative human monocytes.

Monocyte activation induced by an anti-CD163 Ab is inhibited by TWEAK

We evaluated whether TWEAK and CD163 can interact functionally. Cross-linking of the CD163 receptor by an anti-CD163

ng/ml rHuTWEAK coincubated with 100 μM CWDDGWSFC peptide or control peptide. Culture medium, SN-1 supernatant and medium with 100 ng/ml rHuTWEAK were used as controls (*t* test; ∗, *p* < 0.005; ∗∗, *p* < 0.001).
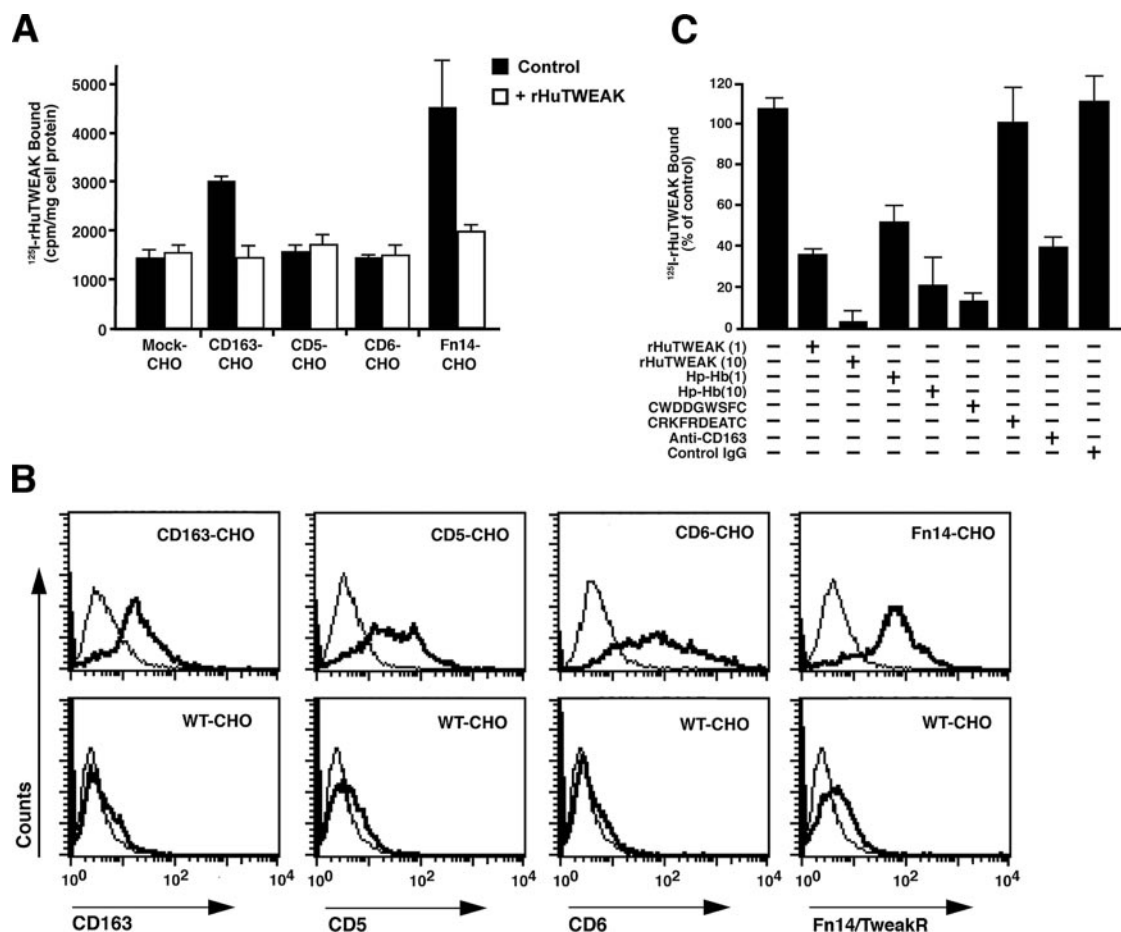
FIGURE 11. Cellular binding of ^{125}I-rHuTWEAK to the CD163-expressed CHO cells. *A*, CHO cells were transiently transfected with or without plasmids encoding human SRCR (CD163, CD5, and CD6) or Fn14/TweakR. The CHO cells transiently expressing SRCR, Fn14/TweakR, or mock-transfectant control were incubated at 4°C for 3 h with 100 ng/ml ^{125}I-rHuTWEAK in the presence (open bar) or absence (filled bar) of an excess amount of unlabeled rHuTWEAK (10 μg/ml). After washing, cells were lysed with 0.1 M NaOH and the radioactivity of the whole cell lysates was determined. *B*, Cell surface expression by flow cytometry of CD163, CD5, CD6, and Fn14/TweakR on the CHO cells. CHO cells transiently transfected with CD163, CD5, CD6, or Fn14/TweakR (*upper histograms*) and wild-type (WT) CHO cells (*lower histograms*) were incubated with each mouse mAb (bold line), or control mouse IgG (standard line). *C*, Effects of the CD163 ligands on the binding of the ^{125}I-rHuTWEAK. CD163-expressed CHO cells were incubated at 4°C for 3 h with ^{125}I-rHuTWEAK (100 ng/ml) in the presence or absence of various ligands (1 or 10 μg/ml rHuTWEAK or Hb-Hp complexes, 100 μM CWDDGWSFC or control peptide CRKFRDEATC) or 10 μg/ml Abs (anti-CD163 AM-3K or control mouse IgG). An amount of ^{125}I-rHuTWEAK bound to the CD163 was determined. Specific amounts were plotted after subtracting nonspecific binding by mock transfectants. Values represent mean ± SD (*n* = 3).

mAb induces signaling and macrophage activation (28). There are two technical considerations that may well be relevant to interpreting this set of experiments. First, culturing normal monocytes results in an ~60% decrease in cell number after 48 h, with most of those cells being lost during the first 6 h of culture (40). Second, the ability of viable cells to metabolize tetrazolium salts (indicated as WST-1 reduction), generally used as a quantitative measure of cell number, can also reflect cell activation from an increase in the overall activity of mitochondrial dehydrogenases (34, 41).

We sought to determine whether incubation with the anti-CD163 Ab GHI/61 activated CD14-positive human monocytes and whether coincubation with TWEAK changed such an effect. The ability of cells to metabolize tetrazolium salts was used as a cell activation marker to evaluate differences in cell viability (34). Activation was higher for monocytes incubated with anti-CD163 Ab relative to buffer (Fig. 10A) or isotype control (data not shown). This effect was abrogated by the addition of rHuTWEAK. In comparison to control cultures, monocytes incubated with rHuTWEAK alone showed no difference in activation level. The ad-

dition of dexamethasone, which up-regulates CD163 (24), did not change the results. Thus, TWEAK appears to inhibit anti-CD163-Ab-induced activation by competing for the same or perhaps a close overlapping binding site (Fig. 10A).

TWEAK-mediated programmed cell death can be inhibited by preincubation with monocytes

TWEAK-induced programmed cell death in several tumor cell lines has been extensively characterized. In particular, Nakayama et al. (12) described the mechanisms mediating the apoptosis of IFN-γ-treated HT-29 cells. Based on the results described above, we hypothesized that CD163, a scavenger receptor, might be acting as a receptor "decoy" for the ligand TWEAK. To test this hypothesis experimentally, we evaluated whether human monocytes (either freshly isolated or after plating for 24 h) could bind and functionally sequester the rHuTWEAK added to the culture medium. Indeed, we show that the ability of TWEAK to induce apoptosis is abrogated from TWEAK-containing monocyte supernatants compared with controls (Fig. 10B). To rule out the possibility that TWEAK was actually being degraded or consumed by

monocyte-secreted proteins, we incubated monocyte-conditioned medium (collected at 30 min and at 1 and 2 h) with the same amounts of TWEAK used above. No differences were observed compared with the curve for untreated TWEAK (data not shown). Moreover, TWEAK-mediated programmed cell death was observed when monocytes were treated with an anti-CD163 Ab (Fig. 10*B*) or by preincubating TWEAK with the CWDDGWSFC peptide (Fig. 10*C*).

Cellular binding of ^{125}I-rHuTWEAK to CD163

To examine the cellular interaction of CD163 with TWEAK, we determined the binding of ^{125}I-rHuTWEAK by SRCR (CD163, CD5, and CD6) or TWEAK receptor Fn14 compared with mock-transfected CHO cells. Fig. 11*A* shows that CHO cells transiently expressing CD163 exhibited the specific binding of ^{125}I-rHuTWEAK but that mock-transfected CHO cells did not. As positive control, ^{125}I-rHuTWEAK bound to the Fn14-expressed cells. In contrast, CHO cells expressing CD5 or CD6 have no specific binding activity. These results indicate that TWEAK is specifically recognized by CD163 as well as Fn14, but not by CD5 and CD6. Cell membrane expression of CD163, CD5, CD6, and Fn14/TweakR on CHO cells was demonstrated by flow cytometry (Fig. 11*B*).

Next, we examined the effects of various ligands and Abs on the binding of TWEAK to the CHO cells transiently expressing CD163. ^{125}I-rHuTWEAK binding to the CD163 was inhibited completely by unlabeled rHuTWEAK in a dose-dependent manner and almost inhibited by an excess of Hb-Hp complexes (Fig. 11*C*). In addition, the CD163-like peptide CWDDGWSFC and the anti-CD163 mAb AK-3K (30) also decreased this activity by 15 and 37%, respectively. By contrast, two controls (CRKFRDEATC peptide and mouse IgG) had no effects. Furthermore, CD163-CHO cells mediated the specific degradation of ^{125}I-rHuTWEAK, but mock-transfected or cells expressing CD5 or CD6 had no such activity (data not shown). These results indicate that the TWEAK binding site(s) within CD163 shares their recognition site(s) with that of Hb-Hp complexes, suggesting that CD163 serves as a scavenger receptor for both ligands.

Discussion

Several studies based on TWEAK-induced migration, proliferation, and angiogenesis in endothelial cells and apoptosis in tumor cells have long suggested a role for the TWEAK receptor Fn14/TweakR (1–3, 17). However, the wide range of biological effects in cells deficient for that receptor raises the possibility that cells may express other TWEAK receptors. First, we screened a combinatorial library to find TWEAK-binding peptides and found motifs similar to that of CD163. Moreover, we validated functional protein-protein interactions between TWEAK and CD163. Finally, we show that the binding is specific. The findings reported here support the candidacy of the cell surface protein CD163 as a TWEAK-binding protein and a possible alternative TWEAK receptor in Fn14/TweakR-deficient cells.

After the selection of a random peptide library on immobilized TWEAK, marked enrichment was obtained. Upon DNA sequencing of the selected phage clones, it became apparent that many of the peptides displayed contained the predominant motif WXDDG or its permutations (flanked by cysteine residues engineered into the libraries). Of note, we have previously identified similar peptide motifs as structural sites in certain integrins (19) and aminopeptidases (22), indicating that this motif is both conserved in several protein families and functional in ligand-receptor binding interactions.

In this study, sequence homology analysis of the predominant motifs recovered from the selection (Figs. 2 and 4) suggest that the peptides mimic the structure of CD163, a member of the class B SRCR restricted to the monocyte/macrophage lineage. SRCR domains are widely found in cell surface molecules where they are thought to mediate ligand binding (39); in particular, the CD163 sequence has nine extracellular cystein-rich domains. Indeed, repeated units of cysteine clusters also define the TNFR superfamily (42). The presence of this motif suggested the possibility that such domains may mediate a putative protein interaction between TWEAK and CD163. The crystal structure of another member of the SRCR family, the glycoprotein M2BP (Mac-2 binding protein; M2BP) (43), has been considered a general template for the cysteine-rich domains in proteins of this ancient superfamily (43, 44), including CD163. It consists of a curved six-stranded β-sheet cradling an α-helix. When TWEAK-binding peptides were aligned with the CD163 sequence, the putative sites of interaction were identified in eight of the nine cysteine-rich domains (excepting SRCR5), 42 peptides were matched to the β-sheets, and only two were matched to the corresponding α-helix of SRCR2 (residues 192–196) and SRCR9 (residues 954–960). No peptide appeared to interact with the transmembrane or intracellular domains, indicating that the interactions are limited to regions of the protein known to be extracellular. Supporting these observations, an anti-CD163 mAb inhibited binding of the CWDDGWSFC phage, which displays a peptide that matches several different regions of the extracellular domain of CD163, to TWEAK.

Other unexpected aspects of our results merit further discussion. The CD163 macrophage-restricted Ag is an established scavenger receptor of circulating Hp-Hb complexes (29, 36), but not of Hp or Hb separately (29). The binding region to CD163 is likely to be represented by structural components created by both Hp and Hb molecules or by an unfolding of a neo-epitope upon complex formation. The residues in the complexes containing the CD163-recognition site have not yet been characterized. However, the Hp β-chain (the major protein of the complex) harbors the receptor-recognition site exposed during complex formation because of its location in Hp (45, 46). Comparison of protein sequences of TWEAK with Hp and Hb reveals similarity in a region that comprised >30% of the secreted TWEAK. In addition, the hypervariable region of a Fab Ab that specifically recognizes the Hp-Hb complex revealed >40% homology with two TWEAK-binding peptides isolated from our panning, supporting the hypothesis that TWEAK may also mimic a neo-epitope generated in the Hp-Hb complex (37).

Madsen et al. (39) have recently shown that the anti-CD163 Ab clone Ki-M8 blocks the binding of the ligand complexes to SRCR domain 3 while clone GHI/61 binds to SRCR domain 7, not affecting the specific ligand-binding site. In this study we have shown that TWEAK binds in vitro to purified CD163 in a dose-dependent manner and that this binding is inhibited by preincubation of CD163 with mAbs raised against CD163. Moreover, TWEAK binding to Fn14/TweakR or CD163 can be displaced by the addition of the opposite soluble receptor, indicating a competition between both receptors. These results lend further support to our hypothesis of a TWEAK-CD163 protein interaction.

Because CD163 is expressed exclusively on monocytes and macrophages, we investigated the putative interactions of TWEAK and CD163 in this cell lineage. In agreement with previous reports (9), the established TWEAK receptor is not present at detectable levels on the surface of freshly isolated CD14-positive monocytes from healthy human donors. Nevertheless, such cells are capable of binding TWEAK as shown here. Thus, CD14-positive/CD163-positive cells not expressing Fn14/TweakR still bind TWEAK.

These results suggest that other receptor(s) may mediate the interaction. We show that preincubation with TWEAK inhibited recognition by a specific Ab of CD163 on the monocyte surface.

Therefore, we used cross-linking of CD163 by a specific Ab to activate tyrosine kinases in human monocytes. Given that the CD14-positive human monocytes in our system were nonproliferating (40), we demonstrated that incubation with an anti-CD163 Ab induced a metabolic activation relative to controls. Coincubation with TWEAK abrogated this activation. In contrast, monocytes incubated with TWEAK alone showed no change in the same conditions. Thus, TWEAK can inhibit the activating effect of the anti-CD163 mAb through biochemical competition for the binding site, steric hindrance, or both.

Also, we have shown that human monocytes can sequester soluble TWEAK from the culture medium. Consistently, monocytes are not able to bind TWEAK in the presence of either an anti-CD163 mAb or a peptide motif mimicking CD163. In light of these findings, TWEAK and CD163 seem to be functionally linked. In addition, TWEAK mediates monocyte death induced by autologous T cells in patients with certain autoimmune diseases (10) and previous reports have shown that TWEAK is produced by monocytes stimulated by IFN-γ, an anti-inflammatory cytokine that also negatively regulates CD163 (26), again suggesting that both proteins function in interacting pathways.

Finally, by using CHO cells transiently expressing the scavenger receptor CD163, we demonstrated that rHuTWEAK specifically binds to this receptor in a similar manner as to its natural receptor (Fn14/TweakR); such binding is reverted by unlabeled rHuTWEAK or the Hp-Hb complex. Moreover, the CD163 receptor also mediates rHuTWEAK degradation (data not shown), an observation consistent with a scavenger function for this ligand.

In summary, our results demonstrate that a protein-protein interaction occurs between TWEAK and CD163 at the cell surfaces of human CD14-positive monocytes. Several lines of evidence are presented in support of this hypothesis. First, phage clones displaying peptides that bind to TWEAK mimic the several SRCR domains in CD163. Furthermore, we also observed that the TWEAK protein structure mimics the Hp-Hb complex, an established CD163 ligand. TWEAK and CD163 also interact at the surface of Fn14/TweakR-negative human monocytes, and TWEAK competes for CD163 binding to these cells. Recently, it was reported that TWEAK promotes tumor cell invasion rather than apoptosis (47), an event that correlates with the overexpression of Fn14/TweakR. According to our findings, it could be proposed that CD163 is a scavenger receptor for TWEAK, thus preventing TWEAK from exerting its biological function(s) by sequestering it from the tumor environment. In accordance with the competition between TWEAK and Hp-Hb shown in the binding experiment, one might also propose that TWEAK could act as an antagonist for CD163. Future research efforts regarding the functional effects of TWEAK-CD163 interaction need to be performed to validate one of these hypotheses. A detailed understanding of this possible functional link between TWEAK and CD163 may have impact on conditions such as inflammation and cancer (10, 47, 48).

Acknowledgments

Disclosures

References

1. Locksley, R. M., N. Killeen, and M. J. Lenardo. 2001. The TNF and TNF receptor superfamilies: integrating mammalian biology. *Cell* 104: 487–501.
2. Ware, C. F. 2002. Tumor necrosis factors. In *Encyclopedia of Cancer*, 2nd Ed., J. R. Bertino, ed. Academic Press, San Diego, pp. 475–489.
3. Bodmer, J. L., P. Schneider, and J. Tschopp. 2002. The molecular architecture of the TNF superfamily. *Trends Biochem. Sci.* 27: 19–26.
4. Chicheportiche, Y., P. R. Bourdon, H. Xu, Y. M. Hsu, H. Scott, C. Hession, I. Garcia, and J. L. Browning. 1997. TWEAK, a new secreted ligand in the tumor necrosis factor family that weakly induces apoptosis. *J. Biol. Chem.* 272: 32401–32410.
5. Lynch, C. N., Y. C. Wang, J. K. Lund, Y. W. Chen, J. A. Leal, and S. R. Wiley. 1999. TWEAK induces angiogenesis and proliferation of endothelial cells. *J. Biol. Chem.* 274: 8455–8459.
6. Jakubowski, A., B. Browning, M. Lukashev, I. Sizing, J. S. Thompson, C. D. Benjamin, Y. M. Hsu, C. Ambrose, T. S. Zheng, and L. C. Burkly. 2002. Dual role for TWEAK in angiogenic regulation. *J. Cell Sci.* 115: 267–274.
7. Harada, N., M. Nakayama, H. Nakano, Y. Fukuchi, H. Yagita, and K. Okumura. 2002. Pro-inflammatory effect of TWEAK/Fn14 interaction on human umbilical vein endothelial cells. *Biochem. Biophys. Res. Commun.* 299: 488–493.
8. Chicheportiche, Y., R. Chicheportiche, I. Sizing, J. Thompson, C. B. Benjamin, C. Ambrose, and J. M. Dayer. 2002. Proinflammatory activity of TWEAK on human dermal fibroblasts and synoviocytes: blocking and enhancing effects of anti-TWEAK monoclonal antibodies. *Arthritis Res.* 4: 126–133.
9. Nakayama, M., N. Kayagaki, N. Yamaguchi, K. Okumura, and H. Yagita. 2000. Involvement of TWEAK in interferon γ-stimulated monocyte cytotoxicity. *J. Exp. Med.* 192: 1373–1379.
10. Kaplan, M. J., E. E. Lewis, E. A. Shelden, E. Somers, R. Pavlic, W. J. McCune, and B. C. Richardson. 2002. The apoptotic ligands TRAIL, TWEAK, and Fas ligand mediate monocyte death induced by autologous lupus T cells. *J. Immunol.* 169: 6020–6029.
11. Desplat-Jego, S., S. Varriale, R. Creidy, R. Terra, D. Bernard, M. Khestchatisky, S. Izui, Y. Chicheportiche, and J. Boucraut. 2002. TWEAK is expressed by glial cells, induces astrocyte proliferation and increases EAE severity. *J. Neuroimmunol.* 133: 116–123.
12. Nakayama, M., K. Ishidoh, N. Kayagaki, Y. Kojima, N. Yamaguchi, H. Nakano, E. Kominami, K. Okumura, and H. Yagita. 2002. Multiple pathways of TWEAK-induced cell death. *J. Immunol.* 168: 734–743.
13. Schneider, P., R. Schwenzer, E. Haas, F. Muhlenbeck, G. Schubert, P. Scheurich, J. Tschopp, and H. Wajant. 1999. TWEAK can induce cell death via endogenous TNF and TNF receptor 1. *Eur. J. Immunol.* 29: 1785–1792.
14. Kaptein, A., M. Jansen, G. Dilaver, J. Kitson, L. Dash, E. Wang, M. J. Owen, J. L. Bodmer, J. Tschopp, and S. N. Farrow. 2000. Studies on the interaction between TWEAK and the death receptor WSL-1/TRAMP (DR3). *FEBS Lett.* 485: 135–141.
15. Marsters, S. A., J. P. Sheridan, R. M. Pitti, J. Brush, A. Goddard, and A. Ashkenazi. 1998. Identification of a ligand for the death-domain-containing receptor Apo3. *Curr. Biol.* 8: 525–528.
16. Wiley, S. R., L. Cassiano, T. Lofton, T. Davis-Smith, J. A. Winkles, V. Lindner, H. Liu, T. O. Daniel, C. A. Smith, and W. C. Fanslow. 2001. A novel TNF receptor family member binds TWEAK and is implicated in angiogenesis. *Immunity* 15: 837–846.
17. Nakayama, M., K. Ishidoh, Y. Kojima, N. Harada, E. Kominami, K. Okumura, and H. Yagita. 2003. Fibroblast growth factor-inducible 14 mediates multiple pathways of TWEAK-induced cell death. *J. Immunol.* 170: 341–348.
18. Polek, T. C., M. Talpaz, B. G. Darnay, and T. Spivak-Kroizman. 2003. TWEAK mediates signal transduction and differentiation of RAW264.7 cells in the absence of Fn14/TweakR: evidence for a second TWEAK receptor. *J. Biol. Chem.* 278: 32317–32323.
19. Pasqualini, R., E. Koivunen, and E. Ruoslahti. 1995. A peptide isolated from phage display libraries is a structural and functional mimic of an RGD-binding site on integrins. *J. Cell Biol.* 130: 1189–1195.
20. Mintz, P. J., J. Kim, K. A. Do, X. Wang, R. G. Zinner, M. Cristofanilli, M. A. Arap, W. K. Hong, P. Troncoso, C. J. Logothetis, R. Pasqualini, and W. Arap. 2003. Fingerprinting the circulating repertoire of antibodies from cancer patients. *Nat. Biotechnol.* 21: 57–63.
21. Cardó-Vila, M., W. Arap, and R. Pasqualini. 2003. $\alpha_v\beta_5$ integrin-dependent programmed cell death triggered by a peptide mimic of annexin V. *Mol. Cell* 11: 1151–1162.
22. Pasqualini, R., E. Koivunen, R. Kain, J. Lahdenranta, M. Sakamoto, A. Stryhn, R. A. Ashmun, L. H. Shapiro, W. Arap, and E. Ruoslahti. 2000. Aminopeptidase N is a receptor for tumor-homing peptides and a target for inhibiting angiogenesis. *Cancer Res.* 60: 722–727.
23. Giordano, R. J., M. Cardó-Vila, J. Lahdenranta, R. Pasqualini, and W. Arap. 2001. Biopanning and rapid analysis of selective interactive ligands. *Nat. Med.* 7: 1249–1253.
24. Hogger, P., J. Dreier, A. Droste, F. Buck, and C. Sorg. 1998. Identification of the integral membrane protein RM3/1 on human monocytes as a glucocorticoid-inducible member of the scavenger receptor cysteine-rich family (CD163). *J. Immunol.* 161: 1883–1890.
25. Backe, E., R. Schwarting, J. Gerdes, M. Ernst, and H. Stein. 1991. Ber-MAC3: new monoclonal antibody that defines human monocyte/macrophage differentiation antigen. *J. Clin. Pathol.* 44: 936–945.
26. Buechler, C., M. Ritter, E. Orso, T. Langmann, J. Klucken, and G. Schmitz. 2000. Regulation of scavenger receptor CD163 expression in human monocytes and macrophages by pro- and anti-inflammatory stimuli. *J. Leukocyte Biol.* 67: 97–103.

27. Pulford, K., K. Micklem, S. McCarthy, J. Cordell, M. Jones, and D. Y. Mason. 1992. A monocyte/macrophage antigen recognized by the four antibodies GHI/61, Ber-MAC3, Ki-M8 and SM4. *Immunology* 75: 588–595.

28. Van den Heuvel, M. M., C. P. Tensen, J. H. Van As, T. K. Van den Berg, D. M. Fluitsma, C. D. Dijkstra, E. A. Dopp, A. Droste, F. A. Van Gaalen, C. Sorg, et al. 1999. Regulation of CD163 on human macrophages: cross-linking of CD163 induces signaling and activation. *J. Leukocyte Biol.* 66: 858–866.

29. Kristiansen, M., J. H. Graversen, C. Jacobsen, O. Sonne, H. J. Hoffman, S. K. Law, and S. K. Moestrup. 2001. Identification of the haemoglobin scavenger receptor. *Nature* 409: 198–201.

30. Komohara, Y., J. Hirahara, T. Horikawa, K. Kawamura, E. Kiyota, N. Sakashita, N. Araki, and M. Takeya. 2006. AM-3K, an anti-macrophage antibody, recognizes CD163, a molecule associated with an anti-inflammatory macrophage phenotype. *J. Histochem. Cytochem.* 54: 763–771.

31. Barbas, C. F., III, D. R. Burton, J. K. Scott, and G. J. Silverman. 2000. *Phage Display: A Laboratory Manual*. Cold Spring Harbor Laboratory Press, Cold Spring Harbor, NY.

32. Arap, W., M. G. Kolonin, M. Trepel, J. Lahdenranta, M. Cardó-Vila, R. J. Giordano, P. J. Mintz, P. U. Ardelt, V. J. Yao, C. I. Vidal, et al. 2002. Steps toward mapping the human vasculature by phage display. *Nat. Med.* 8: 121–127.

33. Thompson, J. D., D. G. Higgins, and T. J. Gibson. 1994. CLUSTAL W: improving the sensitivity of progressive multiple sequence alignment though sequence weighting, position-specific gap penalties and weight matrix choice. *Nucleic Acids Res.* 22: 4673–4680.

34. Virella, G., J. F. Muñoz, G. M. P. Galbraith, C. Gissinger, C. Chassereau, and M. F. Lopes-Virella. 1995. Activation of human monocyte-derived macrophages by immune complexes containing low-density lipoprotein. *Clin. Immunol. Immunopathol.* 75: 179–189.

35. Kuniyasu, A., N. Ohgami, S. Hayashi, A. Miyazaki, S. Horiuchi, and H. Nakayama. 2003. CD36-mediated endocytic uptake of advanced glycation end products (AGE) in mouse 3T3-L1 and human subcutaneous adipocytes. *FEBS Lett.* 537: 85–90.

36. Graversen, J. H., M. Madsen, and S. K. Moestrup. 2002. CD163: a signal receptor scavenging haptoglobin-hemoglobin complexes from plasma. *Int. J. Biochem. Cell Biol.* 34: 309–314.

37. Yoshioka, N., and M. Z. Atassi. 1986. Hemoglobin binding with haptoglobin: localization of the haptoglobin-binding sites on the β-chain of human haemoglobin by synthetic overlapping peptides encompassing the entire chain. *Biochem. J.* 234: 453–456.

38. Horn, I. R., M. J. Nielsen, M. Madsen, C. Jacobsen, J. H. Graversen, S. K. Moestrup, and C. Jacobsen. 2003. Generation of a haptoglobin-hemoglobin complex-specific Fab antibody blocking the binding of the complex to CD163. *Eur. J. Haematol.* 71: 289–293.

39. Madsen, M., H. J. Moller, M. J. Nielsen, C. Jacobsen, J. H. Graversen, T. van den Berg, and S. K. Moestrup. 2004. Molecular characterization of the haptoglobin.hemoglobin receptor CD163: ligand binding properties of the scavenger receptor cysteine-rich domain region. *J. Biol. Chem.* 279: 51561–51567.

40. Lund, P. K., E. Namork, S. H. Brorson, A. B. Westvik, G. B. Joo, R. Ovstebo, and P. Kierulf. 2002. The fate of monocytes during 24 h of culture as revealed by flow cytometry and electron microscopy. *J. Immunol. Methods* 270: 63–76.

41. Takase, S., G. Schmid-Schonbein, and J. Bergan. 1999. Leukocyte activation in patients with venous insufficiency. *J. Vasc. Surg.* 30: 148–156.

42. Idriss, H. T., and J. H. Naismith. 2000. TNF α and the TNF receptor superfamily: structure-function relationship(s). *Microsc. Res. Tech.* 50: 184–195.

43. Koths, K., E. Taylor, R. Halenbeck, C. Casipit, and A. Wang. 1993. Cloning and characterization of a human Mac-2-binding protein, a new member of the superfamily defined by the macrophage scavenger receptor cysteine-rich domain. *J. Biol. Chem.* 19: 14245–14249.

44. Hohenester, E., T. Sasaki, and R. Timpl. 1999. Crystal structure of a scavenger receptor cysteine-rich domain sheds light on an ancient superfamily. *Nat. Struct. Biol.* 6: 228–232.

45. Javid, J., and P. K. Pettis. 1975. The modification of hemoglobin-antihemoglobin reaction by haptoglobin. *J. Lab. Clin. Med.* 86: 777–784.

46. Wejman, J. C., D. Hovsepian, J. S. Wall, J. F. Hainfeld, and J. Greer. 1984. Structure and assembly of haptoglobin polymers by electron microscopy. *J. Mol. Biol.* 174: 343–368.

47. Tran, N. L., W. S. McDonough, B. A. Savitch, S. P. Fortin, J. A. Winkles, M. Symons, M. Nakada, H. E. Cunliffe, G. Hostetter, D. B. Hoelzinger, et al. 2006. Increased fibroblast growth factor-inducible 14 expression levels promote glioma cell invasion via Rac1 and nuclear factor-κB and correlate with poor patient outcome. *Cancer Res.* 66: 9535–9542.

48. Perper, S. J., B. Browning, L. C. Burkly, S. Weng, C. Gao, K. Giza, L. Su, L. Tarilonte, T. Crowell, L. Rajman, et al. 2006. TWEAK is a novel arthritogenic mediator. *J. Immunol.* 177: 2610–2620.

Applications of nanoparticles to diagnostics and therapeutics in colorectal cancer

Paolo Fortina[1,2], Larry J Kricka[3], David J Graves[4], Jason Park[3], Terry Hyslop[5,6,7], Felicia Tam[8], Naomi Halas[9], Saul Surrey[10] and Scott A. Waldman[6,7]

[1] Department of Cancer Biology, Kimmel Cancer Center, Thomas Jefferson University, Jefferson Medical College, Philadelphia, PA 19107, USA
[2] Dipartimento di Medicina Sperimentale, Universita' La Sapienza, 00185, Roma, Italy
[3] Department of Pathology and Laboratory Medicine, University of Pennsylvania Medical Center, Philadelphia, PA 19104, USA
[4] Department of Chemical and Biomolecular Engineering, University of Pennsylvania School of Engineering and Applied Science, Philadelphia, PA 19104, USA
[5] Division of Biostatistics, Thomas Jefferson University, Jefferson Medical College, Philadelphia, PA 19107, USA
[6] Division of Clinical Pharmacology, Thomas Jefferson University, Jefferson Medical College, Philadelphia, PA 19107, USA
[7] Department of Pharmacology and Experimental Therapeutics, Thomas Jefferson University, Jefferson Medical College, Philadelphia, PA 19107, USA
[8] Department of Physics and Astronomy, Rice University, Houston, TX 77005, USA
[9] Department of Electrical and Computer Engineering, Rice University, Houston, TX 77005, USA
[10] Cardeza Foundation for Hematologic Research, Department of Medicine, Thomas Jefferson University, Jefferson Medical College, Philadelphia, PA 19107, USA

Nanotechnology has considerable promise for the detection, staging and treatment of cancer. Here, we outline one such promising application: the use of nanostructures with surface-bound ligands for the targeted delivery and ablation of colorectal cancer (CRC), the third most common malignancy and the second most common cause of cancer-related mortality in the US. Normal colonic epithelial cells as well as primary CRC and metastatic tumors all express a unique surface-bound guanylyl cyclase C (GCC), which binds the diarrheagenic bacterial heat-stable peptide enterotoxin ST. This makes GCC a potential target for metastatic tumor ablation using ST-bound nanoparticles in combination with thermal ablation with near-infrared or radiofrequency energy absorption. Furthermore, the incorporation of iron or iron oxide into such structures would provide advantages for magnetic resonance imaging (MRI). Although the scenarios outlined in this article are hypothetical, they might stimulate ideas about how other cancers could be attacked using nanotechnology.

Introduction

Colorectal cancer is the third most common neoplasm and the second leading cause of cancer-related mortality in the US (Table 1) [1]. Surgery continues to have a major role in colorectal cancer survival in early-stage disease, by removing detectable tumor; however, residual micrometastases might cause a relapse [2]. Recurrence rates vary from 3% for disease limited to the mucosa (stage I) to >50% for tumors that have spread to regional lymph nodes (stage III). Overall, ~50% of surgically treated patients suffer

from a relapse, with 30% recurring locally or regionally and 70% recurring at distant sites – primarily the liver and lung [3]. There is an unmet clinical need for image-based detection, targeted delivery, and ablation of metastases, to affect survival in this disease. In this context, guanylyl cyclase C (GCC), the intestinal receptor for bacterial diarrheagenic heat-stable enterotoxins (STs), which is selectively expressed in the apical membranes of intestinal mucosa cells in normal adults and in colon cancer cells, might be the 'magic bullet' for targeted ablation of colorectal cancer micrometastases [4–6].

Here, we present GCC as a receptor target in colorectal cancer, discuss diagnostics using nanostructures, and address *in vivo* imaging using iron oxide nanoparticles and near-infrared (NIR) fluorescence imaging – approaches that could be extended to other tumor types that have unique receptor functionalities. Novel therapeutic approaches based on functionalized nanoshells and iron-oxide nanoparticles for NIR and radio frequency (RF)-mediated thermal ablation, respectively, of micrometastases as well as nanostructure-based drug delivery are also evaluated. Regulatory issues related to use of nanostructures are not addressed here and have been reviewed previously [7,8].

Nanotechnology

In the past five years, the applications of nanotechnology have been realized in clinical laboratory analysis, imaging and therapeutics [9–16]. The versatility and broad applicability of nanotechnology reflect the spectra of composite materials (e.g. metals, semiconductors or polymers), geometries (e.g. sphere, prism or rod), and structures (e.g. solid, core or shell or dendrimers) that have been generated. This rapidly increasing activity is due to several

---

Corresponding author: Fortina, P. (paolo.fortina@jefferson.edu).
Available online 21 February 2007.

Table 1. Causes of cancer and cancer-related mortality by site

	ESTIMATED US CANCER CASES[a]		
	Men	Women	
New cancers anticipated	720 280	679 510	
Prostate	33%	31%	Breast
Lung and bronchus	13%	12%	Lung and bronchus
Colon and rectum	10%	11%	Colon and rectum
Urinary bladder	6%	6%	Uterine corpus
Melanoma of skin	5%	4%	Melanoma of skin
Non-Hodgkin's lymphoma	4%	4%	Non-Hodgkin's lymphoma
Kidney	3%	3%	Thyroid
Oral cavity	3%	3%	Ovary
Leukemia	3%	2%	Urinary bladder
Pancreas	2%	2%	Pancreas
All other sites	18%	22%	All other sites
	ESTIMATED US CANCER DEATHS		
	Men	Women	
	291 270	273 560	
Lung and bronchus	31%	26%	Lung and bronchus
Colon and rectum	10%	15%	Breast
Prostate	9%	10%	Colon and rectum
Pancreas	6%	6%	Pancreas
Leukemia	4%	6%	Ovary
Liver and bile duct	4%	4%	Leukemia
Esophagus	4%	3%	Non-Hodgkin's lymphoma
Non-Hodgkin's lymphoma	3%	3%	Uterine corpus
Urinary bladder	3%	2%	Multiple myeloma
Kidney	3%	2%	Brain/ONS
All other sites	23%	23%	All other sites

[a]Excludes basal and squamous cell skin cancers and *in situ* carcinoma except urinary bladder. Abbreviation: ONS, other nervous systemSource: American Cancer Society, 2006 (http://www.cancer.org/docroot/PRO/content/PRO_1_1_Cancer_Statistics_2006_Presentation.asp)

factors, including: i) the discovery of new forms of matter, such as buckministerfullerenes (buckyballs) and nanotubes made of carbon [17,18]; ii) the increasing ability of materials scientists to produce reagents on a small but controlled size scale; ii) the availability of instruments, such as the atomic force microscope and the scanning tunneling microscope, to complement traditional instrumentation for viewing and characterizing nanoparticles [19]; iv) the discovery of quantum effects, such as size-dependent fluorescent emission in small particles; and v) the stimulation provided by new funding initiatives from worldwide government agencies (http://nano.cancer.gov/).

Nano-sized structures range from 1–100 nm – for comparative purposes, a single turn of the DNA helix is ~3.4 nm in length, and a eukaryotic cell has dimensions in the range 10–100 μm. Nanoparticles have been used in biology and medicine for >50 years [20]. In earlier times, they were generally called colloids, emulsions or aerosols, and included many natural and man-made suspensions. Colloidal radioactive gold or gold salts were used as therapeutic agents for intra-articular injection in patients with rheumatoid arthritis – a practice that continues in the current clinical management of this disease – and for treating cancer in the 1950s [21], and colloidal gold or gold granules were used as electron-opaque labels in electron microscopy in the 1960s.

Some of the newer techniques for producing nanoparticles involve: i) cooling them from a hot gas or plasma; ii) reacting a gaseous mixture at a hot surface; iii) designing a system with defined properties so it forms a geometrically precise multi-phase structure as it solidifies; and iv) forming by self-assembly, in which components are designed so that intermolecular forces cause them to come together in a pre-

determined fashion. Multi-step procedures can be used to produce sophisticated core and shell structures that can be further engineered to have highly controlled and 'tunable' properties. These include paramagnetic nanoparticles, which can serve as contrast agents for the MRI of tumors [22–24], and nanoshells, which can be fabricated with defined metal shell thicknesses to absorb specific wavelengths of NIR light, resulting in their plasmon resonance and transfer of thermal energy to the surrounding environment [25,26]. In this latter example, NIR wavelengths have minimal optical absorption and, consequently, optimum penetration in tissues, resulting in minimal thermal injury to structures that lack the nanoparticles.

Furthermore, nanostructures can be conjugated to biological molecules, including hormones and antibodies, which enables their targeting to tissues expressing their cognate receptors [27–29]. For example, fluorescent quantum dots conjugated to various peptides specifically target either the vasculature of normal tissues or, alternatively, of cancer cells [30]. Tumor-specific monoclonal antibodies can be conjugated to nanostructures. Monoclonal antibodies directed against a prostate-specific membrane antigen (PSMA) were attached to the surface of triblock copolymer-modified quantum dots and used to image prostate cancer cells, both *in vitro* and *in vivo*, in tumor xenografts [31]. Indeed, anti-PSMA quantum dots injected IV and visualized fluorescently by macro-illumination accumulate in and are retained by prostate cancer xenografts in nude mice.

Nanoshells
Nanoparticles composed of metallic shells with dielectric cores have a tunable plasmon resonance based on the

relative dimensions of the dielectric core and metallic shell [23–26]. Nanoshells composed of metallic gold coating a dielectric core, such as silica, resonate at specific wavelengths of light ranging from 500 nm to 2 μm, depending on their core:shell thickness ratio. Indeed, gold shells of 10 nm encasing a 110 nm silica core resonate in the NIR spectrum (~800 nm); these wavelengths exhibit minimal optical absorption by, and consequently optimum penetration through, overlying tissues, with minimal attendant thermal injury (Figure 1). In the context of specifically absorbing energy in the NIR spectrum, these nanoshells are extremely efficient in converting optical energy into heat. When exposed to NIR light, nanoshells with a 10 nm gold shell and a 110 nm silica core induce thermal damage in adjacent cells [25]. Similarly, direct injection of nanoshells into subcutaneous tumors in a mouse xenograft model resulted in temperature increases of ~37 °C greater than the surrounding normal tissue after ~6 min of exposure to 808 nm at 4 Watts/cm^2, associated with thermal damage to tumors [26]. Separately, nanoshells injected IV into mice with subcutaneous tumors resulted in NIR heating of tumors compared with non-tumor sites and control animals; most probably, this damage resulted from the enhanced permeability of, and retention by, the tumor neovasculature compared with the established vasculature in normal tissues [26]. Differential heating was associated with complete regression of subcutaneous tumor xenografts in animals receiving gold nanoshells compared with control animals. Nanoshells that specifically target tumor cell receptors might be expected to perform even better, particularly on larger and more mature tumors.

Targeting nanoshells and iron-oxide nanoparticles for receptor-directed thermal ablation

The realization of the full diagnostic and therapeutic potential of nanoparticles *in vivo*, in part, reflects the ability to target their localization and uptake to specific cells and tissues. Initial studies with nanoshells for thermal ablation depended on preferential delivery to tumors by exploiting the increased permeability and retention within the tumor neovasculature [32,33]. However, the gold surface of nanoshells can be readily conjugated to biologically active molecules, including antibodies [34]. Thus, an ortho-pyridyl-disulfide-*N*-hydroxysuccinimide polyethylene glycol polymer was used to conjugate HER2-specific IgG antibodies to gold nanoshell surfaces. Under conditions of dark-field microscopy, binding of the anti-HER2 nanoshells to HER2-positive SKBr3 human mammary adenocarcinoma cells was detected by gold-specific silver enhancement staining. These observations highlight the ability of gold nanoshells that are suitable for thermal ablation to be conjugated to targeting molecules for tumor-specific delivery. Iron-oxide or iron-cored nanoshells should provide contrast agents suitable for MRI imaging, which, in addition to their non-invasive nature, would provide even more powerful and generally useful diagnostic tools [14].

Nanometer-sized particles of different shapes and compositions are emerging as important new tools for cancer
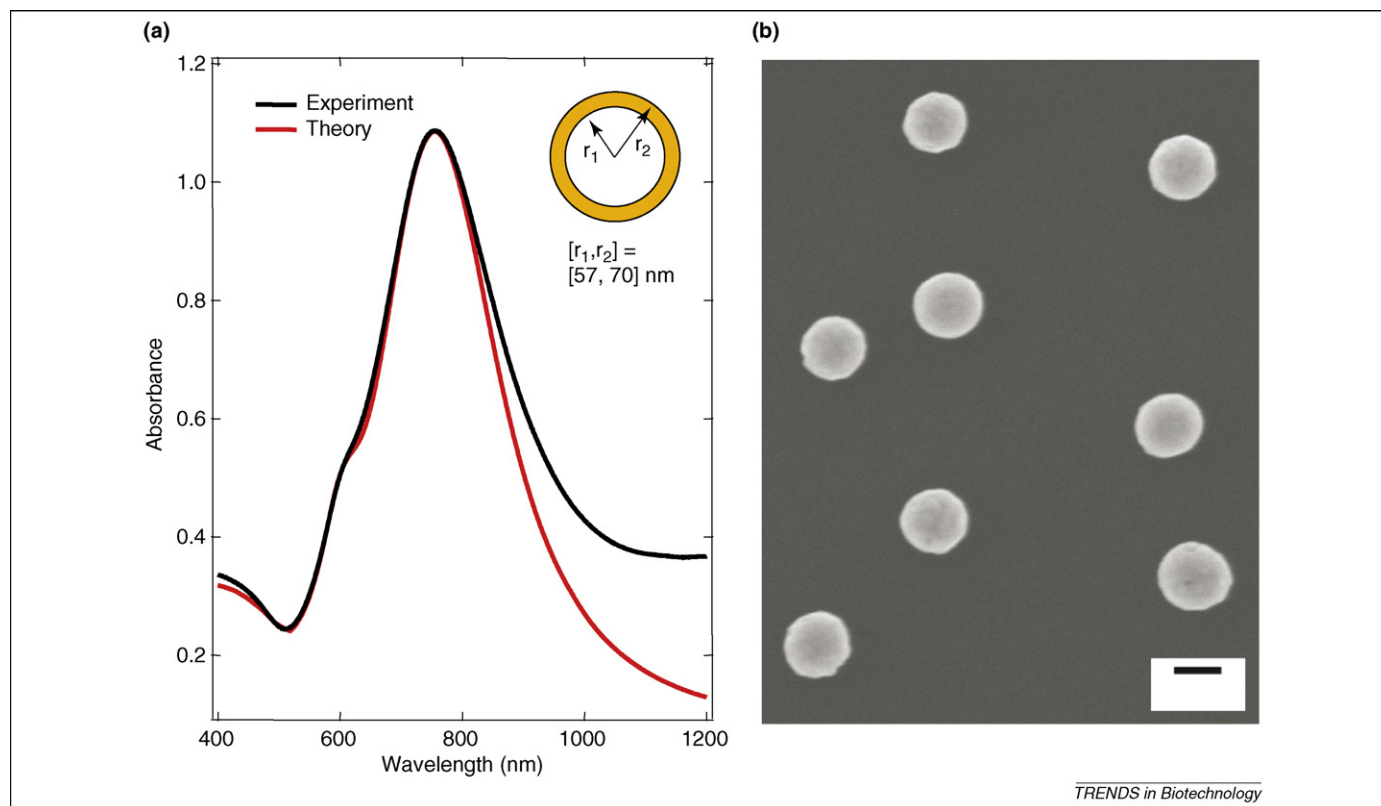

Figure 1. Gold–silica nanoshells tuned to NIR wavelengths. Gold nanoshells are synthesized using SiO$_2$ cores (~114 nm diameter) with surface seeding using 1–3 nm gold particles on cores, followed by controlled surface fill-in with gold by reductive deposition from a gold salt solution. **(a)** The experimental and theoretical extinction spectra of nanoshells with [r$_1$, r$_2$] = [57,70] nm (inset). The radii define the inner and outer diameters of the shell and hence its thickness, leading to the generation of gold nanoshells with an absorption maximum in the NIR (~780 nm). **(b)** Scanning electron micrograph of synthesized gold nanoshells. Bar = 100 nm.

diagnosis, staging and therapeutics. The lack of broader adoption might reflect the considerable barriers to implementation (e.g. availability of particles and suitable automated detection systems) and the absence of biosafety data [35]. Potential applications of thermal-induced tumor ablation by targeted delivery of gold nanoshells to colon cancer cells and, by analogy, to other types of tumors with unique receptors will be addressed below.

Colorectal cancer
Guanylyl cyclase C
GCC is the intestinal receptor for the high-affinity, bacterial, diarrheagenic, heat-stable enterotoxins (STs) and the lower affinity endogenous ligands guanylin and uroguanylin, which induce accumulation of cGMP [4]. In turn, cGMP activates a protein kinase that phosphorylates ion channels, mediating the efflux of salt and water and, in the case of ST, causes diarrhea (Figure 2). GCC is selectively expressed in the apical membranes of intestinal mucosa cells and colon cancer cells. Indeed, expression of GCC has been detected in all colorectal tumors, but not in extragastrointestinal tissues or tumors [4,36] Selective overexpression of GCC by colorectal cancer cells and its anatomical compartmentalization – it is normally confined to mucosa but is accessible to the systemic vasculature in metastatic disease – suggests its utility as a target for delivering therapeutic agents *in vivo*.

GCC as a specific receptor target in colon cancer cells
GCC might be uniquely suited for targeting novel therapeutic agents to metastatic colorectal cancer cells [36]. More specifically, if nanoshells of defined optical resonance frequencies or RF absorptivity can be conjugated to ST for specific delivery, targeted by GCC, it might prove possible to thermally ablate metastatic colorectal tumors. The use of infrared energy in a band where there is minimal absorption by normal tissues is attractive and has been explored experimentally in animals. Unfortunately, thicker tissue masses, such as those found in humans, and highly vascularized (IR absorbing) tissue, such as the liver, present potential problems. RF heating is an alternative with some experimental foundation. It could prove useful, particularly if MRI imaging is used first to locate metastases for focused energy application.

Conjugation of ST to organic and inorganic molecules preserves ligand binding
The 18 amino acid core peptide of ST is sufficient for GCC receptor binding with nanomolar affinity and full biological activity, *in vitro* and *in vivo*. Although manipulation of the ST carboxyl terminus eliminates receptor binding and biological activity, manipulation of the N-terminus preserves binding and enables delivery of large, conjugated, heterologous molecules to colorectal cancer cells. ^{125}I-ST conjugated to biotin, using a long-chain hydrocarbon linker arm coupled to *N*-hydroxy-succinimide, was found to bind to receptors in the GCC positive T84 cell membranes in a time- and concentration-dependent fashion. Binding was also quantitatively competed out by unlabeled ST, demonstrating specificity of the receptor interaction [36]. Analyses of equilibrium binding

by the method of Scatchard demonstrated curvilinear isotherms, and the binding parameters derived from those analyses were comparable to those obtained with unconjugated ^{125}I-ST. In addition, labeled ST conjugated to biotin and avidin was specifically internalized in a time-dependent fashion by T84 cells [37,38]. Similarly, biotinylated ST was immobilized on streptavidin or anti-biotin antibody coated polyvinylchloride plates and used to capture cells expressing ST receptors, with high affinity and specificity [39]. Furthermore, biotinylated ST was coupled to streptavidin–gold and used to label cells expressing GCC, with high affinity and specificity. These data demonstrate that ST can be conjugated to molecules with dimensions and compositions comparable to gold nanoshells and retain full receptor-binding function and the ability to undergo internalization.

Hence, ST attached to gold nanoshells, when injected, should target to micrometastases and/or tumor sites. ST-binding selectively occurs through surface-bound GCC on cancer cells followed by ST-bound nanoshell internalization. NIR radiation could then be used, and the energy absorbed by the internalized gold nanoshells results in heat emission and thermal ablation of the micrometastases. Alternatively, RF-induced ablation of targeted iron-oxide particles could be used; studies are underway using cell lines and animal models of colon cancer to validate such an approach.

Colon cancer diagnostics and therapeutics using nanostructures
The application of nanotechnology to the diagnosis and treatment of colorectal cancer has the promise of enhancing conventional methods as well as fostering the development of novel approaches for detection and therapy. With respect to diagnostics, assays can be divided into *in vitro* (e.g. diagnostic tests on blood serum) and *in vivo* (e.g. imaging of administered agents) applications. Expected improvements for *in vitro* diagnostics include increases in analytical sensitivity without sacrificing specificity. The expected benefits of improved analytical performance include non-amplification assays that are faster and require smaller sample sizes and less expensive detection technologies, which can be readily miniaturized. These benefits might result in greater accessibility of diagnostic tools to clinicians and patients. With regard to *in vivo* imaging, enhancement of conventional imaging agents has resulted in higher sensitivity and finer resolution of tumors. Furthermore, the application of nanotechnology to develop novel imaging agents has resulted in new roles for non-invasive imaging in the detection, staging and overall management of patients with cancer [10–16]. With respect to therapy, targeted nanostructures offer potential solutions to the limitations of standard chemo- and radiotherapeutic modalities, particularly in the context of collateral damage to normal tissues in proximity to, and distant from, tumors and the associated dose-limiting clinical toxicities, which severely restrict the efficacy of the current therapeutic armamentarium.

Although there are many examples of the application of nanotechnology to various analyses and diseases, there are few examples that directly address the *in vitro* diagnosis of
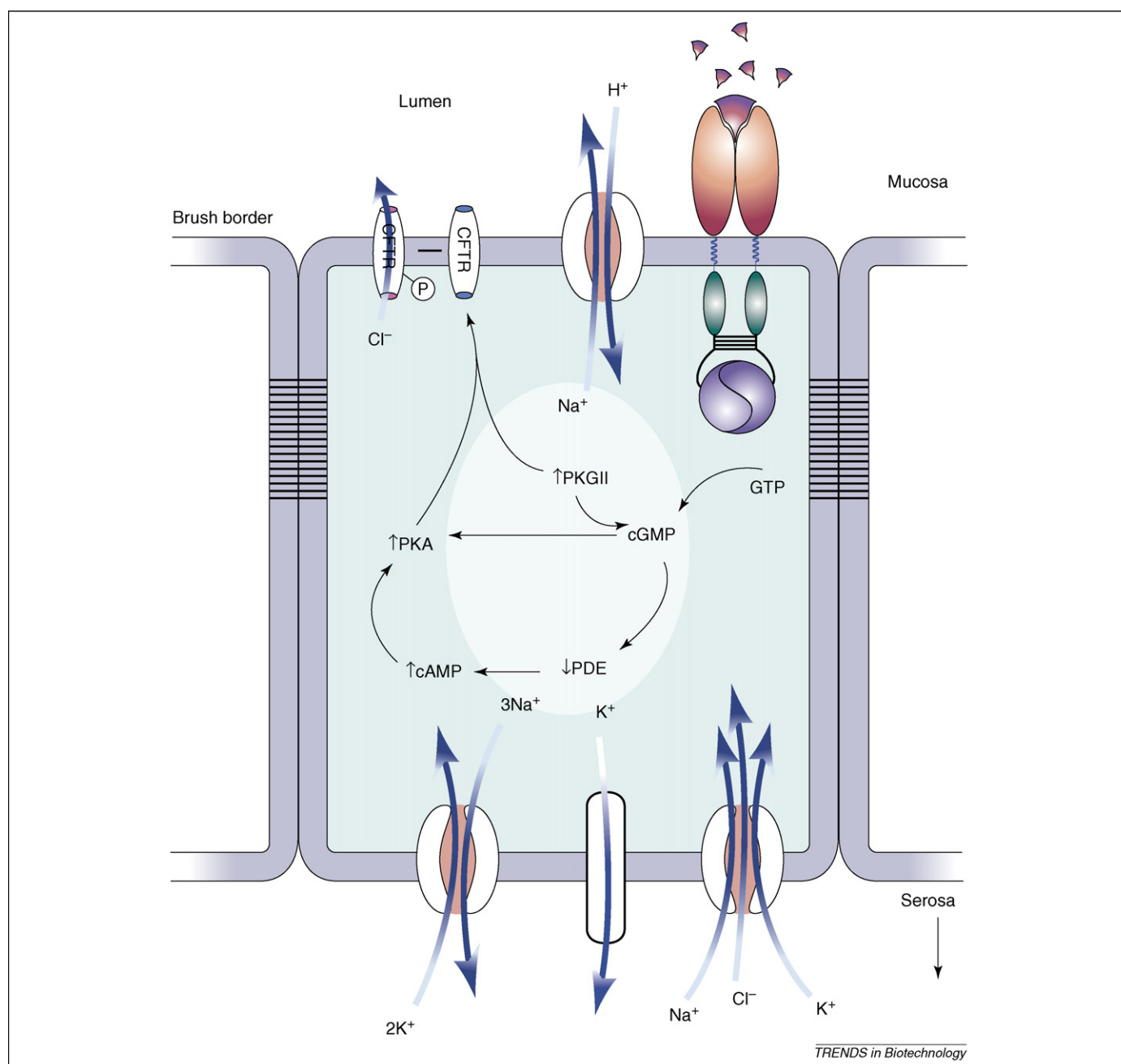
Figure 2. Regulation of intestinal secretion by the heat-stable enterotoxin (ST) and GCC. Bacteria, such as *E. coli*, containing plasmids that encode a member of the homologous peptide family of STs colonize the intestine following the consumption of contaminated food and/or water. Bacterial colonization leads to production of ST in the gut lumen. ST specifically recognizes and binds to the extracellular domain of GCC, which is expressed in the brush border membranes of intestinal mucosa cells from the duodenum to the rectum. The interaction of ST and the extracellular domain of GCC is translated across the plasma membrane to activate the cytoplasmic catalytic domain, resulting in the production and accumulation of cGMP. This cyclic nucleotide binds to and activates cGMP-dependent protein kinase II (PKG II), also localized in the intestinal cell brush border membrane. Furthermore, cGMP can activate cAMP-dependent protein kinase (PKA), either directly or by inhibiting a cAMP-specific phosphodiesterase (PDE), and induces the accumulation of cAMP. The cystic fibrosis transmembrane conductance regulator (CFTR), which is co-localized with GCC and PKG II in brush border membranes, is a substrate for this protein kinase and PKA. CFTR is a chloride channel, and its phosphorylation by PKA or PKG results in a persistent open state, permitting chloride to flow down its concentration gradient from the intracellular to the extracellular compartment. Other ion channels and transporters in the cell maintain the electroneutrality of ST-induced chloride efflux. Vectoral water flux from the basolateral to the apical surface is driven by these ionic conductances, resulting in the accumulation of fluid and electrolytes in the intestinal lumen and secretory diarrhea.

CRC. However, the potential of nanostructures is apparent from the results from other disease systems. Nanostructures, particularly nanoparticles, offer a diverse range of labels that provide direct visual detection and multiplexing capabilities for assaying proteins or detecting nucleic acids [40]. Some of the many types of nanostructures that have been used as components of *in vitro* diagnostic tests for protein markers or nucleic acid targets are presented in

Table 2, and a comprehensive bibliography is available from the National Cancer Institute (http://nano.cancer.gov/resource_center/scientific_bibliography.asp). These nanostructure-based analytical strategies could also be applied to the analysis of specific colon cancer-related markers or nucleic acid sequences.

Similar to *in vitro* diagnostics, the use of nanostructures for *in vivo* imaging is also a particularly promising area of

Table 2. Nanostructures for diagnostic applications

In vitro diagnostic		
Nanostructure	**Application**	**Refs**
Nanochannel		
Glass	DNA sequencing	a
Nanocrystal		
CdS, CuS, PbS	Single-nucleotide polymorphism	[48]
Fluorescein diacetate	IgG	[49]
Nanoparticle		
EuIII-chelate-doped polystyrene	PSA	[50]
Au	Prion protein	[51]
2-methacryloyloxyethyl phosphorylcholine	C-reactive protein	[52]
Polystyrene	Single-base mutation	[53]
Silica	Calf thymus DNA	[54]
Ag on Au	IgG	[55]
Tris (2,2′-bipyridyl) dichloroRu (II) hexahydrate-doped silica	IgG, DNA	[56]
Nanopore		
Silicon nitride	DNA sequencing	[57]
Nanoprism		
Ag	–	[58]
Au	–	[59]
Nanorod		
Au/Ag/Ni/Pd/Pt	IgG	[60]
Nanotube		
Carbon	DNA	[61]
Nanowire		
Si	Influenza A	[62]
Au	*E. coli*	[63]
Polypyrrole	DNA	[64]
In vivo diagnostic		
Nanostructure	**Application**	**Refs**
Liposome		
Gadolinium	MRI imaging	[65,66]
Dual-fluorescence or iron oxide	Optical and MRI imaging	[67]
Dendrimer		
Gadolinium	MRI imaging	[41,42]
Nanoparticle		
Dextran-coated iron oxide	MRI imaging	[45]
Quantum dots	Near-infrared imaging	[46,47,68]
Gold	Optical detection	[69]
Nanoshell		
Gold	Optical detection	[70]
Nanotube		
Ultrashort Gd packed nanotubes	MRI imaging	[71]

ahttp://www.ece.cmu.edu/~mems/pubs/show.php?pub_id=160

colon cancer diagnostics. However, there are few examples of the application of nanotechnology to the imaging of CRC. Several examples that have been applied to enhancing detection and management of various diseases are outlined in Table 2. The technology most readily applicable to colorectal cancer includes novel contrast agents for MRI.

Nanostructures that modify conventional contrast agents, such as gadolinium, or imaging agents, such as iron oxide, have the potential to enhance the diagnostic power of clinical imaging [41–45]. Not only do these nanostructures improve the features of conventional MRI imaging, they also present opportunities to change how colorectal cancer is detected and managed.

Among the technologies in development that might result in the introduction of new modalities in CRC imaging is the use of near-infrared fluorescence imaging (NIRF). NIRF can be useful for imaging gastrointestinal diseases such as CRC because the current clinical evaluation of CRC already uses fiber optic examination of luminal surfaces [46]. This standard of practice can be enhanced by endoscopic visualization of near-infrared fluorescing imaging agents such as tunable quantum dots. Indeed, a murine model of colon cancer has already been studied using a NIRF agent [47].

Beyond imaging and detection, targeted nanostructures offer opportunities to develop novel approaches to treat colorectal and other tumors [10]. Liposomal encapsulation of anthracyclins, including doxorubicin, has had success as an FDA-approved treatment for metastatic ovarian cancer refractory to paclitaxel- and platinum-based agents. Moreover, these stealth nanostructures have been investigated for the treatment of breast cancer, non-Hodgkin's lymphoma and small-cell lung cancer. Similarly, nanoparticle delivery of paclitaxel is being used for the treatment of patients with metastatic breast cancer who have failed standard adjuvant chemotherapy, including anthracycline-based regimens. In preclinical development, nanostructures that are targeted specifically to tumor-expressed molecules are being used to improve the specificity of delivery of cytotoxic chemotherapeutics and limit the collateral damage to normal tissues that is normally associated with their use. Indeed, nanostructures have been used in conjunction with antibodies, proteins and small-molecule ligands targeted to specific tumor-associated receptors to deliver chemotherapeutic agents. This results in greater pharmacological and clinical efficacy and is associated with lower adverse events in animal tumor-xenograft models. In this context, antibody-targeted liposomes effectively accumulate in colorectal cancer cells in mouse xenograft models. These next generation of nanostructured delivery systems, with demonstrated efficacy in animal models, will be translated into early-phase clinical trials in the near-term for the delivery of chemotherapy to cancer patients.

Conclusion

The broad field of cancer management has a history of quickly replacing existing methodologies with ones that offer advantages in terms of improved diagnostic capabilities, increased sensitivity for tumor staging, and better therapeutic approaches and drug delivery. Nanotechnology has several beneficial attributes that might improve the management of colon cancer patients. Indeed, there are now signs that the potential provided by nanotechnology is being evaluated, and the first steps are being taken in the development of improved colorectal cancer imaging, therapeutics and the eventual implementation of targeted

strategies for ablation. Although this Opinion has focused on CRC as a particularly tempting target for the early application of nanotechnology-based approaches, the potential for other tumors with similar highly specific target molecules should be clear.

References

1 Meyerhardt, J.A. and Mayer, R.J. (2005) Systemic therapy for colorectal cancer. N. Engl. J. Med. 352, 476–487
2 Pantel, K. et al. (1999) Detection and clinical importance of micrometastatic disease. J. Natl. Cancer Inst. 91, 1113–1124
3 O'Connell, J.B. et al. (2004) Colon cancer survival rates with the new American Joint Committee on Cancer sixth edition staging. J. Natl. Cancer Inst. 96, 1420–1425
4 Carrithers, S.L. et al. (1996) Guanylyl cyclase C is a selective marker for metastatic colorectal tumors in human extraintestinal tissues. Proc. Natl. Acad. Sci. U. S. A. 93, 14827–14832
5 Wolfe, H.R. et al. (2002) In vivo imaging of human colon cancer xenografts in immunodeficient mice using a guanylyl cyclase C-specific ligand. J. Nucl. Med. 43, 392–399
6 Frick, G.S. et al. (2005) Guanylyl cyclase C: a molecular marker for staging and postoperative surveillance of patients with colorectal cancer. Expert Rev. Mol. Diagn. 5, 701–713
7 Nel, A. et al. (2006) Toxic potential of materials at the nanolevel. Science 311, 622–627
8 Service, R.F. (2006) Science policy. Priorities needed for nano-risk research and development. Science 314, 45
9 Ferrari, M. (2005) Cancer nanotechnology: opportunities and challenges. Nat. Rev. Cancer 5, 161–171
10 Couvreur, P. and Vauthier, C. (2006) Nanotechnology: intelligent design to treat complex disease. Pharm. Res. 23, 1417–1450
11 Cuenca, A.G. et al. (2006) Emerging implications of nanotechnology on cancer diagnostics and therapeutics. Cancer 107, 459–466
12 Farokhzad, O.C. and Langer, R. (2006) Nanomedicine: developing smarter therapeutic and diagnostic modalities. Adv. Drug Deliv. Rev. 58, 1456–1459
13 Grodzinski, P. et al. (2006) Nanotechnology for cancer diagnostics: promises and challenges. Expert Rev. Mol. Diagn. 6, 307–318
14 Qiang, Y. et al. (2006) Iron/iron oxide core-shell nanoclusters for biomedical applications. J. Nanoparticle Res. 8, 489–496
15 Sinha, R. et al. (2006) Nanotechnology in cancer therapeutics: bioconjugated nanoparticles for drug delivery. Mol. Cancer Ther. 5, 1909–1917
16 Yih, T.C. et al. (2006) Engineered nanoparticles as precise drug delivery systems. J. Cell. Biochem. 97, 1184–1190
17 Kroto, H.W. et al. (1985) C60: buckminsterfullerene. Nature 318, 162–163
18 Li, J. et al. (2005) Carbon nanotubes and nanowires for biological sensing. Methods Mol. Biol. 300, 191–123
19 Woolley, A.T. et al. (2000) Structural biology with carbon nanotube AFM probes. Chem. Biol. 7, R193–R204
20 Moses, C. et al. (1955) Experimental and clinical studies with radioactive colloidal gold in the therapy of serous effusions arising from cancer. Cancer 8, 417–423
21 Ahlberg, A. et al. (1969) Intra-articular injection of radioactive gold in treatment of chronic synovial effusion in the knee. Acta Rheumatol. Scand. 15, 81–89
22 West, J.L. and Halas, N.J. (2003) Engineered nanomaterials for biophotonic applications, improving sensing, imaging and therapeutics. Annu. Rev. Biomed. Eng. 5, 285–292

23 Loo, C. et al. (2005) Immunotargeted nanoshells for integrated cancer imaging and therapy. Nano Lett. 5, 709–711
24 Thorek, D.L. et al. (2006) Superparamagnetic iron oxide nanoparticle probes for molecular imaging. Ann. Biomed. Eng. 34, 23–38
25 Hirsch, L.R. et al. (2003) Nanoshell-mediated near-infrared thermal therapy of tumors under magnetic resonance guidance. Proc. Natl. Acad. Sci. U. S. A. 100, 13549–13554
26 O'Neal, D.P. et al. (2004) Photo-thermal tumor ablation in mice using near infrared-absorbing nanoparticles. Cancer Lett. 209, 171–176
27 Devalapally, H. et al. (2007) Poly(ethylene oxide)-modified poly(beta-amino ester) nanoparticles as a pH-sensitive system for tumor-targeted delivery of hydrophobic drugs. Part 3: Therapeutic efficacy and safety studies in ovarian cancer xenograft model. Cancer Chemother. Pharmacol. 59, 477–484
28 van Vlerken, L.E. and Amiji, M.M. (2006) Multi-functional polymeric nanoparticles for tumour-targeted drug delivery. Expert Opin. Drug Deliv. 3, 205–216
29 Farokhzad, O.C. et al. (2006) Targeted nanoparticle–aptamer bioconjugates for cancer chemotherapy in vivo. Proc. Natl. Acad. Sci. U. S. A. 103, 6315–6320
30 Akerman, M.E. et al. (2002) Nanocrystal targeting in vivo. Proc. Natl. Acad. Sci. U. S. A. 99, 12617–12621
31 Gao, X. et al. (2004) In vivo cancer targeting and imaging with semiconductor quantum dots. Nat. Biotechnol. 22, 969–976
32 Matsumura, Y. and Maeda, H. (1986) A new concept for macromolecular therapeutics in cancer chemotherapy: mechanism of tumoritropic accumulation of proteins and the antitumor agent smancs. Cancer Res. 46, 6387–6392
33 Hainfeld, J.F. et al. (2004) The use of gold nanoparticles to enhance radiotherapy in mice. Phys. Med. Biol. 49, N309–N315
34 Loo, C. et al. (2004) Nanoshell-enabled photonics-based imaging and therapy of cancer. Technol. Cancer Res. Treat. 3, 33–40
35 Kommareddy, S. and Amiji, M. (2007) Biodistribution and pharmacokinetic analysis of long-circulating thiolated gelatin nanoparticles following systemic administration in breast cancer-bearing mice. J. Pharm. Sci. 96, 397–407
36 Birbe, R. et al. (2005) Guanylyl cyclase C is a marker of intestinal metaplasia, dysplasia, and adenocarcinoma of the gastrointestinal tract. Hum. Pathol. 36, 170–179
37 Urbanski, R. et al. (1995) Internalization of E. coli ST mediated by guanylyl cyclase C in T84 human colon carcinoma cells. Biochim. Biophys. Acta 1245, 29–36
38 Hakki, S. et al. (1993) Solubilization and characterization of functionally coupled Escherichia coli heat-stable toxin receptors and particulate guanylate cyclase associated with the cytoskeleton compartment of intestinal membranes. Int. J. Biochem. 25, 557–566
39 Hugues, M. et al. (1992) Affinity purification of functional receptors for Escherichia coli heat-stable enterotoxin from rat intestine. Biochemistry 31, 12–16
40 Seydack, M. (2004) Nanoparticle labels in immunosensing using optical detection methods. Biosens. Bioelectron. 20, 2454–2469
41 Kobayashi, H. et al. (2005) Detection of lymph node involvement in hematologic malignancies using micromagnetic resonance lymphangiography with a gadolinum-labeled dendrimer nanoparticle. Neoplasia 7, 984–991
42 Kobayashi, H. et al. (2004) Lymphatic drainage imaging of breast cancer in mice by micro-magnetic resonance lymphangiography using a nano-size paramagnetic contrast agent. J. Natl. Cancer Inst. 96, 703–708
43 Mahmood, U. and Weissleder, R. (2003) Near-infrared optical imaging of proteases in cancer. Mol. Cancer Ther. 2, 489–496
44 Perez, J.M. et al. (2003) Viral-induced self-assembly of magnetic nanoparticles allows the detection of viral particles in biological media. J. Am. Chem. Soc. 125, 10192–10193
45 Harisinghani, M.G. et al. (2003) Noninvasive detection of clinically occult lymph-node metastases in prostate cancer. N. Engl. J. Med. 348, 2491–2499
46 Weissleder, R. et al. (2005) Cell-specific targeting of nanoparticles by multivalent attachment of small molecules. Nat. Biotechnol. 23, 1418–1423
47 Weissleder, R. et al. (1999) In vivo imaging of tumors with protease-activated near-infrared fluorescent probes. Nat. Biotechnol. 17, 375–378

48 Liu, G. *et al.* (2005) Nanocrystal-based bioelectronic coding of single-nucleotide polymorphisms. *J. Am. Chem. Soc.* 127, 38–39

49 Chan, C.P. *et al.* (2004) Nanocrystal biolabels with releasable fluorophores for immunoassays. *Anal. Chem.* 76, 3638–3645

50 Huhtinen, P. *et al.* (2004) Immunoassay of total prostate-specific antigen using europium(III) nanoparticle labels and streptavidin–biotin technology. *J. Immunol. Methods* 294, 111–122

51 Henry, J. *et al.* (2004) Development of a nanoparticle-based surface-modified fluorescence assay for the detection of prion proteins. *Anal. Biochem.* 334, 1–8

52 Park, J. *et al.* (2004) Evaluation of 2-methacryloyloxyethyl phosphorylcholine polymeric nanoparticle for immunoassay of C-reactive protein detection. *Anal. Chem.* 76, 2649–2655

53 Sato, K. *et al.* (2004) Single-base mutation detection using neutravidin-modified polystyrene nanoparticle aggregation. *Anal. Sci.* 20, 893–894

54 Zhang, D. *et al.* (2004) Silica-nanoparticle-based interface for the enhanced immobilization and sequence-specific detection of DNA. *Anal. Bioanal. Chem.* 379, 1025–1030

55 Chu, X. *et al.* (2005) An electrochemical stripping metalloimmunoassay based on silver-enhanced gold nanoparticle label. *Biosens. Bioelectron.* 20, 1805–1812

56 Lian, W. *et al.* (2004) Ultrasensitive detection of biomolecules with fluorescent dye-doped nanoparticles. *Anal. Biochem.* 334, 135–144

57 Li, J. *et al.* (2003) DNA molecules and configurations in a solid-state nanopore microscope. *Nat. Mater.* 2, 611–615

58 Jin, R. *et al.* (2001) Photoinduced conversion of silver nanospheres to nanoprisms. *Science* 294, 1901–1903

59 Hao, E. *et al.* (2004) Synthesis and optical properties of anisotropic metal nanoparticles. *J. Fluoresc.* 14, 331–341

60 Nicewarner-Pena, S.R. *et al.* (2001) Submicrometer metallic barcodes. *Science* 294, 137–141

61 Wang, J. *et al.* (2004) Ultrasensitive electrical biosensing of proteins and DNA: carbon-nanotube-derived amplification of the recognition and transduction events. *J. Am. Chem. Soc.* 126, 3010–3011

62 Patolsky, F. *et al.* (2004) Electrical detection of single viruses. *Proc. Natl. Acad. Sci. U. S. A.* 101, 14017–14022

63 Basu, M. *et al.* (2004) Nano-biosensor development for bacterial detection during human kidney infection: use of glycoconjugate-specific antibody-bound gold nanowire arrays (GNWA). *Glycoconj. J.* 21, 487–496

64 Ramanathan, K. *et al.* (2005) Bioaffinity sensing using biologically functionalized conducting polymer nanowire. *J. Am. Chem. Soc.* 127, 496–497

65 Parac-Vogt, T.N. *et al.* (2005) Paramagnetic liposomes containing amphiphilic bisamide derivatives of Gd-DTPA with aromatic side chain groups as possible contrast agents for magnetic resonance imaging. *Eur. Biophys. J.* 11, 1–9

66 Saito, R. *et al.* (2005) Gadolinium-loaded liposomes allow for real-time magnetic resonance imaging of convection-enhanced delivery in the primate brain. *Exp. Neurol.* 196, 381–389

67 Mulder, W.J. *et al.* (2005) MR molecular imaging and fluorescence microscopy for identification of activated tumor endothelium using a bimodal lipidic nanoparticle. *FASEB J.* 19, 2008–2010

68 Parungo, C.P. *et al.* (2005) Intraoperative identification of esophageal sentinel lymph nodes with near-infrared fluorescence imaging. *J. Thorac. Cardiovasc. Surg.* 129, 844–850

69 Rahman, M. *et al.* (2005) Optical imaging of cervical pre-cancers with structured illumination: an integrated approach. *Gynecol. Oncol.* 99, S112–S115

70 Loo, C. *et al.* (2005) Gold nanoshell bioconjugates for molecular imaging in living cells. *Opt. Lett.* 1, 1012–1014

71 Sitharaman, B. *et al.* (2005) Superparamagnetic gadonanotubes are high-performance MRI contrast agents. *Chem. Commun.* 21, 3915–3917

Polarized Angular Dependent Light Scattering Properties of Bare and PEGylated Gold Nanoshells

Kun Fu[1], Jiantang Sun[2], Alex W. H. Lin[2], Hui Wang[3], Naomi J. Halas[1, 3] and Rebekah A. Drezek*[1, 2,]

Departments of Bioengineering, Electrical and Computer Engineering, and Chemistry, Rice University- Houston, TX 77005;
[1] *Department of Electrical and Computer Engineering;* [2] *Department of Bioengineering;* [3] *Department of Chemistry*

Abstract: Metal nanoshells have found promising applications in biomedical imaging and cancer therapy. To facilitate the application of nanoshells in scattering based imaging techniques, it is essential to characterize their light scattering properties. We have studied the light scattering from nanoshells at the quadrupolar and octupolar frequencies of the surface plasmon resonance, and our measurements are in good agreement with Mie theory calculations for both wavelengths. For *in vivo* use of nanoparticles in biomedical imaging and therapy, surface modification is of great importance in enhancing the stability and biocompatibility of these particles, and polyethylene glycol is commonly used for the surface modification of metal and semiconductor nanoparticles. However, the influence of surface modification on the optical properties of nanoparticles has not been systematically studied yet. Here, we also report the study on the polarized and angularly-resolved light scattering properties of gold nanoshells before and after polyethylene glycol modification. We find that polyethylene glycol does not influence the extinction profile of gold nanoshells. Furthermore, there is no significant change in the scattering phase function of nanoshells after polyethylene glycol modification.

Key Words: Light scattering, Gold nanoshells, Surface modification, Mie theory.

1. INTRODUCTION

Non-invasive optical imaging techniques, such as optical coherent tomography, reflectance confocal microscopy, and diffuse reflectance spectroscopy, have developed very quickly over the past few years because of their high sensitivity, low cost, and strong potential for medical imaging [1, 2]. Moreover, optical contrast agents may play an important role in these scattering-based techniques by enhancing signal-to-background ratio. Various nanoparticles have been investigated as optical contrast agents, e.g., gold nanoparticles [3], gold nanoshells [4-8], gold nanorods [9], gold nanocages [10], etc. There is also a high demand for biocompatible and wavelength-tunable contrast agents for *in vivo* uses.

Previous gold nanoshells have shown promising applications, for biomedical imaging, in general, as well as therapeutic applications in cancer research. This results from the prime property of metal nanoshells: optical tunability. Specifically, by varying the relative dimensions of the silica core and the metallic shell, nanoshells can be intentionally designed to preferentially absorb or scatter light at specific wavelengths of interest. Their optical resonance can thus be tuned over a broad spectra range from the near-UV to the mid-infrared region to meet specific requirements. The strong, near-infrared (NIR) absorption of nanoshells has been applied to assist photo-thermal cancer therapy [11, 12], while scattering nanoshells have been developed as contrast agents for biomedical imaging in the visible and near-infrared regions [4-6]. Gold nanoshells can also be tailored and conjugated to target specific molecules or cells to improve bio-specificity.

Previous work has optimized the optical properties of nanoshells for a variety of biomedical applications, such as whole blood immunoassay [13, 14], photo-thermal tumor ablation [11, 12], cancer imaging [4-6], and tissue welding [15], etc. These works have been based on the extinction spectra of nanoshells. However, the individual effects of extinction, absorption and scattering have not been investigated separately. To help facilitate the development of nanoshell-assisted imaging techniques and non-invasive optical diagnostics, it is essential to characterize the light scattering properties of gold nanoshells. We are interested in the angular dependency of light scattering in nanoshells and the design

and optimization of specific nanoshells to facilitate biomedical applications. For *in vivo* applications of nano-materials, it is necessary to modify the surface of the nano-materials with polyethylene glycol (PEG) or other biomacromolecules to enhance their biocompatibility. This surface modification may influence the optical properties of the nano-materials [16, 17]. Therefore, the potential discrepancy in optical properties between PEGylated and bare nanoshells is also an important subject of this study.

Polarized light scattering has been proven to be sensitive to both the size and shape of the index variation and the refractive index discontinuities in scattering materials. This technique can therefore be used to determine the size of small particles as well as the concentration of dilute suspension of these particles. Polarized light scattering has also been developed as a possible non-invasive tissue diagnostic tool by several research groups [17-21]. Drezek *et al.*, for example, have discovered that cellular scattering is sensitive to changes in the nuclear morphology that accompanies neoplastic progression in cervical cells [18]. Mourant *et al.* have analyzed the polarized angular dependent spectroscopy of epithelial cells and epithelial cell nuclei and have found that light scattering is likely sensitive to structures smaller than those commonly investigated by standard pathology methods [21].

To experimentally study the angular dependent light scattering, a goniometer can be constructed to accurately measure light scattering from dilute suspension of small particles such as polystyrene spheres and gold nanoshells. This device measures the intensity of polarized light scattering as a function of scattering angle, which is known as the scattering phase function P(θ). At the same time, Mie theory can also be utilized to calculate the scattering phase function of gold nanoshells, even though this involves the more complicated concentric sphere geometry of those structures [22, 23]. In our simulations, a refractive index of n=1.45 for silica [24] and the refractive indices published by Johnson and Christy for gold [25] are used. The measured phase function from the goniometer can, in turn, be compared to Mie theory to verify this device's accuracy.

2. METHOD

2.1. Nanoshell Fabrication

Gold-silica nanoshells are fabricated as described by Oldenberg *et al.* [23]. First, nano-sized spherical SiO_2 cores are fabricated using the Stöber method [26]. SiO_2 cores with diameters ranging from 100 nm to 500 nm can be easily synthesized using this method. Silica particle sizes are characterized using scanning elec-

*Address correspondence to this author at the Rice University, Department of Bioengineering; 6100 Main St., MS-142; Houston, TX 77005; Tel: 1-713-348-3011; Fax: 1-713-348-5877; E-mail: drezek@rice.edu

tron microscopy (SEM, Phillips XL30 ESEM-FEG), only the particle polydispersity that is < 10% is considered acceptable. The SiO_2 cores are then functionalized with amine groups by immersing and boiling them with aminopropyl-triethoxysilane (APTES). In the meantime, gold colloid is grown as outlined by Duff *et al.* [27]. In order to grow gold shell on the functionalized silica cores, the cores need to be seeded with concentrated gold colloid, which adsorbs to the amine groups on the silica surface. Then nanoshells are grown by mixing a stock solution of $HAuCl_4$ with the seed particles under formaldehyde catalysis. This process reduces gold onto the adsorbed gold colloid, causing the surface to grow and eventually form a continuous shell over the silica core. The growth of nanoshell is monitored using a UV-Vis spectrophotometer (Varian Cary 300) by comparing the measured extinction spectra to the calculations from Mie theory; the size is further confirmed by SEM. Mie theory can be used to determine the absorption, scattering and extinction coefficients of bare nanoshells with a specific core radius and shell thickness. The concentration of the nanoshells can then be determined by relating the calculated extinction coefficient to the measured extinction from the spectrophotometer. To enhance the stability and biocompatibility, the surface of the nanoshells needs to be modified with polyethylene glycol (PEG) to facilitate further *in vivo* applications.

2.2. PEGylation of Gold Nanoshells

PEG is a water soluble polymer that has the chemical formula of $H-(O-CH_2-CH_2)_n-OH$ [28]. The viscosity and freezing point of liquid PEGs generally increase with greater molecular weights (MW). In this case, PEG-thiol (MW=5000, 0.25μM) is used to modify the nanoshell surface. PEG-SH was synthesized by reacting PEG-amine (MW 5000, Shearwater Polymers, Nektar 2M2U0H21) with Traut's Reagent 137.9 MW (2-iminothiolane, Sigma I-6256) for 1 hour. The product was then dialyzed in deionized water for about 2 hours using a dialysis membrane with a molecular weight cutoff of 1000 to remove excess reagent. Product was stored in working aliquots at -20 °C.

To PEGylate the nanoshells, first, PEG-SH with a series of different concentrations in 10% potassium carbonate is prepared and mixed with nanoshells, and the mixtures is left undisturbed for 1 hour. A positive control of nanoshells without PEG-SH is prepared at the same time. Then 10% NaCl is added to the above suspensions (the same amount of DI water is added to the control to maintain the same concentration). After the lapse of 15 to 30 minutes, the UV-Vis spectrum of each nanoshell sample is recorded and compared with the control. Since NaCl aggregates nanoshells which possess insufficient quantities of the stabilizing PEG-SH, the unstable suspensions will flocculate, and consequently spectral broadening, red-shifting and reduction of peak absorbance can be observed in the extinction spectra [14]. On the contrary, the well PEGylated nanoshells remain stable in the salt solution and do not exhibit such spectral changes, showing enhanced stability and biocompatibility under saline environments.

2.3. Angular Dependent Light Scattering Experiments

As noted above, an automated goniometer has been constructed to perform the angular dependent light scattering measurements, together with different combinations of linear polarizers for light delivery and detection. A schematic of the measurement system is shown in Fig. (**1a**). The light from a 633nm He-Ne laser (or an 830nm GaAlAs laser diode) is incident onto a cylindrical cuvette (1 inch pass length, quartz) containing the samples through the first polarizer (Newport, 10LP-Vis) and a φ500μm Precision Pinhole (Edmund Optics, U56-287), the size of incident beam on the cuvette is about 1mm. The scattered light is then collected by a silicon detector rotating around the cuvette through the second polarizer; the signal is read by a Picowatt Optical Power Meter (Newport® Model 1830-C), which is connected to a computer through a GPIB interface and controlled by LabView. The direction of propagation
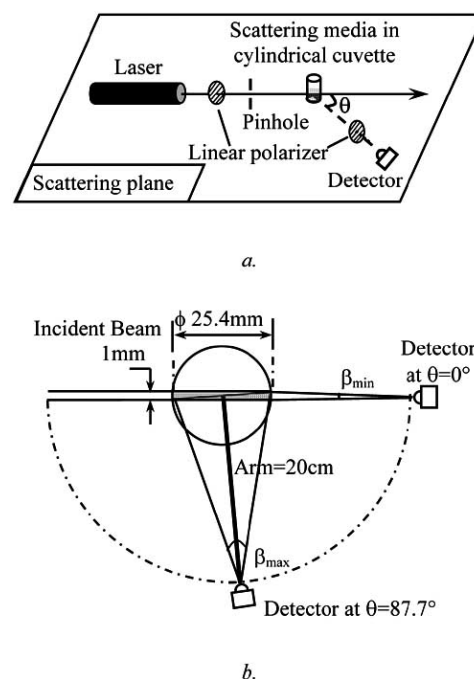

Fig. (1). Schematic of the goniometer system and angular resolution. The light from a 633nm He-Ne laser (or an 830nm GaAlAs laser diode) is incident onto a cylindrical cuvette containing the samples through the first polarizer; the scattered light is then collected by a silicon detector rotating around the cuvette through the second polarizer. The direction of propagation of incident light and the direction of scattered light being detected define a scattering plane. (a) Schematic of the goniometer system. (b) Angular resolution of the goniometer at different viewing angles.

of incident light and the direction of scattered light define a scattering plane. The parallel polarized light scattering is detected when both polarizers are oriented so that to pass light polarized parallel to the scattering plane. The detection of perpendicular polarized light scattering is thus achieved when both polarizers rest on the cross-position. Our measurements range from 20°~160°, with a step size of 1.8°.

The angular resolution of the goniometer is another key issue for the accuracy of the goniometric measurement. The angular resolution is a function of the visible cross section of the beam inside the cuvette and the length of the rotating arm, which is the distance between the detector and the center of the cuvette, as shown in Fig. (**1b**) [29]. The angular resolution is also dependent upon the viewing angle θ. In our experiment, using a 25.4mm (1 inch) pass length cylindrical cuvette and a 20cm rotating arm, the angular resolution ranges between 0.286° and 7.27°, showing that the best angular resolution can be achieved at θ =0° while the angular resolution between θ =87.7° and θ =92.3° is the poorest.

The goniometer is first tested using a dilute aqueous suspension of monodisperse polystyrene spheres with a diameter of 0.17μm (Bangs laboratory) and a concentration of 9.44×10^7/ml. The buffer used for diluting the samples in this paper is deionized water if not otherwise specified, and cuvette filled with deionized water is used as reference. The results of polystyrene spheres are in good agreement with Mie theory calculations, as shown in Fig. (**2**), which demonstrates that the goniometer is functioning properly. Note that the increased measured values relative to Mie theory predictions when approaching 90°. Several reasons may cause this discrepancy: the finite angular resolution of the goniometer in this area, as shown in Fig. (**1b**); the limitation of the detector when detecting very low power; and/or the size distribution of the particles (around 10%).
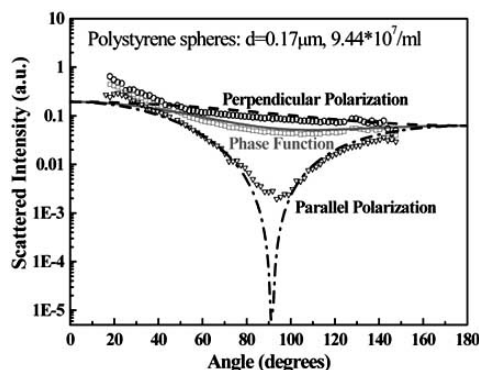
Fig. (2). Comparison of light scattering measurements (scattered symbols) and Mie theory calculations (line curves) for 0.17μm diameter polystyrene spheres; ~9.44×10⁷ particles/ml; top line: Perpendicular polarization; middle line: Unpolarized phase function; bottom line: Parallel polarization.

## 3. RESULTS AND DISCUSSION

Nanoshells with R_1=157±5nm (the dielectric core) and R_2=187±7nm (the whole particle) are designed and fabricated with a strong octupole resonance at 680nm and a quadrupole resonance located at 815nm. Nanoshells with R_1=148±10nm and R_2=168±12nm are also fabricated for the multi-wavelength study, and these nanoshells also have a strong quadrupole resonance at 830nm and an octupole resonance located at 660nm, as shown in Fig. (**3a**)[30]. Fig. (**3b**) shows the measured extinction for nanoshells (R_1=157±5nm, R_2=187±7nm) with and without PEG in comparison to Mie theory calculation for bare nanoshells with R_1=157nm and R_2=192nm. There is little difference between the extinction spectra of the bare and PEGylated nanoshell suspensions, and both are in good agreement with the Mie theory, showing that PEG doesn't influence the extinction spectral shape of the gold nanoshells. The broadened linewidth at the quadrupole and octupole resonances of the nanoshell is dominated by the electron-interface scattering within the shell layer although the size distribution of the core and shell may also contribute to some degree [31].

The angular light scattering properties of bare and PEGylated nanoshells (R_1=157±5nm, R_2=187±7nm) are studied using the goniometer at the wavelength of 633nm, which is near the octupole resonance of the fabricated nanoshells. Nanoshell suspensions are dispersed with an ultrasound probe for 2 minutes before each experiment to ensure the consistency of nanoshell dispersion and homogeneity in suspensions. First, the angular light scattering of the bare nanoshell suspension with a concentration of around 5.2×10⁷/ml is measured. The measurement on another nanoshell suspension diluted by a factor of 4 (~1.3×10⁷/ml) yields no difference in light scattering patterns. This demonstrates that single scattering predominates, while, at the same time, multiple scattering does not occur [19, 20]. PEGylated nanoshell suspension at a concentration of ~1.3×10⁷/ml is prepared for light scattering measurement and compared to the bare nanoshell suspension at an equal concentration. Fig. (**4**) shows that the parallel polarized angular scattering patterns of the bare and PEGylated nanoshells are very similar to each other. Measurements for both the bare and PEGylated nanoshells compare favorably with Mie theory predictions. The Mie theory calculation shown here is based on modeling a particle without any surface modification. In this case, both the shape of the extinction and the scattering phase function could be accurately predicted using this simplified model. Using more sophisticated modeling, a PEG layer can be imported if desired [16, 17]. All of the angular dependent experimental results are averaged over three or more separate measurements. The error bar in Fig. (**4**) represents the standard deviation of the three measurements for each sample.
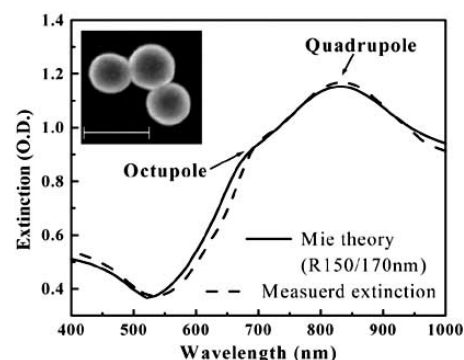
a.
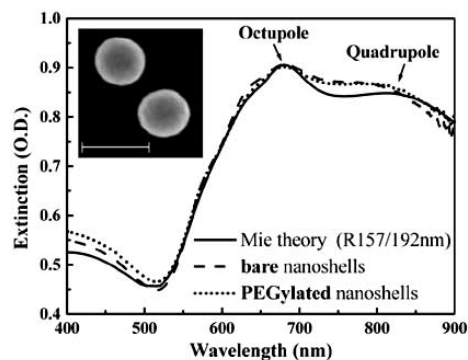
b.

Fig. (3). Comparison of measured extinction spectra to Mie theory calculation of gold nanoshells; SEM images: magnification=50000×; scale bar=500nm. (a) Comparison of measured extinction spectra (dashed line; R_1=148±10nm; R_2=168±12nm) to Mie theory calculation (solid line; R150/170nm). (b) Extinction spectra of bare (dashed line) and PEGylated (dotted line) nanoshells (R_1=157±5nm; R_2=187±7nm) compared to Mie theory (solid line; R157/192nm).

Since it is believed that the scattering of gold nanoshells may be enhanced at certain wavelengths by the surface plasmon resonances [32], the multi-wavelength aspect of our studies is conducted at the quadrupole and octupole resonance frequencies and differences in the scattering patterns at these resonance frequencies are measured. Nanoshells of R_1=148±10nm and R_2=168±12nm with a strong quadrupole resonance at 830nm and an octupole resonance located at 660nm are fabricated for this purpose. Fig. (**5**) shows the comparison of normalized parallel polarized light scattering results with Mie theory predictions for nanoshells (R_1=150nm, R_2=170nm) excited at 830nm where the quadrupole resonance is located, and at 633nm, which is close to the octupole resonance of the nanoshells. The quadrupole and octupole scattering patterns are well shown in the experiments. The scattering patterns for these two wavelengths are very different from each other, but both are well fitted by Mie theory, which therefore shows the potential of gold nanoshells for multi-wavelength imaging applications.

4. CONCLUSIONS

The objectives of this study are (1) to investigate the optical properties of gold nanoshells before and after surface modification using polyethylene glycol (PEG) and (2) to evaluate the results in terms of advancing biomedical imaging applications of gold nanoshells. In summary, we have achieved these goals by successfully studying the angular dependence of light scattering on both
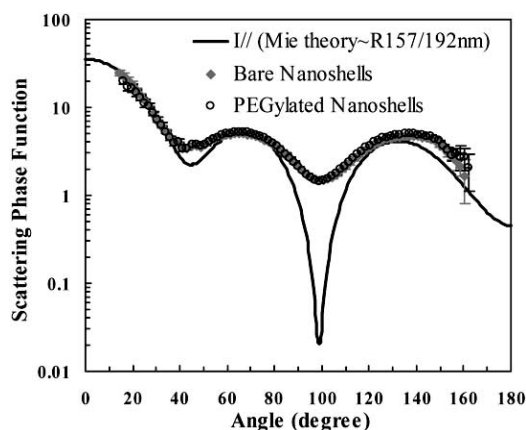
Fig. (4). Normalized parallel polarized light scattering from bare (solid diamonds) and PEGylated (hollow circles) nanoshells (R_1=157±5nm; R_2=187±7nm) compared to Mie theory (solid line; R157/192nm) at 633nm, showing that the scattering phase function of the bare and PEGylated nanoshells are analogous to each other; error bar represents the standard deviation of 3 separate measurements.
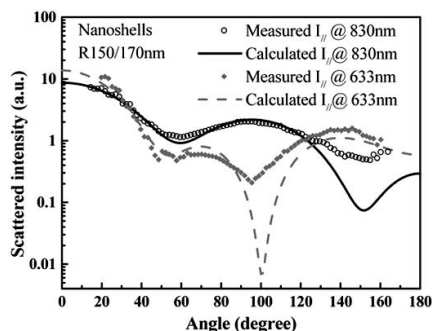

Fig. (5). Parallel polarized light scattering from nanoshells (R_1=148±10nm; R_2=168±12nm) excited at the quadrupole (830nm) and octupole (633nm) plasmon resonances respectively; concentration ~ 1×10^7 /ml; the line curves represent Mie theory calculations for light scattering from nanoshells (R150/170nm) at 830nm (solid line) and 633nm (dashed line); while the scattered symbols represent the normalized experimental data at 830nm (hollow circles) and 633nm (solid diamonds).

bare and PEGylated gold nanoshells (R_1=157±5nm and R_2=187±7nm) near the octupole resonance of the nanoshells, as well as for nanoshells (R_1=148±10nm and R_2=168±12nm) at the quadrupole and octupole resonances respectively. For the multiwavelength study at the quadrupole and octupole resonances of the nanoshells, our measurements are in good agreement with Mie theory calculations at both wavelengths. Our results therefore show that the optical properties of gold nanoshells can be accurately modeled by Mie theory. This offers insight into the efficacy of further design and additional research of gold nanoshells for future application in multi-wavelength *in vivo* imaging techniques. Our study on the PEGylated nanoshells also indicates that PEG doesn't change the scattering phase function of gold nanoshells. Finally, the experiments also indicate that the goniometer could be a very promising instrument for multi-wavelength inspection and for future studies on other nanoparticles being developed as novel contrast agents for biomedical imaging techniques.

REFERENCES

[1]   Lee, T.M.; Oldenburg, A.L.; Sitafalwalla, S.; Marks, D.L.; Luo, W.; Toublan, F.J.-J.; Suslick, K.S.; Boppart, S.A. *Opt. Lett.*, **2003**, *28*, 1546.
[2]   Palmer, G.M.; Zhu, C.; Breslin, T.M.; Xu, F.; Gilchrist, K.W.; Ramanujam, N. *IEEE Tran. Biom. Engineer.*, **2003**, *50*, 1233.
[3]   Sokolov, K.; Aaron, J.; Hsu, B.; Nida, D.; Gillanwater, A.; Follen, M.; Macaulay, C.; Adler-Storthz, K.; Korgel, B.; Discour, M.; Pasqualini, R.; Arap, W.; Lam, W.; Richartz-Kortum, R. *Technol. Cancer Res. Treatment*, **2003**, *2*, 491.
[4]   Loo, C.; Lin, A.; Hirsch, L.; Lee, M.H.; Barton, J.; Halas, N.; West, J.; Drezek, R. *TCRT*, **2004**, *3*, 33.
[5]   Loo, C.; Hirsch, L.R.; Lee, M.-H.; Chang, E.; West, J.; Halas, N.; Drezek, R. *Opt. Lett.*, **2005**, *30*, 1012.
[6]   Loo, C.; Lowery, A.; Halas, N.; West, J.; Drezek, R. *Nano Lett.*, **2005**, *5*, 709.
[7]   Jackson, J.B.; Westcott, S.L.; Hirsch, L.R.; West, J.L.; Halas, N.J. *Appl. Phys. Lett.*, **2003**, *82*, 257.
[8]   Jackson, J.B.; Halas, N.J. *Proc. Natl. Acad. Sci. USA*, **2004**, *101*, 17930.
[9]   Huang, X.; El-Sayed, V.H.; Qian, W.; El-Sayed, M.A. *J. AM. CHEM. SOC.*, **2006**, *128*, 2115.
[10] Chen, J.; Saeki, F.; Wiley, B.J.; Cang, H.; Cobb, M.J.; Li, Z.-Y.; Au, L.; Zhang, H.; Kimmey, M.B.; Li, X.; Xia, Y. *Nano Lett.*, **2005**, *5*, 473.
[11] Hirsch, L.R.; Stafford, R.J.; Bankson, J.A.; S. R. Sershen, B.R.; Price, R.E.; Hazle, J.D.; Halas, N.J.; West, J.L. *Proc. Natl. Acad. Sci. USA*, **2003**, *23*, 13549.
[12] O'Neal, D.P.; Hirsch, L.R.; Halas, N.J.; Payne, J.D.; West, J.L. *Cancer Lett.*, **2004**, *109*, 171.
[13] Hirsch, L.R.; Jackson, J.B.; Lee, A.; Halas, N.J.; West, J.L. *Anal. Chem.*, **2003**, *75*, 2377.
[14] Hirsch, L.R.; Halas, N.J.; West, J.L. *Methods Mol. Biol.*, **2005**, *303*, 101.
[15] Gobin, A.M.; O'Neal, D.P.; Halas, N.J.; Drezek, R.; West, J.L. *Lasers Surg. Med.*, **2005**, *37*, 123.
[16] Khlebtsov, N.G.; Bogatyrev, V.A.; Khlebtsov, B.N.; Dykman, L.A.; Englebienne, P. *Colloid J.*, **2003**, *65*, 622.
[17] Khlebtsov, N.G. *J. Quant. Spectrosc. Radiat. Transfer*, **2004**, *89*, 143.
[18] Drezek, R.; Dunn, A.; Richards-Kortum, R. *Appl. Opt.*, **1999**, *38*, 3651.
[19] Drezek, R.; Collier, T.; MacAulay, C.; Follen, M.; Richards-Kortum, R. *J. Biomed. Opt.*, **2003**, *8*, 7.
[20] Mourant, J.R.; Johnson, T.M.; Doddi, V.; Freyer, J.P. *J. Biomed. Opt.*, **2002**, *7*, 93.
[21] Mourant, J.R.; Johnson, T.M.; Carpenter, S.; Guerra, A.; Aida, T.; Freyer, J.P. *J. Biomed. Opt.*, **2002**, *7*, 378.
[22] Bohren, C.; Huffman, D.R. *Absorption and Scattering of Light by Small Particle*, Wiley: New York, **1983**.
[23] Oldenburg, S.J.; Averitt, R.D.; Westcott, S.L.; Halas, N.J. *Chem. Phys. Lett.*, **1998**, *288*, 243.
[24] Blaaderen, A.V.; Vrij, A. *J. Colloid Interface Sci.*, **1993**, *156*, 1.
[25] Johnson, P.B.; Christy, R.W. *Phys. Rev. B*, **1972**, *6*, 4370.
[26] Stober, W.; Fink, A. *J. Coll. Interf. Sci.*, **1968**, *26*, 62.
[27] Duff, D.G.; Baiker, A.; Edwards, P.P. *Langmuir*, **1993**, *9*, 2301.
[28] Harris, J.M.; Chess, R.B. *Nat. Rev. Drug Discov.*, **2003**, *2*, 214.
[29] Drezek, R.A. *Light Scattering from Cells: Finite-Different Time Domain Simulations and Goniometric Measurements*, Master's Thesis, the University of Texas at Austin, **1998**.
[30] Wang, H.; Fu, K.; Drezek, R.A.; Halas, N.J. *Appl. Phys. B*, **2006**, *84*, 191.
[31] Westcott, S.L.; Jackson, J.B.; Radloff, C.; Halas, N.J. *Phys. Rev. B*, **2002**, *66*, 155431.
[32] Oldenburg, S.J.; Hale, G.D.; Jackson, J.B.; Halas, N.J. *Appl. Phys. Lett.*, **1999**, *75*, 1063.

Letter

Near-Infrared Resonant Nanoshells for Combined Optical Imaging and Photothermal Cancer Therapy

Andr M. Gobin, Min Ho Lee, Naomi J. Halas, William D. James, Rebekah A. Drezek, and Jennifer L. West
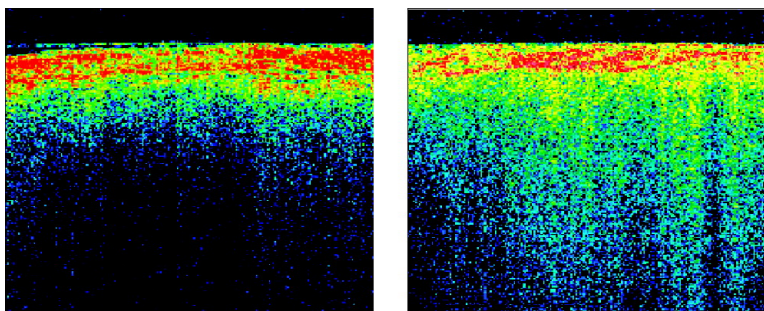
More About This Article

Additional resources and features associated with this article are available within the HTML version:

- Supporting Information
- Links to the 36 articles that cite this article, as of the time of this article download
- Access to high resolution figures
- Links to articles and content related to this article
- Copyright permission to reproduce figures and/or text from this article

View the Full Text HTML

Near-Infrared Resonant Nanoshells for Combined Optical Imaging and Photothermal Cancer Therapy

André M. Gobin,[†] Min Ho Lee,[†] Naomi J. Halas,[‡] William D. James,[§] Rebekah A. Drezek,[†] and Jennifer L. West*,[†]

Department of Bioengineering, Rice University, Houston, Texas 77005, Department of Electrical and Computer Engineering, Rice University, Houston, Texas 77005, and Center for Chemical Characterization and Analysis, Texas A&M University, College Station, Texas 77843

Received March 14, 2007; Revised Manuscript Received May 21, 2007

ABSTRACT

Metal nanoshells are core/shell nanoparticles that can be designed to either strongly absorb or scatter within the near-infrared (NIR) wavelength region (∼650−950 nm). Nanoshells were designed that possess both absorption and scattering properties in the NIR to provide optical contrast for improved diagnostic imaging and, at higher light intensity, rapid heating for photothermal therapy. Using these in a mouse model, we have demonstrated dramatic contrast enhancement for optical coherence tomography (OCT) and effective photothermal ablation of tumors.

Much of the promise for nanotechnology in medicine has focused on the development of multifunctional agents for integrated diagnosis and therapy.[1,2] Here we report on a successful in vivo demonstration of the use of near-infrared resonant nanoparticles, gold nanoshells, to first increase optical contrast in tumors for optical coherence tomography (OCT) imaging and second, to subsequently treat the tumors using nanoshell absorption of near-infrared (NIR) light for photothermal ablation using a single-nanoparticle formulation that has been designed to have both absorption and scattering in the NIR.

Nanoshells consist of a dielectric core nanoparticle surrounded by an ultrathin metal shell with tunable plasmon resonances. Nanoshells offer the ability to manipulate both the resonant wavelength and the relative scattering and absorption efficiencies through the size and composition of each layer of the nanoshell structure.[3−5] Given these advantages, nanoshells can be used as contrast agents for enhanced OCT imaging,[6,7] based on their backscattering properties, as well as cancer therapeutics,[8,9] due to their absorbing properties. Through appropriate nanoparticle design for both strong absorption and scattering, both imaging and therapy should be improved with a single-particle formulation. For these studies, nanoshells were designed for absorption and scat-

tering in the near-infrared (NIR) region.[4,10] This region is of significant biological importance, as it provides a region in the spectrum useful for both therapeutic and imaging applications in tissue because the components of tissue do not have significant absorption in this range of wavelengths.[11] Nanoshells are currently being investigated for use in the NIR region for a variety of applications, including diagnostic assays,[12] modulated drug delivery systems,[13] and for laser tissue welding.[14] We have previously demonstrated photothermal ablation and complete regression of tumors in mice, accomplished through intravenous injection and subsequent passive tumor accumulation, which was followed by external NIR treatment for several minutes.[8,9] We recently reported the development of gold nanoshells suitable for therapy and imaging of cancer cells in in vitro studies.[6,15] This early work imaged human breast cancer cells that had been treated with antibody-conjugated gold nanoshells under darkfield microscopy, followed by NIR laser, inducing cell ablation only within the laser spot. In the present study, we report on the use of nanoshells as contrast agents to enhance OCT imaging of tumors grown in vivo followed by therapeutic application of NIR light.

OCT is an imaging modality that provides cross-sectional subsurface imaging of biological tissue with micrometer-scale resolution. The principles of OCT have been described previously.[16,17] OCT uses a short coherence length light source in a Michelson interferometer to enable high-resolution optical sectioning in tissue. In the system used in this study, low coherence light emitted from the source is

* Corresponding author. E-mail: jwest@rice.edu. Telephone: (713) 348-5955. Fax: (713) 348-5877. Rice University, MS 142, Department of Bioengineering, 6100 S. Main St., Houston, TX 77251.
† Department of Bioengineering, Rice University.
‡ Department of Electrical and Computer Engineering, Rice University.
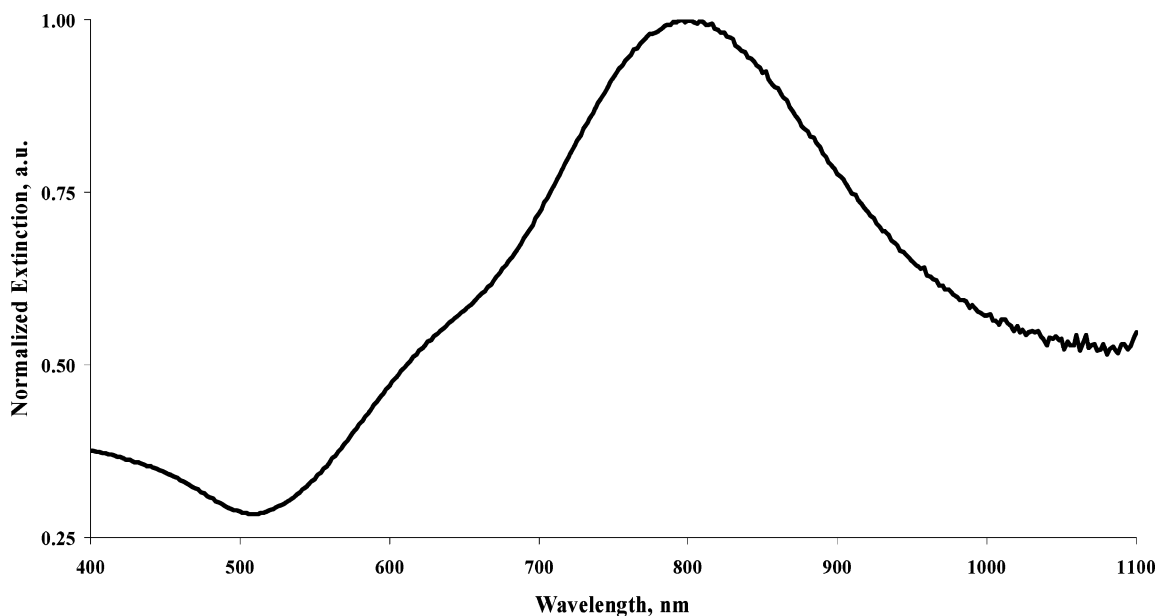§ Center for Chemical Characterization and Analysis, Texas A&M University.

Figure 1. Extinction spectra of nanoshells used in this study. Nanoshells are 143 nm in diameter with a core of 119 nm and a shell thickness of 12 nm.

directed onto a beam splitter. One beam is sent toward a reference mirror of known path length distance while the other is directed toward the sample. The reflected waves from both the reference mirror and sample are recombined at the beam splitter and directed to a detector where interference patterns are monitored as the reference mirror is moved. By monitoring these patterns while scanning the reference mirror, it is possible to map depth-resolved reflectivity of the tissue. The diagnostic potential of OCT was demonstrated by Matheny et al.[18] and has been used for imaging cancers of the gastrointestinal system,[19−22] prostate,[23] and oral mucosal[24] among others.

The use of contrast agents in OCT offers the promise of enhanced diagnostic power, similar to results with contrast agents in computed tomography (CT) and magnetic resonance imaging (MRI). To increase contrast in OCT, imaging agents including microbubbles[25] and microspheres with gold nanoparticles have been employed.[26,27] Optimal contrast agents for OCT would both further enhance contrast in vivo over the ∼5% improvement obtained with microbubbles and offer a smaller alternative to engineered microspheres (∼2−15 μm) to improve distribution into the microcirculation. Because of their biocompatibility, tunable optical properties, and small scale size, nanoshells are well suited to OCT, providing easily detected backscattering of NIR light. Furthermore, nanoshells have been shown to accumulate in tumors due to the leakiness of tumor vasculature, allowing efficient delivery of quantities suitable for both imaging and therapy. For this reason, the current work combines the use of OCT imaging with NIR treatment using an NIR absorbing and scattering nanoshell in a murine in vivo model.

Design of Dual Function Nanoshells. Nanoshells were made with cores that were 119 ± 11 nm in diameter. The shell thickness was approximately 12 nm. The measured extinction spectra of the nanoshells used in this study are shown in Figure 1. Mie theory scattering calculations predict

that these particles have approximately 67% of the extinction due to absorption and 33% due to scattering at 800 nm.

Nanoshells were prepared as previously described.[4,5] Briefly, silica cores were grown using the Stöber process, the basic reduction of tetraethyl orthosilicate (Sigma-Aldrich, Milwaukee, WI) in ethanol. The resultant silica nanoparticles were examined under scanning electron microscopy (SEM; Philips FEI XL30), and particles with a polydispersity of less than 10% were used in subsequent steps. Reaction of the silica core nanoparticles with (3-aminopropyl) triethoxy-silane (APTES, Sigma-Aldrich) provided amine groups on the surface of the core to allow for adsorption of gold colloid. Gold colloid was prepared to a size of 2−4 nm in the method of Duff et al. and aged 2−3 weeks at 4 °C.[28] The colloid was then concentrated 20× through rotary evaporation and mixed with the aminated silica particles, allowing small gold colloid, attached to the larger silica nanoparticle surface, to act as nucleation sites in the subsequent reduction step. This final step, growing the gold shell, was accomplished by the reduction of gold from chloroauric acid ($HAuCl_4$) in the presence of formaldehyde. By this method, the reduction of gold around the initial colloid sites allows gold islands to develop and eventually coalesce to form a contiguous gold shell. The extinction characteristics of the nanoshells were determined using a UV−vis spectrophotometer (Carey 50 Varian, Walnut Creek, CA). Nanoshells were surface-coated with poly(ethylene glycol) PEG to enhance circulation times and reduce immune response. Pegylation was accomplished by adding 20 μL of 5 μM PEG-SH, molecular weight 5 kDa (Nektar, Huntsville, AL) to 1.5 × 10^{10} nanoshells/mL in DI water for a minimum of 8 h. PEG-modified nanoshells were sterilized by filtration using a 0.22 μm filter and subsequently concentrated by centrifugation and re-diluted with sterile phosphate buffered saline (PBS).

Nanoshells Provide Significant Increase in OCT Contrast. PEG-modified nanoshells were injected intravenously
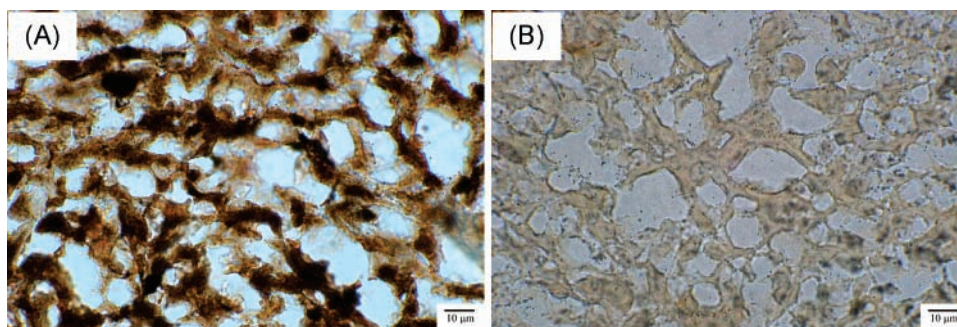
Figure 2. Silver enhancement staining of tissue shows heterogeneous staining of the tumor tissue from mice injected with nanoshells (A) indicating the presence of nanoshells. In contrast, there is little silver enhancement of sections taken from mice with PBS injection (B).

in tumor-bearing mice and allowed to passively accumulate in the tumor tissue due to the leakiness of the tumor vasculature. The significant accumulation of particles within the tumor tissue dramatically increased the NIR scattering within the tumor, enhancing the OCT contrast.

To grow tumors in mice, colon carcinoma cells were cultured and then injected subcutaneously in mice. Murine colon carcinoma cells (CT-26, ATCC, Manassas, VA) were grown at 37 °C in a 5% CO_2 environment in RPMI media supplemented with 4 mM l-glutamine, 1% penicillin, 1% streptomycin, and 10% fetal bovine serum (FBS). Cells were detached from culture with trypsin (0.05%) and EDTA (0.02%). Cells were re-suspended in sterile PBS for inoculation into BALBc mice (Charles River, Willington, MA). BALBc mice were used under an approved protocol of the Institutional Animal Care and Use Committee at Rice University. 150 000 CT-26 cells suspended in 25 μL of PBS were inoculated subcutaneously in the right flank of mice. Tumors were allowed to grow to a diameter of approximately 5 mm ($\sim$10 days). At that point, 150 μL of PEG-modified nanoshells in PBS (1.5×10^{11} nanoshells/mL) were injected into the tail vein 20 h prior to imaging via OCT. Control animals received a PBS injection.

In one set of mice, tumors were excised at 20 h, and nanoshell levels in tumor and normal tissues were assessed. Two methods were used for this. First, excised tumors were cryosectioned and silver stained (Sigma Silver Enhancement system, Sigma, Milwaukee, WI); silver staining allows the nanoshells to act as nucleation sites for deposition of silver to grow large enough to allow for visualization under light microscopy. Other tissue samples were lyophilized for gold content determination using neutron activation analysis (NAA).[29] The blank and the tumor sample were irradiated along with precise calibration standards at the Texas A&M University's Nuclear Science Center 1 MW TRIGA research reactor for 14 h. The irradiation position used in this study has an average neutron flux of approximately 1×10^{13} s^{-1} cm^{-2}. High-purity germanium detectors with nominal resolutions (fwhm) of 1.74 keV or better and efficiencies of 25−47% by industry standard relative measurement were used to quantify the 412 keV gamma line from ^{198}Au. The Canberra Industries OpenVMS alpha processor-based Genie-ESP software was used for acquisition and computation of gold concentrations.

Histological examination of tumors using silver staining confirmed the presence of nanoshells throughout the tumors. Figure 2 shows the silver staining of representative areas of tumors from mice treated with nanoshells (A) or with PBS (B). Additionally, NAA verified nanoshells present in the tumor shown in Figure 2A at 12.5 ppm, which is equivalent to approximately 3 million nanoshells per gram of tumor tissue, compared to 0 ppm for tumors of mice injected with just PBS 2B.

OCT images were collected for nanoshell-injected and control mice 20 h following injection (to allow time for passive accumulation of nanoshells) and analyzed to assess the increase in contrast provided by the nanoshells in tumor tissue compared to normal tissue. This study used a commercially available OCT imaging system (Niris Imaging System, Imalux, Cleveland, OH). The axial and transverse resolutions were measured to be approximately 10 and 15 μm, respectively. OCT images of the tumor and normal tissue was taken after 20 h of circulation. The animals were not anesthetized during the injection or circulation period, only during imaging and treatment. The tumors were imaged using the Niris OCT imaging device by applying glycerol on the shaved tumor site for index matching and placing the probe in contact with the skin directly above the tumor. Images were captured at several locations on each tumor through the integrated computer and image analysis system. Normal tissue images were taken at a location at least 2 cm distant to the tumor on the same animal. Images were analyzed to first quantify the contrast levels using standard thresholding for image analysis, then intensity data were analyzed using an unpaired Student t test assuming equal variance with a confidence interval of 95%, $\alpha < 0.05$ of the two populations of images from PBS-treated and nanoshell-treated mice. Analysis of the tumor regression was performed using the average measurements of the tumor size of the surviving populations at the times shown and compared using an unpaired Student t test assuming equal variance with a confidence interval of 95%, $\alpha < 0.05$.

Figure 3 shows OCT imaging results obtained after PBS injection, panels A and C, and after nanoshell injections, panels B and D. The strata of the skin and underlying muscle can be seen in the OCT image of the normal tissue panel A and B. There is no enhancement in layers of normal tissue in mice treated with nanoshells compared with the PBS-
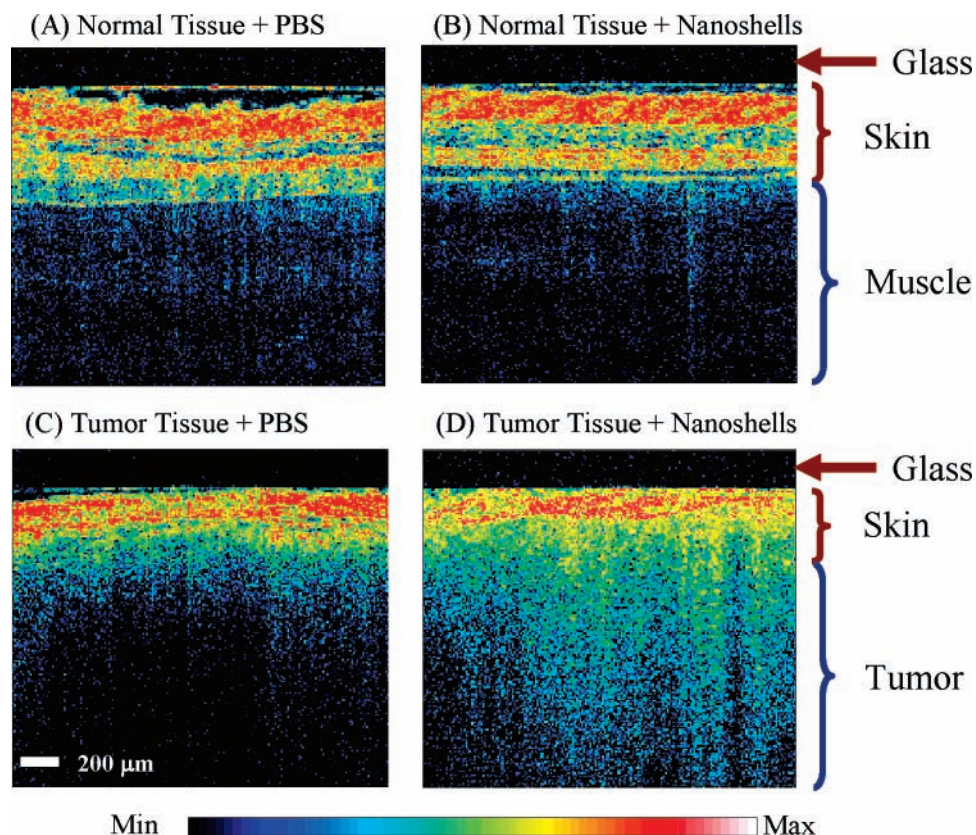
Figure 3. Representative OCT images from normal skin and muscle tissue areas of mice systemically injected with nanoshells (A) or with PBS (B). Representative OCT images from tumors of mice systemically injected with nanoshells (C) or with PBS (D). Analysis of all images shows a significant increase in contrast intensity after nanoshell injection in the tumors of mice treated with nanoshells while no increase in intensity is observed in the normal tissue. The glass of the probe is 200 μm thick and shows as a dark nonscattering layer.
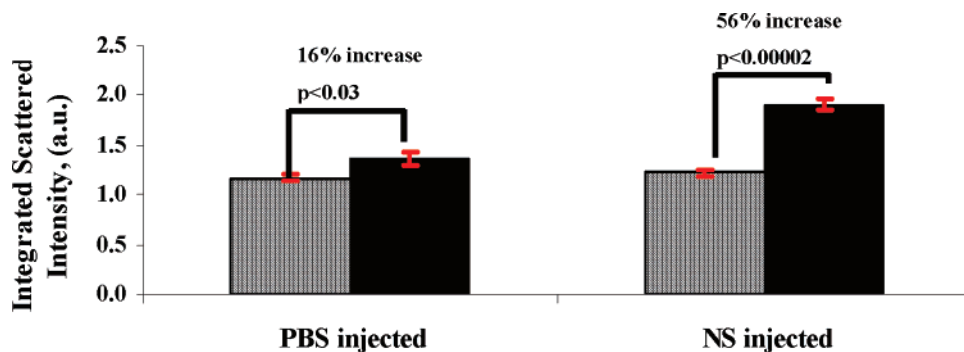
Figure 4. Quantification of OCT images shows a significant increase in intensity of images of tumors from mice with systemic nanoshell injection. Normal muscle tissue is shown in the blue bar while tumor tissue is shown in the black bar. Values are average $\pm$ SEM; p values are shown.

injected mouse because nanoshells do not extravasate appreciably into normal tissues.

The enhanced brightness of the image in panel D relative to panel C of Figure 3, where nanoshells have accumulated in the tumor, indicates that gold nanoshells can provide substantial contrast in OCT imaging. Figure 3D also shows that the borders of tumors (on the left) can more easily be discerned in the OCT images of nanoshell-treated mice compared to those mice that had only PBS injection (Figure 3C). Figure 4 shows the quantification of the image intensity of OCT images of normal tissue ($n = 3$) and tumor tissue ($n = 6$) with PBS injections and nanoshell injections. Images were analyzed to first quantify the contrast and then analyzed

using a Student's t test of the two populations of images from PBS-treated and nanoshell-treated mice. The data show a significant increase in the optical contrast of tumor compared to normal tissue when nanoshells are used, $p <$ 0.00002. No statistical difference is observed in the intensity of the optical contrast of images of normal tissue whether nanoshells are used or PBS.

Nanoshells Also Allow Photothermal Ablation of Tumors with Increased Survival. As described above, tumor-bearing mice received either nanoshell or PBS injections. Animals were randomly assigned to control and treatment groups. Animals were randomly divided into three groups: treatment (nanoshell + laser); sham (PBS + laser), and
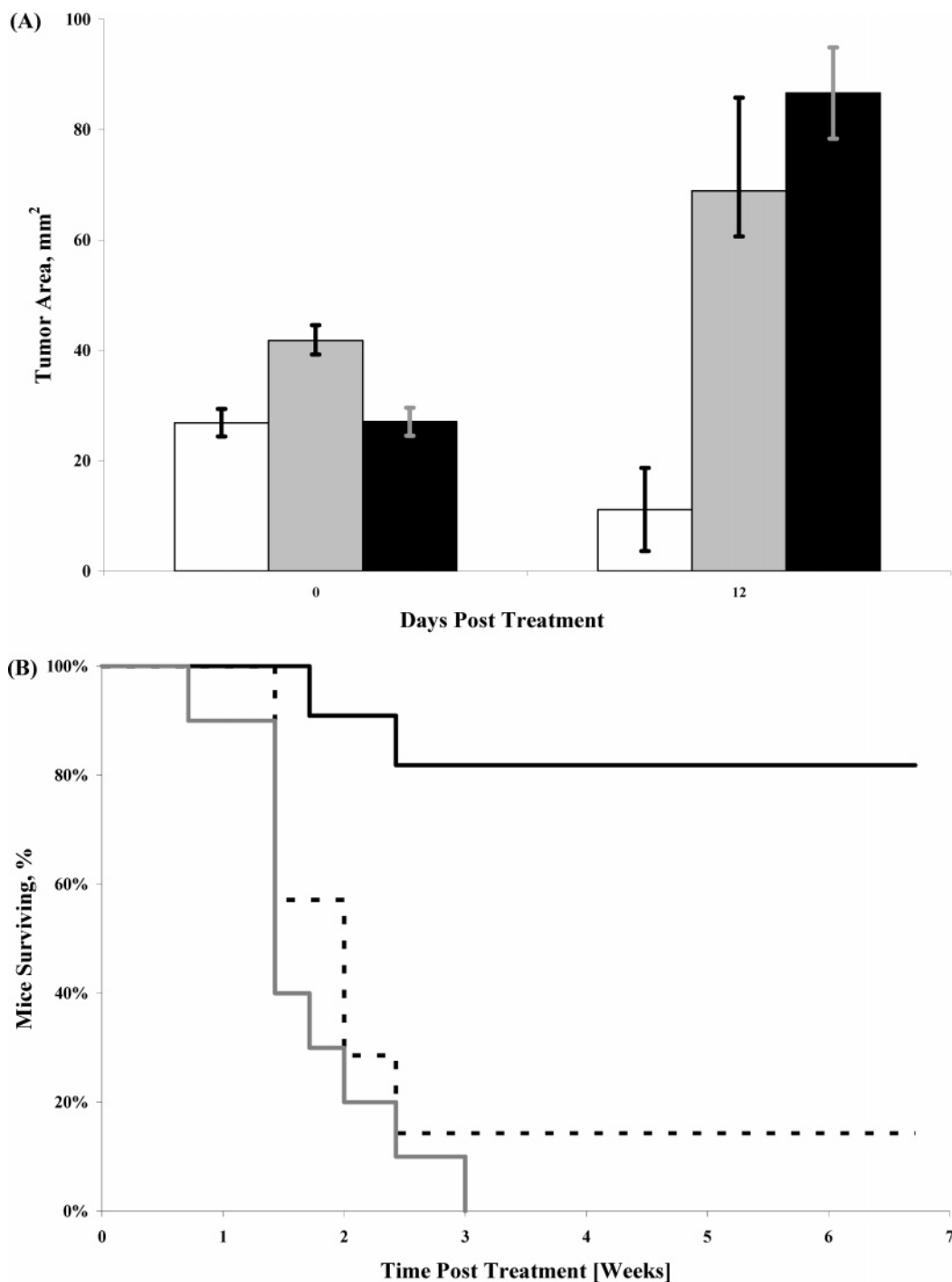
Figure 5. (A) Tumor size before irradiation and 12 days post-irradiation of mice treated with nanoshell + NIR laser irradiation (white bar); PBS sham + NIR laser treatment (gray bar) or untreated control (black bar); values are average ± SEM. (B) Kaplan−Meier survival data for the treatment groups post irradiation; nanoshell + NIR laser irradiation (solid black line); PBS sham + NIR laser treatment (dashed black line) or untreated control (gray line); survival was followed for 7 weeks posttreatment. After 21 days, the nanoshell therapy group survival rate was significantly higher than either control group, $p < 0.001$.

control (untreated). Following OCT imaging as described above, animals in the treatment and sham groups had their tumors irradiated with a NIR laser. In vivo irradiation was accomplished using an Integrated Fiber Array Packet, FAP-I System, with a wavelength of 808 nm (Coherent, Santa Clara, CA) at a power density of 4 W/cm^2 and a spot size of 5 mm diameter for 3 min. Tumor size and animal survival was monitored for 7 weeks after imaging and treatment. Survival

data analysis was performed using the standard Kaplan−Meier analysis using MedCalc software.

Figure 5A shows the tumor sizes on the day of treatment and 12 days after treatment; tumors on all but two nanoshell-treated mice had completely regressed. Figure 5B shows the survival of the mice during the entire study period. Kaplan−Meier statistical analysis shows a median survival of 14 days for the PBS + laser group and 10 days for the untreated

control group. By day 21, the survival of the nanoshell + laser group was significantly greater than either the control or sham groups, $p < 0.001$, and this then continued for the duration of the study. Median survival time could not be calculated for this group, as the long-term survival was 83%.

We have reported the successful in vivo demonstration of a single nanoparticle that enhances the scattering signal for OCT imaging while retaining its properties to affect photothermal ablation of the tumor. Our findings suggest that engineered nanoparticles, such as nanoshells with tunable optical properties, can indeed play a vital role in a number of emerging in vivo molecular imaging modalities and allow integration of diagnostic and therapeutic technologies.

References

(1) Sullivan, D. C.; Ferrari, M. *Mol. Imaging* **2004**, *3*, 364−369.
(2) Ferrari, M. *Nat. Rev. Cancer* **2005**, *5*, 161−171.
(3) Averitt, R.; Wescott, S.; Halas, N. *J. Opt. Soc. Am. B* **1999**, *6*, 1824−1832.
(4) Oldenburg, S. J.; Averitt, R. D.; Westcott, S. L.; Halas, N. J. *Ch. Phys. Lett.* **1998**, *288*, 243−247.
(5) Oldenburg, S. J.; Jackson, J. B.; Westcott, S. L.; Halas, N. J. *Appl. Phys. Lett.* **1999**, *75*, 2897−2899.
(6) Loo, C.; Lowery, A.; Halas, N.; West, J.; Drezek, R. *Nano Lett.* **2005**, *5*, 709−711.
(7) Loo, C. H.; Lin, A.; Hirsch, L.; Lee, M.; Barton, J. K.; Halas, N. J.; West, J. L. *Technol. Cancer Res. Treat.* **2004**, *3*, 33−40.
(8) Hirsch, L. R.; Stafford, R. J.; Bankson, J. A.; Sershen, S. R.; Rivera, B.; Price, R. E.; Hazle, J. D.; Halas, N. J.; West, J. L. *Proc. Natl. Acad. Sci. U.S.A.* **2003**, *100*, 13549−13554.
(9) O'Neal, D. P.; Hirsch, L. R.; Halas, N. J.; Payne, J. D.; West, J. L. *Cancer Lett.* **2004**, *209*, 171−176.
(10) Averitt, R. D.; Westcott, S. L.; Halas, N. J. *J. Opt. Soc. Am. B* **1999**, *16*, 1824−1832.
(11) Weissleder, R. *Nat. Biotechnol.* **2001**, *19*, 316−317.
(12) Hirsch, L. R.; Jackson, J. B.; Lee, A.; Halas, N. J.; West, J. L. *Anal. Chem.* **2003**, *75*, 2377−2381.
(13) Sershen, S. R.; Westcott, S. L.; Halas, N. J.; West, J. L. *J. Biomed. Mater. Res. A* **2000**, *51*, 293−298.
(14) Gobin, A.; O'Neal, D.; Watkins, D.; Halas, N.; Drezek, R.; West, J. *Lasers Surg. Med.* **2005**, *37*, 123−129.
(15) Loo, C.; Hirsch, L.; Lee, M.-H.; Chang, E.; West, J.; Halas, N.; Drezek, R. *Opt. Lett.* **2005**, *30*, 1012−1014.
(16) Fujimoto, J. G.; Brezinsky, M. E.; Tearney, G. J.; Boppart, S. A.; Bouma, B.; Hee, M. R.; Southern, J. F.; Swanson, E. A. *Nat. Med.* **1995**, *1*, 970−972.
(17) Huang, D.; Swanson, E. A.; Lin, C. P.; Schuman, J. S.; Stinson, W. G.; Chang, W.; Hee, M. R.; Flotte, T.; Gregory, K.; Puliafito, C. A. *Science* **1991**, *254*, 1178−1181.
(18) Matheny, E. S.; Hanna, N. M.; Jung, W. G.; Chen, Z.; Wilder-Smith, P.; Mina-Araghi, R.; Brenner, M. *J. Biomed. Opt.* **2004**, *9*, 978−981.
(19) Li, X. D.; Boppart, S. A.; Dam, J. V.; Mashimo, H.; Mutinga, M.; Drexler, W.; Klein, M.; Pitris, C.; Krinsky, M. L.; Brezinski, M. E.; Fujimoto, J. G. *Endoscopy* **2000**, *32*, 921−930.
(20) Izatt, J. A.; Kulkarni, M. D.; Wang, H.-W.; Kobayashi, K.; Sivak, M. V. *IEEE J. Sel. Top. Quantum Electron.* **1996**, *4*, 1017−1028.
(21) Tearney, G. J.; Brezinski, M. E.; Southern, J. F.; Bouma, B. E.; Boppart, S. A.; Fujimoto, J. G. *Am. J. Gastroenterol.* **1997**, *92*, 1800−1804.
(22) Kobayashi, K.; Izaat, J.; Kulkarni, M.; Willis, J.; Sivak, M. *Gastrointest. Endosc.* **1998**, *47*, 515−523.
(23) D'Amico, A. V.; Weinstein, M.; Li, X.; Richie, J. P.; Fujimoto, J. G. *Urology* **2000**, *55*, 783−787.
(24) Sergeev, A. M.; Gelikonov, V. M.; Gelikonov, G. V.; Feldchtein, F. I.; Kuranov, R. V.; Gladkova, N. D. *Opt. Exp.* **1997**, *1*, 432−440.
(25) Barton, J. K.; Hoying, J. B.; Sullivan, C. J. *Acad. Radiol.* **2002**, *9*, S52−S55.
(26) Lee, T. M.; Oldenburg, A. L.; Sitafalwalla, S.; Marks, D. L.; Luo, W. *Opt. Lett.* **2003**, *28*, 1546−1548.
(27) Oldenburg, A. L.; Hansen, M. N.; Zweifel, D. A.; Wei, A.; Boppart, S. A. *Opt. Exp.* **2006**, *14*, 6724−6738.
(28) Duff, D. G.; Baiker, A.; Edwards, P. P. *Langmuir* **1993**, *9*, 2301−2309.
(29) James, W. D.; Hirsch, L. R.; West, J. L.; O'Neal, P. D.; Payne, J. D. *J. Radioanal. Nucl. Chem.* **2006**, *271*, 455−459.

NL070610Y

Design and construction of targeted AAVP vectors for mammalian cell transduction

Amin Hajitou[1], Roberto Rangel[1], Martin Trepel[2], Suren Soghomonyan[3], Juri G Gelovani[3], Mian M Alauddin[3], Renata Pasqualini[1] & Wadih Arap[1]

[1]Department of Genitourinary Medical Oncology, The University of Texas M. D. Anderson Cancer Center, 1515 Holcombe Boulevard, Houston, TX 77030. [2]Department of Hematology and Oncology and Institute for Molecular Medicine and Cell Research, University of Freiburg Medical Center, Hugstetter Strasse 55, D-79106 Freiburg, Germany. [3]Department of Experimental Diagnostic Imaging, The University of Texas M. D. Anderson Cancer Center, 1515 Holcombe Boulevard, Houston, TX 77030. Correspondence should be addressed to R.P. (rpasqual@mdanderson.org) or W.A. (warap@mdanderson.org).

Bacteriophage (phage) evolved as bacterial viruses, but can be adapted to transduce mammalian cells through ligand-directed targeting to a specific receptor. We have recently reported a new generation of hybrid prokaryotic–eukaryotic vectors, which are chimeras of genetic *cis*-elements of recombinant adeno-associated virus and phage (termed AAVP). This protocol describes the design and construction of ligand-directed AAVP vectors, production of AAVP particles and the methodology to transduce mammalian cells *in vitro* and to target tissues *in vivo* after systemic administration. Targeted AAVP particles are made in a two-step process. First, a ligand peptide of choice is displayed on the coat protein to generate a targeted backbone phage vector. Then, a recombinant AAV carrying a mammalian transgene cassette is inserted into an intergenomic region. High-titer suspensions ($\sim 10^{10}$–10^{11} transducing units per μl) can be produced within 3 days after vector construction. Transgene expression by targeted AAVP usually reaches maximum levels within 1 week.

INTRODUCTION

The use of new genetic systems for the study of currently intractable biological questions will require the development of ligand-directed (targeted) vectors that can be systemically delivered. Over the past decade, common approaches at targeted gene delivery have typically relied on ablation of the native tropism of mammalian viruses, redirection to alternative receptors or both[1–8]. Incorporation of homing peptides selected from bacteriophage (phage) display library screenings into mammalian viral vectors has been attempted, but such strategy has the potential to alter the structure of the capsid, affect the targeting attributes of the ligand peptides or even prevent the display within a viable viral capsid altogether[9–13]. In contrast, phage have no intrinsic tropism for mammalian cells[14,15] and can mediate modest gene expression in mammalian cells after genetic manipulation[16–19]. In theory, phage-based vectors have some potential advantages over animal viruses for mammalian cell-targeted delivery of transgenes. First, there are no known natural receptors for phage (which have evolved as prokaryotic viruses) on mammalian cells[14,15]. However, receptor-mediated internalization by mammalian cells occurs if phage vectors are genetically modified to display specific ligands, such as fibroblast growth factor (FGF2), anti-ErbB2 scFv F5 antibody and integrin-binding peptides[16–20]. Moreover, bacteriophage have long been administered to humans, from its antibacterial use in the environment during the preantibiotic era[14] to the very recent Food and Drug Administration approval of certain phage preparations as antibacterial food additives[21]. Indeed, feasibility clinical trials have shown that the selection of phage libraries in cancer patients can yield ligand–receptor systems[22,23] and that serial library administration can be accomplished without major untoward clinical effects[24]. Finally, unlike mammalian viruses, phage do not require further context modification of their capsid because the targeting peptides are actually selected and isolated directly as homing to specific cell-surface receptors[22,25–30].

Despite these potential advantages, phage-based vectors have inherently been considered poor gene delivery vehicles. As a working hypothesis, we proposed that the rate-limiting step might be mechanistically related to the post-targeting fate of the single-stranded DNA of the phage genome[1]. In an attempt to improve phage as targeted vectors for mammalian cells, we reasoned that the genetic incorporation of compatible *cis*-elements (such as inverted terminal repeats (ITRs)) from a mammalian—yet single-stranded—DNA virus such as recombinant adeno-associated virus (AAV) would improve post-targeting transgene expression. Thus, we have developed ligand-directed vectors as a hybrid between AAV and phage (termed AAVP). In our targeted AAVP prototype vector[1], the targeted phage displays an RGD-4C peptide that binds to α_v integrins[26,27,29,31], with the mammalian transgene cassette flanked by full-length ITRs of AAV serotype 2. We reported[1] that the improved mammalian transduction efficiency by targeted AAVP over conventional phage-based vectors is associated with an improved fate of the delivered transgene, through maintenance of the entire mammalian transgene cassette, better persistence of episomal DNA and formation of concatamers of the transgene cassette[1]. Here, we detail how to insert an AAV transgene cassette into the backbone phage vector genome to generate targeted AAVP hybrid constructs (Steps 1–18) and how to produce, purify and titrate the vector preparations (Steps 19–26). We also describe a standard protocol for AAVP-mediated mammalian cell transduction, both in tissue culture and in targeted tissues *in vivo* after systemic administration. Briefly, DNA olignonucleotide sequences encoding peptide ligands are inserted into the *Sfi*I site of the gene of the pIII minor coat protein of fUSE5-MCS (multicloning site)-based filamentous phage[1,32,33]. Phage produced in this manner display 3–5 copies of the specific peptide[32]. The fUSE5-MCS-based filamentous phage display vector is then genetically modified to generate the corresponding targeted AAVP vector, by inserting a recombinant AAV (carrying the desirable promoter/transgene cassette) into an intergenomic region of the phage genome. This strategy also serves to construct

PROTOCOL

non-targeted control vectors (either displaying no peptides or displaying mutant/scrambled versions of the peptide). Targeted and control AAVP particles are amplified, isolated and purified by adapting the protocols used for phage[30,32]. AAVP particles are then resuspended in phosphate-buffered saline (PBS; pH 7.4) and recentrifuged to remove residual bacterial debris. Next, AAVP particles in suspension are sterile-filtered through 0.45-μm pores, then titrated by infection of host bacteria for colony counting on Luria–Bertani (LB) agar plates under a double antibiotic selection and expressed as bacterial transducing units (TU). Transduction of mammalian cells in culture is performed by incubation with the targeted AAVP for 4 h in serum-free medium with a ratio of at least 10^6 TU per cell. Transgene expression begins 48–72 h later and reaches a maximum level by 1 week. Typically, non-targeted AAVP vectors or AAVP displaying mutated and/or scrambled versions of the targeting peptide serve as negative controls for the ligand-directed (i.e., targeting) experiments; either a corresponding version of a targeted phage vector "AAV-less" or a targeted AAVP containing an "ITR-less" or mutant ITR serves as a suitable control for post-internalization (i.e., integration, concatemerization) experiments.

Under these conditions, ∼10–20% of cells are transduced in culture. Specificity can be demonstrated by blocking the interaction of the targeted AAVP by preincubating the target cells with the corresponding synthetic peptide. In our prototype RGD-4C AAVP,

transduction inhibition was dose-dependent, greater than 99% inhibition was observed and incubation with nonspecific negative control peptides had no detectable effects[1]. This data set showcases an example of targeted AAVP transduction of mammalian cells expressing a specific receptor and mediated by an established ligand–receptor system. Transduction of a target tissue *in vivo* will vary among ligand–receptors but one can attempt to use increasing doses of targeted AAVP, starting at 10^{10} TU per mouse, administered intravenously (tail vein). Transgene expression should be monitored and its detection can be expected starting from day 3 after delivery. Depending on the specific reporter used, one can determine gene expression initiation in the target and maximal expression timing. Evidently, different organs will require different ligand peptides and particular conditions should be anticipated for optimal temporal and spatial transduction. In an unpublished work, we have shown systemic targeted tissue-specific transduction of the lung tissue in wild-type mice via a homing peptide[34] that targets membrane dipeptidase in the lung endothelium[35]; we have also tested a tumor-homing peptide[25] that targets MMP-2 and MMP-9 to transduce human tumor xenografts with phage-based vectors. In addition to the suicide gene therapy strategy previously reported[1], other targeted AAVP including applications for delivery of therapeutic genes (unpublished observations) will follow.

MATERIALS
REAGENTS
- Plasmids:
  fUSE5[1,32,33,36] phage plasmid, accession number AF218364
  fd-tet[1,32,33,36] phage plasmid, accession number AF217317
  fMCS[1,36] phage plasmid, accession number AF218733
  fUSE5-MCS[1] phage plasmid
  pAAV-GFP plasmid (Stratagene)
  pMOD-Luc-Sh (Luciferase reporter; InvivoGen)
  pCMVβ (β-galactosidase reporter; Clontech)
- Bacterial strains:
  XL1-Blue MR supercompetent cells (Stratagene)
  Escherichia coli (MC1061 and k91Kan) (see ref. 36)
- LB–tetracycline plates, LB–tetracycline–kanamycin plates and media
- Terrific broth (TB) medium
- SOC medium (Invitrogen)
- Polyethylene glycol (PEG)/NaCl
- QIAquick Nucleotide removal kit (Qiagen)
- Essential restriction enzymes: *Bgl*I, *Bgl*II, *Hind*III, *Pst*I, *Pvu*II, *Sac*I, *Sfi*I and *Xho*I. Other restriction enzymes will be required depending on the specific sequences of the construct
- Phosphatase alkaline (Roche)
- T4 DNA ligase with ligase buffer (Invitrogen)
- Rapid DNA ligation kit (Roche)
- Agarose, electrophoresis (IscBioExpress)
- E-Gel 0.8% agarose (Invitrogen)
- QIAquick Gel extraction kit (Qiagen)
- Phosphorylated DNA linkers (NEB)
- *Taq*-DNA polymerase with supplied buffer (Promega)

- 100 mM dNTPs (Fisher)
- Oligonucleotides (Sigma-Genosys) (see **Table 1**)
- DMSO ❗ **CAUTION** DMSO is readily absorbed through the skin. When handling DMSO, wear appropriate gloves, safety glasses and use a pipeting aid under a safety chemical hood.
- Transfection reagent: Fugene (Roche)
- Human embryonic kidney cells (HEK293; ATCC)
- HEK293 cells are maintained in Dulbecco's modified Eagle's medium (Gibco), supplemented with 10% fetal bovine serum (Gibco), L-glutamine and penicillin/streptomycin
- D-Luciferin potassium salt (InvivoGen)
- Immunocompetent and immunodeficient mice (Harlan–Sprague–Dawley)
  ▲ **CRITICAL** Mice must be used according to the national and institutional guidelines concerning use of animals.
EQUIPMENT
- Fluorescent microscope (Olympus or equivalent).
- Fluorescence-activated cell sorting (FACS) to analyze and sort the cells by using a BD FACS Vantage (Becton-Dickinson)
- 0.22 μm filter units (Corning)
- 0.45 μm filter units (Corning)
- 24-well tissue culture plates
- Tissue culture incubator at 5% CO_2 for HEK293 cells and other cell lines
- Shaker at 37 °C
- Centrifuge Sorvall SA-600 and SLA-3000 rotors
- Cell electroporator (Life Technologies)
- *In vivo* Bioluminescence Imaging (BLI) System 200 (IVIS200; Xenogen)
- PCR machine (Eppendorf)
- DNA electrophoresis equipment (Bio-Rad)

TABLE 1 | Primer set sequences.

Primer set	Sequence	Function
A	5′-CACTCGGCCGACG-3′ 5′-TTCGGCCCCAGCGGC-3′	Oligonucleotide conversion from single- to double-stranded DNA
B	5′-TAATACGACTCACTATAGGGCAAG CTGATAAACCGATACAATT-3′ 5′-CCCTCATAGTTAGCGTAACGATCT-3′	Primers routinely used to amplify the oligonucleotide sequences after insertion into the construct

REAGENT SETUP
PEG/NaCl solution stock   500 g of PEG and 584.5 g of NaCl in 2,380 ml H_2O (double-distilled) and store at 4 °C for up to 1 year.
TB medium   9.6 g of tryptone, 19.2 g of yeast extract and 3.2 ml of glycerol in 1 liter of H_2O. Autoclave, add 100 ml of TB supplements and 50 mg of kanamycin
TB supplements   To prepare 1 liter of TB supplements, add 23.1 g of KH_2PO_4 and 125.4 g of K_2HPO_4 in 1 liter of H_2O (double distilled). Filter through 0.22 µm filter unit and store at 4 °C.

EQUIPMENT SETUP
Whole-body BLI of luciferase   Mice are first anesthetized inside a clear plexiglass box by using an anesthetic gas admixture (2% isofluorane, 98% oxygen) and are then transferred to nose cones attached to the manifold in the imaging chamber. The imaging time is 5 min per side (dorsal/ventral), depending on the experiment. Imaging parameters are as follows: image acquisition time, 1 min; binning, 2; no filter; f/stop (aperture size), 1. Regions of interest can be defined manually over the tumors or target tissues for measuring signal intensities, expressed as photons s^{-1} cm^{-2} sr^{-1}.

PROCEDURE
Insertion of the targeted peptide into the pIII coat protein of fUSE5-MCS phage
1| Generate phage clones displaying targeting peptides by cloning the corresponding oligonucleotide sequences flanked by *Bgl*I restrictions sites into the *Sfi*I site of the gene for the pIII coat protein of fUSE5-MCS. The fUSE5-MCS plasmid can also be generated by replacing the 5.4 kb *Bam*HI–*Sac*II fragment of the fUSE5 with the 4.1 kb *Bam*HI–*Sac*II fragment from the fMCS plasmid that contains an MCS.

2| Design and convert the synthetic oligonucleotide templates flanked by *Bgl*I restriction sites (500 ng) to double-stranded DNA by PCR amplification. We use the following 57 bp oligonucleotide as a template: 5′-**CACTCG GCCGACG**GGGCTXXXXXXXXXX XXXXXXXXXXXGGG**GCCGCTGGG GCCGAA**-3′. This template is flanked by the *Bgl*I restriction sites (GCCNNNNNGGC: underlined). The bold nucleotides in the above template sequence indicate the annealing of the sense and antisense primers, respectively. The nucleotide sequence encoding the displayed peptide is marked "X".

Finally, we use primer set A (see **Table 1**) and 2.5 U of *Taq* DNA polymerase (Promega) in 20 µl. Use the following setup: 94 °C for 2 min, followed by 35 cycles at 94 °C for 30 s, 60 °C for 30 s and 72 °C for 30 s, followed by 72 °C for 5 min, held at 4 °C and stored at −20 °C until ready for Step 3.
▲ **CRITICAL STEP** For effective PCR, it is recommended to add DMSO (2% final) to weaken hydrogen bonding and prevent formation of hairpin structures.

3| Purify and elute the double-stranded DNA sequences containing *Bgl*I restriction sites by using a QIAquick nucleotide removal kit.

4| Digest oligonucleotides with *Bgl*I restriction enzyme for 4 h at 37 °C, then inactivate *Bgl*I activity by incubation at 65 °C for 20 min. Digestion with *Bgl*I restriction enzyme generates the following sticky ends:
5′-   GGGCTXXXXXXXXXXXXXXXXXXXXXXXGGGGCCGCTG-3′
3′-TGCCCCGAXXXXXXXXXXXXXXXXXXXXXXXCCCCGGC-5′.

5| Digest the fUSE5-MCS plasmid with *Sfi*I restriction enzyme for 1–2 h at 50 °C. Run the ∼9.5-kb linearized fUSE5-MCS plasmid on an agarose gel or E-Gel 0.8% agarose to confirm digestion. The fUSE 5 backbone vector contains two *Sfi*I restriction sites[36] (GGCCNNNN/NGGCC) in the pIII gene. After digestion, the *Sfi*I restriction enzyme will generate non-identical, non-complementary three bases 3′-overhanging ends[36]. This will allow directional cloning after removal of the stuffer that lies between these sites in the phage vector. A schematic representation of the final vector sequences is shown below.

fUSE5	Stuffer	fUSE5
5′-TCGGCCGACG	TGGCCTGGCCTCTG	GGGCCGAA-3′
3′-AGCCGGC	TGCACCGGACCGGA	GACCCCGGCTT-5′

? TROUBLESHOOTING

6| Ligate the *Sfi*I-digested fUSE5-MCS vector plasmid with the *Bgl*I-digested oligonucleotides by using the Rapid Ligation Kit for 5–10 min at room temperature (25 °C, **Fig. 1**). It is recommended not to inactivate *Sfi*I and not to dephosphorylate the linearized fUSE5-MCS plasmid, as this markedly reduces the efficiency of ligation. Ligate immediately after digestion. Also, set up a reaction with the fUSE5-MCS plasmid alone and no insert to estimate the bacterial transformation due to autoligation of the fUSE5-MCS plasmid and/or the presence of non-digested fUSE5-MCS plasmid.

7| Use 2 µl of the ligation product to transform MC1061 or XL1-Blue MR bacteria according to the manufacturer's instructions. Incubate transformed bacteria on LB–tetracycline plates for 24 h at 37 °C.

8| Verify the correct insertion and nucleotide sequence by PCR of the bacterial colonies generated. Pick single colonies (at least ten single colonies plus colonies from vector alone as controls) in 20 µl of medium. Use the primer set B (see **Table 1**) and 2 U of *Taq* DNA polymerase (Promega) in 20 µl. Use the following setup: 94 °C for 3 min, followed by 35 cycles at 94 °C for 10 s, 60 °C for 30 s and 72 °C for 30 s.
▲ **CRITICAL STEP** It is recommended to add 2% DMSO to weaken hydrogen bonding and prevent formation of hairpin structures.

9| Run 2 µl of PCR product on a 2% agarose gel or E-Gel 0.8% agarose to verify the insertion. Include the product of an fUSE5-MCS without insert, which will be smaller in size on the gel.

Insertion of recombinant (r) AAV into the MCS of the fUSE5-MCS plasmid displaying the targeting peptide

10| Prepare the rAAV carrying the trangene of interest. Remove and replace GFP from the pAAV-GFP plasmid with the transgene of interest if applicable. GFP can also be replaced with a GFP variant for maximal fluorescence such as eGFP (enhanced GFP, catalog number 6084-1 from ClonTech). Thus, the transgene of interest must be flanked by restriction sites compatible with the MCS of the pAAV plasmid.

11| Remove the transgene cassette flanked by the ITRs from the pAAV plasmid created in Step 10. Use the *Pvu*II restriction enzyme that digests adjacent to the ITRs and gel-purify the released transgene-ITR-segment using the gel extraction kit (**Fig. 1**). Note that expression cassettes of interest should not have any *Pvu*II site. Otherwise, alternative strategies should be used. Then, use an rAAV plasmid with a restriction map compatible with that of the expression cassette of interest. For instance, some AAV plasmids from Stratagene (or other commercial outfits) have convenient rare cutter restriction enzyme sites such as *Sbf*I or *Sse*8387I adjacent to each *Pvu*II site. Sometimes, these can be used for AAV vector genome insertion into the phage vector backbone if other genetic elements permit this utilization.

12| The targeted fUSE5-MCS plasmid has a unique *Pvu*II site in the MCS. Digest with *Pvu*II to linearize and run on an agarose gel or on an E-Gel 0.8% agarose to confirm digestion.

13| Dephosphorylate the targeted fUSE5-MCS plasmid vector by using phosphatase alkaline according to the manufacturer's instructions.
▲ **CRITICAL STEP** It is recommended to dephosphorylate before ligation to reduce background as the fUSE5-MCS plasmid autoligates.

Figure 1 | Targeted AAVP vectors. (**a**) Cloning scheme for generation of targeted AAVP and control vectors. The most convenient procedure is to first clone the *Bgl*I-digested oligonucleotide sequence corresponding to the targeting peptide within the *Sfi*I site of the gene for the pIII coat protein. Next, the *Pvu*II-digested ITR-flanking transgene cassette (rAAV) is cloned into the *Pvu*II site in the MCS of the targeted fUSE5-MCS plasmid or in the cohesive restriction sites after addition of the corresponding linkers. (**b**) Binding of the targeted AAVP particle to a specific cell-surface receptor in the target tissue and internalization after systemic administration. Alternative cloning approaches are discussed in the text.

14| Ligate the ITR-flanked transgene cassette into the *Pvu*II-linearized fUSE5-MCS plasmid for 4 h at 23 °C or 24 h overnight at 16 °C using T4 DNA ligase (**Fig. 1**).
? TROUBLESHOOTING

15| Digestion with *Pvu*II generates blunt ends. Linkers containing recognition sequences of enzymes can be added to the *Pvu*II-recovered ITR-flanked cassette to produce compatible cohesive ends.
    Linkers to *Bgl*II, *Hin*dIII, *Pst*I, *Sac*I and *Xho*I can be used. After determining which restriction site is most appropriate for the construction, add the corresponding restriction enzyme to digest the linkers flanking the ITR transgene cassette. Ligate into the compatible cohesive restriction sites (*Bgl*II, *Hin*dIII, *Pst*I, *Sac*I and *Xho*I) of the MCS of the fUSE5-MCS plasmid.
? TROUBLESHOOTING

16| Use 2 µl of the ligation product to transform MC1061 or XL1-Blue MR bacteria according to the manufacturer's instructions. Plate bacteria on LB-tetracycline and grow overnight at 37 °C for 24 h.

17| Pick ten colonies, grow overnight in 5 ml LB and purify the plasmid DNA by using a QIAprep miniprep kit protocol for low-copy plasmids. Identify the positive clones by enzymatic restriction digestions.
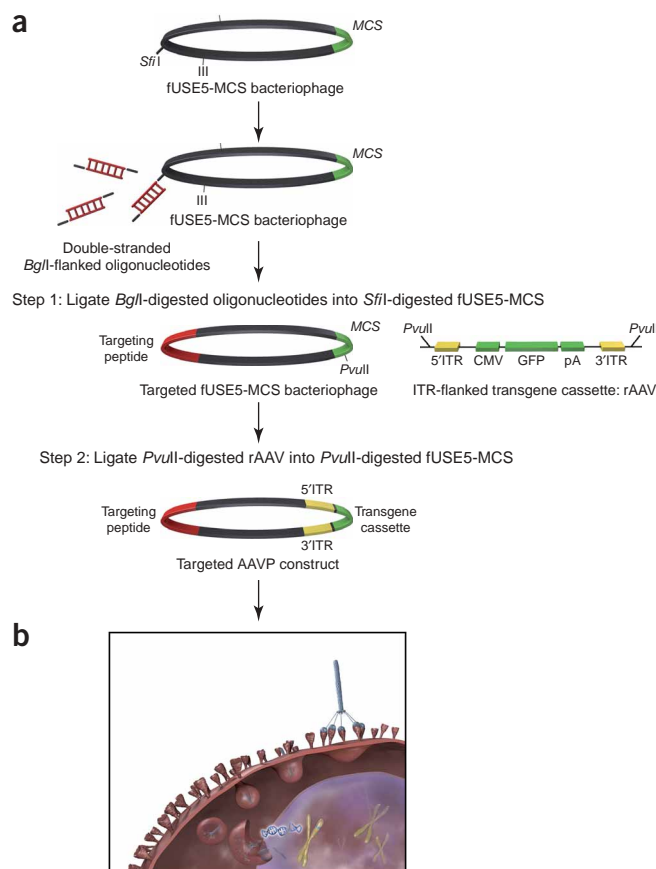
18| Transgene expression can be analyzed at this stage from the AAVP plasmids generated to confirm that the ITR-flanked transgene cassette is functional when inserted into the phage genome (in the context of AAVP). Therefore, transfect human embryonic kidney (HEK293) cells with the AAVP DNA plasmids by using the Fugene transfection reagent (Roche). Different experimental approaches, such as western blots or immunostainings, can be used to detect transgene expression depending on the gene of interest. For reporter *GFP-*, β-*galactosidase-* or *luciferase*-containing cassettes, expression can be analyzed as described in detail in Step 31.

Production, purification and titration of AAVP particles

19| AAVP particles can be amplified either by growing MC1061 colonies (option A) or by infecting and growing K91Kan cells (option B). Following amplification, AAVP particles are isolated and purified from the culture supernatant following a modified phage purification protocol[30,32] by using the steps given below. It is important to note that option A is faster because *E. coli* MC1061 can be used to generate AAVP constructs. This strategy offers the advantage to directly grow positive clones to produce phage particles and to skip the infection step needed for option B. However, *E. coli* K91Kan (option B) are pilus-positive F[+] bacteria and can therefore be infected by the newly produced phage particles during the overnight growth; this phenomenon will result in higher titers compared to MC1061 (option A), which are F^{−} bacteria.

(A) Growth of MC1061 colonies
(i) Amplify AAVP particles directly by growing the MC1061 colonies in LB plus tetracycline overnight at 37 °C.

(B) Infection and growth of K91Kan cells
(i) Incubate 1 ml of growing K91Kan *E. coli* bacteria with 10^{10} TU of AAVP for 1 h at room temperature in TB medium. Then, grow in 500 ml at 37 °C in the presence of tetracycline and kanamycin.

20| After overnight growth, centrifuge cultures at 6,000*g* for 20 min at 4 °C and collect the supernatant. Repeat centrifugation to remove residual bacterial debris.

21| Add PEG/NaCl (15% of the supernatant volume) solution to the supernatant to precipitate the AAVP phage particles. Incubate for 2 h on ice.

22| Centrifuge suspension at 10,000*g* for 30 min at 4 °C. A white pellet should be obtained. Discard the supernatant and centrifuge again for 10 min. Carefully decant the supernatant.

23| Resuspend the AAVP pellet in 10 ml of sterile PBS with agitation at 37°C for 30 min.

24| Repeat the precipitation with PEG/NaCl (15% of the supernatant volume) solution for 30 min on ice. Then, centrifuge at 14,000*g* for 30 min at 4 °C and resuspend in an adequate volume of PBS depending on the size of the pellet.

25| Transfer the solution to an Eppendorf tube, centrifuge at ∼13,000*g* for 10 min at room temperature, transfer to a new tube and recentrifuge to remove residual bacteria and debris.

26| Filter the resulting supernatant containing the AAVP particles in suspension through a 0.45-μm filter. Then, titrate by infection of K91Kan bacteria for 20 min at room temperature and plaque assay according to the standard protocols[30,32]. The AAVP titers are expressed as bacterial TUs per μl. Also, one must keep in mind that bacterial TU and multiplicity of infection are entirely different entities and should not be confused with one another.
▲ **CRITICAL STEP** *E. coli* K91Kan bacteria infection for more than 20 min might generate higher titers due to the newly produced AAVP particles. When comparing two different construct versions of AAVP for transduction efficiency, it is recommended to titrate the preparations side by side to ensure that same doses are compared. Indeed, the titers may vary from one AAVP version to another, depending on the ligand used, the size of the transgene of interest and size of the AAV mammalian cassette. These parameters can affect the coating of the virus in host bacteria during production. Viability of bacteria also plays a role, and it is recommended to infect a log-phase growing bacteria with an optical density ranging between 1.6 and 2.0 at a wavelength of 600 nm (OD_{600}).
■ **PAUSE POINT** AAVP titers are relatively stable and the preparations can be stored at 4 °C for long periods of time (several months) without any significant decrease in the titers. For longer storage times, one should check the titer of the preparation before use.
? TROUBLESHOOTING

Transduction of mammalian cells in culture by targeted AAVP vector and specific inhibition by using synthetic peptides—day 1: cell seeding

27| To transduce mammalian cells by targeted AAVP, it is recommended to incubate at least 10^6 AAVP TUs per cell. Transduction can be performed in any tissue culture dish or flask; however, as an initial experiment to confirm transduction of mammalian cells, it is recommended to work with a 24-well plate to avoid the use of large amounts of AAVP. Therefore, seed 4×10^4 cells in each well of the 24-well plate in a final volume of 0.5 ml of complete medium. Incubate overnight at 37 °C.

▲ **CRITICAL STEP** Factors such as concentration of cells in the edge of the well can affect the efficiency of transduction. Therefore, after seeding, observe the cells under the microscope to determine whether the cells are concentrated in the edge. Then to solve this problem, gently tilt or rock the plates to move the cells from the edge, until they are homogeneously distributed.

28| Analyze the efficiency of transduction of the cell line *in vitro* for each targeted AAVP. This can be carried out using a *GFP* reporter gene, as well as other reporter genes (e.g., *luciferase*, β-*galactosidase*). The *thymidine kinase* of herpes simplex virus type I (*HSV1-tk*) can also be used as a reporter gene[37,38]. Note that transduction with AAVP particles is an approach different from transfection using a naked plasmid containing a reporter cassette. Transfection with naked plasmid DNA is a general, nonspecific strategy aimed at introducing naked DNA into cells, with transgene expression starting after a few hours. However, transduction with a targeted AAVP virus is designed to transduce a specific cell line expressing a specific receptor. It is a process that occurs via a ligand-directed mechanism by binding of the targeting ligand displayed on AAVP virus to its specific receptor on the cell surface. Escape of AAVP from endosomes, the uncoating of the virus and conversion of single- to double-stranded DNA (transcriptionally active) do take time. This causes a delayed initiation of transgene expression from AAVP, starting at day 3 and peaking 7–10 days later. Thus, plasmid transfection and transduction with AAVP are two distinct strategies with different experimental aims. The choice of the cell line will depend on the ligand used and expression of the corresponding receptor on the cell surface. Thus, efficiency of transduction will vary from one cell line to another. For example, HEK293 cells or KS1767 Kaposi sarcoma cells highly express αv-integrin receptors[1,27] and are suitable cell lines to use for transduction by AAVP displaying the αv integrin-binding peptides.

Day 2: targeted AAVP infection

29| When cells are 50–60% confluent, they are ready for infection. Incubate the cells with the AAVP vectors at 10^6 TU per cell in a 0.2 ml total volume of tissue culture medium without serum at 37 °C for 4 h. Manually tilt after 30 min, then continue to gently tilt every 15 min, during incubation.

▲ **CRITICAL STEP** Incubation in the presence of serum markedly decreases the transduction efficiency of RGD-4C-targeted AAVP vector. Serum-mediated decrease of transduction efficiency has already been reported for other gene delivery vectors such as adenoviral vectors or liposomes and for plasmid transfection procedures such as lipofection[39,40]. Moreover, groups that used RGD-targeted adenoviral vectors reported infection of cells *in vitro* in the absence of serum[41]. We have not tested AAVP displaying other ligands.

30| After 4 h of transduction, add 0.3 ml of 10% serum-supplemented medium to each well to have a final volume of 0.5 ml. Incubate the cells at 37 °C and renew the medium every 2 days.
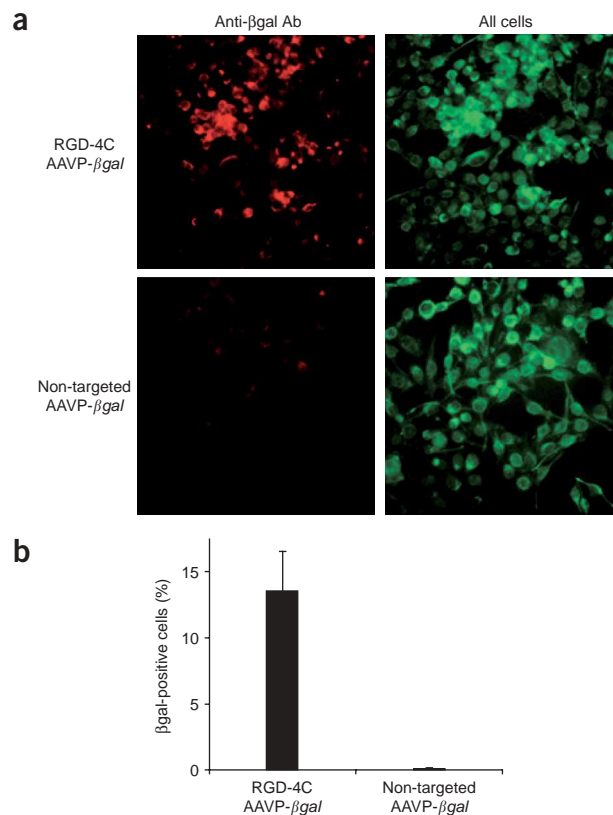
Figure 2 | *In vitro* mammalian cell transduction with targeted AAVP particles. (**a**) MDA-MB-435 breast tumor cells[27,29] were incubated with either targeted RGD-4C AAVP-β*gal* displaying the αv-integrin binding cyclic CDCRGDCFC peptide (termed RGD-4C)[31] or non-targeted AAVP-β*gal* as a control. β*gal* expression was evaluated by using an anti-β*gal* antibody (Sigma). The left panel shows only Texas red-positive cells; the right panel shows the total number of cells in identical fields (green fluorescence). (**b**) Quantitative analysis of cell transduction by targeted or control AAVP. AAVP vectors were incubated with tumor cells as described above. An anti-β*gal* antibody was used for staining; gene expression was detected by immunofluorescence and results are expressed as percentage of β*gal*-positive cells. In each case, s.e.m. was calculated after counting ten fields under the microscope in three independent experiments.

BOX 1 | RESCUE OF rAAV FROM AAVP-TRANSDUCED CELLS

This step is performed to verify the integrity of AAVITRs and their functional ability to rescue a rAAV.

Four days after AAVP transduction, transduced cells are transfected with 170 ng of the rep/cap encoding plasmid pXX2[43] or 500 ng of pDsRed2 (Clontech) as a transfection plasmid control. The cells are then superinfected with wild-type adenovirus at an MOI of 10. Seven days after the initial AAVP transduction, the cells are harvested, freeze/thawed and the adenovirus heat-inactivated by treatment at 50 °C for 20 min. The supernatants containing the rescued rAAV are then used to infect new cells

BOX 2 | TRANSGENE EXPRESSION AND THERAPEUTIC EFFICACY OF AAVP IN MOUSE MODELS *IN VIVO* AFTER SYSTEMIC ADMINISTRATION

A series of increasing vector doses should be tested, starting at 10^{10} TU per administration until a maximum expression of the transgene in the target tissue is obtained. Transfer the AAVP dose to be administered per mouse into a new tube and adjust to $\sim$0.2 ml with PBS. Use a U-100 28 G1/2 insulin syringe to inject a total of 0.2 ml into the tail vein. To perform this, one may choose to anesthetize the mice with Avertin[27, 44] via intraperitoneal injection and warm the tail of the mouse before intravenous injection

Perform a real-time transgene expression analysis, for each AAVP dose level, at different time point after vector administration starting at day 3. When targeting tumor tissue, it is important to avoid large necrotic tumor as this will cause nonspecific AAVP particle trapping. In tumor transduction experiments, cohorts of mice with size-matched tumors are treated. To analyze the efficiency of gene expression by targeted AAVP *in vivo*, it is recommended to start with reporter genes and use more than one (e.g., *GFP, β-galactosidase, luciferase, HSV1-tk*) (see **Box 3**) Specificity of *in vivo* transduction can be assessed using synthetic targeting peptides that are able to block transduction. Therefore, animals are first intravenously injected with the peptides 15 min before AAVP administration. Negative control peptides can be either scrambled or mutated versions of the targeting peptide

The BLI of luciferase experiments will determine the adequate targeted AAVP dose per animal. Therefore, when assessing the therapeutic efficacy of targeted AAVP bearing a therapeutic gene in tumor-bearing mice, the dose of targeted AAVP that results in the maximum of transgene expression in the tumor tissue, without toxicity, should be administered. Monitor tumor growth daily. In the case of using *HSV1-tk/* ganciclovir (GCV) "suicide gene therapy," treatment with GCV should be initiated at a time point that corresponds to a maximum level of gene expression in the target tissue *in vivo*, and should be administered intraperitoneally at 80 mg kg^{-1} day^{-1}

31| Analyze the cells for transgene expression at 48–72 h after transduction. A number of options are available for this, depending on which reporter gene system is used: for example, GFP (option A), β-galactosidase (option B) or luciferase (option C). Maximum levels of gene expression are usually reached by 7–10 days (**Fig. 2**). At this stage, as we previously reported[1], the transduced cells can be used to perform rescue experiments to verify the ITR structure integrity and functional ability to rescue rAAV particles from transduced cells (see **Box 1**).

(A) GFP detection
   (i) For GFP detection, analyze the cells by FACS or count cells by using a standard fluorescence microscope.

(B) Detection of β-galactosidase expression
   (i) Detection of β-galactosidase expression can be performed by X-gal staining[42]. β-Gal activity in cell lysates can also be detected by the Galacto-Star chemiluminescent reporter gene system (Tropix).

(C) Detection of Luciferase expression
   (i) Detect luciferase expression *in vitro* by incubating the cells with the D-luciferin substrate. Aspirate the medium from the cultured cells and add D-luciferin (150 µg ml^{-1} final). Monitor expression with a luminometer, a scintillation counter or a BLI system.

32| After maximum gene expression is obtained, split the transduced cells.
▲ **CRITICAL STEP** Splitting the cells before maximum gene expression is achieved and transferring them into a larger tissue culture dish will stimulate cells to divide and cause dilution of transduced cells within a large background population of non-transduced cells. To circumvent this problem, use a specific selection genetic marker to allow selection of only transduced cells.

33| To determine whether the AAVP particle is transfecting via the correct receptor, carry out a peptide inhibition experiment. For peptide inhibition experiments, seed the cells at 4×10^4 cells per well as in Step 27 and incubate with either 1 mg ml^{-1} of

BOX 3 | DETECTION OF TRANSGENE EXPRESSION *IN VIVO* AFTER SYSTEMIC ADMINISTRATION OF AAVP

To detect transgene expression *in vivo*, a number of options are available depending on which reporter gene system is used. For example:
1. To detect β-galactosidase expression, surgically harvest the tumors or other target tissues from mice under deep anesthesia. β-galactosidase expression is detected in tissue sections by an anti-β-galactosidase antibody and a peroxidase-based immunodetection kit (Vector Labs). For *in vivo* experiments involving tissue extracts, β-galactosidase activity in the tissues is detected by a chemiluminescent assay system (Tropix)
2. To detect GFP expression, anesthetized mice are first systemically perfused with PBS containing 4% paraformaldehyde. Tissues are harvested and processed for GFP immunostaining as previously described[1] (**Fig. 3a**)
3. Luciferase expression can be monitored directly *in vivo* in living mice by BLI (**Fig. 3b**). Each mouse is injected intraperitoneally with a D-luciferin solution (150 mg kg^{-1} in PBS) 10 min before imaging. Luciferase expression can also be confirmed by directly imaging the excised-target tissues
4. Detection of *HSV1-tk* transgene expression by PET-based imaging is detailed in the companion manuscript[45]

the specific targeting or control peptides for 30 min at 37 °C. After 30 min, wash the cells and add 10^6 TU of AAVP per cell for 4 h in serum-free medium as in Step 29. After incubation, add medium supplemented with 10% FCS. Negative control peptide (scrambled and/or mutant sequence) versions of the targeting peptide can be included. Cells are analyzed for transgene expression similar to conventionally transduced mammalian cells (Step 31).

In vivo transduction of target tissues by AAVP vector after systemic administration

34| Analysis of transgene expression *in vivo* was optimized for AAVP targeting systemic gene delivery to murine and human tumors established in mice, but can be applied to target normal tissues or perhaps other pathologically affected tissues. It is important to determine the suitable targeted AAVP dose to be administered to the animal to achieve an efficient and specific transgene expression within the target tissue. Indeed, each target tissue may require a different dose to achieve transduction and transgene expression *in vivo*, depending on the level of expression of the targeted receptor, the ligand used and promoter activity in the tissue. Thus, it is recommended to test different doses and analyze transgene expression over a time course to determine initiation and maximal expression (see **Boxes 2** and **3**).

? TROUBLESHOOTING

? TROUBLESHOOTING
Troubleshooting advice can be found in **Table 2**.

Figure 3 | *In vivo* transduction and molecular-genetic imaging of tumors in mice after systemic delivery of targeted AAVP. Targeted RGD-4C AAVP vectors or controls are intravenously administered to tumor-bearing mice. (**a**) Immunofluoresence analysis of GFP expression in tumors at 1 week after intravenous administration of RGD-4C AAVP-*GFP* or control non-targeted AAVP-*GFP*. (**b**) BLI of luciferase expression in living mice at 1 week after intravenous delivery of RGD-4C AAVP-*Luc* carrying the gene for firefly luciferase or AAVP control (non-targeted AAVP) or AAVP control (displaying CDCGFDCRC, a scrambled RGD-4C version).

TABLE 2 | Troubleshooting table.

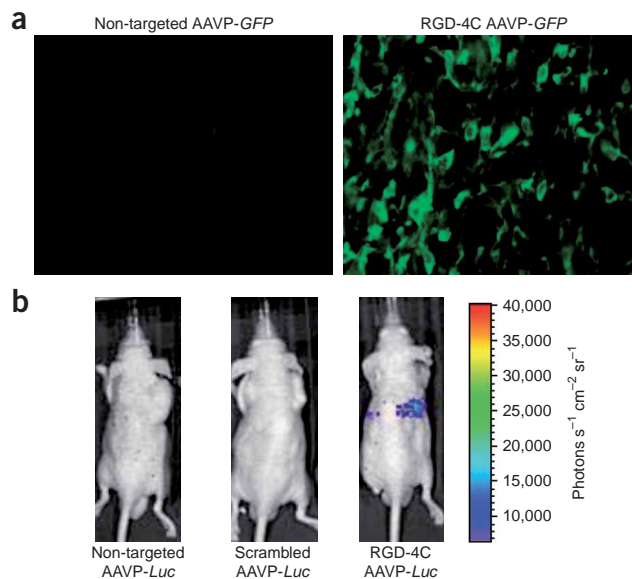| Step	Problem	Solution
Genetic modifications		
5	*Sfi*I digestion generates strong star activity in the phage DNA	Use as few units of *Sfi*I as possible to get a complete digestion. This avoids overdigestion and reduces the final glycerol concentration in the reaction
14	Low efficiency of ligation is caused by autoligation of the vector or by non-digested plasmids	Analyze the complete digestion of the vector by agarose gel. Dephosphorylate and use as little as possible of the vector plasmid
15	Excess of linkers ligate to the vector	Excess linkers are best removed by agarose gel electrophoresis and subsequent gel extraction and purification. Avoid a spinning column
Particle production and purification		
26	Low titers of AAVP preparations	Check bacterial viability. Repeat infection of 1 ml of K91Kan *E. coli* bacteria with the new AAVP preparation for 1 h (10 µl at least). Then grow in 500 ml for up to 16 h
Targeted gene expression		
Boxes 2 and 3	Efficiency of transduction is dependent on the expression of the receptor within the target tissue and its accessibility	Whenever possible, one can increase the expression of the target cell surface receptor by biochemical or genetic methods
		Use the AAVP dose that achieves maximum level of transgene expression in the tumors
	Efficacy of therapy can be heterogeneous from one experiment to another or among different individuals	Use size-matched tumors and at least seven animals per group. When using HSV1-tk/GCV therapy, GCV efficiency is not only dependent on HSV1-tk transgene expression, but also on the rate of tumor growth

ANTICIPATED RESULTS

The protocols described here should result in successful cloning and application of AAVP-based vectors. AAVP preparations of $1-5 \times 10^{10}$ TU μl^{-1} are routinely obtained and are consistent with the titers generated with the parental targeted phage. This shows that insertion of a mammalian transgene cassette in the bacteriophage genome does not affect vector production in bacteria. Transgene expression in cells in culture starts at 48–72 h after incubation with the targeted AAVP vector and reaches maximum levels by days 7–10 (**Fig. 2**). *In vivo*, transgene expression is detectable in target tissues at day 3 after intravenous delivery of targeted AAVP vectors, then it increases gradually until days 7–10 (**Fig. 3**). We previously followed transgene expression until day 10 post-AAVP administration[1]; if required, further reporter detection may be accomplished. For long-term detection of transgene expression, real-time RT-PCR may be used. In recent work (unpublished observation), we have followed transgene expression using BLI of luciferase in a tumor model for 5–6 weeks. Transgene expression started at day 3 after vector delivery and was still detectable at adequate levels upon experiment termination due to tumor burden.

1. Hajitou, A. *et al.* A hybrid vector for ligand-directed tumor targeting and molecular imaging. *Cell* **125**, 385–398 (2006).
2. Watkins, S.J., Mesyanzhinov, V.V., Kurochkina, L.P. & Hawkins, R.E. The 'adenobody' approach to viral targeting: specific and enhanced adenoviral gene delivery. *Gene Ther.* **4**, 1004–1012 (1997).
3. Wickham, T.J. *et al.* Targeted adenovirus-mediated gene delivery to T cells via CD3. *J. Virol.* **71**, 7663–7669 (1997).
4. Miller, C.R. *et al.* Differential susceptibility of primary and established human glioma cells to adenovirus infection: targeting via the epidermal growth factor receptor achieves fiber receptor-independent gene transfer. *Cancer Res.* **58**, 5738–5748 (1998).
5. Martin, F. *et al.* Retrovirus targeting by tropism restriction to melanoma cells. *J. Virol.* **73**, 6923–6929 (1999).
6. Girod, A. *et al.* Genetic capsid modifications allow efficient re-targeting of adeno-associated virus type 2. *Nat. Med.* **5**, 1052–1056 (1999).
7. Vigne, E. *et al.* RGD inclusion in the hexon monomer provides adenovirus type 5-based vectors with a fiber knob-independent pathway for infection. *J. Virol.* **73**, 5156–5161 (1999).
8. Reynolds, P.N. *et al.* A targetable injectable adenoviral vector for selective gene delivery to pulmonary endothelium *in vivo*. *Mol. Ther.* **2**, 562–578 (2000).
9. Wickham, T.J. Targeting adenovirus. *Gene Ther.* **7**, 110–114 (2000).
10. Trepel, M., Grifman, M., Weitzman, M.D. & Pasqualini, R. Molecular adaptors for vascular-targeted adenoviral gene delivery. *Hum. Gene Ther.* **11**, 1971–1981 (2000).
11. Trepel, M., Arap, W. & Pasqualini, R. Exploring vascular heterogeneity for gene therapy targeting. *Gene Ther.* **7**, 2059–2060 (2000).
12. Müller, O.J. *et al.* Random peptide libraries displayed on adeno-associated virus to select for targeted gene therapy vectors. *Nat. Biotechnol.* **21**, 1040–1046 (2003).
13. Lieber, A. AAV display-homing in on the target. *Nat. Biotechnol.* **21**, 1011–1013 (2003).
14. Barrow, P.A. & Soothill, J.S. Bacteriophage therapy and prophylaxis: rediscovery and renewed assessment of potential. *Trends Microbiol.* **5**, 268–271 (1997).
15. Barbas III, C.F., Burton, D.R., Scott, J.K. & Silverman, G.J. *Phage Display: A Laboratory Manual* (Cold Spring Harbor Press, Cold Spring Harbor, NY, 2001).
16. Ivanenkov, V.V., Felici, F. & Menon, A.G. Targeted delivery of multivalent phage display vectors into mammalian cells. *Biochim. Biophys. Acta* **1448**, 463–472 (1999).
17. Larocca, D. *et al.* Gene transfer to mammalian cells using genetically targeted filamentous bacteriophage. *FASEB J.* **13**, 727–734 (1999).
18. Poul, M.A. & Marks, J.D. Targeted gene delivery to mammalian cells by filamentous bacteriophage. *J. Mol. Biol.* **288**, 203–211 (1999).
19. Sergeeva, A., Kolonin, M.G., Molldrem, J.J., Pasqualini, R. & Arap, W. Display technologies: application for the discovery of drug and gene delivery agents. *Adv. Drug Deliv. Rev.* **58**, 1622–1654 (2006).
20. Monaci, P., Urbanelli, L. & Fontana, L. Phage as gene delivery vectors. *Curr. Opin. Mol. Ther.* **3**, 159–169 (2001).
21. http://www.cfsan.fda.gov/~dms/opabacqa.html.
22. Arap, W. *et al.* Steps toward mapping the human vasculature by phage display. *Nat. Med.* **8**, 121–127 (2002).
23. Pentz, R.D. *et al.* Ethics guidelines for research with the recently dead. *Nat. Med.* **11**, 1145–1149 (2005).
24. Krag, D.N. *et al.* Selection of tumor-binding ligands in cancer patients with phage display libraries. *Cancer Res.* **66**, 7724–7733 (2006).
25. Koivunen, E. *et al.* Tumor targeting with a selective gelatinase inhibitor. *Nat. Biotechnol.* **17**, 768–774 (1999).
26. Pasqualini, R., Koivunen, E. & Ruoslahti, E. αv integrins as receptors for tumor targeting by circulating ligands. *Nat. Biotechnol.* **15**, 542–546 (1997).
27. Arap, W., Pasqualini, R. & Ruoslahti, E. Cancer treatment by targeted drug delivery to tumor vasculature in a mouse model. *Science* **279**, 377–380 (1998).
28. Kolonin, MG, Saha, PK, Chan, L, Pasqualini, R & Arap, W. Reversal of obesity by targeted ablation of adipose tissue. *Nat. Med.* **10**, 625–632 (2004).
29. Ellerby, H.M. *et al.* Anti-cancer activity of targeted pro-apoptotic peptides. *Nat. Med.* **5**, 1032–1038 (1999).
30. Pasqualini, R., Arap, W., Rajotte, D. & Ruoslahti, E. *In vivo* phage display. in *Phage Display: A Laboratory Manual* (eds. Barbas III, C.F., Burton, D.R., Scott, J.K. & Silverman, G.J.) Ch. 22, 1–24 (Cold Spring Harbor Laboratory Press, Cold Spring Harbor, NY, 2000).
31. Koivunen, E., Wang, B. & Ruoslahti, E. Phage libraries displaying cyclic peptides with different ring sizes: ligand specificities of the RGD-directed integrins. *BioTechnology* **3**, 265–270 (1995).
32. Smith, G.P. & Scott, J.K. Libraries of peptides and proteins displayed on filamentous phage. *Meth. Enzymol.* **217**, 228–257 (1993).
33. Parmely, S.F. & Smith, G.P. Antibody-selectable filamentous fd phage vectors: affinity purification of target genes. *Gene* **73**, 305–318 (1988).
34. Rajotte, D. *et al.* Molecular heterogeneity of the vascular endothelium revealed by *in vivo* phage display. *J. Clin. Invest.* **102**, 430–437 (1998).
35. Rajotte, D. & Ruoslahti, E. Membrane dipeptidase is the receptor for a lung-targeting peptide identified by *in vivo* phage display. *J. Biol. Chem.* **274**, 11593–11598 (1999).
36. http://www.biosci.missouri.edu/smithGP/PhageDisplayWebsite/PhageDisplayWebsiteIndex.html.
37. Tjuvajev, J.G. *et al.* Imaging herpes virus thymidine kinase gene transfer and expression by positron emission tomography. *Cancer Res.* **58**, 4333–4341 (1998).
38. Tjuvajev, J.G. *et al.* Imaging adenoviral-mediated herpes virus thymidine kinase gene transfer and expression *in vivo*. *Cancer Res.* **59**, 5186–5193 (1999).
39. Serikawa, T., Kikuchi, A., Sugaya, S., Suzuki, N., Kikuchi, H. & Tanaka, K. *In vitro* and *in vivo* evaluation of novel cationic liposomes utilized for cancer gene therapy. *J. Control Rel.* **113**, 255–260 (2006).
40. Abe, A., Miyanohara, A. & Friedmann, T. Polybrene increases the efficiency of gene transfer by lipofection. *Gene Ther.* **5**, 708–711 (1998).
41. Okada, Y., Okada, N., Mizuguchi, H., Hayakawa, T., Nakagawa, S. & Mayumi, T. Transcriptional targeting of RGD fiber-mutant adenovirus vectors can improve the safety of suicide gene therapy for murine melanoma. *Cancer Gene Ther.* **12**, 72–83 (2005).
42. Arap, M. *et al.* Model of unidirectional transluminal gene transfer. *Mol. Ther.* **9**, 305–310 (2004).
43. Xiao, X., Li, J. & Samulski, R.J. Production of high-titer recombinant adeno-associated virus vectors in the absence of helper adenovirus. *J. Virol.* **72**, 2224–2232 (1998).
44. Papaioannou, V.E. & Fox, J.G. Efficacy of tribromoethanol anesthesia in mice. *Lab. Anim. Sci.* **43**, 189–192 (1993).
45. Soghomonyan, S. *et al.* Molecular PET imaging of HSV1-tk reporter gene expression by using ^{18}F-FEAU. *Nat. Protoc.* doi: 10.1038/nprot.2007.49 (2007).

The Original Pathologische Anatomie Leiden-Endothelium Monoclonal Antibody Recognizes a Vascular Endothelial Growth Factor–Binding Site within Neuropilin-1

Diana E. Jaalouk,[1] Michael G. Ozawa,[1] Jessica Sun,[1] Johanna Lahdenranta,[1] Reinier O. Schlingemann,[2] Renata Pasqualini,[1] and Wadih Arap[1]

[1]The University of Texas M. D. Anderson Cancer Center, Houston, Texas and [2]Academic Medical Center, University of Amsterdam, Amsterdam, the Netherlands

Abstract

For two decades, the antigen recognized by the Pathologische Anatomie Leiden-Endothelium (PAL-E) monoclonal antibody, a standard vascular endothelial cell marker, has remained elusive. Here, we used a combinatorial phage display–based approach ("epitope mapping") to select peptides binding to the original PAL-E antibody. We found that a subset of the selected panel of peptides had motifs with strong homology to an exposed site within the b1 domain of human neuropilin-1 (NRP-1). We confirmed peptide binding by ELISA and by surface plasmon resonance. We also showed that the PAL-E antigen colocalizes with NRP-1 staining in endothelial cells. Crystal structure of the b1 domain in NRP-1 suggests that the PAL-E binding site overlaps with a vascular endothelial growth factor (VEGF) binding site. Taken together, these results indicate that NRP-1 is an endothelial cell antigen recognized by the true PAL-E antibody. The consistent biochemical, morphologic, and functional features between the PAL-E antigen and NRP-1 support our interpretation. Given that NRP-1 is a VEGF receptor, these results explain the attributes of the PAL-E antibody as a marker of vascular permeability and angiogenesis. [Cancer Res 2007;67(20):9623–9]

Introduction

The Pathologische Anatomie Leiden-Endothelium (PAL-E) antibody, generated over 20 years ago by injection of human melanoma lymph node metastasis into mice, has since been used as a vascular endothelial cell marker. PAL-E recognizes vascular endothelial cells lining blood capillaries, venules, and small-to-medium sized veins in human frozen tissue sections. On the other hand, it reacts only weakly (if at all) with endothelium of arterioles, arteries, and large veins and does not recognize lymphatic endothelium. Because of these attributes, the PAL-E antibody has become useful (*a*) for delineating phenotypic differences between distinct vascular beds, (*b*) for understanding the endothelial molecular diversity in diseases with an angiogenic component—such as cancer, proliferative retinopathy, or rheumatoid arthritis; and (*c*) for ruling out the predominance of lymphatic endothelium (1, 2).

Indeed, because the PAL-E antibody shows high reactivity to venules in lymph nodes and to tumor blood vessels, it has been extensively used for histopathologic analysis of the endothelium lining tumor vasculature in several premalignant and malignant conditions, including carcinomas and sarcomas (3–5). Moreover, the PAL-E antibody has long served to study the new blood vessel formation that occurs during tumor metastasis and wound healing (6). Notably, unlike endothelial cells in normal brain (with an intact blood-brain barrier), the endothelium in primary malignant gliomas and in secondary brain metastases stain positively with PAL-E, indicating that its reactivity may somehow relate to the altered vascular permeability state observed in angiogenesis (7).

Further insight into the functional relevance of endothelial cell staining by PAL-E antibody was gained by immunoelectron microscopy studies that showed that the PAL-E antibody stains the luminal endothelial surface in a local pattern and is mostly associated with endothelial pinocytotic plasmalemmal vesicles (6, 8). Given that such vesicles (also termed caveolae) function in trans-cellular transport, they are scarce in endothelium, separating blood from intact "sanctuary" tissue sites, such as the blood-brain or the blood-retinal barrier. Thus, studies on the subcellular localization of PAL-E staining have again suggested a role for PAL-E antigen in general trans-endothelial transport and vascular permeability in diverse pathologic conditions varying from inflammatory diseases to malignant tumors to organ transplantation rejection (9–11).

The widespread application of the PAL-E antibody as a marker of vascular endothelium has led to efforts in identifying its corresponding antigen(s); unfortunately, the identification of the elusive "PAL-E antigen" has proved challenging for the past two decades, largely because this unique monoclonal antibody can only be used under a relatively limited set of experimental conditions.

Recently, Xu et al. (12) have attempted to fulfill this objective by combining protein purification to tandem mass spectrometry analysis of tryptic peptides. Although these investigators proposed a secreted isoform of vimentin as a candidate antigen recognized (by invoking the presence of a new so-called "PAL-E–reactive vimentin"), they have actually used and reported (12) on a different isotype from the original PAL-E monoclonal antibody (1).

On the other hand, Niemelä et al. (13) have shown that the plasmalemmal vesicle 1/fenestrated endothelial-linked structure (PV-1/FELS) protein is the antigen recognized by 174/2, a monoclonal antibody generated by immunizing BALB/c mice with vessels from human lymph nodes and fusing lymphocytes with myeloma cells. Next, based on immunostaining and biochemical experiments, the authors have surmised that 174/2 acts as a "PAL-E–like" monoclonal antibody; as such, they have plausibly proposed PV-1/FELS as another PAL-E candidate antigen (13). However,

neither monoclonal antibody inhibits the other in competitive staining experiments (13), bringing such data interpretation into question.

As the identity of the PAL-E monoclonal antibody originally generated by Schlingemann et al. (1) evidently still remains elusive, we used an entirely different approach for the identification of the PAL-E antigen. By screening a phage display random peptide library on the true PAL-E monoclonal antibody, we selected and isolated PAL-E–binding peptides. We reasoned that such selected peptide motifs would mimic the antigenic binding site recognized by the antibody. Indeed, combinatorial epitope mapping of monoclonal antibodies has long served to reveal the identity of target antigens (14) and our group has even adapted this methodology to fingerprint the circulating pool of patient-derived antibodies (15, 16).

Here we show (*a*) that PAL-E–binding consensus peptide motifs reveal an exposed protein site in neuropilin-1 (NRP-1), (*b*) that the original PAL-E antibody binds to NRP-1 and colocalizes with NRP-1 staining in endothelial cells, and (*c*) that the PAL-E binding site within NRP-1 does overlap with a vascular endothelial growth factor (VEGF) binding site. Together, these data indicate that NRP-1 is an endothelial cell antigen recognized by the original PAL-E monoclonal antibody. Given that NRP-1 is a VEGF receptor, these results may explain the attributes of PAL-E as a marker of vascular permeability and angiogenesis.

Materials and Methods

Antibodies, recombinant proteins, and synthetic peptides. Schlingemann et al. (1) generated the original hybridoma corresponding to the monoclonal antibody PAL-E (an isotype IgG2a mouse clone) used throughout this study. A control mouse monoclonal antibody with the same isotype as PAL-E (mIgG2a) and monoclonal antibodies against NRP-1 and NRP-2 were purchased (DAKO and R&D Systems). Polyclonal antibodies against the synthetic cyclic peptide CTQYAMHLC were generated by serial immunization of rabbits with keyhole limpet hemocyanin (KLH)–conjugated peptide (17). Standard IgG purification from rabbit serum (preimmune and anti-CTQYAMHLC IgGs) was accomplished by using Protein A Sepharose Cl-4B resin (Amersham Biosciences). Recombinant NRP-1, NRP-2, semaphorin-3A (Sema3A), and VEGF-A$_{165}$ were commercially obtained (R&D Systems). Unless otherwise specified, all peptides were synthesized, cyclized, and purified at AnaSpec.

Cell culture. Human umbilical vascular endothelial cells (HUVEC) were from Clonetics and cultured in complete endothelial cell basal medium from Cambrex at 37°C in 5% CO$_2$. To minimize tissue culture drifting, only early passage cells (defined as passages 3 and 4) were used.

Selection of combinatorial peptide libraries on immobilized PAL-E. We used a phage display library with an insert displaying random peptides with the general cyclic arrangement CX$_7$C (C, cysteine; X, any amino acid residue). Increasing concentrations of PAL-E and control mIgG2a were immobilized in Protein A–coated strip 96-well plates (Pierce) at 4°C overnight. PBS containing 3% bovine serum albumin (BSA) was used for blocking at 37°C for 1 h. After two washing steps with PBS, 2 × 10^9 transducing units (TU) of CX$_7$C phage library were precleared on mIgG2a at room temperature for 1 h, then incubated with the original PAL-E monoclonal antibody (1) for 3 h after which unbound phage was discarded. After multiple washes in PBS, PAL-E–bound phage was rescued by infection with 200 μL of stationary-phase K91Kan *Escherichia coli* at room temperature for 1 h and then amplified by incubation in 20 mL Luria-Bertani (LB) broth supplemented with 0.2 μg/mL tetracycline and 100 μg/mL kanamycin at 37°C/shaker (225 rpm) for 1 h. Serial dilutions were then plated in triplicates on LB plates supplemented with tetracycline and kanamycin, then incubated at 37°C overnight. Colony counting was done the next day to determine the number of TU. Multiple rounds of panning were

done in a similar manner so that the phage population recovered from one round was used for the subsequent panning round and more stringent washing was applied as the panning progresses.

PCR and sequencing. Colonies from third round of panning on PAL-E antibody were transferred into 30 μL of double-distilled water containing 10% glycerol and stored at −20°C for PCR. PCR mix was prepared such that a 20 μL reaction sample included 2 μL bacteria preserved in double-distilled water containing 10% glycerol, 8 pmol of each of fUSE5 forward primer (5′-TAATACGACTCACTATAGGGCAAGCTGATAAACCGATACAATT-3′) and reverse primer (5′-CCCTCATAGTTAGCGTAACGATCT-3′), 1 μL of 2.5 mmol/L deoxynucleotide triphosphate mix (Promega), 2 μL of 10× Taq polymerase buffer (Promega), and 2.5 units of Taq DNA polymerase (Promega). PCR was done by using 94°C annealing for 3 min, followed by 30 cycles of 94°C for 10 s, 60°C for 30 s, and 72°C for 30 s that were followed by 72°C for 5 min. PCR products were verified by DNA sequencing.

Phage binding assays. PAL-E or mIgG2a were coated at 5 μg in 50 μL PBS per well in Protein A–precoated plates (Pierce) at 4°C overnight. Similarly, recombinant Sema3A or VEGF-A$_{165}$ were coated at 0.25 μg/well. PBS containing 3% BSA served for blocking at 37°C for 1 h followed by two tandem PBS washing steps. Control Fd-tet (insertless) phage or selected PAL-E–binding phage clones were added at 10^9 TU/well and incubated at room temperature for 3 h. After multiple wash steps with PBS, bound phage were recovered by infection in 200 μL of stationary-phase K91Kan *E. coli* at room temperature for 1 h and amplified by overnight culture in 20 mL LB supplemented by tetracycline and kanamycin. Serial dilutions were then plated in triplicates on LB plates supplemented by tetracycline and kanamycin and incubated at 37°C for colony counts overnight to determine the number of TU.

ELISA. Recombinant proteins and synthetic peptides were coated at 0.5 μg/well in 96-well plates (Maxi Sorp, Nunc) at 4°C overnight. PBS containing 3% BSA was used for blocking at room temperature for 1 h. Unless otherwise specified, primary antibody was added at 25 ng/μL in PBS containing 1% BSA and incubated for 2 h at room temperature. After three washing steps with PBS containing 1% BSA plus 0.05% Tween 20 (Sigma), and 100 μL/well of either 1:2,000 dilution of horseradish peroxidase (HRP)–conjugated rabbit anti-total mouse IgG (Zymed) or 1:4,000 dilution of HRP-conjugated goat anti-rabbit IgG (Zymed) prepared in PBS containing 1% BSA was incubated at room temperature for 1 h. Secondary antibody binding was followed by three washing steps as described above, then the signal was developed by using 100 μL/well of TMB soluble substrate (Calbiochem) that was incubated at room temperature while shaking at 75 rpm for 10 min. To stop the reaction, 50 μL of 0.5 N H$_2$SO$_4$ was used per well. Absorbance was determined at 450 nm (Power WaveX340; BIO-TEK Instruments).

Surface plasmon resonance. PAL-E antibody was captured at 5 μg/mL to an anti-mouse-Fc–coated CM5-chip (Biacore, Inc.) by injecting it for 15 min over the chip at 10 μL/min flow rate. Interactions were allowed to stabilize for 5 min then 10 μg/mL of NRP-1 or NRP-2 were captured to PAL-E for 15 min. After injection, dissociation was followed for 5 min. Chips were regenerated by 10 mmol/L glycine (pH 1.7) at 100 μL/min.

Cell staining. HUVEC cells were plated at 10^4 per well in a chamber slide (Lab-Tek II; Nalge Nunc International) in culture medium and allowed to adhere at 37°C, 5% CO$_2$ for 48 h. Cells were washed twice with PBS, then fixed and permeabilized with precooled acetone at −20°C for 10 min. After three PBS washing steps, 5% normal goat serum (NGS) was used for blocking at room temperature for 20 min. Then, 5 μg/250 μL 1% NGS of either mIgG2a or PAL-E were incubated at 4°C overnight. After washing with PBS, cells were incubated with 1:400 μL/well of Cy3-conjugated goat anti-mouse IgG (Jackson ImmunoResearch) at room temperature for 30 min. Vectashield Mounting Medium supplemented with 4′,6-diamidino-2-phenylindole (DAPI; Vector Labs, Inc.) was used for nuclear staining and to mount the slides with coverslips. Slides were then evaluated by using a fluorescent microscope and images were acquired at ×200 magnification with the Magna Fire IX70 software.

Statistical analysis. Results are expressed as the mean of three independent experiments ± SEM. Student's *t* test was used for generation of *P* values and determination of statistical significance.

Results

Combinatorial peptide selection on the original PAL-E monoclonal antibody. To identify peptides that bind to the variable fragment of the PAL-E monoclonal antibody, we used a CX_7C peptide library to profile the surface of PAL-E IgGs immobilized onto Protein A–coated wells via their Fc region. After the third round of serial selection (Fig. 1*A*), we observed marked phage binding to PAL-E compared with negative controls (91-fold relative to BSA and 16-fold relative to mIgG2a isotype control). We next did a comprehensive protein homology analysis of peptide sequences selected and isolated ($N = 85$) from the third round of panning on the PAL-E antibody (Supplementary Table S1). We identified the SQYSTNW motif spanning residues 295 to 301 in the b1 domain of NRP-1 as a strong match such that several PAL-E–binding phage clones share $\geq 50\%$ homology with this motif (Supplementary Table S2).

Next, to validate the selected peptide motifs, we evaluated the binding of three individual phage clones (displaying the inserts CSQYSFNWC, CTQYAMHLC, and CSQWNMLLC) to the immobilized PAL-E monoclonal antibody. In comparison with control insertless phage, all three selected phage clones showed marked binding to PAL-E antibody relative to BSA and mIgG2a (Fig. 1*B*). By arbitrarily setting the binding of the negative control (insertless
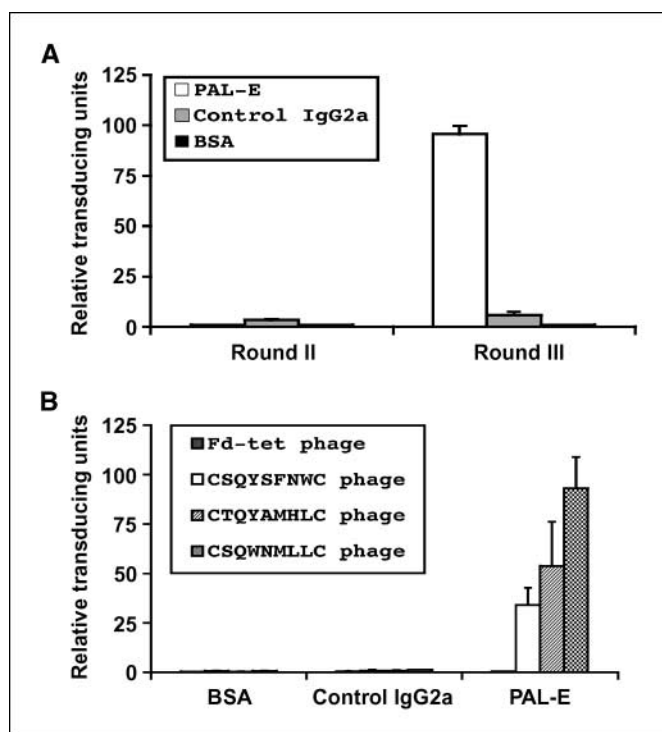
Figure 1. Phage panning on PAL-E antibody and matched sequence alignment. *A,* multiple rounds of panning on PAL-E antibody with CX_7C random phage library resulted in significant enrichment with 91-fold stronger phage binding to PAL-E compared with BSA control after round III. *B,* validation of PAL-E phage clones with NRP-1 sequence homology by phage binding assay ($n = 3$). Compared with Fd-tet insertless phage, all PAL-E phage clones showed strong and specific binding to PAL-E antibody compared with mouse IgG2a isotype or to BSA control. Phage clone with the cyclic insert sequence CSQWNMLLC exhibited the strongest binding to PAL-E antibody with $(93.2 \pm 15.7) \times 10^4$ TU, which is significantly higher compared with $(0.5 \pm 0.2) \times 10^4$ TU with Fd-tet control phage. *Columns,* average; *bars,* SEM ($P = 0.01$).
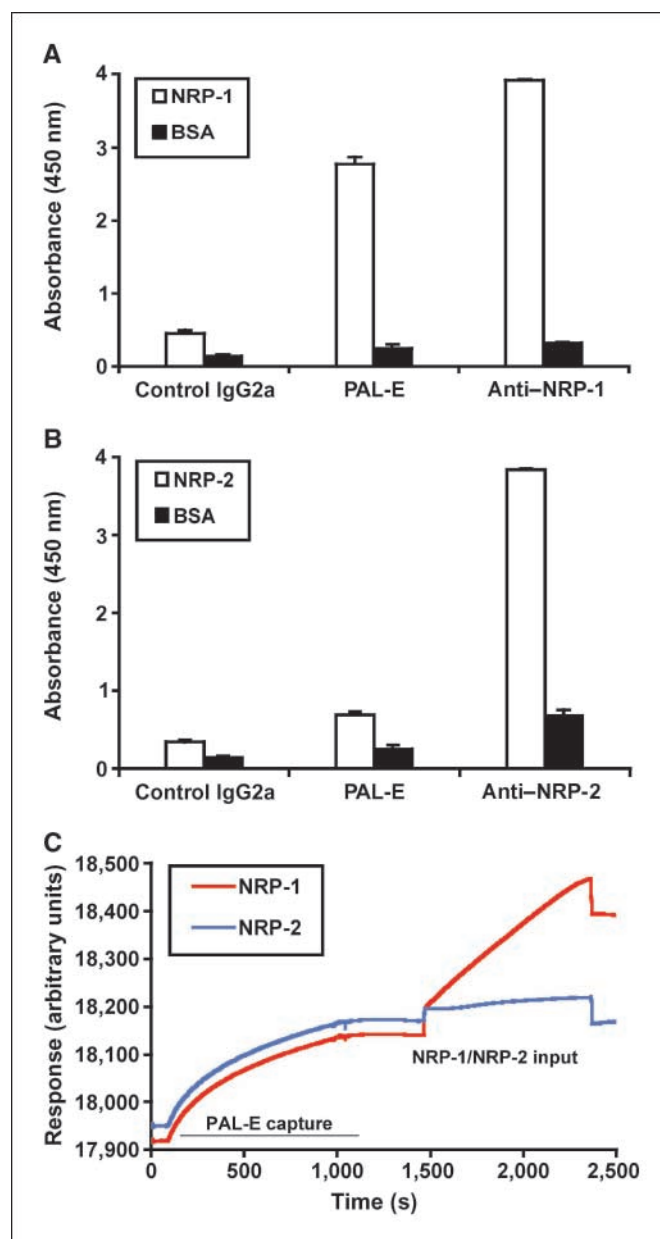
Figure 2. PAL-E antibody recognizes recombinant NRP-1. *A* and *B,* assessing the binding of PAL-E to recombinant NRP-1 to recombinant NRP-2 by ELISA ($n = 3$). Either recombinant protein was coated at 0.5 μg/well. PAL-E antibody, the IgG2a isotype control, anti–NRP-1, or anti–NRP-2 was assayed at 25 ng/μL. Compared with IgG2a, PAL-E reacted positively with both NRP-1 ($P = 0.002$) and NRP-2 ($P = 0.005$) with much higher absorbance measurements with NRP-1. *C,* assessing the binding of PAL-E to recombinant NRP-1 and NRP-2 by Biacore. PAL-E (5 μg/mL) was captured to an anti–mouse-Fc coated CM5-chip. NRP-1 and NRP-2 (10 μg/mL each) were captured to PAL-E. The results show strong binding of PAL-E antibody to NRP-1, whereas no significant binding to NRP-2 was detected.

phage) to PAL-E to one relative TU, CSQYSFNWC-displaying phage yielded 68 ± 18 relative TU, CTQYAMHLC-displaying phage yielded 108 ± 44 relative TU, and CSQWNMLLC-displaying phage yielded 186 ± 32 relative TU (all representing mean $\pm$ SEM). These results establish that peptide motifs with NRP-1 homology mediate binding to the PAL-E monoclonal antibody and suggest that PAL-E may recognize NRP-1.

PAL-E binds to NRP-1. We used ELISA to determine whether the PAL-E monoclonal antibody binds to recombinant NRP-1 *in vitro* (Fig. 2*A*). We also evaluated whether PAL-E binds to recombinant NRP-2, a related receptor that shares 44% identity with NRP-1 at the protein sequence level (Fig. 2*B*). Relative to negative control IgG2a, PAL-E reacted strongly against NRP-1 (A_{450} = 2.77 ± 0.09; t test, P = 0.002). Moreover, PAL-E showed a much weaker binding to NRP-2 (A_{450} = 0.69 ± 0.05; t test, P = 0.005). We next used surface plasmon resonance–based technology (Biacore) as a second independent biochemical method to confirm PAL-E binding to NRP-1. We again observed strong binding of the PAL-E antibody to NRP-1 (Fig. 2*C*). Consistently with our ELISA data showing much lower affinity of PAL-E for NRP-2,

no significant binding to NRP-2 was detected by surface plasmon resonance methodology.

PAL-E staining colocalizes with NRP-1. Furthermore, acetone-fixed HUVEC cells stained positively with PAL-E (Fig. 3*A*). Comparison of double staining in HUVEC cells shows that the fluorescence pattern resulting from PAL-E immunostaining colocalizes to a great extent with that resulting from immunostaining with a commercial anti–NRP-1 antibody, suggesting that PAL-E can also bind to cellular NRP-1 (Fig. 3*B*). Taken together, these data show that NRP-1 is an antigenic target for PAL-E antibody likely through direct recognition of the primary amino acid sequence comprising the SQYSTNW motif. Alternatively, PAL-E may recognize secondary or higher-order protein structure around this motif.
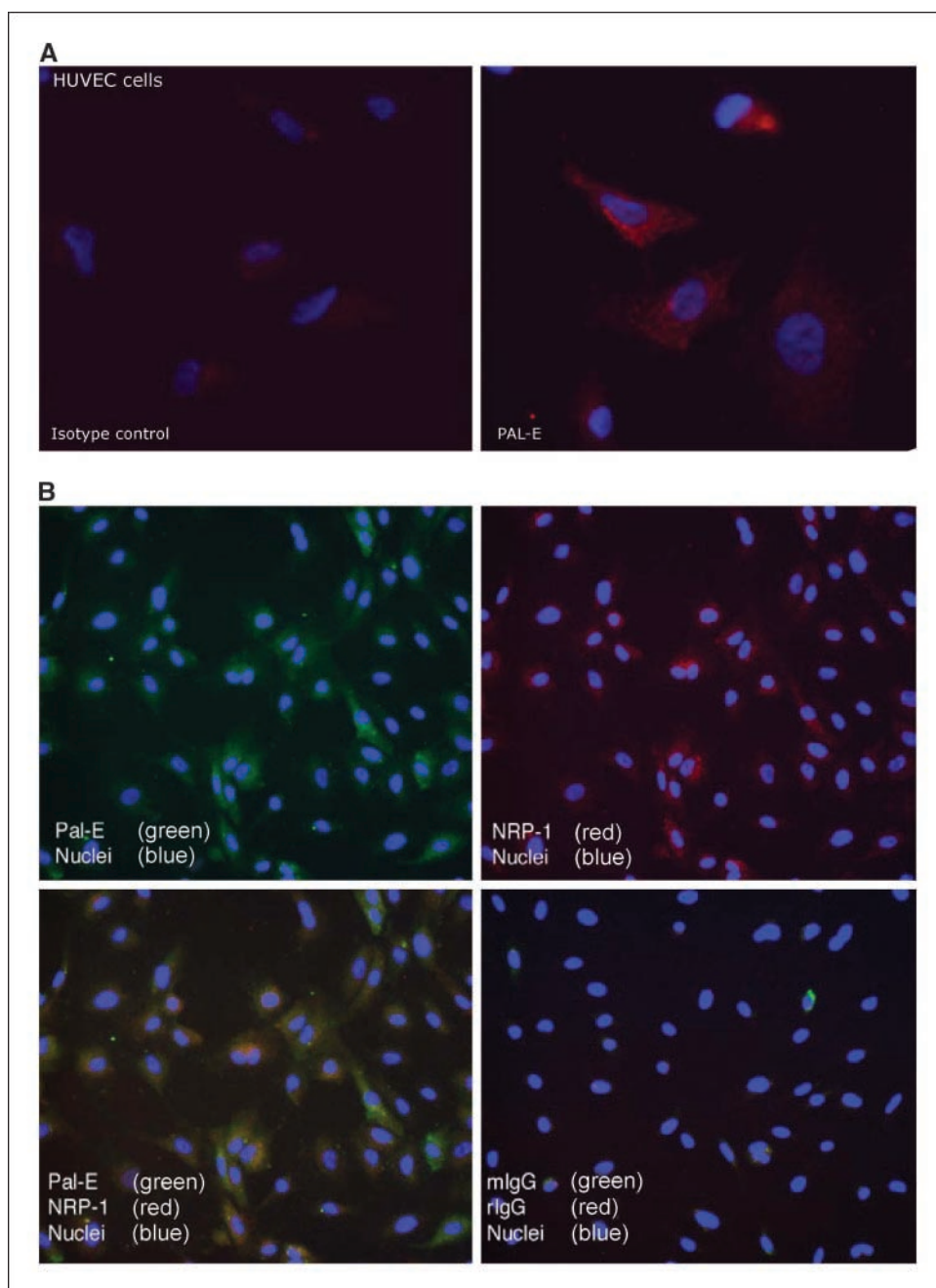
Figure 3. PAL-E stains NRP-1 in HUVEC cells. *A,* acetone-fixed HUVEC cells stain positively with PAL-E. *B,* immunofluorescence patterns indicate that PAL-E staining colocalizes with NRP-1 staining in HUVEC cells adherent in chamber slides. Goat anti–mouse-FITC or Cy3 was used as secondary antibody. Vectashield with DAPI was used for mounting and nuclear staining.
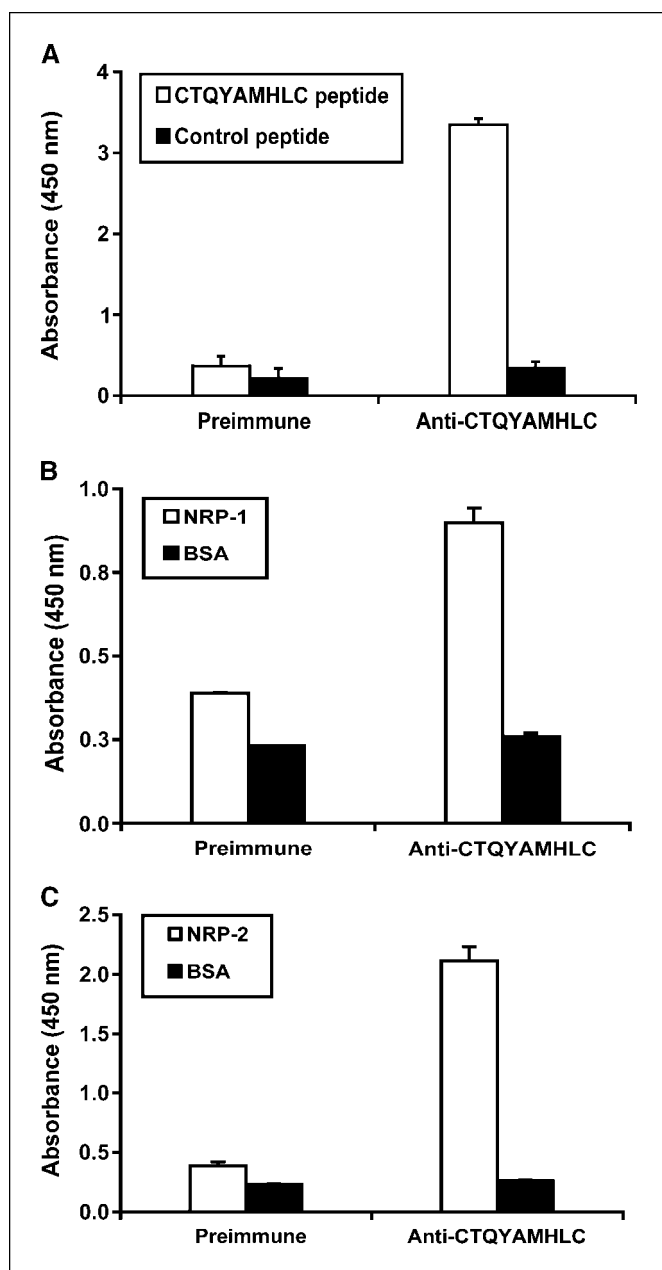
Figure 4. Identification of the PAL-E–binding epitope in NRP-1. *A,* rabbit anti-CTQYAMHLC sera strongly and specifically react with the corresponding cyclic peptide (*n* = 3). The unrelated CGSPGWVRC peptide was used as control. *B* and *C,* purified polyclonal anti-CTQYAMHLC IgGs bind to both recombinant NRP-1 (*P* = 0.004) and NRP-2 (*P* = 0.003) with stronger affinity to NRP-2. Either recombinant protein was coated at 0.1 μg/well. Preimmune and anti-CTQYAMHLC IgGs purified on Protein A Sepharose Cl-4B resin were assayed at 3 ng/μL.

Identification of the antigenic epitope in NRP-1 that is recognized by PAL-E. We used the synthetic peptides CSQYSFNWC, CTQYAMHLC, and CSQWNMLLC corresponding to the cyclic insert sequences in PAL-E–binding phage clones to assess their respective binding to PAL-E antibody by ELISA (data not shown). Relative to IgG2a isotype control, PAL-E reacted positively with CTQYAMHLC peptide, resulting in an average absorbance of 0.64 ± 0.02 (P = 0.002). PAL-E showed no significant binding to either

CSQYSFNWC or CSQWNMLLC peptide. To evaluate whether the CTQYAMHLC motif represents the antigenic epitope in NRP-1 that is targeted by PAL-E, we generated polyclonal anti-CTQYAMHLC antibodies by immunization of rabbits with the KLH counterpart of the peptide. Relative to preimmune sera, the resultant sera were first analyzed for their specific binding to their respective peptide antigen (Fig. 4*A*). The unrelated CGSPGWVRC peptide was used as control. Then, we assessed whether purified polyclonal anti-CTQYAMHLC IgGs can bind to recombinant NRP-1 (Fig. 4*B*). Results show that relative to preimmune sera, anti-CTQYAMHLC IgGs bind positively to NRP-1 with a mean absorbance of 0.90 ± 0.05 (P = 0.004). Interestingly, much stronger binding of anti-CTQYAMHLC IgGs to recombinant NRP-2 was observed with a mean absorbance of 2.11 ± 0.12 (P = 0.003), indicating a stronger affinity of the polyclonal antibody to NRP-2 (Fig. 4*C*). Together,
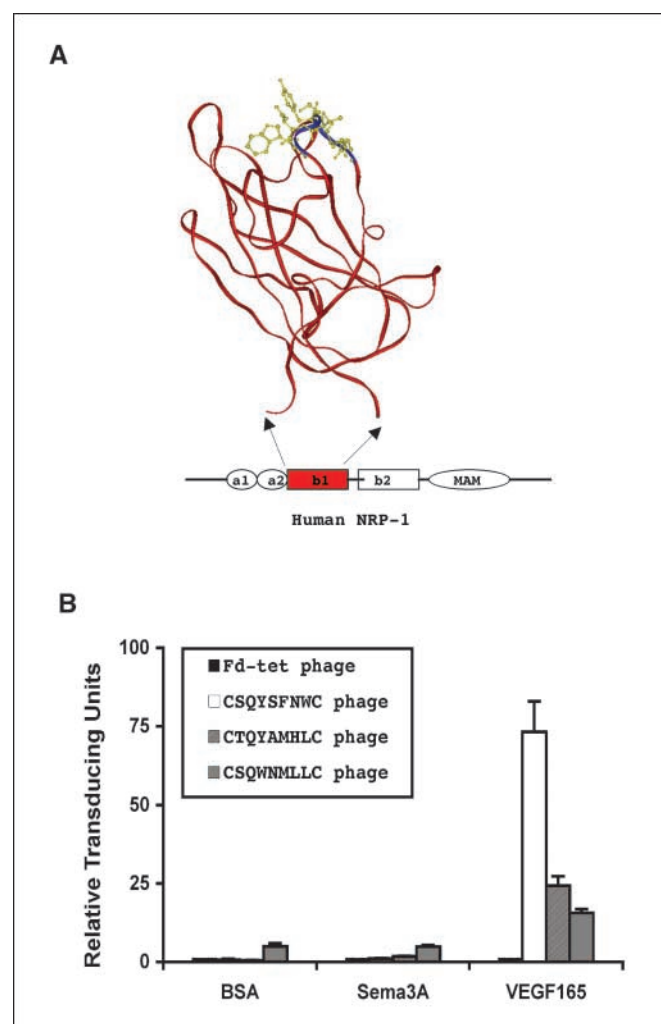
Figure 5. PAL-E–binding epitope in NRP-1 maps to the VEGF$_{165}$ binding site. *A,* PAL-E binding site in NRP-1. A ribbon diagram resembling the crystal structure of the b1 domain in NRP-1 (*red;* http://www.rcsb.org/pdb/cgi/explore.cgi, pdbId=1KEX). The SQYSTNW motif corresponding to the PAL-E binding site in NRP-1 (*blue*). The side-chain amino acid residues (*yellow*). *B,* select phage clones that bind to PAL-E also bind to the NRP-1 ligand VEGF$_{165}$. Compared with Fd-tet insertless phage, clones with the insert sequences CSQYSFNWC and CTQYAMHLC showed strong binding to recombinant human VEGF-A$_{165}$. Recombinant human Sema3A, another NRP-1 ligand, was used as control.

these findings suggest that the CTQYAMHLC motif or its homologous domain in NRP-1 represents, at the least in its secondary peptide structure, the antigenic epitope that is targeted by PAL-E.

PAL-E binding epitope in NRP-1 overlaps with the VEGF-A$_{165}$ binding site. The crystal structure of the b1 domain in NRP-1 (Fig. 5*A*) shows that the SQYSTNW motif (in blue; side chain amino acid residues in yellow) corresponding to the PAL-E binding site in NRP-1 is well exposed on the outer surface of the receptor (18). This suggests that it is accessible not only to circulating antibodies but also to receptor-binding ligands. Because it is known that the NRP-1 ligand VEGF-A$_{165}$ binds to the b1 domain (19), we reasoned that the PAL-E binding site may actually overlap with the VEGF-A$_{165}$ binding region. Thus, we evaluated whether PAL-E–binding phage clones displaying peptide motifs that share homology with NRP-1 also bind to VEGF-A$_{165}$. Relative to Fd-tet insertless phage control, the clones with the peptide insert sequences CSQYSFNWC and CTQYAMHLC showed 73 ± 10-fold and 24 ± 3-fold more binding to human VEGF-A$_{165}$, respectively. This interaction seems to be specific because binding of these phage clones to another NRP-1 ligand (human Sema3A) was negligible (Fig. 5*B*). These data strongly suggest that the PAL-E binding site in NRP-1 overlaps with the binding site for VEGF-A$_{165}$.

Discussion

To identify the PAL-E antigen, we used a phage display–based combinatorial approach to select peptide motifs that preferentially bind to the original PAL-E antibody. We found that these mimics of the antigenic epitope share strong homology with NRP-1. Results from both ELISA-based and surface plasmon resonance–based assays show that PAL-E indeed does bind to NRP-1. Consistently, we show the colocalization of PAL-E and anti–NRP-1 staining in endothelial cells. Notably, the functional and expression profiles of NRP-1 are entirely harmonious with the fact that the endothelial cell entity targeted by PAL-E must play an important role in vascular leakage and angiogenesis. NRP-1 (also known as Npn-1, NP-1, A5-antigen) is a transmembrane glycoprotein that serves versatile roles in the nervous and in the cardiovascular systems mediated by an ability to bind distinct ligands via partnering with other receptors (20). In the developing nervous system, NRP-1 forms functional multireceptor complexes along with NRP-2 and plexins and binds with high affinity to the three classes of structurally related semaphorins (namely semaphorin-3, semaphorin-IV, and semaphorin-E), which function in neuronal guidance and axonal outgrowth (21, 22). In the cardiovascular system, NRP-1 partners with VEGFR-1 and VEGFR-2 and binds to several VEGF family members, including VEGF-A$_{165}$, VEGF-B, VEGF-E, and placental growth factor-2. Consequently, NRP-1 plays a central role in cardiovascular development (20, 23–25). Finally, in endothelial cells, NRP-1 amplifies the mitogenic and chemotactic effects of VEGF-A$_{165}$ by allowing it to bind more efficiently to VEGF receptor-2, resulting in endothelial cell survival, activation, and angiogenesis (26).

In agreement with the PAL-E staining profile, VEGF-A and its cognate receptors are only weakly expressed in quiescent endothelium but are up-regulated in activated endothelium under inflammatory, ischemic, or malignant disease (27). Moreover, increases in PAL-E reactivity in leaky retinal endothelium strongly correlate with increased local expression of VEGF-A and its

receptor VEGFR-2 (28). It is also worth noting that VEGF regulation of vascular permeability is mediated in part by the formation of cell membrane fenestrations associated with caveolae (29); such membrane vesicle structures stain strongly positive with the PAL-E antibody in the vascular endothelium (1, 6, 8). Interestingly, both the PAL-E antigen and NRP-1 are differentially expressed between blood vessel and lymphatic endothelium in that NRP-1 does not partner with VEGFR-3, which is mainly expressed on lymphatic endothelial cells (30, 31). With regard to PAL-E as a tumor cell marker, several studies have shown increased expression of NRP-1 in human prostate, breast, and colorectal cancer cells (32, 33). In these reports, NRP-1 expression correlates with tumor metastasis and aggressiveness by promoting tumor cell growth, survival, invasiveness, and tumor-related angiogenesis.

At a protein-protein biochemical interaction level, we were also able to map the residues likely to comprise a PAL-E binding site. Because the polyclonal antibody raised against the identified motif could bind to both NRP-1 and to the related receptor NRP-2, one might suggest that PAL-E recognizes a secondary structure at the binding site rather than the primary protein sequence. Moreover, our binding results indicate that the PAL-E binding site in NRP-1 overlaps with a VEGF ligand-receptor site. It is known that the binding specificities of the various ligands to NRP-1 are determined by its 860-residue extracellular fragment composed of two tandem repeats of each of complement-like CUB motifs (a1/a2 domains) and coagulation factor V/VIII–like motifs (b1/b2 domains) followed by a short COOH-terminal domain that contains the meprin-like and μphosphatase-like MAM motif. Studies with NRP-1 deletions have shown that Sema3A binding to NRP-1 is mediated through the a1/a2 and b1/b2 domains, whereas only the b1/b2 domains are required for binding of VEGF-A$_{165}$ (19). It is also known that the b1/b2 domains contain an 18-residue stretch that mediates the heterophilic cell-cell adhesion activity of NRP-1; however, this site is evidently distinct from binding sites for Sema3A and VEGF-A$_{165}$ (34). Our own results show that the SQYSTNW motif (corresponding to the PAL-E binding site within the b1 domain of NRP-1) binds to recombinant VEGF-A$_{165}$ but not to Sema3A, suggesting that the PAL-E antigenic epitope on NRP-1 may encompass, overlap, or contain the VEGF-A$_{165}$ binding site. Consistently, the SQYSTNW motif actually maps to the ligand binding site predicted from the crystal structure analysis of the b1 domain within human NRP-1 (18). From detailed analysis of this structure, the ligand-binding site consists of a polar cleft in the b1 domain that is formed by six juxtaposed loops (L1–L6) flanked by electronegative surfaces. In this context, we found that the SQYSTNW motif (spanning residues 295–301) comprises the first loop in the structure in which the Trp^{301} residue falls deep within the formed cleft. Additionally, Tyr^{297}, which lies in perpendicular orientation to Trp^{301}, decorates the side of the cleft along with Ser^{298}, Thr^{299}, and Asn^{300} residues in L1. However, the full understanding of the interaction attributes among the receptor, corresponding known native ligands, synthetic peptides, and PAL-E will have to await elucidation of X-ray crystal structures of the protein complexes. Of course, one cannot entirely rule out the possibility that the true PAL-E antibody may recognize more than one antigen (12, 13), perhaps in different settings. Indeed, cross-reaction of monoclonal antibodies with multiple antigens has long been shown (35, 36). Be that as it may, the common biochemical, morphologic, and

functional features between PAL-E and NRP-1 support the interpretation of our experimental findings.

In summary, we show that a motif within a VEGF binding site in NRP-1 is an antigenic epitope recognized by the original PAL-E antibody. Our findings and reagents enable a suitable interpretation of PAL-E staining of the vascular endothelium and may provide mechanistic insights into the design of new small molecule peptidomimetic leads and other monoclonal antibodies targeting VEGF-mediated pathways.

References

1. Schlingemann RO, Dingjan GM, Emeis JJ, Blok J, Warnaar SO, Ruiter DJ. Monoclonal antibody PAL-E specific for endothelium. Lab Invest 1985;52:71–6.
2. Paavonen K, Mandelin J, Partanen T, et al. Vascular endothelial growth factors C and D and their VEGFR-2 and 3 receptors in blood and lymphatic vessels in healthy and arthritic synovium. J Rheumatol 2002;29:39–45.
3. Nadimi H, Saatee S, Armin A, Toto PD. Expression of endothelial cell markers PAL-E and EN-4 and Ia-antigens in Kaposi's sarcoma. J Oral Pathol 1988;17:416–20.
4. Nakamura S, Muro H, Suzuki S, et al. Immunohistochemical studies on endothelial cell phenotype in hepatocellular carcinoma. Hepatology 1997;26:407–15.
5. Schlingemann RO, Bots GThAM, van Duinen SG, Ruiter DJ. Differential expression of endothelium-specific antigen PAL-E in vasculature of brain tumors and preexistent brain capillaries. Ann N Y Acad Sci 1988;529:111–4.
6. Schlingemann RO, Rietveld FJ, Kwaspen F, van de Kerkhof PC, de Waal RM, Ruiter DJ. Differential expression of markers for endothelial cells, pericytes, and basal lamina in the microvasculature of tumors and granulation tissue. Am J Pathol 1991;138:1335–47.
7. Leenstra S, Das PK, Troost D, Bosch DA, Claessen N, Becker AE. PAL-E, monoclonal antibody with immunoreactivity for endothelium specific to brain tumours. Lancet 1990;335:671.
8. Sauter B, Foedinger D, Sterniczky B, Wolff K, Rappersberger K. Immunoelectron microscopic characterization of human dermal lymphatic microvascular endothelial cells. Differential expression of CD31, CD34, and type IV collagen with lymphatic endothelial cells vs blood capillary endothelial cells in normal human skin, lymphangioma, and hemangioma *in situ*. J Histochem Cytochem 1998;46:165–76.
9. Hengstenberg C, Rose ML, Olsen EG, Maisch B. Immune response to the endothelium in myocarditis, dilated cardiomyopathy and rejection after heart transplantation. Eur Heart J 1991;12:144–6.
10. Rose M, Page C, Hengstenberg C, Yacoub M. Immunocytochemical markers of activation in cardiac transplant rejection. Eur Heart J 1991;12:147–50.
11. Hofman P, Blaauwgeers HG, Vrensen GF, Schlingemann RO. Role of VEGF-A in endothelial phenotypic

shift in human diabetic retinopathy and VEGF-A-induced retinopathy in monkeys. Ophthalmic Res 2001;33:156–62.
12. Xu B, deWaal RM, Mor-Vaknin N, Hibbard C, Markovitz DM, Kahn ML. The endothelial cell-specific antibody PAL-E identifies a secreted form of vimentin in the blood vasculature. Mol Cell Biol 2004;24:9198–206.
13. Niemelä H, Elima K, Henttinen T, Irjala H, Salmi M, Jalkanen S. Molecular identification of PAL-E, a widely used endothelial-cell marker. Blood 2005;106:3405–9.
14. Scott JK, Smith GP. Searching for peptide ligands with an epitope library. Science 1990;249:386–90.
15. Mintz PJ, Kim J, Do KA, et al. Fingerprinting the circulating repertoire of antibodies from cancer patients. Nat Biotechnol 2003;21:57–63.
16. Vidal CI, Mintz PJ, Lu K, et al. An HSP90-mimic peptide revealed by fingerprinting the pool of antibodies from ovarian cancer patients. Oncogene 2004;23:8859–67.
17. Cardó-Vila M, Arap W, Pasqualini R. $\alpha_v\beta_5$ integrin-dependent programmed cell death triggered by a peptide mimic of Annexin V. Mol Cell 2003;11:1151–62.
18. Lee CC, Kreusch A, McMullan D, Ng K, Spraggon G. Crystal structure of the human neuropilin-1 b1 domain. Structure (Camb) 2003;11:99–108.
19. Mamluk R, Gechtman Z, Kutcher ME, Gasiunas N, Gallagher J, Klagsbrun M. Neuropilin-1 binds vascular endothelial growth factor 165, placenta growth factor-2, and heparin via its b1b2 domain. J Biol Chem 2002;277:24818–25.
20. Soker S, Takashima S, Miao HQ, Neufeld G, Klagsbrun M. Neuropilin-1 is expressed by endothelial and tumor cells as an isoform-specific receptor for vascular endothelial growth factor. Cell 1998;92:735–45.
21. Kolodkin AL, Levengood DV, Rowe EG, Tai YT, Giger RJ, Ginty DD. Neuropilin is a semaphorin III receptor. Cell 1997;90:753–62.
22. Takahashi T, Fournier A, Nakamura F, et al. Plexin-neuropilin-1 complexes form functional semaphorin-3A receptors. Cell 1999;99:59–69.
23. Migdal M, Huppertz B, Tessler S, et al. Neuropilin-1 is a placenta growth factor-2 receptor. J Biol Chem 1998;273:22272–8.
24. Makinen T, Olofsson B, Karpanen T, et al. Differential binding of vascular endothelial growth factor B splice and proteolytic isoforms to neuropilin-1. J Biol Chem 1999;274:21217–22.

25. Takashima S, Kitakaze M, Asakura M, et al. Targeting of both mouse neuropilin-1 and neuropilin-2 genes severely impairs developmental yolk sac and embryonic angiogenesis. Proc Natl Acad Sci U S A 2002;99:3657–62.
26. Soker S, Miao HQ, Nomi M, Takashima S, Klagsbrun M. VEGF165 mediates formation of complexes containing VEGFR-2 and neuropilin-1 that enhance VEGF165-receptor binding. J Cell Biochem 2002;85:357–68.
27. Zachary I, Gliki G. Signaling transduction mechanisms mediating biological actions of the vascular endothelial growth factor family. Cardiovasc Res 2001;49:568–81.
28. Ruiter DJ, Schlingemann RO, Rietveld FJ, de Waal RM. Monoclonal antibody-defined human endothelial antigens as vascular markers. J Invest Dermatol 1989;93:1335–47.
29. Roberts WG, Palade GE. Neovasculature induced by vascular endothelial growth factor is fenestrated. Cancer Res 1997;57:765–72.
30. Lymboussaki A, Partanen TA, Olofsson B, et al. Expression of the vascular endothelial growth factor C receptor VEGFR-3 in lymphatic endothelium of the skin and in vascular tumors. Am J Pathol 1998;153:395–403.
31. Paavonen K, Puolakkainen P, Jussila L, Jahkola T, Alitalo K. Vascular endothelial growth factor receptor-3 in lymphangiogenesis in wound healing. Am J Pathol 2000;156:1499–504.
32. Soker S, Kaefer M, Johnson M, Klagsbrun M, Atala A, Freeman MR. Vascular endothelial growth factor-mediated autocrine stimulation of prostate tumor cells coincides with progression to a malignant phenotype. Am J Pathol 2001;159:651–9.
33. Parikh AA, Fan F, Liu WB, et al. Neuropilin-1 in human colon cancer: expression, regulation, and role in induction of angiogenesis. Am J Pathol 2004;164:2139–51.
34. Shimizu M, Murakami Y, Suto F, Fujisawa H. Determination of cell adhesion sites of neuropilin-1. J Cell Biol 2000;148:1283–93.
35. James LC, Roversi P, Tawfik DS. Antibody multispecificity mediated by conformational diversity. Science 2003;299:1362–7.
36. Varga JM, Kalchschmid G, Klein GF, Fritsch P. Mechanism of allergic cross-reactions-I. Multispecific binding of ligands to a mouse monoclonal anti-DNP IgE antibody. Mol Immunol 1991;28:641–54.

Treatment of hypoxia-induced retinopathy with targeted proapoptotic peptidomimetic in a mouse model of disease

Johanna Lahdenranta,*,[1] Richard L. Sidman,[†] Renata Pasqualini,*,[2] and Wadih Arap*,[2]

*The University of Texas, M. D. Anderson Cancer Center, Houston, Texas, USA; and [†]Harvard Medical School and Department of Neurology, Beth Israel Deaconess Medical Center, Harvard Institutes of Medicine, Boston, Massachusetts, USA

ABSTRACT   We have previously identified ligands from combinatorial peptide libraries that target tumor vasculature after *in vivo* selection. These ligands bind to differentially expressed receptors in angiogenic vasculature such as $\alpha_v\beta_3/\alpha_v\beta_5$ integrins, aminopeptidase N, and aminopeptidase A. We hypothesized that we can use these ligands to target angiogenic vasculature in retinopathies. Pathological retinal angiogenesis in conditions such as diabetic retinopathy, retinopathy of prematurity, and age-related macular degeneration is a major cause of blindness for which current treatments are inadequate. Here we tested whether known tumor vasculature targeting peptide ligands displayed on bacteriophage particles would home to the proliferating blood vessels of the retina in a standard mouse model of retinopathy of prematurity. We found that activated retinal blood vessels share many of the endothelial and periendothelial cell receptors expressed in tumor vasculature. Furthermore, these vascular receptors—α_v integrins and aminopeptidases—are accessible through the circulation and mediate phage homing and internalization to endothelial and periendothelial cells. Treatment of mice with a peptide containing a $\alpha_v\beta_3/\alpha_v\beta_5$-integrin targeting domain fused to a proapoptotic domain significantly reduced oxygen-induced retinal angiogenesis by selectively inducing activated endothelial cell apoptosis. Targeted proapoptotic peptides may prove useful in the management of angiogenic retinal diseases.—Lahdenranta, J., Sidman, R. L., Pasqualini, R., Arap, W. Treatment of hypoxia-induced retinopathy with targeted proapoptotic peptidomimetic in a mouse model of disease. *FASEB J.* 21, 3272–3278 (2007)

ANGIOGENESIS, THE FORMATION of new blood vessels from preexisting vasculature, is a major component in several retinal vascular diseases causing blindness, such as retinopathy of prematurity, proliferative diabetic retinopathy, and age-related macular degeneration. Diabetes mellitus is the main cause of new cases of adult blindness. Nearly all individuals with type 1 diabetes show some symptoms of diabetic retinopathy, usually $\sim$ 20 years after clinical recognition of diabetes (1); in the most advanced form of diabetic retinopathy, called proliferative diabetic retinopathy, new blood vessels grow uncontrollably on the retinal inner surface, causing hemorrhages and even retinal detachment (2). Surgical and laser photocoagulation treatments are only partially effective and may further damage the retinal tissue. Neither pathogenetic mechanisms nor effective therapy are in hand for retinopathy of prematurity, diabetic retinopathy, or age-related macular degeneration (3, 4).

Angiogenesis is also a major component in tumor growth (5), and endothelial cells in tumor vessels likewise may show different or much higher concentrations of surface markers than do the corresponding normal tissues (6–8). Our hypothesis in the present study is that angiogenesis, whatever its cause, may involve an increase in the same demonstrable markers so that the extensive data available from study of tumor vessels may also apply to angiogenesis in the common retinal vascular diseases. Among such markers are receptors for vascular growth factors such as specific subtypes of VEGF and basic FGF receptors (9–11), α_v-integrins (12), proteoglycans (13, 14), proteinases (15), and aminopeptidases (16–18). Some of these markers have already been demonstrated in vessels during retinal neovascularization (18–22).

In vivo phage display technology (23) is a powerful method enabling unbiased selection of peptides capable of homing selectively to different vascular beds in mice and humans (6, 24, 25). This method also allows tissue-specific targeting of angiogenesis-related molecules to tumor blood vessels (14, 16, 18, 26–29). Peptide ligands selected through phage display technology can deliver proapoptotic or other toxic peptides

---

selectively, showing marked therapeutic efficacy in tumor-bearing mouse models (30).

Targeted proapoptotic peptides are short peptides composed of two functional domains: a blood vessel homing motif and a programmed cell death-inducing sequence. The homing domain targets endothelial or periendothelial cells and allows for receptor-mediated internalization (30, 31). The proapoptotic domain $_D(KLAKLAK)_2$ is relatively nontoxic outside eukaryotic cells but promotes apoptotic death by disrupting mitochondrial membranes on cell entry (30, 32, 33). In earlier work we showed that the $_D(KLAKLAK)_2$ proapoptotic peptides targeted with peptides that bind to α_v integrins and to aminopeptidase N (CD13/APN), when administered systemically, home to angiogenic tumor vasculature and are selectively toxic to angiogenic endothelial cells after internalization by these receptors, thus exhibiting antitumor activity (30).

In the present study we investigate the accessibility of known angiogenic markers to either intravenously administered peptide ligands presented on a filamentous phage particle or to antibodies. Peptide ligands include the $\alpha_v\beta_3$ binding peptide ACDCRGDCFC (termed RGD-4C; ref. 34), aminopeptidase A (APA) binding peptide CPKVCPRECESNC (termed CPRECES; ref. 18), and the aminopeptidase N binding peptide CNGRC (termed NGR; ref. 16). In the absence of a satisfactory rodent model of diabetic retinopathy, we chose to study angiogenesis in a standard mouse model of retinopathy of prematurity (35) with which we had prior experience (18, 36). We find that *1)* the new blood vessels in retinas exposed to oxygen share accessible endothelial and periendothelial cell receptors with tumor vasculature, *2)* homing peptides can specifically target circulating phage to angiogenic endothelial cells in retinal vasculature, and *3)* targeted proapoptotic peptides can reduce oxygen-induced retinal neovascularization.

MATERIALS AND METHODS

Antibodies and reagents

The anti-mouse CD13 antibody R3–63 was from Serotec (Oxford, UK), anti-mouse CD61 (β_3 integrin) was from BD PharMingen (San Jose, CA, USA), anti-mouse CD31 was from Chemicon (Temecula, CA, USA), and the isotype control antibodies were from DAKO (Glostrup, Denmark). The anti-APA antibody ASD-37 has been described (37). FITC- and Cy3-conjugated secondary antibodies were from Jackson ImmunoResearch Laboratories (West Grove, PA, USA). The peptides $_D(KLAKLAK)_2$, ACDCRGDCFC-GG-$_D(KLAKLAK)_2$, and ACDCRGDCFC (RGD-4C) were synthesized to our specifications at higher than 90% purity by high-performance liquid chromatography (Anaspec, San Jose, CA, USA). The identities of the peptides were verified by mass spectrometry.

Animals

Institutional animal care and utilization committee of the University of Texas M.D. Anderson Cancer Center approved all animal experiments. This study adhered to the Association

for Research in Vision and Ophthalmology (ARVO) guidelines. Nude mice and C57BL/6 mice were obtained from Harlan (Indianapolis, IN, USA).

Mouse model of retinal neovascularization

We used a hypoxia-induced retinopathy in which mouse pups with their nursing mothers were exposed to 75% O_2 from postnatal day 7 (P7) to P12. On P12, mice were returned to room air (20.8% O_2) for 7 days (35). The exposure of neonatal mice to high O_2 levels causes vasoconstriction of the central retinal blood vessels and, subsequently, a decreased retinal perfusion. Returning the mice to lower oxygen levels (room air), which coincides with the rapid development of rod outer segments and an increased retinal oxygen demand, is believed to lead to relative retinal tissue hypoxia and ischemia. The relative hypoxia of the retinal tissue results in the observed retinal neovascularization (4, 35). For phage homing and antibody targeting assays, mice were used on P19, at which point the retinal neovessels are protruding into the vitreal space at the inner retinal surface (35, 36).

Immunofluorescence microscopy and intravascular imaging studies

Enucleated eyes from (P19) mouse pups that had been exposed to 75% O_2 from P7 to P12 were fixed for 1–2 h by immersion in 4% paraformaldehyde in PBS, incubated for 16 h in 30% sucrose in PBS, frozen, and sectioned at 60 μm. Tissue sections were blocked with 5% normal goat serum in 0.3% Triton X-100/PBS and incubated for 16 h at room temperature with 10 μg/ml R3–63 (anti-APN/CD13), 10 μg/ml ASD-37 (anti-APA), or 1 μg/ml anti-CD61 (β3 integrin) in combination with 10 μg/ml anti-CD31 antibody. Secondary antibodies (1:400 dilutions of FITC- or Cy3-conjugated anti-rat IgG and anti-hamster IgG) were incubated with the sections for 4 h at room temperature. After thorough washing, eye sections were mounted, cover slipped, and analyzed with a fluorescence microscope. For the intravascular imaging study, 10 μg of the anti-CD61 (β3 integrin) antibody or a negative control antibody were injected in 50 μl of Dulbecco's modified Eagle's medium (DMEM) intravenously through the tail vein into P19 C57B/6 mice that had been exposed to 75% oxygen from days P7-P12 or into control P19 C57B/6 mice that had not been treated with oxygen. Antibodies were allowed to circulate for 30 min before mice were perfused through the left ventricle with 5 ml of DMEM. Eyes and the brain were collected, fixed, and sectioned at 60 μm as described previously. Tissue sections were blocked with 5% normal goat serum in 0.3% Triton X-100/PBS and incubated for 16 h at room temperature with 2 μg/ml anti-CD31 antibody. Secondary antibodies (1:400 dilutions of FITC- or Cy3-conjugated anti-rat IgG and anti-hamster IgG) were incubated with the sections for 4 h at room temperature. After thorough washing, eye sections were mounted, cover slipped, and analyzed with a fluorescence microscope.

Phage targeting

For the retina-targeting experiments, 1×10^9 transducing units (TUs) of CPRECES- (displaying the peptide insert CPKVCPRECESNC), NGR- (displaying the peptide insert CNGRC), RGD-4C- (displaying the peptide insert ACDCRG-DCFC), or fd-tet-phage in 100 μl of DMEM were injected intravenously through the tail vein into either P18 C57B/6 mice that had been exposed to 75% oxygen from days P7-P12 or into P18 C57B/6 mice not treated with oxygen. Phage were

allowed to circulate for 40 min, then mice were perfused with 5 ml of DMEM through the left ventricle of the heart. The eyes were surgically removed and the retinas dissected under a stereomicroscope. Retinas were homogenized in a Dounce homogenizer with ice-cold DMEM containing proteinase inhibitors aprotinin (20 µg/ml), leupeptin (1 µg/ml), and 1 mM phenylmethylsulfonyl fluoride and the retinal homogenates were washed with the above buffer. Retina-bound phage were recovered by infection of K91kan *Escherichia coli* with the retinal homogenates. Serial dilutions of the infected K91kan were plated on Luria-Bertani agar plates with tetracycline (40 µg/ml) and kanamycin (50 µg/ml). The number of recovered phage TUs was determined by bacterial colony counting. For the tumor-homing experiments, 1×10^9 TU of CPRECES-, NGR-, RGD-4C-, or fd-tet-phage in 100–200 µl of DMEM were injected intravenously through the tail vein into nude mice bearing tumor xenografts derived from MDA-MB-435 human breast cancer cells (27). Phage were allowed to circulate for 5 min and the animals were perfused through the left ventricle of the heart with 10 ml of DMEM. Tumor and control organs were dissected and equal amounts of tissue were homogenized. Homogenates were washed with ice-cold DMEM containing a protease inhibitor and 0.1% bovine serum albumin. Tissue-bound phage were recovered as described above.

Systemic treatment of retinal neovascularization

Mice with hypoxia-induced retinal neovascularization received vehicle alone, 150 µg of targeted proapoptotic peptide ACDCRGDCFC-GG-$_D$(KLAKLAK)$_2$ (termed RGD-GG-$_D$(KLAKLAK)$_2$), or 150 µg of equimolar mixture of RGD-4C and $_D$(KLAKLAK)$_2$ control peptides on P17 (*n*=9 mice/group). On P21, mice were sacrificed and their eyes were enucleated, fixed in 4% paraformaldehyde in PBS, serially sectioned after embedding in paraffin, and stained with hematoxylin and eosin (H&E) for histological analysis. Endothelial cell nuclei on the vitreous side of the internal limiting membrane extending into the vitreous were counted to quantify retinal neovascularization (35, 36).

RESULTS

Tumor targeting with APN, APA, and $\alpha_v\beta_3/\alpha_v\beta_5$ integrin binding ligands

Phage displaying peptide ligands ACDCRGDCFC (termed RGD-4C; refs. 26, 27), CNGRC (27), or CP-KVCPRECESNC (termed CPRECES; ref. 18) were first tested for tumor homing *in vivo*. To confirm findings from previous studies (18, 26, 27), we performed a side-by-side analysis of RGD-4C-, NGR-, CPRECES-, or a negative control phage (insertless fd-tet-phage) for their ability to home to tumor xenografts. RGD-4C-, NGR-, CPRECES-, or a negative control phage were administered intravenously into mice bearing MDA-MB-435-derived human tumor xenografts. Tumor- and control organ (brain) -bound phage were recovered and titered from the tissue homogenates after a 5 min circulation, followed by perfusion. RGD-4C-, NGR-, and CPRECES-phage were enriched in tumors with a minimum of 10-fold enrichment compared with the control organ; in contrast, negative control phage did not enrich in tumors (**Fig. 1**). These results show that APA-,
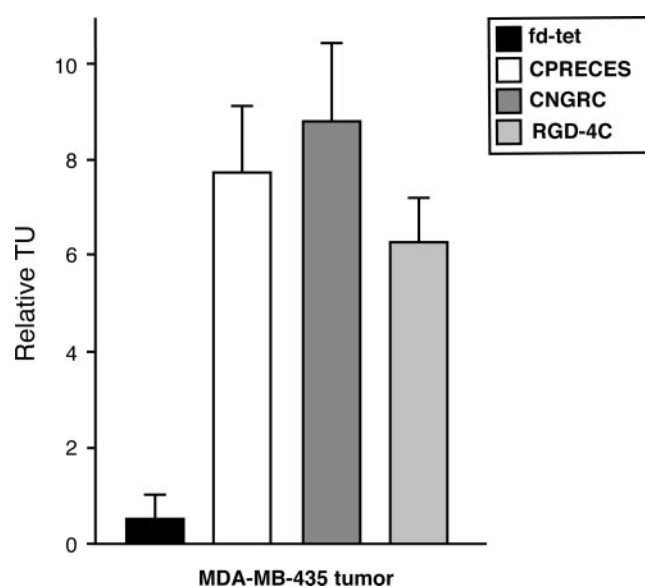
Figure 1. Side-by-side comparison of the tumor homing peptides in mice with MDA-MB-435 xenografts. The ability of APA binding, APN binding, and $\alpha_v\beta_3$ integrin binding phage, compared with control fd-tet phage, to home to tumor vasculature was evaluated after intravenous phage administration into mice bearing human MDA-MB-435 breast carcinoma-derived tumor xenografts. Phage were recovered from tumors after perfusion. Shown are mean ± SE of TU from triplicate platings.

APN-, and $\alpha_v\beta_3/\alpha_v\beta_5$ integrin binding phage target tumor blood vessels *in vivo*.

Receptors for the tumor-targeting peptide ligands are expressed in the proliferating retinal blood vessels

Next we wanted to determine whether the receptors for the identified tumor-homing peptide ligands are expressed during retinal neovascularization. We performed immunofluorescence staining for APA, APN, and β_3 integrin (which partners with α_v integrin) on eye and brain sections from P19 mice with hypoxia-induced retinal neovascularization after an exposure to 75% O_2 from P7-P12. We could detect expression of APA, APN, and β_3 integrin in the blood vessels of angiogenic retinas. We could not detect expression of β_3 integrin in quiescent brain blood vessels; in contrast, however, we did detect APA and APN expression in brain blood vessels, presumably in pericytes. Isotype control antibody served as a negative staining control (**Fig. 2**). These results show that receptors for the tumor homing peptide ligands, APA, APN, and $\alpha_v\beta_3$ integrin, are expressed in blood vessels of retinas undergoing neovascularization.

Tumor-targeting phage home to angiogenic retina

We next evaluated the ability of tumor-targeting phage to home to angiogenic retina. Tumor-targeting phage displaying RGD-4C, NGR, or CPRECES peptide and an insertless control phage (fd-tet) were administered
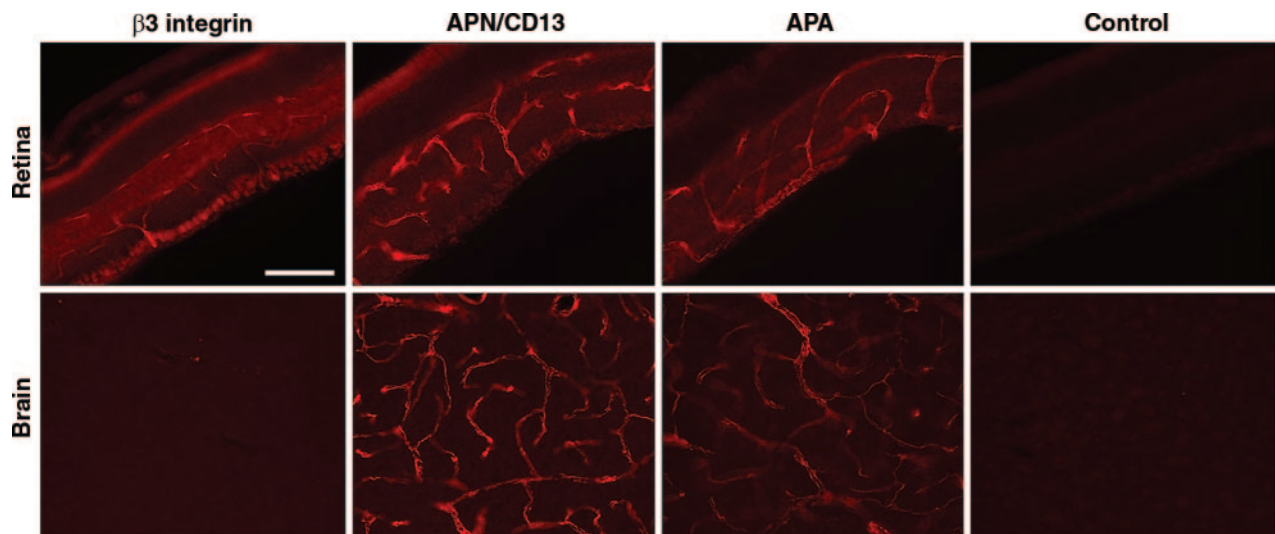
Figure 2. $\alpha_v\beta_3$ integrin, APN, and APA are expressed in the retinal vasculature during oxygen-induced retinal neovascularization. 60 μm eye and brain sections from P19 mouse pups that had been exposed to 75% O_2 from P7 to P12 were stained for $\alpha_v\beta_3$ integrin (anti-CD61), APN (R3–63), and APA (ASD-37). Isotype control antibody was used as a negative control. Target expression was detected by Cy3-conjugated secondary antibody. Scale bar: 100 μm.

intravenously to mice on P18 with hypoxia-induced retinal neovascularization after exposure to 75% O_2 from P7-P12 or to control mice not treated with O_2. Retina-bound phage were recovered and titered from the tissue homogenates after a 40 min circulation, which was followed by perfusion. RGD-4C-, NGR-, and CPRECES-phage were significantly enriched in angiogenic retinas with 4.6 ± 0.9-, 3.5 ± 0.5-, or 5.7 ± 1.3-fold enrichment, respectively (*t* test, $P<0.03$ in each case compared with non-oxygen-treated retinas); in contrast, negative control phage did not enrich in angiogenic retinas (1.2±0.1-fold enrichment, *t* test, $P=0.17$; **Fig. 3**). These results show that APA-, APN-, and $\alpha_v\beta_3/\alpha_v\beta_5$ integrin binding phage target angiogenic retinal blood vessels *in vivo*.

Receptors for the tumor targeting peptide ligands in proliferating retinal blood vessels are accessible to antibodies from the circulation

Next we analyzed the accessibility of the endothelial cell receptor for the RGD-4C peptide ($\alpha_v\beta_3$ integrin) after intravenous injection of anti-β3 integrin antibody. P19 mice without oxygen treatment and with hypoxia-induced retinal neovascularization after exposure to 75% O_2 from P7-P12 received 10 μg of anti-CD61 (β3 integrin) antibody or a negative control antibody intravenously. Antibodies were allowed to circulate for 30 min before mice were perfused. The eyes and brain were collected, sectioned, and stained for the CD31 endothelial cell marker (detected with FITC-conjugated secondary antibody). Anti-CD61 and negative control antibodies were detected in the tissues by Cy3-conjugated secondary antibody. Our results (**Fig. 4**) demonstrate that β3 integrin is accessible to circulating antibodies in retinas with proliferating blood vessels, in contrast to normal retinas without blood

vessel proliferation. Control antibody showed no vascular staining. No anti-CD61 antibody staining was detected in the brain vasculature.

Targeted proapoptotic peptides reduce retinal neovascularization

Finally, we designed studies to assess the effects of $\alpha_v\beta_3/\alpha_v\beta_5$ integrin-targeting proapoptotic peptides
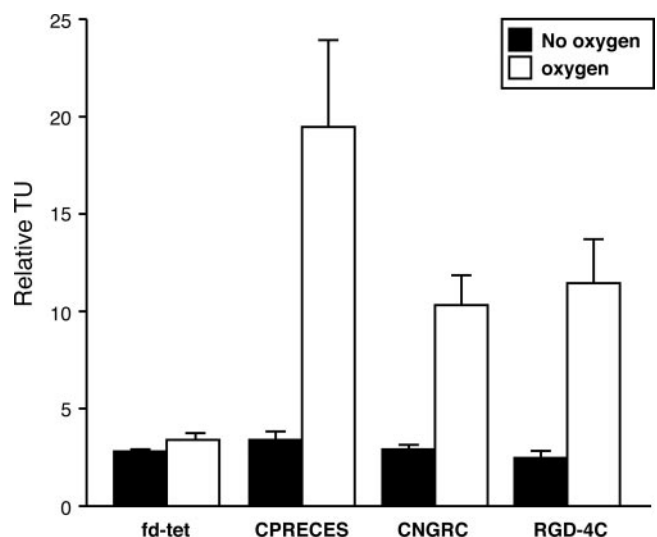
Figure 3. $\alpha_v\beta_3$ integrin, APN, and APA are accessible to their peptide ligands in the retinal vasculature during oxygen-induced retinal neovascularization. The ability of APA binding, APN binding, and $\alpha_v\beta_3$ integrin binding phage to home to retinal neovasculature was evaluated after intravenous phage administration into P18 mice that had been exposed to 75% oxygen between days P7 and P12 or into P18 mice without oxygen treatment. Phage were recovered from retinas after perfusion. Shown are mean ± SE of TU from triplicate platings. Fd-tet served as a negative control phage.
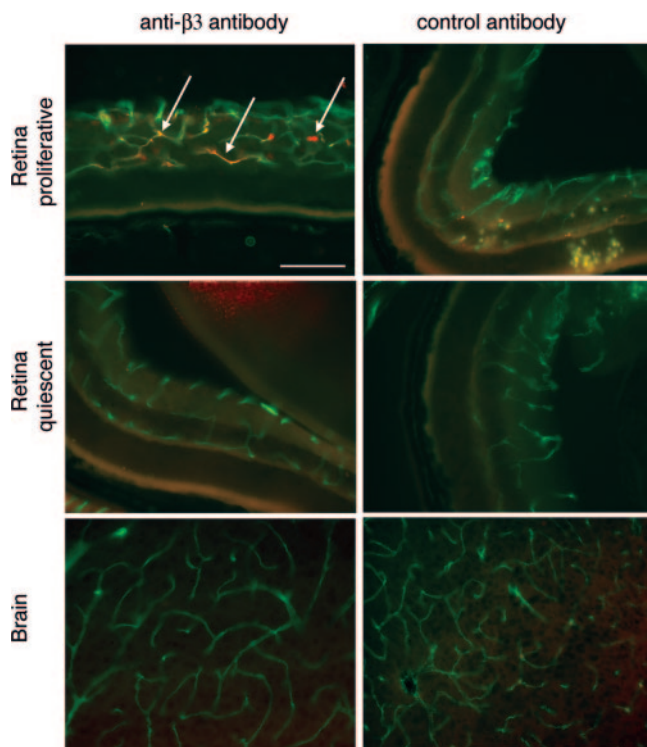
Figure 4. Accessibility of β_3-integrin in retinal blood vessels. Intravenous injection of anti-CD61 (β_3-integrin) antibody or a control antibody into P19 mice with or without hypoxia-induced retinal neovascularization illustrates that the β_3-integrin-positive cells in angiogenic vessels of the retina (arrows) are accessible to the antibodies after 30 min circulation. The control IgG did not stain tissues in any of the experimental settings. β_3-Integrin immunoreactivity is seen in red and CD31 immunoreactivity indicating the endothelium in all blood vessels is seen in green. Scale bar: 100 µm.

(30) in the mouse model of hypoxia-induced retinal neovascularization. Mice received 150 µg of targeted proapoptotic [RGD-4C-GG-$_D$(KLAKLAK)$_2$], control

[equimolar mixture of RGD-4C and $_D$(KLAKLAK)$_2$] peptides, or vehicle alone on P17. On P21, eyes were enucleated, fixed, embedded in paraffin, and stained with H&E. Retinal neovascularization was analyzed by counting endothelial cell nuclei protruding into the vitreous space (35, 36). Induction of retinal neovascularization was seen in vehicle- or control-treated mice on P21, but the number of retinal neovessels was reduced by up to 70% on systemic treatment of mice with the targeted proapoptotic peptide (48±1) endothelial cell nuclei/section (*t* test, $P<0.01$; **Fig. 5**). No endothelial cell nuclei protruding into the vitreous space were found in mice exposed only to room air (data not shown).

DISCUSSION

Several novel approaches have been developed to prevent and treat proliferative diabetic retinopathy. Some experimental approaches aim to block the metabolic pathways inducing hyperglycemic damage in the retina, including increased formation of advanced glycation end product, hexosamine pathway flux, polyol pathway flux, and diacylglycerol activation of a protein kinase C pathway (2, 19, 38). Other approaches aim to prevent vascular leakage and neovascularization *via* inhibition of growth factors and integrins as well as their intracellular signaling cascades (reviewed in ref. 2). In the present study, we showed that endothelial cell surface markers previously demonstrated in tumor vasculature may also serve as suitable receptors in proliferating retinal blood vessels for selective targeting of phage carrying both a peptide-ligand for the receptor and a therapeutic moiety.

We previously identified APN and APA as cell surface receptors in endothelial and periendothelial cells of angiogenic vasculature that are accessible to circulating
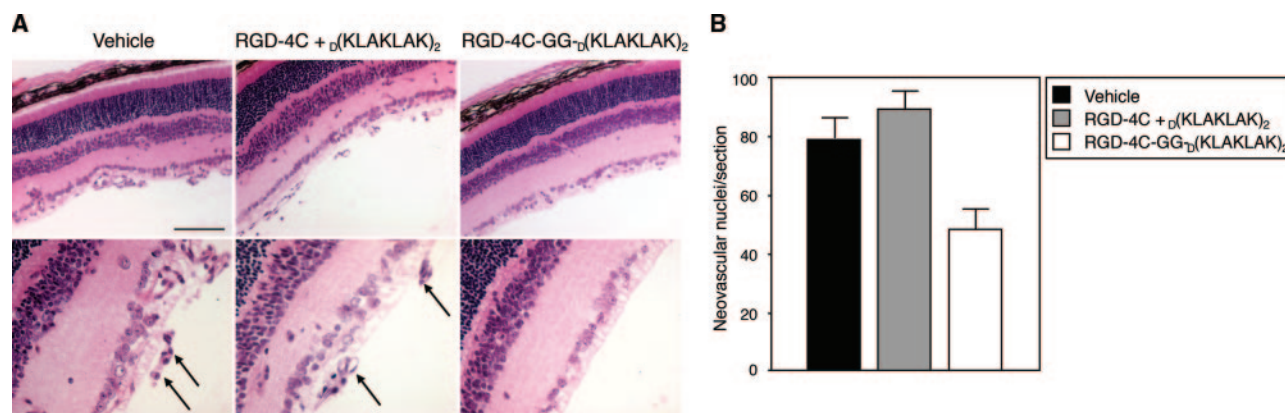
Figure 5. Treatment of hypoxia-induced retinopathy with $\alpha_v\beta_3$ integrin-targeting proapoptotic peptide. P17 mice with hypoxia-induced retinal neovascularization received targeted proapoptotic [RGD-4C-GG-$_D$(KLAKLAK)$_2$] (right column) or control [RGD-4C and $_D$(KLAKLAK)$_2$ peptides separately] (middle column) on P17. Retinal neovascularization was analyzed on P21 in paraffin-embedded H&E-stained eye sections. *A)* Blood vessels are seen protruding from the retina into the vitreous space in eyes from mice treated with vehicle or control peptides (arrows point to endothelial cell nuclei), while few neovascular nuclei are present in eyes from mice treated with targeted proapoptotic peptide. Scale bar: 100 µm (upper panels), 50 µm (lower panels). *B)* The number of neovascular nuclei protruding into the vitreous space was quantified by evaluating several (≥5) serial sections of multiple (≥8) eyes. Shown are mean ± sᴇ.

ligands such as peptides carried on phage particles. Since APN and APA enzymatic activities regulate angiogenesis, blocking their enzymatic activities genetically or biochemically significantly reduces the formation of new blood vessels in tumors and in the mouse model of retinopathy of prematurity (16, 18). The regulatory role for $\alpha_v\beta_3$ and $\alpha_v\beta_5$ integrins in angiogenesis has been established for tumor angiogenesis and angiogenesis in proliferative retinopathies (12, 19, 39). We have further identified peptide ligands for APA (CPRECES peptide), APN (NGR peptide), and $\alpha_v\beta_3/\alpha_v\beta_5$ (RGD-4C peptide) integrins from combinatorial peptide libraries and have shown that these peptide ligands can target tumor vasculature (16, 18, 27, 34). We have both indirect and direct experimental evidence that the identified peptide ligands undergo receptor-mediated internalization into the target cell (18, 30). After identification of both RGD-4C and NGR-peptides as ligands for targeting tumor vasculature, they have been widely used for targeting an array of therapies to tumor vasculature, including cytotoxic drugs (27), proapoptotic peptides (30), cytokines (40), liposomes (41), and gene delivery vehicles (42, 43).

Our objective was to determine whether we can use the tumor-homing peptide ligands RGD-4C, NGR, and CPRECES for targeting the blood vessels of angiogenic retina and for intravenous delivery of therapeutic agents in proliferative retinopathies. After a side-by-side validation of the targeting properties of the CPRECES-, NGR-, and RGD-4C-peptide displaying phage to proliferating blood vessels in human breast carcinoma tumor xenografts, we analyzed the expression of APA, APN, and α_v-integrins in a mouse model of retinal neovascularization using *in vivo* phage targeting and immunostaining. We showed by immunofluorescence microscopy the expression of APA, APN, and β_3-integrins in the blood vessels of the retina after hypoxia-induced retinal neovascularization, and we demonstrated the accessibility of these molecules to circulating ligands by phage homing experiments where phage displaying of APA, APN, and $\alpha_v\beta_3/\alpha_v\beta_5$-integrin ligands specifically targeted retinal vessels, but only in those mice that had been induced to develop neovascularization. For the therapy experiments, we chose the $\alpha_v\beta_3/\alpha_v\beta_5$ integrin binding peptide ligand RGD-4C fused to the proapoptotic moiety $_D$(KLAKLAK)$_2$ as a prototype-targeted peptide. We first assessed the tissue-confined accessibility of β_3-integrins to intravenously administered antibodies and showed that α-β_3-integrin antibody specifically stained the retinal vessels only after the induction of retinal neovascularization and that the staining was specific to the retina, since we did not detect staining in the control organ (brain). Intravenous treatment with the prototype-targeted peptide RGD-4C-GG-$_D$(KLAKLAK)$_2$ markedly reduced the number of retinal neovessels compared with controls consisting of injection of vehicle alone or of an equimolar mixture of RGD-4C and $_D$(KLAKLAK)$_2$ peptides. Of note, cyclic α_v peptide antagonist (RGDfV; ref. 44) has been shown to inhibit retinal neovascularization partially when administered

twice a day (20–100 μg/injection) for 5 days (19). We did not detect a decrease in retinal neovascularization with an injection of our control peptide mixture (90 μg of RGD-4C peptide, which is also an α_v-integrin antagonist), perhaps because our experimental protocol involved only a single injection. In contrast, a single injection of the RGD-4C-peptide fused to the proapoptotic moiety was sufficient to induce endothelial cell apoptosis and a subsequent reduction in retinal neovascularization.

In summary, our data indicate that APA, APN, and $\alpha_v\beta_3/\alpha_v\beta_5$ integrins are not only selectively present in oxygen-induced new retinal blood vessel endothelial cells, but are also accessible targets for therapy in at least one experimental model of a proliferative retinopathy. Since the proliferating blood vessels in the retina share common angiogenic markers with tumor vasculature, and tumor-homing peptides can specifically target circulating phage to activated endothelial and periendothelial cells in retinal vasculature, an experimental model of neovascularization such as the mouse model of retinopathy of prematurity allows more thorough and rapid studies of ligands originally isolated as tumor targeting moieties for their ability to also target angiogenic vasculature in general. In addition, we demonstrated the suitability of activated endothelial cell surface markers as receptors for targeting of therapeutic compounds to angiogenic retinal vasculature in experimental mice and propose that they may have a selective therapeutic effect against proliferative retinopathies such as human diabetic retinopathy and retinopathy of prematurity. [FJ]

REFERENCES

1. Klein, R., Klein, B. E., Moss, S. E., Davis, M. D., and DeMets, D. L. (1984) The Wisconsin epidemiologic study of diabetic retinopathy. III. Prevalence and risk of diabetic retinopathy when age at diagnosis is 30 or more years. *Arch. Ophthalmol.* **102,** 527–532

2. Frank, R. N. (2004) Diabetic retinopathy. *N. Engl. J. Med.* **350,** 48–58

3. Diabetes Control and Complications Trial Research Group (1993) The effect of intensive treatment of diabetes on the development and progression of long-term complications in insulin-dependent diabetes mellitus. *N. Engl. J. Med.* **329,** 977–986

4. Arden, G. B., Sidman, R. L., Arap, W., and Schlingemann, R. O. (2005) Spare the rod and spoil the eye. *Br. J. Ophthalmol.* **89,** 764–769

5. Folkman, J. (2006) Angiogenesis. *Annu. Rev. Med.* **57,** 1–18

6. Trepel, M., Arap, W., and Pasqualini, R. (2002) In vivo phage display and vascular heterogeneity: implications for targeted medicine. *Curr. Opin. Chem. Biol.* **6,** 399–404

7. Luttun, A., and Carmeliet, P. (2004) Angiogenesis and lymphangiogenesis: highlights of the past year. *Curr. Opin. Hematol.* **11,** 262–271

8. St. Croix, B., Rago, C., Velculescu, V., Traverso, G., Romans, K. E., Montgomery, E., Lal, A., Riggins, G. J., Lengauer, C.,

Vogelstein, B., and Kinzler, K. W. (2000) Genes expressed in human tumor endothelium. *Science* **289,** 1197–1202

9. Plate, K. H., Breier, G., Millauer, B., Ullrich, A., and Risau, W. (1993) Up-regulation of vascular endothelial growth factor and its cognate receptors in a rat glioma model of tumor angiogenesis. *Cancer Res.* **53,** 5822–5827

10. Brekken, R. A., Huang, X., King, S. W., and Thorpe, P. E. (1998) Vascular endothelial growth factor as a marker of tumor endothelium. *Cancer Res.* **58,** 1952–1959

11. Valtola, R., Salven, P., Heikkila, P., Taipale, J., Joensuu, H., Rehn, M., Pihlajaniemi, T., Weich, H., deWaal, R., and Alitalo, K. (1999) VEGFR-3 and its ligand VEGF-C are associated with angiogenesis in breast cancer. *Am. J. Pathol.* **154,** 1381–1390

12. Brooks, P. C., Clark, R. A., and Cheresh, D. A. (1994) Requirement of vascular integrin alpha v beta 3 for angiogenesis. *Science* **264,** 569–571

13. Schrappe, M., Klier, F. G., Spiro, R. C., Waltz, T. A., Reisfeld, R. A., and Gladson, C. L. (1991) Correlation of chondroitin sulfate proteoglycan expression on proliferating brain capillary endothelial cells with the malignant phenotype of astroglial cells. *Cancer Res.* **51,** 4986–4993

14. Burg, M. A., Pasqualini, R., Arap, W., Ruoslahti, E., and Stallcup, W. B. (1999) NG2 proteoglycan-binding peptides target tumor neovasculature. *Cancer Res.* **59,** 2869–2874

15. Koivunen, E., Arap, W., Valtanen, H., Rainisalo, A., Medina, O. P., Heikkila, P., Kantor, C., Gahmberg, C. G., Salo, T., Konttinen, Y. T., *et al.* (1999) Tumor targeting with a selective gelatinase inhibitor. *Nat. Biotechnol.* **17,** 768–774

16. Pasqualini, R., Koivunen, E., Kain, R., Lahdenranta, J., Sakamoto, M., Stryhn, A., Ashmun, R. A., Shapiro, L. H., Arap, W., and Ruoslahti, E. (2000) Aminopeptidase N is a receptor for tumor-homing peptides and a target for inhibiting angiogenesis. *Cancer Res.* **60,** 722–727

17. Essler, M., and Ruoslahti, E. (2002) Molecular specialization of breast vasculature: a breast-homing phage-displayed peptide binds to aminopeptidase P in breast vasculature. *Proc. Natl. Acad. Sci. U. S. A.* **99,** 2252–2257

18. Marchiò, S., Lahdenranta, J., Schlingemann, R. O., Valdembri, D., Wesseling, P., Arap, M. A., Hajitou, A., Ozawa, M. G., Trepel, M., Giordano, R. J., *et al.* (2004) Aminopeptidase A is a functional target in angiogenic blood vessels. *Cancer Cell* **5,** 151–162

19. Hammes, H. P., Du, X., Edelstein, D., Taguchi, T., Matsumura, T., Ju, Q., Lin, J., Bierhaus, A., Nawroth, P., Hannak, D., *et al.* (2003) Benfotiamine blocks three major pathways of hyperglycemic damage and prevents experimental diabetic retinopathy. *Nat. Med.* **9,** 294–299

20. Aiello, L. P., Pierce, E. A., Foley, E. D., Takagi, H., Chen, H., Riddle, L., Ferrara, N., King, G. L., and Smith, L. E. (1995) Suppression of retinal neovascularization in vivo by inhibition of vascular endothelial growth factor (VEGF) using soluble VEGF-receptor chimeric proteins. *Proc. Natl. Acad. Sci. U. S. A.* **92,** 10457–10461

21. Luttun, A., Tjwa, M., Moons, L., Wu, Y., Angelillo-Scherrer, A., Liao, F., Nagy, J. A., Hooper, A., Priller, J., De Klerck, B., *et al.* (2002) Revascularization of ischemic tissues by PlGF treatment, and inhibition of tumor angiogenesis, arthritis and atherosclerosis by anti-Flt1. *Nat. Med.* **8,** 831–840

22. Ozerdem, U., and Stallcup, W. B. (2004) Pathological angiogenesis is reduced by targeting pericytes via the NG2 proteoglycan. *Angiogenesis* **7,** 269–276

23. Pasqualini, R., and Ruoslahti, E. (1996) Organ targeting in vivo using phage display peptide libraries. *Nature* **380,** 364–366

24. Arap, W., Kolonin, M. G., Trepel, M., Lahdenranta, J., Cardo-Vila, M., Giordano, R. J., Mintz, P. J., Ardelt, P. U., Yao, V. J., Vidal, C. I., *et al.* (2002) Steps toward mapping the human vasculature by phage display. *Nat. Med.* **8,** 121–127

25. George, A. J., Lee, L., and Pitzalis, C. (2003) Isolating ligands specific for human vasculature using in vivo phage selection. *Trends Biotechnol.* **21,** 199–203

26. Pasqualini, R., Koivunen, E., and Ruoslahti, E. (1997) Alpha v integrins as receptors for tumor targeting by circulating ligands. *Nat. Biotechnol.* **15,** 542–546

27. Arap, W., Pasqualini, R., and Ruoslahti, E. (1998) Cancer treatment by targeted drug delivery to tumor vasculature in a mouse model. *Science* **279,** 377–380

28. Hoffman, J. A., Giraudo, E., Singh, M., Zhang, L., Inoue, M., Porkka, K., Hanahan, D., and Ruoslahti, E. (2003) Progressive vascular changes in a transgenic mouse model of squamous cell carcinoma. *Cancer Cell* **4,** 383–391

29. Joyce, J. A., Laakkonen, P., Bernasconi, M., Bergers, G., Ruoslahti, E., and Hanahan, D. (2003) Stage-specific vascular markers revealed by phage display in a mouse model of pancreatic islet tumorigenesis. *Cancer Cell* **4,** 393–403

30. Ellerby, H. M., Arap, W., Ellerby, L. M., Kain, R., Andrusiak, R., Rio, G. D., Krajewski, S., Lombardo, C. R., Rao, R., Ruoslahti, E., *et al.* (1999) Anti-cancer activity of targeted pro-apoptotic peptides. *Nat. Med.* **5,** 1032–1038

31. Kolonin, M. G., Saha, P. K., Chan, L., Pasqualini, R., and Arap, W. (2004) Reversal of obesity by targeted ablation of adipose tissue. *Nat. Med.* **10,** 625–632

32. Javadpour, M. M., Juban, M. M., Lo, W. C., Bishop, S. M., Alberty, J. B., Cowell, S. M., Becker, C. L., and McLaughlin, M. L. (1996) De novo antimicrobial peptides with low mammalian cell toxicity. *J. Med. Chem.* **39,** 3107–3113

33. Ellerby, H. M., Martin, S. J., Ellerby, L. M., Naiem, S. S., Rabizadeh, S., Salvesen, G. S., Casiano, C. A., Cashman, N. R., Green, D. R., and Bredesen, D. E. (1997) Establishment of a cell-free system of neuronal apoptosis: comparison of premitochondrial, mitochondrial, and postmitochondrial phases. *J. Neurosci.* **17,** 6165–6178

34. Koivunen, E., Wang, B., and Ruoslahti, E. (1995) Phage libraries displaying cyclic peptides with different ring sizes: ligand specificities of the RGD-directed integrins. *Bio/Technology (NY)* **13,** 265–270

35. Smith, L. E., Wesolowski, E., McLellan, A., Kostyk, S. K., D'Amato, R., Sullivan, R., and D'Amore, P. A. (1994) Oxygen-induced retinopathy in the mouse. *Invest. Ophthalmol. Vis. Sci.* **35,** 101–111

36. Lahdenranta, J., Pasqualini, R., Schlingemann, R. O., Hagedorn, M., Stallcup, W. B., Bucana, C. D., Sidman, R. L., and Arap, W. (2001) An anti-angiogenic state in mice and humans with retinal photoreceptor cell degeneration. *Proc. Natl. Acad. Sci. U. S. A.* **98,** 10368–10373

37. Assmann, K. J., van Son, J. P., Dijkman, H. B., and Koene, R. A. (1992) A nephritogenic rat monoclonal antibody to mouse aminopeptidase A. Induction of massive albuminuria after a single intravenous injection. *J. Exp. Med.* **175,** 623–635

38. Brownlee, M. (2001) Biochemistry and molecular cell biology of diabetic complications. *Nature* **414,** 813–820

39. Cheresh, D. A., Smith, J. W., Cooper, H. M., and Quaranta, V. (1989) A novel vitronectin receptor integrin (alpha v beta x) is responsible for distinct adhesive properties of carcinoma cells. *Cell* **57,** 59–69

40. Curnis, F., Sacchi, A., Borgna, L., Magni, F., Gasparri, A., and Corti, A. (2000) Enhancement of tumor necrosis factor alpha antitumor immunotherapeutic properties by targeted delivery to aminopeptidase N (CD13). *Nat. Biotechnol.* **18,** 1185–1190

41. Pastorino, F., Brignole, C., Marimpietri, D., Cilli, M., Gambini, C., Ribatti, D., Longhi, R., Allen, T. M., Corti, A., and Ponzoni, M. (2003) Vascular damage and anti-angiogenic effects of tumor vessel-targeted liposomal chemotherapy. *Cancer Res.* **63,** 7400–7409

42. Hood, J. D., and Cheresh, D. A. (2002) Role of integrins in cell invasion and migration. *Nat. Rev. Cancer* **2,** 91–100

43. Moffatt, S., Wiehle, S., and Cristiano, R. J. (2005) Tumor-specific gene delivery mediated by a novel peptide-polyethylenimine-DNA polyplex targeting aminopeptidase N/CD13. *Hum. Gene Ther.* **16,** 57–67

44. Aumailley, M., Gurrath, M., Muller, G., Calvete, J., Timpl, R., and Kessler, H. (1991) Arg-Gly-Asp constrained within cyclic pentapeptides. Strong and selective inhibitors of cell adhesion to vitronectin and laminin fragment P1. *FEBS Lett.* **291,** 50–54

Enhanced gold nanoshell scattering contrast using angled fiber probes

Vengadesan Nammalvar*, Adrien Wang*, Rebekah Drezek
Department of Bioengineering
Rice University, 6100 Main St., MS-142, Houston, TX   77005
drezek@rice.edu
*Shared principal authorship

Abstract. Gold nanoshells are positioned to become a scattering-based contrast agent to improve the reflectance signals of nanoshell-targeted tissue. However, our study shows that a greater enhancement of nanoshell-induced reflectance signals can now be achieved when angularly oblique fiber geometries are used in place of the conventional orthogonal fiber geometry. This important finding was confirmed by conducting two experiments. First, diffuse reflectance spectra were collected from nanoshell-infused polystyrene phantoms at 0, 10, 20, 30 and 40 degree collection angles. At the 40 deg. fiber angle, the nanoshell-induced reflectance contrast, with respect to the native polystyrene phantom, is significantly increased. Based on these results, a reflectance study was then conducted for human cervical tissue treated with gold nanoshells at the 0 and 40 degree collection angles. Again, at the 40 deg. fiber angle, the signal level of the nanoshell-induced contrast in tissue is determined as statistically significant. Taken together, these results demonstrate that the use of the angularly oblique fiber geometry does significantly improve reflectance contrast.

Keywords: nanoshells, fiber probes, reflectance spectroscopy, scattering contrast.

1 INTRODUCTION

Of all gynecologic diseases in the United States, uterine-cervical cancer leads in mortality rate. Hence, early detection of cervical epithelial abnormalities is believed to be the best strategy in reducing this alarming statistic. However, many currently available screening techniques for epithelial cancers do not provide adequate sensitivity and specificity at the earliest stages of diagnosis and treatment. Thus, a more sensitive and quantitative diagnostic technique is required in order to identify diseased tissue at the early malignant stages.

A promising candidate, which meets these requirements, is reflectance spectroscopy because it has been shown that this method can characterize morphological changes in diseased tissue at various organ sites [1,2]. Since nearly 85% of all cancers originate in epithelia, specific probing of epithelia may help extract diagnostically useful information from this thin tissue. To accomplish this, recent studies have demonstrated that fiber geometry directly affects the spatial distribution of the detected reflectance and consequently changes the probing depths in tissue [3-8]. This then results in refining the selection and separation of epithelia from surrounding biological materials, which will, in turn, improve the accuracy of disease diagnosis for epithelial cancers.

Spatially-resolved reflectance spectroscopy has shown promising results in overcoming the spatial limitations associated with conventional reflectance-based techniques when implemented in turbid biological media. Indeed, optical contrast agents attract considerable attention in biophotonics because of their potential for detecting pathogenesis at molecular levels. For example, gold nanoshells can be labeled with particular antibodies that specifically conjugate to targeted proteins preferentially expressed by malignant cancer cells [9-11]. Consequently, a significant accumulation of nanoshells around cells, or in tissue, due

to this selective binding, can indicate the presence of malignancies which otherwise would remain undetected by traditional white light endoscopy. In addition to their utility as a contrast agent, gold nanoshells may also be used in photo-thermal therapy [12,13]. This procedure takes advantage of the ability of nanoshells to absorb NIR radiation and thus cause cancer cells to be thermally ablated by intense, albeit locally confined, heat. This procedure is highly selective and specific and results in minimal damage to the surrounding healthy tissue [12-14].

By varying their core/shell ratio and overall size, nanoshells can be produced with strong scattering or absorption efficiencies. Therefore, nanoshells can be used for either scattering-based contrast enhancements in imaging applications [12] or photo-thermal tissue ablation in therapeutic procedures [13,14]. Unfortunately, the scattering and absorptive properties of nanoshells are size-dependent, making it rather difficult to maximize one aspect of the nanoshells' optical characteristics without sacrificing the other. However, the use of an angularly-oblique fiber probe can overcome this complication. Specifically, the geometry of such probes results in more efficient detection of back-scattered photons and, thus, more efficiently detects the back-scattered reflectance from nanoshells. The consequence of using such fiber geometry is that nanoshell signals can be significantly increased to exceed those levels currently detectable with conventional orthogonal fiber probes.

2 METHODS AND MATERIALS
2.1 Nanoshell preparation

The gold nanoshells used in this study have two core sizes: 86 and 200 nm in diameter. The silica cores are synthesized using the Stöber method [15], with which tetraethylorthosilicate is synthesized into spherical colloids in ethanol. These Stöber spheres are then functionalized with aminopropyltriethoxysilane, resulting in silica cores with attached amine groups. Then, gold colloids (1-3 nm in diameter) adsorb to the amine group and provide nucleation for further reduction of gold [16]. The reduction of additional gold colloids onto the seeded cores results in a complete coalescence of gold shell. Prior to reflectance experiments, nanoshell surfaces are modified with thiolated polyethylene glycol to provide steric stabilization.

In all, four sizes of nanoshells are used for the phantom study. Beginning with the smallest, these nanoshells have core/shell diameters of 86/104, 86/124, 200/228 and 200/262 nm, as empirically determined by SEM measurements. Among the four types of nanoshells, the 86/104 nm nanoshells are particularly strong in their absorption efficiency, while the 200/268 nm nanoshells are, predominantly, strong in scattering efficiency. The other two sizes (86/124 and 200/228 nm) have similar levels of scattering and absorption efficiency at the targeted spectral wavelengths of this study (400 – 1000 nm).

For the tissue study, nanoshells with the core/shell diameters of 86/114 nm are used because they are produced after the completion of the phantom study. It should be noted that reproducing any one specific size of nanoshells is extremely difficult. Therefore, although it is certainly ideal to employ the same sizes of nanoshells for both the phantom and tissue experiments, the use of the 86/114 nm nanoshells for the latter is a reasonable compromise.

2.2 Polystyrene microsphere phantoms with gold nanoshells

Polystyrene phantoms are used to mimic the optical properties of human cervical tissue. These tissue phantoms have a depth of 25 mm, which is sufficient to represent an optically semi-infinite tissue, and a diameter of 22 mm, which is wide enough to encompass all optical paths collectible by our particular fiber geometry.

Mono-dispersed polystyrene microspheres are the sources of scattering for the phantoms. A mixture of polystyrene microspheres (5.43 µm in diameter) in water is used in

this study to provide scattering properties similar to those of human cervical tissue. India ink is added to the phantoms to provide adequate levels of absorption coefficients. The optical properties of human cervical tissue are based on the values reported by Collier [17], Drezek [18], and Chang [19] et al. that were previously adopted by Zhu [20], Skala [3] and Wang [5,7,8] et al. in their respective studies on epithelial tissue. The scattering coefficients (μ_s) and anisotropies (g) of the phantoms are calculated in accordance with Mie theory, and the absorption coefficients are experimentally determined. The values for the scattering (μ_s) and absorption (μ_a) coefficients of the polystyrene phantoms can be found in Fig. 1.
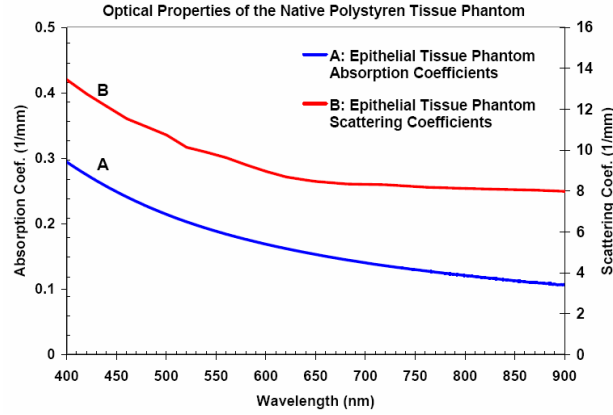
Fig. 1. The scattering and absorption coefficients of the native polystyrene phantom (5.43 µm) before addition of nanoshells.

To assess changes in reflectance signal after nanoshell addition, the four sizes of gold nanoshells, as noted above, are then mixed with the tissue phantoms. No more than 300 µL of nanoshell-suspensions are added to the phantoms, which have the original volume of 9.5 mL. The perturbation on the overall phantom volumes due to the added nanoshell suspensions is no more than 3%, thus eliminating the concern of significant dilution of the native phantom properties. By estimation using Mie theory, there are roughly 3 x 10^{10} nanoshells per cm^3 inside the phantoms.

2.3 Tissue preparation

Eight malignant and eight normal cervical tissue samples are infused with gold nanoshells. After removal from the freezer, the frozen tissue samples are placed and maintained on a cold plate for the duration of the experiment. The cold plate stabilizes at approximately 6 deg. Celsius and therefore retards the rate of structural degradation in tissue due to thawing. Consequently, the tissue sample properties remain reasonably constant during the experiment (approximately 1 hour from the time of tissue retrieval from the freezer). As noted above, we use only the 86/114 nm nanoshells for the tissue study. Two hundred µL of nanoshell fluid (5 x 10^{10}/mL) are directly injected into the cervical tissue samples via 25 gauge needles. The needles penetrate no more than 1 mm into the tissue. Fifteen minutes after the injection, the tissue samples are rinsed with buffered saline to remove loose nanoshells on or above the tissue, and the reflectance is measured.

It should be noted that, due to phenomenon such as loss of nexus [21] and increased extra-cellular space [22, 23], the physical structures of dysplastic tissue is more porous than those of normal tissue. As a consequence, abnormal tissue is receptive to nanoshell injection.

In contrast, it is much more difficult to pierce normal tissue, which has strong structural resilience against the introduction of foreign objects or elements. While we did successfully pierce the normal tissue, nanoshell retention in this tissue is less than optimal. By our visual observations, the abnormal tissue seems to absorb more nanoshell fluid than the normal tissue; therefore, we believe that the increased permeability of particles in dysplastic tissue would facilitate nanoshell redistribution and retention. On the other hand, a large portion of the injected nanoshell fluid leaked out of the normal tissue because the space between tissue fibers was insufficient to accommodate the entire 200 µL of nanoshell fluid.

Since the normal and abnormal tissues retain unequal amounts of nanoshells, quantitative comparisons between the two are slightly less straightforward. Nonetheless, epidermal injection of nanoshells in tissue, in our opinion, is still valid since the unequal nanoshell retentions directly result from the tissues' natural physical properties. Thus, similar observations would appear in all tissue studies, both *in vitro* and *in vivo*. Significantly, we believe that the preferential retention of nanoshells is a natural attribute of the dysplastic tissue. This creates conditions which, in fact, improve the ability of nanoshells to preferentially target diseased tissue. This study focuses on enhancing the capabilities of nanoshell-induced signals in tissue, regardless of the tissue types. Since we are primarily interested in comparing spectra obtained from the same tissue at different fiber angles, the amount of nanoshells retained by either tissue type is, from our perspective, not the focus of this study.

2.4 Fiber geometry

The configuration of the source and collection fibers is controlled with a fiber stage that independently adjusts the fiber obliquity with respect to the normal and malignant tissues. Throughout this study, we maintain the source fiber at the orthogonal orientation and only investigate the angles of the collection fiber in relation to the target surface. Tissue phantom reflectance is sampled at 0, 10, 20, 30 and 40 degrees; based on the phantom study, tissue reflectance is sampled at two collection angles, 0 and 40 degrees, measured out of the plane of tissue surface. The operational uncertainty of the fiber angles is smaller than 0.5° in magnitude. The source and collection fibers, of which the core diameter and nominal numerical aperture are 200 µm and 0.22, are connected to a broadband light source and spectrophotometer, respectively. The distance between the source and collection fibers, measured from their respective geometric center, is 300 µm. All reflectance measurements are referenced to a 99% reflectance standard when the fibers are at 0 degree. Since reflectance intensities collected at the 40 deg. angle are in multiples of those collected at the 0 deg. angle, the reflectance reading for the 40 deg. fibers may exceed 100%.

3 RESULTS
3.1 Nanoshells in tissue phantoms

Figures 2A and B show the reflectance spectra obtained from the 86/104 and 86/124 nm nanoshell-phantoms and native polystyrene phantom at 0 and 40 deg. fiber angles, respectively. At the 0 degree, both nanoshell-infused polystyrene phantoms, in fact, have lower reflectance than the native polystyrene (non-nanoshell) phantom at wavelengths smaller than 700 nm. At longer wavelengths, where the nanoshell scattering efficiency surpasses that of the polystyrene microspheres, we begin to observe noticeable nanoshell signals, and the reflectance levels are enhanced due to the nanoshell infusions. However, when the fiber angle increases to 40 degrees, we observe significant increases of reflectance from the nanoshell-phantoms relative to those of the native polystyrene phantom. Similar trends are seen for the

200/228 and 200/268 nm nanoshell-phantoms with respect to the native polystyrene phantoms, as shown in Fig. 3A and B.
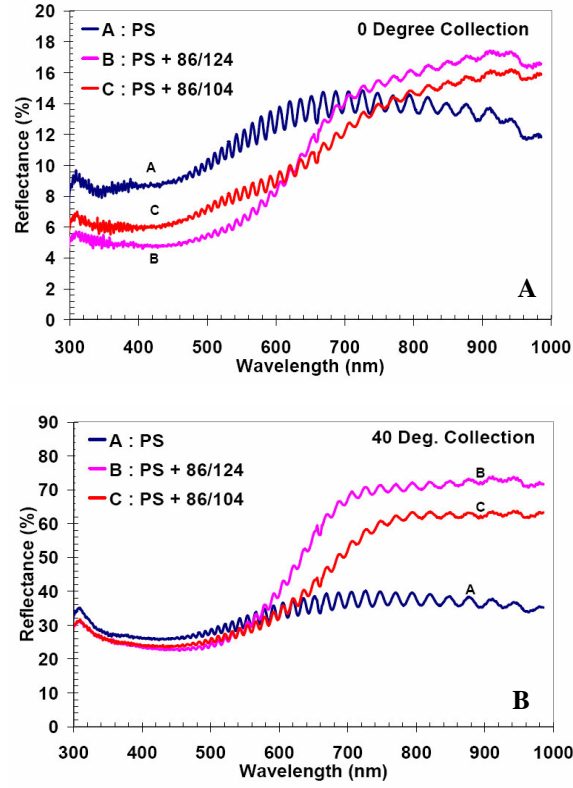
Fig. 2. Reflectance spectra of native polystyrene phantom and nanoshell-infused (86/104 and 86/124 nm) phantoms at (A) 0 deg. and (B) 40 deg. collection fiber angles.

In order to quantitatively assess the contributions of nanoshell reflectance relative to those of the polystyrene beads, we calculate the integrated reflectance intensity of the phantoms across the wavelength spectrum (400 – 1000 nm). The term "area under curve" or AUC is used to denote this metric. We then define the contrast supplied by the nanoshells in the phantoms as a ratio between the AUC of the nanoshell-infused phantoms and the AUC of the native polystyrene phantom. The mathematical formulation of the nanoshells' contrast in the phantoms is expressed in Eq. (1).

$$Contrast(Nanoshell + PS\ Phantom) \equiv \frac{AUC(Nanoshell + PS\ Phantom)}{AUC(PS\ Phantom)} \qquad (1)$$

This ratio thus serves as a quantitative measurement of the nanoshells' contribution to the detected reflectance as an exogenous contrast agent in the tissue phantoms. As shown in Fig. 4A and B, invariantly stronger reflectance contrasts are detected from the nanoshell-infused phantoms at higher angles than those detected at lesser angles. More significantly, with the orthogonal fiber geometry (0 deg.), three of the four nanoshell-infused phantoms produce lower reflectance intensities than the native polystyrene phantom, indicating that the absorptive effect due to nanoshells may, in fact, supersedes the scattering increase and

consequently results in lower reflectance signals. Effectively, their AUC ratios are smaller than 1, which equivalently signifies a negative contrast that actually diminishes the reflectance signal from the phantoms. Since our premise of using exogenous contrast agent is to increase the reflected signal, the instances of diminished reflectance from the nanoshell-infused phantoms are undesirable.
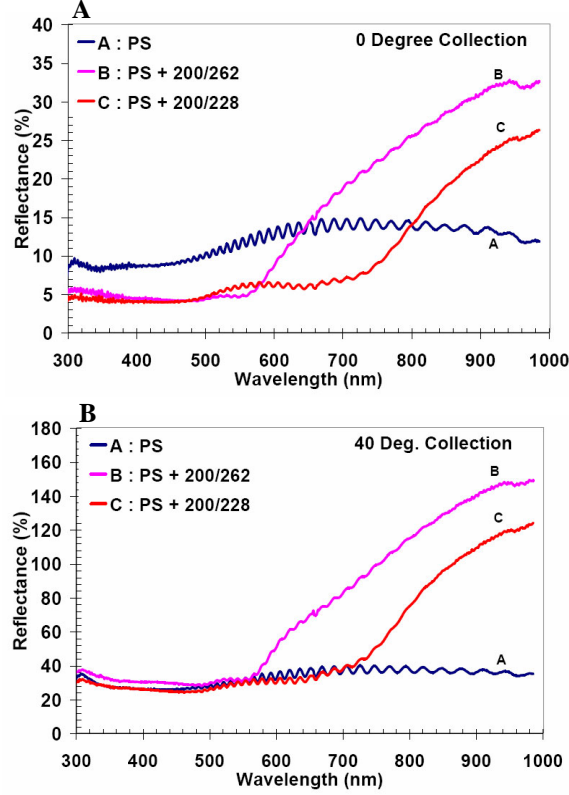
Fig. 3. Reflectance spectra of native polystyrene phantom and nanoshell-infused (200/228 and 200/262 nm) phantoms at (A) 0 deg. and (B) 40 deg. collection fiber angles.

Table 1 lists the contrast levels induced by nanoshells when the nanoshell-phantoms are measured at both 0 and 40 deg. fiber angles. The level of contrast increase is defined as the difference of the contrast ratios, as defined in Eq. (1), between the nanoshell-infused and native polystyrene phantoms. The explicit formulation of this metric is shown in Eq. (2).

$$Contrast\,Increase \equiv \frac{AUC(Nanoshell + PS\ Phantom)}{AUC(PS\ Phantom)} - \frac{AUC(PS\ Phantom)}{AUC(PS\ Phantom)}$$

$$= \frac{AUC(Nanoshell + PS\ Phantom)}{AUC(PS\ Phantom)} - 1 \qquad (2)$$
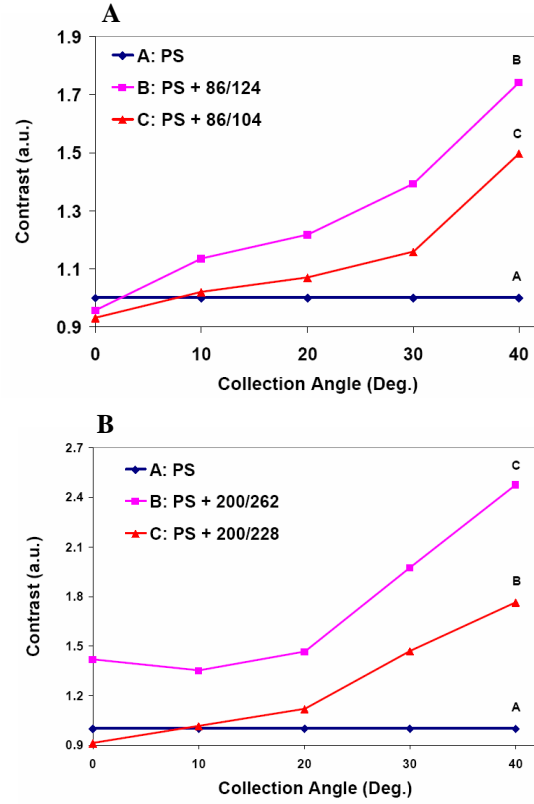
Fig. 4. Nanoshell-induced contrast with respect to the native polystyrene phantom of (A) 86/104 and 86/124 and (B) 200/228 and 200/262 nm sizes of gold nanoshells.

Table 1. Nanoshells-induced contrast with respect to the native PS phantom at 0 and 40 deg. collection fiber angles.

Fiber Angles	Types of Nanoshells in PS Phantoms			
	86/124 nm	86/104 nm	200/262 nm	200/228 nm
0 Deg.	-4.36%	-6.86%	41.72%	-8.95%
40 Deg.	74.07%	49.54%	147.4%	76.34%

Among the four different sizes of nanoshells (86/104, 86/124, 200/228 and 200/262 nm) infused in the polystyrene phantoms, we obtain a consistent trend which indicates that nanoshell-induced reflectance contrasts, when sampled at the 40 deg. angle, are considerably higher than those sampled at the orthogonal fiber geometry. This, in turn, leads us to conclude that nanoshell-induced scattering signals can be better detected at higher fiber angles, and the expected contrast enhancement is, consequently, more significant. In contrast, at the 0 deg. fiber angle, 3 out of the 4 nanoshell-infused phantoms exhibit negative contrasts with respect to the native polystyrene phantom.

3.2 Nanoshells in cervical tissue

Figures 5A and B contain the reflectance spectra measured from the human cervical tissues both before and after the injection of nanoshells. Figure 5A contains the data collected from the normal cervical tissues, and Fig. 5B contains the abnormal tissue data. The standard deviations of the measurements are displayed at the 750 nm wavelength, where the peak of nanoshell reflectance is located. With the 0 deg. fiber geometry, the resultant reflectance spectra of the tissue after nanoshell injection virtually overlap those measured before the nanoshell introduction in tissue, and consequently little evidence of nanoshell scattering is present in the reflectance spectra for either tissue type. On the other hand, significant nanoshell-induced contrast is present in the tissue spectra when the 40 deg. fibers are used.
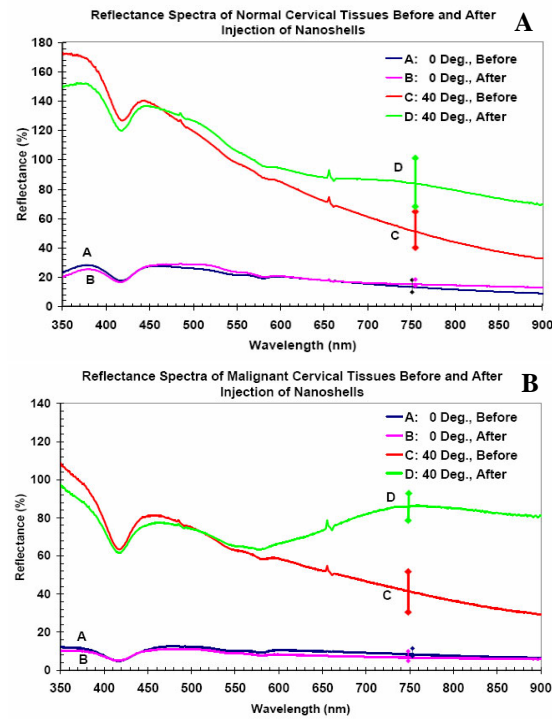
Fig. 5. Reflectance spectra measured from the (A) normal and (B) abnormal human cervical tissues both before and after the injection of nanoshells.
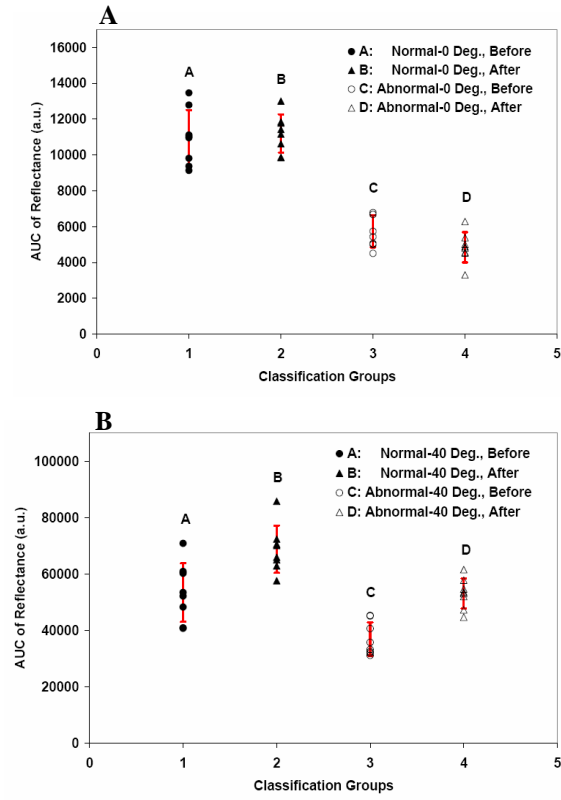
Fig. 6. AUC distributions of the classification groups (normal and abnormal tissues before and after nanoshell application) when measured at (A) the 0 deg. and (B) 40 deg. fiber angle.

Table 2. Significance levels (p-values) of Wilcox rank-sum test (two-tailed) between the tissue samples before and after application of gold nanoshells at 0 and 40 deg. collection fiber angles.

Group Discrimination: Before v. After Nanoshell Application	Fiber Angles	
	0 Deg.	40 Deg.
Normal Tissues	0.430	0.013
Abnormal Tissues	0.066	0.001

In the abnormal cervical tissue, the nanoshell signals are especially strong and definitive. In order to quantify the level of significance of nanoshell-induced contrast, we calculated the integrated intensity of the spectra, or AUC, of the tissue samples before and after the injection of nanoshells for both normal and malignant tissues. The AUC values of the individual tissue samples are shown in Fig. 6A and B. Figure 6A, which represents the AUC distributions of the tissue spectra when the 0 deg. fibers are used, indicates a limited intensity difference caused by the application of nanoshells in tissue. In contrast, Fig. 6B shows that significant intensity differences are observable, particularly for the abnormal tissues, when the 40 deg. fibers are used. Further, based on the AUC value, we calculated the statistical significance of nanoshell-induced contrast among the tissue samples by using Wilcox rank-sum test (two-tailed). The Wilcox test is a non-parametric test, which is appropriate for the small number of samples used in this study, for which a normal distribution can not be assumed. The results of the Wilcox rank-sum test are shown in Table 2, and, based on these data, we observe that the level of nanoshell-induced contrast is significantly stronger when tissue-nanoshell reflectance is collected at the 40 deg. fiber angle than instances where the 0 deg. angle is used. However, more interestingly, the nanoshell-induced contrast in the abnormal tissue (p-value = 0.001) is more significant than that in the normal tissue (p-value = 0.013), even when the 40 deg. fiber angle is used for both tissue types. The stronger significance of nanoshell-induced contrast in the abnormal tissue is most likely the consequence of the preferential retention of nanoshell fluids following the epidermal injection, as previously discussed in the penultimate paragraph of section 2.3.

4 DISCUSSION
4.1 The phantom study

Our initial hypothesis speculates that nanoshell signals can be better collected with oblique fiber geometry than with the conventionally utilized orthogonal fibers. This hypothesis originates from the anisotropic behavior of nanoshell scattering. To explain, the nanoscopic dimensions of nanoshells induce particularly strong back-scattering, while most tissues and cellular elements are predominantly forward scattering. This makes nanoshells a strong candidate for use as a scattering-based contrast agent. However, this enhanced back-scattering may not necessarily translate to increased reflectance measurements when the geometry of the detector is not correspondingly optimized for back-scattered signals from shallow depths of tissue. Specifically, because the 0 deg. fiber geometry is primarily sensitive to deeper tissue depths, the superficially scattered light by nanoshells is unlikely to be detected by the same fiber geometry. The contribution of nanoshell-induced contrast is consequently diminished. The oblique fiber geometry [3-8], on the other hand, is particularly sensitive to superficially scattered light in tissue and is, therefore, more likely to enhance the nanoshell signals, consequently producing greater contrast in tissue reflectance.

The phantom study is an appropriate model by which to confirm the validity of our hypothesis. Accordingly, the data shown in section 3.1 do substantially confirm our hypothesis because the results demonstrate that the nanoshell-infused phantoms do exhibit stronger reflectance than the native polystyrene phantoms when the 40 deg. fibers are used in place of the conventional orthogonal fibers. Interestingly, due to the absorptive properties of nanoshells, the added nanoshells actually result in less reflectance signal and an equivalence of "negative" contrast, when the orthogonal fiber geometry used. This is undesirable for applications of scattering-based imaging or spectroscopy that demand exogenous contrast agents to augment the reflected signal levels beyond those of native cellular or tissue materials. However, by using an epithelial-simulating polystyrene phantom, we have successfully demonstrated that, with gradual increase of the collection angle, the contrast between the nanoshell-infused and native polystyrene phantoms consistently increases, as noted above. More importantly, by applying the 40 deg. fibers, we are able to use the 86/104

nm nanoshells, which are conventionally regarded as strongly absorbing nanoshells and thus not suitable for imaging applications, to produce at least 50% more reflectance than the native polystyrene phantoms.

4.2 The tissue study

Reflectance measurements are taken from the normal and malignant cervical tissues before and after application of nanoshells. Based on the data shown in section 3.2, we are able to achieve consistent results, which confirm the enhanced nanoshell contrast in tissue. From the results shown in Fig. 5A and B, it is clear that nanoshell-induced contrast is much more conspicuous when the collection fiber is oriented at 40 degrees. On the other hand, little differentiation can be made between the naked and nanoshell-infused tissue when the orthogonal fiber geometry is used, which limits the potential of using nanoshells as effective scattering-based tumor markers when the fiber geometry is not optimized. In particular, the spectral characteristics of the nanoshells are best manifested in the reflectance spectra of the abnormal tissue. This is true because nanoshells can preferentially accumulate in abnormal tissue due to its porous and permeable structure, as previously discussed in the penultimate paragraph in section 2.3. In addition, the preferential accumulation of nanoshells in tissue can be further amplified when nanoshells are labeled with antibodies that specifically conjugate to malignant cells. Because of this selective binding, nanoshell-specific spectral signals can indicate the presence of pathogenesis which otherwise would remain undetected by traditional white light endoscopy. However, in order to determine the level of nanoshell accumulation in tissue and successfully implement this strategy, two requirements must be met: (1) the excitation of strong nanoshell signals from the nanoshell-rich tissue regions and, more importantly, (2) significant differentiation based on the reflected signals (in the context of this work, the reflectance levels, or AUC). However, based on the result given in section 3.2, virtually no spectral or intensity difference is seen after the nanoshell injection in tissue when the 0 deg. fiber is the selected fiber geometry for reflectance measurement.

Comparing the normal and malignant tissue, it is also clear that the malignant tissue, as expected, favorably retains the injected nanoshells and, therefore, exhibits greater nanoshell-induced reflectance contrast than the normal tissue. It is also encouraging to observe significant nanoshell-induced contrast in the abnormal tissue samples, although we did not administer antibody conjugation in this study. As discussed in section 2.3, the preferential retention of nanoshells in abnormal tissue is most likely attributed to the increased permeability of the malignant tissue, a phenomenon which should be consistent for all *in vitro* and *in vivo* studies. Thus, we expect even greater improvement of nanoshell-induced contrast when specific antibodies are conjugated onto the nanoshell surface. As noted above, antibody targeting is not used in this study. Nevertheless, we can still identify the pathological status of the tissue samples (normal v. malignant) based on the nanoshell-induced signals present in the overall reflectance spectra, as shown in Fig. 6A and B. In the malignant tissue, the nanoshell-induced contrast is considerably stronger than that for the normal tissue. The affirming observations that nanoshells are an effective source of exogenous scattering contrast can be seen from the AUC results shown in Table 2 and Fig. 6A and B. These data, based on the statistical discrimination of the Wilcox rank-sum test, also confirm that the use of nanoshells results in more significant reflectance contrast in the malignant tissue than in the normal tissue, as demonstrated by their respective AUC values. Most importantly, we consistently observed increased nanoshell-induced contrast for both tissue types when the 40 deg. fiber is used in place of the 0 deg. fiber. This strongly suggests the possibility of enhancing nanoshell signals in tissue environments by using obliquely oriented fiber geometry.

5 CONCLUSION

We have found that the detection capability of nanoshell-induced scattering contrast, in both tissue phantoms and human cervical tissues, increases as the obliquity of collection fibers increases. More specifically, by using an oblique collection fiber at the 40 deg. angle, the nanoshell-induced signals in both tissue phantoms and cervical tissues are significantly higher and discernable than those detected with the conventional orthogonal fiber geometry. In the phantom study, we have also demonstrated that the 86/104 nm nanoshells, which are conventionally regarded as absorbing nanoshells, can be used in applications that demand high scattering contrast. With the 86/104 nm nanoshells, we were able to produce at least 50% more reflectance than the native polystyrene phantom by using the 40 deg. fibers, indicating the possibility of using predominantly absorbing nanoshells for scattering-based contrast enhancement.

For the tissue study, the same conclusion is drawn: that the use of a higher fiber angle (40 deg.) considerably increases nanoshell-induced contrast. Based on the results of this *in vitro* experimentation, we have established a pilot study that addresses the possibility of combining nanoshells and angularly-variable fiber geometries to increase the level of nanoshell-induced contrast in tissue reflectance, which may consequently result in more accurate diagnoses of tissue pathologies, particularly cancer. This study, then, lays a substantial foundation upon which to build future efforts focusing on the development of specialized nanoshells for tissue imaging and reflectance enhancement. Such efforts include the use of antibody conjugation to specifically target tissue dysplasia, the use of larger sizes of tissue and nanoshell samples, and the design of fiber geometry with respect to specific types of nano-particles and *in vivo* experimentation.

Acknowledgements

References

[1] I. Bigio and J. R. Mourant, "Ultraviolet and visible spectroscopies for tissue diagnostics: fluorescence spectroscopy and elastic-scattering spectroscopy," *Phys. Med. Biol.* **42**, 803–814 (1997) [doi:10.1088/0031-9155/42/5/005].

[2] K. Sokolov, R. Drezek, K. Gossage, and R. Richards-Kortum, "Reflectance spectroscopy with polarized light: is it sensitive to cellular and nuclear morphology," *Opt. Exp.* **5**(13), 302-17 (1999).

[3] M. Skala, G. Palmer, C. Zhu, Q. Liu, K. Vrotsos, C. Marshek-Stone, A. Gendron-Fitzpatrick, and N. Ramanujam, "Investigation of fiber-optic probe designs for optical spectroscopic diagnosis of epithelial pre-cancers," *Lasers Surg. Med.* **34**, 25–38 (2004) [doi:10.1002/lsm.10239].

[4] L. Nieman, A. Myakov, J. Aaron, and K. Sokolov, "Optical sectioning using a fiber probe with an angled illumination-collection geometry: evaluation in engineered tissue phantoms," *Appl. Opt.* **43**(6), 1308-19 (2004) [doi:10.1364/AO.43.001308].

[5] A. Wang, J. Bender, J. Pfefer, U. Utzinger, and R. A. Drezek, "Depth-sensitive reflectance measurements using obliquely oriented fiber probes," *J. Biomed. Opt.* **10**(4), 044017 (2005) [doi:10.1117/1.1989335].

[6] D. Arifler, R. Schwarz, S. Chang, and R. Richards-Kortum, "Reflectance spectroscopy for diagnosis of epithelial precancer: model-based analysis of fiber-optic probe designs to resolve spectral information from epithelium and stroma," *Appl. Opt.* **44**(20), 4291-305 (2005) [doi:10.1364/AO.44.004291].

[7] A. Wang, V. Nammalvar, R. Drezek, "Targeting spectral signatures of progressively dysplastic stratified epithelia using angularly-variable fiber geometry in reflectance Monte Carlo simulations," *J. Biomed. Opt.*, Under Review (2007).

[8] A. Wang, V. Nammalvar, R. Drezek, "Experimental evaluation of angularly-variable fiber geometry for targeting depth-resolved reflectance from layered epithelial tissue phantoms," *J. Biomed. Opt.*, Under Review (2007).

[9] C. Loo , A. Lowery, N. Halas, J. West & R. Drezek, "Immunotargeted nanoshells for integrated cancer imaging and therapy," *Nano. Lett.* **5**(4), 709–711 (2005) [doi:10.1021/nl050127s].

[10] C. Loo , L. Hirsch, M. Lee, E. Chang, J. West, N. Halas & R. Drezek, "Gold nanoshell bioconjugates for molecular imaging in living cells," *Opt. Lett.* **30**(9), 1012–1014 (2004) [doi:10.1364/OL.30.001012].

[11] M. H. Lee, V. Nammalvar, A. Gobin, J. Barton and J. West, "Nanoshells as contrast agents for scatter-based optical imaging," *Biomedical Imaging: Macro to Nano, 2006. 3rd IEEE International Symposium.*, 371-374 (2006) [doi: 10.1109/ISBI.2006.1624930].

[12] L. R. Hirsch, R. J. Stafford, J. A. Bankson, S. R. Serchen, B. Rivera, R. E. Price, J. D. Hazle, N. J. Halas, J. L. West, "Nanoshell-mediated near-infrared thermal therapy of tumors under magnetic resonance guidance," *PNAS.* **100** (11), 13549. (2003) [doi:10.1073/pnas.2232479100].

[13] D.P O'Neal, L.R Hirsch, N.J Halas, J.L West "Nanoshell-assisted photothermal ablation of colon carcinoma-derived tumors in mice." *Cancer Lett.* **209**, 171-6 (2004).

[14] A. Gobin, D. O'Neal, N. Halas, R. Drezek, and J. West, "Near infrared laser tissue welding using nanoshells as an exogenous absorber," *Lasers in Surg. and Med.* **37**, 123-129 (2005) [doi:10.1002/lsm.20206].

[15] W. Stober, A. Fink and E. Bohn " Controlled growth of nanodisperse silica spheres in the micron size range," *J. Colliod Interface Sci.* **26**, 62-69 (1968) [doi:10.1016/0021-9797(68)90272-5].

[16] D. G. Duff, A. Baiker, "A new hydrosol of gold clusters,. 1. formation and particle size variation," *Langmuir* **9,** 2301 (1993) [doi:10.1021/la00033a010].

[17] T. Collier, P. Shen, B. de Pradier, K. B. Sung, R. Richards-Kortum, "Near real time confocal microscopy of amelanotic tissue: dynamics of aceto-whitening enable nuclear segmentation," *Opt. Exp.* **6**(2), 40-48 (2000).

[18] R. Drezek, R. Richards-Kortum, M. Brewer, M. Feld, C. Pitris, A. Ferenczy, M. Faupel, and M. Follen, "Optical imaging of the cervix," *Second Intl. Conf. Cervical Cancer*, 2015–2027 (2003).

[19] S. Chang, D. Arifler, R. Drezek, M. Follen, and R. Richards-Kortum, "Analytical model to describe fluorescence spectra of normal and preneoplastic epithelial tissue: comparison with Monte Carlo simulations and clinical measurements," *J. Biomed. Opt.* **9**(3), 511–522 (2004) [doi:10.1117/1.1695559].

[20] C. Zhu, Q. Liu, and N. Ramanujam, "Effect of fiber optic probe geometry on depth-resolved fluorescence measurements from epithelial tissues: a Monte Carlo simulation," *J. Biomed. Opt.* **8**(2), 237–247 (2003) [doi:10.1117/1.1559058].

[21] N. McNutt, R. Hershberg, R. Weinstein, "Further observations on the occurrence of nexuses in benign and malignant human cervical epithelium," *J. Cell Biology* **51**, 805-825 (1971) [doi:10.1083/jcb.51.3.805].

[22] J. Sugar, "An electron microscopic study of early invasive growth in human skin tumors and laryngeal carcinoma," *Eur. J. Cancer* **4**, 33-38 (1968) [doi:10.1016/0014-2964(68)90067-4].

[23] F. White, K. Gohari, "Alterations in the volume of the intracellular space between epithelial-cells of the hamster cheek-pouch," *J. Oral Pathol. Med.* **13,** 244-54 (1984) [doi:10.1111/j.1600-0714.1984.tb01422.x].

Impaired angiogenesis in aminopeptidase N-null mice

Roberto Rangel*, Yan Sun*, Liliana Guzman-Rojas*, Michael G. Ozawa*, Jessica Sun*, Ricardo J. Giordano*, Carolyn S. Van Pelt†, Peggy T. Tinkey†, Richard R. Behringer‡, Richard L. Sidman§¶, Wadih Arap*¶‖, and Renata Pasqualini*¶‖

Departments of *Genitourinary Medical Oncology, ‖Cancer Biology, ‡Molecular Genetics, and †Veterinary Medicine and Surgery, University of Texas M.D. Anderson Cancer Center, 1515 Holcombe Boulevard, Houston, TX 77030; and §Harvard Medical School and Department of Neurology, Beth Israel Deaconess Medical Center, Harvard Institutes of Medicine, 77 Avenue Louis Pasteur, Boston, MA 02115

Aminopeptidase N (APN, CD13; EC 3.4.11.2) is a transmembrane metalloprotease with several functions, depending on the cell type and tissue environment. In tumor vasculature, APN is overexpressed in the endothelium and promotes angiogenesis. However, there have been no reports of _in vivo_ inactivation of the APN gene to validate these findings. Here we evaluated, by targeted disruption of the APN gene, whether APN participates in blood vessel formation and function under normal conditions. Surprisingly, APN-null mice developed with no gross or histological abnormalities. Standard neurological, cardiovascular, metabolic, locomotor, and hematological studies revealed no alterations. Nonetheless, in oxygen-induced retinopathy experiments, APN-deficient mice had a marked and dose-dependent deficiency of the expected retinal neovascularization. Moreover, gelfoams embedded with growth factors failed to induce functional blood vessel formation in APN-null mice. These findings establish that APN-null mice develop normally without physiological alterations and can undergo physiological angiogenesis but show a severely impaired angiogenic response under pathological conditions. Finally, in addition to vascular biology research, APN-null mice may be useful reagents in other medical fields such as malignant, cardiovascular, immunological, or infectious diseases.

CD13 | knockout mice | retinopathy | vasculogenesis

The aminopeptidases are a large family of proteolytic enzymes that affect protein maturation, degradation, and regulation (1, 2). Aminopeptidase N (APN) is a membrane-bound zinc-dependent metalloprotease originally identified as a surface marker in myeloid cells (3, 4). APN is widely distributed in many cell types, and its role in hydrolyzing unsubstituted N-terminal residues with neutral side chains varies in different locations. In the epithelium of the renal proximal tubule, APN cleaves its only known natural substrate, angiotensin (ang) III, to ang IV; in synaptic membranes, APN metabolizes enkephalins and endorphins; in the heart, it is an integral component of cardiac remodeling postmyocardial infarction (5–10); and in the respiratory system, APN is the cell surface receptor for certain human coronaviruses and potentially for the severe acute respiratory syndrome (SARS) virus (11–13). Additionally, APN functions in signal transduction, cell cycle control, and differentiation (14, 15).

We have developed an _in vivo_ system by using ligand peptides displayed on the surface of phage to study organ- and tumor-specific vascular homing; this methodology enables the identification of vascular markers (16, 17). We have isolated phage displaying an asparagine-glycine-arginine (NGR)-containing peptide in a tumor-homing selection and have shown that these phage bind selectively to angiogenic blood vessels. When coupled to a cytotoxic drug (18) or fused to a proapoptotic peptide (19) or to tumor necrosis factor (20), NGR-targeted compounds were more effective and less toxic than the respective controls. The cell surface receptor for NGR-containing ligands was then shown to be APN (21). Of note, although a single gene encodes APN, specific phenotypic forms of APN (CD13) in angiogenic

vasculature relative to normal tissues further enhance the targeting attributes of the NGR motif (22).

To evaluate the effects of the APN gene on development and organ function, we produced a knockout mouse lacking APN. This has been technically challenging because of the incomplete genomic characterization and complex APN gene structure. Here we report the generation of an APN-null mouse by homologous recombination and a description of its phenotype. Despite its broad expression, the APN gene is not essential for development, because the null was not embryonically lethal and developed normally. Standard phenotype characterization revealed no differences between WT and APN-null mice. However, in a model of retinal neovascularization, APN-null mice had a significant decrease in blood vessel growth compared with WT. Moreover, gelfoam plug assays demonstrated a reduction in hemoglobin content within the plugs, indicating lack of a functional vasculature. Thus, although APN activity is not essential for embryonic and fetal development including _de novo_ blood vessel formation (i.e., vasculogenesis) and normal adult function, it is critical for the pathological development of new blood vessels from existing blood vessels (i.e., angiogenesis) in disease.

Results

APN-Null Mouse Generation. Early attempts to isolate the APN gene have been problematic because of the absence of genomic clones in the 5′ region of the gene. To overcome this limitation, a combined screening of 129S6/SvEv Tac BAC libraries and BLAST analysis served to obtain the complete sequence of the mouse APN gene in a C57BL/6 background. Indeed, previous reports on gene characterization revealed variation in restriction enzyme maps between different genetic backgrounds. Integrated Southern blot and bioinformatics revealed that the APN gene in C57BL/6 and 129Sv/Ev backgrounds possessed the same restriction enzyme map (data not shown). APN exon–intron boundary analysis showed that exon 5 contained the nucleotide sequence that encodes the zinc-binding domain. Thus, our strategy (Fig. 1) was to eliminate expression and enzymatic activity by replacing APN exons 1–6 (Fig. 1a). After mouse embryonic stem (ES) cell screening, we detected 3 of 600 ES cell clones that contained the APN mutant allele; mutant ES clones were injected into C57BL/6 blastocysts and produced a single

Fig. 1. Generation and characterization of the APN-null mouse. (*a*) Schema of the APN gene-targeting strategy. The APN gene contains 20 exons (black boxes); the 3′ external probe is located in exon 14. The targeting vector contains a β-galactosidase transgene and a floxed neomycin resistant gene. (*b*) Southern blot of genomic DNA from WT (+/+), APN-heterozygous (+/−), and APN-null (−/−); the mutant allele (8 kb) and the WT allele (11 kb) are noted. The APN heterozygous contains both alleles. (*c*) PCR genotyping reveals unique products for WT (879-bp) and APN-null (320-bp) mice. The APN heterozygous contains both PCR products.

chimeric mouse, which was used for mating with C57BL/6 mice. After 5 mo, we detected the first germ-line transmission in a 129Sv/Ev-C57BL/6 genetic background. The first three generations of progeny were genotyped by either Southern blot (Fig. 1*b*) or PCR (Fig. 1*c*). Despite strong RNA expression during embryogenesis, Mendelian inheritance of the APN-null allele occurred [supporting information (SI) Fig. 8].

Inactivation of APN in the Null Mouse. APN expression was examined at the RNA and protein level, focusing initially on the nervous and renal systems, because APN is highly expressed in the pericytes associated with the brain endothelium and in the proximal tubules of the kidney. RT-PCR and immunohistochemical analysis showed a total absence of mRNA and protein in the brain and kidney of APN-null mice (Fig. 2). In contrast, WT mice displayed a strong expression of mRNA and protein in those organs. Similar results were observed in the spleen, liver, pancreas, intestine, and ovary (Fig. 3). Notably, a gene dosage

Fig. 2. Expression analysis of the APN-null mouse. (*a*) RT-PCR analysis of total RNA. The WT (+/+) and heterozygous (+/−) mice contain the 1.2-kb PCR product representing the APN mRNA transcript that is undetectable in the APN-null mouse (−/−). The G3PDH transcript served as a loading control. (*b*) Immunohistochemical analysis of the APN protein in brain (*Upper*) and kidney (*Lower*). APN immunoreactivity (red fluorescence) is detected in renal tubules and in pericytes within brain vasculature of WT and heterozygous mice but not in the APN-null mice (*Right*). (Scale bar, 100 μm.)

Fig. 3. Immunohistochemical analysis of APN and CD31. Colocalization studies in pancreas, liver, and spleen for APN (red fluorescence) and CD31 (green fluorescence) were performed in frozen tissue sections (*Upper*). The WT and APN-heterozygote mice contain dual fluorescence signals; in APN-null mice, only CD31 immunoreactivity is detected. Ovary and intestine were also evaluated (*Lower Left*). Brain was costained with anti-CD31 and -APA antibodies. The yellow fluorescence reflects the localization of both proteins in pericytes in brain vasculature (*Lower Right*).

effect was observed for the heterozygous animal (Figs. 2 and 3). Because aminopeptidase A (APA) is another member of the aminopeptidase family with similar expression patterns to that of APN (23), APA expression was examined as a surrogate to ensure that loss of APN did not affect normal tissue organization. Colocalization analysis between WT and the APN-null revealed no change in the expression profile of APA in brain pericytes despite the loss of APN (Fig. 3). These data support the genetic generation of a viable APN-null mouse.

Histopathological Studies in the APN-Null Mouse. A comprehensive panel of organs of 12-wk-old male and female mice was examined in H&E-stained sections. No structural differences were found between WT and APN-null mice (SI Fig. 9 *a–d*). Blood counts showed no differences in all parameters (SI Table 1), and serum chemistries indicated there were no significant electrolyte imbalances between WT and APN-null mice (SI Table 2). These results are consistent with full APN-null mouse viability.

Noninvasive Phenotypic Studies in the APN-Null Mouse. The function of APN appears to depend on its tissue localization. Thus, system functions (i.e., neurological, cardiovascular, metabolic, and locomotor) were compared to explore whether the deficiency of APN altered physiology (Fig. 4). First, activity tests were performed in an open field to determine any behavioral alterations
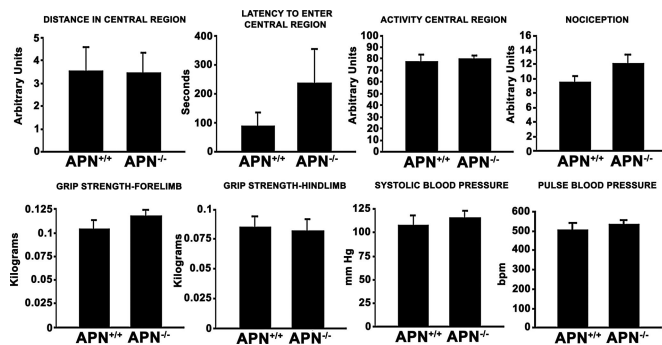
MEDICAL SCIENCES

Fig. 4. Noninvasive phenotypic studies. Spontaneous locomotor activity in WT mice and APN-null littermates are represented as distance in central region, latency central region, and activity central region. Nociception was measured by using a hot-plate analgesia meter. Neuromuscular function was determined by grip strength of the forelimb and hindlimb. Pulse and blood pressure were measured by the tail-cuff method. Error bars indicate SEM of WT and APN-null mice ($n = 6$ per group).

Fig. 5. Comprehensive in-cage monitoring system. The WT and APN-null mice littermates were examined for respiratory exchange ratio, oxygen uptake, and carbon dioxide production. Caloric intake and energy metabolism were measured for heat production, food, and water consumption. Ambulation and rearing activity were determined by using the comprehensive laboratory animal-monitoring system. Error bars indicate SEM of WT and APN-null mice ($n = 6$ per group).

in the APN-null mouse. Data were plotted for the time required for the mice to reach the central region, latency to enter it, and activity within that area of the field. No statistically significant differences in behavior were found. Next, neuromuscular function was assessed by muscle grip strength and showed no differences between the two groups. Finally, thermal and pain reflexes were assessed when the APN-null mouse footpad was placed against a heated surface; we noted a small increase in pain resistance when compared with the WT mouse (Fig. 4).

Noninvasive tail cuff measurements were used for blood pressure and pulse measurements. APN-null mice had normal baseline pulse and blood pressure (Fig. 4). Cardiovascular analysis by noninvasive unrestrained measurements revealed no statistical differences in baseline electrocardiogram heart rate and its variability or waveform intervals (SI Figs. 10 a and b). These data indicate that APN is not critical in regulation of cardiovascular function under normal conditions.

Body composition and whole-body metabolism served as surrogates for endocrine and renal function. Bone mineral density, content, and body fat content were measured by dual energy x-ray absorptiometry. No statistically significant differences between the two groups of mice were found (SI Fig. 11). Moreover, comprehensive in-cage monitoring was performed for O_2 uptake, CO_2 production, food and water intake, locomotor activity, and circadian patterns to assess total body metabolism and energy balance. Results revealed a trend toward reduction in food and water intake for the APN-null mouse, but the results did not reach statistical significance; all other measures were similar between the two groups (Fig. 5). Thus, under normal conditions, WT and APN-null mice have similar behavioral phenotypes and physiological regulation. Null female mice were fertile and carried normal numbers of progeny through full pregnancy and nursing phases.

Reduced Angiogenesis in the APN-Null Mouse. We next evaluated whether the APN-null mouse had a normal angiogenic response to hypoxic conditions. Neonatal mice were exposed to 75% oxygen between postnatal days (P)7–P12 and then returned to room air. By P18, retinal neovascularization is observed in WT mice; in contrast, histological examination of similarly treated APN-null mice revealed a marked reduction in the formation of new blood vessels at the retinal inner surface compared with the response in WT mice (Fig. 6). Consistently, an intermediate dose response was observed in the APN heterozygotes. Thus, the APN-null mouse has a severely reduced angiogenic response to hypoxic conditions.

Next, angiogenic responses to growth factors *in vivo* were tested by s.c. implanting gelfoam sponges saturated with VEGF, basis FGF, and TGF-α. To quantify vascularization, hemoglobin concentrations were compared (Fig. 7). Plugs from WT mice contained $\approx$5-fold more hemoglobin than those from APN-null mice. These results show that APN deficiency reduces the angiogenic response and supports a role in pathological angiogenesis.

Discussion

This study reports the generation of an APN-null mouse and an evaluation of its phenotype. APN-null mice exhibit no developmental, fertility, or behavioral or physiological abnormalities. Interestingly, inactivation of APN gene expression impaired the formation of new blood vessels under pathological conditions.
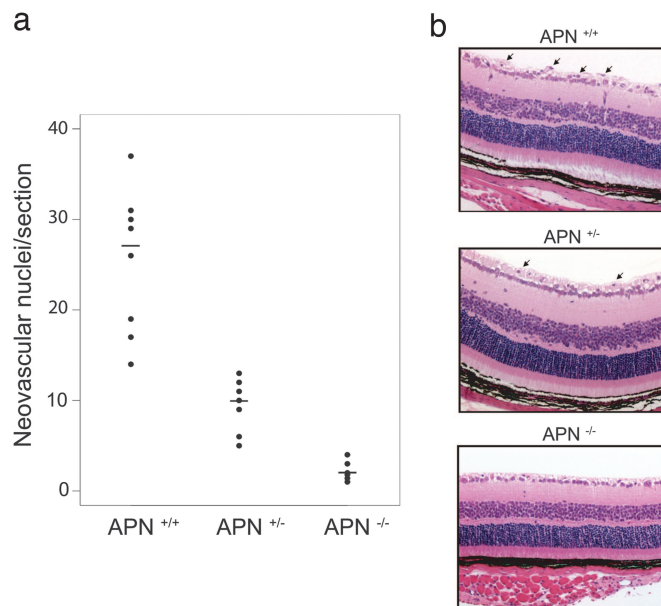
Fig. 6. Failed retinal neovascularization in APN-null mice under hypoxic conditions. (*a*) Quantification of endothelial cells nuclei extended across the inner surface of the retina into the vitreous space. Data from WT, APN-heterozygous, and APN-null mice were compared ($P < 0.001$). (*b*) APN-null mice lack the nuclei protruding into the vitreous space of the eye, as observed in the WT and heterozygote representative examples (arrows). Five independent experiments were performed with similar results.

a

b

APN $^{+/+}$ APN$^{-/-}$
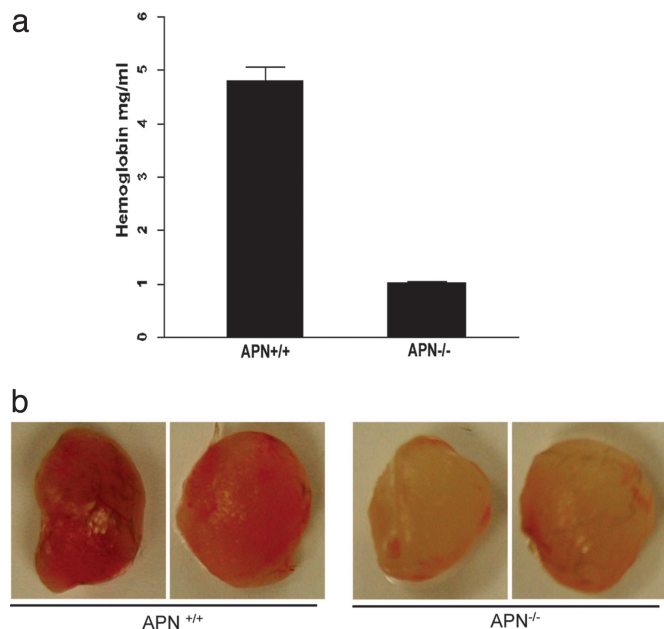
Fig. 7. APN-null mice have severely impaired angiogenesis upon growth factor stimulation. (*a*) Hemoglobin content of the gelfoam from WT and APN-null mice were analyzed. (*b*) Gelfoam plugs implanted in the s.c. tissue were removed after 14 days and analyzed. Plugs in WT mice contained significantly more hemoglobin (4.8 $\pm$ 0.3 mg/ml) than those in APN$^{-/-}$ mice (1.0 $\pm$ 0.1 mg/ml; $P < 0.0001$). Five independent experiments were performed with similar results.

The genetic results presented here not only expand the knowledge of APN in angiogenesis but also provide a tool to study APN function in other fields.

Angiogenesis is critical to pathological conditions, including cancer, inflammation, and retinopathies (21, 24, 25). The present study shows that APN-null mice display a severely impaired angiogenic response to oxygen-induced retinopathy and respond far less strongly to angiogenic growth factors *in vivo* than do WT animals. These data are consistent with our original biochemical observation regarding a functional role for APN in angiogenesis, where the administration of blocking antibodies or chemical inhibitors of APN suppressed new blood vessel formation in several mouse models (21). Shapiro and colleagues later showed that APN is transcriptionally activated by angiogenic signals, mediated by the renin-ang system /MAPK/Ets-2 signaling pathway, and essential for endothelial morphogenesis and capillary tube formation (26–28). Recently, by using RNA interference, Fukasawa *et al.* (29) confirmed that APN is selectively expressed in vascular endothelial cells, and that the enzyme plays multiple roles in angiogenesis. These results (21, 26–29) are in agreement with our findings in the APN-null mouse. However, future experiments are required to determine the precise downstream mechanism(s) through which APN regulates neovascularization. Indeed, APN-null mice develop normally despite strong gene expression during embryogenesis. These contrasting observations indicate that APN is not an essential enzyme for vasculogenesis during development and suggest genetic redundancy or compensation. Of note, similar angiogenic defects were observed in the APA-null mouse, suggesting that both aminopeptidases are required for new blood vessel formation (30). Furthermore, APA and APN serially cleave molecules of the renin–ang system: APA cleaves ang II into ang III, and APN cleaves ang III into ang IV (31). It is tempting to speculate that ang IV is an angiogenic molecule; thus, an enzymatic deficiency (in APN or APA) could ultimately limit the generation of ang

IV and be one possible mechanism leading to reduced angiogenesis in APN-null mice. It is also plausible that other substrate(s) might exist. Interestingly, in pilot experiments, wound-healing assays showed no significant differences between WT and APN-null mice (unpublished results); these results, along with the observed normal fertility and litter sizes suggest that physiological angiogenesis is not affected in APN-null mice. The phenotype in the double (APN/APA)-null mouse remains to be determined; these experiments are ongoing.

Remarkably, APN-null mice have no apparent alterations in blood pressure or electrolytes. These findings are somewhat unexpected, because increased levels of ang III alter water balance and blood pressure (31–33). One possible reason why hemodynamics and electrolyte homeostasis remain normal with no APN activity may be that a mouse homologue of the human adipocyte-derived leucine aminopeptidase (A-LAP) can directly cleaves ang II to produce ang IV (34). The expression of mouse A-LAP is yet to be measured, but it could conceivably compensate for decreased production of ang IV in APN-null mice.

Several reports have demonstrated that enkephalins are neuropeptides cleaved by APN (35–37). Enkephalins are predominantly detected in the thalamus and spinal cord and regulate pain perception, memory, and satiety (38, 39). Experimental manipulation of the brain renin–ang system has shown that exogenous administration of high doses of ang III can modify thirst and sodium appetite, and that doses of ang IV can alter learning and memory (40, 41). Recently, proteomic analysis revealed that APN hydrolyzed leucine and methionine enkephalins in exosomes of microglial cells (42). In line with these studies, a subtle trend toward reduction of water and food consumption was noted in APN-null mice. Although modest, these data suggest that the catabolism of enkephalins might be slightly altered in the APN-null mouse, but that redundancy or compensatory mechanisms are present. Moreover, the APN-null mouse has a small but significantly increased tolerance to heat and pain stimuli. These data again support the enzymatic role of APN in inactivation of enkephalin, leading to pain resistance. However, more refined neurological experiments are needed to better define these minor phenotypes.

Additional insights into APN function may be gained by considering its role as a cell surface receptor for human coronaviruses (11, 12). The SARS virus is a coronavirus that produces severe respiratory infection in patients (43). The mechanism of SARS virus internalization is through binding to the host receptors ACE-2 and L-SIGN (CLEC4M/CD209) in lung epithelial cells (44, 45); we (13) and other investigators (44, 45) have speculated that APN may be a coreceptor for the SARS virus. Because APN is expressed in the lung epithelium, it is worthwhile to evaluate the APN-null mouse as an experimental model for SARS or other coronavirus-induced human diseases.

In summary, we generate and describe the phenotype of an APN-null mouse. Despite the broad range of APN functions, APN-null mice develop and function normally. However, our results provide a clear role for APN in angiogenesis under pathological conditions and provide a genetic model to explore further the role of this enzyme in other biological processes.

Materials and Methods

Generation of Knockout Mice. Commercially available BAC mouse 129S6/SvEv Tac genomic libraries (Research Genetics, Huntsville, AL) were screened by using a ^{32}P-labeled APN cDNA probe. Filters were hybridized at 60°C, washed, and exposed for 4 h at −80°C on x-ray films. Bioinformatics and Southern blot analysis were used to characterize the *Anpep* gene and generate a restriction map for the gene targeting strategy. The 5′ and 3′ arms of homology of the targeting vector (4.5- and 5.5-kb, respectively) were obtained by PCR (Expand Long PCR template kit; Roche, Indianapolis, IN) and confirmed by DNA

MEDICAL SCIENCES

sequencing. A diphtheria toxin gene driven by the pMC1 promoter was cloned at the 3′ end of the construct for negative selection. The targeting vector was linearized by NotI and electroporated into mouse ES cells. DNA from neomycin-resistant ES cell colonies was digested by EcoRI (Roche), separated by agarose gel electrophoresis, blotted onto nylon membranes, and hybridized with a 250-bp external probe. Homologous recombination events were identified by Southern blot (11-kb, WT allele; 8-kb, mutant allele). Targeted ES cell clones were injected into the blastocyst of C57BL/6 mice, and a single chimeric mouse was intercrossed with C57BL/6 mice to establish a germ-line transmission. This study adhered to the ARVO Statement for the Use of Animals in Ophthalmology and Vision Research. The Institutional Animal Care and Use Committee of the University of Texas M. D. Anderson Cancer Center Animal approved all experimentation.

Genotyping. Genotyping was performed by Southern blot and PCR with three primer combinations: forward, 5′-CAC-CCCCATCCCCCATCCCTTAC-3′; reverse, 5′-GTGC-CCACGCCCTTGAACCTTACTT-3′; and IRES-rev, 5′-ACAAACGCACACCGGCCTTATTCC-3′. PCR with the forward/reverse and forward/IRES-rev primer pairs generated an 879-bp WT product and a 320-bp mutant product. For PCR-based genotyping, a hot-start (Qiagen, Valencia, CA) initial step of denaturation (95°C for 15 min) was then followed by 35 cycles (denaturation, 94°C for 30 s; annealing, 65°C for 1 min; extension at 68°C for 1 min).

RT-PCR. Mice were killed by cervical dislocation and tissues removed and incubated in TRIzol reagent (Invitrogen, Carlsbad CA) for total RNA isolation. cDNA was obtained with the reverse transcriptase (RT) superScript III kit (Invitrogen). To detect the expression of the APN transcript, we used the PCR primers: forward 5′-CCCCGGGGCTGCTGTTCTTT-3′ and reverse 5′-ACCACCCGCTCCTTGTTGCTAATG-3′. PCR amplification consisted of an initial step (94°C for 3 min) followed by 35 cycles (94°C for 30 s, 65°C for 1 min, 72°C for 1 min). The housekeeping gene glycerol-3-phosphate dehydrogenase (G3PDH) served as an internal loading control.

Histopathology. Three- and 6-mo-old WT and APN-null male and female mice (at least three mice on each group) were used for histopathological analysis. Blood samples were collected for hematology and serum chemistry studies from each mouse.

Tissue Processing and Immunohistochemistry. WT (APN$^{+/+}$), heterozygous (APN$^{+/-}$), and null (APN$^{-/-}$) mice were anesthetized with Avertin and perfused with 4% paraformaldehyde in PBS (pH 7.4). Organs were removed, incubated in the same fixative solution for 1 h, and then infiltrated with 30% sucrose in PBS containing 0.002% sodium azide overnight at 4°C. The next day, the organs were frozen in OCT and stored at −80°C. Frozen

tissue sections were cut, air-dried on slides, rinsed twice for 5 min with PBS and once with PBS containing 1% Triton X-100 (PBST), and then blocked with 5% normal goat serum (Jackson ImmunoResearch, West Grove, PA) in PBST for 30 min. Tissue sections were incubated for 1 h in primary antibody solution containing monoclonal Armenian hamster anti-CD31 (1:500 dilution, clone 2H8; Chemicon, Temecula, CA), monoclonal rat anti-CD13 (1:500 dilution, clone R3–63; Serotec, Raleigh, NC), and 1% normal goat serum in PBST. Slides were then rinsed three times with PBST for 5 min each and incubated for 30 min with a 0.45-μm-filtered secondary antibody solution containing FITC-conjugated goat anti-hamster IgG (1:200; Jackson ImmunoResearch) and Cy3-conjugated goat anti-rat IgG (1:400; Jackson ImmunoResearch) in PBST. Finally, slides were rinsed three times for 5 min each with PBST, fixed with 4% PFA in PBS for 1 min, rinsed three times with PBS for 5 min each, and mounted (Vectashield; Vector Laboratories, Burlingame, CA).

Noninvasive Phenotypic Analysis. Age- and sex-matched WT, heterozygous, and null ($n = 6$/group) were evaluated for fertility, litter size, locomotor activity, nociception, grip strength, blood pressure, in-cage comprehensive monitoring system, dual energy x-ray absorptiometry, and electrocardiogram.

Retinal Neovascularization Assay. Mice were exposed to 75% oxygen (P7–P12) and killed (P19). Eyes were enucleated and fixed in Bouin's solution. Tail snips were taken to determine the genotype. Fixed and alcohol-dehydrated eyes were embedded in paraffin, serially sectioned and H&E-stained. Endothelial cell nuclei on the vitreous side of the internal limiting membrane were counted.

***In Vivo* Angiogenesis Assay.** To induce the formation of new blood vessels *in vivo*, gelfoam sponges (Johnson & Johnson, Somerville, NJ) were saturated with growth factors (200 ng/ml each; R&D Systems, Minneapolis, MN) including VEGF, basis FGF, and TGF-α. Sponges were implanted s.c. After 14 days, mice were killed, and gelfoams were homogenized and incubated with Drabkin's reagent (Sigma, St. Louis, MO). Hemoglobin content was reported as mean ± SEM. WT, heterozygous, and null mice were compared.

Statistical Analysis. An ANOVA test of variance served to determine significant differences among multiple groups. Paired *t* test comparisons were used for applied posthoc analysis and adjusted by Bonferroni correction.

1. Hooper NM, Lendeckel U, eds (2004) *Aminopeptidases in Biology and Disease* (Kluwer Academic/Plenum, New York).
2. Barrett AJ, Rawlings ND, Woessner JF, eds (2004) *Handbook of Proteolytic Enzymes* (Elsevier, London).
3. Amoscato AA, Alexander JW, Babcock GF (1989) *J Immunol* 142:1245–1252.
4. Favaloro EJ, Bradstock KF, Kabral A, Grimsley P, Zowtyj H, Zola H (1988) *Br J Haematol* 69:163–171.
5. Mechtersheimer G, Moller P (1990) *Am J Pathol* 137:1215–1222.
6. Menrad A, Speicher D, Wacker J, Herlyn M (1993) *Cancer Res* 53:1450–1455.
7. Riemann D, Kehlen A, Langner J (1999) *Immunol Today* 20:83–88.
8. Lalu K, Lampelo S, Vanha-Perttula T (1986) *Biochim Biophys Acta* 873:190–197.
9. Chansel D, Czekalski S, Vandermeersch S, Ruffet E, Fournie-Zaluski MC, Ardaillou R (1998) *Am J Physiol* 275:535–542.
10. Matsas R, Turner AJ, Kenny AJ (1984) *FEBS Lett* 175:124–128.
11. Delmas B, Gelfi J, L'Haridon R, Sjöström H, Norén O, Laude H (1992) *Nature* 357:417–420.
12. Yeager CL, Ashmun RA, Williams RK, Cardellichio CB, Shapiro LH, Look AT, Holmes KV (1992) *Nature* 357:420–422.
13. Kontoyiannis DP, Pasqualini R, Arap W (2003) *The Lancet* 361:1558.
14. Santos AN, Langner J, Herrmann M, Riedmann D (2000) *Cell Immunol* 201:22–32.
15. Mina-Osorio P, Ortega E (2005) *J Leukocyte Biol* 77:1008–1017.
16. Hajitou A, Pasqualini R, Arap W (2006) *Trends Cardiovasc Med* 16:80–88.
17. Sergeeva A, Kolonin MG, Molldrem JJ, Pasqualini R, Arap W (2006) *Adv Drug Deliv Rev* 58:1622–1654.
18. Arap W, Pasqualini R, Ruoslahti E (1998) *Science* 279:377–380.
19. Ellerby HM, Arap W, Ellerby LM, Kain R, Andrusiak R, Rio GD, Krajewski S, Lombardo CR, Rao R, Ruoslahti E, *et al.* (1999) *Nat Med* 5:1032–1038.

20. Curnis F, Sacchi A, Borgna L, Magni F, Gasparri A, Corti A (2000) *Nat Biotechnol* 18:1185–1190.
21. Pasqualini R, Koivunen E, Kain R, Lahdenranta J, Sakamoto M, Stryhn A, Ashmun RA, Shapiro LH, Arap W, Ruoslahti E (2000) *Cancer Res* 60:722–727.
22. Curnis F, Arrigoni G, Sacchi A, Fischetti L, Arap W, Pasqualini R, Corti A (2002) *Cancer Res* 62:867–874.
23. Mentzel S, Dijkman HBPM, Van Son JPHF, Koene RAP, Assmann KJM (1996) *J Histochem Cytochem* 44:445–461.
24. Folkman J (2006) *Annu Rev Med* 57:1–18.
25. Lahdenranta J, Pasqualini R, Schlingemann RO, Hagedorn M, Stallcup WB, Bucana CD, Sidman RL, Arap W (2001) *Proc Natl Acad Sci USA* 98:10368–10373.
26. Bhagwat SV, Petrovic N, Okamoto Y, Shapiro LH (2003) *Blood* 101:1818–1826.
27. Petrovic N, Bhagwat SV, Ratzan WJ, Ostrowski MC, Shapiro LH (2003) *J Biol Chem* 278:49358–49368.
28. Bhagwat SV, Lahdenranta J, Giordano R, Arap W, Pasqualini R, Shapiro LH (2001) *Blood* 97:652–659.
29. Fukasawa K, Fujii H, Saitoh Y, Koizumi K, Aozuka Y, Sekine K, Yamada M, Saiki I, Nishikawa K (2006) *Cancer Lett* 243:135–143.
30. Marchiò S, Lahdenranta J, Schlingemann RO, Valdembri D, Wesseling P, Arap MA, Hajitou A, Ozawa MG, Trepel M, Giordano RJ, *et al.* (2004) *Cancer Cell* 5:151–162.
31. Reaux A, Fournie-Zaluski MC, Llorens-Cortes C (2001) *Trends Endocrinol Metab* 12:157–162.
32. Faber F, Gembardt F, Sun X, Mizutani S, Siems W-E, Walter T (2006) *Regul Pept* 136:130–137.
33. Wright JW, Tamura-Myers E, Wilson WL, Roques BP, Llorens-Cortes C, Speth RC, Harding JW (2002) *Am J Physiol* 284:725–733.
34. Goto Y, Hattori A, Ishii Y, Tsujimoto M (2006) *FEBS Lett* 580:1833–1838.
35. Gros C, Giros B, Schwartz JC (1985) *Biochemistry* 24:2179–2185.
36. Churchill L, Bausback HH, Gerritsen ME, Ward PE (1987) *Biochim Biophys Acta* 923:35–41.
37. Giros B, Gros C, Solhonne B, Schwartz JC (1986) *Mol Pharmacol* 29:281–287.
38. Holden JE, Jeong Y, Forrest JM (2005) *AACN Clin Issues* 16:291–301.
39. Lullmann H, Mohr K, Ziegler A, Bieger D (1993) *Color Atlas of Pharmacology* (Thieme, Stuttgart, Germany).
40. Wilson WL, Roques BP, Llorens-Cortes C, Speth RC, Harding JW, Wright JW (2005) *Brain Res* 1060:108–117.
41. Albiston AL, McDowall SG, Matsacos D, Sim P, Clune E, Mustafa T, Lee J, Mendelsohn FAO, Simpson RJ, Connolly LM, Chai SY (2001) *J Biol Chem* 276:48623–48626.
42. Potolicchio I, Carven GJ, Xu X, Stipp C, Riese RJ, Stern LJ, Santambrogio L (2005) *J Immunol* 175:2237–2243.
43. Yeung KS, Yamanaka GA, Meanwell NA (2006) *Med Res Rev* 26:414–433.
44. Li W, Moore MJ, Vasilieva N, Sui J, Wong SK, Berne MA, Somasundaran M, Sullivan JL, Luzuriaga K, Greenough TC, *et al.* (2003) *Nature* 426:450–454.
45. Chan VSF, Chan KYK, Chen Y, Poon LLM, Cheung ANY, Zheng B, Chan K-H, Mak W, Ngan HYS, Xu X, *et al.* (2006) *Nat Gen* 38:38–46.

MEDICAL SCIENCES

A preclinical model for predicting drug response in soft-tissue sarcoma with targeted AAVP molecular imaging

Amin Hajitou*, Dina C. Lev, Jonathan A. F. Hannay, Borys Korchin, Fernanda I. Staquicini, Suren Soghomonyan, Mian M. Alauddin, Robert S. Benjamin, Raphael E. Pollock, Juri G. Gelovani, Renata Pasqualini†, and Wadih Arap†

The University of Texas M. D. Anderson Cancer Center, 1515 Holcombe Boulevard, Houston, TX 77030

Human sarcomas are rare but diverse malignant tumors derived from mesenchymal tissue. Clinical response to therapy is currently determined by the modified World Health Organization (WHO) criteria or the Response Evaluation Criteria in Solid Tumors (RECIST), but these standards correlate poorly with sarcoma patient outcome. We introduced ligand-directed particles with elements of AAV and phage (AAVP) to enable integration of tumor targeting to molecular imaging. We report drug-response monitoring and prediction in a nude rat model of human sarcoma by AAVP imaging. As a proof-of-concept, we imaged *Herpes simplex* thymidine kinase in a clinic-ready setting with PET to show that one can *a priori* predict tumor response to a systemic cytotoxic. Given the target expression in patient-derived sarcomas, this platform may be translated in clinical applications. Sarcoma-specific ligands and promoters may ultimately lead to an imaging transcriptome.

Human sarcomas are rare yet heterogeneous malignant tumors from mesenchymal tissues (1). Monitoring drug responses in soft-tissue sarcoma has long been clinically problematic. Currently, responses are determined by the modified World Health Organization (WHO) criteria (2–4) or the Response Evaluation Criteria in Solid Tumors (RECIST) (5–7), which require marked tumor size decrease for patients to be considered responding to therapy. A major assumption of these criteria is that a solid tumor volume is directly proportional to the cancer cell number. However, in soft-tissue sarcomas, there are reasons to challenge such an assumption (8). First, in addition to tumor cells, sarcomas contain nonmalignant stromal cells and extracellular matrix (ECM) that do not disappear, even if the malignant component is treated. Moreover, when cytotoxics are used against sarcomas, there is often associated necrosis resulting in reduced total cell number but not necessarily overall tumor size changes. Finally, even if a soft-tissue sarcoma is predominantly or entirely composed of cancer cells, its remnant composition may not be fully eliminated when tumor cells are destroyed by therapy, because myxoid-type degeneration is not always promptly removed. Ultimately, the modified WHO criteria and RECIST correlate poorly with drug response and outcome in patients with soft-tissue sarcomas; validation in this setting is sporadic and restricted. In another level of complexity, drug responses in patients with soft-tissue sarcoma are determined through standard methods, such as CT, MRI, or PET scans. However, because systematic quantitative measurements have not been established because of the rarity and diversity of soft-tissue sarcomas, decreases in tumor size and/or density are not accepted as unequivocal evidence of response. Consequently, many conventional soft-tissue sarcoma responses in individual patients are evaluated qualitatively. Thus, new or alternative quantitative imaging criteria to improve management and follow-up of responses were proposed in ref. 9.

We have introduced a hybrid vector that enables convergence of ligand-directed targeting and molecular imaging (10–12); such vector incorporates genomic *cis*-elements of adeno-associated virus (AAV) and of an M13-derived (13) phage [AAV phage (AAVP)]. Our prototype displays CDCRGDCFC (RGD-4C) to target αv

integrins (14, 15) and systemically deliver transgenes to tumors (10–12).

The present work offers insight into the use of systemically administered RGD-4C AAVP as a targeted imaging tool to monitor—but also to possibly predict—drug response in soft-tissue sarcoma. We used a model of athymic rnu/rnu (nude) rats bearing human soft-tissue sarcoma xenografts (16). We show that targeted AAVP (*i*) allows ligand-directed targeting of human sarcoma xenografts in a preclinical setting; (*ii*) provides molecular imaging of reporters; (*iii*) is suitable for serial noninvasive monitoring of soft-tissue sarcoma; and, as a proof-of-concept, (*iv*) enables response prediction to a cytotoxic. We also show that αv integrins are expressed in vascular endothelium and tumor cells in human soft-tissue sarcomas. AAVP-mediated PET scan of *HSVtk* expression (12, 17–19) enables molecular prediction of drug response in a preclinical model of soft-tissue sarcoma. Translation of this potential strategy in sarcoma patients might be achievable.

Results

Targeted AAVP Binds to Sarcoma Cell Surfaces and Mediates Transduction. We reported the efficacy of a targeted AAVP vector (10–12) in which a CMV promoter drives a mammalian expression cassette containing a reporter transgene, and systemic tumor homing is ligand-directed through an RGD-4C peptide that binds to αv integrins within tumors (10, 14, 15).

We first examined ligand binding to target sarcoma cells by comparing the binding capacity of tumor-homing peptides to human Sloan–Kettering Leiomyosarcoma-1 (SKLMS1) cells in an aqueous-to-organic phase separation assay (20). To determine the best homing, SKLMS1 cells were incubated with targeted phage displaying one of the following: RGD-4C (10, 14, 15), the interleukin-11 receptor (IL11R)-targeting peptide CGRRAGGSC (21), or the aminopeptidase A (APA)-targeting peptide CPRECES (22); insertless phage and phage displaying an unrelated peptides served as negative controls. RGD-4C had the highest binding to sarcoma cell surfaces (Fig. 1A). Next, we evaluated the magnitude and specificity of targeted RGD-4C AAVP binding compared with negative controls, including nontargeted (insertless) AAVP or mutant (Asp → Glu) RGE-4C AAVP. Under nonsaturated conditions, we found that the ratio of specific binding of RGD-4C AAVP to SKLMS1 cell surfaces (relative to negative controls) was
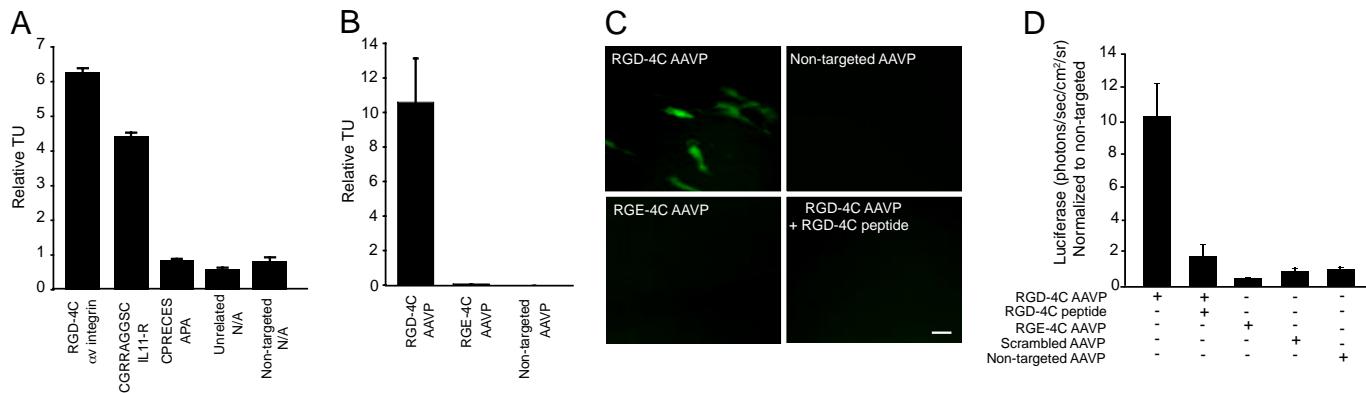
PHARMACOLOGY

Fig. 1. Ligand-directed binding and gene transduction by targeted AAVP. (*A*) Binding of targeted phage displaying tumor-homing peptides or negative controls (as indicated) to the surface of SKLMS1 cells in aqueous-to-organic phase separation assays (20) was performed. (*B*) Binding of RGD-4C AAVP or negative controls (nontargeted AAVP or mutant RGE-4C AAVP) to the surface of SKLMS1 cells. (*C*) Targeted gene transduction mediated by RGD-4C AAVP-*GFP* to SKLMS1 cells relative to negative controls; inhibition by soluble RGD-4C peptide confirms specificity. (Scale bar, 10 μm.) (*D*) Quantitative analysis of cell transduction by targeted or several nontargeted AAVP-*Luc* controls. AAVP-*Luc* vectors were incubated with tumor cells. Error bars represent the SD of the means. Each experiment was repeated twice with similar results. In each case, a representative experiment is shown.

≈10-fold; controls had barely detectable cell binding (Fig. 1*B*). Finally, we analyzed SKLMS1 cell transduction by targeted AAVP vectors carrying two reporters: *green fluorescence protein* (RGD-4C AAVP-*GFP*) or *Luciferase* (RGD-4C AAVP-*Luc*). We observed GFP expression in cells incubated with RGD-4C AAVP-*GFP*, but no GFP was detected in cells incubated with negative controls (Fig. 1*C*). Similar results were obtained by RGD-4C AAVP-*Luc* transduction (Fig. 1*D*). Quantification of luciferase showed ≈10-fold more activity in cells treated with targeted RGD-4C AAVP-*Luc* compared with controls (Fig. 1*D*). We also showed that SKLMS1 cell transduction by RGD-4C AAVP-*GFP* and RGD-4C AAVP-*Luc* is specific because it is inhibited by the RGD-4C peptide (Fig. 1 *C* and *D*); negative control peptides had no detectable inhibitory effect.

AAVP Targeting Sarcoma Xenografts. We next attempted to determine the ability of RGD-4C AAVP to target a model of soft-tissue sarcoma *in vivo*. We systemically (tail vein) administered RGD-4C AAVP or controls to nude rats bearing SKLMS1 sarcoma xenografts in the right hind limbs. At 9 h after vector administration, sarcoma-bearing nude rats were killed, and tumors and control organs were collected. Relative targeted AAVP homing was quantified (11, 23) by recovery from tissue homogenates, bacterial infection, and counting transducing units (TU).

We observed marked enrichment of RGD-4C AAVP in SKLMS1 sarcoma xenografts. Specifically, we found ≈25-fold enrichment compared with homing of nontargeted AAVP control to size-matched tumors and ≈10-fold compared with control organs (Fig. 2*A*). Dose-dependent inhibition of homing to SKLMS1 sarcomas by RGD-4C peptide—but not by control peptides—was observed. These data establish that RGD-4C AAVP targets SKLMS1 xenografts in nude rats upon systemic administration.

Targeted Transgene Delivery. Having shown that RGD-4C AAVP specifically transduces human SKLMS1 cells and homes to SKLMS1 xenografts in nude rats, we set out to evaluate the systemic delivery efficacy of targeted reporter transgenes. We assessed bioluminescence imaging (BLI) and PET imaging with [^{18}F]-FEAU for noninvasive monitoring of spatial diversity and temporal dynamics of *Luc* and *HSVtk* expression in nude rats bearing SKLMS1 xenografts after RGD-4C AAVP administration. We first used a laboratory setup for *in vivo* imaging of *Luc* transgene in sarcoma-bearing rats. We selected BLI of Luc expression as a scout reporter because it is a simple, cost-effective, and sensitive technique for gene expression monitoring in rodents with virtually no unspecific

background (17, 24). On day 0 of a typical repetitive BLI experiment, rats bearing SKLMS1 sarcomas in the right hind limb received RGD-4C AAVP-*Luc* or nontargeted AAVP-*Luc*. BLI corresponding to *Luc* expression started at day 3 after vector delivery and was serially monitored for 5–6 weeks, at which time the experiments were terminated and sarcoma-bearing rats killed (days 38–40); specific expression of *Luc* was detected in sarcoma xenografts of rats receiving RGD-4C AAVP-*Luc* at day 3 after systemic delivery. From day 3 after targeted vector delivery, BLI yielded a gradual increase in the levels of *Luc* expression in tumors during the initial week after administration of RGD-4C AAVP-*Luc* [Fig. 2*B* and supporting information (SI) Fig. 6]. Thereafter, two general outcomes were observed. In some cohorts of sarcoma-bearing rats, a gradual decrease of gene expression was found, ending with nonimageable low levels of reporter transgene expression within the tumors by experimental day 24 (SI Fig. 6). In other cohorts, *Luc* expression in the tumors continued to increase and achieved a very high-level peak by day 20 (the maximum *Luc* expression, coincidentally at approximately the half time point of the experiment), followed by a gradual decrease in gene expression until the experiment termination (Fig. 2*B*). In contrast, no specific BLI signals could be observed in control sarcoma-bearing rats receiving non-targeted AAVP-*Luc*. Administration of any AAVP did not result in reporter transgene expression in normal organs such as liver, spleen, or kidneys (Fig. 2*B*) as evident by the absence of specific BLI signals. These results show that targeted RGD-4C AAVP specifically and efficiently transduces sarcoma xenografts. Transduction of sarcoma-derived xenografts in rats with RGD-4C AAVP appears to be heterogeneous within tumors (up to ≈13-fold differential in *Luc* expression levels and ≈2.5-fold differential in *Luc* expression timelines (Fig. 2*C* and SI Fig. 6*B*). Tumor-specific expression of *Luc* was detected and monitored in follow-up of SKLMS1 sarcomas in rats receiving RGD-4C AAVP-*Luc*; in contrast, tumor-associated BLI signals were not observed in control sarcoma-bearing rats (Fig. 2*B*). No BLI was observed in normal control organs with any AAVP.

Experimental Modeling of Drug Response. To confirm target presence in this system, we examined αv integrin expression in SKLMS1 xenografts. Immunofluorescence analysis showed strong expression in SKLMS1 xenografts (Fig. 3*A*, anti-αv integrin). Double-staining with anti-CD31 antibody (Fig. 3*A*, anti-CD31) showed that αv integrins also localized in tumor blood vessels (Fig. 3*A*, merge). We noticed differences in αv integrin expression among various tumor-
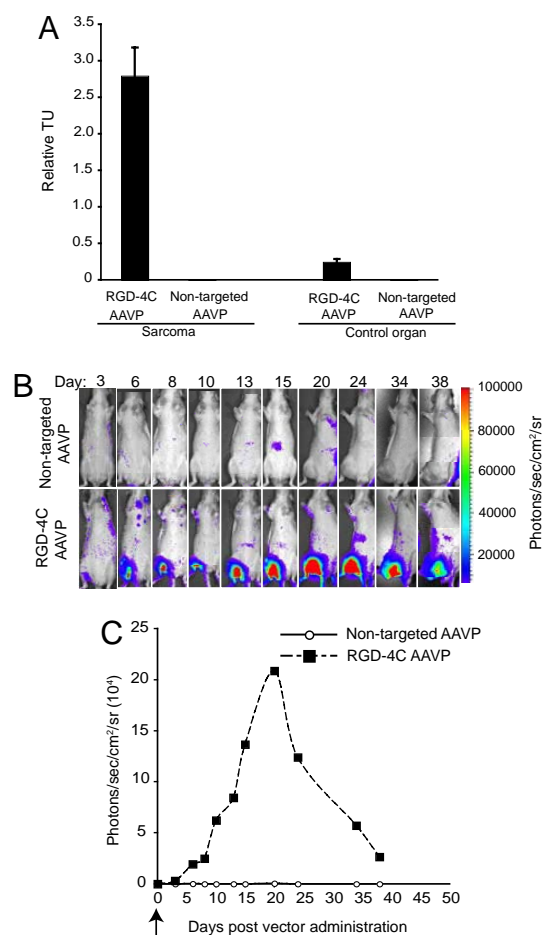
Fig. 2. Targeting soft-tissue sarcoma xenografts and spatial–temporal dynamics of reporter transgene expression. (*A*) Systemic homing ability of the RGD-4C AAVP in nude rats bearing SKLMS1 xenografts was evaluated after i.v. administration of targeted AAVP or control. Nude rats (*n* = 2) bearing established and size-matched SKLMS1 xenografts (≈200 mm³) in the right hind limbs received a single dose (3 × 10¹² TU) of RGD-4C AAVP or nontargeted AAVP. After 9 h, sarcoma-bearing rats were killed, and targeted and control AAVP were recovered from tumors and control normal tissues (shown is pancreas). Experiments were repeated twice. A representative experiment is shown. Error bars represent the SD of the means. (*B*) BLI of luciferase expression after systemic delivery of targeted AAVP or control AAVP. Nude rats bearing size-matched SKLMS1 sarcoma xenografts (≈200 mm³) received a single dose (3 × 10¹² TU) of RGD-4C AAVP-*Luc* or negative control (nontargeted) AAVP-*Luc*. Serial temporal and spatial monitoring of luciferase (*Luc*) gene expression was determined by repetitive BLI at different days after AAVP administration as indicated. A standard calibration scale is provided. Experiments were repeated twice. A representative experiment is shown. (*C*) Serial real-time quantification of *Luc* expression in the animals depicted above. Arrow (day 0) indicates systemic administration of a single dose of targeted AAVP or control.

Fig. 3. Drug response to targeted AAVP-mediated systemic cytotoxic therapy. (*A*) Immunofluorescence analysis of αv integrin in frozen serial sections of SKLMS1 xenografts in nude rats. Representative H&E staining of the tumor sections are shown (far left). Antibodies anti-αv integrins and anti-CD31 antibody for blood vessel staining were used. Merge images (far right) confirm αv integrin expression in the vascular and tumor components. Arrows indicate αv integrins in the tumor blood vessels. (*B*) Cohorts of nude rats (*n* = 8) bearing established, size-matched (≈200 mm³) human SKLMS1-derived sarcomas received two i.v. doses (3 × 10¹² TU per dose, indicated by arrows at days 0 and 19) of targeted RGD-4C AAVP-*HSVtk* or control nontargeted AAVP-*HSVtk* followed by systemic GCV therapy as indicated. Therapeutic tumor responses to two serial drug treatment cycles (first cycle, days 10–19; second cycle, days 24–31) were evaluated by serially measuring sarcoma xenografts. Shown are the mean tumor volumes ± SD. (*C*) Posttreatment histological evaluation of tumors by H&E staining of SKLMS1 sarcoma xenografts. Nontargeted AAVP-*HSVtk*-treated tumors (*Left*) and targeted RGD-4C AAVP-*HSVtk*-treated tumors (*Right*) are shown as high-magnification views from the low-magnification inserts of serial tumor sections. Arrows point to the border between the viable tumor rim and central necrotic area in the targeted images. M, muscle; T, tumor. (Scale bars, 25 μm.)

bearing rat cohorts (Fig. 3*A*), consistently with—and likely accounting for—the serial BLI variability (Fig. 2 and SI Fig. 6).

Although serial BLI of *Luc* expression provides a cheap strategy to initially analyze the specificity, temporal dynamics, and spatial heterogeneity of reporters, BLI is unlikely to be applicable in patients. In contrast, AAVP-mediated delivery of *HSVtk* has been established in preclinical tumor targeting and molecular imaging studies. A potential advantage of a targeted *HSVtk*-based methodology is that it serves as a suicide gene strategy [if combined with ganciclovir (GCV)] or as a reporter for imaging (if combined with *HSVtk*-specific radiolabeled nucleoside analogues). Thus, we reasoned that a targeted AAVP might become translatable as a

clinically applicable PET imaging modality in human soft-tissue sarcomas. To evaluate responses by tumor measurements during physical examination (Fig. 3*B*) and histopathology (Fig. 3*C*), we delivered *HSVtk* by targeted RGD-4C AAVP or controls to cohorts of rats with SKLMS1 sarcomas. We treated both groups with systemic GCV and compared responses by *HSVtk* imaging (Figs. 3 and 4).

Predicting and Monitoring Sarcoma Response. The *HSVtk* gene was used as a reporter in combination with a radiolabeled nucleoside analogue 2′-[¹⁸F]-fluoro-2′-deoxy-1-β-ᴅ-arabino-furanosyl-5-ethyl-uracil ([¹⁸F]-FEAU), a radiolabeled substrate for the HSVtk enzyme; biochemical attributes, such as its high uptake rate and selectivity, render FEAU a suitable PET tracer for *HSVtk* expression (12, 25, 26). Nude rats with SKLMS1 xenografts received targeted or control AAVP-*HSVtk* intravenously. PET imaging with

PHARMACOLOGY
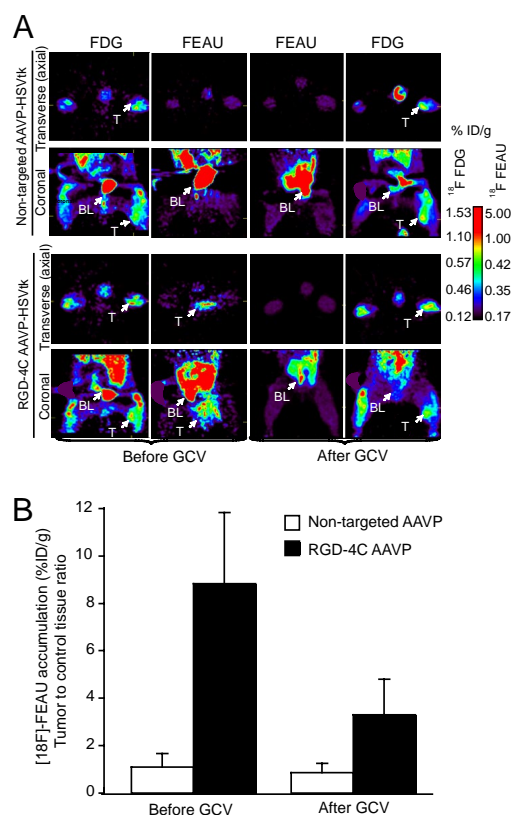
Fig. 4. Predicting and monitoring drug response in a preclinical model of human sarcoma. PET imaging of *HSVtk* transgene expression was performed in sarcoma-bearing rats after i.v. delivery of RGD-4C targeted AAVP or nontargeted control. The first GCV treatment cycle (see Fig. 3) was initiated at 24 h after [^{18}F]-FEAU administration and imaging to enable the molecular–genetic imaging of the corresponding drug response. (*A*) Cohorts of nude rats bearing human SKLMS1-derived xenografts (*n* = 8) received a single i.v. dose (3 × 10^{12} TU) of RGD-4C AAVP-*HSVtk* or control nontargeted AAVP-*HSVtk*. PET imaging of [^{18}F]-FEAU was performed after AAVP administration (day 9) and then again after drug treatment with GCV (day 15). PET imaging of [^{18}F]-FDG was performed (day 8) and then again after the second [^{18}F]-FEAU (day 16). PET imaging with [^{18}F]-FDG and with [^{18}F]-FEAU are presented (before and after treatment with GCV) as indicated. Transverse (axial) and coronal sections are shown. A standard calibration scale is provided, and correspondence of [^{18}F]-FDG and [^{18}F]-FEAU PET imaging is indicated. (*B*) Relative sarcoma expression of *HSVtk* as assessed by repetitive PET imaging with [^{18}F]-FEAU before and after initiation of cytotoxic drug treatment with GCV. A mesenchymal-derived normal tissue (muscle) served to normalize the tumor-to-control reporter transgene expression ratio.

[^{18}F]-fluorodeoxyglucose (FDG) was performed at day 8 after AAVP administration to evaluate tumor viability, and [^{18}F]-FEAU PET was performed 24 h afterward (day 9) to assess localization and magnitude of *HSVtk* expression. [^{18}F]-FDG images (day 8) demonstrated metabolically viable tumors located in the right hind limb of each sarcoma-bearing rat with similar levels of activity of tumors in rats receiving RGD-4C AAVP-*HSVtk* or nontargeted AAVP-*HSVtk* (Fig. 4*A*). In contrast, PET imaging with [^{18}F]-FEAU showed *HSVtk* transgene reporter expression specifically in sarcoma xenografts in rats receiving RGD-4C AAVP-*HSVtk* (Fig. 4*A*). No *HSVtk* expression was detected in tumors in rats receiving nontargeted AAVP-*HSVtk* (Fig. 4*A*). As before, PET with [^{18}F]-FEAU revealed intratumoral heterogeneity and interanimal variability of *HSVtk* transgene expression, consistent with our BLI results. GCV was initiated at day 10 after AAVP administration in these same animals, whereas sarcoma growth was monitored in each rat by caliper serial measurements (SI Fig. 7). After 5 days of
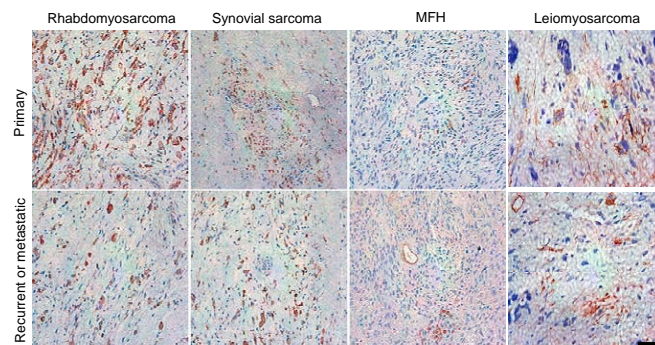
Fig. 5. Analysis of αv integrin expression in human soft-tissue sarcomas. Shown is αv integrin expression in paraffin-embedded sections from a panel of the following patient-derived soft-tissue sarcoma specimens: rhabdomyosarcomas, synovial sarcomas, and malignant fibrous histiocytoma (MFH). Representative images of primary, recurrent, or metastatic tumors are shown as indicated. (Scale bar, 25 μm.)

systemic GCV treatment, PET imaging of [^{18}F]-FEAU showed marked decrease in the levels of *HSVtk* expression (expressed as percentage of administered i.v. dose per gram of tissue) in sarcoma xenografts from the RGD-4C AAVP-*HSVtk*-treated rat cohort (Fig. 4). Moreover, suppression of sarcoma growth and even regression of primary tumors (in some animals) were observed with GCV (Fig. 3*B*). However, all tumors eventually recurred (Fig. 3*B*) with confirmatory analysis of viability with [^{18}F]-FDG PET (Fig. 4*A*). To assess the potential of repetitive AAVP-mediated gene transfer, a second RGD-4C AAVP-*HSVtk* dose was administered to sarcoma-bearing rats and GCV was initiated 5 days later. Again, regression of the SKLMS1 sarcomas in rats was observed between days 26 and 30, followed by tumor regrowth (Fig. 3*B*); tumors were recovered and processed for analysis. Hematoxylin and eosin (H&E) staining revealed destruction of the central area of tumor tissue after treatment with targeted RGD-4C AAVP-*HSVtk* plus GCV (Fig. 3*C*). Notably, a viable peripheral rim was found in these tumors. In contrast, nontargeted AAVP-*HSVtk* plus GCV had no such effect (Fig. 3*C*). These results are consistent with reports in other cell type or species (10, 22).

Target Analysis in Human Sarcomas. To begin to translate this strategy into clinical applications, we analyzed the presence of αv integrins in a patient-derived sarcoma set (*n* = 28). This panel of tumors (SI Table 1) included primary, recurrent, and metastatic soft-tissue sarcomas of many subtypes. We found that expression of αv integrins in sarcomas is consistently positive within the vascular and tumor compartments. These data suggest that this cell surface target may be suitable for translation into patient applications. Expression of αv integrins in representative specimens is shown (Fig. 5).

Discussion

Reliable assessment of tumor response in human soft-tissue sarcoma remains a challenge since the report of a ''meaningful'' response classification by Karnofsky (26) nearly half-century ago. Despite sequential improvements, modifications, and revisions over the ensuing decades, the problem is still unsolved. Currently, tumor response evaluation is established by criteria originally developed in ref. 2 and subsequently modified in refs. 3 and 4 by the WHO and, since the year 2000, by the RECIST methodology (5–7). A recent prospective trial suggested that RECIST is equivalent to the modified WHO criteria in soft-tissue sarcoma patients (6). However, the unprecedented development of imaging methodology in cancer medicine has led to clinical settings in which current guidelines, with predetermined evaluation criteria for anti-tumor drug activity, might no longer be adequate (19, 27–29).

Conventionally, RECIST requires a 30% decrease in the sum of the longest dimension of tumors to be considered a partial response to therapy (5). Historically, one can trace the origins of this arbitrary standard to >30 years ago, when physical examination was the predominant methodology available to determine tumor response to chemotherapy (30). However, in soft-tissue sarcoma patients, RECIST may be too stringent. First, anatomically based imaging measurements are rarely used to determine drug responses today because of the increased sophistication in imaging (27). Moreover, in soft-tissue sarcoma patients, RECIST does miss "true" (i.e., biopsy-proven) pathological responses; consequently, anything less than RECIST-defined progression may represent a tumor response (8). Although contemporary imaging allows accurate sarcoma size measurement, marked required decreases in tumor diameter have been questioned on the empirical basis that any sarcoma size reduction—or even tumor growth stabilization or decreasing tumor density (indicating necrosis or degeneration)—in response to therapy might be clinically significant. Choi *et al.* (9) have proposed that a 10% tumor size decrease or 15% tumor density decrease (the so-called "Choi criteria") in contrast enhanced-CT imaging is evidence of response in patients with soft-tissue sarcomas (8, 9, 29). Finally, RECIST does not adequately evaluate activity of targeted agents that may be predominantly cytostatic rather than cytotoxic. Brennan and colleagues have reported a postoperative algorithm for sarcoma-specific death (31); in addition to this valuable tool, earlier biological endpoints other than patient survival might be desirable. Because functional imaging (FDG PET) has shown clinical promise to monitor disease in soft-tissue sarcoma (27, 32), we reasoned that a PET-based system could also be potentially developed to predict tumor response.

Here, we report a targeted AAVP-based monitoring of response to a drug in a preclinical experimental model of human soft-tissue sarcoma xenografts in nude rats. Specifically, we demonstrated ligand-directed targeting, noninvasive serial imaging of reporter transgenes, and drug response prediction and monitoring in human xenografts established in nude rats with PET-based imaging of RGD-4C AAVP-delivered *HSVtk* incorporating specific radiotracers. We first sought to determine whether RGD-4C AAVP would bind to and transduce SKLMS1 cells. We showed that the RGD-4C peptide is a consistent and specific ligand *in vitro*. Next, we administered the RGD-4C AAVP or nontargeted controls to tumor-bearing nude rats to evaluate whether RGD-4C AAVP would home to SLMS1 xenografts. Again, we observed specific localization of RGD-4C AAVP to tumors. The magnitude and specificity of these results are consistent with *in vitro* and *in vivo* data in other experimental systems (10). We then used luciferase BLI to serially analyze the potential of RGD-4C AAVP for targeted delivery and to monitor the distribution and persistence of reporter expression. Our data show that systemic delivery of RGD-4C AAVP-*Luc* results in efficient and specific gene expression within human soft-tissue sarcoma xenografts but that the tumor transduction is heterogeneous, even in a carefully standardized experimental model. This result suggests that RGD-4C AAVP can be used to target gene therapy to distant tumors after systemic administration, a route that is applicable for localized and metastatic disease. Such diversity in sarcoma transduction could be due to many factors (i.e., heterogeneity in the expression and receptor accessibility to circulating ligands), resulting in variability in the magnitude of targeted delivery and gene transduction. These results and others (17) indicate that targeted molecular imaging is a promising approach to study the persistence of transgene expression in tumors after systemic administration of targeted AAVP, and also provides the ability to visualize and quantify not only the magnitude and spatial distribution of transgene expression, but also the temporal dynamics (with repetitive molecular imaging). In a previous report (10), we followed the levels of transgene expression of *HSVtk* by PET imaging of both human tumor xenografts and isogenic tumors in mice until day 10 (before GCV treatment) after i.v. AAVP delivery,

and observed a stabilization between days 5–10 consistent with the possibility that proliferating cells continue to pass the transgene without a noticeable dilution effect in this period. In the current study, a biphasic and heterogeneous pattern of AAVP-mediated transgene expression emerged in growing sarcoma xenografts. BLI revealed a gradual, almost linear increase in BLI signal in sarcomas beginning 3 days after AAVP administration, reaching a plateau of transgene expression between days 5 and 10 that lasted only briefly, followed by a decrease in transgene expression. Thus, dynamics and magnitude of transgene expression may be variable with each tumor type. These observations could well be explained by dilution effect of proliferating transduced cells within a larger population of proliferating nontransduced cells. Indeed, in some animals, the decrease of luciferase expression in tumors coincided with a striking increase of tumor growth rate. However, the CMV promoter that drives transgene expression in the current version of the AAVP is notorious for silencing its own transcriptional activity. Any of these phenomena could have played a role in the occasional observed decrease of AAVP-*Luc* expression in sarcomas. These questions notwithstanding, our results are in agreement with other studies that have demonstrated transgene silencing with CMV promoters and reporters such as *GFP* or *βgal*. Although the CMV promoter is active in mammalian cells, it is susceptible to transcriptional inactivation because of DNA methylation and histone acetylation; the possibility of such inactivation in human soft-tissue sarcoma cells is an open question. Despite this potential limitation, BLI of the *Luc* reporter transgene provided the yield initial cost-effective scout imaging for 2D monitoring of targeted delivery, tumor expression levels, and longitudinal persistence needed to optimize the preclinical sarcoma model used here. Subsequently, we designed and developed a clinic-ready AAVP-based candidate approach for translation in human soft-tissue sarcomas: by using [¹⁸F]-FEAU PET imaging, we were able to repetitively monitor the location, magnitude, and temporal dynamics of *HSVtk* expression in nude rats bearing human sarcoma xenografts *in vivo* after i.v. administration of targeted AAVP-*HSVtk*. Such targeted molecular–genetic imaging provides a potential advantage because of its ability to monitor the efficiency and specificity of *HSVtk* delivery before and to predict tumor response after GCV. Our proof-of-concept results suggest that targeted AAVP can be integrated with PET imaging to predict sarcoma response.

In addition to SKLMS1, the susceptibility of other human sarcoma lines to the *HSVtk* plus GCV has been established. Based on these data, targeted AAVP particles may provide a systemic mean to deliver imaging reporters at sufficient expression levels to accomplish imaging of tumor response to drugs in soft-tissue sarcomas patients.

A few translational aspects merit comment. First, discovery of sarcoma-specific cell surface ligands and sarcoma-specific (or radiation-induced) promoters may improve the efficacy of this system; genetic targets, such as PAX3-FKHR, EWS-FLI1, and SYT-SSX1 fusion proteins (33), may provide imaging opportunities. Second, in addition to reporters, targeted delivery of therapeutic transgenes may also be feasible. Third, both SKLMS1 sarcoma cells and the tumor blood vessels express αv integrins; the relative tumor targeting versus vascular targeting will depend on the relative levels of receptor expression and accessibility (10). Consistently, αv integrins are expressed in the tumor vascular endothelium and in sarcoma cells in patient-derived specimens (Fig. 5 and SI Table 1).

The results reported here serve as a preclinical blueprint for design of translational clinical trials with targeted AAVP-mediated molecular imaging in human soft-tissue sarcoma; if so, targeted AAVP molecular imaging applications in patients with soft sarcoma may eventually become possible.

Materials and Methods

Cell Culture. SKLMS1 cells were grown at 37°C in 5% CO_2 in DMEM supplemented with 10% FCS, penicillin, and streptomycin. A model of nude rat-bearing SKLMS1-derived xenografts is described in ref. 16.

PHARMACOLOGY

Targeted Phage and AAVP. αv integrin-binding (10, 14, 15), IL11R-binding (21), and APA-binding (22) phage were described; the insertless fd-tet phage (13) or phage displaying unrelated peptide sequences served as controls. Design and genetic construction of targeted AAVP-based vectors is detailed in ref. 11. Vectors were purified from MC1061 *Escherichia coli*, resuspended in PBS and recentrifuged to remove residual debris. Supernatant containing AAVP was titrated by k91Kan *E. Coli* infection. Serial dilutions were plated on LB agar plates with tetracycline and kanamycin. TU were determined by colony counting.

Cell Surface Binding Assay. We used the biopanning and rapid analysis of selective interactive ligands (BRASIL) methodology (20) to evaluate sarcoma cell binding. SKLMS1 cells were detached by EDTA and resuspended in DMEM containing 1% BSA at 4×10^6 cells per ml. SKLMS1 cell suspensions (50 μl each) were incubated with 10^9 TU of RGD-4C AAVP or controls. After 2 h, the admixture was transferred to the top of a nonmiscible organic phase and centrifuged. Binding clones were recovered by k91Kan *E. coli* infection (20).

Sarcoma Cell Transduction. SKMLS1 cell transduction of was carried out as reported in ref. 11. Cells (4×10^4) were cultured on 24-well plate, and the culture medium was replaced by 200 μl of serum-free DMEM and 10^6 TU per cell of targeted AAVP and controls. Vectors were incubated with cells followed by medium change to DMEM containing 10% FCS. For binding inhibition, SKLMS1 cells were incubated with peptides in normal growth medium. Then, cells were washed with PBS and incubated with AAVP for transduction. Cells were analyzed for gene expression after transduction. D-Luciferin (Invivogen) was added to transduced cells at 20 μg/ml and activity was quantified with the BLI system 200 (Xenogen); luciferase activity was measured as photons per sec per cm^2 per sr and normalized to activity in cells treated with controls.

Nude Rat Model of Human Sarcoma. The Institutional Animal Care and Use Committee approved all experimentation. Rats were anesthetized by gas (2% isoflurane and 98% O_2) inhalation. To establish human sarcoma xenografts, 10^6 SKLMS1 cells were suspended in Matrigel and implanted in the right hind limb of 8-week-old female nude rats. When size-matched tumors reached $\approx$200 mm^3 (day 0), tumor-bearing rats received a single i.v. dose (3×10^{12} TU per rat) of RGD-4C AAVP-*HSVtk* or control. After 9 h, xenografts and control organs were removed and vectors recovered. GCV (100 mg·kg^{-1}·day^{-1}) was administered i.p. as indicated. Tumor volumes were determined as described in refs. 10, 14, and 15.

BLI of Sarcoma-Bearing Rats. To image the *Luc* expression, rats received a dose (150 mg/kg) of D-luciferin. Photonic emission was imaged after i.v. adminis-

tration of targeted RGD-4C AAVP-*Luc* or control. BLI parameters are described in ref. 10.

PET Scanning. Sarcoma-bearing nude rats were imaged at 1 h after i.v. administration of [^{18}F]-FDG (PETNet) at 200 μCi/rat. To image *HSVtk* expression, PET scans were performed at 2 h after i.v. administration of the radiolabeled nucleoside analogue [^{18}F]-FEAU. A microPET R4 (Concorde Microsystems) equipped with a computer-controlled positioning bed in a 10.8-cm transaxial and 8-cm axial field of view with no septa and operating in 3D list mode was used (10).

Radiolabeled Substrate Synthesis. Radiolabeled [^{18}F]-FEAU was synthesized to radiochemical purity >99% by using 5-ethyluracil-2,5-bis-trimethylsilyl ether as the pyrimidine base for condensation with 1-bromo-2-deoxy-2-[^{18}F]-fluoro-3,5-di-*O*-benzoyl-α-D-arabinofuranose (12, 34). To quantitate [^{18}F]-FEAU or [^{18}F]-FDG radioactivity, regions of interest were drawn on images and the measured values converted from nCi/mm^3 into percentage of injected dose per gram [%ID/g (18, 30)]. Repetitive [^{18}F]-FEAU PET imaging scans were performed after administration of targeted AAVP carrying the *HSVtk* gene or controls. PET imaging was performed at 24 h after GCV dosing to allow for sufficient elimination of GCV.

Immunohistochemistry. αv integrin expression in SKLMS1 xenografts in rats was analyzed in frozen samples. Cryosections were fixed in cold acetone for 10 min, washed with PBS, and blocked with 5% normal horse serum and 1% normal goat serum in PBS. Tissue sections were then incubated with a polyclonal antibody against αv integrin (AB1930; Chemicon) at 1:400 dilution ON at 4°C. Sections were rinsed with PBS, blocked, and incubated for 1 h at RT with a goat anti-rabbit Alexa488 secondary antibody. Tumor vascularization was assessed on frozen sections with a rat anti-mouse CD31 antibody (BD PharMingen). Sections were stained with a goat anti-rat Alexa Fluor 594 secondary antibody. A nuclear counter stain with Hoechst 33342 was applied. Analysis of αv integrin expression in human specimens was carried out on paraffin-embedded sections with a mouse anti-integrin monoclonal (MAB 1976; Chemicon). Sections were deparaffinized, rehydrated in PBS, and incubated ON at 4°C with the primary antibody at 1:100. A peroxidase-conjugated goat anti-mouse IgG (Jackson ImmunoResearch) was added for 1 h at RT. Sections were counterstained with hematoxylin.

1. Kotilingam D, Lev DC, Lazar AJ, Pollock RE (2006) Staging soft tissue sarcoma: Evolution and change. *CA Cancer J Clin* 56:282–291.
2. Miller AB, Hoogstraten B, Staquet M, Winkler A (1981) Reporting results of cancer treatment. *Cancer* 47:207–214.
3. Van Glabbeke M, van Oosterom AT, Steward W, Verweij J, Mouridsen H (1993) Selection of large and objectively measurable target lesions in EORTC phase II trials: Impact on recruitment and response rate. EORTC Soft Tissue and Bone Sarcoma Group (STBSG). *Eur J Cancer* 29:1943–1947.
4. Van Glabbeke M, et al. (1999) Prognostic factors for the outcome of chemotherapy in advanced soft tissue sarcoma: An analysis of 2,185 patients treated with anthracycline-containing first-line regimens—a European Organization for Research and Treatment of Cancer Soft Tissue and Bone Sarcoma Group study. *J Clin Oncol* 17:150–157.
5. Therasse P, et al. (2000) New guidelines to evaluate the response to treatment in solid tumors. European Organization for Research and Treatment of Cancer, National Cancer Institute of the United States, National Cancer Institute of Canada. *J Natl Cancer Inst* 92:205–216.
6. Therasse P, Le Cesne A, Van Glabbeke M, Verweij J, Judson I (2005) RECIST vs. WHO: Prospective comparison of response criteria in an EORTC phase II clinical trial investigating ET-743 in advanced soft tissue sarcoma. *Eur J Cancer* 41:1426–1430.
7. Therasse P, Eisenhauer EA, Verweij J (2006) RECIST revisited: A review of validation studies on tumour assessment. *Eur J Cancer* 42:1031–1039.
8. Benjamin R (2006) Measuring drug response in sarcoma. *Clin Adv Hematol Oncol* 4:513–514.
9. Choi H, et al. (2007) Correlation of computed tomography and positron emission tomography in patients with metastatic gastrointestinal stromal tumor treated at a single institution with imatinib mesylate: Proposal of new computed tomography response criteria. *J Clin Oncol* 25:1753–1759.
10. Hajitou A, et al. (2006) A Hybrid vector for ligand-directed tumor targeting and molecular imaging. *Cell* 125:385–398.
11. Hajitou A, et al. (2007) Design and construction of targeted AAVP vectors for mammalian cell transduction. *Nat Protoc* 2:523–531.
12. Soghomonyan S, et al. (2007) Molecular Pet imaging of HSV1-tk reporter gene expression using ^{18}F-FEAU. *Nat Protoc* 2:416–423.
13. Zacher III AN, Stock CA, Golden II JW, Smith GP (1980) A new filamentous phage cloning vector: fd-tet. *Gene* 9:127–140.
14. Arap W, Pasqualini R, Ruoslahti E (1998) Cancer treatment by targeted drug delivery to tumor vasculature in a mouse model. *Science* 279:377–380.
15. Ellerby HM, et al. (1999) Anti-cancer activity of targeted pro-apoptotic peptides. *Nat Med* 5:1032–1038.
16. Hannay J, et al. (2007) Isolated limb perfusion: A novel delivery system for wild-type p53 and fiber-modified oncolytic adenoviruses to extremity sarcoma. *Gene Ther* 14:671–681.
17. Gross S, Piwnica-Worms D (2005a) Spying on cancer: Molecular imaging *in vivo* with genetically encoded reporters. *Cancer Cell* 7:5–15.
18. Tjuvajev JG, et al. (1998) Imaging *Herpes virus* thymidine kinase gene transfer and expression by positron emission tomography. *Cancer Res* 58:4333–4341.
19. Tjuvajev JG, et al. (1999) Imaging adenoviral-mediated herpes virus thymidine kinase gene transfer and expression *in vivo*. *Cancer Res* 59:5186–5193.
20. Giordano RJ, Cardó-Vila M, Lahdenranta J, Pasqualini R, Arap W (2001) Biopanning and rapid analysis of selective interactive ligands. *Nat Med* 11:1249–1253.
21. Arap W, et al. (2002) Steps toward mapping the human vasculature by phage display. *Nat Med* 8:121–127.
22. Marchiò S, et al. (2004) Aminopeptidase A is a functional target in angiogenic blood vessels. *Cancer Cell* 5:151–162.
23. Pasqualini R, Arap W, Rajotte D, Ruoslahti E (2001) in *Phage Display: A Laboratory Manual*, eds Barbas CF, III, Burton DR, Scott JK, Silverman GJ (Cold Spring Harbor Press, New York), pp 22.1–22.24.
24. Gelovani-Tjuvajev J, Blasberg RG (2003) *In vivo* imaging of molecular-genetic targets for cancer therapy. *Cancer Cell* 3:327–332.
25. Serganova I, et al. (2004) Molecular imaging of temporal dynamics and spatial heterogeneity of hypoxia-inducible factor-1 signal transduction activity in tumors in living mice. *Cancer Res* 64:6101–6108.
26. Karnofsky DA (1961) Meaningful clinical classification of therapeutic responses to anti-cancer drugs. *Clin Pharmacol Ther* 2:709–712.
27. Jaffe CC (2006) Measures of response: RECIST, WHO, and new alternatives. *J Clin Oncol* 24:3245–3251.
28. Michaelis LC, Ratain MJ (2006) Measuring response in a post-RECIST world: From black and white to shades of grey. *Nat Rev Cancer* 6:409–414.
29. Tuma RS (2006) Sometimes size doesn't matter: Reevaluating RECIST and tumor response rate endpoints. *J Natl Cancer Inst* 98:1272–1274.
30. Moertel CG, Hanley JA (1976) The effect of measuring error on the results of therapeutic trials in advanced cancer. *Cancer* 38:388–394.
31. Kattan MW, Leung DH, Brennan MF (2002) Postoperative nomogram for 12-year sarcoma-specific death. *J Clin Oncol* 20:791–796.
32. Schuetze SM (2006) Utility of positron emission tomography in sarcomas. *Curr Opin Oncol* 18:369–373.
33. Helman LJ, Meltzer P (2003) Mechanisms of sarcoma development. *Nat Rev Cancer* 3:685–694.
34. Alauddin MM, Fissekis JD, Conti PS (2003) A general synthesis of 2′-deoxy-2′-([^{18}F]fluoro-5-methyl-1-β-D-arabinofuranosyluracil and its 5-substituted nucleosides. *J Labelled Compds Radiopharm* 46:285–289.

Circulation Research

American Heart Association®

*Learn and Live*sm

A Population of Multipotent CD34-Positive Adipose Stromal Cells Share Pericyte and Mesenchymal Surface Markers, Reside in a Periendothelial Location, and Stabilize Endothelial Networks

Dmitry O. Traktuev, Stephanie Merfeld-Clauss, Jingling Li, Mikhail Kolonin, Wadih Arap, Renata Pasqualini, Brian H. Johnstone and Keith L. March

The online version of this article, along with updated information and services, is located on the World Wide Web at:

http://circres.ahajournals.org/cgi/content/full/102/1/77

Cellular Biology

A Population of Multipotent CD34-Positive Adipose Stromal Cells Share Pericyte and Mesenchymal Surface Markers, Reside in a Periendothelial Location, and Stabilize Endothelial Networks

Dmitry O. Traktuev, Stephanie Merfeld-Clauss, Jingling Li, Mikhail Kolonin, Wadih Arap, Renata Pasqualini, Brian H. Johnstone, Keith L. March

Abstract—It has been shown that stromal–vascular fraction isolated from adipose tissues contains an abundance of CD34$^+$ cells. Histological analysis of adipose tissue revealed that CD34$^+$ cells are widely distributed among adipocytes and are predominantly associated with vascular structures. The majority of CD34$^+$ cells from freshly isolated stromal–vascular fraction were CD31$^-$/CD144$^-$ and could be separated from a distinct population of CD34$^+$/CD31$^+$/CD144$^+$ (endothelial) cells by differential attachment on uncoated plastic. The localization of CD34$^+$ cells within adipose tissue suggested that the nonendothelial population of these cells occupied a pericytic position. Analysis of surface and intracellular markers of the freshly isolated CD34$^+$/CD31$^-$/CD144$^-$ adipose-derived stromal cells (ASCs) showed that >90% coexpress mesenchymal (CD10, CD13, and CD90), pericytic (chondroitin sulfate proteoglycan, CD140a, and CD140b), and smooth muscle (α-actin, caldesmon, and calponin) markers. ASCs demonstrated polygonal self-assembly on Matrigel, as did human microvascular endothelial cells. Coculture of ASCs with human microvascular endothelial cells on Matrigel led to cooperative network assembly, with enhanced stability of endothelial networks and preferential localization of ASCs on the abluminal side of cords. Bidirectional paracrine interaction between these cells was supported by identification of angiogenic factors (vascular endothelial growth factor, hepatocyte growth factor, basic fibroblast growth factor), inflammatory factors (interleukin-6 and -8 and monocyte chemoattractant protein-1 and -2), and mobilization factors (macrophage colony-stimulating factor and granulocyte/macrophage colony-stimulating factor) in media conditioned by CD34$^+$ ASCs, as well a robust mitogenic response of ASCs to basic fibroblast growth factor, epidermal growth factor, and platelet-derived growth factor-BB, factors produced by endothelial cells. These results demonstrate for the first time that the majority of adipose-derived adherent CD34$^+$ cells are resident pericytes that play a role in vascular stabilization by mutual structural and functional interaction with endothelial cells. (*Circ Res*. 2008;102:77-85.)

Key Words: adipose stromal cells ∎ pericytes ∎ growth factors/cytokines

O ver the past decade, interest has grown in identifying and characterizing progenitor cells isolated from a range of types of adult tissues, such as subtypes of endothelial progenitor cells,[1–4] bone marrow–derived mesenchymal cells,[1,5,6] and satellite cells from skeletal muscles.[7–10] Experimental models and clinical trials have shown that these cells stimulate angiogenesis in ischemic tissues and may preserve or rescue cardiac and brain function in the context of ischemic insult. Despite potentially significant therapeutic effects demonstrated by a majority of these cell types, their relatively limited availability in adult organisms (endothelial progenitor cells and mesenchymal stem cells [MSCs]) or invasive nature of their procedures of their harvest (MSCs and myoblasts) may pose a challenge to their extensive clinical application.

Accordingly, adipose-derived stromal cells (ASCs), which can be obtained in abundance through minimally invasive harvest procedures (lipoaspiration or abdominoplasty), present an important alternative for autologous cell transplantation.

Recently it has been shown that the ASC population, which includes cells that function as adipocyte progenitors (preadipocytes),[11] contains cells able to differentiate in vitro into multiple mesenchymal cell types[12–16] as well as hepatocytes,[17] neuronal cells,[18] endothelial cells (ECs),[19,20] and cardiomyocytes.[21,22] In addition, locally or systemically injected ASCs, whether freshly isolated or expanded, stimulate angiogenesis and mediate recovery of muscle tissues following ischemic insult.[19,22–26]

Despite the plasticity of ASCs in vitro, and their effects in experimental models in vivo, there is little knowledge of their natural localization, characteristics, and physiologic role(s) in vivo. Initial enzymatic liberation of ASCs yields a mixture of stromal and vascular cells (referred to as the stromal–vascular fraction [SVF]), indicating a spatial proximity. Several studies have examined surface marker profiles of the ASC population within the SVF and have observed that the total nonendothelial population is highly enriched for CD34-expressing cells.[19,23,24]

This study was designed to define the in vivo localization of CD34$^+$ ASCs in adipose tissue and to further characterize their phenotype with respect to expression of surface markers and factors important for intracellular interactions, to help uncover their normal physiological functions, and to shed further light on their angiogenic properties.

To this end, we demonstrate, for the first time, the existence of a periendothelial subpopulation of ASCs that bear many hallmarks of pericytes and provide vascular stability through functional interaction with ECs. This information may help to delineate both their capabilities and limitations with respect to their potential clinical translation.

Materials and Methods

Isolation and Culture of Human ASCs

Human subcutaneous adipose tissue samples (N=10), obtained from lipoaspiration/liposuction procedures were digested in collagenase type I solution (Worthington Biochemical, Lakewood, NJ) under agitation for 2 hours at 37°C and centrifuged at 300g for 8 minutes to separate the stromal cell fraction (pellet) from adipocytes. The pellet was resuspended in DMEM/F12 containing 10% FBS (Hyclone, Logan, Utah) filtered through 250-μm Nitex filters (Sefar America Inc, Kansas City, Mo) and centrifuged at 300g for 8 minutes. The cell pellet was treated with red cell lysis buffer (154 mmol/L NH$_4$Cl, 10 mmol/L KHCO$_3$, 0.1 mmol/L EDTA) for 10 minutes. The final pellet was resuspended in EBM-2/5% FBS or EGM2-MV (Cambrex, Baltimore, Md).

Flow Cytometric Characterization of Human ASCs

Freshly isolated SVF cells, and cells cultured for 2 days on culture plastic, were analyzed for surface marker expression using a Calibur flow cytometer analyzer and Cell QuestPro software (Becton Dickinson Immunocytometry Systems). Day 2 cells were harvested with 2 mmol/L EDTA/PBS. All of the following steps were performed on ice. Cell pellets were incubated for 20 minutes with primary antibodies or matching isotype controls (5 μg/mL). The primary antibodies used were CD10-phycoerythrin (PE), CD13-PE, CD31-PE, CD45–fluorescein isothiocyanate, CD34-allophycocyanin, CD90-PE, CD140a-PE, CD140b-PE, CD144-PE, and chondroitin sulfate proteoglycan (NG2) (Chemicon, Temecula, Calif). To detect nonlabeled primary antibodies, samples were incubated for 20 minutes with PE-conjugated antibodies (BD, San Diego, Calif), then washed with 2% FBS/PBS, and fixed with 2% paraformaldehyde.

Immunofluorescent Analysis of Adipose Tissue

Frozen sections of human fat tissue were simultaneously stained with rabbit anti-CD31 and mouse anti-human CD34 or with mouse anti-human CD31 and rabbit anti-CD140b antibodies. See the online data supplement, available at http://circres.ahajournals.org, for detailed procedures.

Immunofluorescent Analysis of Isolated ASCs

Freshly isolated ASCs were stained by immunofluorescence, 3 days after plating, against caldesmon, calponin, and α-smooth muscle actin antigens. See the online data supplement for detailed procedures.

Matrigel Assay

Human microvascular ECs (HMVECs) (passage 7) and ASCs (day 2 or passage 1) were labeled with PKH2 (green) and PKH-26 (red) (Sigma, St Louis, Mo), respectively. Twelve-well plates were coated with 600 μL per well of growth factor–reduced Matrigel (BD). Plates were incubated at 37°C for 2 hours. Cells (10^5 cells/well). HMVECs and ASCs were plated separately or together at a ratio of 1:3 (7.5×10^4 HMVECs+2.5×10^4 ASCs) in 600 μL of DMEM/10% FBS and were cultured at 37°C with 10% CO$_2$ and monitored frequently by fluorescent microscopy.

Generation of Conditioned Media

Human (h)ASCs and HMVECs were grown in EGM-2MV, in T75 flasks, until confluent, and media were changed to 10 mL of EBM-2/5% FBS. Seventy-two hours later, conditioned media (CM) was collected, centrifuged at 300g for 5 minutes, and frozen at −80°C. Cell counts were determined in a standard manner.

Proliferation Assay

Cells were grown for 24 hours in EBM-2/5% FBS before detachment with 0.05% trypsin/EDTA and replating into 12-well plates at 10^4 cells per well. Four hours postplating, media were changed to fresh EBM-2/5% FBS (control) or CM prepared as above. Four days later, cells were detached and counted.

Migration Assay

The bottom surfaces of Costar Transwell insert membranes, with pore diameters of 5 μm for ASCs and 8 μm for HMVECs, were coated with 50 μg/mL rat tail collagen I (BD). Cells (3×10^4) in 0.1 mL of EBM-2/5% FBS were added into each insert, and the inserts were placed into 24-well plates, with wells containing either controls or CM. Cells were allowed to migrate for 4 hours, after which the downward aspect of the inserts were stained for transmigratory cells with Diff-Quick (Dade Behring). Cells retained on the top surface of the membranes were eliminated using a cotton swab. Insert undersides were imaged and migratory cells quantitated using ImageJ software.

Evaluation of hASC Mitogenic Response to Individual Growth Factors

Freshly isolated ASCs were adhered on cell culture plastic for 2 days before harvesting attached cells with 0.05% trypsin/EDTA. Cells were seeded at 3×10^3 cells/cm^2 in 12-well plates and allowed to attach overnight in EBM-2/5% FBS medium, which was then replaced with EBM-2/5% FBS alone (control) or EBM-2/5% FBS supplemented with basic fibroblast growth factor (bFGF), epidermal growth factor (EGF), or platelet-derived growth factor (PDGF)-BB individually at final concentrations of 10 pg, 100 pg, 1 ng, or 10 ng each or the mixture of all of these, each at the specified concentration. Cells were cultured for 4 days, with a medium change after 48 hours, and then detached using 0.05% trypsin/EDTA, and viable cells were counted using a hemacytometer and trypan blue. Proliferation data are presented as the ratio of cells per well supplemented with growth factor to cells per well in control media.

See the online data supplement for detailed information regarding analysis of factor accumulation in CM of hASC and HMVECs, quantitative assessment of growth factors accumulated in HMVEC CM, and statistical analysis.

Results

Defining the Subpopulation of SVF Corresponding to ASCs

The objective of this study was to define the location of ASCs within adipose tissues. Initially, it was necessary to carefully
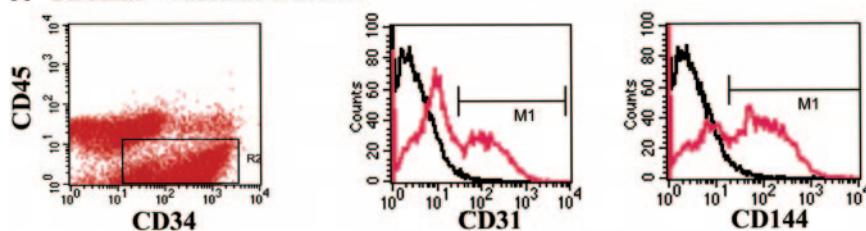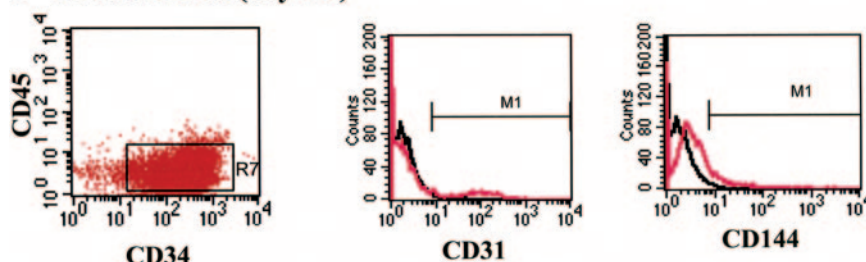
Figure 1. Fluorescence-activated cell sorting analyses of SVF of adipose tissue. Analysis of cells, either freshly isolated or adherently cultured for 2 days, was performed using CD34 (allophycocyanin), CD45 (fluorescein isothiocyanate), CD144 (PE), and CD31 (PE) antibodies. Cell populations in flow cytometric gates outlined by black boxes (R2 and R7), representing CD34$^+$/CD45$^-$ populations, were evaluated for the presence of ECs (CD144$^+$/CD31$^+$). Signals for fluorescent isotype IgG are shown as black and antigen-specific signals are shown as red curves.

define the phenotype of the ASC subpopulation contained within the mixed population comprising SVF. Multilabel flow cytometric analysis was performed using markers that allowed differentiation among 3 main cell types: ASCs, ECs, and leukocytes. In addition, we used dissimilar attachment and growth properties to further distinguish these. Endothelial and leukocyte cells use protein matrices to promote attachment and growth in culture.[27–29] A limited plating time (1 to 2 days) of SVF on uncoated tissue culture plastic resulted in selective adherence of a population that was greatly reduced in the percentage of endothelial (CD31 and CD144) and leukocytic (CD45) cells (Figure 1). Staining of freshly isolated cells for CD34 and CD45 revealed 3 major subpopulations: CD34$^-$/CD45$^+$, CD34$^+$/CD45$^+$, and CD34$^+$/CD45$^-$ (Figure 1a). The CD45$^+$ cells (47.6±5.8% of SVF) likely include a mixture of leukocytes contained within vasculature as well as resident in the adipose tissue.[11,30] Analysis of the CD34$^+$/CD45$^-$ population revealed a significant subpopulation (20±5%) that coexpressed the EC markers CD31 and CD144. Culturing isolated cells on plastic

resulted in enrichment to >85% of cells bearing the surface marker profile CD34$^+$/CD31$^-$/CD45$^-$/CD144$^-$ (Figure 1b). Accordingly, this adherent fraction of nonendothelial CD34$^+$/CD31$^-$/CD45$^-$/CD144$^-$ cells broadly defines the ASC population that has been previously characterized as pluripotent. The differentiation capacity of this purified population was confirmed by the demonstration that these undergo both osteogenesis and adipogenesis at high frequency (Figures I and II in the online data supplement).

CD34$^+$ Cells in Adipose Tissue Are Associated With the Vasculature

Immunofluorescent analysis of human adipose tissue sections established that the majority of CD34$^+$ cells were associated with vessels within the tissue (Figure 2). A significant portion of these cells also coexpressed CD31, and therefore were presumably capillary ECs. However, a separate and predominant population of CD34$^+$ cells, which did not express CD31, was
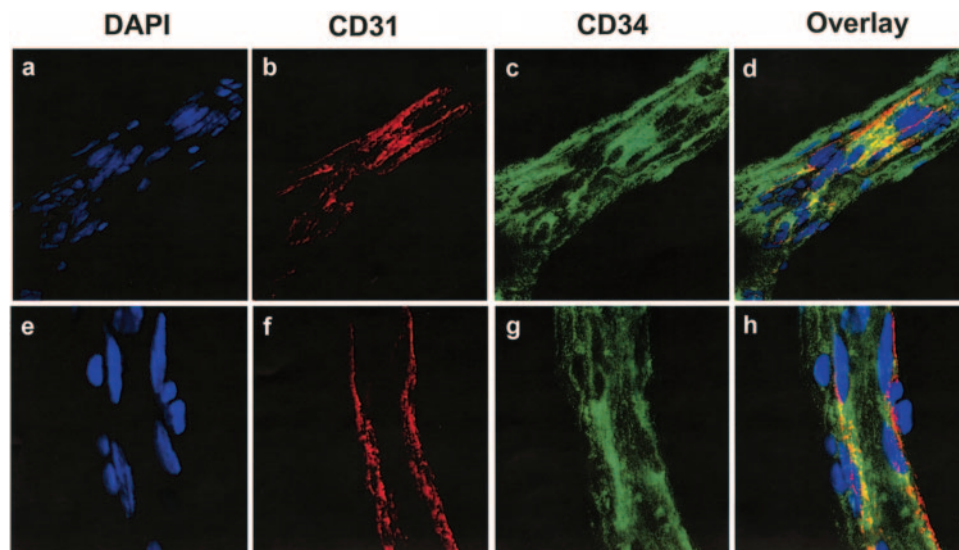
Figure 2. Histological analysis of human adipose tissue. Frozen sections of human fat were stained for the endothelial marker CD31 (red) and a major fresh ASC marker CD34 (green). Nuclei are revealed by 4′,6-diamidino-2-phenylindole (DAPI) staining.
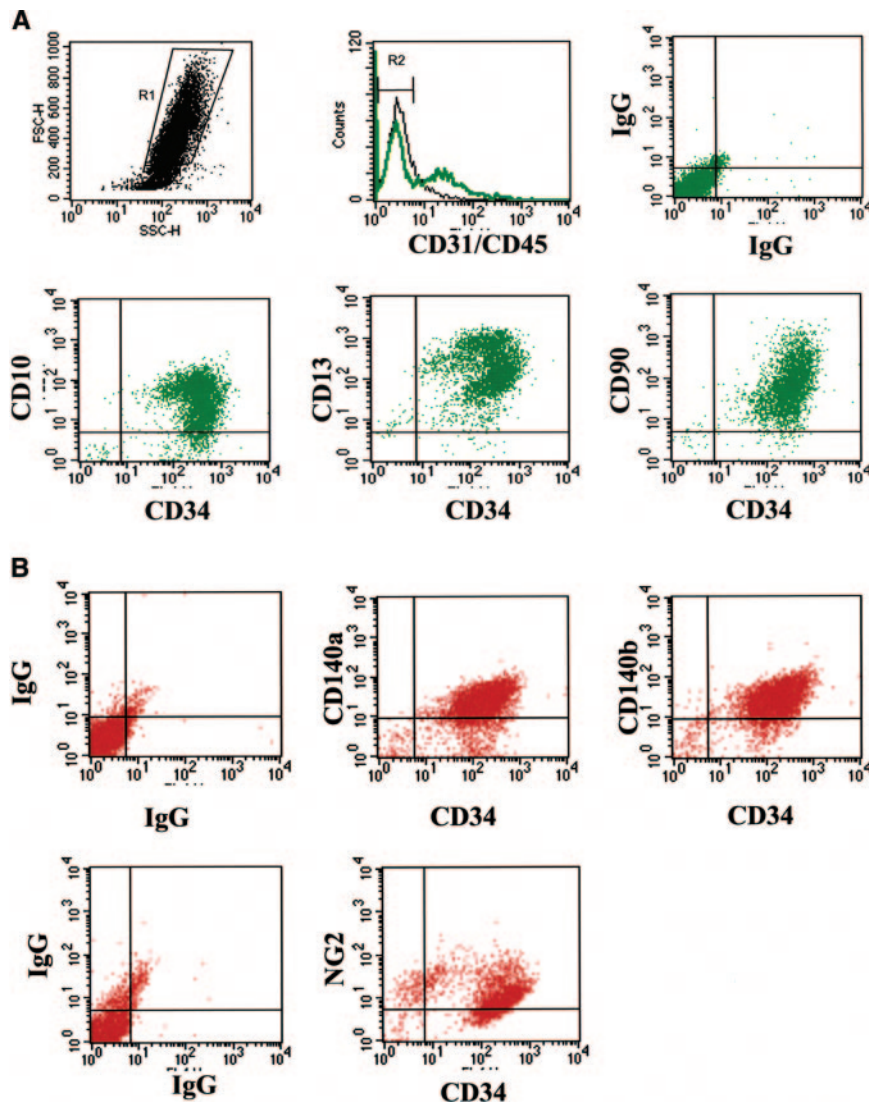
Figure 3. Fluorescence-activated cell sorting analysis of ASCs for coexpression of CD34 with mesenchymal (a) and pericyte (b) markers, assessed 2 days postadherence to plastic. Analysis was performed for CD34, CD45, CD10, CD13, CD90, CD140a, CD140b, NG2, and isotype IgGs.

observed in proximity to ECs. The perivascular location of the CD34$^+$/CD31$^-$ cells suggested their pericytic identity.

Adipose-Derived CD34$^+$/CD31$^-$ Cells Display Pericytic Markers In Vitro

The predominantly perivascular location of the CD34$^+$/CD31$^-$ cells suggested that these cells were pericytes, mural cells, which line and stabilize vascular endothelium in vivo.[27] The adherent CD34$^+$/CD31$^-$ population of SVF was thus characterized for expression of mesenchymal, pericytic, and smooth muscle cell markers. More than 95% of the adherent CD34$^+$/CD45$^-$/CD31$^-$ population coexpressed the mesenchymal cell markers CD10, CD13, and CD90 (Figure 3a). Analysis of surface markers used to define pericytes[28–30] (Figure 3b) revealed that the majority of the ASCs expressed chondroitin sulfate proteoglycan (NG2), CD140a, and CD140b (PDGF receptor-α and -β, respectively). Analysis of cytoskeletal markers performed by immunocytochemistry of freshly isolated ASCs revealed that many ASCs also expressed the smooth muscle cell antigens caldesmon, calponin, and α-smooth muscle actin (Figure 4).

The ASC antigen profile by flow cytometry was confirmed by PCR analysis of mRNA expression corresponding with multiple proteins (supplemental Figure III).

ASCs Occupy a Perivascular Position in Adipose Tissue In Vivo

The spatial relationship between EC and ASCs was evaluated by colabeling adipose tissue sections with antibodies specifically decorating each cell type. The surface antigen CD140b was highly expressed by ASCs (Figure 3b) but not microvascular EC (data not shown), whereas, as shown above, ASCs did not express the EC antigen CD31. Cells comprising capillary vessels in adipose tissue exhibited spatially separated expression of each antigen; CD31 (green) was specifically associated with cells forming the vessel lumen, whereas CD140b (red) was displayed on the surface of cells lining the exterior surface of the vessels (Figure 5). Taken together, these data demonstrate that ASCs are pericytic cells that occupy a perivascular position in vivo.
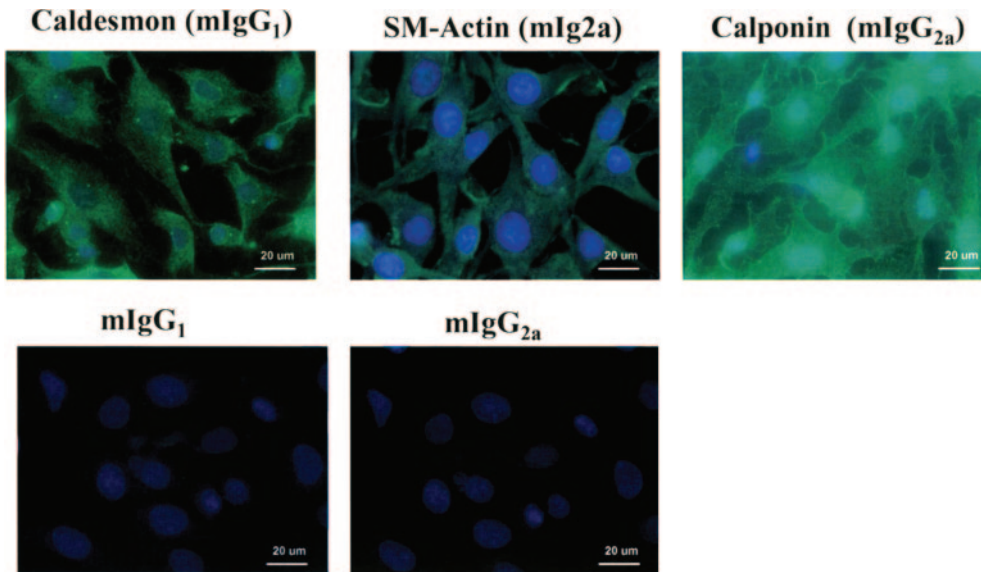
Figure 4. Immunocytochemistry of cytoskeletal antigens in ASCs 2 days postadherence to plastic. Formaldehyde-fixed cells were permeabilized and stained against α-smooth muscle actin, caldesmon, and calponin or with isotype-matched IgGs. Nuclei are revealed by DAPI staining.

ASCs Coassemble With and Stabilize Newly Forming EC Networks

To test for a functional correlate of the ASC–EC proximity in vascular structures, we evaluated the effect of ASCs on formation and stabilization of EC network on Matrigel. As shown in Figure 6a, HMVECs cultured in growth factor–free media form temporary networks that started dissociating after 24 hours. Plating ASCs alone also revealed formation of networks on Matrigel. However, coculturing HMVECs with ASCs produced stabilized cell networks that remained intact for up to 5 days (n=9), when experiments terminated. Coculture of fluorescently labeled HMVECs and ASCs revealed that the cells formed a cooperative network of tubular structures on Matrigel matrix with HMVECs (green) forming the lumen and ASCs (red) overlaying tubes formed by HMVECs (Figure 6b). Extending this finding into an in vivo system, we found that subcutaneous implantation of collagen/fibronectin gels containing ASCs admixed with ECs into
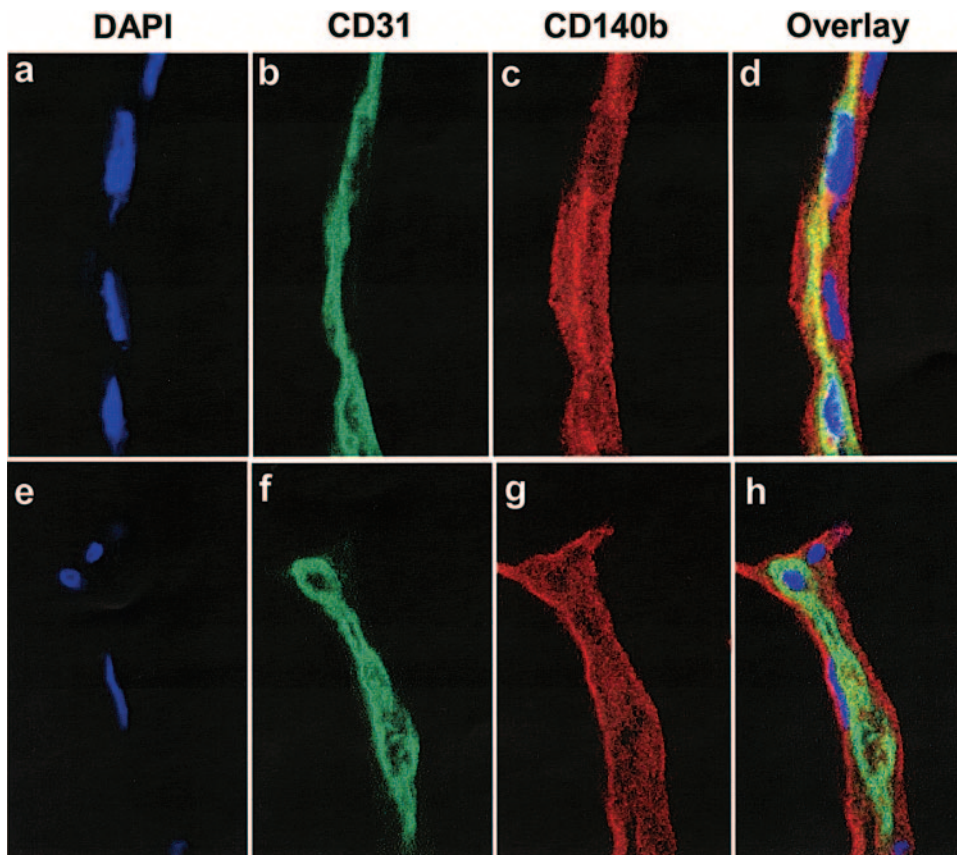
Figure 5. Histological analysis of human adipose tissue for microvascular endothelium and CD140b-expressing cells. Frozen sections of human fat were stained against endothelial CD31 (green) and ASC/pericyte CD140b (red) markers. Nuclei are revealed by DAPI staining.
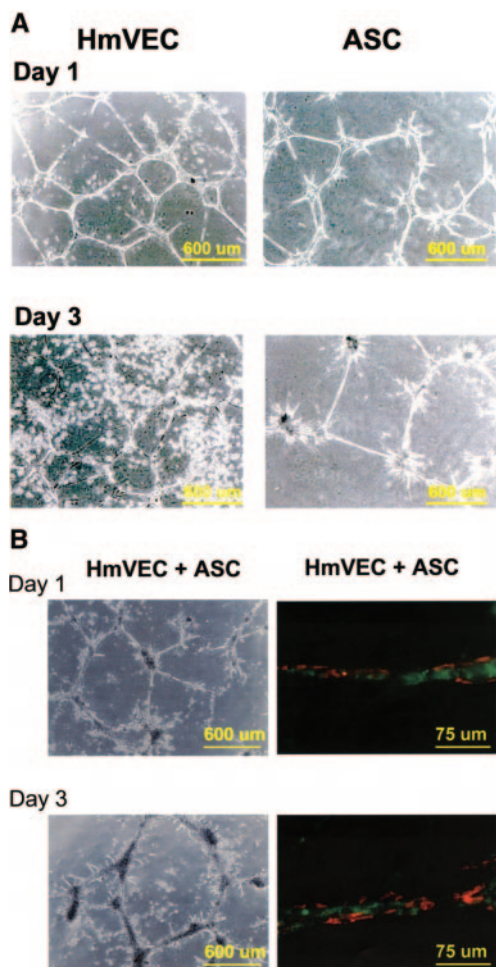
Figure 6. A, Evaluation of cord formation by HMVECs and hASCs on Matrigel surface. Cord formation was evaluated (phase contrast) on days 1 and 3 postplating. B, Fluorescent dye–labeled ECs (green) and hASCs (red) were mixed and plated on Matrigel. Cord formation was evaluated on days 1 and 3 postplating by fluorescence.

nude mice (n=4) also demonstrated formation of human-derived vascular structures with both endothelial and mural layers, with the mural layer comprising ASCs (supplemental Figure IV).

Paracrine Crosstalk Between ASCs and EC

To evaluate for paracrine crosstalk between ASCs and ECs, we evaluated the effects of CM collected from each of HMVECs and ASCs on the proliferation and migration of the complementary cell types. As is shown in Figure 7a, CM manifested strong mitogenic effects on ASCs. In 4-hour experiments, more than twice as many cells migrated through the filter in response to HMVEC CM as to control media EBM-2/5% FBS ($P<0.001$). In parallel with this chemotactic effect, HMVEC CM stimulated more than 3.5-fold expansion of ASCs compare with control media ($P<0.001$) (Figure 7b).

We evaluated the complementary effects of ASC-secreted factors on EC. Unlike the finding with EC CM, ASC CM did not stimulate proliferation to cell numbers above those originally seeded but rather demonstrated a strong prosurvival effect on microvascular EC, markedly limiting their

death in basal medium. As is shown in Figure 7d, HMVECs cultured in EBM-2/5% FBS for 4 days exhibit cell loss, with 50% remaining viable ($P<0.001$), whereas exposing cells to ASC CM (at 1:1 dilution) for the same time supports 100% cell survival ($P<0.001$). Evaluation for HMVEC chemotaxis toward ASC CM (Figure 7c) showed a modest but significant increase in migration compared with control media (n=9).

To evaluate factors responsible for such effects, we analyzed proteins secreted by freshly isolated ASCs and cultured HMVECs using antibody Arrays (RayBiotech). The protein profile in CM from ASCs revealed multiple angiogenic factors, including angiogenin, vascular endothelial growth factor, hepatocyte growth factor, bFGF, and β-nerve growth factor; the cytokines interleukin-6, -8, -11, and -17; and the cell-mobilizing factors monocyte chemoattractant proteins 1 and 2, granulocyte/macrophage colony-stimulating factor, and macrophage colony-stimulating factor (supplemental Figure Va and Vb). Notably absent were EGF, PDGF-BB, transforming growth factors, stromal cell–derived factor-1, and stem cell factor. See the online data supplement for all proteins detected, as well as their respective detection limits.

On the other hand, cultured HMVEC CM included multiple factors, such as bFGF, EGF, and PDGF-AA, -AB, and -BB (supplemental Figure Vc). Several of these were quite distinct, whereas a few overlapped with the profile of ASC secretion (eg, bFGF). Quantitative analysis revealed that in HMVEC CM (72 hours), the concentration of factors were as follows: EGF, 83.6 ± 51.0 pg/mL; bFGF, 243.0 ± 46.4 pg/mL; and PDGF-BB, 405.2 ± 85.0 pg/mL. The concentration of these in basal media before conditioning was below 2 pg/mL. The dose dependence of the effects of these factors on ASC proliferation was evaluated by the addition of each factor to basal medium. As shown in Figure 8, these factors exert strong mitogenic effects on ASCs over concentrations that overlap with those secreted by ECs. Further evaluation revealed synergy among factors with respect to mitogenesis of ASCs. We observed significantly higher mitogenesis of ASCs to the factor mixture compared with individual factors at concentrations of 100 pg/mL for bFGF ($P<0.05$) and PDGF-BB ($P<0.001$) and 1 ng/mL for EGF ($P<0.05$) and PDGF-BB ($P<0.01$).

Discussion

This study demonstrates for the first time that stromal cells derived from subcutaneous adipose tissue, which have properties of preadipocytes[12,15,31] and manifest clonal pluripotency along multiple lineage pathways,[15,32,33] serve structurally and functionally as pericytes within adipose tissue. This finding sheds a unique light on their importance in normal adipose biology as well as the biological basis for their ability to promote vascularization and accelerate tissue perfusion in the context of ischemia.

Our study shows the prominent and consistent presence of the marker CD34 on freshly isolated ASCs, occurring in the absence of CD45, which distinguishes ASCs from cells of hematopoietic lineage. The variability in reports of ASC as $CD34^+$, as well as $CD34^-$ cells,[12,15,24] is likely a consequence of its consistent downregulation during culturing over a
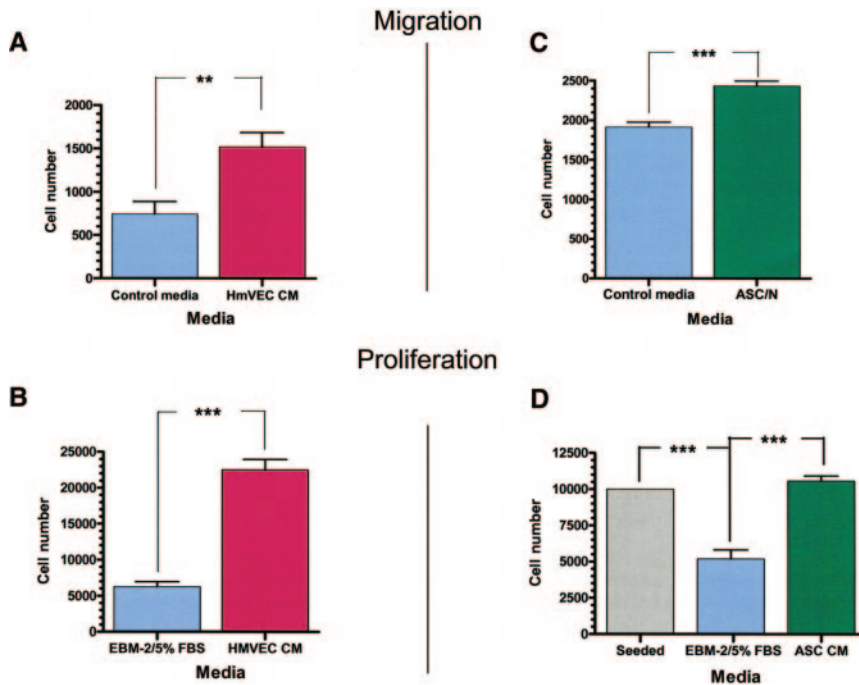
Figure 7. Effects of media conditioned for 72 hours by HMVECs (A and B) or ASCs (C and D) on ASC and HMVEC migration (A and C) and proliferation (B and D). The cells were added to collagen-coated Costar Transwell inserts and were allowed to migrate for 4 hours toward the lower wells containing control or CM (migration). The attached cells were exposed to either control or CM for 4 days and were detached and counted subsequently (proliferation).

several-day period[24]; passaged ASCs have been characterized as CD34^{low} or CD34^{−}.[12,15,24] We have found that CD34 antigen serves as a convenient tool for identifying the majority of freshly isolated ASCs, when used with the CD45^{−} and CD31^{−} phenotypes to exclude leukocytic and endothelial populations respectively.

This study also demonstrates that the marker profile of ASCs shares much in common with bone marrow–derived MSCs, as also found in analyses of gene expression.[34–36] One apparent distinction is a widespread and prominent degree of CD34 expression on ASCs, contrasting with descriptions of MSCs as lacking CD34.[37–39] Based on our observation that ASC expression of CD34 is rapidly downregulated in culture,[24] and that most isolation protocols for MSCs require
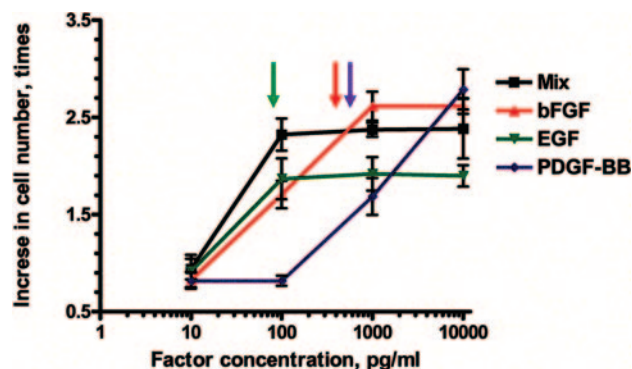

Figure 8. Mitogenic response of hASCs to bFGF, EGF, and PDGF-BB factors (known to be produced by ECs). hASCs were cultured in EBM-2/5% FBS media in the presence of 1 of bFGF, EGF, PDGF-BB, or their mixture in a range of concentrations between 10 pg/mL and 10 ng/mL for 4 days. ***$P<0.001$. Data are presented as ratios (in percentages) of the cell counts in wells containing growth factor(s) to wells with basal media (n=3). Arrows represent concentrations of factors secreted by HMVECs.

extended culture periods before availability of MSCs for study, we hypothesize that MSC in situ may indeed express the CD34 antigen but this property is lost during expansion between isolation and surface marker evaluation. Indeed, early descriptions of MSCs reported enrichment of their colony-forming activity using CD34^{+} selection[40]

ASCs Express Pericyte Markers

The perivascular location of CD34^{+}/CD31^{−} cells suggested a pericytic identity, which was confirmed by flow cytometry and further immunolocalization of these cells using a panel of markers associated with pericytes, including CD140a and CD140b (PDGF receptor-α and -β), and NG2. Staining for these markers in adipose tissue confirmed a perivascular location for the ASC population. It is notable that these markers were present on most ASCs, as defined above (>95%), reflecting that pericytic cells are not a minor subset of ASCs isolated using standard methods but rather are substantially identical to these cells, at least in subcutaneous adipose tissue.

ASCs and Endothelial Cells Are Linked by Physical and Paracrine Interactions

Exploration of the relationship of ASCs with ECs clearly revealed their capacity for both structural and functional interactions. ASCs and EC in coculture exhibited preferential heterotypic assembly into vascular networks in vitro, which demonstrate a stability advantage in comparison with polygonal networks of ECs alone. This model for vascular assembly should permit in vitro screening and analyses of molecules mediating assembly by selective disruption of interactions. Exploration of paracrine interactions between ASCs and EC by CM transfer demonstrated mutual chemoattraction, consistent with their association in coculture. In addition, EC CM exhibited a mitogenic effect on ASCs,

whereas ASC CM supported endothelial survival. Analysis of secreted proteins revealed candidates for mediating these responses, extending our previous description of vascular endothelial growth factor, bFGF, and hepatocyte growth factor secreted by ASCs associated with antiapoptotic effects on ECs.[24] Complementary factors secreted by HMVECs included isoforms of PDGF (AA, AB, and BB) as well as EGF, which showed potent mitogenic effects on ASCs, confirming functionality of PDGF receptors identified on ASCs by immunostaining. The heterotypic assembly as well as paracrine crosstalk are consistent with interactions described between microvascular ECs and pericytes from other sources.[27]

Dual Roles for ASCs In Situ: Tissue and Vascular Support

Our findings that ASCs are components of the vascular wall functioning in paracrine support of microvasculature, complements previous understanding of their role as preadipocytes, which are able to differentiate and form new adipocytes.[11,31] The location of the ASCs in the vessel at the interface between endothelium and adipocytes and their ability to both support vascular structure and generate adipocytes suggests a key hypothesis that they play an important role linking adipose tissue parenchymal mass with provision of its vascular supply. Indeed, forced regression of adipose tissue vasculature has been identified as an approach to reducing adipose mass.[41,42] The novel recognition of a dual role for ASCs in adipogenesis and vascular stabilization also suggests new approaches to manipulation of adipose tissue mass.

It is tempting to speculate that this role for ASCs/pericytes in physiological vascular stabilization could underlie potential mechanisms by which exogenous ASCs enhance vascular supply and limit ischemic tissue loss in models of limb ischemia, as consistently reported.[19,23,24,43] This has suggested that the readily available ASCs be tested as a therapy for ischemic diseases.

ASCs: Multipotent Perivascular Cells

At least 3 lines of investigation point to the notion that stem or progenitor cells in many tissues are deployed on blood vessels. Several studies have shown that pericytes isolated from different tissues are pluripotent.[44–46] Complementary literature has suggested that MSCs are found in perivascular sites in many tissues: in bone marrow, where they interact with both sinusoidal ECs and hematopoietic precursors; in central nervous system[47]; in dental pulp[48]; and in others.[49] Furthermore, developmental studies have identified a perivascular mesangioblast population of dorsal aorta and other vessels that gives rise to multiple cell types, including smooth muscle cells, skeletal and cardiac muscle cells, and bone.[50,51] The findings of our study indicate that multipotent ASCs also have a perivascular location and express pericytic markers. Analysis of all these findings suggests that in adult tissues, the perivascular compartment represents a niche for multipotent cells. The interaction of EC with these multipotent cells, including ASCs, implies that endothelium modulates their function within this niche.

We have shown that ASCs express the pericyte markers CD140a, CD140b, NG2, and α-smooth muscle actin occasionally express CD146 but lack 3G5, also a pericyte marker.[48,52] Taking these together, it may be best to describe ASCs as a cell with pericytic properties. Without direct comparison of ASCs with pericytes from other sources, their precise relationship is difficult to assess. Also, it may be that pericytes from a range of tissues differ in antigen expression because of unique local environments. Furthermore, we would propose that pericytic identity should be primarily established by physiological properties and function rather than by surface markers.

In conclusion, the highly defined ASC population (CD34$^+$/140a$^+$/140b$^+$/31$^-$/45$^-$/117$^-$/144$^-$) is a subset of adipose-derived cells, which in quiescent adipose tissue, possesses a majority of pericytic properties, while harboring the ability to enter into multiple other distinct lineages.

Disclosures

None.

References

1. Assmus B, Schachinger V, Teupe C, Britten M, Lehmann R, Dobert N, Grunwald F, Aicher A, Urbich C, Martin H, Hoelzer D, Dimmeler S, Zeiher AM. Transplantation of Progenitor Cells and Regeneration Enhancement in Acute Myocardial Infarction (TOPCARE-AMI). *Circulation*. 2002;106:3009–3017.
2. Kawamoto A, Gwon HC, Iwaguro H, Yamaguchi JI, Uchida S, Masuda H, Silver M, Ma H, Kearney M, Isner JM, Asahara T. Therapeutic potential of ex vivo expanded endothelial progenitor cells for myocardial ischemia. *Circulation*. 2001;103:634–637.
3. Masuda H, Kalka C, Asahara T. Endothelial progenitor cells for regeneration. *Hum Cell*. 2000;13:153–160.
4. Ingram DA, Mead LE, Tanaka H, Meade V, Fenoglio A, Mortell K, Pollok K, Ferkowicz MJ, Gilley D, Yoder MC. Identification of a novel hierarchy of endothelial progenitor cells using human peripheral and umbilical cord blood. *Blood*. 2004;104:2752–2760.
5. Perin EC, Dohmann HF, Borojevic R, Silva SA, Sousa AL, Mesquita CT, Rossi MI, Carvalho AC, Dutra HS, Dohmann HJ, Silva GV, Belem L, Vivacqua R, Rangel FO, Esporcatte R, Geng YJ, Vaughn WK, Assad JA, Mesquita ET, Willerson JT. Transendocardial, autologous bone marrow cell transplantation for severe, chronic ischemic heart failure. *Circulation*. 2003;107:2294–2302.
6. Prockop DJ, Sekiya I, Colter DC. Isolation and characterization of rapidly self-renewing stem cells from cultures of human marrow stromal cells. *Cytotherapy*. 2001;3:393–396.
7. Menasche P, Hagege AA, Vilquin JT, Desnos M, Abergel E, Pouzet B, Bel A, Sarateanu S, Scorsin M, Schwartz K, Bruneval P, Benbunan M, Marolleau JP, Duboc D. Autologous skeletal myoblast transplantation for severe postinfarction left ventricular dysfunction. *J Am Coll Cardiol*. 2003;41:1078–1083.
8. Menasche P, Hagege AA, Scorsin M, Pouzet B, Desnos M, Duboc D, Schwartz K, Vilquin JT, Marolleau JP. Myoblast transplantation for heart failure. *Lancet*. 2001;357:279–280.
9. Pagani FD, DerSimonian H, Zawadzka A, Wetzel K, Edge AS, Jacoby DB, Dinsmore JH, Wright S, Aretz TH, Eisen HJ, Aaronson KD. Autologous skeletal myoblasts transplanted to ischemia-damaged myocardium in humans. Histological analysis of cell survival and differentiation. *J Am Coll Cardiol*. 2003;41:879–888.
10. Goodell MA, Jackson KA, Majka SM, Mi T, Wang H, Pocius J, Hartley CJ, Majesky MW, Entman ML, Michael LH, Hirschi KK. Stem cell plasticity in muscle and bone marrow. *Ann N Y Acad Sci*. 2001;938:208–218.

11. Sengenes C, Lolmede K, Zakaroff-Girard A, Busse R, Bouloumie A. Preadipocytes in the human subcutaneous adipose tissue display distinct features from the adult mesenchymal and hematopoietic stem cells. *J Cell Physiol*. 2005;205:114–122.

12. Gronthos S, Franklin DM, Leddy HA, Robey PG, Storms RW, Gimble JM. Surface protein characterization of human adipose tissue-derived stromal cells. *J Cell Physiol*. 2001;189:54–63.

13. Wickham MQ, Erickson GR, Gimble JM, Vail TP, Guilak F. Multipotent stromal cells derived from the infrapatellar fat pad of the knee. *Clin Orthop*. 2003;196–212.

14. Mizuno H, Zuk PA, Zhu M, Lorenz HP, Benhaim P, Hedrick MH. Myogenic differentiation by human processed lipoaspirate cells. *Plast Reconstr Surg*. 2002;109:199–209.

15. Zuk PA, Zhu M, Ashjian P, De Ugarte DA, Huang JI, Mizuno H, Alfonso ZC, Fraser JK, Benhaim P, Hedrick MH. Human adipose tissue is a source of multipotent stem cells. *Mol Biol Cell*. 2002;13:4279–4295.

16. Jonasson L, Hansson GK, Bondjers G, Bengtsson G, Olivecrona T. Immunohistochemical localization of lipoprotein lipase in human adipose tissue. *Atherosclerosis*. 1984;51:313–326.

17. Seo MJ, Suh SY, Bae YC, Jung JS. Differentiation of human adipose stromal cells into hepatic lineage in vitro and in vivo. *Biochem Biophys Res Commun*. 2005;328:258–264.

18. Safford KM, Hicok KC, Safford SD, Halvorsen YD, Wilkison WO, Gimble JM, Rice HE. Neurogenic differentiation of murine and human adipose-derived stromal cells. *Biochem Biophys Res Commun*. 2002;294:371–379.

19. Miranville A, Heeschen C, Sengenes C, Curat CA, Busse R, Bouloumie A. Improvement of postnatal neovascularization by human adipose tissue-derived stem cells. *Circulation*. 2004;110:349–355.

20. Cao Y, Sun Z, Liao L, Meng Y, Han Q, Zhao RC. Human adipose tissue-derived stem cells differentiate into endothelial cells in vitro and improve postnatal neovascularization in vivo. *Biochem Biophys Res Commun*. 2005;332:370–379.

21. Planat-Benard V, Menard C, Andre M, Puceat M, Perez A, Garcia-Verdugo JM, Penicaud L, Casteilla L. Spontaneous cardiomyocyte differentiation from adipose tissue stroma cells. *Circ Res*. 2004;94:223–229.

22. Strem BM, Zhu M, Alfonso Z, Daniels EJ, Schreiber R, Begyui R, Maclellan WR, Hedrick MH, Fraser JK. Expression of cardiomyocytic markers on adipose tissue-derived cells in a murine model of acute myocardial injury. *Cytotherapy*. 2005;7:282–291.

23. Planat-Benard V, Silvestre JS, Cousin B, Andre M, Nibbelink M, Tamarat R, Clergue M, Manneville C, Saillan-Barreau C, Duriez M, Tedgui A, Levy B, Penicaud L, Casteilla L. Plasticity of human adipose lineage cells toward endothelial cells: physiological and therapeutic perspectives. *Circulation*. 2004;109:656–663.

24. Rehman J, Traktuev D, Li J, Merfeld-Clauss S, Temm-Grove CJ, Bovenkerk JE, Pell CL, Johnstone BH, Considine RV, March KL. Secretion of angiogenic and antiapoptotic factors by human adipose stromal cells. *Circulation*. 2004;109:1292–1298.

25. Kang SK, Lee DH, Bae YC, Kim HK, Baik SY, Jung JS. Improvement of neurological deficits by intracerebral transplantation of human adipose tissue-derived stromal cells after cerebral ischemia in rats. *Exp Neurol*. 2003;183:355–366.

26. Nakagami H, Maeda K, Morishita R, Iguchi S, Nishikawa T, Takami Y, Kikuchi Y, Saito Y, Tamai K, Ogihara T, Kaneda Y. Novel autologous cell therapy in ischemic limb disease through growth factor secretion by cultured adipose tissue-derived stromal cells. *Arterioscler Thromb Vasc Biol*. 2005;25:2542–2547.

27. von Tell D, Armulik A, Betsholtz C. Pericytes and vascular stability. *Exp Cell Res*. 2006;312:623–629.

28. Ozerdem U, Stallcup WB. Early contribution of pericytes to angiogenic sprouting and tube formation. *Angiogenesis*. 2003;6:241–249.

29. Hughes S, Chan-Ling T. Characterization of smooth muscle cell and pericyte differentiation in the rat retina in vivo. *Invest Ophthalmol Vis Sci*. 2004;45:2795–2806.

30. Bergers G, Song S, Meyer-Morse N, Bergsland E, Hanahan D. Benefits of targeting both pericytes and endothelial cells in the tumor vasculature with kinase inhibitors. *J Clin Invest*. 2003;111:1287–1295.

31. Van Harmelen V, Rohrig K, Hauner H. Comparison of proliferation and differentiation capacity of human adipocyte precursor cells from the omental and subcutaneous adipose tissue depot of obese subjects. *Metabolism*. 2004;53:632–637.

32. Case J, Horvath TL, Howell JC, Yoder MC, March KL, Srour EF. Clonal multilineage differentiation of murine common pluripotent stem cells isolated from skeletal muscle and adipose stromal cells. *Ann N Y Acad Sci*. 2005;1044:183–200.

33. Guilak F, Lott KE, Awad HA, Cao Q, Hicok KC, Fermor B, Gimble JM. Clonal analysis of the differentiation potential of human adipose-derived adult stem cells. *J Cell Physiol*. 2006;206:229–237.

34. Bunnell BA, Ylostalo J, Kang SK. Common transcriptional gene profile in neurospheres-derived from pATSCs, pBMSCs, and pNSCs. *Biochem Biophys Res Commun*. 2006;343:762–771.

35. Lee RH, Kim B, Choi I, Kim H, Choi HS, Suh K, Bae YC, Jung JS. Characterization and expression analysis of mesenchymal stem cells from human bone marrow and adipose tissue. *Cell Physiol Biochem*. 2004;14:311–324.

36. Izadpanah R, Trygg C, Patel B, Kriedt C, Dufour J, Gimble JM, Bunnell BA. Biologic properties of mesenchymal stem cells derived from bone marrow and adipose tissue. *J Cell Biochem*. 2006;99:1285–1297.

37. Muller I, Kordowich S, Holzwarth C, Spano C, Isensee G, Staiber A, Viebahn S, Gieseke F, Langer H, Gawaz M, Horwitz E, Conte P, Handgretinger R, Dominici M. Animal serum-free culture conditions for isolation and expansion of multipotent mesenchymal stromal cells from human BM. *Cytotherapy*. 2006;8:437–444.

38. Kassis I, Zangi L, Rivkin R, Levdansky L, Samuel S, Marx G, Gorodetsky R. Isolation of mesenchymal stem cells from G-CSF-mobilized human peripheral blood using fibrin microbeads. *Bone Marrow Transplant*. 2006;37:967–976.

39. Igura K, Zhang X, Takahashi K, Mitsuru A, Yamaguchi S, Takashi TA. Isolation and characterization of mesenchymal progenitor cells from chorionic villi of human placenta. *Cytotherapy*. 2004;6:543–553.

40. Simmons PJ, Torok-Storb B. CD34 expression by stromal precursors in normal human adult bone marrow. *Blood*. 1991;78:2848–2853.

41. Dallabrida SM, Zurakowski D, Shih SC, Smith LE, Folkman J, Moulton KS, Rupnick MA. Adipose tissue growth and regression are regulated by angiopoietin-1. *Biochem Biophys Res Commun*. 2003;311:563–571.

42. Kolonin MG, Saha PK, Chan L, Pasqualini R, Arap W. Reversal of obesity by targeted ablation of adipose tissue. *Nat Med*. 2004;10:625–632.

43. Moon MH, Kim SY, Kim YJ, Kim SJ, Lee JB, Bae YC, Sung SM, Jung JS. Human adipose tissue-derived mesenchymal stem cells improve postnatal neovascularization in a mouse model of hindlimb ischemia. *Cell Physiol Biochem*. 2006;17:279–290.

44. Collett GD, Canfield AE. Angiogenesis and pericytes in the initiation of ectopic calcification. *Circ Res*. 2005;96:930–938.

45. Doherty MJ, Ashton BA, Walsh S, Beresford JN, Grant ME, Canfield AE. Vascular pericytes express osteogenic potential in vitro and in vivo. *J Bone Miner Res*. 1998;13:828–838.

46. Farrington-Rock C, Crofts NJ, Doherty MJ, Ashton BA, Griffin-Jones C, Canfield AE. Chondrogenic and adipogenic potential of microvascular pericytes. *Circulation*. 2004;110:2226–2232.

47. Dore-Duffy P, Katychev A, Wang X, Van Buren E. CNS microvascular pericytes exhibit multipotential stem cell activity. *J Cereb Blood Flow Metab*. 2006;26:613–624.

48. Shi S, Gronthos S. Perivascular niche of postnatal mesenchymal stem cells in human bone marrow and dental pulp. *J Bone Miner Res*. 2003;18:696–704.

49. da Silva Meirelles L, Chagastelles PC, Nardi NB. Mesenchymal stem cells reside in virtually all post-natal organs and tissues. *J Cell Sci*. 2006;119:2204–2213.

50. Tagliafico E, Brunelli S, Bergamaschi A, De Angelis L, Scardigli R, Galli D, Battini R, Bianco P, Ferrari S, Cossu G, Ferrari S. TGFbeta/BMP activate the smooth muscle/bone differentiation programs in mesoangioblasts. *J Cell Sci*. 2004;117:4377–4388.

51. Minasi MG, Riminucci M, De Angelis L, Borello U, Berarducci B, Innocenzi A, Caprioli A, Sirabella D, Baiocchi M, De Maria R, Boratto R, Jaffredo T, Broccoli V, Bianco P, Cossu G. The meso-angioblast: a multipotent, self-renewing cell that originates from the dorsal aorta and differentiates into most mesodermal tissues. *Development*. 2002;129:2773–2783.

52. Nayak RC, Berman AB, George KL, Eisenbarth GS, King GL. A monoclonal antibody (3G5)-defined ganglioside antigen is expressed on the cell surface of microvascular pericytes. *J Exp Med*. 1988;167:1003–1015.

Article

Nanoshell-Enabled Photothermal Cancer Therapy: Impending Clinical Impact

Surbhi Lal, Susan E. Clare, and Naomi J. Halas

More About This Article

Additional resources and features associated with this article are available within the HTML version:

- Supporting Information
- Access to high resolution figures
- Links to articles and content related to this article
- Copyright permission to reproduce figures and/or text from this article

View the Full Text HTML

ACCOUNTS
of chemical research

Nanoshell-Enabled Photothermal Cancer Therapy: Impending Clinical Impact

SURBHI LAL,[†,⊥] SUSAN E. CLARE,[‖] AND NAOMI J. HALAS*[,†,‡,§,⊥]

†Department of Electrical and Computer Engineering, ‡Department of Chemistry, §Department of Bioengineering, and ⊥The Laboratory for Nanophotonics, Rice University, 6100 Main Street, Houston, Texas 77005, and ‖Department of Surgery, Indiana University School of Medicine, Indianapolis, Indiana 46202

CONSPECTUS

Much of the current excitement surrounding nanoscience is directly connected to the promise of new nanoscale applications in cancer diagnostics and therapy. Because of their strongly resonant light-absorbing and light-scattering properties that depend on shape, noble metal nanoparticles provide a new and powerful tool for innovative light-based approaches.

Nanoshells—spherical, dielectric core, gold shell nanoparticles—have been central to the development of photothermal cancer therapy and diagnostics for the past several years. By manipulating nanoparticle shape, researchers can tune the optical resonance of nanoshells to any wavelength of interest. At wavelengths just beyond the visible spectrum in the near-infrared, blood and tissue are maximally transmissive. When nanoshell resonances are tuned to this region of the spectrum, they become useful contrast agents in the diagnostic imaging of tumors. When illuminated, they can serve as nanoscale heat sources, photothermally inducing cell death and tumor remission. As nanoshell-based diagnostics and therapeutics move from laboratory studies to clinical trials, this Account examines the highly promising achievements of this approach in the context of the challenges of this complex disease. More broadly, these materials present a concrete example of a highly promising application of nanochemistry to a biomedical problem.

We describe the properties of nanoshells that are relevant to their preparation and use in cancer diagnostics and therapy. Specific surface chemistries are necessary for passive uptake of nanoshells into tumors and for targeting specific cell types by bioconjugate strategies. We also describe the photothermal temperature increases that can be achieved in surrogate structures known as tissue phantoms and the accuracy of models of this effect using heat transport analysis. Nanoshell-based photothermal therapy in several animal models of human tumors have produced highly promising results, and we include nanoparticle dosage information, thermal response, and tumor outcomes for these experiments.

Using immunonanoshells, infrared diagnostic imaging contrast enhancement and photothermal therapy have been integrated into a single procedure. Finally, we examine a novel "Trojan horse" strategy for nanoparticle delivery that overcomes the challenge of accessing and treating the hypoxic regions of tumors, where blood flow is minimal or nonexistent. The ability to survive hypoxia selects aggressive cells which are likely to be the source of recurrence and metastasis. Treatment of these regions has been incredibly difficult. Ultimately, we look beyond the current research and assess the next challenges as nanoshell-based photothermal cancer therapy is implemented in clinical practice.
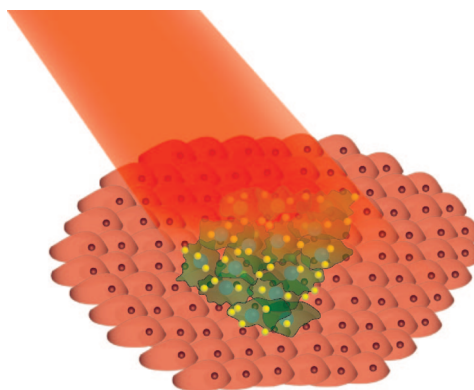
Introduction

It is projected that a total of 1,437,180 new cancer cases and 565,650 deaths from cancer will occur in the United States in 2008,[1] accounting for one in four deaths. Since the U.S. population 65 years and older will double in the next few

decades,[2] cancer diagnoses are expected to increase by 38% between 2005 and 2020.[3] While improvements in traditional cancer therapies have resulted in a continued decrease in cancer death rates since the early 1990s,[1] if we are to permanently reverse the trends reflected in these statistics and strike a decisive blow against this disease, the following critical challenges must be addressed:

1. **We need to understand the causes of cancer, so that interventions can be developed for prevention.**

2. **We must develop tools for early detection.** For example, ovarian cancer is curable if detected in its earliest stage; the 5-year survival for localized disease is 92% versus 30% for metastatic disease.[1] To address this challenge, nanotechnology may substantially increase the sensitivity and specificity of current diagnostic techniques and may enable the development of completely novel imaging modalities.

3. **We need to devise effective treatments for all stages of cancer, in particular, advanced stage metastatic disease and especially for metastatic disease in privileged sites, that is, the brain.** Much of the recent progress in cancer therapy has involved the treatment of early stage, localized disease where conventional surgical approaches followed by chemotherapy or radiation therapy provide standard protocols. However, the majority of cancer diagnoses are for more advanced stages of the disease. For example, 70% of ovarian cancers are already metastatic when diagnosed.[1] As technology advances are developed for cancer therapy, it is important that strategies for all stages of the disease are developed, in particular for those cases where no surgical option currently exists.

Much of the current excitement surrounding nanoscience and nanotechnology is focused on the potential use of chemically synthesized and functionalized nanoparticles designed specifically for biomedical applications. Indeed, perhaps the greatest promise of impact for nanochemistry is in nanoparticle-based approaches designed to address the specific diagnostic and therapeutic challenges of cancer. While many approaches are being developed for nanotechnology-enabled cancer diagnostics and therapeutics, a remarkably promising strategy involves the combination of noble metal nanoparticles and light. The uniquely vivid colors of metallic nanoparticles such as gold or silver are a result of their strong optical resonances.[4] When illuminated by light, metal nanoparticles support coherent oscillations of their valence electrons known as surface plasmons. The plasmon resonance wavelength depends strongly on the shape and size of the metal nano-

particle, as well as the type of metal and its local environment.[5] There is very strong enhancement of absorption or scattering at the plasmon resonant wavelength of the nanoparticle, depending on nanoparticle size: smaller plasmonic nanoparticles are better absorbers, and increasing size increases the nanoparticle scattering cross section.[6] Fortuitously, nanoparticles in the 100 nm diameter size range can possess both strong resonant absorption and scattering characteristics. The resonant absorption properties of metallic nanoparticles result in strong, highly localized photothermal heating upon laser illumination, an effect that can be exploited to induce cancer cell death and tumor remission. The light scattering properties can be utilized for contrast enhancement in bioimaging. These two inherent properties of nanoparticles can be combined for integrated diagnostic imaging and therapeutics.

Nanoshells, spherical nanoparticles consisting of a dielectric (silica) core and a metallic shell layer, provide a systematic approach to "nanoengineering" the optical resonance wavelength of a metallic nanoparticle.[7] By variation of the relative size of the inner and outer shell layer, the plasmon resonance of a nanoshell can be "tuned" to any wavelength desired across a large region of the visible and infrared spectrum.[5] In particular, the optical resonance of nanoshells can be tuned to the near-infrared between 700−1100 nm in wavelength, where water absorption is minimal and blood and tissue are maximally transmissive.[8] Nanoshells with resonances in this region of the spectrum can serve as strong absorbers or scatterers of near-infrared light as desired, determined by their size. In this way, gold nanoshells combine the biocompatibility of gold nanoparticles with a new tailored infrared plasmon resonance wavelength, which enables their use *in vivo* for biomedical applications. Subsequent to the development of Au nanoshells, gold nanoparticles such as nanorods or nanocages have been developed with shape-dependent near-IR optical resonances and are also being applied to cancer therapy.[9,10]

In the past five years, nanoshell-based photothermal cancer therapy has been realized, and the transition from bench to bedside for this potentially revolutionary approach has begun. As this application transitions from initial proof-of-concept studies to clinical settings in an expanding number of research groups and hospitals, we provide a view of the current state of nanoshell-based therapeutics and diagnostics for cancer.

Nanoparticle Properties Specific to *in Vivo* Applications

Most nanoparticle-based diagnostic and therapeutic techniques rely on the accumulation of nanoparticles at the tumor site, which can occur by several different mechanisms. One approach relies on the passive accumulation of nanoparticles at the tumor site through the leaky tumor vasculature. Malignant tumors rapidly develop new vasculature to supply the expanding tumor mass. These new blood vessels are structurally abnormal and irregularly shaped with inconsistent diameters and large gaps (up to 2 μm).[11] These gaps are large enough to allow large molecules and nanoparticles in the blood stream to be taken up into the tumor. This property is referred to as the "enhanced permeability and retention (EPR) effect".[12,13] Without an appropriate surface coating, nanoparticles in the blood stream are rapidly removed from circulation, limiting their availability for tumor uptake.[14] Nanoparticles can be protected from this fate by chemically functionalizing their surfaces. In particular, attaching poly(ethylene glycol) (PEG) to the nanoparticle surface has proven to be quite successful for extending the circulation time of nanoparticles in the bloodstream and enhancing passive accumulation in tumors.[15] The thiol ($-$SH) moiety is a facile group for conjugation to a gold nanoparticle surface. Nanoshells coated with thiol-modified PEG (PEG-SH) are used to protect nanoshells injected into the bloodstream from being removed before they can accumulate in the tumors. Details on PEGylating nanoshells may be found in ref 16.

In addition to passive accumulation, nanoshell delivery may be directed by conjugating the nanoparticles to antibodies, proteins, or ligands specific to surface markers overexpressed by cancer cells. Many solid tumors are known to express proteins such as HER2, α_v integrin receptor, and interleukin receptor, all of which have been used to target the delivery of nanoparticles to tumor sites.[17] A successful protocol that has been used for attaching antibodies to nanoshells is using bifunctional PEG linker molecules. Antibodies such as anti-HER2 are conjugated to orthopyridyl disulfide-PEG-*n*-hydroxysuccinimide (OPSS-PEG-NHS). The resulting OPSS-PEG-antibody conjugates react with the gold surface to form a layer of PEG-antibody on the nanoshell surface.[16]

Heating Profiles

Nanoshells used in photothermal ablation of cells are designed to be highly absorbing in the NIR region of the spectrum, resulting in preferential heating upon laser illumination only in the direct vicinity of the nanoshells. Heating of the tar-
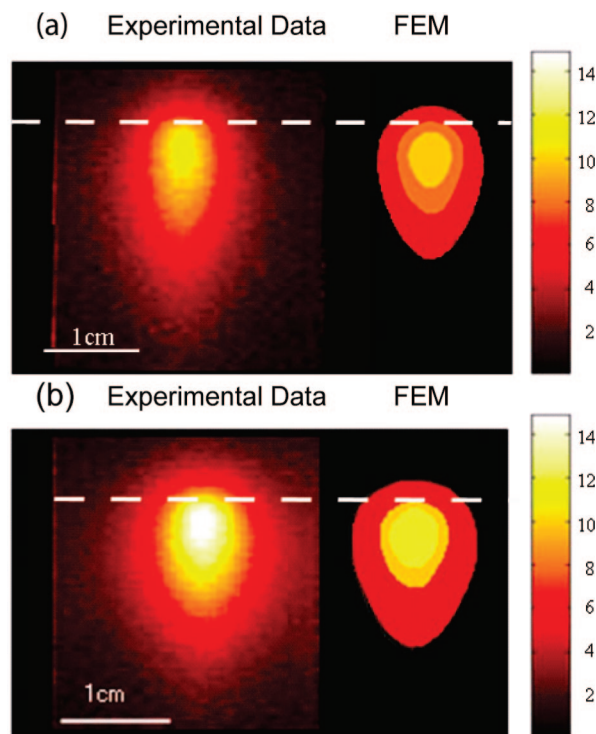

FIGURE 1. Nanoshell-based photothermal heating in (a) 0.55 OD and (b) 0.695 OD nanoshell-laden tissue phantoms consisting of a synthetic scattering medium (Lipsyn), which replicates the optical scattering properties of tissue, incorporating nanoshells for contrast enhancement and photothermal therapy. The color bar indicates the change in temperature of the tissue phantom. Dashed line indicates boundary of nanoshells in gel. Reprinted with permission from ref 18, copyright 2007 AAPM.

get region is controlled by both nanoshell concentration and laser power.

Elliot et al. have quantified this nanoshell$-$laser interaction to determine the effect of nanoshell concentration and laser power in light-induced thermal therapy.[18] Tissue phantoms (1.5% agarose gel) with 110 nm diameter nanoshells at 0.55 optical density (OD) and 180 nm diameter nanoshells at 0.695 OD were prepared. The gels were irradiated with a Diomed 15 Plus cw laser at 808 nm wavelength. The laser power was varied from 0.4 to 1.5 W, and the laser spot was maintained at $\sim$0.5 cm. The spatiotemporal distribution of heat was measured using magnetic resonance thermal imaging, a technique based on the temperature sensitivity of the proton resonance frequency, implemented in a commercial magnetic resonance imaging (MRI) scanner. The measured temperature distribution for both sets of phantoms are shown in Figure 1. The heat distribution was simulated using a commercial finite element method (FEM) modeling package (COMSOL, Multiphysics). An overlay of the isotherms at 5, 8, and 10 °C rise

in temperature, generated by the FEM model, are shown alongside in Figure 1. The theoretical spatiotemporal distribution, the heating (cooling) profile while the nanoshell-laden phantom is irradiated by the laser, and the laser power dependence of the temperature distribution compare very well with experimentally measured quantities. This demonstrates that FEM modeling can provide quantitative agreement with the effective heating profiles obtained in nanoshell-based therapeutics and should be applicable, with appropriate modifications, to optimizing nanoshell dosages for clinical applications.

Biodistribution of Nanoshells

Neutron activation analysis (NAA) studies have been undertaken to determine optimal nanoshell accumulation times in tumors and biodistribution of nanoshells in various organs.[19] NAA is a highly sensitive technique to identify and quantify various elements in a sample and can be used to determine the quantity of gold present in tissue samples. The technique relies on the transformation of atoms to different radioisotopes following irradiation with neutrons and subsequent γ ray emission as the radioisotopes decay. The emission consists of signatures of the nuclei of the specific elements from which the γ rays are emitted.

For these studies, mice with subcutaneous tumors were injected with PEGylated nanoshells. The mice were then sacrificed at different times, and tissue samples were prepared for neutron activation analysis. γ-ray spectroscopy was carried out 4−8 days after irradiation to quantify the gold content in blood, tumor, spleen, liver, lungs, kidney, brain, bone, and muscle tissues.

The NAA data indicate that nanoshells are cleared from the blood stream in a day and are scavenged by the liver and spleen. The nanoshell concentrations in the liver and spleen continue to increase after a day and do not reach normal levels even after 28 days, the longest time point in the study. The nanoshells accumulate in the tumor and reach a maximum concentration after 24 h after which the nanoshell concentration in the tumor diminishes.

While NAA remains the standard to determine nanoshell concentrations, alternate techniques for faster determination of blood circulation times that ultimately determine accumulation in tumors are being developed. A nondestructive optical approach developed by Xie et al. utilizes dynamic light scattering (DLS) from nanoshell and Triton X-100 solutions in whole blood.[20] The Triton X-100 acts as a standard against which the scattering from the nanoshells in blood may be quantified. For *in vivo* determination of nanoshell circulation

times, mice were injected with a PEGylated nanoshell solution. Fifteen microliter blood samples were taken at various time points, and a known amount of Triton X-100 solution was added to each sample. DLS measurements were performed to quantify the scattering, yielding the nanoshell concentrations. The same samples were then analyzed using NAA, where a correlation between the nanoshell concentrations obtained using these two techniques showed excellent agreement.

Nanoshell-Enabled Tumor Imaging and Therapy

Nanoshell-based photothermal therapy of cancer relies strongly on the absorption of NIR light by nanoshells and the efficient conversion of the light to heat. The nanoshells heat the tumor in which they are embedded. When a temperature increase of 30−35 °C is photothermally induced, significant cell death is observed.[21] Similarly, the diagnostic imaging of tumors at laser power levels that do not induce heating has been shown to be enhanced by using nanoshell-based contrast agents. Nanoshells designed to scatter light in the NIR physiological transparency window have been shown to act as stable contrast agents for imaging modalities such as dark field scattering,[22,23] diffuse light scattering,[24] photoacoustic tomography (PAT),[25] and optical coherence tomography (OCT).[22,26]

Nanoshell-based therapy was first demonstrated in tumors grown in mice.[21] Subcutaneous tumors were grown in mice to a size of ~1.0 cm in diameter. PEGylated nanoshells were directly injected into the tumors under magnetic resonance imaging (MRI) guidance. Control tumors received saline injections. The tumors were subsequently exposed to NIR light, and the tumor temperature, as well as the temperature of the adjacent tissue, was monitored during and after laser irradiation. The mice were euthanized, and tumors were excised for histological evaluation. Analysis of the nanoshell-based photothermal treatment reveals tissue damage in an area of similar extent as that exposed to laser irradiation (Figure 2).

Magnetic resonance thermal imaging (MRTI) was used to monitor the temperature profile of the tumor during and after irradiation. Analysis of these temperature maps reveals an average temperature increase of 37.4 ± 6.6 °C after 4−6 min of irradiation. These temperatures were sufficient to induce irreversible tissue damage. Nanoshell-free control samples show an average temperature rise of 9.1 ± 4.7 °C, considered to be safe for cell viability.
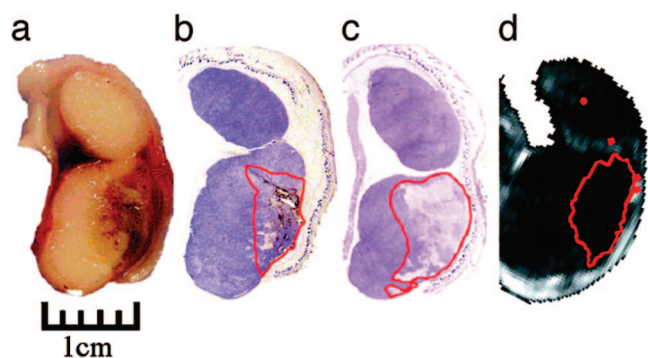
FIGURE 2. (a) Gross pathology after *in vivo* treatment with nanoshells and NIR laser reveal hemorrhaging and loss of tissue birefringence beneath the apical tissue surface. (b) Silver staining of a tissue section reveals region of localized nanoshells (red). (c) Hematoxylin/eosin staining within the same plane clearly shows tissue damage within the area occupied by nanoshells. (d) MRTI calculations reveal area of irreversible thermal damage similar to that in panel a, b, and c. Reprinted with permission from ref 21. Copyright 2003 National Academy of Sciences, U.S.A.

FIGURE 3. (a) Mean tumor size on treatment day and day 10 for the treatment group (green), control group (red), and sham treatment (blue). (b) Survival for first 60 days. Average survival time for the nanoshell-treated group was >60 days, control group was 10.1 days, and sham treatment group was 12.5 days. Reprinted with permission from ref 27. Copyright 2004 Elsevier.

Subsequent experiments were then conducted to determine the therapeutic efficacy and animal survival times by monitoring the tumor growth and regression over a period of 90 days.[27] In these studies, tumors were grown subcutaneously in mice, and PEGylated nanoshells were injected systemically via the tail vein, accumulating in the tumor over 6 h. The tumors were then irradiated with a diode NIR laser at a wavelength of 808 nm at a power of 4 W/cm^2 for 3 min. A sham treatment group received the same laser treatment following saline injection, and a control group received no treatment. Following this treatment, the change in tumor size over the first 10 days indicates a dramatic difference in tumor size for the three control groups (Figure 3a). In the nanoshell-treated group there was 100% resorption of the tumor at the 10 day mark. In the rest of the study, this result persisted, whereas in the sham and control groups, the tumor burden became large enough (tumor burden doubled in size corresponding to >5% body weight) that the mice were euthanized. Figure 3b is a plot of the survival statistics for the three groups of mice. At 90 days post-treatment, all mice in the treatment group were healthy and free of tumors.

The passive accumulation of nanoshells in tumors and subsequent ablation relies on a minimum accumulation of nanoshells in the tumor. Stern et al. have evaluated the effect of nanoshell concentration on tumor ablation in a human prostate cancer model in mice.[28] Tumors were grown subcutaneously. PEGylated nanoshells of two different dosages (7.0 μL/gm (low dose) and 8.5 μL/gm of body weight (high dose)) were delivered into the mice via tail vein injection. The nanoshells were allowed to accumulate for 18 h at which time
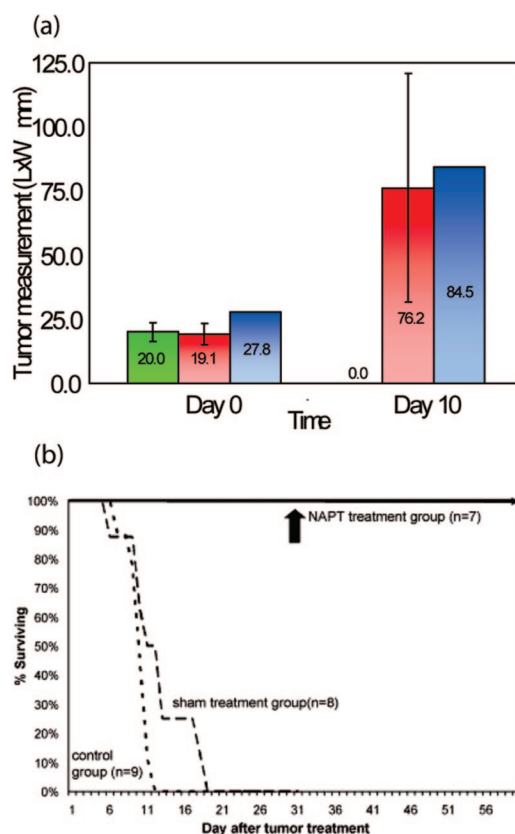
the tumors were irradiated using a Diomed NIR laser at 810 nm for 3 min. Tumor size was measured for 21 days. In the low dose group, only partial tumor ablation was achieved. Nine of the ten tumors showed arrested growth (mean volume 49.2 mm^3 from a baseline of 41.6 mm^3), as opposed to the control sample where the tumor burden tripled in 21 days (126.4 mm^3 from a baseline of 43.5 mm^3). Histologically the tumors showed partial ablation with patchy areas of normal tumor cells. In the high dose treatment group, at 21 days complete tumor deletion was observed (Figure 4). Histological evaluation also confirmed complete tumor necrosis for this dosage. In the high dose treated group, a well circumscribed eschar formed over the laser treated region by day 1. This eschar fell off by day 21 revealing normal healthy skin. The control samples that did not receive any nanoshells did not form an eschar over the laser-treated areas. In the high dose group, the average temperature achieved was 65.4 °C, which is known to be effective in thermal ablation therapy.

FIGURE 4. Photothermal tumor ablation: (A) tumor before treatment; (B) complete ablation of tumor in the high dose group. The eschar formed over the laser-treated region fell off by day 21 exposing healthy skin. Figure reproduced with permission from ref 28. Copyright 2008 Elsevier.

Nanoshells as Contrast Agents

In addition to being strong near-IR absorbers, nanoshells can be strong scatterers of NIR light. This opens up the potential for diagnostic imaging of tumors for early detection. Optical techniques have the advantage of being minimally invasive and offer high resolution images using biocompatible non-photobleaching nanoshells to improve contrast. Compared with molecular contrast agents such as indocyanine green, nanoshells have far larger scattering cross sections and a tunable optical response over a wide wavelength range. Nanoshells synthesized with high scattering cross sections have been used as contrast agents in numerous imaging modalities,[25,26,29,30] enhancing the sensitivity of these imaging techniques.

Loo et al. have demonstrated the use of scattering nanoshells targeted with anti-HER2 as a contrast agent in dark-field microscopy. HER2 positive SK Br3 and HER2 negative MCF7 cell cultures were incubated with anti-HER2 and anti-IgG immunonanoshells.[29] After 1 h, the cells were rinsed and visualized under a high-magnification dark-field microscope. Analysis of the dark-field images shows significantly higher contrast values for anti-HER2 targeted nanoshells compared with the nonspecific IgG targeted nanoshells or untargeted bare nanoshells. HER2-negative MCF 7 cells show significantly less contrast providing additional evidence that enhanced contrast is attributable to the nanoshell binding to SK Br3 cells.

Combined Cancer Imaging and Therapy

Nanoshells have been successfully used for photothermal ablation of cancer cells and for imaging contrast in numerous imaging techniques. It is therefore reasonable to envision a dual diagnostic−therapeutic modality for nanoshells, where the same laser source used for imaging the tumor could at higher laser powers be used to heat and destroy the tumor.

Loo, Lowery, et al.[23] have demonstrated this dual imaging/therapy approach *in vitro* using anti-HER2 immunonanoshells. Nanoshells were designed with a 60 nm core radius, a 10 nm thick shell, and a plasmon resonance at 800 nm. Anti-HER2 or nonspecific anti-IgG were conjugated to nanoshells. SK Br3 breast carcinoma cells were cultured and incubated with immunonanoshells for 1 h. Following rinsing to remove unbound nanoshells, the cells were imaged in a dark-field microscope. Next the cells were irradiated with NIR laser (820 nm wavelength laser 0.008 W/m^2 for 7 min).

Following irradiation the cells were stained and evaluated for nanoshell binding and viability. Figure 5 shows the results of combined imaging and therapy using nanoshells. The controls with no nanoshells or the nonspecific antibody show no contrast in either imaging or therapy. The anti-HER2 nanoshells show a distinct enhancement in the dark-field scattering image and a dark circular area of cell death corresponding to the beam spot upon laser irradiation. The silver stain assay also shows a high density of nanoshells bound to the carcinoma cells.

Gobin et al.[26] have demonstrated *in vivo* imaging via Optical Coherence Tomography (OCT) and therapy using nanoshells. The bifunctional nanoshell designed for the dual role of OCT contrast enhancer and therapeutic heat absorber in tissue has a silica core of 119 nm diameter and a 12 nm gold shell. Mie scattering theory predicts that these particles have approximately 67% of their extinction due to absorption and 33% due to scattering at 800 nm.

Subcutaneously grown tumors in mice (~5 mm in diameter) were injected with PEGylated nanoshells via tail vein injection. The control mice received phosphate buffered solution instead of the nanoshell solution. Twenty hours post injection the tumors were imaged using a commercial OCT setup by applying the probe directly over the tumor touching the skin. Representative OCT images from normal tissue and tumor sites with either PBS or nanoshells are shown in Figure 6. The enhanced brightness in Figure 6, panel D compared with panel C demonstrates that nanoshells provide substantial contrast for OCT imaging. After imaging, the tumors were
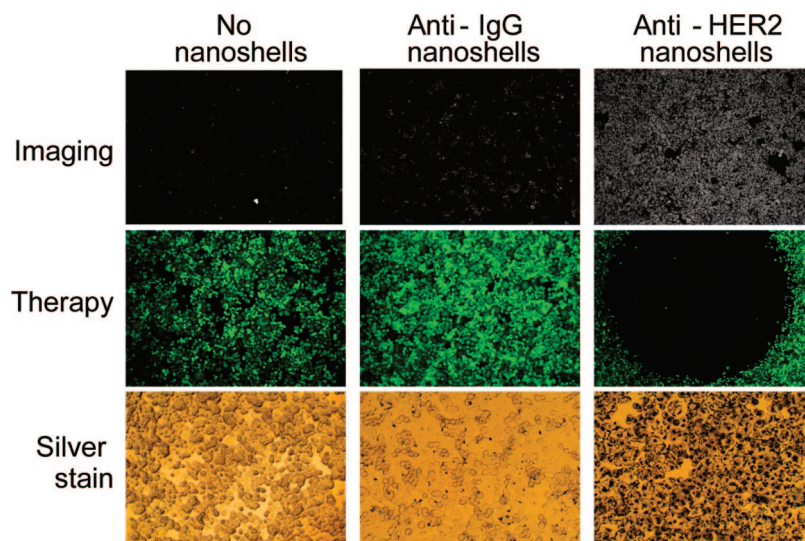
FIGURE 5. Combined imaging and therapy of SKBr3 breast cancer cells using HER2-targeted nanoshells. Scatter-based dark-field imaging of HER2 expression (top row), cell viability assessed via calcein staining (middle row), and silver stain assessment of nanoshell binding (bottom row). Cytotoxicity was observed in cells treated with a NIR-emitting laser following exposure and imaging of cells targeted with anti-HER2 nanoshells only. Figure reproduced with permission from ref 23. Copyright 2005 American Chemical Society.
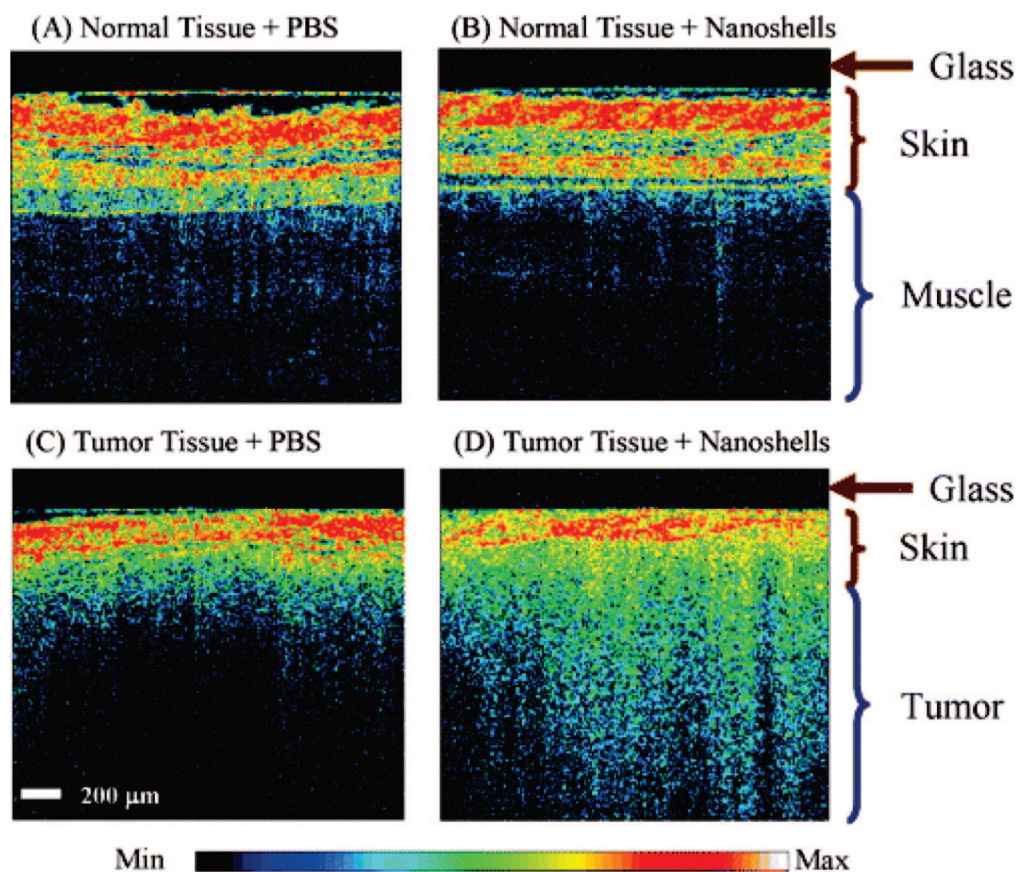
FIGURE 6. Representative OCT images from normal skin and muscle tissue areas of mice systemically injected with PBS (A) or with nanoshells (B). Representative OCT images from tumors of mice systemically injected with PBS (C) or with nanoshells (D). The glass of the probe is 200 μm thick and shows as a dark nonscattering layer. Figure reproduced with permission from ref 26. Copyright 2007 American Chemical Society.

irradiated using a NIR laser (808 nm, 4 W/cm^2, and a spot size of 5 mm) for 3 min. Tumor size and animal survival were monitored for 7 weeks. The median survival for the group receiving sham treatment (laser irradiation with no nanoshells)

was 14 days, while the control group (receiving neither nanoshells nor laser irradiation) was 10 days. The tumors in all but two mice receiving nanoshells and laser treatment had completely regressed in 21 days. Median survival for this group was longer than the 7 weeks of the study period.

Nanoshell Targeting of Tumor Hypoxia

The passive accumulation of nanoshells relies on the EPR effect. However, the centers of large solid tumors are frequently hypoxic, with drastically reduced blood flow. These regions are resistant to nanoparticle accumulation as well as conventional chemotherapy. Since it is believed that these regions are the source of resistant cells which ultimately produce recurrence and metastasis, developing a delivery method for therapeutics to these regions is an important challenge.

Choi et al. have developed a "Trojan Horse" strategy to deliver nanoshells to these hypoxic regions of solid tumors (Figure 7).[31] In response to the presence of hypoxia and necrosis, peripheral blood monocytes enter the tumor due to a chemoattractive gradient. Once inside, the monocytes differentiate into macrophages, which can make up ~70% of the tumor mass. Monocytes loaded with nanoshells are delivered to the tumor periphery where they enter the tumor and differentiate into nanoshell-loaded macrophages. Once distributed inside the tumor mass, irradiation with a NIR laser activates the photothermal destruction of the macrophages and the tumor including the hypoxic regions. Choi et al. have successfully demonstrated several critical steps in this strategy.[31] An in vitro tumor model with a necrotic, hypoxic core was constructed using malignant breast epithelial cells and macrophage loaded with nanoshells, and then irradiated with a pulsed NIR laser (754 nm, 1.54 W total power at source) with varying power at the tumor. Above a certain threshold power, tumor ablation was observed.

The hypoxic regions of the solid tumors are also resistant to traditional treatment modalities. Any strategy to alleviate tissue hypoxia would thus make these aggressive tumors amenable to radiation and chemo- and immunotherapies. One such strategy is mild hyperthermia. Mild hyperthermia allows increased perfusion in the tumor and reduces the hypoxic regions. Although it has been proven in clinical settings that hyperthermia improves the long-term prognosis of radiation therapy, it is underutilized since there are no noninvasive means of achieving local hyperthermia for long periods of time. Diagaradjane et al.[32] have demonstrated the use of nanoshell-mediated hyperthermia as an adjunct to radiation therapy. The nanoshell-induced hyperthermia raises the temperature of the tumors by ~10 °C and allows early perfu-
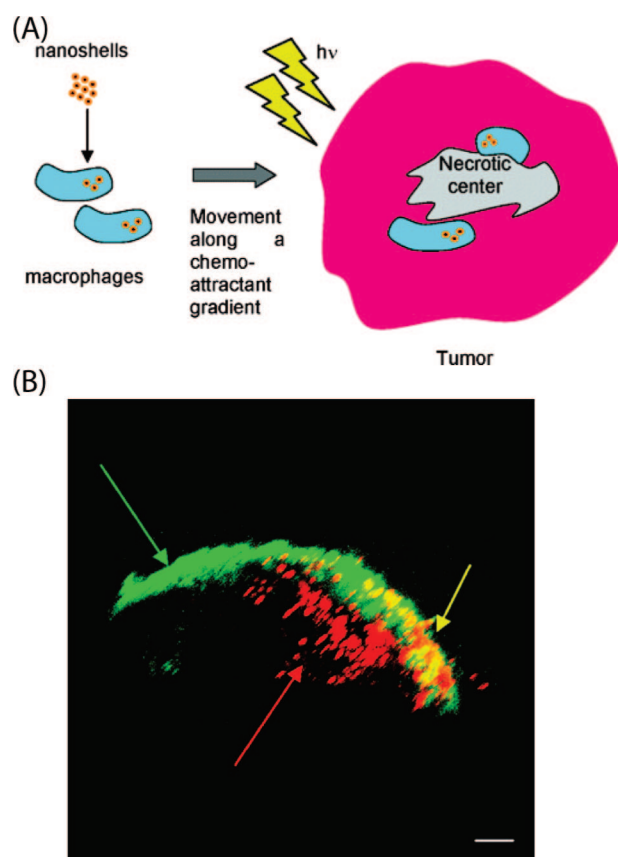

FIGURE 7. (A) Schematic of Trojan Horse therapeutic nanoparticle delivery into hypoxic region of tumor. (B) Frame from three-dimensional reconstruction of tumor spheroid. Viable cells (green fluorescence) form an outer shell around the central necrosis: green arrow, unirradiated cells; red arrow, nanoshell-laden macrophages, which have infiltrated into the area in the center of the spheroid. Yellow cells and arrow may represent cells that have been thermally damaged due to their location next to macrophages. Cells to the left in the photo (green arrow) have not been irradiated, serving as internal control. Scale bar is 50 μm. Figure reproduced with permission from ref 31. Copyright 2007 American Chemical Society.

sion into the tumors, reducing hypoxic regions and leading to necrosis that complements the radiation-induced cell death.

While nanoshells hold tremendous potential in the single point of care integration of imaging and therapy, currently the technology has a few limitations that need to be addressed as this treatment of cancers moves into clinical settings.[28]

1. Currently there is a need for effective quantification methods for nanoshell accumulation in tumors, which when combined with standard illumination geometries for tumors in specific organs will enable complete regression of tumors.[28]

2. Additional research and accurate theoretical models of concentration profiles for nanoshells in tumors and their achievable temperature elevations are needed to apply this technique as generally as possible to tumor remission.

3. Most of the current *in vivo* studies have been on subcutaneous tumors easily accessible to NIR light applied over the skin surface. NIR light penetration in tissue is a few inches. Techniques to deliver NIR light deep into tissue by exploiting fiber optic probes, for example, need to be applied to this therapeutic modality. Imaging modalities may need to be modified for combined imaging and therapeutics in deep tissue.

4. While these studies seem to demonstrate that the EPR effect occurs in animal models of human tumors,[26,28] almost all of these models use ectopic, that is, subcutaneous, injection of malignant cells in order to form tumors. It is a critically important clinical question to consider how faithfully these models recapitulate human malignancy. Interstitial fluid pressure (IFP) in orthotopic versus subcutaneous human osteosarcoma xenografts has been compared,[33] where the baseline IFP was significantly higher in orthotopic than in subcutaneous tumors of comparable size. Therefore, there may be a net flow of nanoparticles into subcutaneous tumors in animal models but not into orthotopic human tumors.

5. Toxicity concerns need to be addressed in a serious and systematic way. Recent publications, such as the report of carbon nanotubes injected into mice resulting in mesothelioma, contribute to the public's unease.[34,35] It is of paramount importance with every novel application of nanotechnology for the detection and treatment of cancer that efforts be made to identify all potential toxicities, both those to the patient and those to the environment. With this diligent oversight, the unreserved enthusiasm of the public should support this potentially revolutionary endeavor.

The ways in which nanotechnology may enter clinical oncology will only be limited by our imagination. Nanotherapy strategies may function as stand-alone therapy but are also likely to be adjunctive to current systemic therapies. Since nanoshell-based photothermal therapy functions in ways completely different from conventional therapies, its resistance mechanisms are unlikely to be similar. We can ultimately envision utilizing nanoparticles as nanovehicles to deliver therapeutics to sites of disease notoriously difficult to treat, that is, the brain. An almost intractable problem in oncology is the treatment of primary brain malignancies and multiple metastatic deposits within the brain. Nanovehicles engineered to penetrate the blood−brain barrier could be utilized to ferry therapeutics across the barrier. Hypoxic brain tumors (glioblastoma multiforme) may be particularly vulnerable to the macrophage "Trojan Horse" approach.[31]

BIOGRAPHICAL INFORMATION

Surbhi Lal received her Ph.D. in Applied Physics in 2006 from Rice University. Since 2006, she has been a Postdoctoral Research Associate in the Halas Nanophotonics Group at Rice University. Her research interests are in the area of nanophotonics and surface enhanced spectroscopy.

Susan E. Clare is an Assistant Professor of Surgery at the School of Medicine at Indiana University. Her current interests are the development of the normal breast particularly with regard to the role of progenitor cells, the effect of surgical extirpation of a primary breast cancer on the growth of micrometastatic disease, and the utilization of nanovectors for the treatment of breast cancer.

Dr. Naomi J. Halas is currently The Stanley C. Moore Professor in Electrical and Computer Engineering and Professor of Chemistry, and Bioengineering at Rice University. She is best known scientifically as the inventor of nanoshells. She has subsequently shown numerous applications for nanoshells in biomedicine and in chemical sensing. She is author of more than 150 refereed publications, has ten issued patents, and more than 275 invited talks. She is Fellow of the SPIE, OSA, IEEE, APS, and AAAS.

FOOTNOTES

REFERENCES

1 Jemal, A.; Siegel, R.; Ward, E.; Hao, Y.; Xu, J.; Murray, T.; Thun, M. J. Cancer statistics, 2008. *CA: Cancer J. Clin.* **2008**, *58* (2), 71–96.

2 U.S. Census Bureau: Projected Population of the United States, by Age and Sex: 2000 to 2050. http://www.census.gov/ipc/www/usinterimproj/natprojtab02b.pdf.

3 Szabo, L. Cancer burden expected to soar, overwhelm doctors. USA Today March 13, 2007.

4 Bohren, C. F.; Huffman, D. R. *Absorption and Scattering of Light by Small Particles*; John Wiley and Sons, Inc: New York, 1983.

5 Halas, N. J. Playing with Plasmons: Tuning the Optical Resonant Properties of Nanoshells. *MRS Bull.* **2005**, *30*, 362–367.

6 Jain, P. K.; Lee, K. S.; El-Sayed, I. H.; El-Sayed, M. A. Calculated Absorption and Scattering Properties of Gold Nanoparticles of Different Size, Shape, and Composition: Applications in Biological Imaging and Biomedicine. *J. Phys. Chem. B* **2006**, *110*, 7238–7248.

7 Oldenburg, S. J.; Averitt, R. D.; Westcott, S. L. Nanoengineering of Optical Resonances. *Chem. Phys. Lett.* **1998**, *288*, 243–247.

8 Weissleder, R. A Clearer Vision for in Vivo Imaging. *Nat. Biotechnol.* **2001**, *19*, 316–317.

9 Huang, X.; El-Sayed, I. H.; Qian, W.; El-Sayed, M. A. Cancer Cell Imaging and Photothermal Therapy in the Near-Infrared Region by Using Gold Nanorods. *J. Am. Chem. Soc.* **2006**, *128*, 2115–2120.

10 Hu, M.; Chen, J.; Li, Z.-Y.; Au, L.; Hartland, G. V.; Li, X.; Marquez, M.; Xia, Y. Gold Nanostructures: Engineering Their Plasmonic Properties for Biomedical Applications. *Chem. Soc. Rev.* **2006**, *35*, 1084–1094.

11 McDonald, D. M.; Baluk, P. Significance of Blood Vessel Leakiness in Cancer. *Cancer Res.* **2002**, *62*, 5381–5385.

12 Maeda, H. The Enhanced Permeability and Retention (EPR) Effect in Tumor Vasculature: The Key Role of Tumor-Selective Macromolecular Drug Targeting. *Adv. Enzyme Regul.* **2001**, *41*, 189–207.

13 Maeda, H.; Fang, J.; Inutsuka, T.; Kitamoto, Y. Vascular Permeability Enhancement in Solid Tumor: Various Factors, Mechanisms Involved and Its Implications. *Int. Immunopharmacol.* **2003**, *3*, 319–328.

14 Moghimi, S. M.; Muir, I. S.; Ilium, L.; Davis, S. S.; Kolb-Bachofen, V. Coating Particles with a Block Co-polymer (Poloxamine-908) Suppresses Opsonization but Permits the Activity of Dysopsonins in the Serum. *Biochim. Biophys. Acta* **1993**, *1179*, 157–165.

15 Crawford, J. Clinical Uses of Pegylated Pharmaceuticals in Oncology. *Cancer Treat. Rev.* **2002**, (Suppl. A), 7–11.

16 Lowery, A. R.; Gobin, A. M.; Day, E. S.; Halas, N. J.; West, J. L. Immunonanoshells for Targeted Photothermal Ablation of Tumor Cells. *Int. J. Nanomed.* **2006**, *1*, 1–6.

17 Arap, W.; Pasqualini, R.; Ruoslahti, E. Cancer Treatment by Targeted Drug Delivery to Tumor Vasculature in a Mouse Model. *Science* **1998**, *279*, 377–380.

18 Elliott, A. M.; Stafford, R. J.; Schwartz, J.; Wang, J.; Shetty, A. M.; Bourgoyne, C.; O'Neal, P.; Hazle, J. D. Laser-Induced Thermal Response and Characterization of Nanoparticles for Cancer Treatment Using Magnetic Resonance Thermal Imaging. *Med. Phys.* **2007**, *34*, 3102–3108.

19 James, W. D.; Hirsch, L. R.; West, J. L.; O'Neal, P. D.; Payne, J. D. Application of INAA to the Build-up and Clearance of Gold Nanoshells in Clinical Studies in Mice. *J. Radioanal. Nucl. Chem.* **2007**, *271*, 455–459.

20 Xie, H.; Gill-Sharp, K. L.; O'Neal, D. P. Quantitative Estimation of Gold Nanoshell Concentrations in Whole Blood Using Dynamic Light Scattering. *Nanomedicene* **2007**, *3*, 89–94.

21 Hirsch, L. R.; Stafford, R. J.; Bankson, J. A.; Sershen, S. R.; Rivera, B.; Price, R. E.; Hazle, J. D.; Halas, N. J.; West, J. L. Nanoshell-Mediated Near-Infrared Thermal Therapy of Tumors under Magnetic Resonance Guidance. *Proc. Natl. Acad. Sci. U.S.A.* **2003**, *100* (23), 13549–13554.

22 Loo, C.; Lin, A.; Hirsch, L.; Lee, M.-H.; Barton, J.; Halas, N.; West, J.; Drezek, R. Nanoshell-Enabled Photonics-Based Imaging and Therapy of Cancer. *Technol. Cancer Res. Treat.* **2004**, *3*, 33–40.

23 Loo, C.; Lowery, A.; Halas, N.; West, J.; Drezek, R. Immunotargeted Nanoshells for Integrated Cancer Imaging and Therapy. *Nano Lett.* **2005**, *5* (4), 709–711.

24 Zaman, R. T.; Diagaradjane, P.; Wang, J. C.; Schwartz, J.; Rajaram, N.; Gill-Sharp, K. L.; Cho, S. H.; Rylander, H. G. I.; Payne, J. D.; Krishnan, S.; Tunnell, J. W. In Vivo Detection of Gold Nanoshells in Tumors Using Diffuse Optical Spectroscopy. *IEEE J. Sel. Top. Quantum Electron.* **2007**, *13*, 1715–1720.

25 Wang, Y.; Xie, X.; Wang, X.; Ku, G.; Gill, K. L.; O'Neal, D. P.; Stoica, G.; Wang, L. V. Photoacoustic Tomography of a Nanoshell Contrast Agent in the in Vivo Rat Brain. *Nano Lett.* **2004**, *4*, 1689–1692.

26 Gobin, A. M.; Lee, M. H.; Halas, N. J.; James, W. D.; Drezek, R. A.; West, J. L. Near-Infrared Resonant Nanoshells for Combined Optical Imaging and Photothermal Cancer Therapy. *Nano Lett.* **2007**, *7*, 1929–1934.

27 O'Neal, D. P.; Hirsch, L. R.; Halas, N. J. D. P. J.; West, J. L. Photo-thermal Tumor Ablation in Mice Using near Infrared-Absorbing Nanoparticles. *Cancer Lett.* **2004**, *209*, 171–176.

28 Stern, J. M.; Stanfield, J.; Kabbani, W.; Hsieh, J.-T.; Cadeddu, J. A. Selective Prostate Cancer Thermal Ablation With Laser Activated Gold Nanoshells. *J. Urol.* **2008**, *179*, 748–753.

29 Loo, C.; Hirsch, L.; Lee, M.-H.; Chang, E.; West, J.; Halas, N.; Drezek, R. Gold Nanoshell Bioconjugates for Molecular Imaging in Living Cells. *Opt. Lett.* **2005**, *30*, 1012–1014.

30 Park, J.; Estrada, A.; Sharp, K.; Sang, K.; Schwartz, J. A.; Smith, D. K.; Coleman, C.; Payne, J. D.; Korgel, B. A.; Dunn, A. K.; Tunnell, J. W. Two-Photon-Induced Photoluminescence Imaging of Tumors Using near-Infrared Excited Gold Nanoshells. *Opt. Express* **2008**, *16*, 1590–1599.

31 Choi, M.-R.; Stanton-Maxey, K. J.; Stanley, J. K.; Levin, C. S.; Bardhan, R.; Akin, D.; Badve, S.; Sturgis, J.; Robinson, J. P.; Bashir, R.; Halas, N. J.; Clare, S. E. A Cellular Trojan Horse for Delivery of Therapeutic Nanoparticles into Tumors. *Nano Lett.* **2007**, *7*, 3759–3765.

32 Diagaradjane, P.; Shetty, A.; Wang, J. C.; Elliott, A. M.; Schwartz, J.; Shentu, S.; Park, H. C.; Deorukhkar, A.; Stafford, R. J.; Cho, S. H.; Tunnell, J. W.; Hazle, J. D.; Krishnan, S. Modulation of in Vivo Tumor Radiation Response via Gold Nanoshell-Mediated Vascular-Focused Hyperthermia: Characterizing an Integrated Antihypoxic and Localized Vascular Disrupting Targeting Strategy. *Nano Lett.* **2008**, *8*, 1492–1500.

33 Brekken, C.; Bruland, O. S.; de Lange Davies, C. Interstitial Fluid Pressure in Human Osteosarcoma Xenografts: Significance of Implantation Site and the Response to Intratumoral Injection of Hyaluronidase. *Anticancer Res.* **2000**, *20* (5B), 3503–3512.

34 Poland, C. A.; Duffin, R.; Kinloch, I.; Maynard, A.; Wallace, W. A. H.; Seaton, A.; Stone, V.; Brown, S.; MacNee, W.; Donaldson, K. Carbon nanotubes introduced into the abdominal cavity of mice show asbestos-like pathogenicity in a pilot study. *Nat. Nanotechnol.* **2008**, *3*, 423–428.

35 Takagi, A.; Hirose, A.; Nishimura, T.; Fukumori, N.; Ogata, A.; Ohashi, N.; Kitajima, S.; Kanno, J. Induction of mesothelioma in p53± mouse by intraperitoneal application of multi-wall carbon nanotube. *J. Toxicol. Sci.* **2008**, *33* (1), 105–116.

A Cellular Trojan Horse for Delivery of Therapeutic Nanoparticles into Tumors

Mi-Ran Choi,[†] Katie J. Stanton-Maxey,[†] Jennifer K. Stanley,[†] Carly S. Levin,[‡,§]
Rizia Bardhan,[‡,§] Demir Akin,[∥] Sunil Badve,[⊥] Jennifer Sturgis,[#] J. Paul Robinson,[#]
Rashid Bashir,[∥,#] Naomi J. Halas,[‡,§,+] and Susan E. Clare*,[†]

*Department of Surgery, Indiana University School of Medicine, Indianapolis,
Indiana 46202, Department of Chemistry, Rice University, Houston, Texas 77005,
Department of Electrical and Computer Engineering, Rice University, Houston, Texas 77005,
Birck Nanotechnology Center, Purdue University, West Lafayette, Indiana 47907,
Department of Pathology and Laboratory Medicine, Indiana University School of Medicine,
Indianapolis, Indiana 46202, Bindley BioScience Center, Purdue University,
West Lafayette, Indiana 47907, and Laboratory for Nanophotonics, Rice University,
Houston, Texas 77005*

ABSTRACT

Destruction of hypoxic regions within tumors, virtually inaccessible to cancer therapies, may well prevent malignant progression. The tumor's recruitment of monocytes into these regions may be exploited for nanoparticle-based delivery. Monocytes containing therapeutic nanoparticles could serve as "Trojan Horses" for nanoparticle transport into these tumor regions. Here we report the demonstration of several key steps toward this therapeutic strategy: phagocytosis of Au nanoshells, and photoinduced cell death of monocytes/macrophages as isolates and within tumor spheroids.

Nanotechnology shows great promise for the diagnosis and treatment of cancer. Nanoparticle-based therapeutics have been successfully delivered into tumors by exploiting the enhanced permeability and retention (EPR) effect, a property that permits nanoscale structures to be taken up passively into tumors without the assistance of antibodies or other targeting moieties.[1] Nanoparticle-based therapies have also been targeted to malignant cells by conjugating the nanoparticles with antibodies or peptides specific to those cells.[2] An alternative strategy for delivering nanoparticle-based therapies within the tumor microenvironment, not previously explored, involves the uptake of nanoparticles within nonmalignant cells which subsequently are recruited into the tumor. These nonmalignant cells, rather than being "innocent bystanders", may actually be the active agents of metastatic disease.

The centers of solid tumors are frequently observed to be largely necrotic, resulting from prolonged hypoxia: insufficient availability of oxygen and glucose to meet the metabolic demands of the malignant cells. During tumor growth, the rapid proliferation of malignant cells places cells within the core of the tumor at increasingly larger distances from their nearest capillaries, drastically compromising blood flow to these cells. In addition to inducing necrosis, this isolation of cells with respect to the tumor vasculature renders the hypoxic areas of tumors inaccessible to virtually all molecular or nanoparticle-based therapies where delivery into the tumor is based on the EPR effect. This not only is a severe limitation to many standard therapeutic strategies such as chemotherapy[3] but also may limit the efficacy of many nanoparticle-based therapeutic approaches currently in development. In fact, one possible scenario for the progression of cancer to its latter, highly fatal stages is that cells which survive in these inaccessible hypoxic regions may themselves be the source of subsequent local recurrence and distant metastasis. It has been shown that hypoxia exerts a selective pressure on tumor cells in that only those with an aggressive phenotype (e.g., mutated p53) are able to survive in a low oxygen tension microenvironment.[4−6]

One of the body's responses to the presence of a malignant neoplasm is the recruitment of peripheral blood monocytes into the tumor, induced into the tumor mass by a chemoattractive gradient. Once the monocytes cross the endothelial basement membrane, they differentiate into macrophages.

* Corresponding author. Phone: (317) 278-3907. Fax (317) 278-3185. E-mail: sclare@iupui.edu.
† Department of Surgery, Indiana University School of Medicine.
‡ Department of Chemistry, Rice University.
§ Laboratory for Nanophotonics, Rice University.
∥ Birck Nanotechnology Center, Purdue University.
⊥ Department of Pathology and Laboratory Medicine, Indiana University School of Medicine.
Bindley BioScience Center, Purdue University.
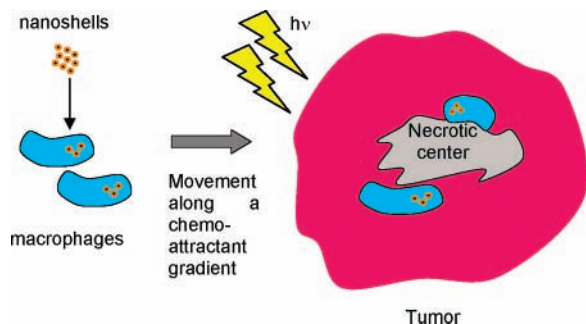+ Department of Electrical and Computer Engineering, Rice University.

Figure 1. Schematic of Trojan Horse therapeutic nanoparticle delivery into the hypoxic region of tumor.

In breast cancer, macrophages may comprise up to 70% of the tumor mass.[7] Macrophages that have infiltrated a tumor are referred to as tumor-associated macrophages or TAMs. There is increasing evidence that suggests that TAMs are "educated" by their microenvironment and promote tumor progression.[8] The presence of large numbers of TAMs is associated with poor prognosis in breast cancer.[9,10] TAMs have been shown to foster invasion,[11−14] proliferation,[10,14−17] tumor neoangiogenesis,[8,18−20] and metastasis[12,14,20−25] and to suppress antitumor immune responses.[26−28]

Destruction of hypoxic regions within tumors, and especially the TAMs recruited into these regions, may well prevent the proliferation, growth, invasion, migration, and metastasis of malignant epithelial cells. This destruction should severely thwart tumor function and metastatic potential, directly impacting the probability of patient mortality. Delivery of therapeutics into the hypoxic regions of tumors, however, presents a major challenge. To address this problem, we hypothesize that the tumor's natural recruitment of monocytes may in fact be exploited for nanoparticle-based drug delivery and therapeutics. Since monocytes possess an innate phagocytotic capability and can be easily loaded with therapeutic nanoparticles, each cell can serve as a "Trojan Horse" delivery vector for nanoparticle therapeutics into these otherwise inaccessible tumor regions (Figure 1). In this treatment scenario, monocytes would be permitted to take up nanoparticle-based therapeutics and deliver them into the tumor site. Once recruited into the tumor, the monocytes differentiate into macrophages, which would also be required to maintain the cargo nanoparticles. The nanoparticle-laden macrophages would then migrate/chemotax to the hypoxic regions of the tumor. Once in place, the nanoparticle-based therapeutic function could be initiated by near-infrared (NIR) illumination into the tumor, destroying the TAMs. Depending on the illumination protocol, this therapeutic response may also include the destruction of adjacent cells or may be combined and coordinated with other chemical, molecular, or nanoparticle-based therapeutics, to result in total tumor destruction and remission with a greatly decreased risk of tumor regrowth and metastasis.

One essential requirement of this delivery and therapeutic strategy is that the intracellular cargo of the monocytes/macrophages remains inactive and harmless to its cellular host until delivery into the hypoxic tissue is accomplished. Au nanoshell-based photoinduced therapy is particularly amenable to this approach. Au nanoshells are nanoparticles consisting of a silica core surrounded by a thin Au shell.[29,30] By modifications of their relative core and shell dimensions, their plasmon resonances can be tuned such that they absorb light in the NIR,[31] a region of the spectrum where optical absorption of the tissue is minimal and penetration by the radiation is optimal for deep tissue treatments.[32] Au nanoshells can be designed and fabricated to either preferentially absorb or scatter light by varying the size of the particle relative to the wavelength of the light at their optical resonance.[32] Prior to resonant illumination, nanoshells are likely to remain entirely inert within cells or tissue, allowing for the viability of the monocytes/macrophages during recruitment into the tumor, differentiation to macrophages, and transport into hypoxic tumor regions. Upon illumination by NIR light at a wavelength corresponding to a nanoshell resonance, absorbed continuous wave (CW) laser light is converted to heat and has been shown to increase the temperature in the tissue in which the nanoshells are embedded by over 30 °C upon resonant illumination.[33] The resonant properties of nanoshells are dependent on their local environment,[34,35] and are preserved in the presence of defects or roughness on the nanoshell surface.[36,37] Nanoshell-based photothermal ablation therapy has been shown to successfully treat tumors in mice with tumor remission rates over 90%.[38]

Here we report the successful demonstration of several critical steps toward the ultimate goal of Trojan Horse therapeutics: the efficient phagocytosis of Au nanoshells by both monocytes and macrophages, photoinduced ablation of Au nanoshell-laden monocytes/macrophages, and the ability of nanoshell laden monocytes/macrophages to be taken up into a tumor and, once in place, to succumb to Au nanoshell-based photoinduced cell death using NIR light. Human breast tumor spheroids, an in vitro model of the hypoxic tumor microenvironment, were utilized to examine the efficacy of cellular uptake and nanoshell-assisted photoinduced ablation in the hypoxic tumor region using this approach.

Au nanoshells with a core radius 60 nm and shell thickness 27 nm were fabricated as previously described.[29] The internal and overall dimensions of the nanoparticles were confirmed using UV−visible extinction measurements, comparison with Mie scattering theory, and scanning electron microscopy (SEM). Absorbance spectra were obtained using a Varian Cary 5000 UV−vis-NIR spectrophotometer. SEM images were obtained using a FEI XL-30 environmental scanning electron microscope (ESEM). Figure 2 displays the extinction spectra of the Au nanoshells used, whose extinction peak maximum is at 754 nm. SEM images of these nanoshells are also shown.

Since monocytes become macrophages once they migrate from the capillary into the tumor, it is necessary to demonstrate Au nanoshell loading and subsequent survival in both monocytes and macrophages. To pursue this investigation, human whole blood was obtained from the Indiana Blood Center. Lymphocytes, monocytes, and platelets, i.e., the Buffy coat, were isolated using Ficoll density gradient centrifugation.[39] Monocytes were separated from the other components of the Buffy coat using anti-CD14 antibody
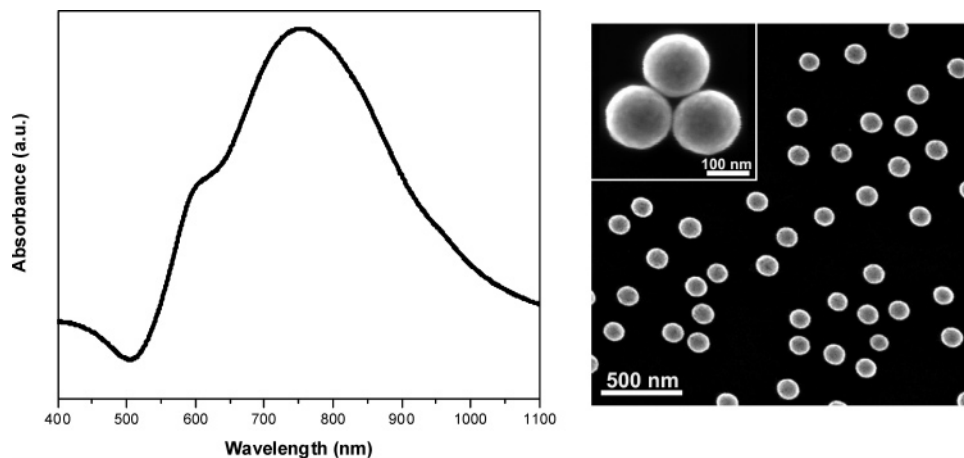
Figure 2. Left: Extinction spectra of $[r_1, r_2]$ = 60, 87 nm Au nanoshells where r_1, r_2 denote the inner and outer Au shell layer radii, respectively. The peak extinction wavelength corresponds to the nanoshell surface plasmon resonance. Right: SEM images of the $[r_1, r_2]$ = 60, 87 nm Au nanoshells at two different magnifications. The images reveal complete spherical shells (inset).
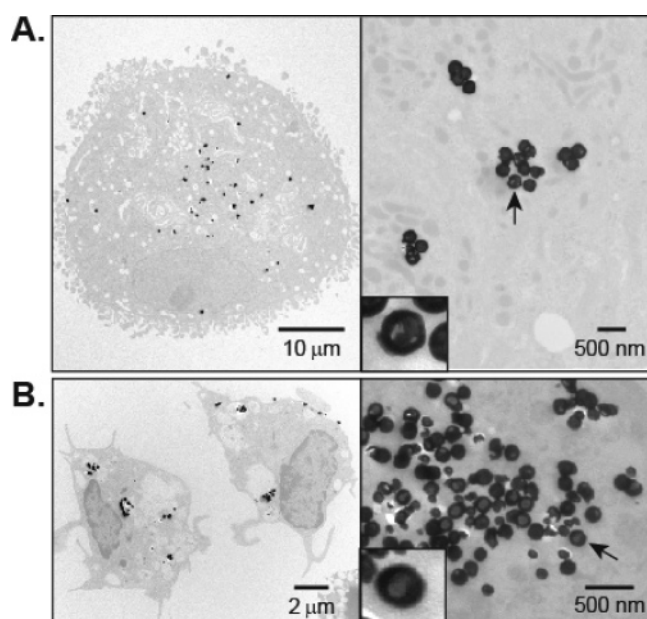

Figure 3. (A) Transmission electron micrograph of a nanoshell-laden macrophage. Au nanoshells are dispersed within vacuoles (left). Enlarged picture of aggregates of nanoshells in the macrophage in the right panel. The clear silica−core of the nanoshells surrounded with the black gold shells is shown in the inset (arrow). (B) Transmission electron micrograph of a nanoshell-laden monocytes.

bound to magnetic beads (MACS cell separation system, Miltenyi Biotec, Auburn, CA). Monocytes were differentiated into macrophages in vitro by culturing the isolated monocytes for 7 days in Teflon bags in the presence of recombinant human macrophage-colony stimulating factor (R & D Systems, Minneapolis, MN).[40] Macrophages or monocytes were incubated with Au nanoshells for 24 h. Figure 3 shows a transmission electron microscope (TEM) images of phagocytosed Au nanoshells in macrophages and monocytes. When the Au nanoshells are phagocytosed, they are taken up in vacuoles and dispersed in the cytoplasm. Uptake of Au nanoshells into monocytes and macrophages was observed to be equally effective. It can be observed in these images that the intracellular environment may modify and

somewhat reshape the morphology of the nanoparticle's shell layer. This reshaping has been observed in the context of several types of chemical treatments,[41,42] and can be minimized by suitable functionalization of the nanoparticles prior to use. It is important to note, however, that the defects observed in the nanoshells in these images would not be sufficient to destroy their resonant optical absorption properties.[36,37]

To determine the treatment parameters for producing optimal macrophage destruction in vitro, macrophages loaded with Au nanoshells and control macrophages (without nanoshells) were irradiated using varying power densities and irradiation durations. Twenty thousand macrophages in 200 μL of Macrophage-SFM (serum free medium) (Gibco, Invitrogen, Carlsbad, CA) per well in a 96-well plate were incubated with unfunctionalized Au nanoshells overnight. An identical number of macrophages were used as a control sample. One microliter of propidium iodide (PI, 1 mg/mL in phosphate-buffered saline), normally cell impermeant at this concentration, was added to each well of the microtiter plate to study the membrane damage caused by photoinduced ablation of the macrophages. Macrophage death was quantified using the Cytotoxicity Detection Kit (Roche Applied Science, Indianapolis, IN). This assay is a colorimetric assay which measures the amount of lactate dehydrogenase (LDH) released from the cytosol of damaged cells into the supernatant. The NIR irradiation source as well as the visualization system used in our study was a Bio-Rad Radiance 2100 MP Rainbow Confocal/Multiphoton System. The laser source produces pulses with widths of 100 fs at a repetition rate of 80 MHz, and in our experiments this pulsed laser excitation was used to investigate protocols and characteristics of Au-nanoshell-based photoinduced cell death in this very different ablation regime. The total power at the source was 1.54 W at 754 nm. The cells were scanned through a 4× microscope objective within a fixed 1028 μm × 1028 μm area. A single scan was performed in 1 s at 500 lines/s, in which the 1028 μm × 1028 μm area is divided into the 500 lines. The pixel dwell time was on the order of 2.6 μs over a pixel area of approximately 2 μm × 2 μm. Immediately after
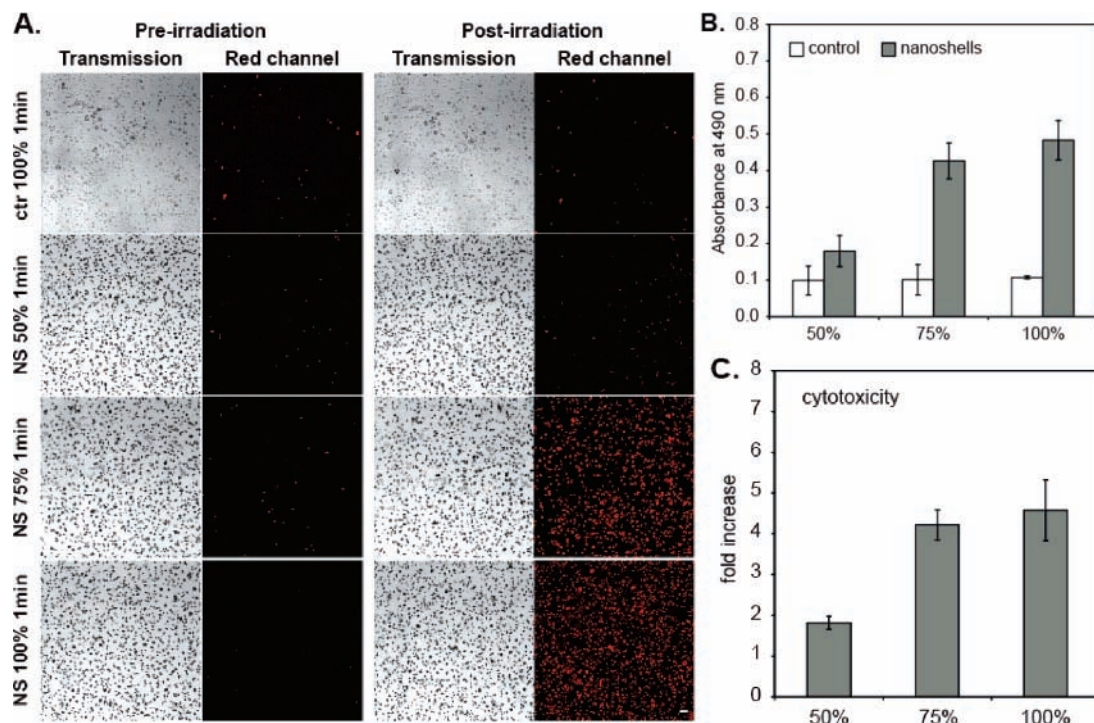
Figure 4. Effect of increasing power on the cytotoxicity of macrophages. Power was increased from 50% to 100% in increments of 25%. (A) Increasing PI uptake with increasing laser power: ctr, macrophages alone; NS, macrophages loaded with gold−silica nanoshells. Scale bar is 50 μm in A (bottom, right corner). (B and C) Determination of cytotoxicity after irradiation. Supernatant was removed from the irradiated wells, and the activity of the released LDH was measured.

irradiation, a transmission image and red channel image were acquired using the 10× objective of the confocal microscope, and the images were overlaid. Power at the source was varied in increments of 25%. All experiments were repeated in triplicate.

Upon the irradiation of the nanoshell-laden cells, a dose−response corresponding to increasing uptake of propidium iodide (Figure 4A) and release of LDH (Figure 4B,C) as a function of power is observed. Irradiation with 75% laser power showed a cytotoxic effect comparable to 100% laser power. Control macrophages without Au nanoshells showed no PI uptake as well as no increase in the release of LDH. A 75% laser power produced effective photothermal ablation of TAMs, and therefore, this power density was utilized in the subsequent duration experiments.

The macrophages were then irradiated at 75% power to determine the optimum duration of NIR irradiation for cell destruction. By visual inspection, the amount of PI uptake appears relatively similar at all time points (Figure 5). However, quantification of the PI signal (Supporting Information) reveals that PI uptake is greatest at 10 s of irradiation. This is confirmed by the observed LDH release: the extent of cytotoxicity is greatest at 10 s irradiation duration. However, given the error of the measurements, the cytotoxicities at 10 and 30 s are not significantly different. The cytotoxicity assay for the sample irradiated at 75% for 1 min showed almost the same increase (4×) of LDH release (Figure 4C). These results are as expected since, in the two-photon system used, the time of irradiation (*x*-axis in parts B and C of Figure 5) indicates the number of scans, where each scan is performed in 1 s. Thus for the 10 s case, 10

consecutive scans are performed and the time between irradiation of each 2.6 μm × 2.6 μm pixel would still be about 1 s. Performing additional scans at 1 Hz did not cause additional cell damage, indicating that at this scan rate, accumulated thermal effects are negligible and the photo-induced ablation resulting from the initial 10 scans is sufficient to cause lethal cell damage. It should also be noted that at any given time a region smaller than an individual cell is being illuminated (2.6 μm × 2.6 μm) and, hence, the mechanism of cell death may also include localized disruption of the cell membrane or local thermal ablation of vital intracellular compartments. Further experiments are warranted to examine the differences between femtosecond and CW Au-nanoshell-based photoinduced cell death in greater physiological detail and present an opportunity to understand the mechanism of cell death based on disruption of intracellular components, e.g., organelles.

The hypoxic tumor microenvironment can be modeled in vitro using tumor spheroids. These structures, composed of malignant breast epithelial cells, have a central necrotic area of cell debris surrounded by layers of hypoxic cells; the outer layer is comprised of normoxic cells (Supporting Information). Lewis and colleagues[43] have shown that macrophages infiltrate the spheroid and accumulate in the inner hypoxic rim around the central necrosis. Breast tumor spheroids were established by culturing human T47D cells on agarose for 20 days at 37 °C, 5% CO_2. The culture medium was replaced with fresh culture medium on alternate days. Five thousand macrophages and 8.3×10^8 gold−silica nanoshells were added to each well of a 96-well plate; each well contained a single spheroid. The spheroids, macrophages, and nanoshells
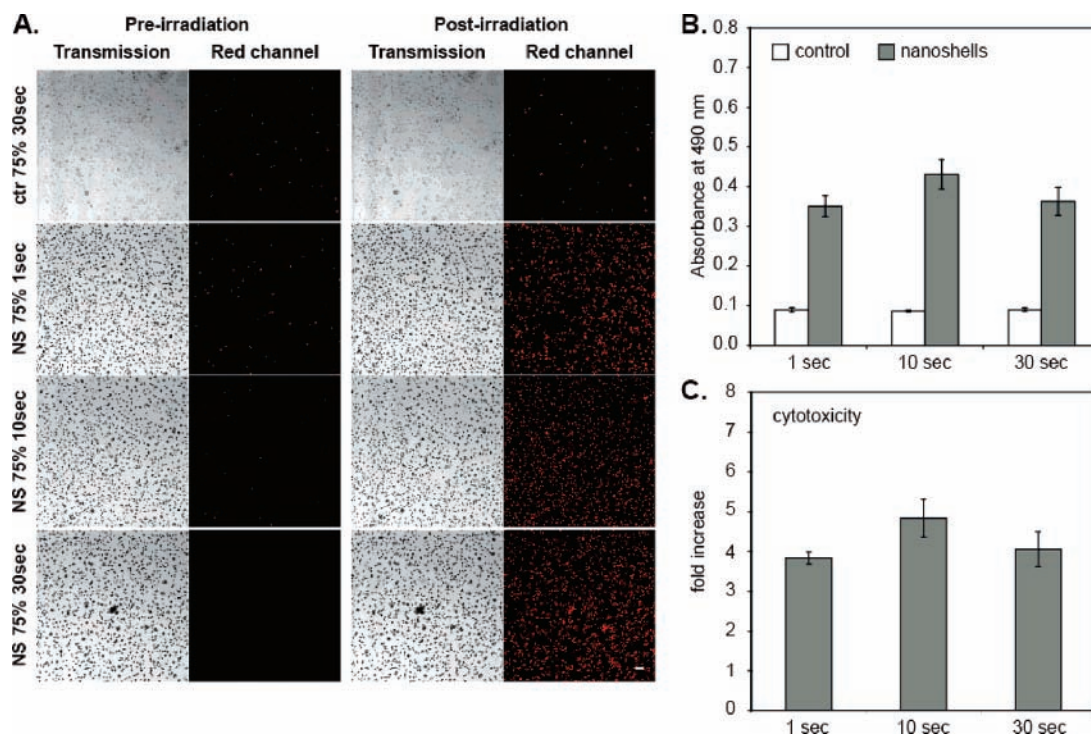
Figure 5. Effect of increasing irradiation duration on the cytotoxicity of macrophages. Macrophages loaded with gold–silica nanoshells were irradiated at 754 nm at 75% power for 1, 10, and 30 s, respectively. (A) PI uptake does not appear markedly different at the three time points. Scale bar is 50 μm in A (bottom, right corner). (B and C) The amount of LDH released increases between 1 and 10 s. Additional irradiation does not result in an increase in cytotoxicity (30 s). All experiments were repeated in triplicate.
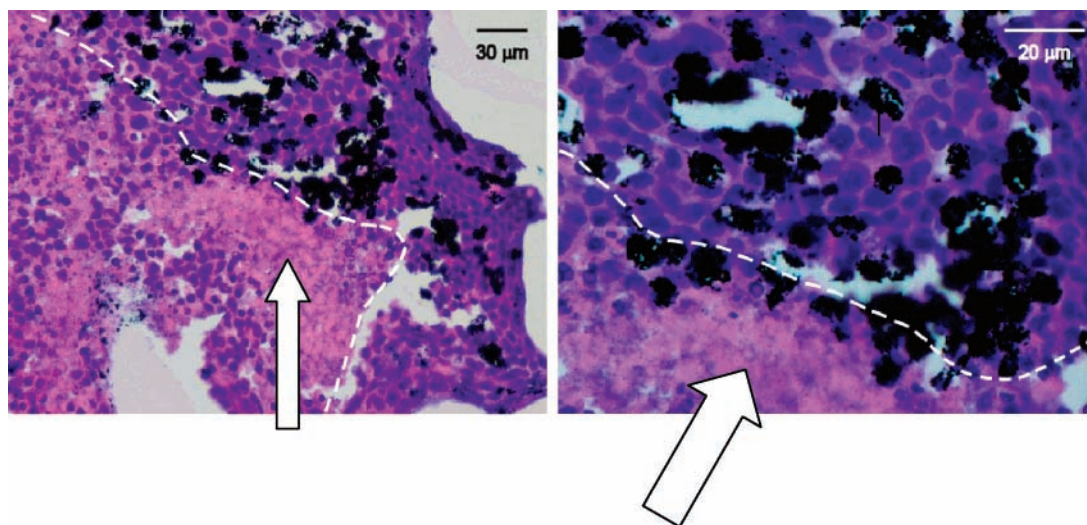
Figure 6. Photomicrograph of hematoxylin and eosin stained section of T47D tumor spheroid infiltrated with nanoshell-laden macrophages: left, 40×; right, 100×. Scale included in photomicrographs. The nanoshell-laden macrophages (black areas) have infiltrated the spheroid and reside within the viable tumor cells as well as near areas of necrosis (pink staining; white arrow). The dotted red line divides the central area of necrosis (white arrow) from the rim of viable cells which stain a dark purple due to the presence of nuclei.

were incubated for 3 days at 37 °C, 5% CO_2. Phagocytosis of the Au nanoshells as well as infiltration of macrophages into the tumor spheroid was monitored by transmission light microscopy and confirmed by H & E staining. The infiltrated macrophages accumulate within the hypoxic rim and around the central necrosis (Figure 6). The tumor spheroids had reached approximately 780 μm in diameter at the time of irradiation. The T47D breast tumor spheroids infiltrated with macrophages were irradiated through the 10× microscope objective of the Bio-Rad Radiance 2100 MP Rainbow Confocal/Multiphoton System at 100% power for 2 s (i.e., Two scans). Tumor spheroid infiltrated with macrophages without nanoshells were utilized as a control. A green fluorescent dye (CellTracker, Molecular Probes, Invitrogen, Carlsbad, CA) was added to each well plate to facilitate identification of cells. After irradiation, a transmission image and a green as well as a red channel image were acquired using the 10× objective of the confocal microscope, and the images were overlaid (Figure 7). Irradiation of a tumor spheroid infiltrated with nanoshell-laden macrophages re-
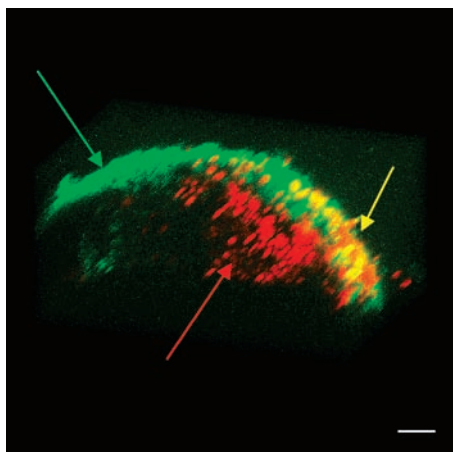
Figure 7. Frame from three-dimensional reconstruction of tumor spheroid. Perspective: looking out from necrotic center toward normoxic rim of cells. Viable cells (green fluorescence) form an outer shell around the central necrosis: green arrow, unirradiated T47D cells; red arrow, nanoshell-laden macrophages which have infiltrated into the area cell debris and necrosis in the center of the spheroid. Macrophages are propidium iodide positive following irradiation. Yellow cells/arrow: May represent T47D cells which have been thermally damaged due to their location next to macrophages. Cells to the left in the photo (green arrow) have not been irradiated, serving as an internal control. Scale bar is 50 μm.

sulted in death of cells within the irradiated area which are identified by propidium iodide fluorescence (Figure 7). There are no viable malignant epithelial cells in the center of the spheroid; this area is composed of cellular debris/necrotic cells. The area of red signal toward the center of the spheroid is from thermally damaged macrophages which were attracted into the center by signals released by the cellular debris.[44] Macrophages are also recruited to areas of hypoxia within the rim of viable malignant epithelial cells by a chemoattractant gradient established by the anoxic and hypoxic cells. This results in the intercalation of the macrophages among the epithelial cells as seen in Figure 6 and Supporting Information. Yellow-orange fluorescence in the outer layer of the spheroid as seen in Figure 7 may represent damaged/dead T47D tumor cells. The irradiation of the control spheroid with nonladen macrophages under the same conditions showed no increase in the number of dead cells. The extent to which femtosecond laser versus CW laser ablation may be more effective at destroying the extended hypoxic region based Trojan Horse delivery is the subject of future experiments.

In conclusion, we have reported the successful demonstration of several critical steps toward the ultimate goal of Trojan Horse nanoparticle delivery and therapeutics. The efficient phagocytosis of Au nanoshells by both monocytes and macrophages, photoinduced ablation of Au-nanoshell-laden monocytes/macrophages, tumor recruitment, and photoinduced cell death of macrophages in the hypoxic microenvironment of a human breast tumor spheroid have all been successfully demonstrated. It was observed that even though the irradiation source focuses the energy within subcellular volumes, cell death resulted for incident laser powers above a power threshold. This may indicate that nanoshell-based photoinduced ablation using femtosecond

NIR sources may be a consequence of local subcellular thermal ablation. Although the essential steps for Trojan Horse delivery have been demonstrated specifically for nanoshell-based therapy, this general approach might be useful for delivery of a large variety of therapies to the hypoxic regions in tumors. Such therapies may be either nanoparticle or molecule based, developed with the requirement that the cell's cargo remains noncytotoxic until the macrophages enter the tumors' hypoxic regions. Infrared-stimulated photothermal therapeutics using Au nanorods or carbon nanotubes, nanoparticle-based therapeutics triggered by application of external magnetic fields, or molecular therapies activated by the unique chemical microenvironment of the hypoxic region may all be ultimately suitable for this delivery mechanism.

Supporting Information Available: Description of analysis of cell membrane damage as a function of irradiation duration. Photomicrographs of hematoxylin and eosin stained sections of tumor spheroids at varying magnification. This material is available free of charge via the Internet at http://pubs.acs.org.

References

(1) Maeda, H.; Wu, J.; Sawa, T.; Matsumura, Y.; Hori, K. *J. Controlled Release* **2000**, *65*, 271−284.
(2) Loo, C.; Lowery, A.; Halas, N.; West, J.; Drezek, R. *Nano Lett.* **2005**, *5*, 709−711.
(3) Primeau, A. J.; Rendon, A.; Hedley, D.; Lilge, L.; Tannock, I. F. *Clin. Cancer Res.* **2005**, *11*, 8782−8788.
(4) Brown, J. M. *Cancer Res.* **1999**, *59*, 5863−5870.
(5) Cairns, R. A.; Khokha, R.; Hill, R. P. *Curr. Mol. Med.* **2003**, *3*, 659−671.
(6) Christofori, G. *Nature* **2006**, *441*, 444−450.
(7) Kelly, P. M.; Davison, R. S.; Bliss, E.; McGee, J. O. *Br. J. Cancer* **1988**, *57*, 174−177.
(8) Lewis, C. E.; Pollard, J. W. *Cancer Res.* **2006**, *66*, 605−612.
(9) Leek, R. D.; Landers, R. J.; Harris, A. L.; Lewis, C. E. *Br. J. Cancer* **1999**, *79*, 991−995.
(10) Tsutsui, S.; Yasuda, K.; Suzuki, K.; Tahara, K.; Higashi, H.; Era, S. *Oncol. Rep.* **2005**, *14*, 425−431.
(11) Lin, E. Y.; Nguyen, A. V.; Russell, R. G.; Pollard, J. W. *J. Exp. Med.* **2001**, *193*, 727−740.
(12) Hagemann, T.; Robinson, S. C.; Schulz, M.; Trümper, L.; Balkwill, F. R.; Binder, C. *Carcinogenesis* **2004**, *25*, 1543−1549.
(13) Hagemann, T.; Wilson, J.; Kulbe, H.; Li, N. F.; Leinster, D. A.; Charles, K.; Klemm, F.; Pukrop, T.; Binder, C.; Balkwill, F. R. *J. Immunol.* **2005**, *175*, 1197−1205.
(14) Goswami, S.; Sahai, E.; Wyckoff, J. B.; Cammer, M.; Cox, D.; Pixley, F. J.; Stanley, E. R.; Segall, J. E.; Condeelis, J. S. *Cancer Res.* **2005**, *65*, 5278−5283.
(15) O'Sullivan, C.; Lewis, C. E.; Harris, A. L.; McGee, J. O. *Lancet* **1993**, *342*, 148−149.
(16) Lewis, C.; Murdoch, C. *Am. J. Pathol.* **2005**, *167*, 627−635.

(17) van Netten, J. P.; George, E. J.; Ashmead, B. J.; Fletcher, C.; Thornton, I. G.; Coy, P. *Lancet* **1993**, *342*, 872−873.

(18) Sunderkotter, C.; Goebeler, M.; Schulze-Osthoff, K.; Bhardwaj, R.; Sorg, C. *Pharmacol. Ther.* **1991**, *51*, 195−216.

(19) Lewis, C. E.; Leek, R.; Harris, A.; McGee, J. O. *J. Leukocyte Biol.* **1995**, *57*, 747−751.

(20) Leek, R. D.; Lewis, C. E.; Whitehouse, R.; Greenall, M.; Clarke, J.; Harris, A. L. *Cancer Res.* **1996**, *56*, 4625−4629.

(21) Mantovani, A.; Sozzani, S.; Locati, M.; Allavena, P.; Sica, A. *Trends Immunol.* **2002**, *23*, 549−555.

(22) Hanada, T.; Nakagawa, M.; Emoto, A.; Nomura, T.; Nasu, N.; Nomura, Y. *Int. J. Urol.* **2000**, *7*, 263−269.

(23) Wyckoff, J.; Wang, W.; Lin, E. Y.; Wang, Y.; Pixley, F.; Stanley, E. R.; Graf, T.; Pollard, J. W.; Segall, J.; Condeelis, J. *Cancer Res.* **2004**, *64*, 7022−7029.

(24) Ohno, S.; Ohno, Y.; Suzuki, N.; Kamei, T.; Koike, K.; Inagawa, H.; Kohchi, C.; Soma, G.; Inoue, M. *Anticancer Res.* **2004**, *24*, 3335−3342.

(25) Oosterling, S. J.; van der Bij, G. J.; Meijer, G. A.; Tuk, C. W.; van Garderen, E.; van Rooijen, N.; Meijer, S.; van der Sijp, J. R.; Beelen, R. H.; van Egmond, M. *J. Pathol.* **2005**, *207*, 147−155.

(26) Zeineddine, N. S.; Avina, M. D.; Williams, C. C.; Wepsic, H. T.; Jadus, M. R. *Immunol. Lett.* **1999**, *70*, 63−68.

(27) Elgert, K. D.; Alleva, D. G.; Mullins, D. W. *J. Leukocyte Biol.* **1998**, *64*, 275−290.

(28) Wojtowicz-Praga, S. *J. Immunother.* **1997**, *20*, 165−177.

(29) Oldenburg, S. J.; Averitt, R. D.; Westcott, S. L.; Halas, N. *Chem. Phys. Lett.* **1998**, *288*, 243−247.

(30) Prodan, E.; Radloff, C.; Halas, N. J.; Nordlander, P. *Science* **2003**, *302*, 419−422.

(31) Prodan, E.; Nordlander, P. *Nano Lett.* **2003**, *3*, 543−547.

(32) Loo, C.; Lin, A.; Hirsch, L.; Lee, M. H.; Barton, J.; Halas, N.; West, J.; Drezek, R. *Technol. Cancer Res. Treat.* **2004**, *3*, 33−40.

(33) Hirsch, L. R.; Stafford, R. J.; Bankson, J. A.; Sershen, S. R.; Rivera, B.; Price, R. E.; Hazle, J. D.; Halas, N. J.; West, J. L. *Proc. Natl. Acad. Sci. U.S.A.* **2003**, *100*, 13549−13554.

(34) Prodan, E.; Lee, A.; Nordlander, P. *Chem. Phys. Lett.* **2002**, *360*, 325−332.

(35) Tam, F.; Moran, C.; Halas, N. *J. Phys. Chem. B* **2004**, *198*, 17290−17294.

(36) Oubre, C.; Nordlander, P. *J. Phys. Chem. B* **2004**, *108*, 17740−17747.

(37) Wang, H.; Fu, K.; Drezek, R.; Halas, N. *J. Appl. Phys. B* **2006**, *84*, 191−196.

(38) O'Neal, D. P.; Hirsch, L. R.; Halas, N. J.; Payne, J. D.; West, J. L. *Cancer Lett.* **2004**, *209*, 171−176.

(39) http://www6.amershambiosciences.com/applic/upp00738.nsf/vLook-upDoc/224505666−P516/$file/71716700AF.pdf.

(40) van der Meer, J. W.; van de Gevel, J. S.; Blussé van Oud Alblas, A.; Kramps, J. A.; van Zwet, T. L.; Leijh, P. C.; van Furth, R. *Immunology* **1982**, *47*, 617−625.

(41) Aguirre, C. M.; Kaspar, T. R.; Radloff, C.; Halas, N. J. *Nano Lett.* **2003**, *3*, 1707−1711.

(42) Wang, H.; Goodrich, G. P.; Tam, F.; Oubre, C.; Nordlander, P.; Halas, N. *J. Phys. Chem. B* **2005**, *109*, 11083−11087.

(43) Owen, M. R.; Byrne, H. M.; Lewis, C. E. *J. Theor. Biol.* **2004**, *226*, 377−391.

(44) Azenshtein, E.; Luboshits, G.; Shina, S.; Neumark, E.; Shahbazian, D.; Weil, M.; Wigler, N.; Keydar, I.; Ben-Baruch, A. *Cancer Res.* **2002**, *62*, 1093−1102.

(45) http://rsb.info.nih.gov/ij/.

NL072209H